Advances in Civil Engineering

Fiber Reinforced Concrete (FRC) with Applications in Civil Engineering 2020

Lead Guest Editor: Peng Zhang
Guest Editors: Grzegorz Ludwik Golewski, Soner Guler, and Yifeng Ling

Fiber Reinforced Concrete (FRC) with Applications in Civil Engineering 2020

Advances in Civil Engineering

Fiber Reinforced Concrete (FRC) with Applications in Civil Engineering 2020

Lead Guest Editor: Peng Zhang
Guest Editors: Grzegorz Ludwik Golewski, Soner Guler, and Yifeng Ling

Contents

Hindawi
Advances in Civil Engineering
Volume 2021, Article ID 8827124, 24 pages
https://doi.org/10.1155/2021/8827124

Review Article

A Critical Review on Effect of Nanomaterials on Workability and Mechanical Properties of High-Performance Concrete

Peng Zhang,[1] **Lei Wang**,[1] **Hua Wei**,[2] **and Juan Wang**[1]

[1]*School of Water Conservancy Engineering, Zhengzhou University, Zhengzhou 450001, China*
[2]*Henan Quality Testing Supervision Station of Basic Transportation Construction, Zhengzhou 450003, China*

Correspondence should be addressed to Juan Wang; wangjuan@zzu.edu.cn

Received 12 June 2020; Revised 18 February 2021; Accepted 25 February 2021; Published 8 March 2021

Academic Editor: Chao Wu

The application of nanomaterials in high-performance concrete (HPC) has been extensively studied worldwide due to their large surface areas, small particle sizes, filling effects, and macroquantum tunneling effects. The addition of nanomaterials in HPC has great contribution to enhancing the pore size of the cementitious matrix, improving the hydration of cement, and making the matrix much denser. In order to present an exhaustive insight into the feasibility of HPC reinforced with nanomaterials, the new development of HPC was summarized and the influence of different nanomaterials on the properties of HPC was reviewed based on more than 100 recent studies in this literature review. Workability, compressive strength, tensile strength, and flexural strength properties of HPC with nanomaterials were discussed in detail. In addition, nanomaterial-modified HPC was compared with the traditional concrete and obtained a lot of valuable results. The results in the present review indicate that the addition of various nanomaterials improves the mechanical properties of HPC, while reducing the workability of HPC. However, there is an optimal dosage of nanomaterial for improving the mechanical properties of HPC. Improving the properties of HPC by adding nanomaterials is expected to become a mainstream technique in the future. This literature review can provide comprehensive and systematic knowledge to researchers and engineers working on HPC and promote the application of this new HPC in modern civil engineering.

1. Introduction

Compared with masonry structure and wood structure, the development history of concrete structure is relatively short, but with the advantages of concrete materials such as high strength, high elastic modulus, good plasticity and workability, wide source of raw materials, convenient local materials, and convenient construction, concrete has been widely used in the world since the mid-19th century, and the development speed of concrete structure has also rapidly increased, making it an irreplaceable and widely used material in engineering construction for a long period of time. Concrete material has become one of the most widely used and most consumable building materials in the world. It has made important contributions to the development and progress of the human society [1]. Concrete starts from a low strength grade [2]. With the development of modern civil engineering projects toward high long-span bridges and large-scale water conservancy projects, the demand for concrete having strength, rigidity, durability, and crack resistance continues to increase. However, traditional concrete cannot meet these requirements. This issue led to the development of a new concrete technology, high-strength concrete (HSC), which can bear a load capacity of up to approximately 90 MPa [3]. Subsequently, high-performance concrete (HPC) and then ultrahigh-performance concrete (UHPC) were produced, and these can meet the strict structural design and durability requirements of modern construction projects. Compared with conventional concrete, HPC is the most comprehensive concrete at present because of its excellent performance in terms of workability, durability, strength, and volume stability. Moreover, it is receiving increasing attention in civil engineering construction and is expected to become the

development direction of concrete technology in the future [4–8]. HPC is composed of more cementing materials, well-graded aggregates, less water, and high-efficiency water-reducing agent to ensure excellent mechanical properties, durability, and stable working performance. Traditional materials and preparation methods of ordinary concrete are not available [9]. Adding admixtures such as fly ash (FA), silica fume, slag powder, metakaolin, and other volcanic ashes to concrete [10, 11] is an effective way to achieve high performance [12–14]. Mixing these mineral powder active materials into HPC can enhance various properties of concrete. Above all, it will replace some cement, which can realize the recycling of waste, reduce carbon dioxide emissions, and achieve environmental protection [15]. Compared with other pozzolans, silica fume has a high specific surface area and a fast pozzolanic reaction speed, which can effectively replace cement and improve concrete strength [16–20]. Fly ash is also a widely used mineral admixture. It mainly contains aluminate glass beads with smooth surfaces and small-size particle. The addition of FA to concrete can play the role of ball bearing, which will reduce the water demand of cement slurry, enhance the workability of fresh concrete, and increase the compactness of hardened concrete [21–24].

Nanomaterials, having been developed in the early 1980s, are a fairly new type of material. Nanomaterials refer to ultra-fine materials with particle sizes in the order of nanometers (1–100 nm). They include a variety of powder materials, such as metal, nonmetal, organic, inorganic, and biological materials [25], and are often located in the transition region between atomic clusters and macroscopic objects. Nanomaterials have small particles and large specific surface areas. When the particle size is as low as 10 nm, the proportion of the surface atoms is 20%, and the number of atoms distributed on the surface of the particles increases sharply with decreasing particle size. When the particle size is 1 nm, almost all atoms are concentrated on the surface of the particles, resulting in the surface effect, volume effect, filling effect, and other special properties of nanomaterials. Therefore, ultrafine powder has a host of unusual mechanical, electrical, magnetic, catalytic, and optical properties compared with traditional granular materials. As a new material, nanomaterials have shown remarkable application prospects in fine ceramics, microelectronics, bioengineering, light industry, and medicine. They are already one of the hotspots in scientific research due to their successful application and regarded as another industrial revolution of the century. Furthermore, they have cross-era significance [1]. The reason why ultrafine particles can be used well in concrete performance is mainly due to the continuous filler of cementitious material composition, as presented in Figure 1 [26]. Silica fume provides UHPC with better strength and durability because of its smaller granularity and high activity [17]. However, its output is low, and its price is high. Generally, silica fume is not considered when the concrete strength is lower than 80 MPa. With the increasing demand for HPC, nanotechnology has produced nanomaterials to replace silica fume. Nanomaterials are widely used in concrete owing to their special nanoeffects. The results show that the workability, mechanical properties, durability, and microstructure of concrete have been improved with the addition of nanoparticles [27]. Table 1 lists the comparison results for the performances of ordinary concrete, HPC, UHPC, and nanoconcrete. Several nanomaterials are used to reinforce ordinary concrete; examples of such materials include nano-SiO_2 (NS) [32], nano-$CaCO_3$ [33], nano-Al_2O_3 (NA) [34], nano-Fe_3O_4 (NF) [35], nano-TiO_2 (NT) [36], nano-ZnO_2 [37], nano-limestone [38], nano-FA [39], carbon nanotubes (CNTs) [40], and nano-metakaolin (NMK) [41]. Among many nanomaterials, NS has successfully replaced the traditional silica fume with its high pozzolanic activity, making it extensively applicable in HPC. One of the important reasons why NS can considerably improve the mechanical strength of concrete is that the calcium-silicate-hydrate (C-S-H) gel formed by the reaction of calcium hydroxide crystals distributed between the cement-based material matrix and aggregate can heighten the strength of the hardened cement stone matrix due to the high activity of NS [42]. In recent years, with extensive research being conducted on the performance of nano-modified concrete, several studies have found that nanomaterials are very effective as cementing materials in improving the properties of concrete. They can not only considerably reduce the amount of cement but also fill the gaps of materials, thus making a great contribution in enhancing the performance of traditional concrete. Accordingly, the main task of this paper is to summarize and review the latest progress of different nano particles in the research of normal concrete and HPC. The workability, compressive strength, and tensile strength of nanoparticles in HPC under single or mixed conditions are also discussed.

2. Workability

Workability is a comprehensive technical property used to ensure the construction operation of each process and obtain the stable performance of fresh concrete. Based on previous experimental research, a slump height of approximately 650 mm is acceptable for fresh concrete and is a sign of sufficient strength for high-quality concrete. In fact, within a certain range, the larger the slump, the better the workability, which indicates that concrete can easily flow without segregation [43, 44]. Moreover, the strength of concrete is related to workability. To ensure maximum strength of fresh concrete, the concrete should have sufficient workability, owing to its self-compacting capability. Therefore, controlling the workability of concrete is meaningful. Slump and slump flow are important parameters for evaluating high-performance concrete.

2.1. Influence of NS on the Workability of HPC. A slump is regarded as a suitable indicator of the fluidity of fresh concrete. A lot of studies have shown that NS has an effect on the slump of concrete [45]. Aydın et al. [46] observed the effect of changes in NS and FA on the slump flow of fresh concrete at optimal replacement rates of 2% and 40%, respectively. Their investigation revealed that NS considerably

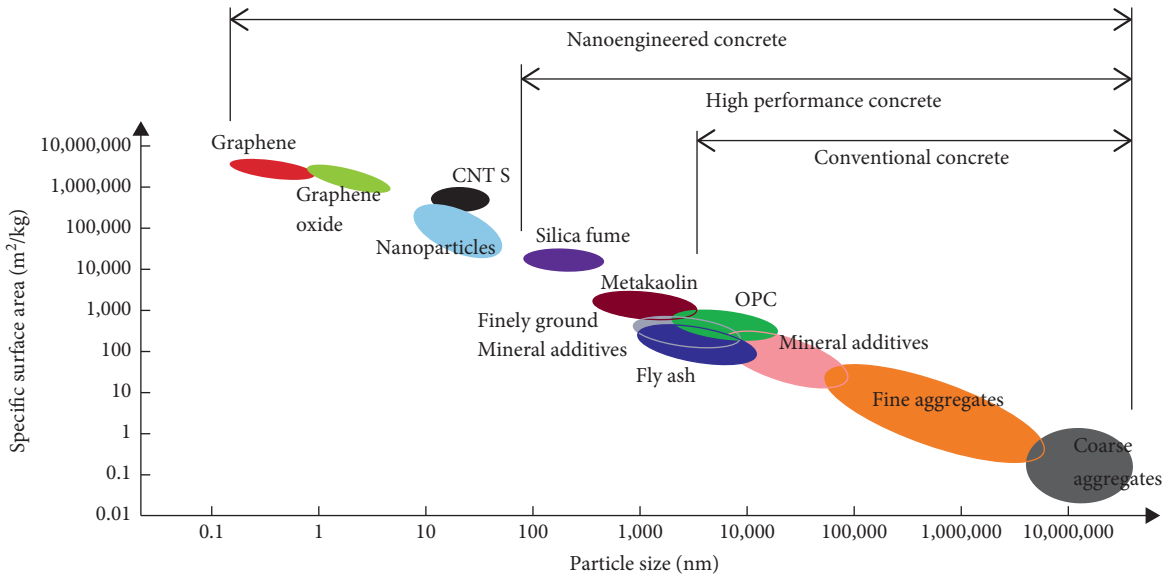

Figure 1: Relationship between the particle size and specific surface area of concrete materials [26].

Table 1: Summary of the performance of diverse kinds of concrete based on previous studies.

	Compressive strength (MPa)	Flexural strength (MPa)	Water absorption (%)	Reference
Ordinary concrete	10–40	1–10	<30	Mehta and Monteiro [28]
HPC	40–100	11–20	12–25	Hamid et al. [29]
UHPC	100	20–30	<12	Hartmann and B. Graybeal [30]
Nanoconcrete	70	12–20	<12	Aïtcin [31]

improved the performance of fresh concrete and eliminated the segregation of 40% FA when mixing [46]. Hani et al. [47] stated the influence of self-compacting concrete with four contents of NS on a slump under different water-binder ratios. In this investigation, the water-binder ratios of the three series are 0.41, 0.45, and 0.5. In addition, 0%, 0.25%, 0.5%, and 0.75% of cement are planned to be substituted by NS in each series. The most important finding from this study is that the fluidity of all NS mixtures is reduced. Moreover, the addition of 0.75% NS has the greatest influence on the slump of the three water-cement ratios, reducing by 15.2%, 15.5%, and 14.1%, respectively [47]. As shown in Figure 2, NS reduces the slump loss and slump flow loss of concrete mixtures with different water-binder ratios, and these losses increase with the increase in nanoparticle content. This conclusion was supported by Naji Givi et al. [48], who found that low workability may be associated with an increase in the surface area of the mixture upon addition of nanomaterials, which necessitates more cement slurry to wrap the NS. Furthermore, to confirm these results, they obtained through a slump test that the content of NS has a distinct impact on the flowability of fresh concrete. Compared with the control group, the slump of all mixtures containing NS is reduced under a water-binder ratio of 0.4. Moreover, according to ASTM C143 (2015), slump loss is usually used to evaluate the influence of NS on the workability of concrete.

Supit and Shaikh [49] found that adding 2%–4% NS to concrete can observably reduce slump loss, which reaches 60%. Meanwhile, Bahadori and Hosseini [50] observed that the slump loss of concrete containing NS is severe when the ratio of super-plasticizer to cementitious material is unchanged. Zhang et al. [51] also revealed that the slump and slump flow of 15% FA concrete decreased after adding NS. We can observe the influence trend of NS content on the slump and slump flow in Figure 3. In addition, to evaluate the flowability of fresh concrete, Jalal et al. [52] and Güneyisi et al. [53] tested the time and slump diameter of a slump flow test and V-funnel flow test, respectively. They concluded that the fluidity of self-compacting HPC declined after adding NS particles. Nevertheless, the particle size of NS is a contributing factor on the rheological and fresh properties of concrete. Durgun and Atahan [54] studied the influence of colloidal NS (CNS) on the flow performance and rheological parameters of concrete. Self-compacting concrete was modified using CNS with different average particle sizes of 35, 17, and 5 nm. Experiments show that adding CNS increases the T_{500} time, however, reducing the content of FA decreases the T_{500} time. These factors show opposite results for the slump flow diameter. When the content of CNS with a particle size of 35 nm exceeds 1.5%, the slump flow time at 500 mm is considerably higher than that of the control group. Senff et al. [55] demonstrated that adding NS can cause a severe slump loss in concrete, which can be attributed to the content of nanoparticles. The main reason for this result is that nano-ultrafine particles contributing to the increasing specific surface area will absorb part of the mixed water. Finally, some scholars pointed out that to avoid a

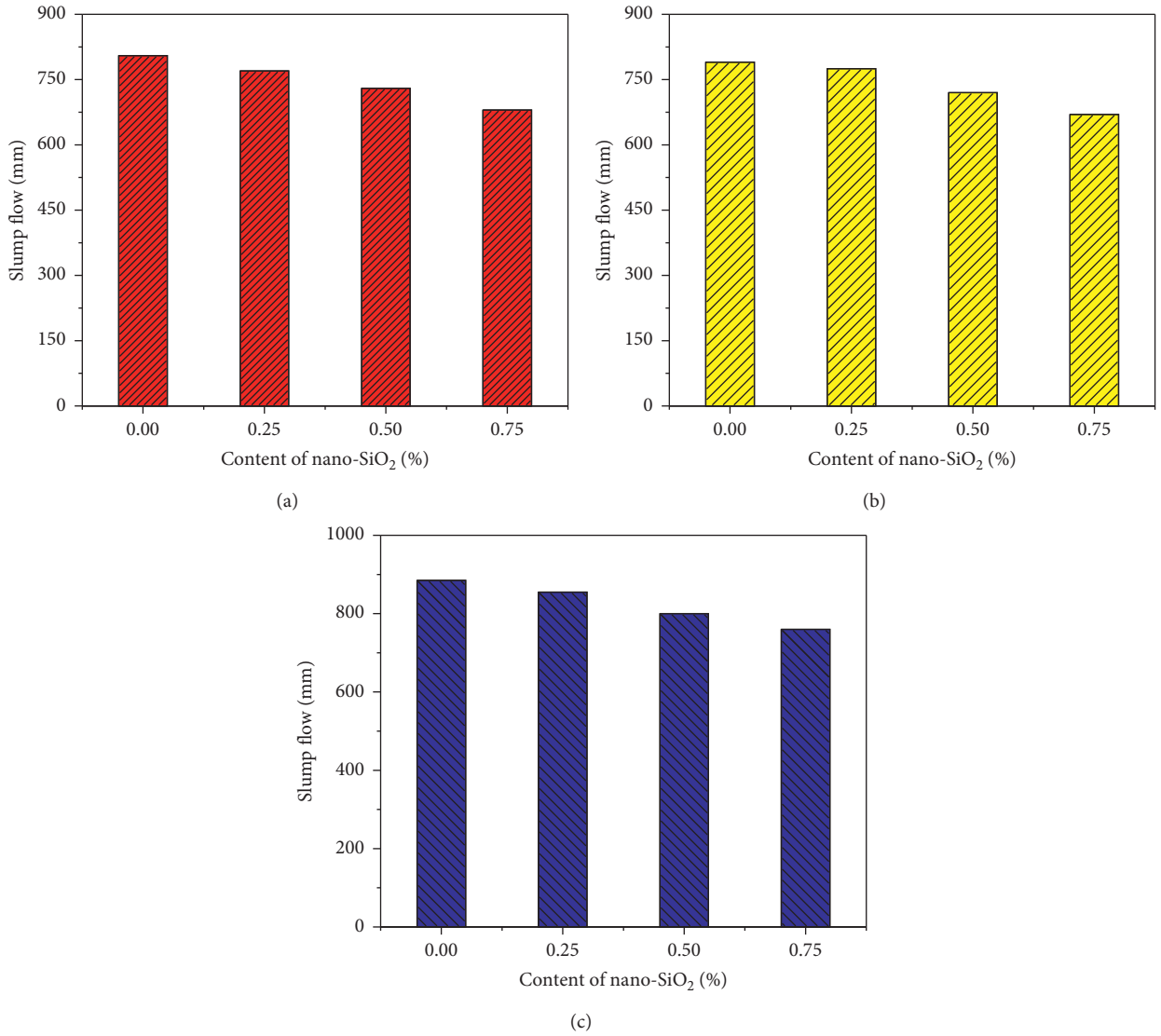

Figure 2: Relationship between the slump flow and w/b [47]. (a) w/b = 0.45; (b) w/b = 0.41; (c) w/b = 0.5.

certain degree aggregation of nanoparticles in the dispersion process, the content of NS should be as small as possible (1%–5%) [56, 57].

2.2. Effect of Nano-$CaCO_3$ on the Workability of HPC. Nano-$CaCO_3$ is a type of nanomaterial with a certain activity, and its cost is only one tenth of that of nanosilicon. As a result, researchers have been interested in applying it to concrete materials. A large number of researchers have demonstrated that the specific surface area of a cement slurry will be sharply increased due to the incorporation of small-sized nano-$CaCO_3$ particles, which will increase the water demand of the cement slurry. Meng et al. [58] found an association between the water demand of nano-$CaCO_3$ and cement slurry. They identified that the water demand increases with the increase in the nano-$CaCO_3$ content. Specifically, when the content of nano-$CaCO_3$ is 2%, 5%, and 8%, the water demand will rise by 0.4%, 1.8%, and 3.2%, respectively. However, this effect is suppressed when using a nano-$CaCO_3$ intermediate slurry. When the content of nano-$CaCO_3$ is 2% and 5%, the water demand will only decrease by 0.3%. By contrast, when the dosage is 8%, the water demand is essentially the same as the reference water supply. The main reason for this change is that the nano-$CaCO_3$ intermediate slurry is easier to evenly disperse and can markedly improve the particle size distribution.

The application of nano-$CaCO_3$ to cement can not only promote the hydration of cement but also cut down the setting time. Wei [59] found that the increase in nano-$CaCO_3$ content will shorten the initial setting and final setting time of the cement paste. When the content increased from 0.44% to 4.88%, the initial setting time increased from 35 min to 81 min and the final setting time increased from 23 min to 71 min. This effect also occurs for concrete, and a study [60] on UHPC has similar results. Their investigation revealed that 5% nano-$CaCO_3$ will make UHPC achieve the best workability. Liu [61] explored the workability of steel

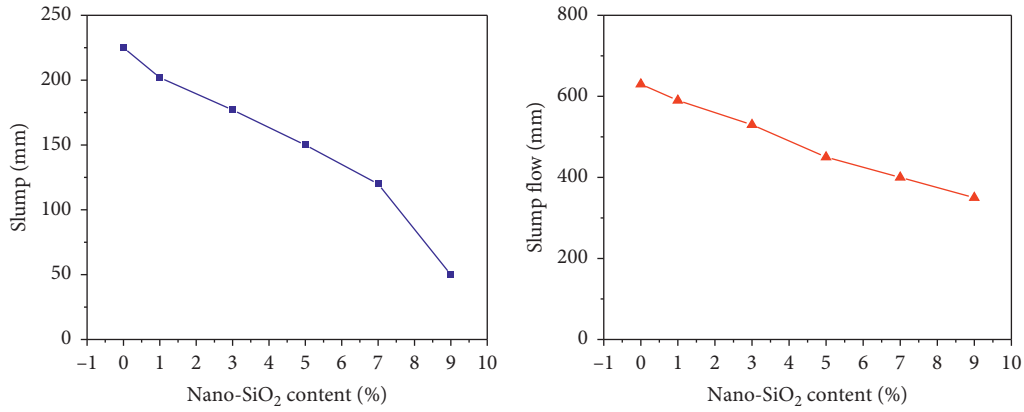

Figure 3: Effect of NS content on the (a) slump and (b) slump flow [51].

fiber-reinforced concrete with different amounts of nano-$CaCO_3$. It was found that the workability of concrete improved considerably after the addition of nano-$CaCO_3$. These data are presented in Figure 4. Clearly, when the content of nano-$CaCO_3$ varies from 0% to 0.5%, the slump grows slightly. When the added amount of NC increases, the slump increases sharply, and a maximum value of 184 mm is obtained when 1.5% NC is added. However, with the continuous increase in the nano-$CaCO_3$ content, the slump begins to decline steadily. A number of studies have demonstrated that for ordinary concrete, the optimal content of nano-$CaCO_3$ is 1.5%, which may be due to the addition of steel fiber that increases the porosity of concrete compared with ordinary concrete, and thus, the optimal content is also increased. This increased content is used to fill the pores in the concrete. However, when the content of nano-$CaCO_3$ exceeds 2.0%, more free water will be increased and absorbed by the surface area of the mixture, thus causing the slump of concrete to slowly drop. Contrarily, Shaikh and Supit [62] performed experiments to examine the influence of nano-$CaCO_3$ content on the workability of an ordinary cement mortar, high-volume fly ash (HVFA) mortar, and concrete. Figure 5 shows that as the proportion of cement replaced by nano-$CaCO_3$ increases, the workability of the mortar or concrete will decrease.

Shaikh and Supit [33] explored the effect of the content of nano-$CaCO_3$ on the workability of cement mortar and HVFA mortar, through a flow meter test, in accordance with ASTM C1437 (2012). Compared with the control group, the workability of mortar containing nano-$CaCO_3$ is lower. As the content of nano-$CaCO_3$ used to replace cement increases, the fluidity decreases. Similar to the control mortar, the workability of the HVFA mortar is reduced upon adding 1% nano-$CaCO_3$. The decrease in the workability of mortar or concrete is caused by the high-specific surface area of nano-$CaCO_3$. However, research by Xu et al. [63] revealed that the application of nano-$CaCO_3$ in concrete improves the workability of fresh concrete. The slump will gradually rise with the increase in nano-$CaCO_3$ content. Compared with the concrete without nano-$CaCO_3$, the slump of the concrete with 2% nano-$CaCO_3$ is increased by 8.5%. Nano-$CaCO_3$ can be well dispersed in concrete, which

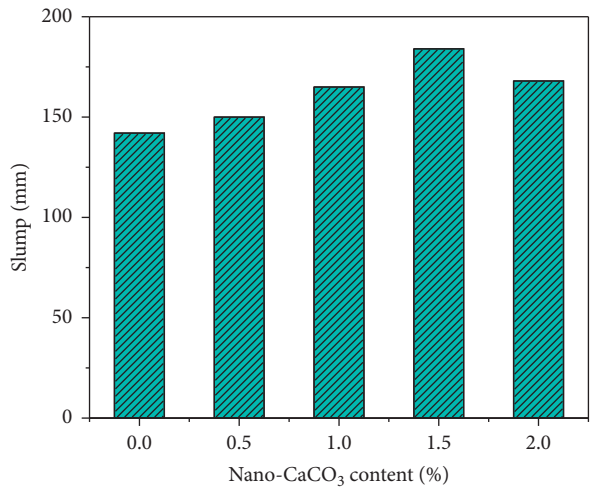

Figure 4: Relationship between the slump and NC content [61].

plays a key role in effectively improving the grading of fine particles, reducing accumulation voids, and strengthening the effect of microaggregates, thus improving its water-reducing effect and enhancing the workability of concrete under the same water-binder ratio. Li et al. [38] explored the fluidity curve of a UHPC matrix with different NS and NC contents. Compared with the control mixture, all UHPC substrates containing NS or NC showed lower fluidity. In the mixture containing 1.0% NS and 3.0% NC, the fluidity decreased by 20% and 34%, respectively. Similarly, at a constant NC substitution rate, the fluidity of the UHPC matrix decreases with the increase in NS content. For example, when the content of NS varies from 0.5% to 1.5%, the fluidity of the mixture containing 3.0% NC is reduced by 23% and 35%, respectively. Therefore, the greater the amount of cement replacement, the lower the fluidity.

2.3. Effect of CNT on the Workability of HPC. CNT is an allotrope of carbon with a cylindrical nanostructure. Nanotubes are members of the fullerene structural family. It also determines the performance of nanotubes [40]. Wang

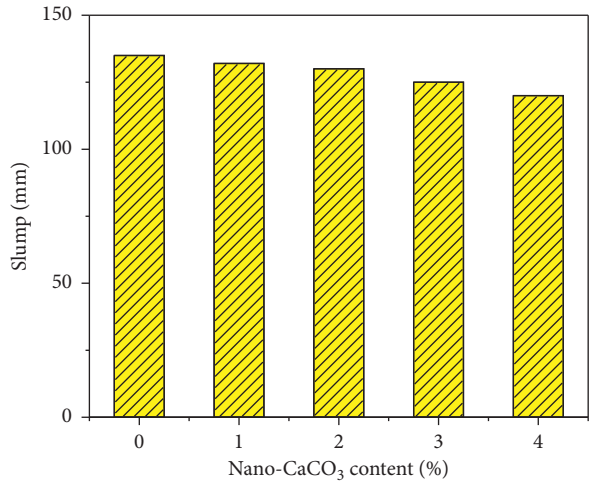

Figure 5: Relationship between the slump and NC content [62].

et al. [64] examined the influence of CNT on the workability of concrete through experiments. Figure 6 shows that, when concrete is not mixed with CNT, the slump of the mixture can reach 150 mm. The slump of the concrete mixture gradually decreases, and its fluidity becomes worse, with the increase in CNT contents. When a suitable amount of water-reducing agent (<1.0%) is added to the concrete mixtures with different CNT contents, the slump of the mixture reaches 150–160 mm, meeting the construction requirements. Moreover, CNT has a considerable impact on the adhesion of concrete. In Sun et al.'s study [65], to observe the effect of changes in multiwalled carbon nanotubes (MWCNTs) on the workability of 3D printing polyvinyl alcohol mortar ink, MWCNTs with different volume contents were applied to 3D printing polyvinyl alcohol fiber-reinforced mortar ink. It was found that, compared with the control mixture, the flow value of the new 3D printing mortar modified with MWCNTs can be reduced by a maximum of 3.7%. The addition of MWCNTs will not considerably affect the fluidity of 3D printing mortar, which was also recognized by Sun et al. [66]. Several studies have examined the dispersion of CNTs in polymer composites; however, few studies have investigated the dispersion of CNTs in ordinary Portland cement (OPC) paste. In Figure 7, the slump values of CNT-modified slurry with water-cement ratios of 0.4, 0.5, and 0.6 and a control group (mixed with 0% CNT) are compared. From the figure, we can see that the slump of the control group increases with the increase in water-cement ratio. Moreover, in each mix proportion, the slump is reduced when CNTs are added in small amounts (0.5%, 1%, and 2%) [67].

2.4. Effect of Titanium Oxide on the Workability of HPC. Titanium oxide, usually known as titanium dioxide (TiO_2), is a natural oxide of titanium. Adding TiO_2 to concrete will change its performance. Joshaghani et al. [68] obtained the dosage of high-range water-reducing admixture (HRWRA) required for each mixture to achieve a slump of 650 ± 25 mm. The solidification delay caused by a high HRWRA dosage is the main

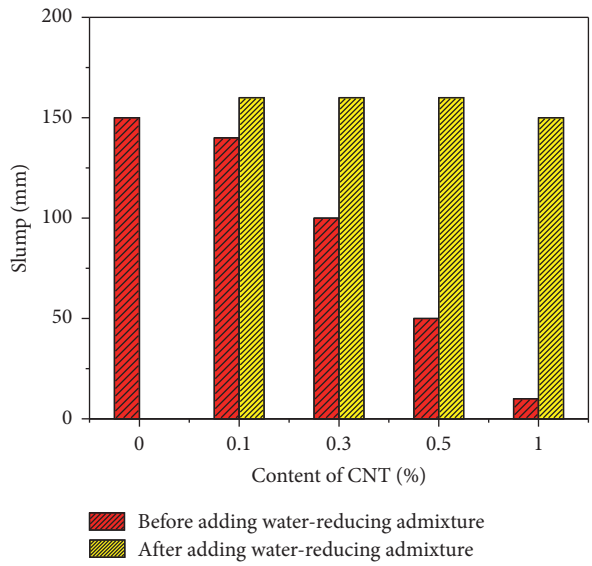

Figure 6: Slump of fresh concrete with different amounts of CNTs [64].

reason for the surface subsidence of self-compacting concrete. They observed that the addition of 5% TiO_2 resulted in a high demand for HRWRA under different water-binder ratios. Moreover, adding 5% of nano-Fe_2O_3 and nano-Al_2O_3 into concrete resulted in a high demand for HRWRA. The water demand of the mixture was increased because the high surface area of the nanoparticles led to more water being absorbed on their surfaces. The data from Figure 8 show the relationship between the content of nano-TiO_2 and the slump of the mixture when the water-binder ratio is 0.40. They concluded that compared with the mixture without nano-TiO_2, all the mixtures modified with nano-TiO_2 revealed lower slump in a small dosage range [69].

2.5. Effect of Nano-Kaolin on the Workability of HPC. NMK is a derivative of industrial mineral kaolin. Kaolin ($Al_2Si_2O_5(OH)_4$) is a layered silicate composed of tetrahedral

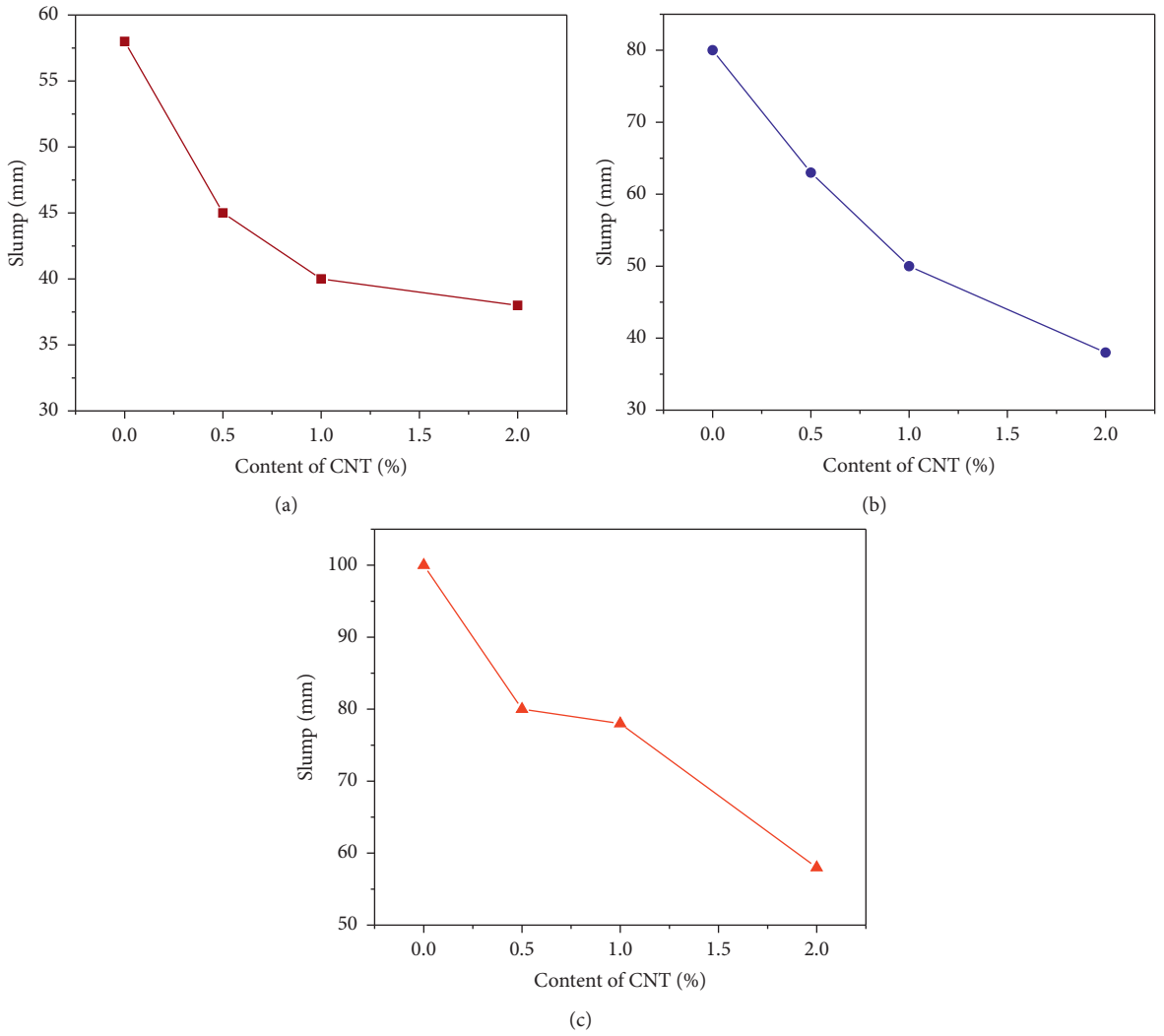

Figure 7: Effect of CNT dosage and water/cement on the measured minislump [67]: (a) w/b = 0.4, (b) w/b = 0.5, and (c) w/b = 0.6.

and octahedral coordinated SiO_2 and Al_2O_3. Its main components are hydrated aluminum disilicate, Shi Ying, muscovite, and rutile. NMK is a kind of supplementary material that can be used in concrete to improve its properties. It is based on metakaolin which can considerably modify the performance of various kinds of concrete. The addition of NMK and metakaolin will reduce the workability of UHPC, as presented in Figure 9 [41]. The data reveal that the slump decrease is indeed due to the addition of NMK. Compared with OPC and MK10, the slump decreases with an increase in the NMK content. A number of published papers have reported that the decrease in workability caused by NMK is caused by two factors: namely, high chemical activity and high specific surface area, which can increase the water demand for a hydration reaction. In similar tests, when the NMK content is increased from 0% to 6%, the fluidity of cement mortar decreases by 5.61%–12.47% compared with reference [70]. In addition, the slump of concrete containing 9% NMK decreased by approximately 15.7% [41]. This conclusion was also recognized by Senff et al. [55]. Therefore, controlling the NMK content is beneficial to obtain the concrete mixture with appropriate workability.

2.6. Effect of NA on the Workability of HPC. Al_2O_3 is not only the main product in cement hydration but also controls the setting time of cement. NA is actually alumina, and the application of NA to concrete has rarely been studied. Adding NA can better modify some properties of concrete as it can control the setting time of cement. In UHPC, NA is used as a dispersant in cement particles. In addition, because the size of NA is nanoform, NA as a nanofiller can also refine the voids in hydrated gel. Because of the high content of cement in UHPC, the dispersion of cement particles in UHPC must simultaneously occur with the action of silica in the hydration process. However, silica, which is usually used to modify concrete, cannot penetrate the hydration gel; this slows the hydration reaction. However, the addition of NA can accelerate cement hydration by refining cement hydration products. Therefore, adding NA can improve the microstructure of hydrated gel. A research by Gowda et al.

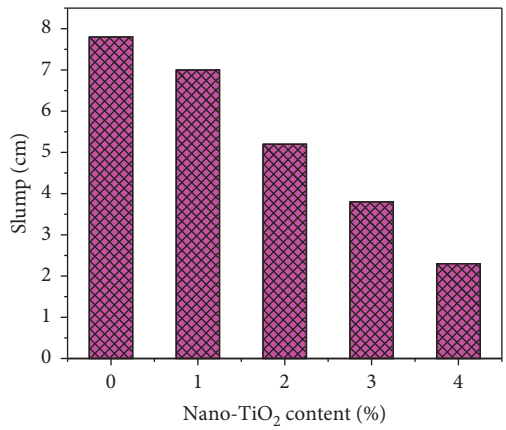

Figure 8: Effects of TiO_2 nanoparticles on the workability of concrete [69].

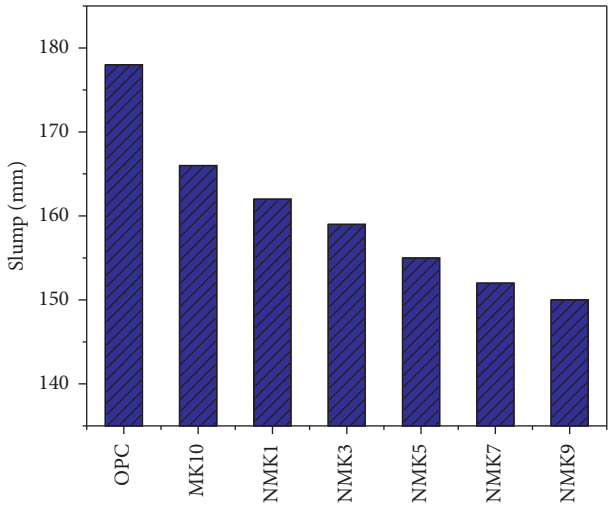

Figure 9: Effect of NMK content on the slump of UHPC [41].

[71] stated that adding NA into concrete reduces workability. The workability of the mortar mixture decreases with the increase in NA replacement amount. When the doping amount reaches 5%, the workability considerably decreases. The reason is that the large surface area of NA particles leads to an increased demand for water. The results are shown in Figure 10.

3. Mechanical Properties

3.1. Influence of Nano-SiO_2 on the Mechanical Properties of Concrete. Adding various nanomaterials to modify the concrete matrix to obtain concrete with excellent mechanical properties is one of the most promising research fields of nanomaterials in concrete application. Several experiments have been performed to examine the mechanical properties, including compressive strength, elastic tensile strength, and flexural strength, of nanoconcrete. NS is a kind of nanomaterial often used to modify HPC. It can be used as a substitute for cement and provides a ball bearing function in cement particles. In addition, NS is used as a superfiller in concrete owing to its particle size, which makes the concrete structure denser and helps improve the performance of concrete.

3.1.1. Compressive Strength. Several studies have identified that the compressive strength of concrete modified by NS is indeed considerably enhanced. The 28-day compressive strengths of the mixtures modified with NS are shown in Table 2. Many experiments have revealed that the compressive strength of cementitious materials can be improved by adding NS within a certain range of dosage. The optimum doping amount has also been considered. The strength will decrease if it exceeds the optimal dosage mainly because a large amount of NS will aggregate and cannot be well dispersed in the mixture [47, 74, 76, 77]. Amin and Abu el-Hassan [81] investigated the influence of the content of NS between 0% and 1.8% and basalt fiber with different contents on the compressive strength and tensile strength. Further research revealed that a large number of C-S-H gels and alumina, ferric oxide, and trisulfate crystals will be produced when the content of NS increases. When the optimal dosage is 1.2%, the amount of the C-S-H gel is the largest, which makes the concrete denser. These results are consistent with those observed in the compressive strength test. The study of Li et al. [38] indicated that 2% is the best dosage to improve concrete performance. Sadrmomtazi et al. [83] found that the optimal content of NS is between 5% and 7%. Compared with the control mixture, the compressive strength will be improved even if the optimum content is exceeded. However, the maximum strength still occurs at the optimum content. An experiment [72] also revealed that a mortar mixed with NS after curing for 7 and 28 days has advantages over a mortar mixed with silica fume in terms of improving strength. In this study, cement was replaced by NS with contents of 5%, 10%, and 15%. The influence of the partial replacement of cement by NS on the compressive strength of HVFA mortar and concrete was also explored [73]. The compressive strength of the mortar was analyzed after curing for 7 and 28 days, and that of concrete was analyzed after curing for 3, 7, 28, 56, and 90 days. The results show that in the range of 1%–6%, the compressive strength of cement mortar in 7 and 28 days reaches the maximum when the content of NS is 2%. Moreover, the compressive strength of the mortar mixed with 40% and 50% FA increases by 5% and 7%, respectively, after 7 days of curing with the addition of 2% slag micropowder. However, when the content of FA in the ordinary mortar exceeds 50%, no evident improvement is observed. By contrast, the 28-day compressive strength of all HVFA mortars is improved by adding 2% NS, and the most significant improvement occurred in mortars with FA contents over 50%. In HVFA concrete, the compressive strength at the early stage (3 days) is also improved owing to the addition of 2% NS. The results are presented in Figures 11 and 12.

3.1.2. Tensile Strength and Flexural Strength. The tensile strength of concrete is low, generally 1/10–1/20 of the compressive strength. Amin and Abu el-Hassan [81] found that an HSC composed of 1.2% NS and 3 kg/m^3 basalt fiber

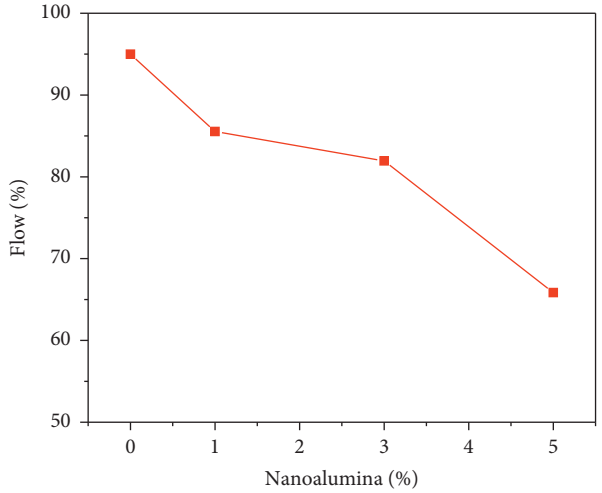

Figure 10: Percentage of flow [71].

Table 2: Compressive strengths of cementitious materials with NS at 28 days.

Cementitious materials	w/b ratio	Content of NS	Optimum content	Compressive strength increment	Reference
Cement Mortar	0.3–0.5	5%–15%	10%	—	[72]
HVFA cement paste	0.4	1%–6%	2%	5%	[73]
Lightweight aggregate concrete	0.35	1%–3%	3%	3.2%–16.8%	[74]
		0%–7%	5%		[75]
	0.4	2% NS + 0.08% CNT + 40% FA	2%	20%	[46]
SCC	0.5	0%–0.75%	0.75%	26.9%–48.8%	[47]
	0.4	0.5%–2%	2% + 15 mm	—	[76, 77]
			1.5% + 80 mm	—	
	0.5	Basalt fiber + NS	6%	10.4%–19.6%	[78]
	0.5	0%–6%	6%	12.45%	[79]
Ordinary concrete	0.3	5% MS + 1% NS	1%	—	[80]
	0.2	1%–4%	3%	10%	[81]
	0.48	0%–1.8%	1.2%	9.04%	[81]
	0.34	3%–5%	3%	—	[82]
HPC	0.16	0.5%–1.5%	1%	3%	[38]
	0.35	0.75%–1.5%	1.5%	12%	[32]

can achieve the best splitting tensile strength. They revealed that the tensile strength can be increased by 17.42% compared with a control mixture concrete (see Figure 13). Jalal et al. [84] pointed out that the splitting tensile strength of self-compacting concrete can be increased by 25.6%, 30.7%, and 35.9% after curing for 90 days with 10% FA and 2% NS in different cementitious material contents. Fallah and Nematzadeh [85] explored the mechanical strength of HPC mixed with polymer fiber and NS. Tests show that after replacing cement with 1%, 2%, and 3% NS, the tensile strength of cement increased by 12.96%, 7.82%, and 16.10%, respectively. This increase in strength is mainly due to the increased bonding force between the cement base and aggregate. Mohamed's research [86] shows that adding 0.75% NS and 3% nanoclay (NC) to concrete can increase the flexural strength by 4% and 9%, respectively, after curing for 90 days. They also pointed out that adding 3% nanoparticles consisting of 25% NS and 75% NC has great advantages in improving mechanical properties. Amin and Abu el-Hassan [81] also revealed that, compared with a control group, the flexural strength of concrete after adding NS and $NiFe_2O_4$ nanoparticles is increased by approximately 23%.

3.2. Influence of Nano-$CaCO_3$ on the Mechanical Properties of Concrete. According to several studies worldwide, nano-$CaCO_3$ modified cement-based materials generally have three functions, namely, the chemical, nucleation, and filling functions. Among them, nano-$CaCO_3$ effects on the hydration process of cement are mainly chemical and nucleation. Detwiler and Tennis provided that calcium carbonate powder particles act as nucleation sites in the process of cement hydration, which increases the precipitation probability of the hydration product C-S-H gel on limestone powder particles and accelerates the hydration of C_3S. Many hydrated calcium aluminate particles grow on the surfaces of

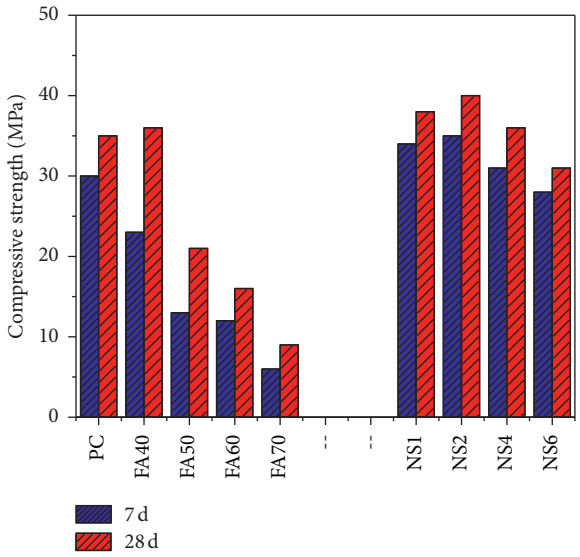

Figure 11: Compressive strength of mortars containing NS and FA [73].

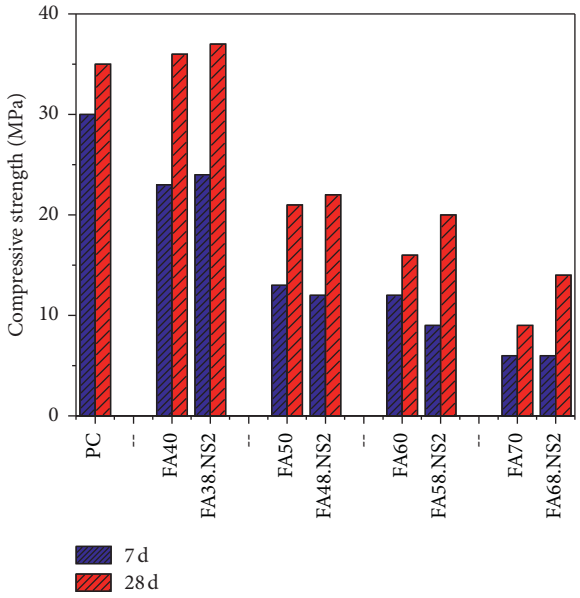

Figure 12: Effects of 2% NS on the compressive strength of mortars containing HVFA [73].

major products, such as C-S-H and $Ca(OH)_2$. Calcium aluminate ($CaO.3Al_2O_3.CaCO_3.11H_2O$) is produced by the hydration reaction between nano-$CaCO_3$ and C_3A, and it can improve the early strength of cement-based materials.

The compressive strength of the cementing material modified by a proper amount of nano-$CaCO_3$ is enhanced, and adding nano-$CaCO_3$ can exert the combined microaggregate, pinning, and crystal nucleus effects, so as to make the particle gradation more perfect, fill each other, reduce the void ratio, increase the bulk density, and contribute in the enhancement of the flexural and compressive strength. However, this characteristic is related to the content of nano-$CaCO_3$, and an optimal

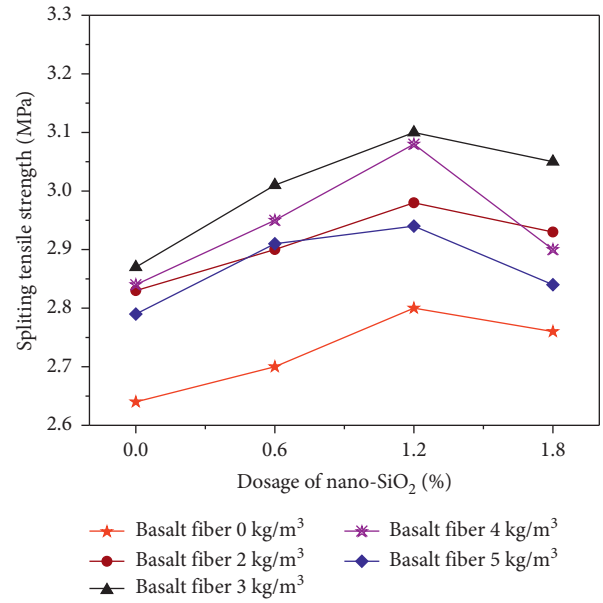

Figure 13: Effect of the NS dosage on the splitting tensile strength [81].

content is generally considered. When the content of nano-$CaCO_3$ exceeds the optimal content, it will not be conducive to improving the performance of the cementitious materials. The main reason is that the van der Waals force of nano-$CaCO_3$ is higher than that of cement, which easily causes nano-$CaCO_3$ with fine particles to aggregate in the mixture. According to the literature [59], for a 29.0% FA content, the optimal content of nano-$CaCO_3$ to enhance the compressive and flexural strength is 2.2%. With this content, the flexural and compressive strengths of cement-based materials are increased by 27.3% and 19%, respectively, compared with the control group. Huang and Zu [60] found that the optimal content of nano-$CaCO_3$ to improve the UHPC strength (accounting for cement quality) is 3%, and the water-cement ratio should be 0.15, as presented in Figure 14. Meng et al. [58] observed the influence of nano-$CaCO_3$ content with an average particle size of 60 nm on OPC. The results show that when the content is 2%, the early hydration strength of cement is improved, but when the content exceeds 5%, the strength decreases due to the relative decrease in cement content. Similar findings have been reported in other publications as well [87–91].

When nano-$CaCO_3$ is mixed into concrete with FA, the early strength hysteresis effect caused by FA can be improved, and the early and late strength of cement-based materials containing FA can be further developed. The composite mineral admixture modified by nano-$CaCO_3$ prepared in reference [92] can exert the composite function of the early strength of calcium carbonate intermediate and high activity of mineral powder in the later period, so the early and later strengths of concrete are superior. Shaikh and Supit [62] revealed that the optimal content of nano-$CaCO_3$ modified high-performance FA concrete (e.g., concrete with 40% and 60% FA

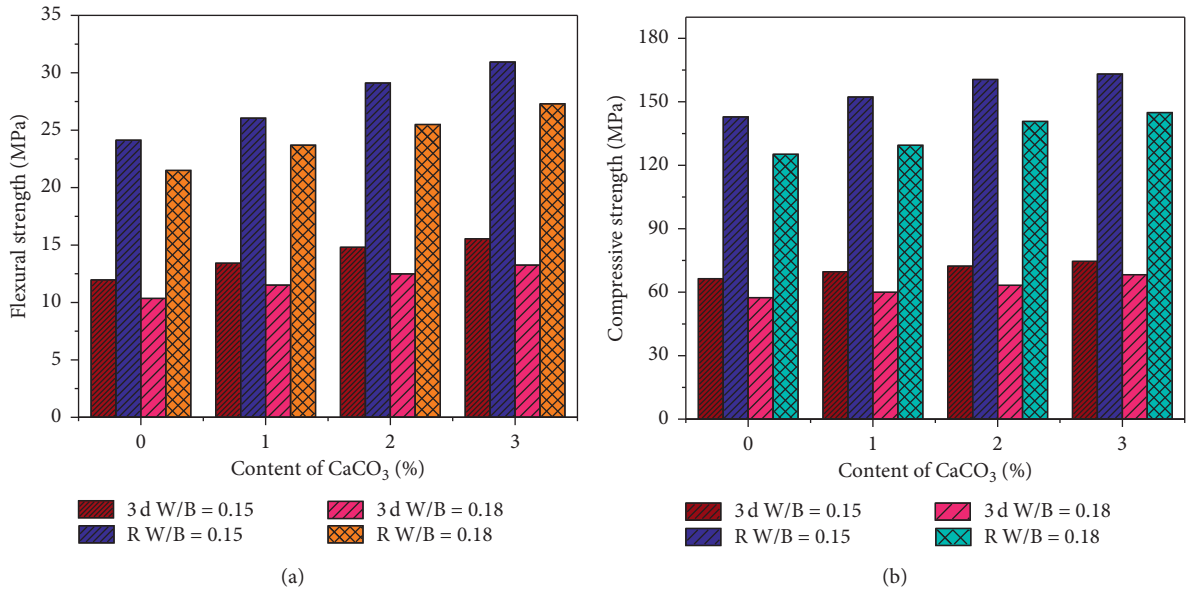

Figure 14: Influence of nano-$CaCO_3$ content on the (a) flexural strength and (b) compressive strength [60].

content, respectively) is 1%. Moreover, the concrete with this content has reasonable compressive strength, low permeable pore volume, and low porosity. Wu et al. [93] found that the addition of 3.2% nano-$CaCO_3$ considerably improved the bonding performance of the fiber-matrix and the bending performance of UHPC. The main reason is that nano-$CaCO_3$ improves the densification of the interfacial transition zone from the perspective of microstructure. However, when the content of nano-$CaCO_3$ exceeds 3.2%, the mechanical properties of UHPC will decrease due to the increase in porosity caused by nano-$CaCO_3$ agglomeration. Meng et al. [94] also explored the relationship between the mechanical properties of nano-$CaCO_3$ and concrete with or without FA. They concluded that nano-$CaCO_3$ has a positive effect on the early mechanical strength of concrete mixed with FA and concrete not mixed with FA. The main reason is that the seed crystal effect of nano-$CaCO_3$ accelerates the hydration of cement and also produces a filling effect, making the microstructure of cement paste more compact. Shaikh and Supit [62] and Supit and Shaikh [33] investigated the influence of nano-$CaCO_3$ on the compressive strength of concrete with a large amount of FA. The results show that adding 1% nano-$CaCO_3$ allows HVFA concrete to have an excellent compressive strength.

In addition, in Xu et al.'s study [63], the changes in the compressive strength of HSC caused by nano-$CaCO_3$ under a standard curing temperature ($21 \pm 1^{\circ}C$) and low-temperature curing ($6.5 \pm 1^{\circ}C$) were investigated. It was observed that the compressive strength of concrete modified by adding 1% and 2% nano-$CaCO_3$ can be increased by 13% and 18% at a standard curing temperature. However, the compressive strength increased by 17% and 14% after curing at low temperature for 3 days. Moreover, the effect of NC on the mechanical properties of concrete under different curing conditions was investigated by Li et al. [38]. They found that the compressive and flexural strengths increase as the NC content increases. Meanwhile, the optimal content of NC is approximately 2.0%. The influence of nano-$CaCO_3$ content on the compressive strength and tensile strength of concrete under different curing conditions is presented in Figure 15.

3.3. Influence of CNT on the Mechanical Properties of Concrete. The flexibility of CNTs can also be used to modify UHPC. Compared with other nanomaterials, CNTs have great advantages in enhancing the toughness and strength of UHPC [40]. In recent years, CNTs have been widely examined to modify and obtain cement-based composites with excellent properties. However, obtaining uniform CNT dispersions is extremely difficult because they are prone to aggregation. Accordingly, Parveen et al. [95] used Pluronic F-127 as a new dispersant to blend CNT-modified cement composites with excellent performance. In addition, adding 0.1% single-walled nanotube dispersion increases the flexural modulus of mortar by 72%. Moreover, the flexural strength and compressive strength increased by 7% and 19%, respectively, after curing for 28 days. Gillani et al. [96] also addressed this shortcoming. To realize a uniform dispersion of MWCNT, high-energy ultrasonic treatment was performed on the modified acrylic polymers. The amount of MWCNTs added to the cement was 0.05% and 0.1%. They pointed out that the splitting tensile strength, bending strength, and compressive strength of the mixture increased by 20.58%, 26.29%, and 15.60%, respectively, after adding 0.05% MWCNT compared with the control mixture cured for 28 days, as presented in Figure 16. However, the mixing duration is also a factor that affects the strength of CNTs' cementitious composites. The bending strength of materials containing 0.03%, 0.08%,

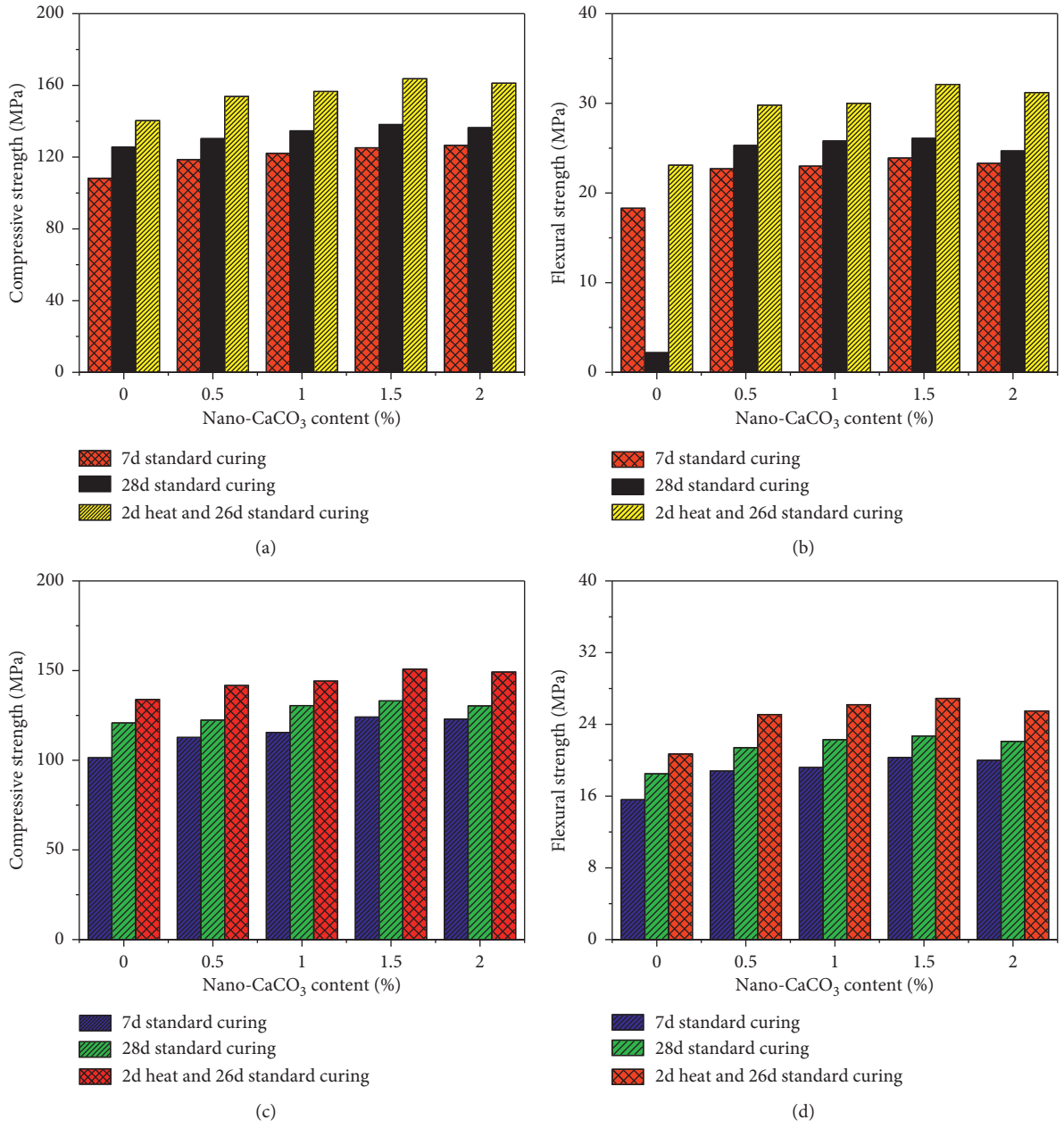

Figure 15: Effect of nano-$CaCO_3$ content on the mechanical strength of UHPC under different water-binder ratios [38]: (a) w/b = 0.16, (b) w/b = 0.16, (c) w/b = 0.17, and (d) w/b = 0.17.

0.15%, or 0.25% MWCNT prepared using stirring times of 1.5, 15, 30, and 60 min, respectively, was studied on the 28th day. These data reveal that the flexural strength of the cement materials added with 0.25% CNTs increased a lot. Compared with the test results of ordinary cement, the flexural strength of the mixture mixed with 0.15% and 0.25% CNTs is considerably increased when the mixing time exceeded 30 min. The mixing effect of CNT cement is presented in Figure 17, and the flexural strength results are shown in Figure 18 [97]. Meanwhile, AI-Rub et al. [98] found the effect of different concentrations of long MWCNTs in cement paste. They showed that nanocomposites modified with low concentrations of long CNTs have the same mechanical properties as those modified with high concentrations of short CNTs. Many studies have shown that CNTs can be uniformly dispersed in concrete using a certain dispersion method, and the compressive strengths of concrete with CNT can be remarkably enhanced. However, the performance of concrete will deteriorate when the content is excessively high [99–103]. The findings of Jung et al. are shown in Figure 19. The mechanism of influence involves adding a proper amount of CNTs into the concrete and evenly distributing the CNTs in the concrete material, which can better exert its nanonucleation effect, thus enhancing the compressive strength and flexural strength of the concrete. However, when the content of CNTs is too much, it is difficult to

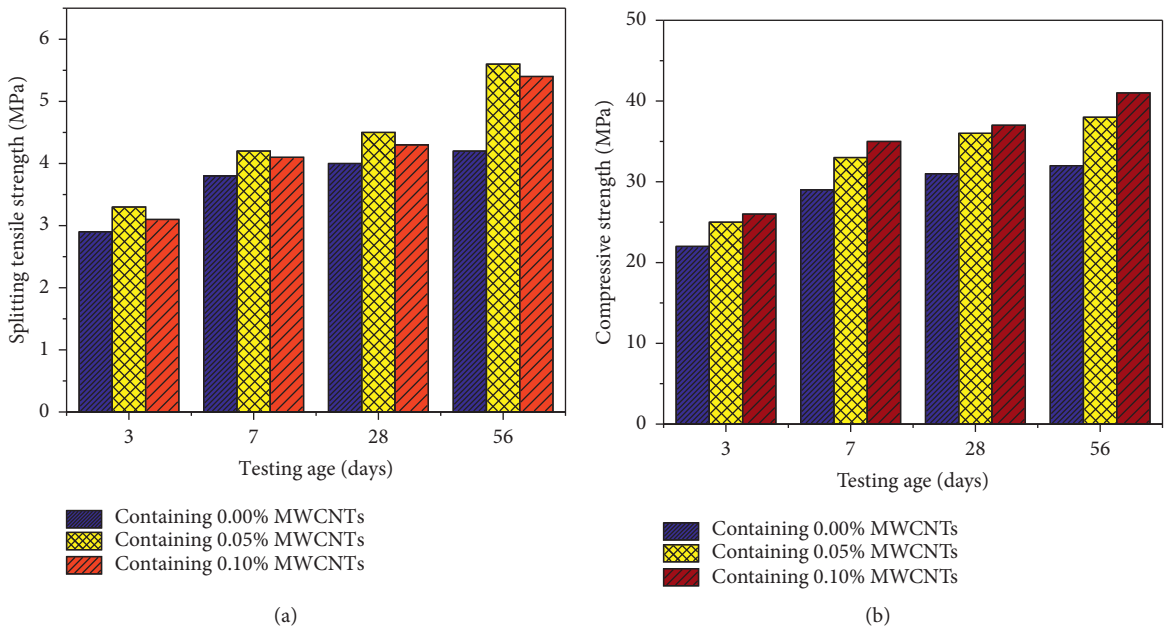

Figure 16: . (a) Splitting tensile strength and (b) compressive strength of concrete with different contents of MWCNTs at different ages [96].

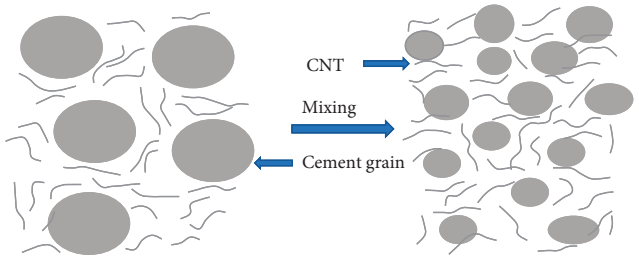

Figure 17: Schematic of the mixing effect on the cement grain size [97].

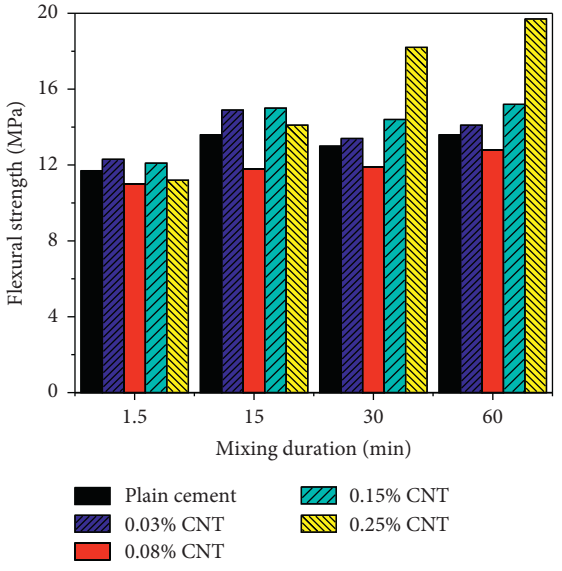

Figure 18: Effect of the mixing time on the flexural strength of CNT cement composites [97].

disperse and aggregate inside the concrete, which reduces the bridging effect and leads to the performance degradation of the concrete.

3.4. Influence of TiO_2 on the Mechanical Properties of Concrete. The application of TiO_2 in UHPC and ordinary concrete has generally resulted in a strong self-cleaning ability, which enables application of green materials in buildings. Meanwhile, it accelerates the early strength of concrete [36]. However, TiO_2 particles are dusty and small and have a considerable environmental impact during the packaging and production process. Adding a small amount of NT into concrete can effectively improve its compressive strength and flexural strength. The strength of concrete specimens increases first and then decreases with the increase in NT contents. Adding very fine NT will increase the specific surface area of the material and the water demand of the mixture, which will make the matrix material unevenly distributed in the mixture, thus reducing the strength of concrete. The effect of FA and TiO_2 on the flexural strength of self-compacting concrete replacing cement was analyzed by Jalal et al. [104–106]. They found that fly ash will reduce the bending strength at the early curing stage. Therefore, measures to increase curing time can be adopted to improve the bending strength. Replacing cement with 4% TiO_2 nanopowder can increase the content of crystal $Ca(OH)_2$ at the early stage of hydration and accelerate the formation of the C-S-H gel; this can enhance the strength of concrete. The relevant data are presented in Figure 20. The compressive strength of cement-based materials modified by nano-TiO_2 was explored in Meng et al.'s [107] and Zhang et al.'s [108] experiments. When cement was replaced by NT, the compressive strength of the cement mortar increases at early age because NT promotes cement hydration and refines pores. Duan et al. [109] stated that adding a certain amount of

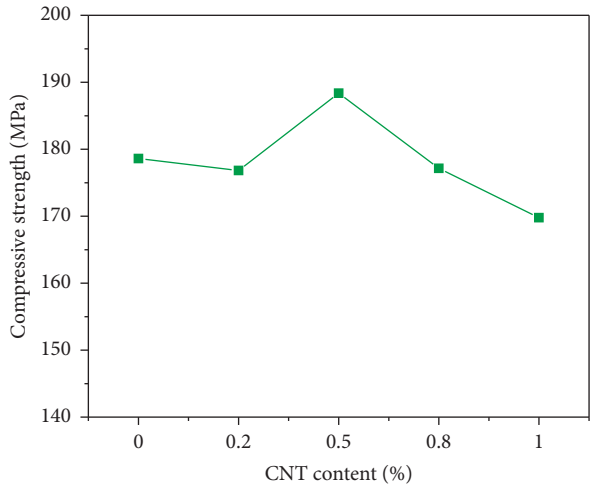

Figure 19: Compressive strength of the UHPC-CNT composites [99].

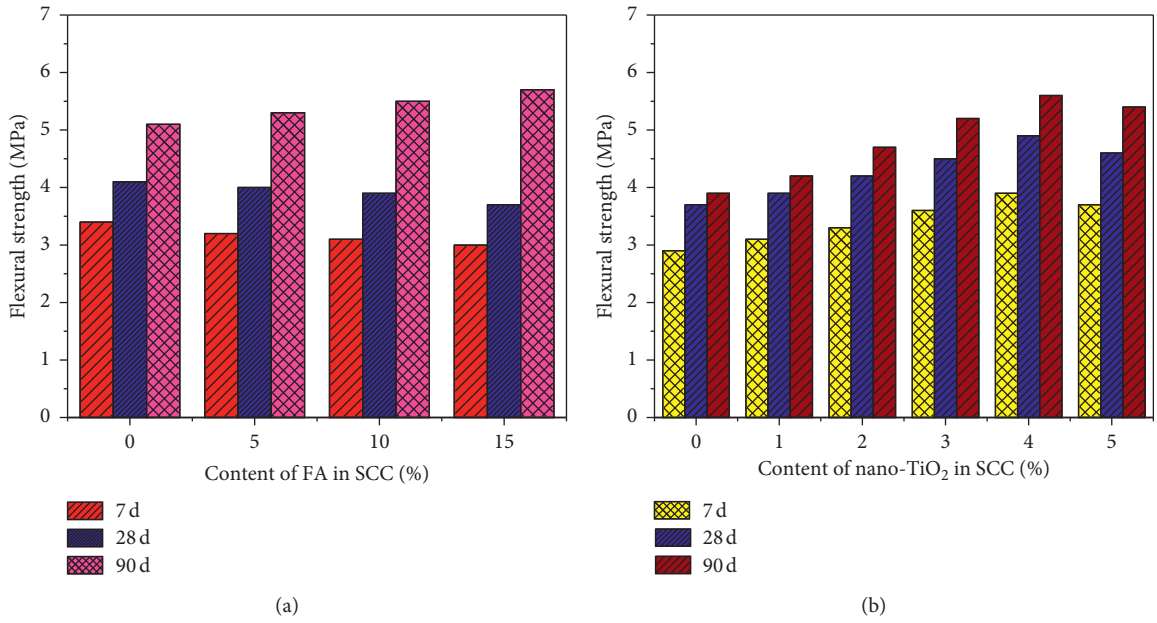

Figure 20: Flexural strength results of SCC-FA mixtures (a) and SCC-NT mixtures (b) [104]. (a) Content of FA in SCC, (b) Content of NT in SCC.

nano-TiO_2 can improve the early and late compressive strengths of the mixture. When the optimal content is 5%, NT shows evident effect on the performance of the modified polymer.

3.5. Influence of Nano-Kaolin on the Mechanical Properties of Concrete

3.5.1. Compressive Strength. Several researchers regard NMK as a suitable mineral admixture precisely because metakaolin can effectively enhance the microstructure of cement-based materials and substantially increase their strength. A number of studies have revealed that the compressive strengths of cement-based composites can be remarkably enhanced with an appropriate amount of NMK [110, 111], as presented in Table 3. Adding an appropriate amount of NMK can improve the compressive strength of cementitious materials. The results [112, 113] show that the optimum dosage of NMK is 10%. However, the compressive strength and bending strength gradually decrease when the content exceeds optimum value (10%), and the compressive strength of samples containing 12% and 14% NMK is close to the control group. Similar results were obtained by Shoukry and AI-Jabri [114]. By contrast, El-Gamal et al. [115] and Kaur et al. [116] found that the optimal NMK content in cement mortar is 3% and 4%, respectively. Morsy et al. [40] revealed that the compressive strength of a cement mortar modified by 6% NMK and 0.02% CNTs for 28 days increased by 29% and 11%, respectively. These findings show that NMK and CNTs have good synergy.

Table 3: Compressive strength of NMK cement-based materials at 28 days.

Cementitious material	w/b ratio	Content of NMK	Compressive strength increment (%)	Reference
Cement paste	0.27	10% NMK	20	[112]
Cement paste	0.3	10% NMK	48	[113]
Cement mortar	0.54	10% NMK	42	[114]
Cement mortar	0.48	3% NMK	54	[115]
Cement mortar	0.3	4% NMK	22.6	[116]
Cement mortar	0.5	6% NMK	18	[40]
		6% NMK + 0.02% CNT	29	
Ordinary concrete	0.5	10% NMK	63.1	[117]
UHPC	0.2	1% NMK	7.88	[41]

Some contrasting findings have also been reported in the literature. Muhd Norhasri et al. [41] examined the mechanical properties of UHPC with NMK content of 1%–9%; the compressive strength of the 1% NMK sample was observed to be the highest. This finding is corroborated by previous studies. However, NMK had no significant effect on the early strength of UHPC, not even a slight decrease. This occurs mainly because the cement and aggregate in the UHPC mixture provide less space, which hinders the filling effect of NMK and reduces the amount C_3S and β-C_2S phases in the matrix; this results in a slight decrease in the early strength of UHPC.

3.5.2. Flexural Strength and Splitting Tensile Strength. NMK is generally used to modify cementing materials; it can remarkably enhance the flexural strength and splitting tensile strength, and its optimal content is approximately 8%–10%. Shoukry et al.'s [118] examined the modification effect of NMK. They found that the bending strength is improved using 2%–14% NMK instead of cement and through surface plastering with 2% fiber content. They also observed that the bending strength increased by approximately 67% compared with the control FRCC when the NMK content was 10%. However, the strength gradually decreases with the increase in the NMK content. As shown in Figure 21, Habeeb et al. [119] provided that the splitting tensile strength was increased by 3.04%–3.41% and 6.95%–7.98%, respectively, with the addition of 2% and 5% NMK into reactive powder concrete (RPC). In Morsy et al.'s [120] study, the influence of 800°C high temperature on the mechanical properties of NMK-modified cement mortar with a cement-sand ratio of 1 : 3 and water-binder ratio of 0.6 was explored. They found that 250°C is the appropriate temperature to maximize the compressive strength (see Figure 22). However, Braganca et al. [35] found that the splitting tensile strength of NMK concrete with 3% content does not improve appreciably when the water-cement ratio is 0.53.

3.6. Influence of NA on the Mechanical Properties of Concrete. In the current research, the compressive strength and pore structure of cement can be modified with nanomaterials, such as NS, NA, and CNTs. If nanocement can be economically manufactured and used on a large scale, concrete construction will enter a new era defined by stronger

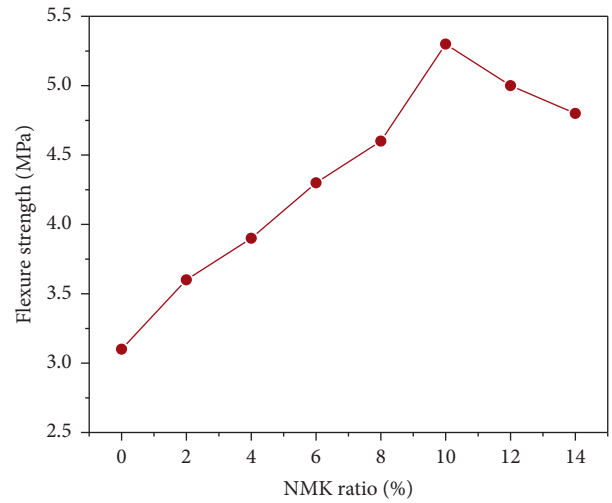

Figure 21: Flexural strength of NMK-modified FRCC as a function of the NMK ratio at 28 days of curing [118].

concrete durability. Alumina, as the main chemical substance in the hydration process of cement, can control the setting time of cement. Adding NA into concrete, especially UHPC, substantially influences the performance of concrete. However, research NA concrete is limited.

According to the literature [71], the maximum early strength can be obtained by adding 1% NA instead of cement. The influence of NS, NA, and NT on the mechanical properties of self-compacting mortar containing FA under single and double doping was studied by Mohseni et al. [121]. The content of the three nanoparticles is 1%, 3%, and 5%, respectively. They observed that the compressive strength of the mixture increased with an increase in the curing age, reaching the maximum value at 90 days; this is mainly due to the pozzolanic activities of FA. The results also show that when the contents of NA, NS, and NT are 1%, 3%, and 5%, respectively, the best compressive strength can be achieved. When the mixture is modified with two types of nanoparticles, the combination of NST achieves the highest strength. On the one hand, NT plays an important role in improving the strength. On the other hand, the combined action of FA and NS increases the pozzolanic reaction in mortar. The experimental results under single and double doping are shown in Figures 23(a)–23(c) and 24(a)–24(c). Hamed et al. [122] revealed the effects of adding constant contents of nano-ZrO_2 (NZ), NF, NT, and NA on the

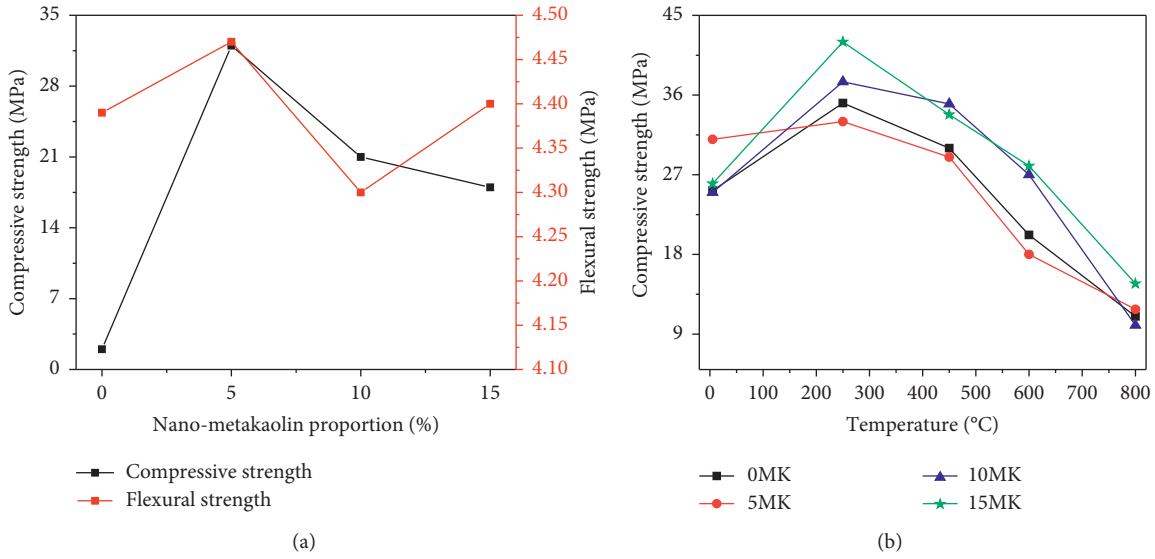

FIGURE 22: Compressive and flexural strength of NMK-cement mortar and NMK proportion and temperature [120]. (a) Different contents of NMK. (b) Different temperatures.

properties of concrete. They proved that NA has unique advantages in improving the mechanical properties of HPC (see Figure 25).

3.7. Influence of NC on the Mechanical Properties of Concrete. NC is a type of mineral silicate nanoparticle and is also one of the most economical nanomaterials. It offers several advantages with regard to modifying mixtures. The effects of NC addition on the mechanical performances of the SCC were investigated. Mohammadi and Mirgozar Langaroudi [123] found that compared with the replacement rates of NC at 1% and 2%, the compressive strength is considerably improved when 3% NC is used to replace cement. Moreover, 3% is considered the optimal content of NC for SCC. However, Hamed et al.'s [122] investigated influence of different contents of NC (5%, 7.5%, and 10%) on concrete performance. They found that compared with the as-received NC concrete, the properties of concrete are obviously improved through the sonication of NC particles and the optimum content of NC to replace cement was 7.5%, as shown in Figure 26.

3.8. Influence of Other Nanomaterials on the Mechanical Properties of Concrete. Finally, paper [35] indicates that using 1% NF to replace cement can ensure that concrete has better mechanical properties. The reason is that micro-nanomaterial fills the surplus pores and voids of the mixture, which promotes the matrix material to be denser. Joshaghani et al. [68] used the mechanical properties as the starting point and analyzed the influence of different types of nanoparticles (including nano-TiO_2, NA and nano-Fe_2O_3) on the properties of self-compacting concrete through different test methods. Compared with NA and NT, nano-Fe_2O_3 is considerably better at enhancing compressive strength because hydrated ferric calcium gel is formed in the microstructure. To handle the large amounts of carbon dioxide emitted and energy consumed during cement production [124], two different proportions of nano palm oil fly ash (NPOFA) were used to replace cement to improve the mechanical properties of concrete. Test data show that the compressive strength of concrete increases gradually when the content of NPOFA is as high as 30%. Ruan et al. [125] and Han et al. [126] found that the mechanical properties of RPC with NZ at a curing age of 28 days improve the compressive strength in comparison with plain RPC.

4. Effect of Different Nanomaterials on Workability and Mechanical Properties of HPC

In summary, a large number of research results show that adding nanomaterials to concrete will reduce its workability. As the content of nanomaterials used to replace cement increases, the workability decreases. Therefore, many scholars believe that in order to maintain a good workability of concrete, the content of nanomaterials should be as small as possible (1%–5%). However, Lui [61] found that the workability of concrete improved considerably after the addition of nano-$CaCO_3$ when the content of nano-$CaCO_3$ varies from 0% to 0.5%, the slump grows slightly, and the optimal content of nano-$CaCO_3$ is 1.5%.

A lot of study results show that adding nanomaterials can exert crystal nucleus effect so as to make the particle gradation more perfect, fill each other, reduce the void ratio, increase the bulk density, and contribute in the enhancement of the flexural and compressive strength. The overall trend is increasing first and then decreasing, and an optimal content is generally considered. There are inconsistent conclusions in the current research on the optimal content. Amin and Abu el-Hassan found that the optimal dosage is 1.2% and the amount of the C-S-H gel is the largest, which

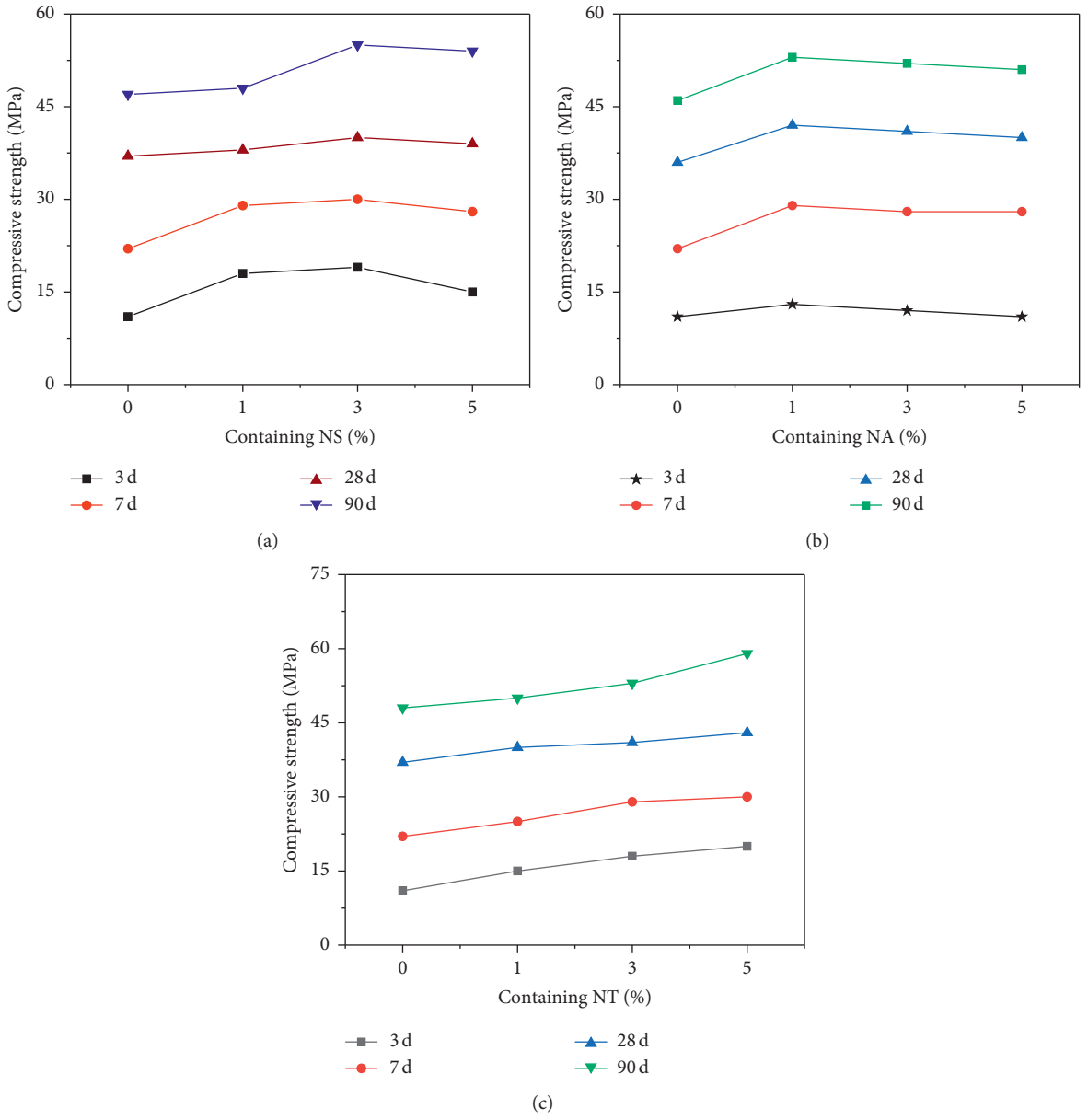

Figure 23: Variation of the compressive strengths of self-compacting mortars containing (a) NS, (b) NA, and (c) NT, at different ages [121].

makes the concrete denser [81]. The study of Li et al. indicates that 2% is the best dosage to improve concrete performance [38]. Sadrmomtazi et al. found that the optimal content of NS is between 5% and 7% [83]. It can be concluded that the optimal content of nano-$CaCO_3$ to enhance the compressive and flexural strength is 2.2% [59]. Huang and Zu found that the optimal content of nano-$CaCO_3$ to improve the UHPC strength (accounting for cement quality) is 3% [60]. The related results show that when the content is 2%, the early hydration strength of cement is improved [58]. Shaikh and Supit show that adding 1% nano-$CaCO_3$ allows HVFA concrete to have an excellent compressive strength [62]. Wu et al. found that the addition of 3.2% nano-$CaCO_3$ considerably improved the bonding performance of the fiber-matrix and the bonding performance of UHPC [93]. Gillani et al. revealed that the flexural strength of the cement materials added with 0.25% CNTs increased a lot [96]. Duan et al. stated that adding a certain amount of nano-TiO_2 can improve the early and late compressive strengths of the mixture [109]. When the optimal content is 5%, NT shows evident effect on the performance of the modified polymer. The results show that the optimum dosage of NMK is 10% [112, 113], and the similar results were obtained by Shoukry and AI-Jabri [114]. By contrast, El-Gamal et al. [115] and Kaur et al. [116] found that the optimal NMK content in cement mortar is 3% and 4%, respectively. However, Muhd Norhasri et al. found that the compressive strength of the 1% NMK sample was observed to be the highest [41]. Shoukry et al. observed that the bending strength increased by approximately 67% compared with the control FRCC when the NMK content was 10% [118]. Mohseni et al. also showed that when the contents of NA, NS, and NT are 1%, 3%, and

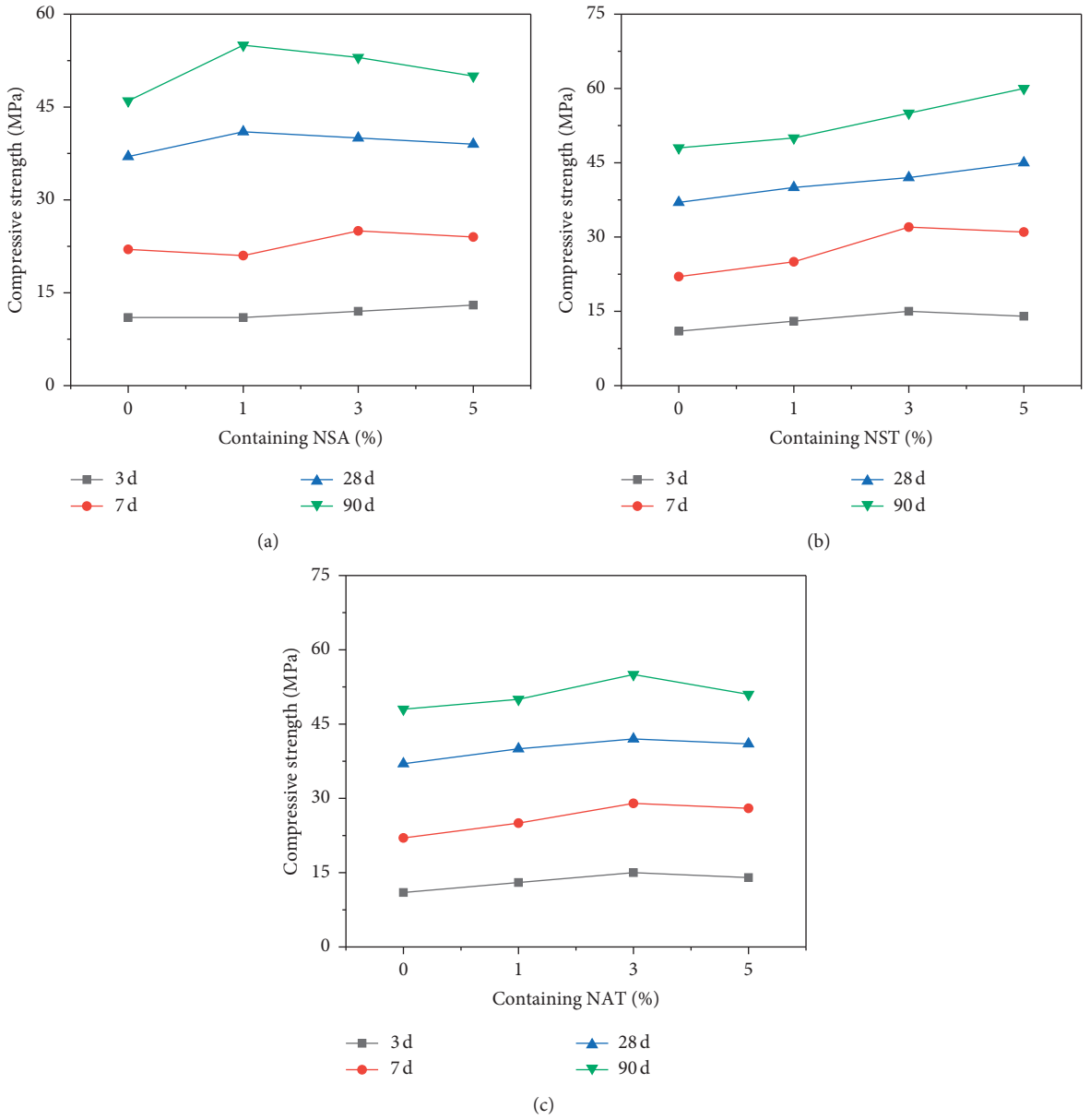

Figure 24: Variation of the compressive strengths of self-compacting mortars containing (a) NSA, (b) NST, and (c) NAT at different ages [121].

5%, respectively, the best compressive strength can be achieved [121].

5. Effect of Different Nanomaterials on Microstructure of HPC

The microstructure of concrete materials is the most essential factor that determines its mechanical properties and durability. The size of nanoparticle is about 1–100 nm, which is advantageous for the nanoparticle to take part in reactions as a nucleus. The nanoparticles pozzolanic reaction with calcium hydroxide produces more C-S-H gels. Using different electronic microscope techniques (SEM, ESEM, and XRD) to conduct microstructural analyses of concrete showed that the microstructure of concrete with nanoparticles is more uniform and dense than concrete without nanoparticles. Therefore, this section will summarize the effects of adding different nanomaterials on the microstructure of concrete.

Khaloo et al. through mercury intrusion porosimetry (MIP) analyzed the pore size distributions of the HPC mixtures with and without 1.5% nano-SiO_2 particles, at the w/b ratio of 0.30 [32]. They show that the pore distributions of the HPC mixtures containing pyrogenic nanosilica with different specific surface areas were finer than those of control HPC mixture. Said et al. through MIP found that the total porosity was significantly lower for mixtures containing nanosilica [42]. More refinement of the pore structure was achieved with increasing the nanosilica dosage up to 6%. Through the BSEM test, they showed notable densification

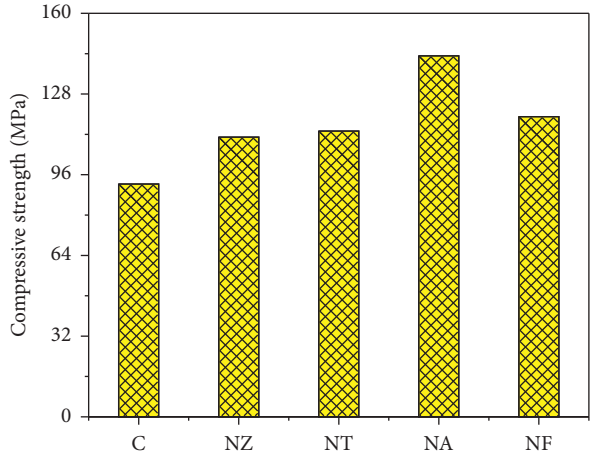

Figure 25: Compressive strength of different nanoparticles after 28 days [122].

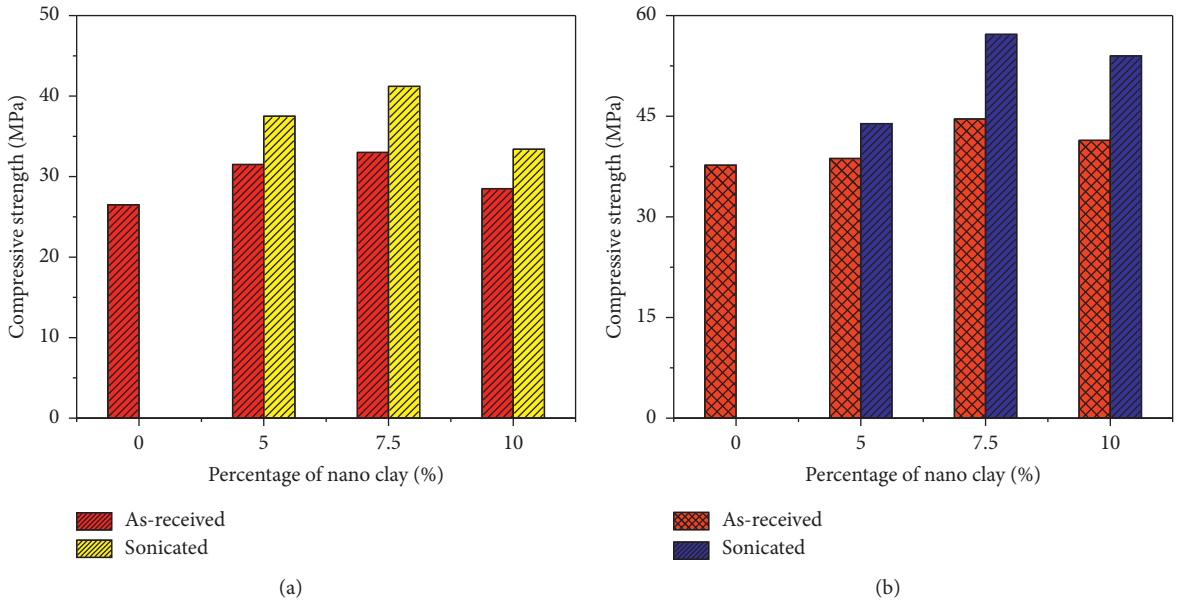

Figure 26: Compressive strength of concrete treated with as-received and sonicated NC after (a) 7 days standard curing and (b) 28 days standard curing [122].

in the ITZ for specimens containing nanosilica. Also, for specimens containing Class F fly ash and nanosilica, BSEM showed higher degree of hydration at 28 days relative the control mixture containing only Class F fly ash. Nazerigivi and Najigivi showed that the addition of 80 nm SiO_2 nanoparticles in ternary blended concrete can fill the cement pores and produce much more C–S–H gel resulting in better mechanical performance of the ternary blended concrete with respect to control concrete [77]. The study of Supivt and Shaikh indicated that NS can react more rapidly with the free lime in the course of hydration reaction than fly ash, and more secondary C-S-H gel can be produced to fill into the microvoids due to the fairly tiny particle size and large specific surface area of SiO_2 nanoparticles in high volume fly ash concrete [73]. Supit and Shaikh [33] showed that calcium carbonate powder particles act as nucleation sites in the process of cement hydration, which increases the precipitation probability of the hydration product C-S-H gel on limestone powder particles and accelerates the hydration of C_3S. Many hydrated calcium aluminate particles grow on the surfaces of major products, such as C-S-H and $Ca(OH)_2$ through (SEM). And the XRD analysis results showed that nano-$CaCO_3$ is effective in reducing the CH and CS in HVFA and hence the formation of additional CSH gels. Jalal et al. found that replacing cement with 4% TiO_2 nanopowder can increase the content of crystal $Ca(OH)_2$ at the early stage of hydration and accelerate the formation of the C-S-H gel [104]. According to SEM, Parveen et al. indicated that CNTs were well wetted by cement forming a dense reinforcing network, and the presence of CNT all over the fracture surface was identified indicating their homogeneous distribution within the cementitious matrix [95]. It was also observed that CNTs were very tightly inserted between the hydration products of cement (C–S–H phases). This was due

to the fact that CNTs acted as the nucleating agent for C–S–H gel which formed as a coating along the CNT bundles. Al-Jabri and Shoukry indicated that the microstructure of the hardened mortar containing NMK appeared quite dense and compact with relatively less capillary pores as compared with the control mix, causing disappearance of large CH crystals [114]. The NMK modified the interfacial transition zone and increased the bond between the cement paste and aggregate due to its pozzolanic activity. And NMK consumes the CH crystals and results in the creation of supplementary CSH. Therefore, nanomaterials can promote the hydration of concrete, improve the internal structure, and enhance the mechanical strength and durability.

6. Conclusions

This review paper reveals the influence of various nanoparticles on the fresh performance and mechanical performance of HPC. NS, nano-$CaCO_3$, NA, and TiO_2 are among the nanomaterials currently researched for the development of nanoconcrete. This paper discusses in detail the available information on the workability, compressive strength, and flexural properties of concrete modified with nanoparticles. The analyses of the existing literature provide important insights into the role of nanomaterials in improving the performance of concrete. This paper also intends to compare the performance of concrete modified by nanoparticles with that of control concrete to obtain more valuable results. Therefore, based on a review of more than 100 papers, the conclusions are as follows:

(1) The slump flow and slump of concrete modified by NS are reduced. The greater the amount of cement replacement, the lower the workability. In this case, an appropriate amount of water-reducing agent should be used to ensure the working performance of HPC containing NS.

(2) The addition of nano-$CaCO_3$ reduces the workability of mortar and concrete with high content of FA, and the workability decreases with the increase in cement replacement.

(3) The slump of HPC is significantly affected by adding CNTs. With the increase in CNT content, the slump drops, and when it reaches 1%, the slump drops below 20 mm. However, the workability of HPC is improved by adding a water-reducing agent.

(4) The addition of various nanomaterials reduces the workability of HPC, such as NT, Al_2O_3, and metakaolin.

(5) The HPC modified by NS has excellent compressive strength mainly because a large amount of C-S-H gel is generated after NS replaces cement, and the microstructure is more compact. Hence, it is related to the optimal dosage of NS. Researchers have proposed different thresholds to optimize NS replacement. However, the replacement rate of NS cannot be excessively high; a value lower than 5% is generally recommended. The compressive strength will be reduced owing to the agglomeration of nanoparticles when adding more than the optimal content in the mixture. At the same time, the type, dosage, and size of NS will affect the compressive strength of HPC.

(6) With the addition of NS, the increasing trends of tensile strength and bending strength are similar to those of compressive strength. NS has an optimal dosage for the influence trend of these strengths.

(7) Most studies show that adding nanomaterials (e.g., nano-$CaCO_3$, CNTs, TiO_2, and Al_2O_3) to HPC not only reduces the amount of cement but also promotes the hydration of C_3S and increases the mechanical properties of concrete. The change in performance depends on the dosage, and exceeding the optimal dosage will reduce the strength.

Conflicts of Interest

The authors declare that they have no conflicts of interest in this paper.

Acknowledgments

The authors acknowledge the financial support received from the National Natural Science Foundation of China (grant nos. 51979251 and U2040224), Natural Science Foundation of Henan (grant no. 212300410018), Program for Innovative Research Team (in Science and Technology) in University of Henan Province of China (grant no. 20IRTSTHN009), and Program for Science & Technology Innovation Talents in Universities of Henan Province, China (grant no. 21HASTIT013).

References

[1] J.-X. Wang and L.-J. Wang, "Advances in the applied research of nano-material in concrete," *Concrete*, vol. 11, 2004.

[2] N. Crainic and A. T. Marques, "Nanocomposites: a state-of-the-art review," *Key Engineering Materials*, vol. 230–232, pp. 656–660, 2002.

[3] C. Wang, C. Yang, F. Liu, C. Wan, and X. Pu, "Preparation of ultra-high performance concrete with common technology and materials," *Cement and Concrete Composites*, vol. 34, no. 4, pp. 538–544, 2012.

[4] P. Zhang, C. Liu, and Q. Li, "Application of gray relational analysis for chloride permeability and freeze-thaw resistance of high-performance concrete containing nanoparticles," *Journal of Materials in Civil Engineering*, vol. 23, no. 12, pp. 1760–1763, 2011.

[5] A. Alsalman, C. N. Dang, and W. Micah Hale, "Development of ultra-high performance concrete with locally available materials," *Construction and Building Materials*, vol. 133, pp. 135–145, 2017.

[6] P. Zhang, Q. Li, and H. Zhang, "Fracture properties of high-performance concrete containing fly ash," *Proceedings of the Institution of Mechanical Engineers, Part L: Journal of Materials: Design and Applications*, vol. 226, no. 2, pp. 170–176, 2012.

[7] P. Zhang, C.-H. Liu, Q.-F. Li, T.-H. Zhang, and P. Wang, "Fracture properties of steel fiber reinforced high

performance concrete containing nano-SiO_2 and fly ash," *Current Science*, vol. 106, no. 7, pp. 980–987, 2014.

[8] N. T. Tran and D. J. Kim, "Synergistic response of blending fibers in ultra-high-performance concrete under high rate tensile loads," *Cement and Concrete Composites*, vol. 78, pp. 132–145, 2017.

[9] B. J. Olawuyi and W. P. Boshoff, "Influence of SAP content and curing age on air void distribution of high performance concrete using 3D volume analysis," *Construction and Building Materials*, vol. 135, pp. 580–589, 2017.

[10] P. Zhang and Q.-F. Li, "Durability of high performance concrete composites containing silica fume," *Proceedings of the Institution of Mechanical Engineers, Part L: Journal of Materials: Design and Applications*, vol. 227, no. 4, pp. 343–349, 2013.

[11] L. Wang, M.-M. Jin, Y.-H. Wu, Y. Zhou, and S. Tang, "Hydration, shrinkage, pore structure and fractal dimension of silica fume modified low heat Portland cement-based materials," *Construction and Building Materials*, vol. 272, 2021.

[12] K. Sobolev, "The development of a new method for the proportioning of high-performance concrete mixtures," *Cement and Concrete Composites*, vol. 26, no. 7, pp. 901–907, 2004.

[13] A. M. Rashad, "Metakaolin as cementitious material: history, scours, production and composition - a comprehensive overview," *Construction and Building Materials*, vol. 41, pp. 303–318, 2013.

[14] E. Güneyisi, M. Gesoğlu, S. Karaoğlu, and K. Mermerdaş, "Strength, permeability and shrinkage cracking of silica fume and metakaolin concretes," *Construction and Building Materials*, vol. 34, pp. 120–130, 2012.

[15] P. Richard and M. Cheyrezy, "Composition of reactive powder concretes," *Cement and Concrete Research*, vol. 25, no. 7, pp. 1501–1511, 1995.

[16] V. Matte and M. Moranville, "Durability of reactive powder composites: influence of silica fume on the leaching properties of very low water/binder pastes," *Cement and Concrete Composites*, vol. 21, no. 1, pp. 1–9, 1999.

[17] A. A. A. Hassan, M. Lachemi, and K. M. A. Hossain, "Effect of metakaolin and silica fume on the durability of self-consolidating concrete," *Cement and Concrete Composites*, vol. 34, no. 6, pp. 801–807, 2012.

[18] L. Senff, D. Hotza, S. Lucas, V. M. Ferreira, and J. A. Labrincha, "Effect of nano-SiO_2 and nano-TiO_2 addition on the rheological behavior and the hardened properties of cement mortars," *Materials Science and Engineering: A*, vol. 532, pp. 354–361, 2012.

[19] M. Mazloom, A. A. Ramezanianpour, and J. J. Brooks, "Effect of silica fume on mechanical properties of high-strength concrete," *Cement and Concrete Composites*, vol. 26, no. 4, pp. 347–357, 2004.

[20] M. Kumar, S. K. Singh, N. P. Singh, and N. B. Singh, "Hydration of multicomponent composite cement: OPC-FA-SF-MK," *Construction and Building Materials*, vol. 36, pp. 681–686, 2012.

[21] L. Wang, F. Guo, H. Yang, Y. Wang, and S. Tang, "Comparison of fly ash, PVA fiber, MgO and shrinkage-reducing admixture on the frost resistance of face slab concrete via pore structural and fractal analysis," *Fractals*, vol. 29, Article ID 2140002, 2020.

[22] H. Yazıcı, S. Aydın, H. Yiğiter, and B. Baradan, "Effect of steam curing on class C high-volume fly ash concrete mixtures," *Cement and Concrete Research*, vol. 35, no. 6, pp. 1122–1127, 2005.

[23] L. Wang, M. Jin, F. Guo, Y. Wang, and S. Tang, "Pore structural and fractal analysis of the influence of fly ash and silica fume on the mechanical property and abrasion resistance of concrete," *Fractals*, vol. 29, Article ID 2140003, 2020.

[24] J. M. Khatib, "Performance of self-compacting concrete containing fly ash," *Construction and Building Materials*, vol. 22, no. 9, pp. 1963–1971, 2008.

[25] L.-D. Zhang, "Nanomaterials and nanotechnology in China: current status of application and opportunities for commercialization," *Materials Reports*, vol. 15, pp. 2–5, 2001.

[26] K. Sobolev and M. Ferrada Gutierrez, "How nanotechnology can change the concrete world: Part 1," *American Ceramic Society Bulletin*, vol. 10, pp. 14–17, 2005.

[27] L. Senff, D. Hotza, W. L. Repette, V. M. Ferreira, and J. A. Labrincha, "Mortars with nano-SiO_2 and micro-SiO_2 investigated by experimental design," *Construction and Building Materials*, vol. 24, no. 8, pp. 1432–1437, 2010.

[28] P. Mehta and P. Monteiro, *Concrete: Structure, Properties and Materials*, Taylor & Francis, Abingdon, UK, 1993.

[29] R. Hamid, K. M. Yusof, and M. F. M. Zain, "A combined ultrasound method applied to high performance concrete with silica fume," *Construction and Building Materials*, vol. 24, no. 1, pp. 94–98, 2010.

[30] B. Graybeal and J. L. Hartman, "Ultra-high performance concrete material properties," *Transportation Research Board*, vol. 2003, 2003.

[31] P.-C. Aïtcin, "Cements of yesterday and today: concrete of tomorrow," *Cement and Concrete Research*, vol. 30, no. 9, pp. 1349–1359, 2000.

[32] A. Khaloo, M. H. Mobini, and P. Hosseini, "Influence of different types of nano-SiO_2 particles on properties of high-performance concrete," *Construction and Building Materials*, vol. 113, pp. 188–201, 2016.

[33] S. Supit and F. Shaikh, "Effect of Nano-$CaCO_3$ on Compressive strength development of high volume fly ash mortars and concretes," *Journal of Advanced Concrete Technology*, vol. 12, no. 6, pp. 178–186, 2014.

[34] R. Ismael, J. V. Silva, R. N. F. Carmo et al., "Influence of nano-SiO_2 and nano-Al_2O_3 additions on steel-to-concrete bonding," *Construction and Building Materials*, vol. 125, pp. 1080–1092, 2016.

[35] M. O. G. P. Bragança, K. F. Portella, M. M. Bonato, E. Alberti, and C. E. B. Marino, "Performance of Portland cement concretes with 1% nano-Fe_3O_4 addition: electrochemical stability under chloride and sulfate environments," *Construction and Building Materials*, vol. 117, pp. 152–162, 2016.

[36] H. Jafari and S. Afshar, "Improved photodegradation of organic contaminants using nano-TiO_2 and TiO_2-SiO_2 deposited on Portland cement concrete blocks," *Photochemistry and Photobiology*, vol. 92, no. 1, pp. 87–101, 2016.

[37] F. Vazinram, M. Jalal, and M. Y. Foroushani, "Effect of nano ZnO_2 and lime water curing on strength and water absorption of concrete," *International Journal of Materials and Product Technology*, vol. 50, no. 3/4, pp. 356–365, 2015.

[38] W. Li, Z. Huang, F. Cao, Z. Sun, and S. P. Shah, "Effects of nano-silica and nano-limestone on flowability and mechanical properties of ultra-high-performance concrete matrix," *Construction and Building Materials*, vol. 95, pp. 366–374, 2015.

[39] P. Arulraj and M. Carmichael, "Effect of nano-flyash on strength of concrete," *International Journal for*

Computational Civil and Structural Engineering, vol. 2, no. 2, pp. 475–482, 2011.

[40] M. S. Morsy, S. H. Alsayed, and M. Aqel, "Hybrid effect of carbon nanotube and nano-clay on physico-mechanical properties of cement mortar," *Construction and Building Materials*, vol. 25, no. 1, pp. 145–149, 2011.

[41] M. S. Muhd Norhasri, M. S. Hamidah, A. Mohd Fadzil, and O. Megawati, "Inclusion of nano metakaolin as additive in ultra high performance concrete (UHPC)," *Construction and Building Materials*, vol. 127, pp. 167–175, 2016.

[42] A. M. Said, M. S. Zeidan, M. T. Bassuoni, and Y. Tian, "Properties of concrete incorporating nano-silica," *Construction and Building Materials*, vol. 36, pp. 838–844, 2012.

[43] Y.-H. Lin, Y.-Y. Tyan, T.-P. Chang, and C.-Y. Chang, "An assessment of optimal mixture for concrete made with recycled concrete aggregates," *Cement and Concrete Research*, vol. 34, no. 8, pp. 1373–1380, 2004.

[44] G. H. Tattersall and P. H. Baker, "An investigation on the effect of vibration on the workability of fresh concrete using a vertical pipe apparatus," *Magazine of Concrete Research*, vol. 41, no. 146, pp. 3–9, 1989.

[45] G. Quercia, A. Lazaro, J. W. Geus, and H. J. H. Brouwers, "Characterization of morphology and texture of several amorphous nano-silica particles used in concrete," *Cement and Concrete Composites*, vol. 44, pp. 77–92, 2013.

[46] A. C. Aydın, V. J. Nasl, and T. Kotan, "The synergic influence of nano-silica and carbon nano tube on self-compacting concrete," *Journal of Building Engineering*, vol. 20, pp. 467–475, 2018.

[47] N. Hani, O. Nawawy, K. S. Ragab, and M. Kohail, "The effect of different water/binder ratio and nano-silica dosage on the fresh and hardened properties of self-compacting concrete," *Construction and Building Materials*, vol. 165, pp. 504–513, 2018.

[48] A. Naji Givi, S. Abdul Rashid, F. N. A. Aziz, and M. A. M. Salleh, "The effects of lime solution on the properties of SiO_2 nanoparticles binary blended concrete," *Composites Part B: Engineering*, vol. 42, no. 3, pp. 562–569, 2011.

[49] S. W. M. Supit and F. U. A. Shaikh, "Durability properties of high volume fly ash concrete containing nano-silica," *Materials and Structures*, vol. 48, no. 8, pp. 2431–2445, 2015.

[50] H. Bahadori and P. Hosseini, "Reduction of cement consumption by the aid of silica nano-particles (Investigation on Concrete Properties)," *Journal of Civil Engineering and Management*, vol. 18, no. 3, pp. 416–425, 2012.

[51] P. Zhang, Y.-N. Zhao, Q.-F. Li, T. Zhang, and P. Wang, "Mechanical properties of fly ash concrete composite reinforced with nano-SiO_2 and steel fibre," *Current Science*, vol. 106, no. 11, pp. 1529–1537, 2014.

[52] M. Jalal, A. Pouladkhan, O. F. Harandi, and D. Jafari, "Comparative study on effects of class F fly ash, nano silica and silica fume on properties of high performance self compacting concrete," *Construction and Building Materials*, vol. 94, pp. 90–104, 2015.

[53] E. Güneyisi, M. Gesoglu, A. Al-Goody, and S. İpek, "Fresh and rheological behavior of nano-silica and fly ash blended self-compacting concrete," *Construction and Building Materials*, vol. 95, pp. 29–44, 2015.

[54] M. Y. Durgun and H. N. Atahan, "Rheological and fresh properties of reduced fine content self-compacting concretes produced with different particle sizes of nano SiO_2," *Construction and Building Materials*, vol. 142, pp. 431–443, 2017.

[55] L. Senff, J. A. Labrincha, V. M. Ferreira, D. Hotza, and W. L. Repette, "Effect of nano-silica on rheology and fresh properties of cement pastes and mortars," *Construction and Building Materials*, vol. 23, no. 7, pp. 2487–2491, 2009.

[56] J.-Y. Shih, T.-P. Chang, and T.-C. Hsiao, "Effect of nanosilica on characterization of Portland cement composite," *Materials Science and Engineering: A*, vol. 424, no. 1-2, pp. 266–274, 2006.

[57] Y. Qing, Z. Zenan, K. Deyu, and C. Rongshen, "Influence of nano-SiO_2 addition on properties of hardened cement paste as compared with silica fume," *Construction and Building Materials*, vol. 21, no. 3, pp. 539–545, 2007.

[58] T. Meng, K.-L. Qian, X.-Q. Qian et al., "Effect of composite nano-addition on mechanics strength and microstructure of cement paste," *Rare Metal Materials and Engineering*, vol. 37, pp. 631–633, 2008.

[59] H.-H. Wei, "Study on effect and mechanism of nano-CaCO3 in cement-based materials," Master thesis, Harbin Institute of Technology, Harbin, China, 2013.

[60] Z.-Y. Huang and T.-Y. Zu, "Influence of nano-$CaCO_3$ on ultra high performance concrete," *Bulletin of the Chinese Ceramic Society*, vol. 32, pp. 1103–1109, 2013.

[61] L.-J. Liu, "Study on increasing the toughness of cement concrete by using nano-CaCO3/steel fiber composite," Master thesis, Tianjin University, Tianjin, China, 2009.

[62] F. U. A. Shaikh and S. W. M. Supit, "Mechanical and durability properties of high volume fly ash (HVFA) concrete containing calcium carbonate ($CaCO_3$) nanoparticles," *Construction and Building Materials*, vol. 70, pp. 309–321, 2014.

[63] Q. L. Xu, T. Meng, and M. Z. Huang, "Effects of nano-$CaCO_3$ on the compressive strength and microstructure of high strength concrete in different curing temperature," *Applied Mechanics and Materials*, vol. 121-126, pp. 126–131, 2011.

[64] J.-L. Wang, Y.-L. Zhao, X.-B. He et al., "Influence of carbon nanotubes on the properties of concrete," *Bulletin of the Chinese Ceramic Society*, vol. 35, pp. 2193–2197, 2016.

[65] X. Sun, Q. Wang, H. Wang, and L. Chen, "Influence of multi-walled nanotubes on the fresh and hardened properties of a 3D printing PVA mortar ink," *Construction and Building Materials*, vol. 247, 2020.

[66] D.-X. Sun, C.-J. Yang, X.-D. Qi, J.-H. Yang, and Y. Wang, "Largely enhanced fracture toughness of the PP/EPDM blends induced by adding carbon nanofibers," *Composites Science and Technology*, vol. 164, pp. 146–152, 2018.

[67] F. Collins, J. Lambert, and W. H. Duan, "The influences of admixtures on the dispersion, workability, and strength of carbon nanotube-OPC paste mixtures," *Cement and Concrete Composites*, vol. 34, no. 2, pp. 201–207, 2012.

[68] A. Joshaghani, M. Balapour, M. Mashhadian, and T. Ozbakkaloglu, "Effects of nano-TiO_2, nano-Al_2O_3, and nano-Fe_2O_3 on rheology, mechanical and durability properties of self-consolidating concrete (SCC): an experimental study," *Construction and Building Materials*, vol. 245, 2020.

[69] A. Nazari and S. Riahi, "RETRACTED: the effects of TiO_2 nanoparticles on properties of binary blended concrete," *Journal of Composite Materials*, vol. 45, no. 11, pp. 1181–1188, 2011.

[70] X.-Y. Guo, K. Yang, and Y.-F. Fan, "Study on reasonable addition of nano metakaolin in cement mortar in chloride environment," *Concrete*, vol. 40, pp. 110–114, 2018.

[71] R. Gowda, H. Narendra, D. Rangappa, and R. Prabhakar, "Effect of nano-alumina on workability, compressive strength and residual strength at elevated temperature of

cement mortar," *Materials Today: Proceedings*, vol. 4, no. 11, pp. 12152–12156, 2017.

[72] A. Hosseini, S. H. Hosseini, and A. Zadeh, "Study of compress strength and time setting of concrete by additives of silica fume and nano silica," *Asian Journal of Chemistry*, vol. 24, no. 2, pp. 903–907, 2012.

[73] F. U. A. Shaikh, S. W. M. Supit, and P. K. Sarker, "A study on the effect of nano silica on compressive strength of high volume fly ash mortars and concretes," *Materials & Design*, vol. 60, pp. 433–442, 2014.

[74] X. F. Wang, Y. J. Huang, G. Y. Wu et al., "Effect of nano-SiO_2 on strength, shrinkage and cracking sensitivity of lightweight aggregate concrete," *Construction and Building Materials*, vol. 175, pp. 115–125, 2018.

[75] J. Cui, "The mechanical properties that nano-SiO_2 affect EPS light-aggregate concrete," *Advanced Materials Research*, vol. 571, pp. 86–90, 2012.

[76] A. Naji Givi, S. Abdul Rashid, F. N. A. Aziz, and M. A. M. Salleh, "Experimental investigation of the size effects of SiO_2 nano-particles on the mechanical properties of binary blended concrete," *Composites Part B: Engineering*, vol. 41, no. 8, pp. 673–677, 2010.

[77] A. Nazerigivi and A. Najigivi, "Study on mechanical properties of ternary blended concrete containing two different sizes of nano-SiO_2," *Composites Part B: Engineering*, vol. 167, pp. 20–24, 2019.

[78] Y. Wang, P. Hughes, H. Niu, and Y. Fan, "A new method to improve the properties of recycled aggregate concrete: composite addition of basalt fiber and nano-silica," *Journal of Cleaner Production*, vol. 236, 2019.

[79] M. Mahdikhani, O. Bamshad, and M. Fallah Shirvani, "Mechanical properties and durability of concrete specimens containing nano silica in sulfuric acid rain condition," *Construction and Building Materials*, vol. 167, pp. 929–935, 2018.

[80] L. G. Li, J. Y. Zheng, J. Zhu, and A. K. H. Kwan, "Combined usage of micro-silica and nano-silica in concrete: SP demand, cementing efficiencies and synergistic effect," *Construction and Building Materials*, vol. 168, pp. 622–632, 2018.

[81] M. Amin and K. Abu el-hassan, "Effect of using different types of nano materials on mechanical properties of high strength concrete," *Construction and Building Materials*, vol. 80, pp. 116–124, 2015.

[82] B. M. Wang, "Influence of nano-SiO_2 on the strength of high performance concrete," *Materials Science Forum*, vol. 686, pp. 432–437, 2011.

[83] A. Sadrmomtazi, A. Fassihi, F. Balalaei, and A. K. Haghi, "Investigation of mechanical and physical properties of mortars containing silica fume and nano-SiO_2," in *Proceedings of the Third International Conference on Concrete and Development*, pp. 1153–1161, Tehran, Iran, April 2009.

[84] M. Jalal, A. R. Pouladkhan, A. Ramezanianpour, and H. Norouzi, "Effects of silica nanpowder and silica fume on rheology and strength of high strength self compacting concrete," *Journal of American Science*, vol. 8, no. 4, pp. 270–277, 2012.

[85] S. Fallah and M. Nematzadeh, "Mechanical properties and durability of high-strength concrete containing macro-polymeric and polypropylene fibers with nano-silica and silica fume," *Construction and Building Materials*, vol. 132, pp. 170–187, 2017.

[86] A. M. Mohamed, "Influence of nano materials on flexural behavior and compressive strength of concrete," *HBRC Journal*, vol. 12, no. 2, pp. 212–225, 2016.

[87] S.-S. Ying, *Nano Calcium Carbonate Modification of Aerated Concrete and Preparation of High Aluminum Aerated concrete*, Doctor Thesis, Zhengjiang University, Hangzhou, China, 2014.

[88] L. Liu, *Study on Properties and Mechanism of Nano-$CaCO_3$ in Fly Ash concrete*, Master Thesis, Harbin Institute of Technology, Harbin, China, 2014.

[89] Y.-C. Zhang, "Effect of nano $CaCO_3$ on mechanical properties of concrete," *New Materials and Application*, vol. 21, pp. 74-75, 2011.

[90] D.-Z. Wang, Y.-F. Meng, and T.-Y. Li, "Test of improving frost resistance of concrete with nano-SiO_2 and nano-$CaCO_3$," *China Concrete and Cement Products*, vol. 43, pp. 6–10, 2015.

[91] S. Yang and F.-Q. Ji, "Effect of nano calcium carbonate on physical and mechanical properties of steel fiber reinforced concrete," *Railway Engineering*, vol. 51, pp. 133–135, 2011.

[92] K.-L. Qian, J.-J. Zhang, X.-Q. Qian et al., "Effects of nano-$CaCO_3$ intermediate on physical and mechanical properties of cement-based materials," *Journal of Materials Science & Engineering*, vol. 29, pp. 692–697, 2011.

[93] Z. Wu, C. Shi, and K. H. Khayat, "Multi-scale investigation of microstructure, fiber pullout behavior, and mechanical properties of ultra-high performance concrete with nano-$CaCO_3$ particles," *Cement and Concrete Composites*, vol. 86, pp. 255–265, 2018.

[94] T. Meng, Y. Yu, and Z. Wang, "Effect of nano-$CaCO_3$ slurry on the mechanical properties and micro-structure of concrete with and without fly ash," *Composites Part B: Engineering*, vol. 117, pp. 124–129, 2017.

[95] S. Parveen, S. Rana, R. Fangueiro, and M. C. Paiva, "Microstructure and mechanical properties of carbon nanotube reinforced cementitious composites developed using a novel dispersion technique," *Cement and Concrete Research*, vol. 73, pp. 215–227, 2015.

[96] S. S.-U.-H. Gillani, A. Khitab, S. Ahmad et al., "Improving the mechanical performance of cement composites by carbon nanotubes addition," *Procedia Structural Integrity*, vol. 3, pp. 11–17, 2017.

[97] M. O. Mohsen, N. Al-Nuaimi, R. K. Abu Al-Rub, A. Senouci, and K. A. Bani-Hani, "Effect of mixing duration on flexural strength of multi walled carbon nanotubes cementitious composites," *Construction and Building Materials*, vol. 126, pp. 586–598, 2016.

[98] R. K. Abu Al-Rub, A. I. Ashour, and B. M. Tyson, "On the aspect ratio effect of multi-walled carbon nanotube reinforcements on the mechanical properties of cementitious nanocomposites," *Construction and Building Materials*, vol. 35, pp. 647–655, 2012.

[99] M. Jung, Y.-S. Lee, S.-G. Hong, and J. Moon, "Carbon nanotubes (CNTs) in ultra-high performance concrete (UHPC): dispersion, mechanical properties, and electromagnetic interference (EMI) shielding effectiveness (SE)," *Cement and Concrete Research*, vol. 131, 2020.

[100] A. Hawreen and J. A. Bogas, "Creep, shrinkage and mechanical properties of concrete reinforced with different types of carbon nanotubes," *Construction and Building Materials*, vol. 198, pp. 70–81, 2019.

[101] A. J. N. MacLeod, A. Fehervari, W. P. Gates et al., "Enhancing fresh properties and strength of concrete with a pre-dispersed carbon nanotube liquid admixture," *Construction and Building Materials*, vol. 247, 2020.

[102] M. Saafi, K. Andrew, P. L. Tang et al., "Multifunctional properties of carbon nanotube/fly ash geopolymeric

nanocomposites," *Construction and Building Materials*, vol. 49, pp. 46–55, 2013.

[103] Y.-Y. Liu, M. Sun, F. Feng et al., "The influence of the incorporation of modified carbon nanotubes on the mechanical properties of concrete," *China Concrete and Cement Products*, vol. 45, pp. 26–30, 2018.

[104] J. Mostafa and T. Mostafa, "Assessment of nano-TiO_2 and class F fly ash effects on flexural fracture and microstructure of binary blended concrete," *Science and Engineering of Composite Materials*, vol. 22, no. 3, pp. 263–270, 2015.

[105] M. Jalal, M. Fathi, and M. Farzad, "Effects of fly ash and TiO_2 nanoparticles on rheological, mechanical, microstructural and thermal properties of high strength self compacting concrete," *Mechanics of Materials*, vol. 61, pp. 11–27, 2013.

[106] M. Jalal, A. A. Ramezanianpour, and M. K. Pool, "Split tensile strength of binary blended self compacting concrete containing low volume fly ash and TiO_2 nanoparticles," *Composites Part B: Engineering*, vol. 55, pp. 324–337, 2013.

[107] T. Meng, Y. Yu, X. Qian, S. Zhan, and K. Qian, "Effect of nano-TiO_2 on the mechanical properties of cement mortar," *Construction and Building Materials*, vol. 29, pp. 241–245, 2012.

[108] R. Zhang, X. Cheng, P. Hou, and Z. Ye, "Influences of nano-TiO_2 on the properties of cement-based materials: hydration and drying shrinkage," *Construction and Building Materials*, vol. 81, pp. 35–41, 2015.

[109] P. Duan, C. Yan, W. Luo, and W. Zhou, "Effects of adding nano-TiO_2 on compressive strength, drying shrinkage, carbonation and microstructure of fluidized bed fly ash based geopolymer paste," *Construction and Building Materials*, vol. 106, pp. 115–125, 2016.

[110] M. S. M. Norhasri, M. S. Hamidah, and A. M. Fadzil, "Applications of using nano material in concrete: a review," *Construction and Building Materials*, vol. 133, pp. 91–97, 2017.

[111] M. Heikal and N. S. Ibrahim, "Hydration, microstructure and phase composition of composite cements containing nano-clay," *Construction and Building Materials*, vol. 112, pp. 19–27, 2016.

[112] S. M. A. El-Gamal, M. S. Amin, and M. Ramadan, "Hydration characteristics and compressive strength of hardened cement pastes containing nano-metakaolin," *HBRC Journal*, vol. 13, no. 1, pp. 114–121, 2017.

[113] A. E. Al-Salami, M. S. Morsy, S. Taha, and H. Shoukry, "Physico-mechanical characteristics of blended white cement pastes containing thermally activated ultrafine nano clays," *Construction and Building Materials*, vol. 47, pp. 138–145, 2013.

[114] K. Al-Jabri and H. Shoukry, "Influence of nano metakaolin on thermo-physical, mechanical and microstructural properties of high-volume ferrochrome slag mortar," *Construction and Building Materials*, vol. 177, pp. 210–221, 2018.

[115] S. M. A. El-Gamal, F. S. Hashem, and M. S. Amin, "Influence of carbon nanotubes, nanosilica and nanometakaolin on some morphological-mechanical properties of oil well cement pastes subjected to elevated water curing temperature and regular room air curing temperature," *Construction and Building Materials*, vol. 146, pp. 531–546, 2017.

[116] M. Kaur, J. Singh, and M. Kaur, "Microstructure and strength development of fly ash-based geopolymer mortar: role of nano-metakaolin," *Construction and Building Materials*, vol. 190, pp. 672–679, 2018.

[117] S. Salih, A. Ibrahim, and Z. Naji, "The effect of nano metakaolin material on some properties of concrete," *Diyala Journal of Engineering Sciences*, vol. 6, pp. 50–61, 2013.

[118] H. Shoukry, M. F. Kotkata, S. A. Abo-el-Enein, and M. S. Morsy, "Flexural strength and physical properties of fiber reinforced nano metakaolin cementitious surface compound," *Construction and Building Materials*, vol. 43, pp. 453–460, 2013.

[119] G. Mohsin Habeeb, J. Mahdi Al-Jeabory, and M. Hamed Majeed, "Sustainable performance of reactive powder concrete by using nano meta kaolin," *Journal of Engineering and Sustainable Development*, vol. 22, no. 2, pp. 96–106, 2018.

[120] M. S. Morsy, Y. A. Al-Salloum, H. Abbas, and S. H. Alsayed, "Behavior of blended cement mortars containing nano-metakaolin at elevated temperatures," *Construction and Building Materials*, vol. 35, pp. 900–905, 2012.

[121] E. Mohseni, B. M. Miyandehi, J. Yang, and M. A. Yazdi, "Single and combined effects of nano-SiO_2, nano-Al_2O_3 and nano-TiO_2 on the mechanical, rheological and durability properties of self-compacting mortar containing fly ash," *Construction and Building Materials*, vol. 84, pp. 331–340, 2015.

[122] N. Hamed, M. S. El-Feky, M. Kohail, and E.-S. A. R. Nasr, "Effect of nano-clay de-agglomeration on mechanical properties of concrete," *Construction and Building Materials*, vol. 205, pp. 245–256, 2019.

[123] M. A. Mirgozar Langaroudi and Y. Mohammadi, "Effect of nano-clay on workability, mechanical, and durability properties of self-consolidating concrete containing mineral admixtures," *Construction and Building Materials*, vol. 191, pp. 619–634, 2018.

[124] H. M. Hamada, F. M. Yahaya, K. Muthusamy, G. A. Jokhio, and A. M. Humada, "Fresh and hardened properties of palm oil clinker lightweight aggregate concrete incorporating Nano-palm oil fuel ash," *Construction and Building Materials*, vol. 214, pp. 344–354, 2019.

[125] Y. Ruan, B. Han, X. Yu et al., "Mechanical behaviors of nano-zirconia reinforced reactive powder concrete under compression and flexure," *Construction and Building Materials*, vol. 162, pp. 663–673, 2018.

[126] B. Han, Z. Wang, S. Zeng et al., "Properties and modification mechanisms of nano-zirconia filled reactive powder concrete," *Construction and Building Materials*, vol. 141, pp. 426–434, 2017.

Hindawi
Advances in Civil Engineering
Volume 2020, Article ID 8899630, 26 pages
https://doi.org/10.1155/2020/8899630

Research Article

Experimental Study and Reliability Analysis of Flexural Capacity of RC Beams Reinforced with 600 MPa Grade Steel

Xianhua Yao, Yulong Zhang, Junfeng Guan, Lielie Li, Haichao Liu, Ruicong Han, and Junyi Xi

School of Civil Engineering and Communication, North China University of Water Resources and Electric Power, Zhengzhou 450045, China

Correspondence should be addressed to Junfeng Guan; shuaipipi88@126.com

Received 31 August 2020; Revised 11 November 2020; Accepted 23 November 2020; Published 17 December 2020

Academic Editor: Yifeng Ling

Flexural capacity of beams reinforced with 400 or 500 MPa grade steel can be accurately estimated by using equations provided in design codes. Recently, 600 MPa grade steel has evolved in the construction industry, and the applicability of existing equations for this grade of steel should be verified by performing experimental investigation. By conducting tests on concrete beams reinforced with 600 MPa grade high-strength steel, this study investigates the flexural performance for different concrete strength grades and different reinforcement ratios. Flexural capacities of concrete beams reinforced with 400 MPa, 500 MPa, and 600 MPa grade steel are analyzed based on equations in various codes and based on experimental studies in the literature. Furthermore, this study performs reliability analysis and verifies the three design values of 600 MPa grade steel yield strength in relation to the experimental performance and recommends the appropriate design values of 600 MPa grade steel yield strength. Research results show that when the measured values of yield strength of the steel bars and concrete strength are used, the ratio of the measured failure moment value to the calculated value for various beams based on different codes is nearly 1.0, demonstrating the high degree of fitting. Finally, the reliability analysis shows that the design yield strength of the 600 MPa grade high-strength steel bars should be taken as 520 MPa.

1. Introduction

In recent years, use of high-strength steel bars has improved the performance of concrete structures and reduced the amount of steel bars. High-strength steel bars (with yield strength > 500 MPa) have evolved as a new type of environmentally friendly building materials [1–4]. In the United States, South Korea, Canada, and Japan, 70% of the steel reinforcement in reinforced concrete has the strength of 400 MPa and above 25% has the strength of 500 MPa. In Germany, France, and the United Kingdom, the amount of the 500 MPa steel bar has reached 70% of the total reinforcement, and the construction industry is demanding for the 600 MPa steel bar. Based on the data of steel processing, saving 10 million tons of steel is equivalent to saving 18 million tons of iron ore, saving 6.5 million tons of standard coal, and reducing a large amount of exhaust gas and dust emissions. Therefore, the application of high-strength reinforcement can not only save energy and resources but also reduce emissions. In addition, new materials and environmentally friendly materials have always been the goal pursued by engineers and researchers [5–7]. High-strength steel with yield strength (f_y) greater than 500 MPa has been developed in several markets worldwide [8]. Development of high-strength steel with different grades has been extensively studied all over the world, such as steel grade 600 MPa [9], steel grade 700 MPa [10], steel grade 700 MPa [11], steel grade 780 MPa [12], and steel grade 800 MPa [13]. Hao et al. [14] studied the mechanical properties and microstructure of HRB600 steel bars (600 MPa grade) after subjecting to high temperature. Zhang et al. [15] studied the mechanical properties of steel fiber concrete at high temperatures. Saleem et al. [16] studied the bonding and deformation properties of reinforced concrete (RC) that used steel with

the yield strength of 690 MPa. Harries et al. [17] believed that the application of high-strength steel bars in concrete can achieve significant economic benefits. Barcley and Kowalsky [18] studied the seismic performance of high-strength RC columns, and the results showed that RC columns with steel having the yield strength of 550 MPa behaved similar to columns with steel having yield strength of 420 MPa steel bars in terms of the early stage of yield, length of plastic hinge, and capacity consumption. However, the yield strength of RC columns having 550 MPa grade steel was markedly improved. The characteristic of steel bar fracture appears under low deformation. Zhang et al. [19] found that high-strength concrete columns with HRB600 steel bars possessed good hysteretic behavior, deformability, and energy dissipation capacity as well as seismic resilience. Aldabagh and Alam [20] found that high-strength steel (HSS), i.e., ASTM A1035 grade 690, has been gaining popularity in the last two decades due to its considerably higher strength and corrosion resistance. Baek et al. [21] revealed that the shear friction resistance of grade 600 MPa (87 ksi) reinforcing bars was greater than that of 400 MPa (58 ksi) reinforcing bars. Li et al. [22] found that the combination of concrete with C80 grade and steel bars with HRB600 grade was a reasonable match for strength.

Definition of high-strength grade differs from specifying institutions. For instance, the International Organization for Standardization Standard ISO6935-2-2015 stipulates the high-strength steel bar grades as B600A-R, B600B-R, and B600C-R, the American standard ASTM A615-18el stipulates the high-strength steel grade as 100 ksi (690 MPa), the Korean standard KSD3504-2011 stipulates the high-strength steel grade as SD600 and SD700, the Singapore standard SS 560-2016 stipulates high-strength steel bar grades as B600A, B600B, and B600C, and the Chinese standard GB/T1499.2-2018, Part 2 of steel for RC, hot-rolled ribbed steel bar stipulates the high-strength steel bar as HRB600 [23]. However, the formulas for calculating the bearing capacity of RC beams made with high-strength steel bars are not the same in various countries, and even, the formulas used by different industries are sometimes different in the same country. For example, in China, reinforcing steel is produced with different standards, namely, GB 50010 [24], DL/T 5057 [25], SL/T 191 [26], JTJ 267 [27], JTG D62 [28], and TB10002.3 [29]. The applicability of equations developed for 400 MPa and 500 MPa steel bars has been generally deemed applicable for high-strength bars by various countries. However, experimental verification is necessary to determine whether high-strength steel bars based on different standards are suitable to be used as 600 MPa steel bars and whether the bars possess sufficient safety reserves. Determining the properties of materials through experiments is also a common method used by researchers [30–36]. In addition, the grades of steel bars are updated quickly, and the codes often lag behind. The current Chinese code GB 50010 Design Code for Concrete Structures stipulates that the highest yield strength of ordinary stressed steel bars is 500 MPa. Therefore, the applicability of high-strength steel bars should be urgently recognized in such codes; otherwise, it will affect its application in engineering.

Table 1: Main physical and mechanical properties of cement.

Compressive strength (MPa)				Flexural strength (MPa)				Density (kg/m^3)	
P.O42.5		P.O52.5		P.O42.5		P.O52.5		P.O42.5	P.O52.5
3 d	28 d	3d	28 d	3d	28 d	3 d	28 d	3043	3244
22.3	49.4	26.5	57.7	5.2	9.1	6.5	9.8		

Researchers have identified the safe design value of 600 MPa steel bars. However, researchers are not unanimous about the yield strength of the 600 MPa steel bar, and this causes inconvenience in design. Chen et al. [37] and Rong et al. [38] studied the flexural performance of RC beams with 600 MPa grade steel under concentrated load. The research results showed that the bending failure mode was the same as that of ordinary reinforced (HRB500 and HRB400) concrete beams. The flexural bearing capacity could still be calculated according to the equations for the flexural bearing capacity of the normal RC section specified in the current codes. When the design tensile strength of the 600 MPa grade steel bar was set to 500 MPa, sufficient safety reserve was maintained. However, Zhang et al. [39] suggested that when the yield strength of 600 MPa grade steel bars was taken as 520 MPa, the equation for design of concrete structures (GB 50010) could be safely used for calculating flexural bearing capacity of RC beams with 600 MPa steel bars. In order to study the applicability of codes from various countries in the design of RC beams with high-strength steel bars, this research experimentally investigates the flexural bearing capacity of beams with 600 MPa high-strength reinforcement and different strengths of concrete and combines the test results with those of other scholars to analyze the bearing capacity of RC beams. Finally, the reliability of the three design values (500 MPa, 520 MPa, and 545 MPa) of 600 MPa grade steel yield strength is verified in relation to the experimental results, and the appropriate design value of 600 MPa grade steel yield strength is selected.

2. Experimental Study for RC Beams with 600 MPa Steel Bars

2.1. Material. Four concrete grades were used in this experiment, denoted by C30, C40, C50, and C60. Physical and mechanical properties of cement are shown in Table 1 (Chinese standard GB 175 2007 [40]). Fine aggregate used in this experiment was river sand with the maximum size of 2.5 mm. Material properties of the river sand are presented in Table 2. Coarse aggregate used in this experiment was crushed aggregate, and its properties are shown in Table 3. A high-range water-reducing admixture was used to achieve good workability. Concrete mixture proportion for the four grades of concrete can be found in Table 4.

The size, reinforcement arrangement, and material properties of tested beams are listed in Table 5. In the table, f_{cu} (average value from three cubes with the dimensions of 150 mm × 150 mm × 150 mm) is the cube compressive strength and f_{ts} (average value from three cubes with the dimensions of 150 mm × 150 mm × 150 mm) is the splitting

Table 2: Machine-made sand.

Apparent density (kg/m^3)	Sediment percentage	Bulk density (kg/m^3)	Fineness modulus
2700	0.5	1610	2.6

Table 3: Coarse aggregate.

Apparent density (kg/m^3)	Sediment percentage	Bulk density (kg/m^3)	Particle size distribution (mm)
2710	0.3	1630	5–20

Table 4: Concrete mixture proportion.

Mixture	Cement, (kg/m^3)	Water, (kg/m^3)	w/c	Aggregate (kg/m^3)			Sand (kg/m^3)	High-range water-reducing admixture (kg/m^3)
				5 to 10 (mm)	10 to 16 (mm)	16 to 20 (mm)		
C30	378 (no. 42.5)	189	0.50	491	328	273	758	1.89
C40	473 (no. 42.5)	189	0.40	491	328	273	670	3.31
C50	473 (no. 52.5)	189	0.40	491	328	273	698	3.31
C60	630 (no. 52.5)	189	0.30	458	305	254	624	5.04

Table 5: Size and reinforcement and material properties of tested beams.

RC beam number	Width b/mm	Depth h/mm	Effective span l_0/mm	Concrete cover c/mm	Steel ratio ρ/100%	Reinforcement			Concrete			
						A_s/mm^2	f_y/MPa	E_s/GPa	f_{cu}/MPa	f_{ck}/MPa	f_{ts}/MPa	$E_c \times 10^4$/MPa
600-C30-1-1	200	350	2550	30	0. 8	509	645.02	195	37.65	26.36	1.97	3.80
600-C30-1-2	200	350	2550	30	0. 8	509	645.02	195	37.65	26.36	1.97	3.80
600-C30-2-1	200	350	2550	30	0. 5	308	635.71	198	37.65	26.36	1.97	3.80
600-C30-2-2	200	350	2550	30	0. 5	308	635.71	198	37.65	26.36	1.97	3.80
600-C40-1-1	200	350	2550	30	0. 8	509	645.02	195	42.55	32.19	2.69	3.70
600-C40-1-2	200	350	2550	30	0. 8	509	645.02	195	42.55	32.19	2.69	3.70
600-C40-2-1	200	350	2550	30	0. 5	308	635.71	198	42.55	32.19	2.69	3.70
600-C40-2-2	200	350	2550	30	0. 5	309	635.71	198	42.55	32.19	2.69	3.70
600-C50-1-1	200	350	2550	30	0.8	509	645.02	195	53.00	33.28	3.40	3.70
600-C50-1-2	200	350	2550	30	0. 8	509	645.02	195	53.00	33.28	3.40	3.70
600-C50-2-1	200	350	2550	30	0. 5	308	635.71	198	53.00	33.28	3.40	3.70
600-C50-2-2	200	350	2550	30	0. 5	308	635.71	198	53.00	33.28	3.40	3.70
600-C60-1-1	200	350	2550	30	0. 8	509	645.02	195	67.14	62.31	3.35	4.10
600-C60-1-2	200	350	2550	30	0. 8	509	645.02	195	67.14	62.31	3.35	4.10
600-C60-2-1	200	350	2550	30	0. 5	308	645.02	198	66.31	61.75	3.35	4.10
600-C60-2-2	200	350	2550	30	0. 5	308	645.02	198	66.31	61.75	3.35	4.10
400-C60-1-1	200	350	2550	30	0. 8	509	428.07	200	67.14	62.31	3.35	4.10
400-C60-1-2	200	350	2550	30	0. 8	509	428.07	200	67.14	62.31	3.35	4.10

tensile strength. Similarly, f_{ck} (average value from three prisms with the dimensions of 150 mm × 150 mm × 300 mm) is the prism compressive strength and E_c (average value from three prisms with the dimensions of 150 mm × 150 mm × 300 mm) is the elastic modulus.

2.2. Design and Test of RC Beams. In this experiment, 8 groups (2 beams from each group based on the concrete grade) of RC beams were tested. All beams were cast using 600 MPa grade reinforcing steel. 2 RC beams with C60 grade concrete and the steel grade of 400 MPa were cast as a control group. As shown in Figure 1, the two points of the midspan section were symmetrically loaded to form an 800 mm pure bending section. The load application was based on the design bending moment of the purely bent section. The concrete beam was tested under static loading with consideration of the effects of the beam's own weight and the loading equipment. The load values at all levels were controlled by the readings of the data acquisition system connected to the sensor.

2.3. Stress-Strain Curves of 600 MPa Steel Bar. In this study, 600 MPa grade reinforcement was used as longitudinal reinforcement of the test beam. Figure 3 shows the stress-strain curve of the 600 MPa rebar as obtained from a test. The stress-strain curve of the 600 MPa steel bar shows three stages with a clear yield plateau: elasticity, yielding, and stress hardening. Yield strength f_y and ultimate strength f_u of the 600 MPa rebar with different diameters were between 635.71 MPa and 645.02 MPa, and 819.92 MPa to 840.38 MPa, respectively. The Chinese standard GB50010-2010 specifies the measured maximum force total elongation A_{gt} of steel bars should not be less than 9%. The measured A_{gt} of 600 MPa grade steel bars was 10.3%.

2.4. Failure Mode and Load-Deformation Curves of RC Beam. The actual failure mode of the RC beam belongs to proper-reinforced beam failure. As shown in Figure 4, the actual failure state of the test beam is shown that the beam has obvious plastic deformation and fracture precursor before failure. In addition, the load-deformation curves show typical three stage of proper-reinforced beam failure, as shown in Figure 5. The deformation of the specimen increased linearly before cracking. When the external load reached the cracking bending moment M_{cr} ((20%–30%)M_u), one or several initial cracks appeared in the pure bending section of the RC beam, the deformation curves exhibited an abrupt transition point, and the slopes of the curves began to decrease. With a further increase in load, when the strength of the 600 MPa steel bar reached its yield strength, the deformation of the specimens increased sharply, a second and more obvious inflection point appeared on the load-deformation curve, and the concrete in the RC beam was crushed. Therefore, the 600 MPa steel RC beam is the balanced-reinforced beam.

As shown in Figure 5, when the strength grade of concrete was the same, the bearing capacity of the specimen increased with an increase in reinforcement ratio. On the other hand, the ductility of specimens decreased with an increase in the reinforcement ratio. When the ratio of reinforcement was the same, the bearing capacity of the specimen increased with an increase in the concrete strength grade.

3. Results and Discussion

3.1. Analytical Ultimate Bearing Capacity Based on Codes from Various Countries. The calculation methods for the bearing capacity from various Chinese standards are based on the test results of 335 MPa, 400 MPa, and 500 MPa RC beams. Whether the method is applicable to the calculation of the bearing capacity of 600 MPa RC beams is still uncertain. This needs to be verified based on the test data of 600 MPa RC beams.

By comparing the bearing capacity equations of various national codes (GB 50010-2010 [24], SL 191-2008 [26],DL/T5057-2009 [25], JTG D62-2004 [27], ACI 318-2014 [41], EN1992-1-1 [42], CRC Press LLC, 1999 [43], BS5400-4 [44, 45], EN1991-2 [46], and AASHTOLRFD Bridge Design Specification [47]), it can be found that the calculation methods for the bearing capacity of rectangular cross section RC beams in the current Chinese codes and European and American codes are consistent in expression and symbolic connotation. However, there are subtle differences in the strength calculation and height calculation methods of the concrete equivalent rectangular stress diagram. Therefore, the actual measured value of the bearing capacity of 400 MPa, 500 MPa, and 600 MPa RC beams and the calculated values based on various codes are compared and analyzed to verify their applicability.

3.2. Analysis of Moment of Resistance of Beams with 400 MPa Grade Steel. The literature [48–53] reports flexural performance tests of concrete beams reinforced with 400 MPa grade steel, and the relevant information of the specimens is shown in Table 6.

In order to verify the applicability of the bearing capacity equations of the existing national codes, measured flexural bearing capacity of RC beams is compared with the calculated value based on various codes. The comparison of the measured value M_u and the calculated value M_{uc} is shown in Table 7 and Figure 6. It can be seen that all codes have good accuracy for the calculation of the flexural bearing capacity of concrete beams using 400 MPa grade steel bars ($\mu = 1.01–1.17$ and $\delta = 0.08–0.1$).

3.3. Analysis of Moment of Resistance of Beams with 500 MPa Grade Steel. References [52, 54–60] conducted flexural performance tests of concrete beams reinforced with 500 MPa grade steel. The relevant information of the specimens is shown in Table 8. In order to verify the applicability of the bearing capacity equations of the existing national codes, measured flexural bearing capacity of RC beams is compared with the calculated value based on various codes. The comparison of the measured value M_u of

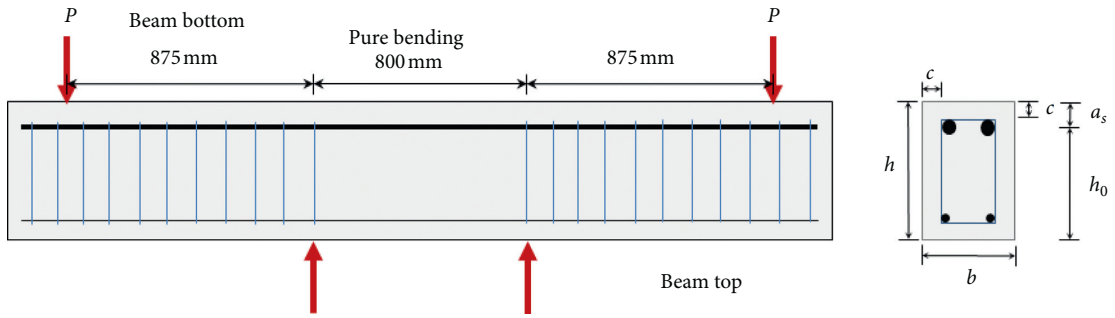

Figure 1: Geometry of RC beams.

Figure 2: Actual RC beams with 600 MPa steel bars and the test device.

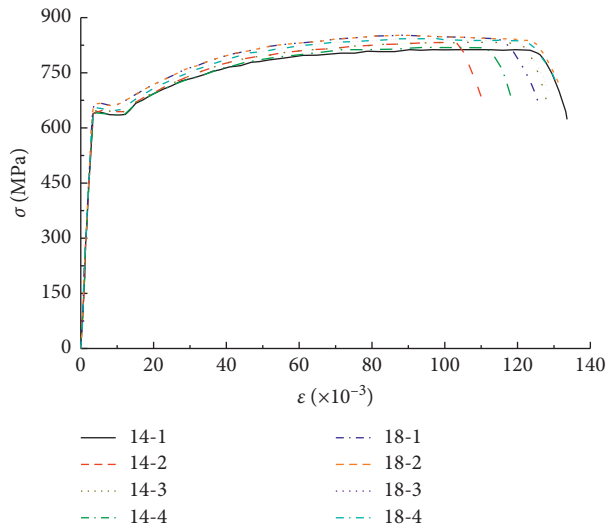

Figure 3: Stress-strain curves of 600 MPa steel bars.

the flexural bearing capacity of the test beams with 500 MPa steel bars and the calculated value M_{uc} based on different codes is shown in Table 9 and Figure 7. It can be seen that all codes have good accuracy for the calculation of the bending bearing capacity of 500 MPa RC beams ($\mu = 1.01–1.22$ and $\delta = 0.09–0.11$).

3.4. Analysis of Moment of Resistance of Beams with 600 MPa Grade Steel. Several studies [39, 52, 53, 61] conducted flexural performance tests of RC beams reinforced with 600 MPa grade steel. The relevant information of the RC beams in those studies is shown in Table 10. In order to verify the applicability of the bearing capacity equation in the current national standard, results from the experiment in this study are compared with the measured values of the flexural bearing capacity of RC beams in the literature and with the calculated value based on the national standard. Measured value M_u of the flexural bearing capacity of the RC beam reinforced with 600 MPa grade steel is compared with

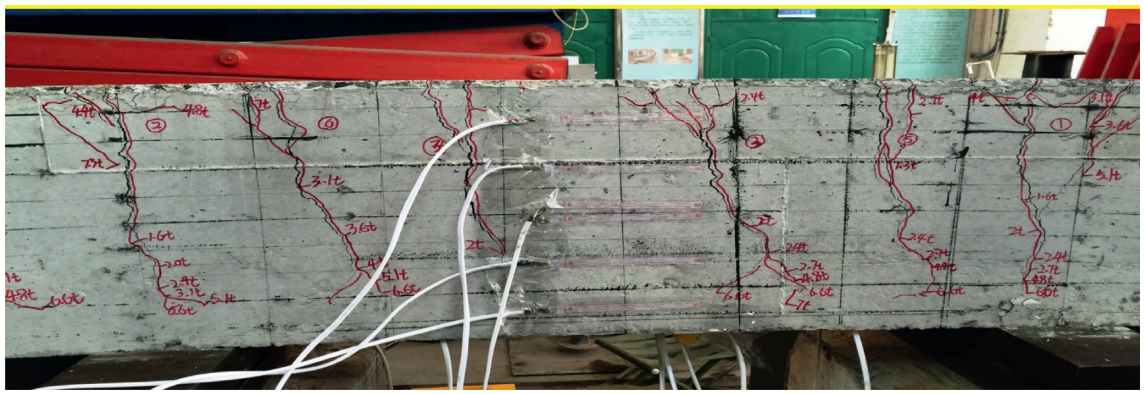

Figure 4: Actual failure mode of the RC beam.

the calculated value M_{uc} based on various codes as shown in Table 11 and Figure 8. Due to the differences in the size of the members designed by different scholars and the properties of the materials used in the experiment and other influencing factors during the experiment, the results have certain differences but the difference is small. The average value μ of the ratio between the measured value and the calculated value of the ultimate bearing capacity based on the codes is 1.10~1.27, and the dispersion coefficient δ is 0.07~0.08. As shown in Figure 8, the measured values of the ultimate bearing capacity of RC beams with 400 MPa and 500 MPa grade steel are in good agreement with the calculated values of various codes. The data of the configuration of RC beams with 600 MPa grade steel and the configuration of RC beams with 400 MPa and 500 MPa grade steel are similar (the ratio of the measured value of the flexural bearing capacity of RC beams to the calculated values of various codes is around 1.0 for all cases), and the dispersion coefficients are small. In general, the measured value of the ultimate bearing capacity of 600 MPa RC beams coincided with the ultimate bearing capacity calculated from various codes. Therefore, the existing equations in the Chinese code are still applicable to RC beams reinforced with high-strength (600 MPa) steel.

4. Reliability Analysis of Bearing Capacity

For an RC beam using 600 MPa grade steel, the design values of the yield strength of reinforcement taken by different scholars are different, such as 500 MPa and 520 MPa. In order to determine the appropriate yield strength design value of the 600 MPa grade steel bar in a design specification, this study took the basis of the experiment and the reference standard GB 50010 [24]. The material subentry coefficients as per the standard are 1.1, 1.1, and 1.15, respectively, for the 335 MPa, 400 MPa, and 500 MPa grade steel (yield strength design value of the steel bar determined by many engineering practice and the material subentry coefficient is the ratio of the standard value to the design value of yield strength). Accordingly, the trial design value of the yield strength of 600 MPa grade steel was taken as 500 MPa, 520 MPa, and 545 MPa, corresponding to the material subentry coefficients of 1.1, 1.15, and 1.2, respectively. Reliability analysis was performed to determine the most appropriate value. On the basis of the experimental study, the reliability analysis of the above three values was carried out to further select the design value of yield strength which would meet the requirements of both strength and reliability.

In the reliability analysis of the flexural bearing capacity of the 600 MPa RC beam, the known function is shown in equation (1), where the structural resistance R obeys the log-normal distribution and the dead load S_G obeys the normal distribution. The load S_Q obeys the extreme value type I distribution [62]. The most commonly used method for reliability calculation is the first-order second-moment method, including the center point method and the checking point method. The center point method does not take into account the probability distribution of variables, while the JC method (checking point method) can handle other random variables of probability distributions [63, 64]. In order to consider the probability distribution and correlation of random variables, this paper used the JC method to calculate the reliability of the flexural bearing capacity of 600 MPa RC beams and used MATLAB software to solve the problem:

$$R - S_G - S_Q = 0. \tag{1}$$

4.1. Reliability Index of Beams with Different Yield Strength Values of Steel Bars. In order to select the most suitable design value of the steel bar, the reliability index was calculated for different strength design values for the steel bar. In the process of determining the reliability index, statistical parameters of various loads of RC beams were referred to the specifications GB 50153 [65] and GB 50009 [66]. The standard value of moment of resistance was calculated by taking the reinforcement strength of 600 MPa and substituting it into the bending bearing capacity formula of GB 50010. Minimum ratio of the dead load to the variable load was determined under the condition that only the self-weight was considered as the dead load. According to the determined calculation parameters, the JC method was used to calculate the reliability index of RC beams.

As shown in Figure 9, for a given constant load to variable load ratio ρ, the reliability index of each RC beam was basically the same for different yield strength values of

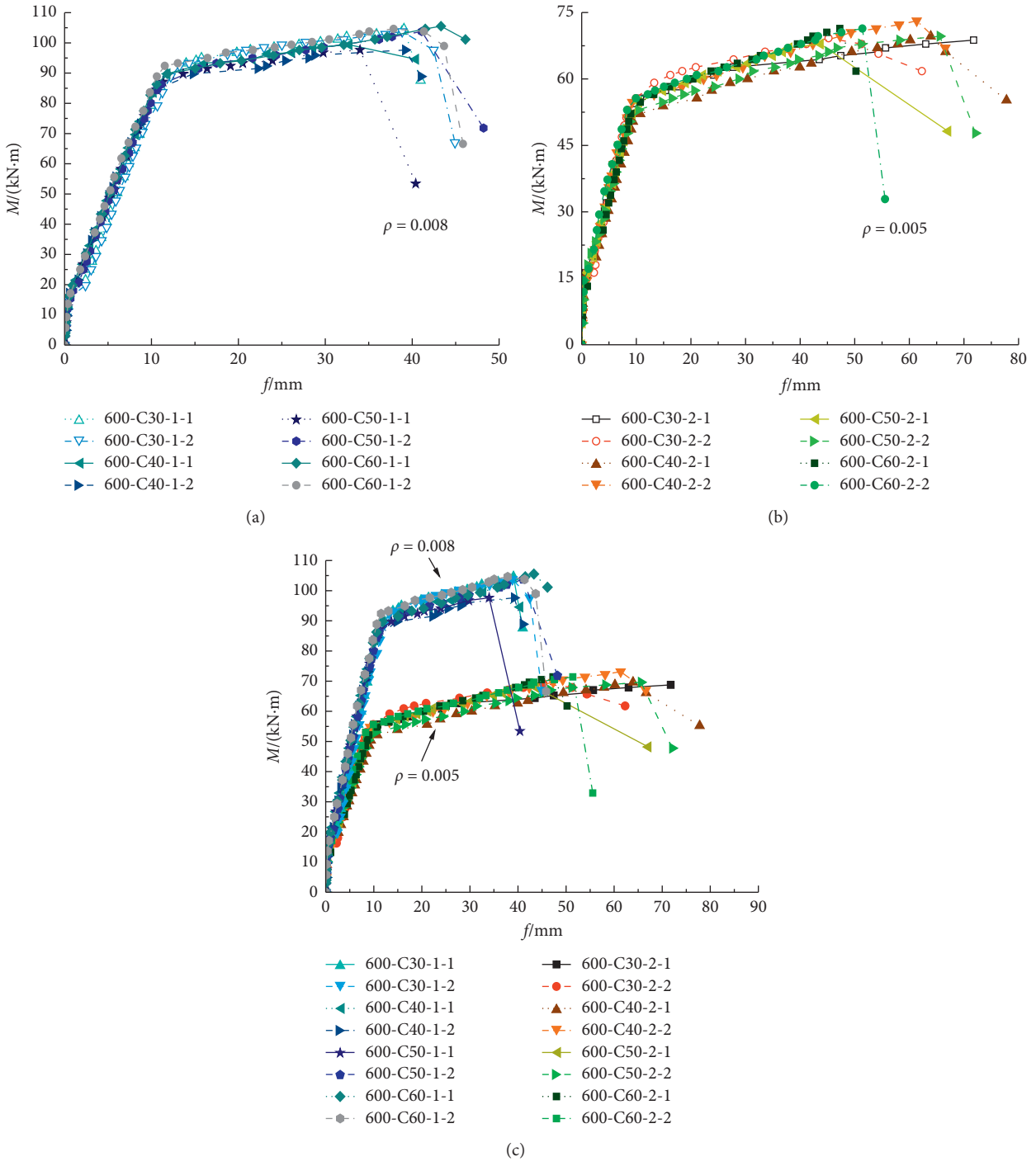

Figure 5: The load-deformation curves for RC beams.

steel. When dead load was the controlling load, that is, when ρ was less than 2.8, the reliability index of the beam increased continuously with an increase in ρ value and with an increased rate. When the loading was dominated by the variable load, that is, when ρ was greater than 2.8, the reliability index still increased to a certain extent as the value of ρ increased. When ρ was approximately 7, the reliability index reached its peak, after which the reliability index decreased marginally and then gradually stabilized. The reliability index of each RC beam was different for different design values of steel yield strength. Generally speaking, the reliability decreased as the design yield strength increased. For the steel with the strength of 600 MPa, when the design yield strength was taken as 500 MPa, the reliability was the largest and it was followed by 520 MPa, and the smallest reliability index was observed corresponding to the yield strength of 545 MPa. For beams with a concrete strength grade of C60, two types of steel bars, namely, HRB600 and

Table 6: Details of beams with 400 MPa steel bars.

Data sources	RC beam number	b/mm	h/mm	l_0/mm	c/mm	ρ/100%	Reinforcement			Concrete			
							A_s/mm^2	fy/MPa	Es/GPa	Fcu/MPa	Fck/MPa	fts/MPa	$Ec \times 104$/MPa
[48]	SB-1	200	400	2210	30	0.9	628	470	200	18.80	14.30	1.99	2.47
	SB-2	200	400	2210	30	0.7	509	533	200	23.50	17.90	2.24	2.72
	SB-3	200	400	2210	30	0.6	461	493	200	15.50	11.80	1.78	2.25
[49]	L-1	200	400	3300	30	0.9	628	450	200	29.67	19.84	1.42	2.97
	L-2	200	400	3300	30	1.3	928	455	200	33.53	22.42	1.48	3.09
	L-3	200	400	3300	30	1.3	942	457	200	24.32	16.26	1.25	2.76
	L-4	200	400	3300	30	0.9	628	485	200	27.64	18.48	1.36	2.89
	TL-1	200	400	4300	30	0.9	628	465	200	27.38	18.50	1.36	2.88
	TL-2	200	400	4300	30	0.9	628	475	200	22.22	14.68	1.18	2.66
[50]	L-1	152	304	1800	30	0.5	226	504	200	47.75	28.64	2.44	3.32
	L-2	150	304	1800	30	0.8	339	504	200	40.90	27.50	2.38	3.28
	L-3	153	305	1800	30	1.2	509	479	200	42.75	28.64	2.44	3.32
	L-4	150	305	1800	30	1.2	509	458	200	41.00	27.47	2.38	3.28
	L-5	151	304	1800	30	—	308	448	200	42.80	28.68	2.44	3.32
	L-6	149	305	1800	30	1.3	509	479	200	44.60	29.88	2.50	3.36
[51]	B4A	180	300	3000	30	0.5	226	405	—	41.60	27.8	2.8	3.31
	B4B	180	300	3000	30	0.7	339	405	—	41.60	27.8	2.8	3.31
	B4C	180	300	3000	30	1.1	515	452	—	41.60	27.8	2.8	3.31
	B4D	180	300	3000	30	1.5	716	452	—	41.60	27.8	2.8	3.31
[52]	L7	250	400	3400	35	1.5	1521	360	200	—	14.3	1.432	3.0
	L8	250	400	3400	35	1.5	1521	360		—	23.1	1.89	3.45
	L9	250	400	3400	35	1.5	1521	360	200	—	27.5	2.04	3.6
[53]	LW-5	200	400	3000	25	2.0	1473	445	—	29.1	19.5	2.22	—

Note. Symbol "—" means that the parameter has no relevant data in the literature.

HRB400, were used. The curve of the reliability of RC beams with ρ value is shown in Figure 10. When the design yield strength of the HRB600 steel bar was taken as 500 MPa and 520 MPa, the reliability of the beam was greater than that when the HRB400 steel bar was used. However, when the design yield strength of the HRB600 steel bar was 545 MPa, the reliability of the beam was less than that of the beam using the HRB400 steel bar.

The minimum reliability index can reflect the reliability performance of the component under the most unfavorable conditions, so statistical analysis was necessary to determine the minimum reliability index of the beam. Table 12 shows the minimum value of the reliability index of the C60 test beams under different conditions. For C60 beams equipped with HRB600 steel bars, the minimum reliability index corresponding to the reinforcement ratio of 0.005 was greater than the index corresponding to the reinforcement ratio of 0.008. For a given reinforcement ratio, the minimum reliability index decreased with an increase in the design yield strength of the steel bar. This study calculated the average value of the minimum reliability index corresponding to HRB600 RC beams under different reinforcement ratios. When the design yield strength was 520 MPa, the minimum reliability index average value was 3.172, which is closest to the code specified value and basically meets the reliability criterion. The failure probabilities of the HRB400 RC beam and that of the HRB600 RC beam with the design yield strength of 500 MPa and 520 MPa were comparable to the standard failure probability. When the design yield strength of the HRB600 steel bar was taken as 545 MPa, the beam's failure probability was an order of magnitude smaller than the normative failure probability.

When designing the bearing capacity of a beam, considering that the beam should have sufficient safety protection, the design value of the bearing capacity of the component is generally less than the ultimate bearing capacity. Table 13 compares the measured value of the bearing capacity for all test beams with the calculated value when design yield strength of the steel bars was taken as 520 MPa. As shown in the table, the calculated value of the ultimate bearing capacity of each test beam obtained from the existing Chinese code <cite> equation is less than the actual measured value of the ultimate bearing capacity, demonstrating a larger safety reserve ($\mu = 1.36$~1.59 and $\delta = 0.05$~0.06).

On the basis of the experiment and practice, 500 MPa, 520 MPa, and 545 MPa were selected as the possibly appropriate design value of yield strength of the 600 MPa grade reinforcement. Reliability analysis showed that 500 MPa and 520 MPa met the reliability requirements. Moreover, use of 520 MPa as the design value showed a large strength surplus

Table 7: Comparison of experimental flexural bearing capacity M_u with M_{uc} calculated by different codes for beams with 400 MPa steel bars.

Data sources	RC beam number	GB50010-2010 M_u/M_{uc}	SL191-2008 M_u/M_{uc}	DL/T5057-2009 M_u/M_{uc}	JTGD62-2012 M_u/M_{uc}	ACI318-2014 M_u/M_{uc}
Test	400-C60-1-1	1.14	1.14	1.14	1.14	1.14
	400-C60-1-2	1.07	1.07	1.07	1.07	1.07
[48]	SB-1	1.17	1.17	1.17	1.17	1.21
	SB-2	0.98	0.98	0.98	0.98	1.00
	SB-3	1.06	1.06	1.06	1.06	1.09
[49]	L-1	0.97	0.97	0.97	0.97	0.99
	L-2	0.95	0.95	0.95	0.95	0.98
	L-3	0.99	0.99	0.99	0.99	1.03
	L-4	1.00	1.00	1.00	1.00	1.02
	TL-1	1.06	1.06	1.06	1.06	1.08
	TL-2	1.10	1.10	1.10	1.10	1.13
[50]	L-1	1.09	1.09	1.09	1.09	1.10
	L-2	1.09	1.09	1.09	1.09	1.11
	L-3	1.04	1.04	1.04	1.04	1.06
	L-4	1.08	1.08	1.08	1.08	1.10
	L-5	1.08	1.08	1.08	1.08	1.09
	L-6	1.12	1.12	1.12	1.12	1.14
[51]	B4A	0.98	0.98	0.98	0.98	0.99
	B4B	0.93	0.93	0.93	0.93	0.94
	B4C	0.89	0.89	0.89	0.89	0.90
	B4D	0.93	0.93	0.93	0.93	0.95
[52]	L7	0.90	0.90	0.90	0.90	0.95
	L8	0.89	0.89	0.89	0.89	0.91
	L9	0.88	0.88	0.88	0.88	0.90
[53]	LW-5	1.10	1.10	1.10	1.10	1.16
μ	—	1.02	1.02	1.02	1.02	1.04
δ	—	0.08	0.08	0.08	0.08	0.08
Data sources	RC beam number	EN 1992-1-1 M_u/M_{uc}	BS5400-4 M_u/M_{uc}	AASHEO M_u/M_{uc}	EN1991-2 2003 M_u/M_{uc}	CRC PRESS M_u/M_{uc}
Test	400-C60-1-1	1.23	1.31	1.14	1.14	1.14
	400-C60-1-2	1.15	1.22	1.07	1.06	1.07
[48]	SB-1	1.17	1.35	1.21	1.17	1.21
	SB-2	0.98	1.13	1.00	0.98	1.00
	SB-3	1.06	1.22	1.09	1.06	1.09
[49]	L-1	0.97	1.12	0.99	0.97	0.99
	L-2	0.95	1.09	0.98	0.95	0.98
	L-3	0.99	1.14	1.03	0.99	1.03
	L-4	1.00	1.15	1.02	1.00	1.02
	TL-1	1.06	1.21	1.08	1.06	1.08
	TL-2	1.10	1.26	1.13	1.10	1.13
[50]	L-1	1.09	1.25	1.10	1.09	1.10
	L-2	1.09	1.25	1.11	1.09	1.11
	L-3	1.04	1.19	1.06	1.04	1.06
	L-4	1.08	1.24	1.10	1.08	1.10
	L-5	1.08	1.24	1.09	1.08	1.09
	L-6	1.12	1.29	1.14	1.12	1.14
[51]	B4A	0.98	1.13	0.99	0.95	0.99
	B4B	0.93	1.07	0.94	0.88	0.94
	B4C	0.89	1.02	0.90	0.81	0.90
	B4D	0.93	1.07	0.95	0.82	0.95
[52]	L7	0.90	1.04	0.95	0.90	0.95
	L8	0.89	1.02	0.91	0.89	0.91
	L9	0.88	1.01	0.90	0.88	0.90
[53]	LW-5	1.10	1.15	1.16	1.13	0.98
μ	—	1.03	1.17	1.04	1.01	1.04
δ	—	0.09	0.08	0.08	0.10	0.08

Note. M_u in the table is the measured ultimate flexural bearing capacity and M_{uc} is the calculated value of ultimate flexural bearing capacity obtained by taking the measured yield strength of reinforcement from the current code formulas.

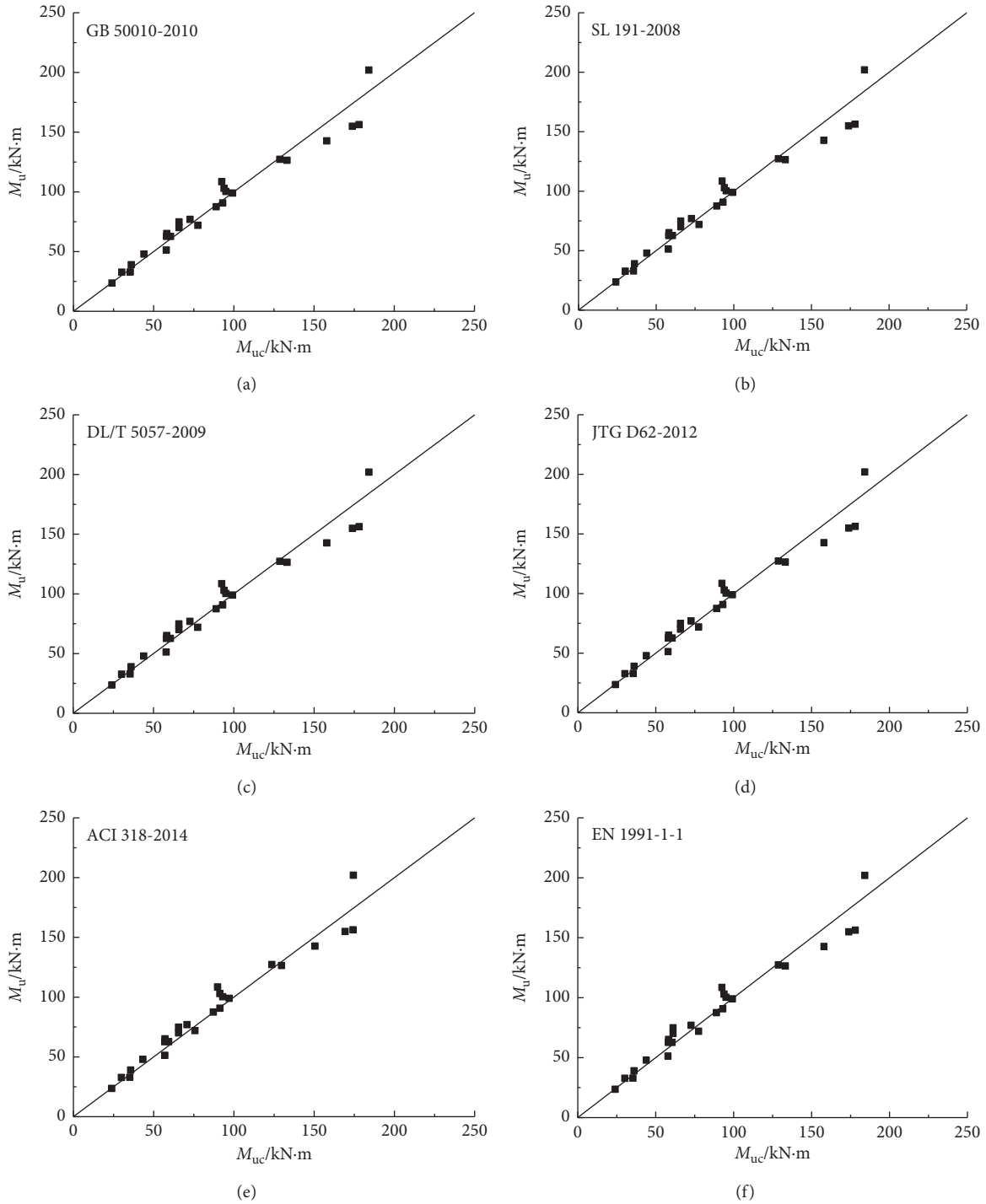

Figure 6: Continued.

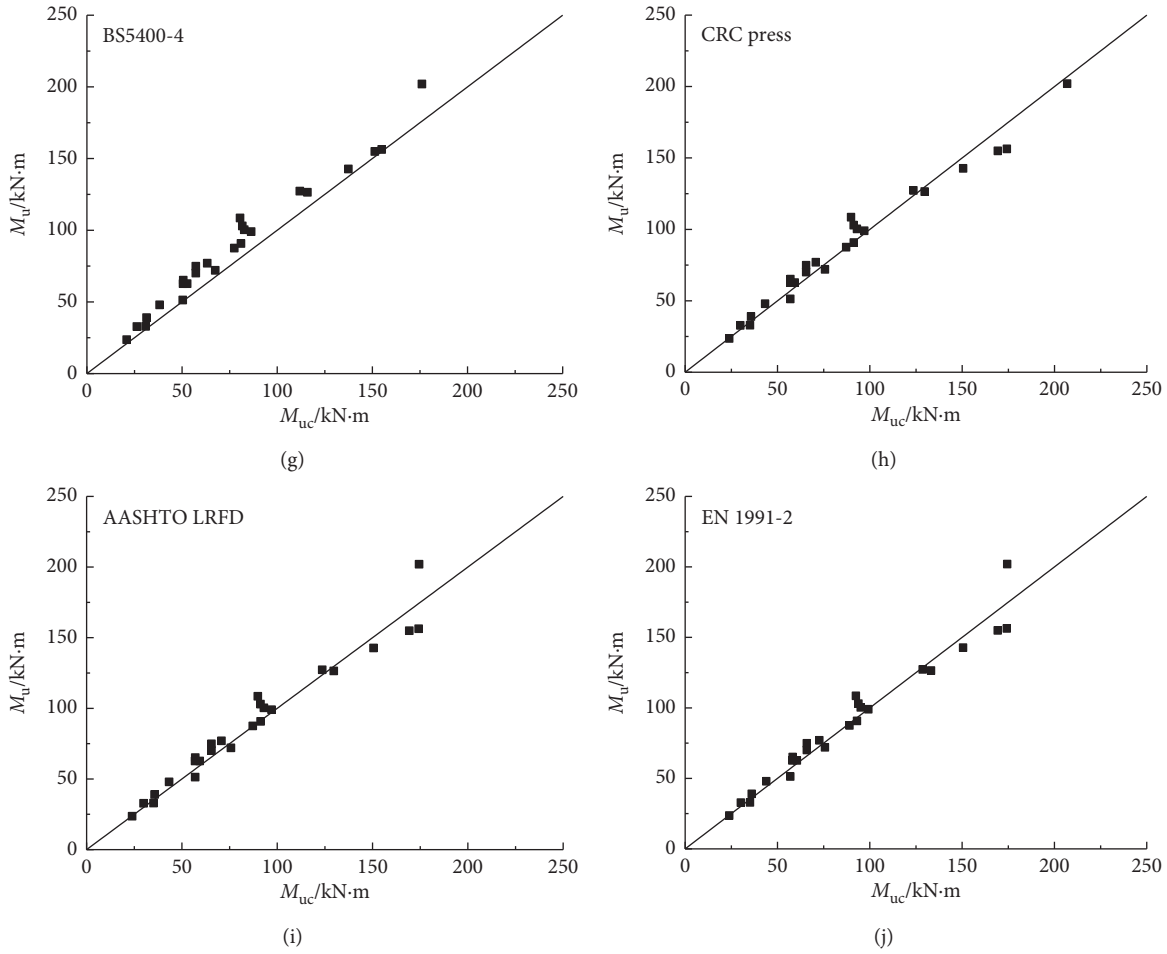

Figure 6: Comparison of experimental flexural bearing capacity M_u with M_{uc} calculated by different codes for beams with 400 MPa steel bars.

Table 8: Details of beams with 500 MPa steel bars.

Data sources	RC beam number	b/mm	h/mm	$l0$/mm	c/mm	ρ/100%	Reinforcement			Concrete			
							A_s/mm^2	f_y/MPa	E_s/GPa	f_{cu}/MPa	f_{ck}/MPa	f_{ts}/MPa	$E_c \times 10^4$/MPa
[54]	LW1	200	400	3200	30	0.8	603	567.3	210	43.4	27.3	2.66	3.33
	LW2	200	400	3200	30	0.8	603	567.3	210	47.8	30.4	2.79	3.42
	LW3	200	400	3200	30	0.8	603	567.3	210	56.2	34.3	2.97	3.55
	LW4	200	400	3200	30	1.3	982	502.8	210	43.4	27.3	2.66	3.33
	LW5	200	400	3200	30	1.3	982	502.8	210	47.8	30.4	2.79	3.42
	LW6	200	400	3200	30	1.3	982	502.8	210	56.2	34.3	2.97	3.55
	LW7	200	400	3200	30	2.1	1608	522.5	210	47.8	30.4	2.79	3.42
[55]	FB1	200	400	3000	30	0.4	339	515	211	23.3	15.6	1.96	2.71
	FB2	200	410	3000	30	0.6	509	567	213	28.1	18.8	2.18	2.91
	FB3	200	399	3000	30	1.2	982	537	205	25.7	17.2	2.07	2.82
	FB4	200	403	3000	30	0.4	339	515	211	33.4	22.3	2.39	3.09
	FB5	200	401	3000	30	0.6	509	567	213	33.5	22.4	2.4	3.09
	FB6	200	405	3000	30	1.2	982	537	205	32.1	21.5	2.34	3.05
	FB7	200	395	3000	30	0.4	339	515	211	40.6	27.1	2.67	3.27
	FB8	200	406	3000	30	0.6	509	567	213	40.7	27.2	2.67	3.28
	FB9	200	402	3000	30	1.2	982	537	205	40.3	27	2.65	3.27
[56]	B5F1	250	400	3600	30	0.7	603	549.5	200	—	22.74	2.16	3.11
	B5F2	250	400	3600	30	1.1	982	495	200	—	22.74	2.16	3.11
	B5F3	250	400	3600	30	0.7	603	549.5	200	—	36.2	2.77	3.55
	B5F4	250	400	3600	30	1.1	982	495	200	—	36.2	2.77	3.55

Table 8: Continued.

Data sources	RC beam number	b/mm	h/mm	$l0$/mm	c/mm	ρ/100%	Reinforcement			Concrete			
							A_s/mm^2	f_y/MPa	E_s/GPa	f_{cu}/MPa	f_{ck}/MPa	f_{ts}/MPa	$E_c \times 10^4$/MPa
[57]	LW1	204	400	3200	30	0.8	603	567.3	200	41.3	27.3	2.66	3.29
	LW2	202	400	3200	30	0.8	603	567.3	200	45.5	30	2.79	3.38
	LW3	202	400	3200	30	0.8	603	567.3	200	53.5	34.3	2.97	3.51
	LW4	199	400	3200	30	1.3	982	502.8	200	41.3	27.3	2.66	3.29
	LW5	200	400	3200	30	1.3	982	502.8	200	45.5	30	2.79	3.38
	LW6	199	400	3200	30	1.3	982	502.8	200	53.5	34.3	2.97	3.51
	LW7	200	400	3200	30	2.2	1608	522.5	200	45.5	30	2.79	3.38
[58]	L1	202	405	3200	30	0.6	462	525	200	21.42	14.33	1.87	2.62
	L2	204	400	3200	30	0.8	603	550	200	21.42	14.33	1.87	2.62
	L3	198	401	3200	30	1.0	760	530	200	21.42	14.33	1.87	2.62
	L4	201	402	3200	30	1.3	982	505	200	21.42	14.33	1.87	2.62
	LX1-A	200	402	3200	30	0.6	462	525	200	22.1	14.78	1.91	2.65
	LX2-A	199	402	3200	30	0.8	603	550	200	22.1	14.78	1.91	2.65
	LX3-A	202	400	3200	30	1.0	760	530	200	22.1	14.78	1.91	2.65
	LX4-A	201	403	3200	30	1.3	982	505	200	22.1	14.78	1.91	2.65
	LX1-B	203	402	3200	30	0.6	462	525	200	21.01	14.05	1.86	2.6
	LX2-B	200	401	3200	30	0.8	603	550	200	21.01	14.05	1.86	2.6
	LX3-B	203	400	3200	30	1.0	760	530	200	21.01	14.05	1.86	2.6
	LX4-B	202	401	3200	30	1.3	982	505	200	21.01	14.05	1.86	2.6
[59]	L1-A	149	305	2800	30	0.2	100	540	200	27.96	18.7	2.47	2.91
	L1-B	253	305	2800	30	0.2	100	540	200	27.96	18.7	2.47	2.91
	L1-C	150	303	2800	30	0.2	100	540	200	42.67	28.54	3.11	3.32
	L2-A	152	310	2800	30	1.0	399	502	200	46.31	30.97	3.26	3.39
	L2-B	150	308	2800	30	1.0	399	502	200	49.51	33.11	3.38	3.45
	L3-A	150	315	2800	30	1.4	599	502	200	48.34	32.33	3.33	3.43
	L3-B	150	301	2800	30	1.5	599	502	200	42.7	28.56	3.11	3.32
	L4-A	151	303	2800	30	2.2	799	502	200	52.1	34.84	3.47	3.49
	L4-B	152	306	2800	30	2.2	799	502	200	52.1	34.84	3.47	3.49
	L5-A	149	303	2800	30	2.8	999	502	200	46.75	31.27	3.27	3.4
	L5-B	148	305	2800	30	2.8	999	502	200	46.75	31.27	2.27	3.4
[60]	B-N2	200	250	3080	26	1.2	509	530	—	—	48.61	3.69	2.46
	B-N3	200	250	3080	26	1.8	763	530	—	—	48.61	3.69	2.46
	B-N4	200	250	3080	26	2.4	1018	530	—	—	48.61	3.69	2.46
	B-M2	200	250	3080	26	1.2	509	530	—	—	78.5	5.05	3.54
	B-M3	200	250	3080	26	1.8	763	530	—	—	78.5	5.05	3.54
	B-M4	200	250	3080	26	2.4	1018	530	—	—	78.5	5.05	3.54
	B-H2	200	250	3080	26	1.2	509	530	—	—	102.4	5.59	3.84
	B-H3	200	250	3080	26	1.8	763	530	—	—	102.4	5.59	3.84
	B-H4	200	250	3080	26	2.4	1018	530	—	—	102.4	5.59	3.84
[52]	L4	250	400	3400	35	1.3	1257	435	200	—	14.3	1.432	3
	L5	250	400	3400	35	1.3	1257	435	200	—	23.1	1.89	3.45
	L6	250	400	3400	35	1.3	1257	435	200	—	27.5	2.04	3.6

Note. Symbol "—" means that the parameter has no relevant data in the literature.

when checked for a strength criterion. According to the analysis results, the strength utilization ratio of reinforcement was considered to meet the requirements of strength and reliability, and hence, the appropriate design yield strength of the 600 MPa grade steel bar was selected as 520 MPa.

4.2. Reliable Indicators of Beams under Different Concrete Strength Grades. In the reliability calculation, parameters are divided into deterministic variables and random variables. The deterministic random variables include geometric parameters and design parameters, such as cover thickness and reinforcement ratio. The random variables are load and material parameters, such as concrete strength, reinforcement strength, constant load, and variable load [67–69]. It can be seen from the above analysis that the influence of constant load and variable load on the reliability index of the beam is such that the reliability index of the test beam increased with an increase in the constant load to variable load ratio. When the load ratio reached a certain value, the reliability index of the beam became approximately constant. In order to study the influence of the concrete strength grade on the reliability index, the index was calculated for RC

Table 9: Comparison experimental flexural bearing capacity Mu with Muc calculated by different codes for beams with 500 MPa steel bars.

Data sources	RC beams number	GB50010 -2010 M_u/M_{uc}	SL191 -2008 M_u/M_{uc}	DL/T5057 -2009 M_u/M_{uc}	JTG D62-2012 M_u/M_{uc}	ACI 318-2014 M_u/M_{uc}
[54]	LW-1	0.93	0.93	0.93	0.93	0.95
	LW-2	1.01	1.01	1.01	1.01	1.02
	LW-3	1.18	1.18	1.18	1.18	1.19
	LW-4	0.99	0.99	0.99	0.99	1.02
	LW-5	1.00	1.00	1.00	1.00	1.02
	LW-6	1.00	1.00	1.00	1.00	1.02
	LW-7	1.06	1.06	1.06	1.06	1.10
[55]	FB-1	1.10	1.10	1.10	1.10	1.12
	FB-2	0.89	0.89	0.89	0.89	0.91
	FB-3	1.07	1.07	1.07	1.07	1.12
	FB-4	1.12	1.12	1.12	1.12	1.13
	FB-5	1.10	1.10	1.10	1.10	1.12
	FB-6	1.01	1.01	1.01	1.01	1.04
	FB-7	1.20	1.20	1.20	1.20	1.21
	FB-8	1.09	1.09	1.09	1.09	1.11
	FB-9	1.18	1.18	1.18	1.18	1.22
[56]	B5F1	1.17	1.17	1.17	1.17	1.18
	B5F2	1.22	1.22	1.22	1.22	1.25
	B5F3	1.09	1.09	1.09	1.09	1.10
	B5F4	1.20	1.20	1.20	1.20	1.22
[57]	LW-1	0.94	0.94	0.94	0.94	0.96
	LW-2	1.05	1.05	1.05	1.05	1.06
	LW-3	1.19	1.19	1.19	1.19	1.21
	LW-4	1.03	1.03	1.03	1.03	1.05
	LW-5	1.02	1.02	1.02	1.02	1.04
	LW-6	1.01	1.01	1.01	1.01	1.03
	LW-7	1.08	1.08	1.08	1.08	1.12
[58]	L1	1.01	1.01	1.01	1.01	1.04
	L2	1.17	1.17	1.17	1.17	1.21
	L3	1.16	1.16	1.16	1.16	1.21
	L4	1.13	1.13	1.13	1.13	1.20
	LX1-A	1.01	1.01	1.01	1.01	1.03
	LX2-A	1.11	1.11	1.11	1.11	1.15
	LX3-A	1.18	1.18	1.18	1.18	1.23
	LX4-A	1.17	1.17	1.17	1.17	1.23
	LX1-A	0.97	0.97	0.97	0.97	0.99
	LX2-A	1.09	1.09	1.09	1.09	1.13
	LX3-B	1.19	1.19	1.19	1.19	1.24
	LX4-B	1.15	1.15	1.15	1.15	1.22
[59]	L1-A	1.18	1.18	1.18	1.18	1.19
	L1-B	1.16	1.16	1.16	1.16	1.17
	L1-C	1.32	1.32	1.32	1.32	1.32
	L2-A	1.07	1.07	1.07	1.07	1.09
	L2-B	1.05	1.05	1.05	1.05	1.07
	L3-A	1.03	1.03	1.03	1.03	1.06
	L3-B	1.09	1.09	1.09	1.09	1.12
	L4-A	0.94	0.94	0.94	0.94	0.97
	L4-B	0.98	0.98	0.98	0.98	1.01
	L5-A	0.93	0.93	0.93	0.93	0.97
	L5-B	0.89	0.89	0.89	0.89	0.93
[60]	B-N2	1.07	1.07	1.07	1.07	1.09
	B-N3	1.03	1.03	1.03	1.03	1.05
	B-N4	0.99	0.99	0.99	0.99	1.01
	B-M2	1.04	1.04	1.04	1.04	1.05
	B-M3	0.98	0.98	0.98	0.98	0.99
	B-M4	0.97	0.97	0.97	0.97	0.99
	B-H2	1.01	1.01	1.01	1.01	1.02
	B-H3	1.00	1.00	1.00	1.00	1.01
	B-H4	0.99	0.99	0.99	0.99	1.00
[52]	L4	0.93	0.93	0.93	0.93	0.97
	L5	0.86	0.86	0.86	0.86	0.89
	L6	0.87	0.87	0.87	0.87	0.89
μ	—	1.06	1.06	1.06	1.06	1.09
δ	—	0.09	0.09	0.09	0.09	0.09

Table 9: Continued.

Data sources	RC beams number	EN1992-1-1 M_u/M_{uc}	BS5400-4 M_u/M_{uc}	AASHEO M_u/M_{uc}	EN1991-2 2003 M_u/M_{uc}	CRC PRESS M_u/M_{uc}
[54]	LW-1	0.93	1.07	0.95	0.93	0.95
	LW-2	1.01	1.16	1.02	1.01	1.02
	LW-3	1.18	1.35	1.19	1.18	1.19
	LW-4	0.99	1.14	1.02	0.99	1.02
	LW-5	1.00	1.15	1.02	1.00	1.02
	LW-6	1.00	1.15	1.02	1.00	1.02
	LW-7	1.06	1.21	1.10	1.06	1.10
[55]	FB-1	1.10	1.27	1.12	1.10	1.12
	FB-2	0.89	1.02	0.91	0.89	0.91
	FB-3	1.07	1.23	1.12	1.07	1.12
	FB-4	1.12	1.28	1.13	1.12	1.13
	FB-5	1.10	1.27	1.12	1.10	1.12
	FB-6	1.01	1.16	1.04	1.01	1.04
	FB-7	1.20	1.38	1.21	1.20	1.21
	FB-8	1.09	1.25	1.11	1.09	1.11
	FB-9	1.18	1.36	1.22	1.18	1.22
[56]	B5F1	1.17	1.37	1.18	1.17	1.18
	B5F2	1.22	1.41	1.25	1.22	1.25
	B5F3	1.09	1.25	1.10	1.09	1.10
	B5F4	1.20	1.38	1.22	1.20	1.22
[57]	LW-1	0.94	1.08	0.96	0.94	0.96
	LW-2	1.05	1.20	1.06	1.05	1.06
	LW-3	1.19	1.37	1.21	1.19	1.21
	LW-4	1.03	1.18	1.05	1.03	1.05
	LW-5	1.02	1.17	1.04	1.02	1.04
	LW-6	1.01	1.16	1.03	1.01	1.03
	LW-7	1.08	1.24	1.12	1.08	1.12
[58]	L1	1.01	1.16	1.04	1.01	1.04
	L2	1.17	1.35	1.21	1.17	1.21
	L3	1.16	1.33	1.21	1.16	1.21
	L4	1.13	1.30	1.20	1.13	1.20
	LX1-A	1.01	1.16	1.03	1.01	1.03
	LX2-A	1.11	1.28	1.15	1.11	1.15
	LX3-A	1.18	1.36	1.23	1.18	1.23
	LX4-A	1.17	1.34	1.23	1.17	1.23
	LX1-B	0.97	1.12	0.99	0.97	0.99
	LX2-B	1.09	1.25	1.13	1.09	1.13
	LX3-B	1.19	1.37	1.24	1.19	1.24
	LX4-B	1.15	1.33	1.22	1.15	1.22
[59]	L1-A	1.18	1.36	1.19	1.18	1.19
	L1-B	1.16	1.34	1.17	1.16	1.17
	L1-C	1.32	1.51	1.32	1.32	1.32
	L2-A	1.07	1.23	1.09	1.07	1.09
	L2-B	1.05	1.21	1.07	1.05	1.07
	L3-A	1.03	1.19	1.06	1.03	1.06
	L3-B	1.09	1.25	1.12	1.09	1.12
	L4-A	0.94	1.03	0.97	0.94	0.97
	L4-B	0.98	1.12	1.01	0.98	1.01
	L5-A	0.93	1.07	0.97	0.93	0.97
	L5-B	0.89	1.02	0.93	0.89	0.93
[60]	B-N2	1.07	1.23	1.09	1.07	1.09
	B-N3	1.03	1.18	1.05	1.03	1.05
	B-N4	0.99	1.13	1.01	0.99	1.01
	B-M2	1.04	1.20	1.05	1.04	1.05
	B-M3	0.98	1.12	0.99	0.98	0.99
	B-M4	0.97	1.12	0.99	0.97	0.99
	B-H2	1.01	1.16	1.02	1.01	1.02
	B-H3	1.00	1.15	1.01	1.00	1.01
	B-H4	0.99	1.14	1.00	0.99	1.00
[52]	L4	0.93	1.07	0.73	0.93	0.87
	L5	0.86	0.99	0.75	0.99	0.83
	L6	0.87	1.00	0.78	1.03	0.84
μ	—	1.06	1.22	1.01	1.06	1.08
δ	—	0.09	0.09	0.11	0.09	0.10

Note. M_u in the table is the measured ultimate flexural bearing capacity and M_{uc} is the calculated value of ultimate flexural bearing capacity obtained by taking the measured yield strength of reinforcement from the current code formulas.

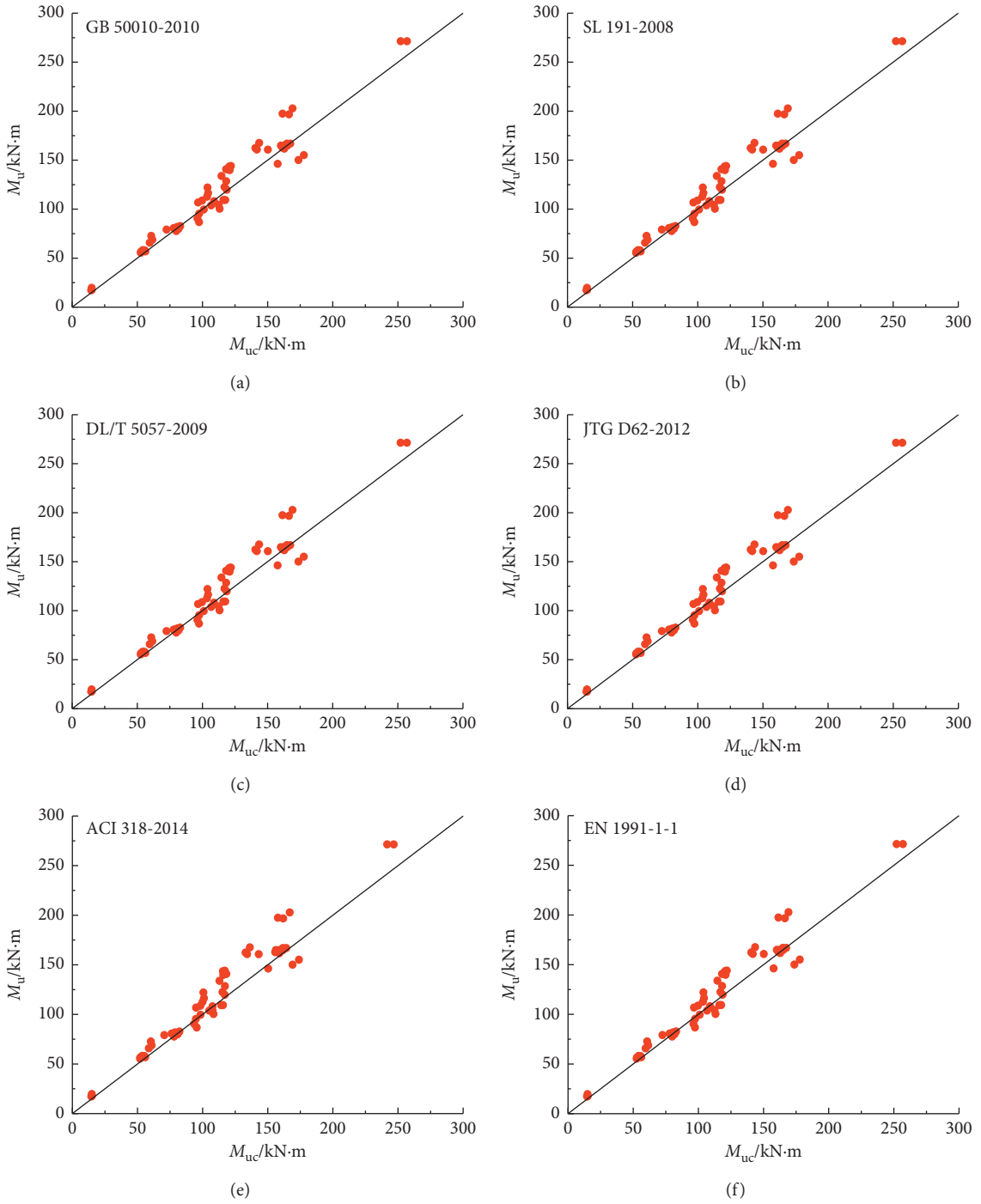

Figure 7: Continued.

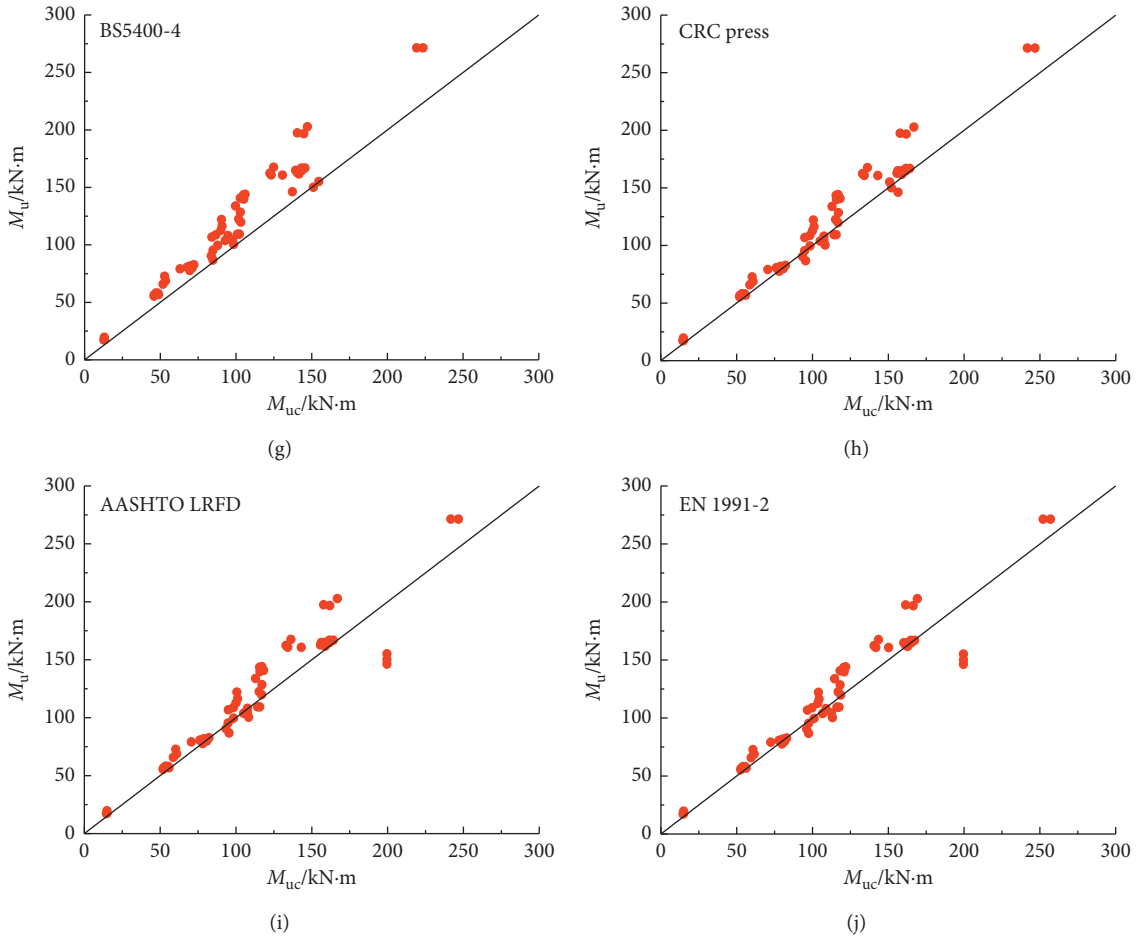

Figure 7: Comparison of experimental flexural bearing capacity M_u with M_{uc} calculated by different codes for beams with 500 MPa steel bars.

beams reinforced with 600 MPa grade steel and having the concrete grade of C40, C50, and C60. The reliability analysis of the flexural bearing capacity of RC beam was calculated by considering the design yield strength of the steel bar as 520 MPa.

As shown in Figures 11 and 12, the trend of change in ρ-β curve corresponding to different concrete strength grades was basically the same for the two reinforcement ratios of 600 MPa grade steel. Generally speaking, the reliability index of the beam increased with an increase in the strength of concrete, but the increase was not large.

The curve of the minimum value of the reliability index of the beam with different concrete strength grades is shown in Figure 13. The trend of change in the minimum value of the reliability index of the beam under different reinforcement ratios was basically the same. With an improvement in the concrete strength grade, the minimum value of the reliability index increased; when the reinforcement ratio is small, the minimum value of the reliability index of the beam is larger.

Table 14 shows the statistical parameters of the minimum reliability index corresponding to different concrete strength grades of the test beams. The average value of the minimum reliability index of the test beams with a reinforcement ratio of 0.005 was 3.172 for each concrete strength grade. The average value of the minimum reliability index corresponded to the failure probability of 7.57×10^{-4}. The average value of the minimum reliability index for different concrete grades with a reinforcement ratio of 0.008 was 3.148, and the average value of the minimum reliability index corresponded to the failure probability of 8.23×10^{-4}. The overall average minimum reliability index of the test beam (irrespective of the reinforcement ratio) was 3.160, and the corresponding failure probability was 7.89×10^{-4}. These values are close to the code specified values. The coefficient of variation of the minimum reliability index corresponding to different concrete strength grades was negligibly small, indicating that the minimum reliability index was less affected by the concrete strength grade and had good stability. The analysis of the minimum reliability index of the beams with different concrete strength grades further verified that the design yield strength of the 600 MPa grade steel bar should be taken as 520 MPa to meet the reliability requirements.

Table 10: Details of beams with 600 MPa steel bars.

Data sources	RC beam number	b/mm	h/mm	l_0/mm	c/mm	ρ/100%	Reinforcement			Concrete			
							A_s/mm^2	fy/MPa	Es/GPa	Fcu/MPa	Fck/MPa	fts/MPa	Ec ×104/MPa
[39]	L-5	200	400	3200	30	1.3	982	622	—	54.67	35.3	2.80	3.52
	L-7	200	400	3200	30	1.3	982	622	—	54.67	35.3	2.80	3.52
	L-8	200	400	3200	30	1.0	763	654	—	54.67	35.3	2.80	3.52
	L-9	200	400	3200	30	0.7	509	654	—	54.67	35.3	2.80	3.52
	L-10	200	400	3200	30	1.0	763	654	—	67.42	45.49	3.68	3.68
	L-11	200	400	3200	30	0.7	509	654	—	67.42	45.49	3.68	3.68
[61]	LW-1	200	400	3200	30	—	509	654	—	54.27	35.11	3.02	—
	LW-2	200	400	3200	30	—	509	654	—	67.42	43.27	3.09	—
	LW-3	200	400	3200	30	—	763	654	—	54.27	35.11	3.02	—
	LW-4	200	400	3200	30	—	763	654	—	67.42	43.27	3.09	—
	LW-5	200	400	3200	30	—	982	622	—	54.27	35.11	3.02	—
	LW-6	200	400	3200	30	—	982	622	—	67.42	43.27	3.09	—
[53]	LW1	200	400	3000	25	0.8	603	645	—	19.5	19.5	2.22	—
	LW2	200	400	3000	25	0.8	603	645	—	31.2	31.2	2.85	—
	LW3	200	400	300	25	1.4	982	610	—	19.5	19.5	2.22	—
	LW4	200	400	3000	25	1.4	982	610	—	31.5	31.2	2.85	—
[52]	L-1	250	400	3400	35	1.1	1140	500	200	—	14.3	1.43	3.0
	L-2	250	400	3400	35	1.1	1140	500	200	—	23.1	1.89	3.45
	L-3	250	400	3400	35	1.1	1140	500	200	—	27.5	2.04	3.6

Note. Symbol "—" means that the parameter has no relevant data in the literature.

Table 11: Comparison of experimental flexural bearing capacity M_u with M_{uc} calculated by different codes for beams with 600 MPa steel bars.

Data sources	RC beam number	GB50010-2010 M_u/M_{uc}	SL191 -2008 M_u/M_{uc}	DL/T5057-2009 M_u/M_{uc}	JTGD62-2012 M_u/M_{uc}	ACI318-2014 M_u/M_{uc}
Test	600-C30-1-1	1.16	1.16	1.16	1.16	1.18
	600-C30-1-2	1.15	1.15	1.15	1.15	1.17
	600-C30-2-1	1.20	1.20	1.20	1.20	1.22
	600-C30-2-2	1.19	1.19	1.19	1.19	1.20
	600-C40-1-1	1.06	1.06	1.06	1.06	1.08
	600-C40-1-2	1.04	1.04	1.04	1.04	1.06
	600-C40-2-1	1.10	1.10	1.10	1.10	1.11
	600-C40-2-2	1.25	1.25	1.25	1.25	1.27
	600-C50-1-1	1.04	1.04	1.04	1.04	1.06
	600-C50-1-2	1.10	1.10	1.10	1.10	1.12
	600-C50-2-1	1.16	1.16	1.16	1.16	1.17
	600-C50-2-2	1.19	1.19	1.19	1.19	1.20
	600-C60-1-1	1.08	1.08	1.08	1.08	1.09
	600-C60-1-2	1.07	1.07	1.07	1.07	1.08
	600-C60-2-1	1.20	1.20	1.20	1.20	1.20
	600-C60-2-2	1.20	1.20	1.20	1.20	1.20
[39]	L-5	1.16	1.16	1.16	1.16	1.29
	L-7	1.11	1.11	1.11	1.11	1.24
	L-8	1.14	1.14	1.14	1.14	1.24
	L-9	1.13	1.13	1.13	1.13	1.19
	L-10	1.13	1.13	1.13	1.13	1.19
	L-11	1.11	1.11	1.11	1.11	1.15
[61]	LW-1	1.13	1.13	1.13	1.13	1.14
	LW-2	1.14	1.14	1.14	1.14	1.15
	LW-3	1.14	1.14	1.14	1.14	1.16
	LW-4	1.13	1.13	1.13	1.13	1.15
	LW-5	1.12	1.12	1.12	1.12	1.14
	LW-6	1.13	1.13	1.13	1.13	1.15

Table 11: Continued.

Data sources	RC beam number	GB50010-2010 M_u/M_{uc}	SL191 -2008 M_u/M_{uc}	DL/T5057-2009 M_u/M_{uc}	JTGD62-2012 M_u/M_{uc}	ACI318-2014 M_u/M_{uc}
[53]	LW1	1.13	1.13	1.13	1.13	1.16
	LW2	1.05	1.05	1.05	1.05	1.07
	LW3	1.08	1.08	1.08	1.08	1.13
	LW4	1.06	1.06	1.06	1.06	1.09
[52]	L-1	0.92	0.92	0.92	0.92	0.97
	L-2	0.90	0.90	0.90	0.90	0.93
	L-3	0.89	0.89	0.89	0.89	0.91
μ	—	1.11	1.11	1.11	1.11	1.14
δ	—	0.07	0.07	0.07	0.07	0.08
Data sources	RC beam number	EN1992-1-1 M_u/M_{uc}	BS5400-4 M_u/M_{uc}	AASHEO M_u/M_{uc}	EN1991-2 2003 M_u/M_{uc}	CRC PRESS M_u/M_{uc}
Test	600-C30-1-1	1.14	1.33	1.18	1.10	1.18
	600-C30-1-2	1.13	1.32	1.17	1.09	1.17
	600-C30-2-1	1.19	1.38	1.22	1.17	1.22
	600-C30-2-2	1.20	1.37	1.20	1.18	1.20
	600-C40-1-1	1.06	1.22	1.08	1.04	1.08
	600-C40-1-2	1.04	1.20	1.06	1.02	1.06
	600-C40-2-1	1.10	1.27	1.11	1.09	1.11
	600-C40-2-2	1.25	1.44	1.27	1.24	1.27
	600-C50-1-1	1.04	1.19	1.06	1.01	1.06
	600-C50-1-2	1.10	1.27	1.12	1.07	1.12
	600-C50-2-1	1.16	1.34	1.17	1.14	1.17
	600-C50-2-2	1.19	1.37	1.20	1.17	1.20
	600-C60-1-1	1.08	1.24	1.09	1.08	1.09
	600-C60-1-2	1.07	1.23	1.08	1.07	1.08
	600-C60-2-1	1.20	1.37	1.20	1.20	1.20
	600-C60-2-2	1.20	1.37	1.20	1.20	1.20
[39]	L-5	1.24	1.33	1.19	1.16	1.19
	L-7	1.20	1.28	1.14	1.11	1.14
	L-8	1.20	1.31	1.16	1.14	1.16
	L-9	1.17	1.29	1.14	1.13	1.14
	L-10	1.17	1.30	1.14	1.13	1.14
	L-11	1.13	1.28	1.12	1.11	1.12
[61]	LW-1	1.13	1.30	1.14	1.13	1.14
	LW-2	1.14	1.31	1.15	1.14	1.15
	LW-3	1.14	1.31	1.16	1.14	1.16
	LW-4	1.13	1.30	1.15	1.13	1.15
	LW-5	1.12	1.28	1.14	1.12	1.14
	LW-6	1.13	1.30	1.15	1.13	1.15
[53]	LW1	1.13	1.30	1.16	1.13	1.16
	LW2	1.05	1.20	1.07	1.05	1.07
	LW3	1.08	1.24	1.13	1.08	1.13
	LW4	1.06	1.22	1.09	1.06	1.09
[52]	L-1	0.92	1.06	0.97	0.92	0.97
	L-2	0.90	1.04	0.93	0.90	0.93
	L-3	0.89	1.02	0.91	0.89	0.91
μ	—	1.12	1.27	1.13	1.10	1.13
δ	—	0.08	0.07	0.07	0.07	0.07

Note. M_u in the table is the measured ultimate flexural bearing capacity and M_{uc} is the calculated value of ultimate flexural bearing capacity obtained by taking the measured yield strength of reinforcement from the current code formulas.

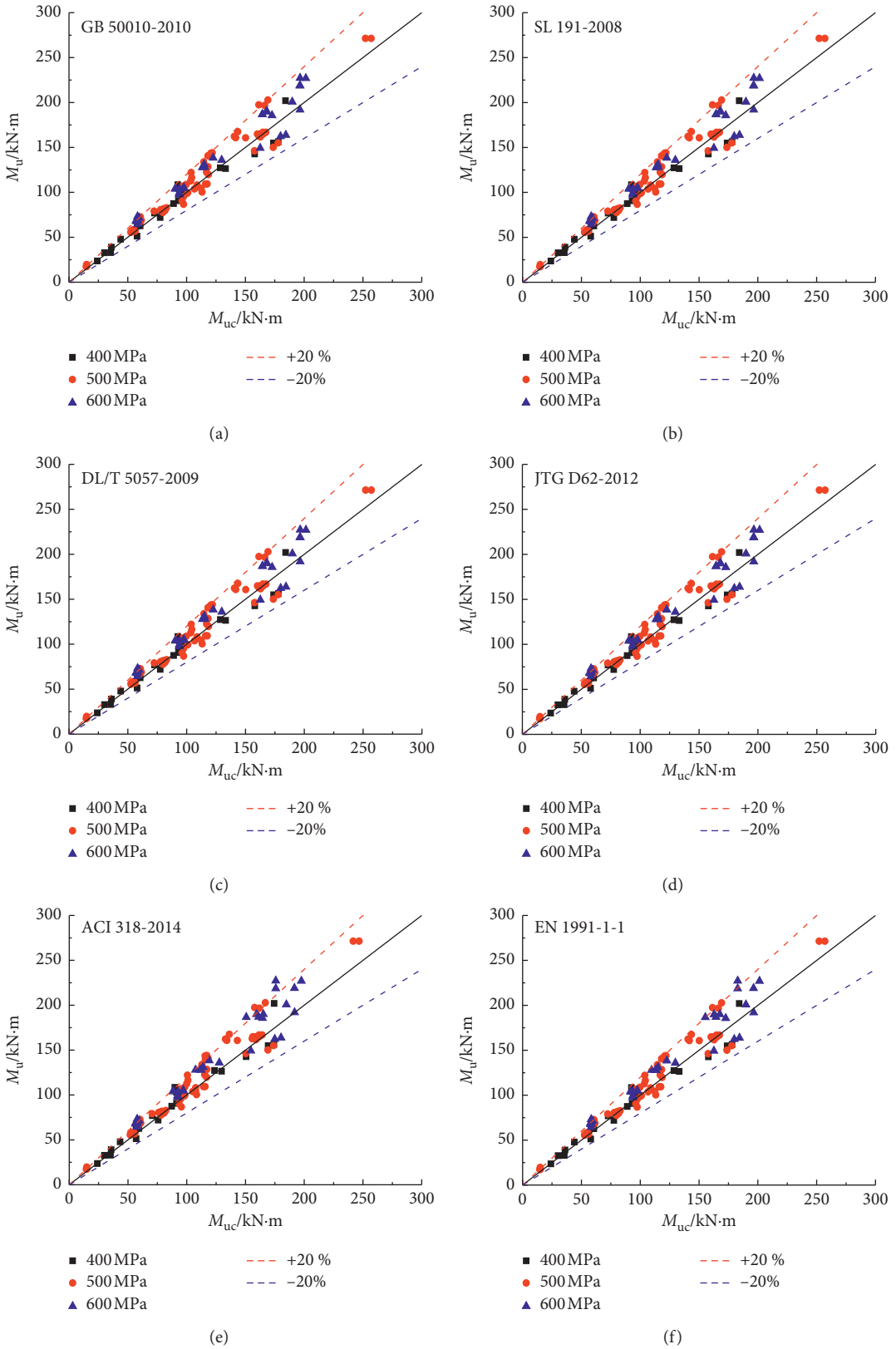

Figure 8: Continued.

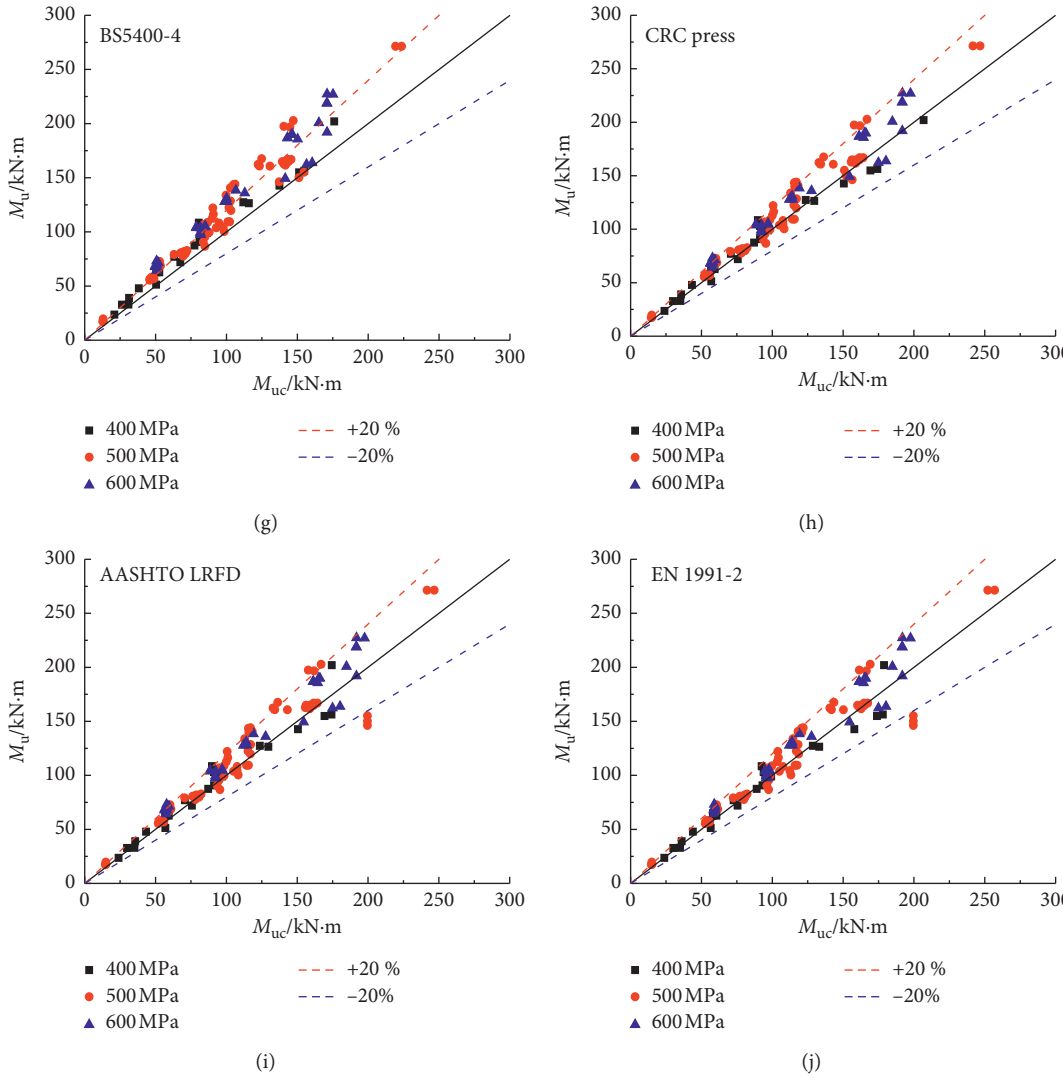

Figure 8: Comparison of experimental flexural bearing capacity M_u with M_{uc} calculated by different codes for beams with 600 MPa steel bars.

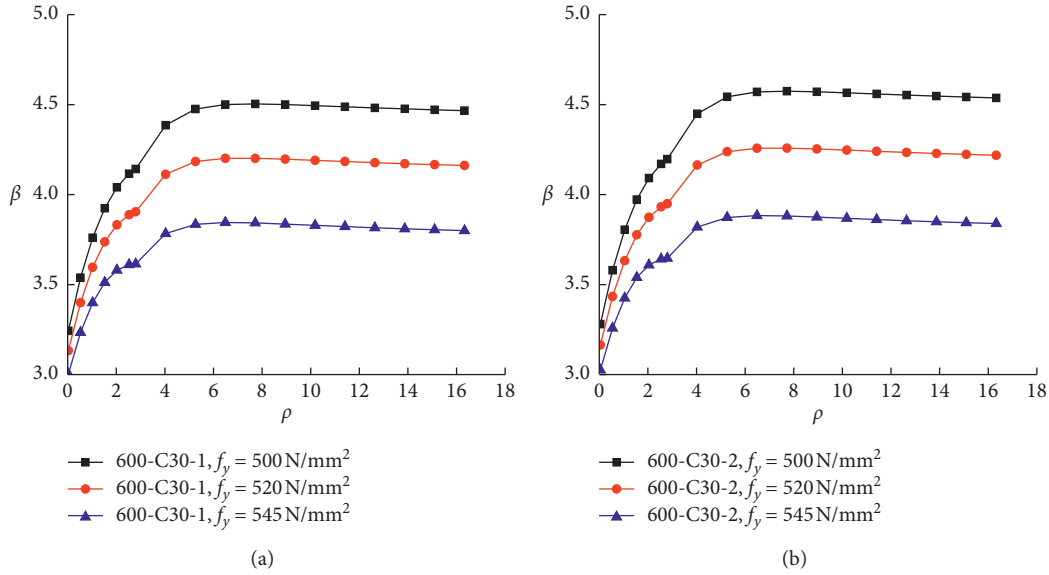

Figure 9: Continued.

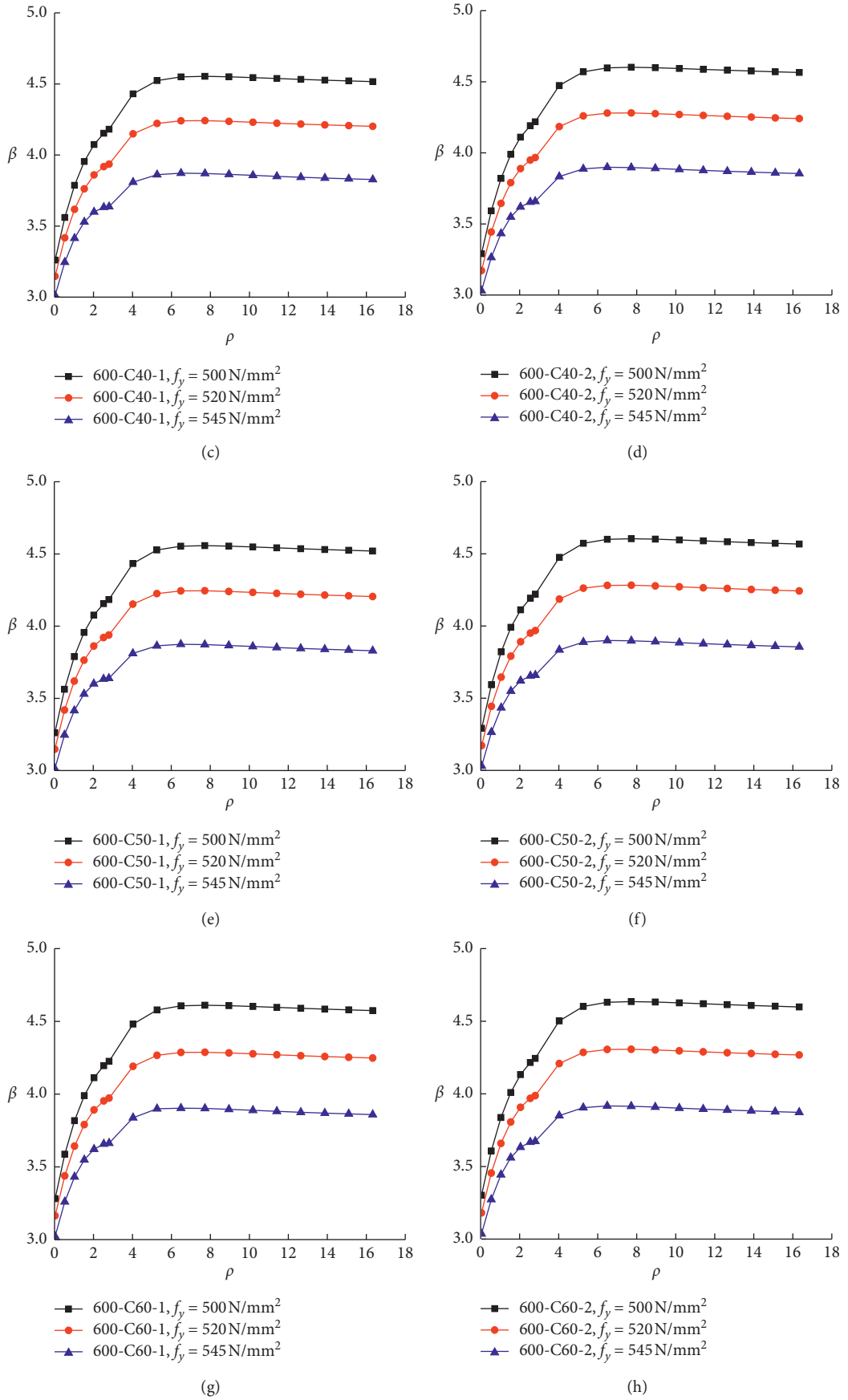

Figure 9: ρ-β Variation curve of each test beam.

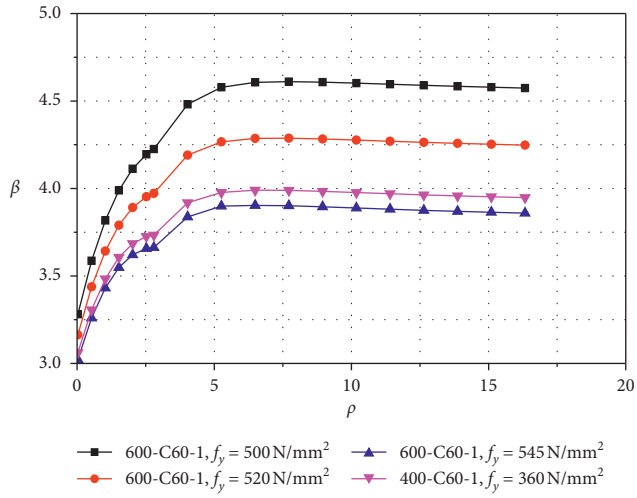

Figure 10: Comparison of the ρ-β variation curve of the test beam 600-C60-1 and 400-C60-1.

Table 12: The minimum reliable indexes and failure probability of the C60 test beam under different conditions.

Rebar category	f_y	Minimum reliable index		Average	Probability of failure	Code value	
		Reinforcement rate 0.008	Reinforcement rate 0.005			β	p_f
HRB400	360	3.062	—	3.095	9.83×10^{-4}	3.2	6.87×10^{-4}
	500	3.281	3.302	3.291	4.99×10^{-4}		
HRB600	520	3.163	3.181	3.172	7.57×10^{-4}		
	545	3.023	3.036	3.030	1.22×10^{-3}		

Table 13: Comparison of experimental flexural bearing capacity M_u with M_{uc} calculated by code of 520 MPa for the reinforcement design strength.

RC beam number	EN1992-1-1 M_u/M_{uc}	BS5400-4 M_u/M_{uc}	AASHEO M_u/M_{uc}	EN1991-2 2003 M_u/M_{uc}	CRC PRESS M_u/M_{uc}
600-C30-1-1	1.40	1.40	1.44	1.40	1.42
600-C30-1-2	1.39	1.39	1.42	1.39	1.41
600-C30-2-1	1.29	1.45	1.33	1.29	1.31
600-C30-2-2	1.27	1.43	1.30	1.27	1.29
600-C40-1-1	1.27	1.29	1.30	1.27	1.28
600-C40-1-2	1.35	1.27	1.38	1.35	1.36
600-C40-2-1	1.33	1.34	1.36	1.33	1.34
600-C40-2-2	1.32	1.52	1.35	1.32	1.32
600-C50-1-1	1.45	1.27	1.49	1.45	1.47
600-C50-1-2	1.43	1.35	1.47	1.43	1.45
600-C50-2-1	1.34	1.41	1.37	1.34	1.35
600-C50-2-2	1.52	1.45	1.56	1.52	1.53
600-C60-1-1	1.41	1.33	1.45	1.41	1.42
600-C60-1-2	1.45	1.32	1.48	1.45	1.46
600-C60-2-1	1.46	1.45	1.49	1.45	1.46
600-C60-2-2	1.46	1.45	1.49	1.45	1.46
M	1.38	1.38	1.42	1.38	1.40
Δ	0.05	0.05	0.05	0.05	0.05

Table 13: Continued.

RC beam number	EN1992-1-1 M_u/M_{uc}	BS5400-4 M_u/M_{uc}	AASHEO M_u/M_{uc}	EN1991-2 2003 M_u/M_{uc}	CRC PRESS M_u/M_{uc}
600-C30-1-1	1.38	1.61	1.42	1.35	1.42
600-C30-1-2	1.37	1.60	1.41	1.34	1.41
600-C30-2-1	1.44	1.49	1.47	1.27	1.47
600-C30-2-2	1.45	1.46	1.45	1.25	1.45
600-C40-1-1	1.29	1.46	1.31	1.24	1.31
600-C40-1-2	1.27	1.55	1.29	1.31	1.29
600-C40-2-1	1.34	1.53	1.35	1.33	1.35
600-C40-2-2	1.52	1.51	1.53	1.32	1.53
600-C50-1-1	1.27	1.67	1.28	1.42	1.28
600-C50-1-2	1.35	1.65	1.36	1.40	1.36
600-C50-2-1	1.41	1.54	1.42	1.32	1.42
600-C50-2-2	1.45	1.75	1.46	1.50	1.46
600-C60-1-1	1.33	1.62	1.34	1.39	1.34
600-C60-1-2	1.32	1.66	1.32	1.42	1.32
600-C60-2-1	1.46	1.67	1.46	1.45	1.46
600-C60-2-2	1.46	1.67	1.46	1.45	1.46
M	1.38	1.59	1.40	1.36	1.40
Δ	0.05	0.05	0.05	0.06	0.05

Note. M_u in the table is the measured ultimate flexural bearing capacity and M_{uc} is the calculated value of ultimate flexural bearing capacity obtained by taking the measured yield strength of reinforcement from the current code formulas.

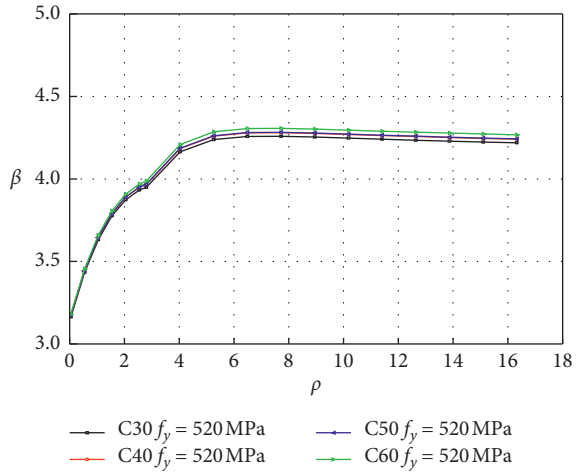

Figure 11: ρ-β Curve of different concrete strength grades with the reinforcement rate of 0.005.

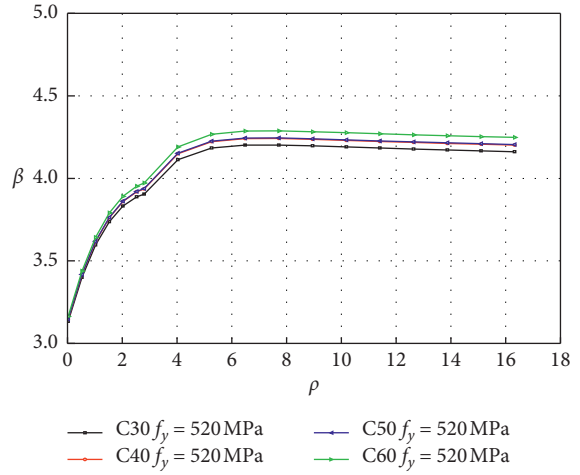

Figure 12: ρ-β Curve of different concrete strength grades with the reinforcement rate of 0.008.

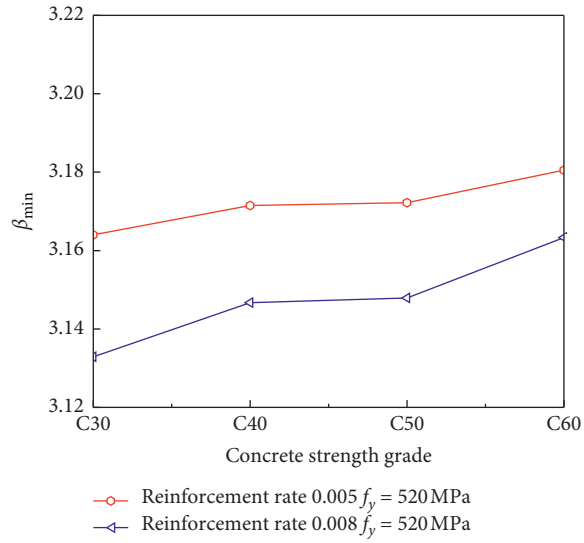

Figure 13: Concrete strength grade-βmin curve.

Table 14: Statistical parameters of the minimum reliable index.

Reinforcement rate	μ_β	δ_β	μ_{pf}	μ'_β	δ'_β	μ'_{p_f}	β	p_f	μ'_{p_f}/p_f
0.005	3.172	0.002	7.57×10^{-4}	3.160	0.005	7.89×10^{-4}	3.2	6.87×10^{-4}	1.15
0.008	3.148	0.003	8.23×10^{-4}						

Note. μ_β is the average reliability index of concrete different strength grades corresponding to the reinforcement ratio; δ_β is the coefficient of variation of different concrete strength grades corresponding to the reinforcement ratio; μ_{pf} is the failure probability of the concrete different strength grades corresponding to the reinforcement rate; μ'_β is the average value of the overall reliability index; δ'_β is the coefficient of variation of the overall reliability index; μ'_{p_f} is the overall average failure probability; β is the reliability index in code; and p_f is the failure probability in code.

5. Conclusion

This paper investigated the flexural bearing capacity of concrete beams reinforced with high-strength steel bars (600 MPa) and concrete of different strengths. Combined with the test data, this study analyzed the applicability of the equations for calculating the flexural capacity an RC beam with 600 MPa grade reinforcement as per different national codes. The reliability of the proposed method of analysis was checked against the experimental performance. The conclusions are as follows:

(1) The expressions and symbols of the equations for calculating the flexural capacity of the normal section of reinforced concrete beams are consistent in various countries, but there are slight differences in the strength calculation and height calculation methods of the equivalent rectangular stress diagram of concrete.

(2) The calculated values of ultimate bearing capacity of RC beams based on codes of different countries were compared with the measured values of ultimate bearing capacity. Equations and calculation procedures that are used to calculate the flexural capacity of beams reinforced with 400 MPa or 500 MPa grade steel could also be used for beams reinforced with 600 MPa grade steel.

(3) On the basis of the experiment, reliability analysis was performed for different design values of yield strength of the 600 MPa grade steel bar. Combined with the experimental results and considering the utilization ratio of steel bar strength, the design value of yield strength of the steel bar was selected to be 520 MPa.

Data Availability

The data used to support the findings of this study are included within the article.

Conflicts of Interest

The authors declare that they have no conflicts of interest.

Acknowledgments

The authors would like to express their gratitude to the National Natural Science Foundation of China (no. 51779095) and the Science Technology Innovation Talents in Universities of Henan Province (no. 20HASTIT013).

References

[1] R. F. Mast, M. Dawood, and S. H. Rizkalla, "Flexural strength design of concrete beams reinforced with high-strength steel bars," *ACI Structural Journal*, vol. 106, no. 4, pp. 551-552, 2009.

[2] T. K. Hassan, H. M. Seliem, and H. Dawiri, "Shear behavior of large concrete beams reinforced with high-strength steel," *ACI Structural Journal*, vol. 105, no. 2, pp. 173–179, 2008.

[3] J. Sperry, D. Darwin, and M. O'Reilly, "Conventional and high-strength steel hooked bars: detailing effects," *ACI Structural Journal*, vol. 115, no. 1, pp. 247–257, 2018.
[4] X. Ni, S. Cao, and S. Liang, "High-strength bar RC walls: cyclic loading test and strength prediction," *Engineering Structures*, vol. 198, pp. 1–18, 2019.
[5] P. Zhang, S. Fu, K. Zhang, and T. Zhang, "Mechanical properties of polyvinyl alcohol fiber-reinforced concrete composite containing fly ash and nano-SiO_2," *Science of Advanced Materials*, vol. 10, no. 6, pp. 769–778, 2018.
[6] P. Zhang, Y. Zheng, K. Wang, and K. Zhang, "Combined influence of nano-$CaCO_3$ and polyvinyl alcohol fibers on fresh and mechanical performance of concrete incorporating fly ash," *Structural Concrete*, vol. 21, no. 2, pp. 724–734, 2019.
[7] P. Zhang, Y. Ling, J. Wang, and Y. Shi, "Bending resistance of PVA fiber reinforced cementitious composites containing nano-SiO_2," *Nanotechnology Reviews*, vol. 8, no. 1, pp. 690–698, 2019.
[8] Y. Li and H. Aoude, "Blast response of beams built with high-strength concrete and high-strength ASTM A1035 bars," *International Journal of Impact Engineering*, vol. 130, no. 8, pp. 41–67, 2019.
[9] S.-H. Lee, K.-J. Shin, H.-D. Lee, W.-B. Kim, and J.-G. Yang, "Behavior of plate-to-circular hollow section joints of 600 MPa high-strength steel," *International Journal of Steel Structures*, vol. 12, no. 4, pp. 473–482, 2012.
[10] H.-L. Yi, L.-X. Du, G.-D. Wang, and X.-H. Liu, "Strengthening mechanism of a new 700 MPa hot rolled high strength steel," *Journal of Iron and Steel Research International*, vol. 15, no. 2, pp. 76–80, 2008.
[11] Y. Yoshida, T. Obinata, M. Nishio, and T. Shiwaku, "Development of high-strength (780 n/mm^2) steel for building systems," *International Journal of Steel Structures*, vol. 9, no. 4, pp. 285–289, 2009.
[12] D.-H. Kim, J.-H. Kim, and S. Chang, "Material performance evaluation and super-tall building applicability of the 800 MPa high-strength steel plates for building structures," *International Journal of Steel Structures*, vol. 14, no. 4, pp. 889–900, 2014.
[13] S. E. Quiel, C. Irwin, and C. J. Naito, "Mechanical characterization of normal and high-strength steel bars in RC members under fire," *Journal of Structural Engineering*, vol. 146, no. 7, pp. 1–17, 2020.
[14] Q. Hao, D. M. Yan, and S. K. Chen, "Effect of high temperature exposure and strain rate on mechanical properties of high-strength steel rebars," *Journal of Materials in Civil Engineering*, vol. 31, no. 11, pp. 1–11, 2019.
[15] P. Zhang, L. Y. Kang, J. Wang, and J. J. Guo, "Mechanical properties and explosive spalling behavior of steel-fiber-RC exposed to high temperature-a review," *Applied Sciences*, vol. 10, no. 7, pp. 1–21, 2020.
[16] M. A. Saleem, A. Mirmiran, J. Xia, and K. Mackie, "Development length of high-strength steel rebar in ultrahigh performance concrete," *Journal of Materials in Civil Engineering*, vol. 25, no. 8, pp. 991–998, 2013.
[17] K. A. Harries, B. M. Shahrooz, and A. Soltani, "Flexural crack widths in concrete girders with high-strength reinforcement," *Journal of Bridge Engineering*, vol. 17, no. 5, pp. 804–812, 2012.
[18] L. Barcley and M. Kowalsky, "Seismic "performance of circular concrete columns reinforced with high-strength steel," *Journal of Structural Engineering*, vol. 146, no. 2, pp. 1–11, 2020.
[19] J. W. Zhang, C. Li, and X. Y. Li, "Experimental study on seismic behavior of high-strength concrete columns with HRB600 steel bars," *China Civil Engineering Journal*, vol. 52, no. 8, pp. 6–17, 2019, in Chinese.
[20] S. Aldabagh and M. S. Alam, "High-strength steel reinforcement (ASTM A1035/A1035M grade 690): state-of-the-art review," *Journal of Structural Engineering*, vol. 146, no. 8, pp. 1–13, 2020.
[21] J. W. Baek, S. H. Kim, and H. G. Park, "Shear-friction strength of low-rise walls with 600 MPa (87 ksi) reinforcing bars," *ACI Structural Journal*, vol. 117, no. 1, pp. 169–182, 2020.
[22] X. Li, J. Zhang, and W. Cao, "Hysteretic behavior of high-strength concrete shear walls with high-strength steel bars: experimental study and modelling," *Engineering Structures*, vol. 214, no. 7, pp. 1–16, 2020.
[23] GB/T. 1499.2-2018, *Steel for the Reinforcement of Concrete-Part 2: Hot Rolled Ribbed Bars*, Standardization Administration of China, Beijing, China, 2018, in Chinese.
[24] GB50010-2010, *Code for Design of Concrete Structures*, China Building Industry Press, Beijing, China, 2010, in Chinese.
[25] DL/T 5057-2009, *Design Specification for Hydraulic Concrete Structures*, China Electric Power Press, Beijing, China, 2010, in Chinese.
[26] SL/T 191-2008, *Design Code for Hydraulic Concrete Structures*, China Water Power Press, Beijing, China, 2009, in Chinese.
[27] JTJ267-98, *Design Code for Harbour Engineering Concrete Structures*, China Communication Press, Beijing, China, 1998, in Chinese.
[28] JTG D62-2012, *Code for Design of Highway RC and Prestressed Concrete Bridges and Culverts*, China Communication Press, Beijing, China, 2012, in Chinese.
[29] TB10002.3-2005, *Code for Design of Railroad RC and Prestressed Concrete Bridges and Culverts*, China Railway Press, Beijing, China, 2005, in Chinese.
[30] P. Zhang, Q. Li, J. Wang, Y. Shi, Y. Zheng, and Y. Ling, "Effect of nano-particle on durability of polyvinyl alcohol fiber reinforced cementitious composite," *Science of Advanced Materials*, vol. 12, no. 2, pp. 249–262, 2020.
[31] P. Zhang, K. X. Wang, and Q. F. Li, "Fabrication and engineering properties of concretes based on geopolymers/alkali-activated binders-a review," *Journal of Cleaner Production*, vol. 258, pp. 1–22, Article ID 120896, 2020.
[32] P. Zhang, K. Wang, J. Wang, J. Guo, S. Hu, and Y Ling, "Mechanical properties and prediction of fracture parameters of geopolymer/alkali-activated mortar modified with PVA fiber and nano-SiO2," *Ceramics International*, vol. 46, no. 12, pp. 20027–20037, 2020.
[33] P. Zhang, Q. F. Li, and Y. Z. Chen, "Durability of steel fiber-RC containing SiO_2 nano-particles," *Materials*, vol. 12, no. 13, pp. 1–18, 2019.
[34] H. Zhao, K. Jiang, R. Yang, Y. Tang, and J Liu, "Experimental and theoretical analysis on coupled effect of hydration, temperature and humidity in early-age cement-based materials," *International Journal of Heat and Mass Transfer*, vol. 146, Article ID 118784, 2020.
[35] H. Zhao, X. Wu, Y. Huang, P. Zhang, Q. Tian, and J Liu, "Investigation of moisture transport in cement-based materials using low-field nuclear magnetic resonance imaging," *Magazine of Concrete Research*, pp. 1–19, 2019.
[36] H. T. Zhao, K. Jiang, and B. Hong, "Experimental and numerical analysis on coupled hygro-thermo-chemo-mechanical effect in early-age concrete," *ASCE Journal of Materials in Civil Engineering*, vol. 67, no. 3, pp. 299–331, 2006.
[37] C. Chen, X. D. Yang, and W. Pan, "Experimental research on flexural performance of RC beams with 600 MPa steel bars

industrial construction," *Building Structures*, vol. 48, no. 6, pp. 1–4, 2018, in Chinese.

[38] X. Rong, H. C. Wu, and P. Liu, "Experimental research on bending behavior of prestressed concrete beams with 600 MPa steel bars," *Journal of Wuhan University*, vol. 51, no. 2, pp. 139–143, 2018, in Chinese.

[39] J. X. Zhang, X. Rong, and P. Liu, "Experimental research on crack and flexural behavior of concrete beams with 600 MPa steel bars," *Building Structures*, vol. 47, no. 24, pp. 89–92, 2017, in Chinese.

[40] GB175-2007, *Common Portland Cement*, Standardization Administration of China, Beijing, China, 2007, in Chinese.

[41] ACI Committee 318, *Building Code Requirement for Structural Concrete (ACI 318-14) and Commentary (ACI 318R-14)*, American Concrete Institute, Detroit, MI, USA, 2014.

[42] EN1992-1-1, *Euro-code2: "Design for Concrete Structures-Part1: General Rules and Rules for Building"*, European Committee for Standardization, London, UK, 2004.

[43] M. Mustafa, *Structural Engineering Handbook*, CRC Press LLC, Boca Raton, FL, USA, 1999.

[44] BS5400S, "Concrete and Composite Bridges Part 4;Code of practice for design of concrete bridges," *British Standard Institution England*, vol. 4, pp. 13–56, 1990.

[45] BS5400S, "Concrete and composite bridges Part 2: specification for loads," *British Standard Institution England*, vol. 2, pp. 15–72, 2006.

[46] EN1991-2-2003, *Eurocode 1;Actions on Structures-Part 2*, Traffic Loads on Bridges, Brussels, Belgium, 2003.

[47] AASHTO, *AASHTOLRFD Bridge Design Specification*, AASHTO, Washington, DC, USA, 2007.

[48] M. Y. Li, *The Study of Mechanical Property of HRB400 reinforced*, Zhengzhou: Zhengzhou University, Zheng Zhou, China, 2003, in Chinese.

[49] L. Y. Na, *The Experimental Study on the Crack Behavior of Concrete Bending Members Reinforced with HRB400 Steel*, Hu Nan: Hunan University, Changsha, China, 2006, in Chinese.

[50] H. J. Xiao, *Experimental Research on Bend Behavior of HRB400 RC Beams*, Zhengzhou: Zhengzhou University, Zheng Zhou, China, 2006, in Chinese.

[51] W. J. Ge and J. W. Z. H. Dai, "Experimental Study on the flexural behavior of concrete beam reinforced with HRBF400 steel bars," *Industrial Construction*, vol. 41, no. 6, pp. 71–74, 2011, in Chinese.

[52] H. L. Shao, R. Q. Ma, and J. Ge, "The theoretical analysis on bend performance of RC beams with 600 MPa," in *Proceedings of the Industrial Construction 2016 Supplement II*, pp. 251–255, Industrial Construction Press, New York, NY, USA, August 2016, in Chinese.

[53] C. Cheng, *Experimental Study on Mechanical Properties of RC Members with 600 MPa Steel Bar*, Kunming University of Science Technology, Kunming, China, 2016, in Chinese.

[54] P. Zhang, *The Experimental Study on Bending Behavior of RC Beams with 500 MPa Steel Bar*, Hebei University of Technology, Tianjin, China, 2007, in Chinese.

[55] T. Zhang, *The Study of Mechanical Property of HRB500 reinforced*, Zhengzhou: Zhengzhou University, Zhengzhou, China, 2004, in Chinese.

[56] S. Z. Shang, *Experimental Research on Flexural Performance of Concrete Beam Reinfored with High-Strength Rebars*, Tongji University, Shanghai, China, 2007, in Chinese.

[57] Y. Y. Li, *Experimental Research on Behaviors of RC Beams with 500 MPa Steel Bars*, Tianjin University, Tianjin, China, 2007, in Chinese.

[58] P. Liu, *Experimental and Theoretical Research on Beams with HRB 500 High Strength Steel Bars*, Hebei University of Technology, Tianjin, China, 2012, in Chinese.

[59] F. B. Xu, *Experimental and Theoretical Research on Flexural Behavior of RC Beams with HRB 500 Bars*, Hu Nan: Hunan University, Changsha, China, 2007, in Chinese.

[60] S. A. Ashour, "Effect of compressive strength and tensile reinforcement ratio on flexural behavior of high-strength concrete beams," *Engineering Structures*, vol. 22, no. 5, pp. 413–423, 2000.

[61] X. Rong, H. T. Wang, and P. Liu, "Experimental study on bending behavior of RC beam with 600 MPa steel bar," *Journal of Harbin University of Technology*, vol. 44, no. 5, pp. 86–89, 2015, in Chinese.

[62] A. .W. Li, *Experimental Research on Flexural Bearing Capacity of RC Beams with HRBF500 and Reliability Analysis*, Huqiao University, Quanzhou, China, 2011, in Chinese.

[63] M. Zhang, *Structural Reliability Analysis: Methods and Procedures*, Science Press, Beijing, China, 2009, in Chinese.

[64] J. X. Gong and W. W. Wei, *The Principle of Engineering Structure Reliability Design*, Machinery Industry Press, Beijing, China, 2007, in Chinese.

[65] GB 50153-2008, *Unified Standard for Reliability Design of Engineering Structures*, China Building Industry Press, Beijing, China, 2008, in Chinese.

[66] GB 50009-2012, *Load Code for the Design of Building Structures*, China Building Industry Press, Beijing. China, 2012, in Chinese.

[67] J. Zhang, S. G. Liu, and J. H. Ding, "Analysis of the reliability of the bending carrying capacity of the RC beams," in *Proceedings of the Beijing Force Society. The Paper Collection of the 20th Annual Conference of the Beijing Force Society*, pp. 750–753, Beijing Force Society, Beijing, China, November 2014, in Chinese.

[68] F. Bai, *Discussion of the Safety and Life Evaluation Methods of RC Flexural and Compression-Flexure Members Based on Reliability*, South China University of Technology, Guangzhou, China, 2012, in Chinese.

[69] Z. He and Y. C. Huang, "Reliability evaluation for flexural capacity sdesign of concrete beams reinforced with FRP rebars," *Journal of Harbin University of Technology*, vol. 4, pp. 650–655, 2007, in Chinese.

Hindawi
Advances in Civil Engineering
Volume 2020, Article ID 8899888, 12 pages
https://doi.org/10.1155/2020/8899888

Research Article

Dynamic Inversion Analysis of Structural Layer Modulus of Semirigid Base Pavement considering the Influence of Temperature and Humidity

Bei Zhang, Xu Zhang, Yanhui Zhong, Xiaolong Li, Meimei Hao, and Jinbo Liu

College of Water Conservancy and Engineering, Zhengzhou University, Zhengzhou 450001, China

Correspondence should be addressed to Yanhui Zhong; zhong_yanhui@163.com and
Xiaolong Li; wennuandeshang@hotmail.com

Received 29 July 2020; Revised 11 September 2020; Accepted 27 September 2020; Published 29 October 2020

Academic Editor: Grzegorz Golewski

This paper is aimed to solve the overlearning problem of the neural network algorithm used to calculate the asphalt concrete pavement structural modulus in reverse. The firefly algorithm was adapted to optimize the selection of support vector machine (SVM) parameters. Based on the optimized SVM model, a new method for dynamic inversion of the semirigid base asphalt concrete pavement structural layer modulus was presented. The results show that the absolute value of relative error of each layer modulus is not more than 3.73% by using the proposed method. Then, the influences of temperature and humidity on the inversion modulus of semirigid base asphalt concrete pavement in the seasonal frozen area were analyzed, and the correction formula of the inversion modulus was established. The paper is of practical significance for improving the safety performance of semirigid base pavement in the seasonal frozen area in China.

1. Introduction

In recent years, China's highway construction has developed rapidly in terms of construction scale and quantity. The highway has reached a total mileage of 5 million kilometers by 2019, including 143,000 km of expressways. The semirigid base asphalt concrete pavement is most widely used in expressways [1]. In seasonal frozen areas such as Northeast China, Inner Mongolia, Qinghai, Gansu, Ningxia, and Tibet, the asphalt concrete pavement structure bears the frost-thawing damage under low temperature and damp environment, and its bearing capacity and stability of material will be greatly affected. These factors result in pavement cracks, cavities, subsidence, rutting, and other diseases, which seriously affect the traffic operation and normal use of expressways and even threaten the development of society and economy [2]. At present, in the design methods of asphalt pavement in the world, static load or approximate equivalent static load is generally used, but the static load mode cannot reflect the actual stress state of the pavement, so the influence of dynamic load on the design of the pavement structure has become the focus of research. Golewski studies the design of the concrete structure under dynamic load and puts forward the reference criteria for the design, construction, and maintenance of the dynamic loading structure, which provides a reference method for the design of pavement concrete structure [3, 4].

The bearing capacity of semirigid base asphalt concrete pavement is important to evaluate pavement performance. Falling weight deflectometer (FWD) is widely used as a kind of nondestructive testing equipment for the asphalt concrete pavement structure. Its principle is to carry out inversion analysis on the modulus of the asphalt concrete pavement structural layer according to the deflection value measured by FWD under impact load [4]. Scrivener et al. first proposed the inverse modulus calculation method of FWD deflection basin by solving the Burmister double layer system and compiled the inversion nomograph [5]. However, the regression analysis method cannot be used to process large-scale FWD-measured data with poor inversion accuracy and

versatility. Bush developed BISDEF and CHEVDEF software for inversion of the pavement structural layer modulus by using the iterative method [6]. Based on the system identification, Wang used this method to develop a software SIDMOD for inversion of the pavement structural layer modulus [7]. Nevertheless, the inversion results obtained by the iterative method are greatly affected by initial value and iterative method, and the iterative method converges slowly. Based on the database search method, Utahj et al. developed the MODULUS software for inversion of the pavement structural layer modulus [8]. Nonetheless, the database search method takes a long time to calculate and needs to select a more strict range of modulus. Meier et al. used the BP neural network to inverse the modulus and developed ANOVA software for inversion of pavement structural layer modulus [9]. There are some problems in using the neural network method such as oscillation and divergence out of improper initial value. Fwa et al. studied the inverse calculation of modulus by adopting the genetic algorithm and developed the inverse software NUS-GABACK [10]. Due to the slow calculation speed, of the genetic algorithm, NUS-GABACK software cannot realize the large-scale inverse calculation needed in practical engineering. The above studies are all static inversion methods. Wang developed a dynamic inversion program integrated with the artificial neural network and genetic algorithm (ANN-GA) to calculate the modulus of the structural layer. According to the asphalt concrete pavement deflection measured by FWD, the service condition of asphalt pavement can be evaluated [11]. You et al. developed a dynamic inversion model based on ANN to predict the interlayer contact conditions and structural layer modulus of the pavement structure in view of the asphalt concrete pavement interlayer contact conditions [12]. Considering the influence of FWD dynamic load characteristics, viscoelastic material parameters, and nonlinear material parameters, Li et al. developed a dynamic inversion program based on ANN in combination with the genetic algorithm [13]. However, the neural network may cause the problem of overlearning.

Asphalt concrete pavement material is a kind of viscoelastic material whose strength and stability are easily affected by temperature changes, so the bearing capacity of the asphalt concrete pavement structure will change with temperature. Subgrade is a linear structure built in the natural environment, and its structural performance will change with the freeze-thaw cycle in the seasonal frozen area. The specific performance is that the change of seasonal climate causes the moisture in the subgrade to freeze-thaw. This affects the structural performance of the subgrade and ultimately leads to the destruction of the asphalt concrete pavement structure. Therefore, the influence of temperature and humidity should be considered when calculating the modulus of the pavement structure layer. Scholars have carried out a lot of research on the relationship between temperature and humidity in seasonally frozen areas and the modulus of pavement material. Chamberlain et al. found that the pore ratio of fine-grained soil changes with freeze-thaw cycle and modulus, and the permeability increases with the continuous freeze-thaw cycle [14]. Observing the change law of soil material properties after the first freeze-thaw change, Simonsen et al. found that the modulus value of subgrade decreased after the first freeze-thaw [15]. Taking remolded soil as the research object, Mao studied the change law of soil modulus of resilience with water content and freeze-thaw cycles. It was found that water content in subgrade is the most important factor affecting the modulus of resilience, and the freeze-thaw cycle is a secondary one under the conditions of optimum water content and degree of compaction [16]. Chen used the self-developed multifunctional subgrade freeze-thaw cycle test device to paper the repeated freeze-thaw characteristics of subgrade soil in a seasonal frozen area under different water compensating state. Analyzing the influence of initial degree of compaction, freeze-thaw cycle times, and water content on modulus of resilience, he revealed the change law of modulus of resilience and gave the modulus reduction coefficient of subgrade in a seasonal frozen area [17]. Wang used the self-developed remote temperature and humidity acquisition system for subgrade in a seasonal frozen area to monitor the temperature and humidity status of subgrade, revealing the temperature and humidity change law of pavement structure in the seasonal frozen area. Meanwhile, he also analyzed the influence of water content, freeze-thaw cycle times, and degree of compaction on subgrade strength in a seasonal frozen area through the indoor freeze-thaw cycle test [18]. To sum up, although there are many research studies on the asphalt concrete pavement in the seasonal frozen area, most of them are about the influence of environmental factors on pavement materials and subgrade physical characteristics in the frozen soil area. There is no relevant research on the influence of temperature and humidity in the seasonal frozen area on the inversion modulus of the semirigid base pavement structure layer.

Therefore, this paper introduces the SVM method, optimizes the inversion of the asphalt concrete pavement structural layer modulus by the firefly algorithm considering the effect of temperature and humidity, and analyzes the influence of temperature and humidity on the inversion modulus of semirigid base asphalt pavement in the seasonal frozen area. The research results have guiding significance to ensure the safety performance of the asphalt concrete pavement structure in the seasonal frozen area and extend its service cycle.

2. Dynamic Response Analysis of Semirigid Base Pavement

2.1. Dynamic Finite Element Analysis Model of Pavement Structure

2.1.1. Basic Assumption. In this paper, the displacement of the elastic layer system is analyzed by assuming that each layer satisfies the following conditions:

(1) Each structural layer is homogeneous and isotropic, which satisfies the deformation law of linear elastic body

(2) The contact surface of each structural layer is continuous

(3) The subgrade extends infinitely in horizontal and longitudinal directions

2.1.2. Semirigid Base Pavement Structure Model. This paper takes FWD load as the research object and selects the depth direction 6m and radial direction 6m as calculation elements. According to the theory of pavement structure mechanics, the displacement, stress, and strain of the axisymmetric structure have nothing to do with the value of θ, but only with the value of R and Z. Therefore, the rectangular ring element is used as the research object of the axisymmetric structure, and only the section on the coordinate R and z plane needs to be studied. The finite element model is shown in Figure 1.

2.2. Calculation of Pavement Dynamic Response. According to Hamilton's variation principle, the dynamic balance equation considering damping effect is [19]

$$[M]\left\{\ddot{\delta}\right\} + [C]\left\{\dot{\delta}\right\} + [K]\{\delta\} = \{P\}, \tag{1}$$

$$[C] = \alpha[M] + \beta[M], \tag{2}$$

where $[M]$ is the global mass matrix; $\left\{\ddot{\delta}\right\}$ is the global acceleration vector; $[C]$ is the global damping matrix; $\left\{\dot{\delta}\right\}$ is the global velocity vector; $[K]$ is the global stiffness matrix ; $\{\delta\}$ is the global displacement vector; $\{P\}$is the equivalent node load vector; α and β are the damping coefficients, $\alpha = \xi\omega_1$ and $\beta = \xi/\omega_1$; ω_1 is the structural fundamental frequency; ξ is the mode damping ratio.

The calculation range of the model, boundary treatment, and characteristics of the rectangular ring element are known from [20, 21].

In this paper, the Wilson-θ direct integration method [20, 21] is selected to calculate the dynamic balance equation, and $\theta = 1.4$ is taken in the calculation. The specific steps are as follows.

2.2.1. Initial Calculation. Calculate the following constants:

$$\tau = \theta\Delta t\,(\theta = 1.4),$$

$$b_0 = \frac{6}{\tau^2},\ b_1 = \frac{3}{\tau},\ b_2 = 2b_1,\ b_3 = \frac{\tau}{2},\ b_4 = \frac{b_0}{\theta}, \tag{3}$$

$$b_5 = \frac{b_2}{\theta},\ b_6 = 1 - \frac{3}{\theta},\ b_7 = \frac{\Delta t}{2},\ b_8 = \frac{\Delta t^2}{6}.$$

The effective stiffness matrix is established:

$$[\overline{K}] = [K] + b_1[C] + b_0[M]. \tag{4}$$

The effective stiffness matrix is decomposed:

$$[\overline{K}] = [L][D][L]^{\mathrm{T}}. \tag{5}$$

2.2.2. Calculation of Each Time Step. Calculate the effective load vector:

$$\begin{aligned}\{\overline{P}(t_1+\tau)\} = {} & \{P(t_1+\tau)\} + [M]\left(2\left\{\ddot{\delta}(t_1)\right\} + b_2\left\{\dot{\delta}(t_1)\right\}\right. \\ & \left. + b_0\{\delta(t_1)\}\right) + [C]\left(b_3\left\{\ddot{\delta}(t_1)\right\}\right. \\ & \left. + 2\left\{\dot{\delta}(t_1)\right\} + b_1\{\delta(t_1)\}\right).\end{aligned} \tag{6}$$

The equation of motion is solved by

$$\{\delta(t_1+\tau)\} = [\overline{K}]^{-1}\{\overline{P}(t_1+\tau)\}. \tag{7}$$

Calculate acceleration, velocity, and displacement of $t_1 + \Delta t$ time:

$$\begin{aligned}\ddot{\delta}(t_1+\Delta t) = {} & b_4[\delta(t_1+\Delta t) - \delta(t_1)] \\ & + b_5\dot{\delta}(t_1) + b_6\ddot{\delta}(t_1),\end{aligned} \tag{8}$$

$$\dot{\delta}(t_1+\Delta t) = \dot{\delta}(t_1) + b_7\left[\ddot{\delta}(t_1) + \ddot{\delta}(t_1+\Delta t)\right], \tag{9}$$

$$\delta(t_1+\Delta t) = \delta(t_1) + \dot{\delta}(t_1)\Delta t + b_8\left[\ddot{\delta}(t_1+\Delta t) + 2\ddot{\delta}(t_1)\right]. \tag{10}$$

Based on the above solution method, the dynamic response calculation program of the semirigid base pavement structure is compiled in this paper.

2.3. Example Analysis

(1) In a three-layer semirigid base pavement system, the elastic modulus of each layer is, respectively, 1200 MPa, 1400 Mpa, and 60 MPa, the thickness 18 cm, 32 cm, and 550 cm, the Poisson's ratio 0.35, 0.30, and 0.40, and the density 2400 kg/m^3, 2300 kg/m^3, and 1800 kg/m^3. In this paper, Dynatest8000 FWD is used as the applied load. In order to simplify the calculation process, the load application curve of FWD is simplified to a sine semiperiodic function with the peak value of 721 kpa, the action time of 32 ms, and the loading radius of 0.15 m. The load time history curve and transducer distribution position of the simplified FWD are shown in Figure 2 and Table 1.

The calculated deflection results in this paper are basically consistent with the measured deflection basin data at different measuring points with small error and high accuracy from Figure 5, which can be applied to actual asphalt concrete pavement engineering.

Eight-node linear hexahedron element (C3D8R) is selected as the calculation element of the finite element model. The boundary conditions are set as follows: there is no X-direction displacement in the left-right direction and no Y-direction displacement in the front-back direction. All nodes on the bottom are completely fixed, and the layers are completely continuous. The finite element model is shown in Figure 3.

It can be seen from Figure 4 that the calculation results at different times obtained by applying the

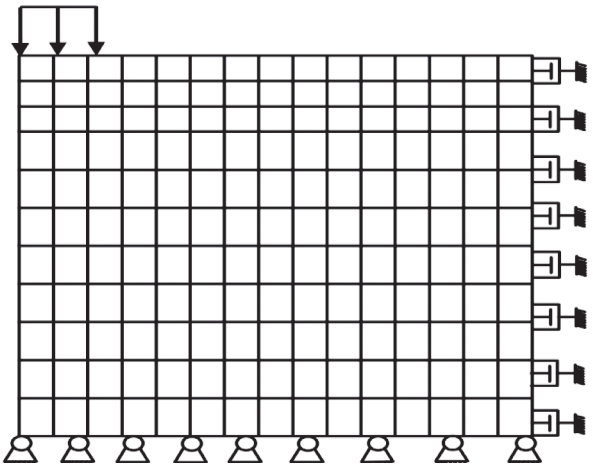

Figure 1: Finite element model of the pavement structure.

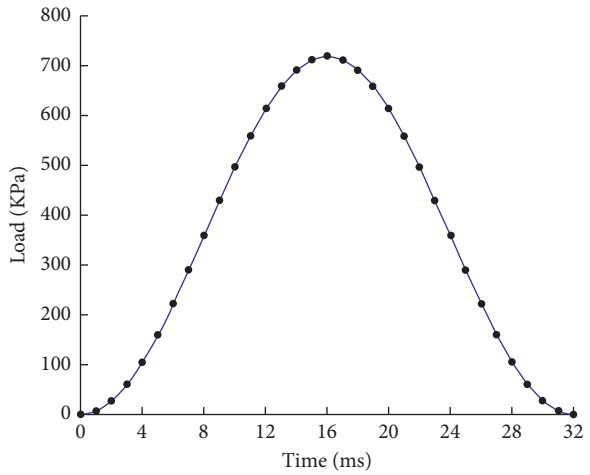

Figure 2: FWD load time history curve.

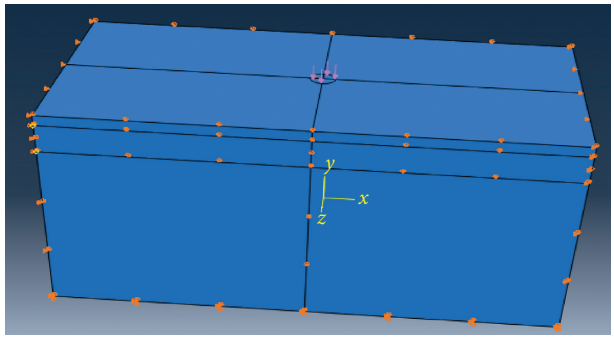

Figure 3: Finite element model.

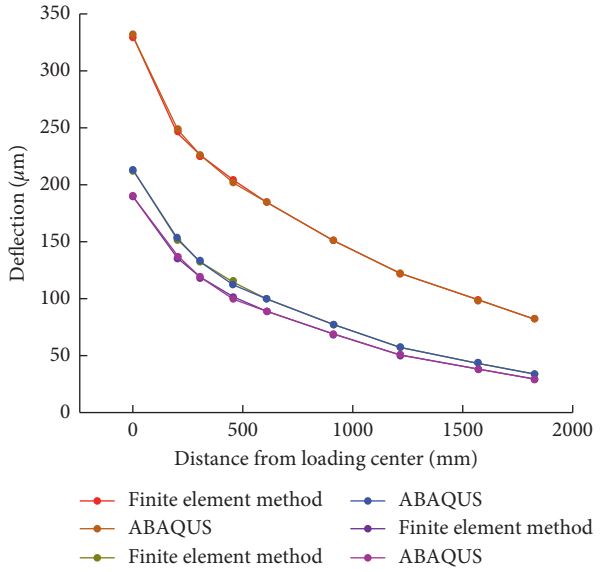

Figure 4: Comparison of pavement deflection calculation results at different time.

Table 1: Dynatest8000 FWD transducer layout.

Transducer number	C1	C2	C3	C4	C5	C6	C7	C8	C9
Distance from loading center (mm)	0	204	305	457	610	914	1219	1574	1829

method in this paper are basically consistent with those of ABAQUS, which proves that the dynamic response calculation program has high accuracy.

(2) In order to further verify the accuracy of the program, based on FWD-measured deflection basin data and the position of the measuring points in [22], the calculation program of this paper is used to calculate the corresponding data. The calculated results are compared with the measured data, as shown in Figure 5.

3. Modulus Inversion of Asphalt Concrete Pavement Structural Layer Based on SVM

3.1. Modulus Inversion of Asphalt Concrete Pavement Structural Layer. This paper introduces the SVM model in the modulus inversion of the asphalt concrete pavement structure layer and uses the SVM model instead of the numerical model to carry out the inversion of the modulus, considering the disadvantages of the previous inversion methods of pavement modulus. Based on the structural risk minimization criterion, SVM can balance the relationship between training error and complexity of learning machine. It can improve inversion efficiency in the application of engineering practice. SVM can solve the "overlearning" problem faced by the neural network well and make the calculation results have better generalization ability. It has been widely used in the fields of automatic control, pattern recognition, and rock mechanic parameter inversion [23].

The inversion process of the pavement structural modulus using the SVM model is as follows [24].

The standard SVM function $\mathrm{SVM}(x_1, x_2, \ldots, x_m)$ is used to reflect the nonlinear relationship between deflection and parameters to be inversed:

$$\mathrm{SVM}(X):\ R^m \longrightarrow R, \tag{11}$$

$$y = \mathrm{SVM}(X), \tag{12}$$

$$X = (x_1, x_2, \ldots, x_m), \tag{13}$$

where $X = (x_1, x_2, \ldots, x_m)$ is the parameter of the pavement structural layer to be inverted and Y is the deflection value of a measuring point measured in the field.

The number of $\mathrm{SVM}(x_1, x_2, \ldots, x_m)$ is the same as the number of deflection transducer, and n SVM models correspond to n deflection values. The SVM model $y(X)$ which reflects the mapping relationship between structural layer modulus and pavement deflection is established by enough learning samples:

$$y(X) = \sum_{i=1}^{l} (\alpha_i - \alpha_i')k(x, x_i) + b, \tag{14}$$

where $y(X)$ is a set of displacements of a line corresponding to parameter $X = (x_1, x_2, \ldots, x_m)$; l is the number of learning samples; $k(x, x_i)$ is the kernel function; α, α^* is the Lagrange multiplier of the SVM algorithm.

From the SVM model, it can be seen that the parameter α, α^* and the offset b are important parameters for creating the SVM model, and their values can be obtained by solving the constrained quadratic programming problem:

$$\max W(\alpha, \alpha^*) = -\frac{1}{2} \sum_{i,j=1}^{l} (\alpha_i - \alpha_i^*)(\alpha_j - \alpha_j^*)k(x_i, x_j) + \sum_{i=1}^{l} y_i(\alpha_i - \alpha_i^*) - \varepsilon \sum_{i=1}^{l} (\alpha_i + \alpha_i^*), \tag{15}$$

$$s.t. \sum_{i=1}^{n} (a_i - a_i^*) = 0, 0 \le a_i, a_i^* \le C, \quad i = 1, \ldots, n. \tag{16}$$

An efficient optimization algorithm is used to solve the parameters α, α^* and the offset b to establish the standard SVM model. The optimal solution is constantly searched in the range of modulus. When the error between the deflection value calculated by the SVM model and the measured deflection reaches the minimum, a set of modulus parameters corresponding to the calculated deflection can be determined as the real modulus of the asphalt concrete pavement structure layer. The inversion process is completed.

3.2. Basic Steps of SVM Inversion Optimization Based on Firefly Algorithm. The selection and optimization of model parameters have a great influence on the establishment of SVM model. The reasonable model parameters are one of the important factors to ensure the accuracy and reliability of the inversion results of the SVM model. The SVM model has two parameters, the basic parameter of the model (such as penalty factor C and insensitive loss parameter ε) and the parameter related to kernel function (such as the kernel width σ in radial basis function, the constant c in polynomial kernel function, and the exponential function d). Previous methods of parameter selection mainly rely on subjective experience and grid search, so it is difficult to find the best parameters [25,26]. In recent years, scholars use the heuristic intelligent search algorithm with global optimization ability to select parameters of SVM and get good results. Therefore, the firefly algorithm is used to obtain the optimal parameters of the SVM model in this paper.

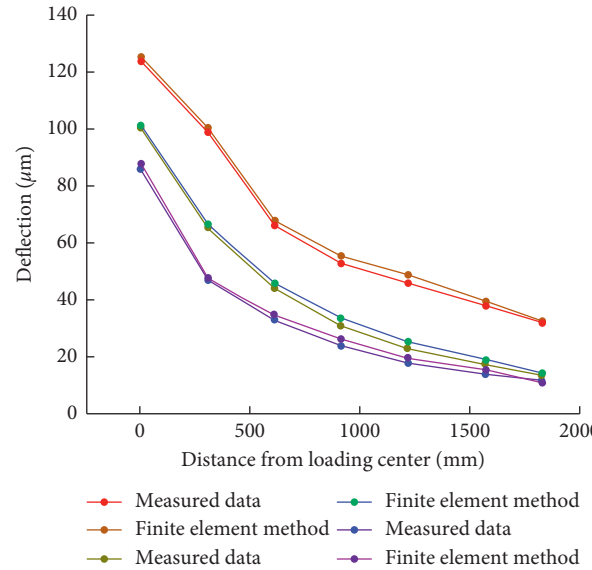

Figure 5: Comparison of deflection results at different measuring points.

3.2.1. Introduction of Firefly Algorithm. Suppose n fireflies are randomly and evenly distributed in the solution space and each firefly is given a unique initial brightness value. The function value of the firefly's position will determine the brightness of the firefly. The relationship between the position and the brightness of the firefly is the better the position, the higher the brightness. Each firefly has its own dynamic decision domain r_d^i, in which the firefly moves towards the brighter firefly, forming a domain set. Then, the position, brightness, and decision domain of the firefly are updated [27]. The main phases of the firefly algorithm are as follows:

(1) The updating phrase of the dynamic decision domain:

$$r_d^i(t+1) = \min\{r_s, \max\{0, r_d^i(t) + \beta(n_t - |N_t(t)|)\}\}, \tag{17}$$

where $r_d^i(t+1)$ is the $t+1$ generation decision range of the t generation firefly i; r_s is the perception range of the firefly; n_t is the domain threshold which can control the number of fireflies; β is the constant

related to the decision domain; $N_t(t)$ is the number of fireflies within the radius of r_d^i.

(2) The updating phrase of position:

In this phase, each firefly first selects the firefly whose brightness is higher than itself within the range of its decision domain to form the domain set. The formula is

$$N_t(t) = \left\{ j: \left\| x_j(t) - x_i(t) \right\| < r_d^i, l_i(t) < l_j(t) \right\}, \tag{18}$$

where $\|x_j(t) - x_i(t)\|$ is the Euclidean distance between two fireflies; $x_j(t)$is the firefly position; $l_i(t)$ is the fluorescein value of the t iteration.

The formula of the moving probability is as follows:

$$p_{ij}(t) = \frac{l_j(t) - l_t(t)}{\sum_{k \in N_t(t)} l_k(t) - l_i(t)}, \tag{19}$$

where p_{ij} is the probability of firefly i moving to firefly j.

After the composition of the domain set, the position is updated according to the following formula:

$$x_i(t+1) = x_i(t) + s\left[\frac{x_j(t) - x_i(t)}{\left\| x_j(t) - x_i(t) \right\|} \right]. \tag{20}$$

(3) The updating phrase of updating fluorescein value:

$$l_i(t) = (1-p) l_i(t-1) + \gamma J\left(x_i(t)\right), \tag{21}$$

where $l_i(t)$ represents the fluorescein value of the firefly i of the t generation; p is the vanishing rate; γ is the parameter to measure the fitness function value; $J(x_i(t))$ is the fitness function value.

The main steps of the firefly algorithm are as follows:

(1) Random initialization of fireflies$i\,(i = 1, 2, \ldots, n)$
(2) Calculating the function value $J(x_i(t))$ corresponding to the position $x_i(t)$ of the firefly i in the t generation and the fluorescein value $l_i(t)$ of the current firefly by formula (20), so as to update the fluorescein value of the firefly
(3) Each firefly looks for the individuals with higher fluorescein value in its dynamic decision domain radiusr_d^i and forms the domain set $N_t(t)$ together with the higher fluorescein value
(4) Getting the moving probability $p_{ij}(t)$of firefly i into the domain set by formula (18)
(5) Obtaining the moving position of firefly by formula (17)
(6) Updating the radius of dynamic decision domain by formula (16)

3.2.2. Optimization of SVM Model Parameters Based on Firefly Algorithm. This paper adopts the firefly algorithm to optimize the SVM model and then solves the problem of "overlearning" and "underlearning" when the SVM model is not the optimal parameter.

The specific steps of the firefly algorithm to optimize SVM model parameters are as follows:

(1) Giving initial values to the parameters of each firefly, and setting the initial position of the firefly with the range of initial position parameters ($C_{\min} \sim C_{\max}$, $\sigma_{\min} \sim \sigma_{\max}$) and the maximum number of iterations;
(2) Calculating brightness value as brightness update;
(3) Obtaining the domain set of each firefly and randomly selecting the firefly i in the set as its moving direction;
(4) Calculating the training value of SVM after position update. If the training value of the updated SVM is better than the previous one, the position will be replaced, otherwise it will not change;
(5) Updating the dynamic decision domain;
(6) Calculating the above process in cycle. If the search times reach its maximum, the cycle process will be interrupted. The SVM will be trained according to the optimal solution in the process until the end condition is satisfied.

3.3. Example Analysis

(1) The thickness of each layer of semirigid base asphalt concrete pavement is 18 mm, 32 mm, and ∞, respectively. Poisson's ratio of each layer is 0.35, 0.30, and 0.40. The number of transducers is $d_1 \sim d_7$. The position of each transducer is 0.0 mm, 304.8 mm, 609.6 mm, 914.4 mm, 1219.2 mm, 1524.0 mm, and 1828.8 mm, respectively.

In this paper, seven groups of different modulus parameters are set up to test the correctness of the inversion results. The corresponding deflection values of each parameter combination are shown in Table 2. The range of modulus parameters of each layer is 1000–4000 MPa for surface course, 400–3000 MPa for base course, and 30–150 MPa for subgrade. The modulus parameters of each layer are substituted into the dynamic response calculation program to obtain the corresponding pavement deflection. These data form a sample pair, and thus 12 test samples and 100 learning samples are obtained.

It can be seen from Figure 6 that the modulus of asphalt concrete pavement surface course, base layer, and subgrade obtained by this method is between the regression model algorithm and the BP model algorithm. Furthermore, the inversion results have good stability by this method. The three methods are basically consistent with each other, which proves that the method in this paper has high accuracy and completely meets the practical engineering calculation requirements.

This paper adopts standard SVM in which the loss function is an insensitive loss function and the kernel function is a radial basis kernel function (RBF) [28]. Through the training of learning samples and test

Table 2: Seven sets of deflection basin data.

Number	Surface course (MPa)	Base course (MPa)	Subgrade (MPa)	Theoretical deflection (μm)						
				d1	d2	d3	d4	d5	d6	d7
1	1200	1400	60	329.63	225.14	184.91	150.78	121.96	99.19	82.42
2	2330	1700	110	293.24	199.33	162.29	132.15	107.16	87.43	72.74
3	1550	2200	140	288.98	190.19	154.85	125.80	101.77	82.82	69.02
4	3600	1300	35	318.47	232.88	192.81	159.02	130.09	106.65	88.16
5	2350	800	50	331.95	234.87	190.54	155.04	125.74	102.62	84.88
6	3200	1400	90	294.92	204.57	166.33	135.55	110.05	89.91	74.76
7	3800	1100	140	286.91	195.02	155.67	125.50	101.24	82.55	68.88

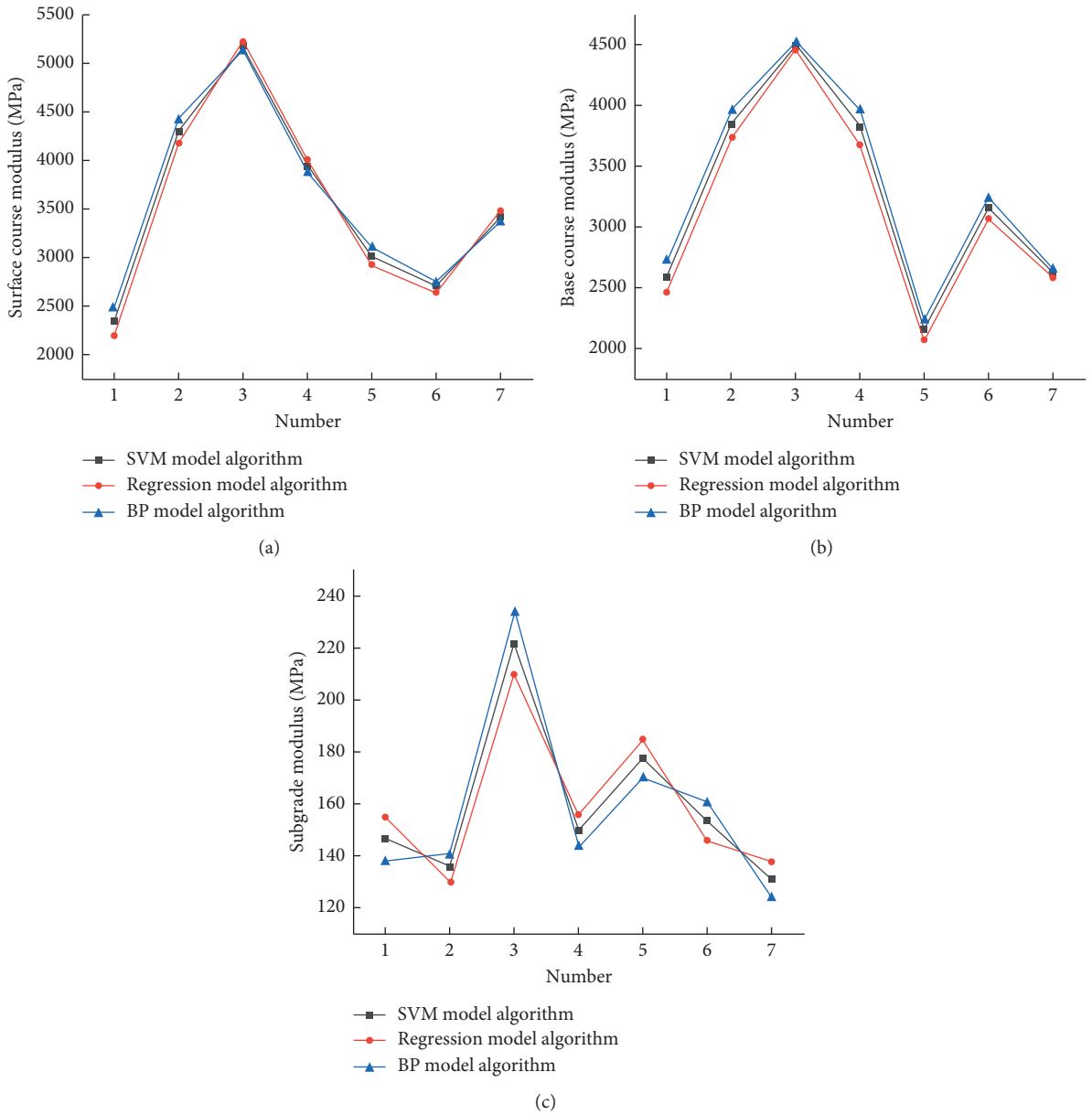

Figure 6: Comparison of inversion results of different inversion methods.

samples, the optimal model parameters and the offset b values of SVM corresponding to each deflection transducer are obtained, as shown in Table 3.

After obtaining the optimal SVM model, the SVM model instead of the numerical model combines with the firefly algorithm to carry out the inversion. The inversion results are shown in Table 4.

The results reveal that the average absolute value of relative error of surface course modulus inversion results is 0.97%, and the maximum value is of 2.16%. The average absolute value of relative error absolute value of the base course modulus inversion result is 0.82%, and the maximum value is of 2.31%. The average absolute value of relative error absolute value of the subgrade structure layer modulus prediction result is 1.91%, and the maximum value is of 3.73%. Based on the results, the SVM model has high inversion efficiency and accuracy, which can fully meet the practical engineering demands.

(2) In order to further verify the accuracy of the inversion program, the inversion method proposed in this paper is used to carry out the modulus inversion of each structural layer of pavement with the measured deflection data [22]. The results are compared with those of the two methods in [22]. The results are presented in Table 5.

4. Correction of Modulus Inversion in Seasonal Frozen Area

4.1. Temperature Correction of Inversion Surface Modulus in Seasonal Frozen Area. For asphalt concrete pavement, the asphalt mixture is a kind of temperature sensitive material. Its strength, stiffness, and deformation resistance will change with temperature. When the asphalt concrete pavement temperature increases, the strength and stiffness of the asphalt mixture will decrease, causing the asphalt concrete pavement to easily undergo high-temperature shear failure under the vehicular load. When the asphalt concrete pavement temperature decreases, the deformation capacity of the asphalt mixture decreases, causing the asphalt concrete pavement to easily undergo low-temperature shrinkage cracking. Pavement modulus which can reflect the strength and stiffness of pavement is the main parameter of pavement structure design. Therefore, the analysis of the relationship between asphalt concrete pavement surface modulus and temperature is of great significance to the evaluation of pavement structure bearing capacity in the seasonal frozen area.

In this paper, the temperature field model of Zhang is selected as the research object [29]. The model is as follows.

Pavement temperature along the depth direction:

$$T_H = T_{60} + (T_s - T_{60}) \times \left(a \times H^3 + b \times H^2 + c \times H + d\right) \times \exp(eH), \tag{22}$$

where H is the distance between a certain point within the asphalt concrete pavement and the surface; T_H is the temperature at the depth of h; T_{60} is the temperature at 60 cm of subgrade; T_S is the asphalt concrete pavement temperature or actual pavement temperature; $a \sim e$ is the undetermined regression coefficient.

According to the hot linear elastic layer system theory and in consideration of the structural characteristics and stress state of asphalt pavement, the following assumptions are set:

(1) Each structural layer of the asphalt concrete pavement is isotropic and homogeneous thermoelasticity material

(2) It is assumed that only the material parameters of the surface course are affected by temperature and the material parameters of the base course and subgrade are regarded as constant

(3) The structural layers are completely continuous

Based on the above hypothesis analysis, the following calculation examples are constructed for analysis: a three-layer semirigid base pavement system in the seasonal frozen area is selected, including 18 cm asphalt concrete surface course and 32 cm cement-stabilized macadam base and subgrade. Poisson's ratio of each layer in the asphalt concrete pavement is, respectively, 0.35, 0.30, and 0.40 and the density is 2400 kg/m^3, 2300 kg/m^3, and 1800 kg/m^3.

The relationship between the inversion modulus of asphalt concrete pavement surface course and temperature can be obtained by embedding the temperature field prediction model into the inversion program. The calculation results are shown in Figure 7 and Table 6.

The inverse modulus of asphalt pavement has a good exponential relationship with the asphalt concrete pavement temperature from Figure 7. The inverse modulus of the surface course will decrease with the increase in temperature. The correlation formula of E-T is obtained by regression analysis:

$$E = 2110e^{-0.033T}. \tag{23}$$

The correlation coefficient R^2 between them is equal to 0.9896.

The temperature correction coefficient K is defined as the ratio of the modulus E of asphalt pavement under T temperature and the modulus E_S under standard temperature T_S. T_S is taken as 20°C, that is,

$$K = \frac{E}{E_S} = \frac{2110e^{-0.033T}}{2110e^{-0.033T_S}} = e^{-0.033(T-20)}, \tag{24}$$

Table 3: Model training results.

Position (mm)	0	304.8	609.6	914.4	1219.2	1524.0	1828.8
C	2000	1870	1968	1580	1856	1920	1740
σ	2.35	2.36	2.36	2.37	2.37	2.38	2.39
b	109.74	104.06	97.43	90.17	82.90	75.88	69.27

Table 4: Modulus inversion results.

Number	Structural layer	Structural layer modulus (MPa)	Inverse modulus (MPa)	Inversion relative error (%)
	Surface course	1200	1190	−0.83
1	Base course	1400	1404	0.29
	Subgrade	60	58	−2.77
	Surface course	2330	2346	0.70
2	Base course	1700	1702	0.14
	Subgrade	110	106	−3.73
	Surface course	1550	1533	−1.12
3	Base course	2200	2229	1.30
	Subgrade	140	140	−0.07
	Surface course	3600	3618	0.49
4	Base course	1300	1290	−0.79
	Subgrade	35	34	−2.86
	Surface course	2350	2401	2.16
5	Base course	800	819	2.31
	Subgrade	50	50	0.00
	Surface course	3200	3169	−0.98
6	Base course	1400	1413	0.90
	Subgrade	90	91	1.11
	Surface course	3800	3819	0.49
7	Base course	1100	1100	−0.01
	Subgrade	140	144	2.86

Table 5: Comparison of inversion results of different inversion methods.

	Surface course modulus (MPa)			Base course modulus (MPa)			Subgrade modulus (MPa)		
Number	SVM model algorithm	Regression model algorithm	BP model algorithm	SVM model algorithm	Regression model algorithm	BP model algorithm	SVM model algorithm	Regression model algorithm	BP model algorithm
1	2342	2198	2486	2599	2466	2732	147	155	138
2	4300	4177	4423	3850	3737	3962	136	130	141
3	5187	5225	5149	4495	4463	4526	222	210	234
4	3938	4003	3872	3819	3679	3957	150	156	144
5	3009	2916	3102	2157	2075	2239	178	185	170
6	2694	2638	2749	3159	3077	3241	154	146	161
7	3427	3481	3372	2629	2595	2663	131	138	124

where K is the correction coefficient of the inversion modulus of the surface course and T is the expressed temperature.

4.2. Humidity Correction of Inversion Subgrade Modulus in Seasonal Frozen Area. Temperature in different seasons fluctuates greatly in the seasonal frozen area. Water in the subgrade turns into ice at the temperature below 0°C, which changes the properties of subgrade structure materials as well as the position and volume of soil particles. In contrast, ice turns into water at the temperature above 0°C, which causes the volume of soil particles to become smaller. Both factors will result in repeated frost heaving and thawing settlement deformation of pavement. Therefore, considering

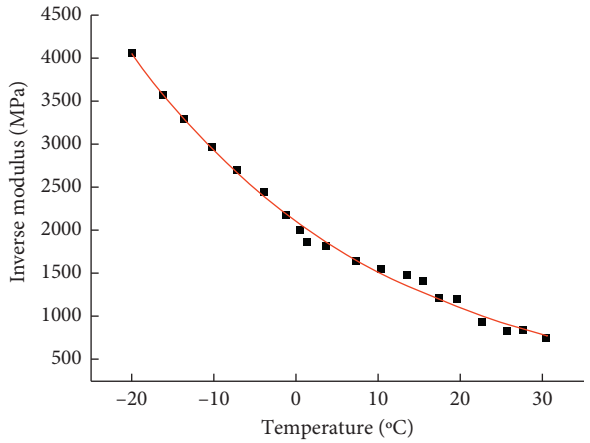

Figure 7: Correlation between inversion modulus of asphalt surface course and temperature.

Table 6: Correlating data of pavement temperature and inversion modulus of surface course.

Temperature (°C)	Inverse modulus (MPa)
−20.1	4059
−16.2	3585
−13.6	3299
−10.2	2964
−7.2	2697
−3.9	2441
−1.2	2186
0.5	2002
1.4	1873
3.7	1816
7.3	1641
10.4	1544
13.5	1481
15.5	1419
17.4	1209
19.6	1200
22.6	939
25.7	8299
27.6	837
30.5	743

the influence of subgrade water content on subgrade modulus inversion is of great significance to evaluate the performance of the asphalt concrete pavement structure layer in the seasonal frozen area.

The following basic assumptions are made to calculate the humidity field:

(1) The asphalt concrete pavement is simplified as a multilayer elastic system, assuming that the layers are continuous and compact and the materials of each layer are homogeneous and isotropic

(2) The moisture transmission only occurs on the cross-section of the asphalt concrete pavement

(3) The moisture change of the subgrade is only related to the initial water content and groundwater without regard to the external moisture movement among the structures

(4) The moisture movement is carried out in the subgrade regardless of moisture migration in other structural layers

The humidity field of subgrade with the above assumption can be described by the following humidity field equation with phase transition:

$$\frac{\partial w}{\partial t} = \frac{\partial}{\partial x}\left[D_x(w)\frac{\partial w}{\partial x}\right] + \frac{\partial}{\partial y}\left[D_y(w)\frac{\partial w}{\partial y} - K_y(w)\right] \quad t > 0, \tag{25}$$

where w is the water content; $K(w)$ is the hydraulic conductivity; $D(w)$ is the diffusivity.

The final moisture content of any point in the seasonal frozen area is calculated as follows: suppose that the phase change interface reaches here at time t_0, and its water content is $w(t_0,x,y)$; when the phase change interface develops downward at time t_1, the final water content of this point is

$$w(x,y) = w(t_0,x,y) + (t_1 - t_0) \cdot \left[\left(D_y(w)\frac{\partial w}{\partial y} - K_y(w)\right) + D_x(w)\frac{\partial w}{\partial x}\right]. \tag{26}$$

The hydraulic conductivity $K(w)$ is related to dry density r_d and saturation G as follows:

$$K(w, r_d) = 0.046\left(\frac{2.7 - r_d}{1.44}\right)^{14.79} G^{9.69}. \tag{27}$$

The diffusivity $D(w)$ is related to dry density r_d and saturation G as follows:

$$D(w, r_d) = 10.28\left(\frac{2.7 - r_d}{1.44}\right)^{11.44} G^{2.72}. \tag{28}$$

The correlation between subgrade modulus and humidity can be obtained by embedding the model into the inversion program. The calculation results are shown in Figure 8 and Table 7.

Figure 8 shows that the inversion modulus of subgrade decreases with the increase of water content, which is an exponential relationship. The correlation formula of inversion modulus of subgrade and water content is obtained from regression analysis as follows:

$$E = 215.97e^{-0.049w}. \tag{29}$$

The correlation coefficient R^2 between them is equal to 0.9833.

The humidity correction coefficient K_E is defined as the ratio between the modulus E of subgrade with water content w and the modulus E_S under the condition of optimal water content w_S. The optimal water content w_S is 16%, that is,

$$K_E = \frac{E}{E_s} = \frac{215.97e^{-0.049w}}{215.97e^{-0.049w_s}} = e^{-0.049(w-16)}, \tag{30}$$

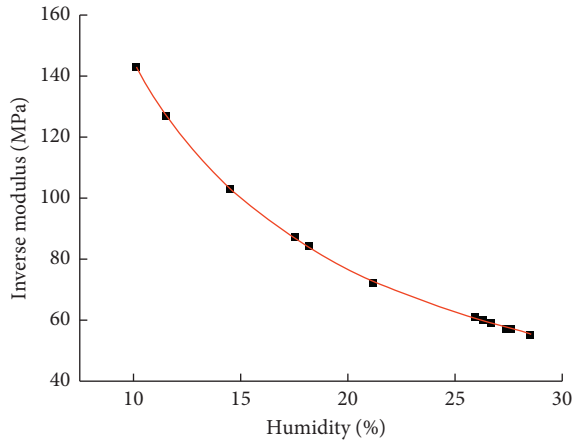

Figure 8: Correlation between inversion modulus of subgrade and humidity.

Table 7: Subgrade humidity and inversion modulus data.

Humidity (%)	Inverse modulus (MPa)
26.70	59
27.60	57
27.40	57
26.30	60
28.50	55
21.20	72
17.50	87
18.20	84
11.50	127
10.10	143
14.50	103
25.90	61

where K_E is the correction coefficient of inversion modulus of subgrade and w is the water content.

5. Conclusion

In this paper, in view of the existing problems in the inversion of the asphalt concrete pavement structure layer modulus, the support vector machine model is introduced into the asphalt concrete pavement modulus inverse analysis to study the influences of the temperature and humidity in the seasonal frozen area on the inversion modulus. The research conclusions are as follows:

(1) After inversion by using the support vector machine model optimized by the firefly algorithm, the average of relative error absolute value of the pavement structural layer modulus is within 2% and the maximum value is within 4%, which meets the accuracy requirements.

(2) Considering the influence of temperature and humidity on the inversion modulus, the inversion modulus of pavement surface layer will decrease with the increase of temperature, and the inversion modulus of subgrade will decrease with the increase of water content.

(3) According to the inversion results, the modified formulas for the inversion modulus of the semirigid base pavement surface layer and subgrade varying with temperature and humidity are established: $K = e^{-0.033(T-20)}$ and $K_E = e^{-0.049(w-16)}$.

Data Availability

The data used to support the findings of this study are not available.

Conflicts of Interest

The authors declare that they have no conflicts of interest.

Acknowledgments

The authors acknowledge the support received from the National Key Research and Development Plan (Grant no. 2018YFB1600200), the National Natural Science Foundation of China (Grant nos. 51878624 and 51878622), the Major Scientific and Technological Special Project in Henan (Grant no. 181100310400), the Program for Innovative Research Team (in Science and Technology) at the University of Henan Province (Grant no. 18IRTSTHN007), the Program for Science and Technology Innovation Talents in Universities of Henan Province (Grant no. 19HASTIT041), and the Key Research Projects of Higher Education in Henan Province (Grant no. 18A580001).

References

[1] C. Jing, J. Zhang, and B. Song, "An innovative evaluation method for performance of in-service asphalt pavement with semi-rigid base," *Construction and Building Materials*, vol. 235, 2020.

[2] A. Meng, "Feasibility of freeze-thaw damage analysis for asphalt mixtures through dynamic nondestructive testing," *Construction and Building Materials*, vol. 233, 2020.

[3] G. L. Golewski, "A novel specific requirements for materials used in reinforced concrete composites subjected to dynamic loads," *Composite Structures*, vol. 223, no. 223, 2019.

[4] G. L. Golewski, "New principles for implementation and operation of foundations for machines: a review of recent advances," *Structurat Engineering and Mechanics*, vol. 71, pp. 317–327, 2019.

[5] M. Li, H. Wang, G. Xu, and P. Xie, "Finite element modeling and parametric analysis of viscoelastic and nonlinear pavement responses under dynamic FWD loading," *Construction and Building Materials*, vol. 141, pp. 23–35, 2017.

[6] H. Scrivner and W. F. Mcfarland, "A systems approach to the flexible pavement design problem," pp. 20–70, 1968, Research report.

[7] N. Sivaneswaran, S. L. Kramer, and J. P. Mahoney, "Advanced backcalculation using a nonlinear least squares optimization technique," *Journal of the Transportation Research Board*, vol. 1239, 1991.

[8] F. Wang and R. L. Lytton, "System identification method for backcalculating pavement layer properties," *Journal of the Transportation Research Board*, vol. 1384, pp. 1–7, 1993.

[9] T. Scullion, J. Uzan, and M. Paredes, "Modulus: a microcomputer-based backcalculation system," *Transportation Research Record*, vol. 1260, pp. 180–191, 1990.
[10] R. W. Meier, D. R. Alexander, and R. B. Freeman, "Using artificial neural networks as a forward approach to backcalculation," *Transportation Research Record: Journal of the Transportation Research Board*, vol. 1570, no. 1, pp. 126–133, 1997.
[11] T. F. Fwa, C. Y. Tan, and W. T. Chan, "Backcalculation analysis of pavement-layer moduli using genetic algorithms," *Transportation Research Record: Journal of the Transportation Research Board*, vol. 1570, no. 1, pp. 134–142, 1997.
[12] H. Wang, M. Li, P. Szary, and X. Hu, "Structural assessment of asphalt pavement condition using back calculated modulus and field data," *Construction and Building Materials*, vol. 211, pp. 943–951, 2019.
[13] L. You, K. Yan, and N. Liu, "Assessing artificial neural network performance for predicting interlayer conditions and layer modulus of multi-layered flexible pavement," *Frontiers of Structural and Civil Engineering*, vol. 12, 2020.
[14] M. Li and H. Wang, "Development of ANN-GA program for back calculation of pavement moduli under FWD testing with viscoelastic and nonlinear parameters," *International Journal of Pavement Engineering*, vol. 20, no. 4, pp. 490–498, 2019.
[15] J. C. Edwin and J. G. Anthony, "Effect of freezing and thawing on the permeability and structure of soils[J]," *Engineering Geology*, vol. 13, no. 1–4, pp. 73–92, 1979.
[16] E. Simonsen, V. C. Janoo, and U. Isacsson, "Resilient properties of unbound road materials during seasonal frost conditions," *Journal of Cold Regions Engineering*, vol. 16, no. 1, pp. 28–50, 2002.
[17] X. Mao, Z. Hou, and W. Wang, "Experimental study on the resilience modulus of remolded soil based on water content and freeze-thaw cycles," *Chinese Journal of Rock Mechanics & Engineering*, vol. 28, pp. 3585–3590, 2009.
[18] W. Chen, "Study on modulus of resilience and humidity of subgrade seasonal frozen region," Master Degree Thesis, Wuhan Polytechnic University, Hubei, China, 2012.
[19] M. Wang, "Research on moisture and temperature monitoring and intensity change of subgrade in seasonal frozen region," Master Degree Thesis, Northeast Forestry University, Harbin, China, 2014.
[20] M. Williams, *Structural Dynamics*, Taylor & Francis, Milton Park, UK, 2016.
[21] I. Babuška and T. Strouboulis, *The Finite Element Method and its Reliability*, Clarendon Press, Oxford, UK, 2001.
[22] X. Qiu, *Research on modulus parameter inversion and correction method of semi-rigid base asphalt pavement based on FWD*, PhD Thesis, Tongji University, Shanghai, China, 2009.
[23] V. Vapnik, "Statistical Learning Theory," *Encyclopedia of the Sciences of Learning*, vol. 41, no. 4, pp. 3185–3185, 1998.
[24] C. Cortes and V. Vapnik, "Support-vector networks," *Machine Learning*, vol. 20, no. 3, pp. 273–297, 1995.
[25] V. Cherkassky and Y. Ma, "Practical selection of SVM parameters and noise estimation for SVM regression," *Neural Networks*, vol. 17, no. 1, pp. 113–126, 2004.
[26] K. Ito and R. Nakano, "Optimizing support vector regression hyperparameters based on cross-validation," in *Proceedings of the 2003 International Joint Conference*, Portland, OR, USA, 2003.
[27] K. N. Krishnanand and D. Ghose, "Detection of multiple source locations using A glowworm mmetaphor with applications to collective robotics," in *Proceedings 2005 IEEE Swarm Intelligence Symposium*, Pasadena, CA, USA, 2005.
[28] F. Budiman, "SVM-RBF parameters testing optimization using cross validation and grid search to improve multiclass classification," *Scientific Visualization*, vol. 11, no. 1, pp. 80–90, 2019.
[29] R. Zhang, "Study on temperature field distribution law of pavement structure in seasonally frozen regions considering extreme climate," Master Degree Thesis, Harbin Institute of Technology, Harbin, China, 2012.

Hindawi
Advances in Civil Engineering
Volume 2020, Article ID 8878974, 7 pages
https://doi.org/10.1155/2020/8878974

Research Article

Study on Temperature Field Massive Concrete in Early Age Based on Temperature Influence Factor

Min Zhang, Xianhua Yao, Junfeng Guan, and Lielie Li

School of Civil Engineering and Communication, North China University of Water Resources and Electric Power, Zhengzhou 450045, China

Correspondence should be addressed to Junfeng Guan; shuaipipi88@126.com and Lielie Li; 13370912@qq.com

Received 27 August 2020; Revised 13 September 2020; Accepted 21 September 2020; Published 12 October 2020

Academic Editor: Yifeng Ling

In order to solve the problem of insufficient accuracy of early temperature field caused by the change of hydration rate under different temperatures, the theoretical formula of finite element calculation based on temperature influence factor is put forward and then the theory is tested. On this basis of this theory, the early temperature field of a RCC dam is numerically simulated and the variation law of concrete hydration rate under different temperatures is studied. The numerical simulation results are compared with the results without considering the temperature effect and the measured temperature data. The results show that the theoretical results are in agreement with the measured temperature data, and the accuracy and applicability of the theoretical formula are proved.

1. Introduction

Due to great temperature difference, the temperature stresses are caused by heat of hydration of cement which leads to temperature cracks during mass concrete construction processing. Temperature cracks seriously affect the durability of concrete structures and reduce the service life of the project [1–3]. Cement hydration of mass concrete produces vast quantities of heat. However, concrete as a poor conductor of heat leads to its slow heat dissipation and high internal temperature. The heat of hydration generation rate of cement varies with different temperatures, and in the first 2 days, the heat of hydration of cement is 40–80% of the total heat [4, 5]. Therefore, it is more significant to simulate accurately the early-age temperature field of mass concrete considering temperature effect.

Considering the temperature influence on the mass temperature field, Saul [6] and Rastrup [7] firstly proposed the concept of equivalent age. Based on the concept of equivalent age, the domestic and foreign scholars have carried out a lot of research. For example, the Jin et al. [8] calculated equivalent age based on the equivalent quantity of cement and determined the concrete temperature field equation; Zhang et al. [9]. studied the influence of equivalent age on the adiabatic temperature rise of concrete; Schindler [10] studied the temperature effect on hydration heat of concrete based on equivalent age; Schutter [11] studied the heat of hydration from concrete based on the degree of hydration, which is consistent with the concept of equivalent age. Dong and Li [12] considered the chemical reaction rate of cement at different curing temperatures and deduced the hydration-heat released model of cement based on equivalent age. In order to directly reflect the change of hydration rate during the actual age, Zhang et al. [4]. proposed the temperature influence factor to accurately simulate the temperature field of PCCP (Prestressed Concrete Cylinder Pipe) on the high temperature curing stage. On this basis, this study presents a finite element theoretical formula based on the temperature influence factor and studies the early-age temperature field variation law of mass concrete considering the influence of temperature. Furthermore, compared with the measured temperature data, the theoretical formula is verified to be the correction and a basis for accurately simulating the temperature field of mass concrete is provided.

2. Hydration Rate Based on Temperature Influence Factor

2.1. Temperature Influence Factor. Arrhenius proposed the empirical formula for the rate of chemical reactions [13–18]:

$$v = Ae^{-(E_a/RT),} \tag{1}$$

where A is the pre-exponential factor and E_a is the reaction activation energy; Ordinary Portland cement E_a is 33500/(J·mol^{-1}), atmospheric constant $R = 8.314$ (J·mol^{-1}); T is temperature (k).

Integral expression of equation (1) is shown as

$$\ln\left(\frac{v_i}{v_r}\right) = \frac{E_a}{R}\left(\frac{1}{T_r} - \frac{1}{T_i}\right). \tag{2}$$

Making temperature influence factor $c_{T_i} = (v_i/v_r)$, c_{T_i} is the temperature influence factor at time i, which is the ratio of the reaction rate corresponding to the temperature at time i to the reaction rate at reference temperature. Formula (3) of temperature influence factor is obtained:

$$c_{T_i} = e^{(E_a/R)((1/T_r) - 1/T_i),} \tag{3}$$

where T_r is the reference temperature and T_i is the concrete temperature at a certain moment i.

2.2. The Equation of Hydration Rate Based on the Temperature Influence Factor. Assuming any point coordinate (x, y, z) in the concrete, the heat conduction equation of the transient temperature field [18] is shown as

$$c\rho\frac{\partial T}{\partial t} = \lambda\left(\frac{\partial^2 T}{\partial x^2} + \frac{\partial^2 T}{\partial y^2} + \frac{\partial^2 T}{\partial z^2}\right) + \frac{\mathrm{d}Q_{(t)}}{\mathrm{d}t}, \tag{4}$$

where c is the specific heat capacity; ρ is the density; T is the temperature; and t is the actual age.

In the temperature field simulation of mass concrete, the temperature influence factor c_T is introduced to the heat conduction equation (4) considering the temperature effect. The modified formula is shown as

$$c\rho\frac{\partial T}{\partial t} = \lambda\left(\frac{\partial^2 T}{\partial x^2} + \frac{\partial^2 T}{\partial y^2} + \frac{\partial^2 T}{\partial z^2}\right) + c_T\frac{\mathrm{d}Q_{(t)}}{\mathrm{d}t}. \tag{5}$$

The heat conduction equation (5) is to consider the temperature effect in transient temperature field, and the innovation is the introduction of temperature influence factorc_T.

Concrete hydration heat is generated and produced, in essence, by the compounds of cement hydration reaction with water hydration heat. Cement hydration heat is not fully released in the hardening process, but gradually released as time [19–22]. The hydration heat of cement changes with time:

$$Q_{(t)} = Q_\infty\left(1 - e^{mt^n}\right), \tag{6}$$

where t is the actual age; Q_∞ is the final hydration heat$t \longrightarrow \infty$; and m and n are the constant coefficients.

The hydration rate equation considering the temperature effect for any element in the finite element model at time t_i is shown as

$$q^T_{(t_i)} = c_{T_i}\frac{dQ_{(t)}}{dt} = e^{(E_a/R)((1/T_r) - 1/T_i)}\, t_i^{n-1} e^{mt_i^n} mnQ_\infty. \tag{7}$$

In formula (7), the temperature influence item is $e^{(E_a/R)((1/T_r) - 1/T_i)}$, namely, the temperature influence factor c_{T_i}. If $T_r = 20^\circ$C, when $T_i \geq 20^\circ$C, $c_{T_i} \geq 1$; when $T_i < 20^\circ$C, $0 < c_{T_i} < 1$. The age effect term is $t_i^{(n-1)}$; moreover, this item declines with the increase of age and changes in (0, 1).

When the initial time ($t = 1$ d) and pouring temperature is T_0, the initial hydration heat rate value is q_1. If the initial value of the hydration heat rate is known, the temperature T_i at a certain unit time t_i can be obtained by program language programming. Thus, the temperature influence factor c_{T_i} at time t_i can be obtained from the heat conduction equation (3). The temperature field of mass concrete affected by temperature is calculated by the heat conduction equation (5).

3. Verify the Theory

In order to study the temperature field variation law of mass concrete under the influence of different temperature, the concrete finite element model of 1m thickness, 5 m long, and 5 m wide is used to verify the theory. The temperature field of the center point in the model is studied under the different ambient temperatures. Three calculation conditions: the 1st condition is cold environment, 5°C ambient temperature and 10°C pouring temperature; the 2nd condition is high temperature environment, 35°C ambient temperature and 10°C pouring temperature; the 3rd condition is high temperature environment, 40°C ambient temperature and 20°C pouring temperature. Under the different conditions, comparison analysis of temperature field in the center point M considering and not considering the temperature effect is studied. The results are shown in Figure 1.

In Figure 1, we can see that

(1) In the 1st condition, the slope of the point on L_1 curve is obviously smaller than that of curve L_{01} after considering temp-effect. Temperature change rate decreases and the peak temperature is decreased from 20.4°C to 17.2°C. After reaching the peak temperature on the 10th day, the slope difference between the curve L_1 and L_{01} becomes weaker and weaker gradually. The reason is that the temperature influence factor $c_{T_i} < 1$ and the heat of hydration rate are lower than that of without considering. It leads to the decrease of the temperature change rate and the temperature field changes obviously. With the increase of age, the age effect term $t_i^{n-1}e^{mt_i^n}$ is gradually reduced to zero. Thus, the temperature change rate is getting smaller and smaller.

(2) In the 2nd condition, when the temperature is between 10 – 20°C, the slope of L_2 curve is smaller than curve L_{02}, the temperature change rate decreases.

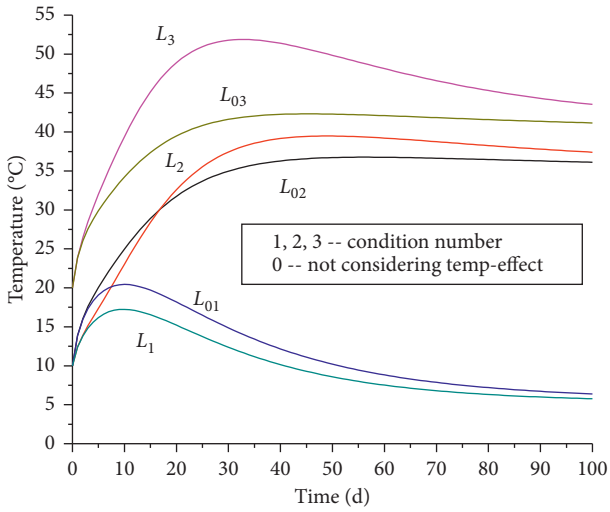

Figure 1: The temperature process curve of point M.

When the temperature is higher than 20°C, the slope of the point on the L_2 curve is obviously larger than that of L_{02} and the peak temperature increases from 36.8°C to 39.5°C. After reaching the peak temperature on the 50th day, the slope difference between the curve L_2 and L_{02} becomes weaker and weaker gradually. The reason is that the temperature influence factor $c_{T_i} > 1$ and the heat of hydration rate is higher than that of without considering temperature influence. It leads to the increase of the temperature change rate and the temperature field changes obviously. With the increase of age, the age effect term $t_i^{n-1}e^{mt_i^n}$ is gradually reduced to zero. Thus, the temperature change rate is getting smaller and smaller.

(3) In the 3rd condition, the slope of curve L_3 is obviously larger than L_{03} in early age. The temperature change rate increases, and the peak temperature increases from 42.3°C to 51.9°C. When after reaching the peak temperature on the 35th day, the slope difference between the curves L_3 and L_{03} becomes weaker and weaker gradually. After considering the temperature effect, the temperature difference between inside and outside increases from 2.3°C to 11.9°C.

(4) The temperature effect is weakened with the increase of age. In order to save the finite element calculation time, the temperature effect is taken into consideration only in early age, which is within two months after pouring concrete. Because after two months, the both temperature changes tend to be consistent. Beyond the time, the temperature effect is not considered. Considering the influence of temperature, the higher the temperature, the faster the hydration rate and the more obvious the change of temperature. It is more unfavorable to the concrete temperature control during the construction period, and vice versa.

The calculation results under the different conditions are shown in Table 1. In Table 1, it can be seen that, in high-temperature areas, the temperature difference has increased by five times after considering the temperature influence factors; however, in cold areas, the temperature difference does not change significantly. For the mass concrete engineering in the high temperature region and the high temperature curing, it is necessary to consider the temperature effect especially in the early temperature field simulation, which can improve the simulation accuracy of the temperature field and better construction temperature control.

4. Engineering Example

4.1. Engineering Overviews. One full section RCC gravity dam is divided into 22 sections. Building surface elevation is 73.0 m, and the crest width is 7 m. The thickness of the roller compacted layer is 30 cm. The interval layer thickness is 2 m, and the interval time is 5–7 days. The typical dam section No. 6 is used for finite element calculation. The length of the dam section is 20 m, and the dam height is 38.5 m. The element type of finite element analysis is solid70. The finite element model has a total of 60102 nodes and 50240 elements, and the finite element model is shown in Figure 2.

4.2. Material Parameters and Hydration Heat Calculation

(1) Material parameters and cement compositions: material parameters and cement components used in the finite element calculation for the RCC dam are shown in Tables 2 and 3, respectively.

(2) m and n parameters: Borg analyzed a large number of cement hydration heat test data, using the least squares method to obtain the empirical formula of multiple regression hydration heat [14, 15]:

$$Q(t) = A_t \times P_a + B_t \times P_b + C_t \times P_c + D_t \times P_d. \quad (8)$$

In formula (8), $Q_{(t)}$ is cement hydration heat on the age of t, kJ/kg; P_a, P_b, P_c, and P_d are C_3S, C_2S, C_3A, and C_4AF percent content, respectively; A_t, B_t, C_t, and D_t corresponding to unit mass C_3S, C_2S, C_3A, and C_4AF hydration heat value in t-age, kJ/kg.

The heating quantity of various hydration substances in cement clinker at different ages at 20°C is shown in Table 4 [18–20].

The empirical formula for the hydration heat of mixed cement with admixture [20–24]:

$$Q_P = Q_0(1 - kp), \quad (9)$$

where Q_p is the hydration heat of the cement mixed with admixture; Q_0 is the hydration heat of the cement without admixture; p is the percentage of the admixture; the maximum value of p is 60%; and k is empirical coefficient 0.55. When the content of admixture is greater than 60%, the empirical coefficient k value is 0.5.

Table 1: The calculation results under different conditions.

Condition number	Ambient temperature (°C)	Pouring temperature (°C)	Peak temperature (°C)		Temperature difference (°C)	
			Without C_T	Considering C_T	Without C_T	Considering C_T
1	5	10	20.4	17.2	15.4	12.3
2	35	10	36.8	39.5	1.8	4.5
3	40	20	42.3	51.9	2.3	11.9

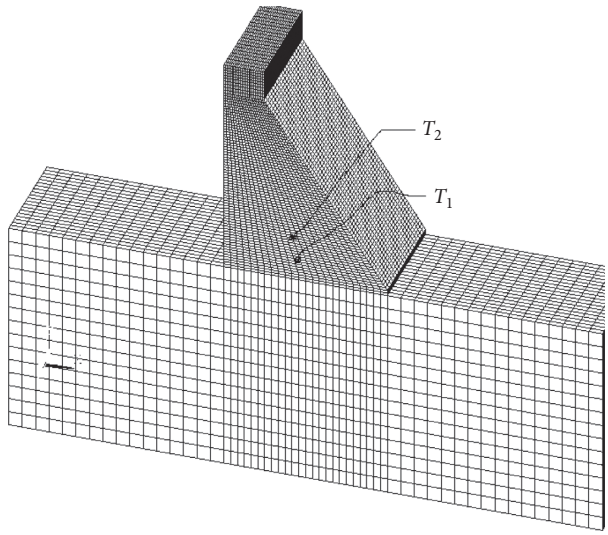

Figure 2: Finite element model.

Table 2: Material parameters.

Material	Density (kg/m^3)	Specific heat capacity (J/kg·K)	Thermal conductivity W/(m·K)	Poisson ratio	Linear expansion coefficient 10^{-6} (m/k)
Normal concrete	2 450	950	1.80	0.166	5.85
RCCII	2 350	950	1.85	0.166	5.85
RCCIII	2 350	950	1.85	0.166	6.75
Bed rock	2 550	780	1.66	0.235	7.10

Table 3: Cement components (%).

SiO_2	Al_2O_3	Fe_2O_3	CaO	MgO	SO_3	C_3S	C_2S	C_3A	C_4AF
20.94	5.59	5.24	63.46	2.88	1.8	51.22	21.43	5.77	16.77

Table 4: Heat of hydration substances.

Hydration substances	Heat of hydration (kJ/kg)					
	3 d	7 d	28 d	90 d	360 d	Q_∞
C_3S	242.9	221.8	376.7	435.5	489.8	510.1
C_2S	50.3	41.8	104.6	175.8	226.2	247.0
C_3A	887.7	1557.4	1377.4	1302.2	1168.2	1355
C_4AF	288.8	494.1	494.1	410.4	376.9	427.0

According to different cement mineral compositions and fly ash contents, the heat of hydration value can be calculated in different ages of the project through formulas (8) and (9). And the heat of hydration formula was fitted with the double exponential formula (6) by the hydration heat value of different ages. The fitting results of m and n coefficients are shown in Table 5.

4.3. Temperature Field Simulation. The ambient temperature of the engineering site varies with time according to the cosine curve of $T = 14.8–13.3\cos[3.14(t–1.1)/6]$ [24–26]. The mean annual temperature is 14.8°C. Roller-compacted concrete dam is compacted layer by layer, and each layer pouring temperature and time are different. The dam's temperature field is simulated using new heat conduction equation (formula (5)). Because the influence of temperature effect is obvious only in the early age, in order to save the calculation time, the calculation example only takes into account the influence of temperature in 30 days. Point T_1 is chosen to study the temperature field of the RCC dam on the early age. The position of T_1 is at the 82.5 m elevation and shown in Figure 1. The temperature history curve and the monitoring temperature data of position T_1 are shown in Figure 3.

Table 5: Hydration heat of concrete.

Type	Fly ash content (%)	Heat of hydration (kJ/kg)						m	n	R^2
		3 d	7 d	28 d	90 d	360 d	Q_∞			
Normal concrete	0	234.8	295.3	377.8	404.6	430.0	464.0	0.54	0.3	0.98
RCCII	50	176.1	214.1	273.9	293.3	311.8	336.4	0.57	0.3	0.98
RCCIII	68	155.0	194.9	249.3	267.0	283.8	306.2	0.54	0.3	0.98

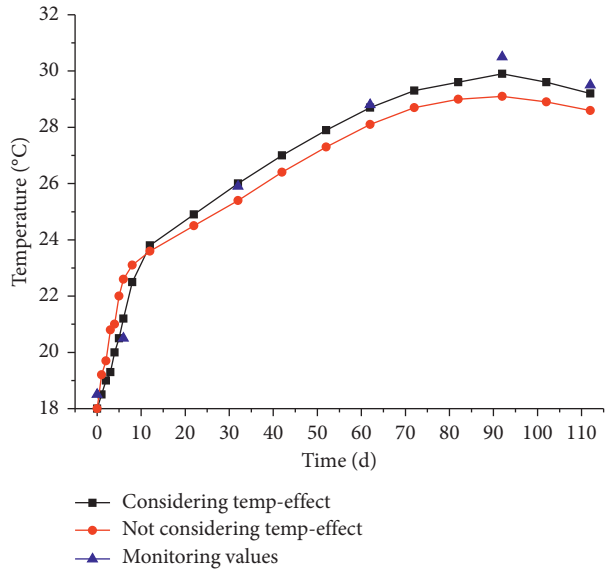

Figure 3: Temperature history curve of position T_1.

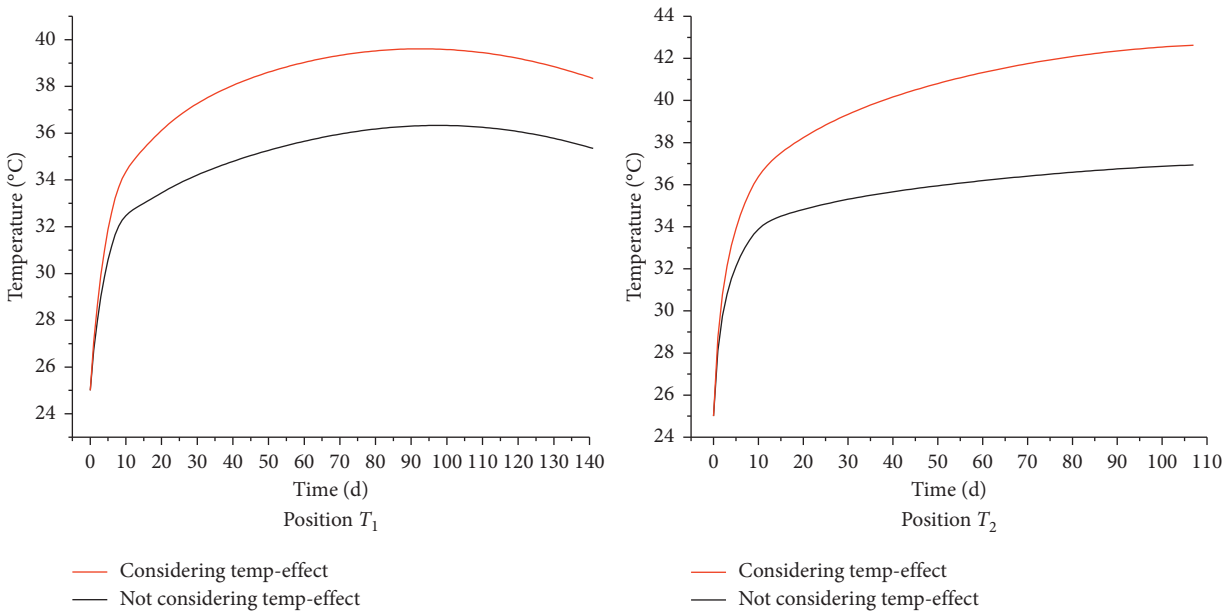

Figure 4: Temperature history curve of position T_1 and position T_2.

In Figure 3, it can be seen that (1) the pouring temperature is 18°C, and the heating rate is slower at the beginning of a few days after considering the influence of temperature. When the temperature is higher than 20°C, the heating rate becomes faster. Maximum temperature increased by 1.2°C. (2) The monitoring data is more consistent with the finite element calculation result considering the temperature effect, which shows that the numerical simulation results are more accurate after considering the temperature effect. (3) The ambient temperature is closer to

the reference temperature of 20°C; thus, the temperature range of change is small.

It is assumed that the RCC dam is constructed in a high temperature region with an average temperature of 28°C and the ambient temperature varies with time according to the cosine curve $T = 28 + 10.8\cos[3.14\ (t - 66.8)/6]$. The position of point T_1 and point T_2 is at 82.5 m and 90.5 m elevation, respectively, as shown in Figure 1. The temperature history curves of point T_1 and point T_2 are shown in Figure 4.

In Figure 4, it can be seen that (1) concrete temperature rising speed increases in high-temperature area after considering temp-effect. Point T_1 reached the peak temperature on 100th day. The peak temperature increased from 36.3°C to 39.9°C, and maximum temperature increased by 3.6°C. Point T_2 reached the peak temperature on 110th day. The peak temperature increased from 36.9°C to 43°C, and maximum temperature increased by 6.2°C. (2) When the ambient temperature drops sharply, the larger temperature difference will lead to higher thermal stress and concrete temperature cracks. Therefore, better temperature control is necessary during the summer construction period in high-temperature areas such as pouring temperature control and take concrete cooling measures.

5. Conclusions

The heat conduction equation and the finite element theory formula based on the temperature influence factor are proposed. The theory is verified and the variation law of temperature field is analyzed. The temperature field of the RCC dam is simulated by an engineering example. The finite element simulation results are in agreement with the measured temperature data after considering the temperature effect, which proves that the theory formula is correct.

Temperature has a great influence on the early temperature field. In order to save the finite element calculation time, the temperature effect is considered only in one to two months after the pouring time.

Especially in the high-temperature region, early ages' accurate simulation of mass concrete temperature field, adopting the reasonable temperature control measures, control right into the molding temperature, and break and intermittent layer thickness is important, such as the choice of which can effectively guide the engineering construction rapidly.

Data Availability

The data used to support the findings of this study are included in the article.

Conflicts of Interest

The authors declare no conflicts of interest.

Acknowledgments

The authors would like to acknowledge the financial support received from National Natural Science Foundation of China (51779095) and Foundation Sponsored by Program for Science and Technology Innovation Talents in Universities of Henan Province (20HASTIT013).

References

[1] P. Zhang, Q. F. Li, Y. Z. Chen et al., "Durability of steel fiber-reinforced concrete containing SiO_2 nano-particles," *Materials*, vol. 12, no. 13, pp. 1–18, Article ID 2184, 2019.

[2] P. Zhang, Q.-F. Li, J. Wang, Y. Shi, and Y.-F. Ling, "Effect of PVA fiber on durability of cementitious composite containing nano-SiO2," *Nanotechnology Reviews*, vol. 8, no. 1, pp. 116–127, 2019.

[3] P. Zhang, Z. Gao, J. Wang et al., "Properties of fresh and hardened fly ash/slag based geopolymer concrete: a review," *Journal of Cleaner Production*, vol. 270, Article ID 122389, 2020.

[4] L. S. Zhang, M. Zhang, W. Ge et al., "PCCP temperature field analysis at steam curing stage considering temperature effect," *Journal of Building Materials*, vol. 13, no. 5, pp. 35–37, 2016, in Chinese.

[5] P. Zhang, Y. Zheng, K. Wang, and K. Zhang, "Combined influence of nano-$CaCO_3$ and polyvinyl alcohol fibers on fresh and mechanical performance of concrete incorporating fly ash," *Structural Concrete*, vol. 21, no. 2, pp. 724–734, 2019.

[6] A. G. A. Saul, "Principles underlying the steam curing of concrete at atmospheric pressure," *Magazine of Concrete Research*, vol. 2, no. 6, pp. 127–140, 1951.

[7] E. Rastrup, "Heat of hydration in concrete," *Magzine of Concrete Research*, vol. 6, no. 17, pp. 127–140, 1954.

[8] N. G. Jin, X. Y. JIN, W. H. Wu et al., "Application of equivalent age method to concrete thermal cracking control at early ages," *Journal of Zhejiang University*, vol. 42, no. 1, pp. 44–47, 2008, in Chinese.

[9] Z. M. Zhang, S. R. Feng, and Q. C. Shi, "Based on the equivalent time of concrete adiabatic temperature rise," *Journal of Hohai University*, vol. 32, no. 9, pp. 573–577, 2004, in Chinese.

[10] A. K. Schindler, "Heat of hydration models for cementitious materials," *Materials Journal*, vol. 100, no. 5, pp. 24–33, 2003.

[11] G. D. Schutter, "Fundamental study of early age on concrete behaviour as a basis for durable concrete structures," *Materials and Structures*, vol. 35, no. 2, pp. 15–21, 2002.

[12] J. H. Dong and Z. Y. Li, "Effect of temperature on heat release behavior of hydration of cement," *Journal of Building Materials*, vol. 13, no. 5, pp. 675–677, 2010, in Chinese.

[13] P. F. Hansen and E. J. Pedersen, "Maturity computer for controlled curing and hardening of concrete," *Nordisk Betong*, vol. 5, no. 1, 61 pages, 1977.

[14] T. C. Clark and J. E. Dove, "Examination of possible non-arrhenius behavior in the reactions," *Canadian Journal of Chemistry*, vol. 51, no. 13, pp. 2147–2154, 2011.

[15] K.-Y. Shin, S.-B. Kim, J.-H. Kim, M. Chung, and P.-S. Jung, "Thermo-physical properties and transient heat transfer of concrete at elevated temperatures," *Nuclear Engineering and Design*, vol. 212, no. 1-3, pp. 233–241, 2002.

[16] K. Meinhard and R. Lackner, "Multi-phase hydration model for prediction of hydration-heat release of blended cements," *Cement and Concrete Research*, vol. 38, no. 6, pp. 794–802, 2008.

[17] B. W. Langan, K. Weng, and M. A. Ward, "Effect of silica fume and fly ash on heat of hydration of portland cement," *Cement and Concrete Research*, vol. 32, no. 7, pp. 1045–1051, 2002.

[18] B. F. Zhu, "Combined exponential formula of thermal and mechanical properties of concrete with age," *Journal of Hydraulic Engineering*, vol. 42, no. 1, 7 pages, 2011, in Chinese.

[19] G. D. Schutter, "Influence of hydration reaction on engineering properties of hardening concrete," *Materials and Structures*, vol. 35, no. 8, pp. 447–452, 2002.

[20] Z. Pytel, "Heat evolution in hydrated cementitious systems admixtured with different set controlling components," *Journal of Thermal Analysis and Calorimetry*, vol. 77, no. 1, pp. 159–164, 2004.

[21] T. Kishi, K. Ozawa, and K. Maekawa, "Multi-component model for hydration heat of concrete based on cement mineral compounds," *Proceedings of the Japan Concrete Institute*, vol. 15, pp. 1211–1216, 1993.

[22] N. B. Singh, M. Kalra, M. Kumar et al., "Hydration of ternary cementitious system: Portland cement, fly ash and silica fume," *Journal of Thermal Analysis and Calorimetry*, vol. 119, no. 1, 9 pages, 2015.

[23] D. G. Snelson, S. Wild, and M. O'Farrell, "Heat of hydration of portland cement-metakaolin-fly ash (PC-MK-PFA) blends," *Cement and Concrete Research*, vol. 38, no. 6, pp. 832–840, 2008.

[24] J. Ding and S. Chen, "Simulation and feedback analysis of the temperature field in massive concrete structures containing cooling pipes," *Applied Thermal Engineering*, vol. 61, no. 2, pp. 554–562, 2013.

[25] P. Zhang, K. X. Wang, Q. F. Li et al., "Fabrication and engineering properties of concretes based on geopolymers/alkali-activated binders - a review," *Journal of Cleaner Production*, vol. 258, Article ID 120896, 22 pages, 2020.

[26] C. P. Bobko, V. Z. Zadeh, and R. Seracino, "Improved schmidt method for predicting temperature development in mass concrete," *ACI Materials Journal*, vol. 112, no. 4, pp. 579–586, 2015.

Hindawi
Advances in Civil Engineering
Volume 2020, Article ID 8881273, 12 pages
https://doi.org/10.1155/2020/8881273

Research Article

Mechanical Properties of SiO_2-Coated Carbon Fiber-Reinforced Mortar Composites with Different Fiber Lengths and Fiber Volume Fractions

Gwang-Hee Heo,[1] Jong-Gun Park,[2] Ki-Chang Song,[3] Jong-Ho Park,[3] and Hyung-Min Jun[4]

[1]*Department of International Civil and Plant Engineering, Konyang University, 121 Daehak-Ro, Nonsan-Si, Chungnam-Do 32992, Republic of Korea*
[2]*Public Safety Research Center (PSRC), Konyang University, 121 Dachak-Ro, Nonsan-Si, Chungnam-Do 32992, Republic of Korea*
[3]*Department of Biomedical Materials, Konyang University, 158 Gwanjedong-Ro, Seo-Gu, Daejeon Metropolitan-Si 35365, Republic of Korea*
[4]*Department of Disaster and Safety Engineering, Konyang University, 121 Dachak-Ro, Nonsan- Si, Chungnam-Do 32992, Republic of Korea*

Correspondence should be addressed to Jong-Gun Park; 2630@hanmail.net

Received 28 May 2020; Revised 9 July 2020; Accepted 22 September 2020; Published 12 October 2020

Academic Editor: Peng Zhang

In the present study, SiO_2 particles were coated on the surface of carbon fibers by means of chemical reaction of silane coupling agent (glycidoxypropyl trimethoxysilane, GPTMS) and colloidal SiO_2 sol to improve the interfacial bonding force between fibers and matrix in cement matrix. The surface of the modified carbon fibers was confirmed through a scanning electron microscope (SEM). The mechanical properties of SiO_2-coated carbon fiber mortar and uncoated carbon fiber mortar with different fiber lengths (6 mm and 12 mm) and fiber volume fractions (0.5%, 1.0%, 1.5%, and 2.0%) were compared and analyzed. The experimental results show that the flow values of the carbon fiber mortar were greatly disadvantageous in terms of fluidity due to the nonhydrophilicity of fibers and fiber balls, and the unit weight decreased significantly as the fiber volume fractions increased. However, the air content increased more or less. In addition, regardless of whether the fibers were coated, the compressive strength of carbon fiber-reinforced mortar (CFRM) composite specimens tended to gradually decrease as the fiber volume fractions increased. On the other hand, in case of the SiO_2-coated CFRM composite specimens, the flexural strength was significantly increased compared to uncoated CFRM composite specimens and plain mortar specimens, and the highest flexural strength was obtained at 12 mm and 1.5%, particularly. It can be seen that the new carbon fiber surface modification method employed in this study was very effective in enhancing the flexural strength as cement-reinforcing materials.

1. Introduction

Fiber-reinforced cement composites (FRCCs) are manufactured by incorporating short fibers, which can suppress the opening and propagation of cracks due to the bridging action of fibers. It not only increases ductility in tension and compression but also provides improved safety performance for dynamic load, impact·explosion, etc. [1–6]. Currently, the main reinforcing materials of fiber-reinforced cement-based composite materials are steel fiber, polypropylene fiber, polyvinyl alcohol (PVA) fiber, carbon fiber, glass fiber, basalt fiber, and cellulose fiber [7–10].

Figure 1 shows the roles of fibers embedded in cement matrix: (a) cracking occurs in cement matrix, (b) cracking is suppressed due to the increased bond between fibers and matrix, (c) the phenomenon of "strain-softening" or "strain-

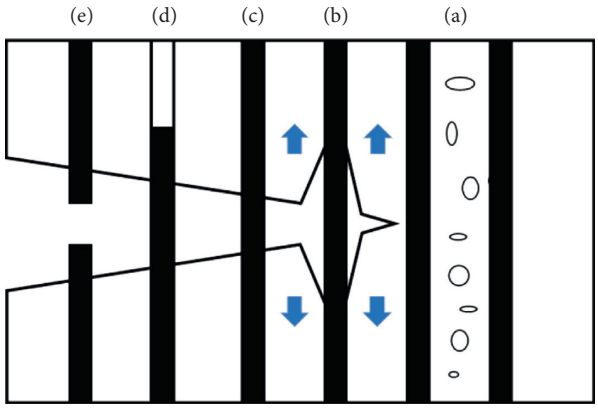

Figure 1: The roles of fiber embedded in cement matrix: (a) matrix cracking, (b) fiber/matrix debonding, (c) fiber bridging, (d) fiber pull-out, and (e) fiber failure.

hardening" by suppressing crack propagation owing to bridging action between fibers and matrix is shown after cracking in cement matrix, (d) fibers are pulled-out from cement matrix, and (e) the performance of FRCC is degraded by fiber failure. As seen above, it has been reported that the mechanical performance of cement-based composites can be improved by effectively preventing the propagation of cracks by stress through bonding between fibers and matrix as well as by controlling crack propagation by means of fiber bridging, fiber debonding, fiber pull-out, fiber failure, etc. [11–16]. Moreover, it is noted that the bond performance between fibers and matrix is very closely related to the performance of FRCC and that the material and surface shape of fibers, matrix strength, etc. play a vastly important role in the interfacial bonding force between fibers and matrix [17, 18]. Such interfacial properties of fibers are directly connected with effective improvement of the flexural performance (flexural strength or toughness) of the cement-based composites and exercise a substantial influence on the flexural and tensile fracture behaviors of FRCC [1, 6, 19, 20].

Recently, carbon fiber (CF) has been drawing wide attention in industries such as ships, automobiles, civil engineering, and construction as well as aerospace due to its lightweight and high mechanical properties [21, 22]. It was once already reported that carbon fiber is very effective in improving the flexural, tensile, and shear strengths when used as cement-reinforcing materials, owing to its high physical properties and chemical stabilities [23–26]. However, when carbon fiber is applied as a construction material, there are some problems to consider despite the excellent mechanical properties it will provide. The carbon fiber, when used cement-reinforcing materials, has an effect of improving the mechanical performance by being uniformly dispersed in cement matrix and inducing bond between fibers and matrix. In particular, a decrease in compressive, flexural, and shear strengths may rather result if carbon fiber is not fully adhered to the cement matrix [27–29]. Therefore, the interfacial bonding force between fibers and matrix is so important that lots of studies on CFRM composites have been conducted and advanced worldwide. To improve the interfacial bonding force between fibers and matrix, sizing treatment of carbon fibers is performed in this regard.

Although FRCC has been reviewed in the previous domestic and foreign studies, research studies to manufacture the carbon fiber with improved bond performance and developments to improve the mechanical performance of CFRM composites are still more or less insufficient [30, 31]. In Korea, the research data which specifically reviewed the bond properties between the carbon fiber and cement matrix are very limited [32]. In fact, there is a need to develop a method to improve the interfacial bonding force by coating the surface of carbon fiber with SiO_2, inducing by this reaction with limestone or $Ca(OH)_2$ in cement matrix and eventually increasing calcium silicate hydrate (C-S-H) gel.

Therefore, the main objective of this study is to develop CFRM composites that can improve the bond performance of carbon fiber and ultimately enhance the mechanical performance of mortar. This study provides a method for producing carbon fiber coated with SiO_2 in order to improve the interfacial bonding force between fibers and matrix in cement matrix, and the mechanical properties of SiO_2-coated CFRM composites and uncoated CFRM composites with different fiber lengths (6 mm and 12 mm) and fiber volume fractions (0.5%, 1.0%, 1.5%, and 2.0%) are compared and analyzed in this study. Then, after the strength test, the fracture surface of the hardened CFRM composites was observed by an SEM.

2. Materials and Methods

In this study, it was found from checking the mechanical properties of SiO_2-coated CFRM composites and uncoated CFRM composites that the lengths of fibers were 6 mm and 12 mm, and the fiber volume fractions varied from 0.5 to 2.0% by 0.5%. This was compared and reviewed with plain mortar. The flow, air content, and unit weight were measured in the fresh mortar state, while the compressive and flexural strengths were measured in the hardened mortar state. Besides, the surface of the carbon fiber was observed by SEM imaging.

2.1. Materials

2.1.1. Cement. The cement used in this study is Ordinary Portland Cement (OPC) produced by S Co., Ltd., with a specific gravity of 3.13 and a powder density of 3,860 cm^2/g. The chemical composites of cement are shown in Table 1.

2.1.2. Fine Aggregate. The standard sand produced by Jumunjin was used as fine aggregate to make uniform mortar. The specific gravity of fine aggregate in the dry saturated state of the surface was 2.65, and the physical properties of fine aggregate are shown in Table 2.

2.1.3. Carbon Fiber. The high-strength carbon fiber based on polyacrylonitrile (PAN) used in this study was manufactured by T company in Japan, which has a tensile strength of

Table 1: Chemical composites of cement (%).

SiO_2	Al_2O_3	Fe_2O_3	CaO	MgO	Na_2O	K_2O	SO_3	F-CaO	Ignition loss
21.47	6.21	3.70	59.24	2.08	0.13	1.08	2.48	0.57	2.87

Table 2: Physical properties of fine aggregate.

Size (mm)	Unit mass (kg/m^3)	Density (g/cm^3)	Fineness modulus (FM)
2≤	1,490	2.65	2.78

4,900 MPa and an elastic modulus of 230 GPa. To secure a uniform carbon fiber length, fibers were cut into the average lengths of 6 mm and 12 mm prior to use. In order to secure the length of the carbon fiber uniformly, it was cut from the long fibers to 6 mm and 12 mm in average length. The physical properties of carbon fiber are shown in Table 3.

2.1.4. Surface Modification of Carbon Fiber. In order to coat the surface of carbon fiber with a sizing agent, the reagents and materials used in this study are colloidal SiO_2 sol (ss-sol 30a, 30%, S-Chemtech Co., Ltd.) in which nano-SiO_2 particles having a size of 10 nm are dispersed, and nitric acid (HNO_3, 60%, Samchun Chemical) was used as a catalyst. GPTMS (99.9%, Sigma-Aldrich) was employed as a silane coupling agent, EDA (99.9%, Sigma-Aldrich) as a hardener, and ethanol (EtOH, 99.0%, Samchun Chemical) as a solvent, respectively. The reagent was used as such without purification and chemical treatment. SiO_2 sol was effective for consistently synthesizing high-purity SiO_2 particles at low temperatures. Based on the reinforcing mechanism of the modified carbon fiber, the SiO_2 particles produced on the surface of carbon fiber react with the hydration product $Ca(OH)_2$ in cement matrix, forming by thus a C-S-H gel which could improve the interfacial bonding force between fibers and matrix. After removing first all impurities attached to carbon fiber using acetone, the carbon fiber was oxidized by immersing it in a nitric acid solution for 24 hours to increase the surface activity, and the oxidized carbon fiber was washed with distilled water and dried in an oven at the temperature of 110°C. Then, the dried carbon fiber was dipped in the hydrophilic SiO_2-coating solution synthesized through the above process for 3 hours to adhere the SiO_2 particles to the surface of the carbon fiber in order to surface-modify the carbon fiber with hydrophilicity. Subsequent to being hardened in an oven at 80°C for 1 hour, the carbon fiber was washed again with distilled water and dried at 120°C for 2 hours in the final process. Figure 2 shows the SiO_2-coated carbon fiber and uncoated carbon fiber used in this experiment.

Table 3: Physical properties and shapes of carbon fiber.

Diameter (μm)	Density (kg/m^3)	Tensile strength (MPa)	Elastic modulus (GPa)	Elongation (%)
7 ± 2	1,800	4,900	230	2.1

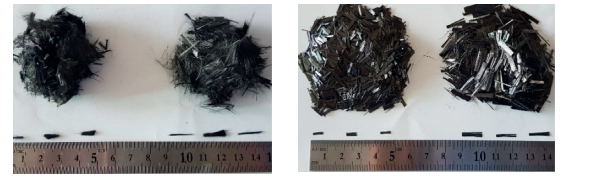

(a) (b)

Figure 2: Shapes of carbon fibers used in this experiment: (a) SiO_2-coated carbon fibers (6 mm and 12 mm) and (b) uncoated carbon fibers (6 mm and 12 mm).

2.2. Methods

2.2.1. Mix Proportions and Preparation of Specimens. The mix proportions of mortar applied in this experiment are shown in Table 4. The water-cement ratio (W/C) was kept constant (equal to 0.5) for all mixtures according to the test regulations of KS L ISO 679 [33], and the ratio (mass ratio) of cement:standard sand:water = 1 : 3 : 0.5 was fixed. At this time, coarse aggregate was not used. That is, the amount of each batch material in the mixing ratio corresponds to 450 ± 2 g of cement, $1{,}350 \pm 5$ g of sand, and 225 ± 1 g of water. The target flow value was mixed to be more than 190 mm or more. The amount of admixture added was adjusted to 1.0% of the cement mass, and in case of plain mortar, no particular admixture was added. The admixture used to ease the fluidity of carbon fiber is light yellow liquid, high-performance AE water reducing agent having a specific gravity of 1.04 and pH 5.0 ± 1.5 in a series of polycarboxylic acid manufactured by D Co., Ltd., in Korea. Figure 3 shows the main experimental process and casting progress of each step for manufacturing of CFRM composite specimens. As for the mixing method, cement and fine aggregate were added first and then mixed, dried for 90 seconds. In order to secure dispersibility of fibers, carbon fibers were added and mixed for 60 seconds. Then, the blended water and admixture were added and immediately mixed for 90 seconds. Following the 30-second pause, the attached mortar was removed and finally a mixer was operated again for further 60 seconds. The total mixing time was about 5 minutes. The specimens were demolded after 24 hours and immersed in a water tank with the temperature maintained at 20 ± 2°C constantly to perform underwater curing for 28 days of age.

2.2.2. Test of Flow and Unit Weight. In order to evaluate the fluidity performance of mortar, a flow test was conducted according to the test method of the "testing method for

Table 4: Mix proportions of mortar.

Type of mortar	W/C (%)	C : S ratio	Fiber volume fractions (%, in vol)	Fiber lengths (mm)	Content of SP (cement × 1.0%)
CC	50	1 : 3	0.5 1.0 1.5 2.0	6, 12	1.0
UC			0.5 1.0 1.5 2.0		
p			—	—	—

CC is the SiO_2-coated carbon fiber mortar, UC is the uncoated carbon fiber mortar, p is the plain mortar, C : S is the cement to fine aggregate ratio, and SP is the superplasticzer

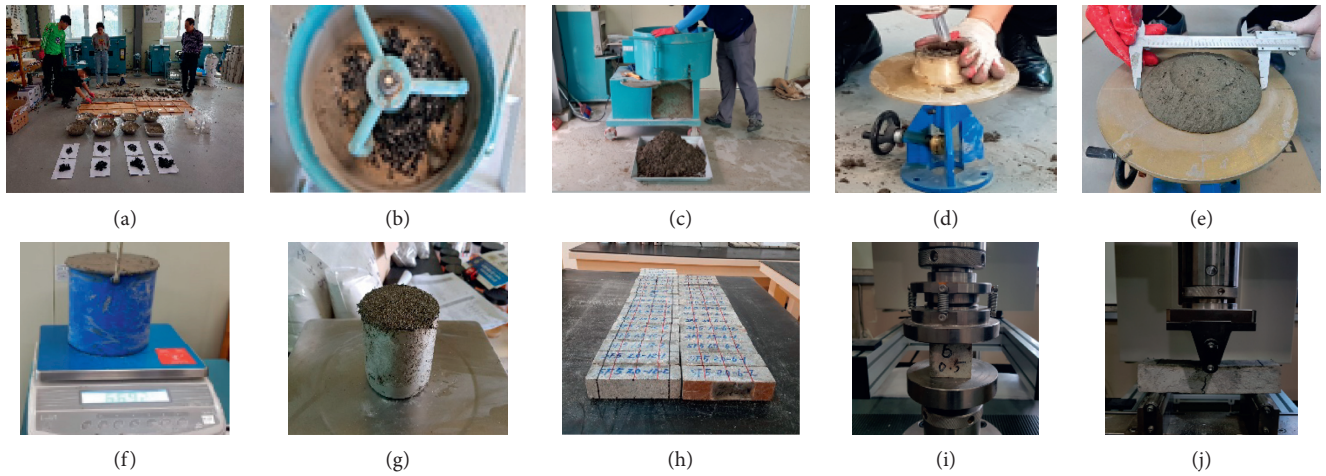

Figure 3: Main experimental process and casting progress of each step for manufacturing of CFRM composite specimens: (a) material metering, (b) fiber mixing, (c) finish mixing, (d) compaction, (e) flow test, (f) unit weight test, (g) air content test, (h) finish of specimens, (i) compressive test, and (j) flexural test.

compressive hydraulic cement mortar" in KS L 5105-2007 using the flow table specified in the "flow table for use in tests of hydraulic cement" in KS L 5111-2017, and a unit weight test was also performed according to the "standard test method for unit weight and air content of fresh concrete" in KS F 2409-2016.

2.2.3. Test of Air Content. Air content was measured using a cylindrical vessel capable of securing 400 ± 1 mL of water at 23°C, having a diameter of 76 ± 1.5 mm and a depth of 88 mm according to the test method specified in the "testing method for air content of hydraulic cement mortar"in KS L 3136-2005:

$$\text{air content } (\%) = 100 - \omega\left(\frac{182.7 + p}{2000 + 4p}\right), \quad (1)$$

where ω is the mass (g) of 400 mL mortar and p is the percentage of mixed water on the basis of cement.

2.2.4. Test of CFRM Composite Mechanical Properties. The compressive and flexural strength test of mortar was performed by preparing a mold according to the test method of KS L ISO 679 [33], and the strengths were all measured at 28 days of age. The cured cubic specimens of 40 × 40 × 160 mm were tested using a universal tester with a capacity of 100 kN (MTDI Co., Ltd., Korea, UT-100F). The flexural strength test was carried out on the basis of a three-point loading, and the specimen of 120 mm in length and 40 mm in height was loaded at a speed of 50 N/s. After the flexural strength test, a compressive strength test was conducted with a cut specimen. In the compressive strength test, the load area was 1,600 mm^2, and the speed was 2,400 N/s.

2.2.5. SEM Observation. SEM images were photographed to confirm whether the SiO_2 particles were coated on the surface of carbon fiber. The equipment used for analysis was MIRA LMH high-resolution SEM model of TESCAN. Besides, after the fibers obtained by pulverization of CFRM composite specimens were dried and coated with platinum in a vacuum state, it was observed whether the SiO_2 particles remained still attached to the surface of carbon fiber.

3. Results and Discussion

3.1. Surface Topography of SiO_2-Coated Carbon Fiber. Figure 4 shows a photograph of the surface topography for SiO_2-coated carbon fiber measured by the SEM. Figure 4(a)

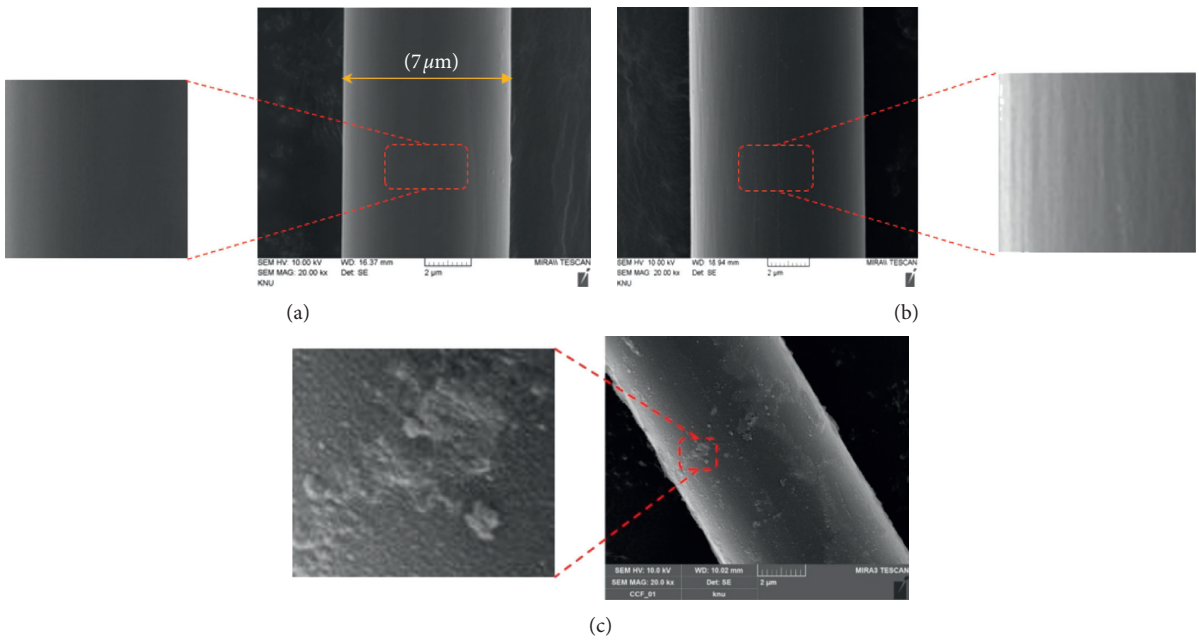

Figure 4: Surface topography of carbon fibers (20000 times): (a) uncoated carbon fiber, (b) nitric acid-treated carbon fiber, and (c) SiO_2-coated carbon fiber.

shows an uncoated carbon fiber, Figure 4(b) shows a carbon fiber pretreated with nitric acid, and Figure 4(c) shows a carbon fiber coated with SiO_2, observed by the SEM, respectively. The uncoated carbon fiber surface was neat and smooth, with a diameter of approximately 7 μm as shown in Figure 4(a). Compared to uncoated carbon fiber of Figure 4(a), the carbon fiber pretreated with nitric acid in Figure 4(b) has a string in the axial direction, increasing the surface roughness of carbon fiber. The objective of the pretreatment with nitric acid as shown in Figure 4(b) is to intensify roughness and to increase the number of COOH or -OH functional groups on the surface of carbon fibers by means of oxidation reaction in order to make SiO_2 particles easily attached to it. As shown in Figure 4(c), it can be seen that, in case of SiO_2-coated carbon fiber, particles of several tens of nanometers in size are spread entirely and attached to the surface of carbon fibers.

3.2. Properties of Fresh Mortar

3.2.1. Fluidity of Mortar. Figure 5 shows the test results of flow values of SiO_2-coated carbon fiber mortar and uncoated carbon fiber mortar with different fiber lengths and fiber volume fractions compared to plain mortar. The flow values were calculated from the average values measured in four directions, and the flow value for mixture of plain mortar was 192 mm, which satisfies more than the target flow value of 190 mm. On the other hand, the flow value for mixture of SiO_2-coated carbon fiber mortar was 114 to 160 mm, while that of uncoated carbon fiber mortar was measured to be 103 ~ 146 mm. As shown in Figure 5, the variation in flow value at the lengths of fibers (6 mm, 12 mm) was insignificant but tended to decrease significantly as the fiber volume fractions increased. When carbon fibers were mixed in the ratio of 2.0% particularly, their flow was drastically reduced and fluidity was very disadvantageous as far as fluidity of fire balls and nonhydrophilicity of the fibers are concerned. These results are due to the fiber balls caused by increase in the viscosity of mortar and by partial absorption of the mixed water during the mixing process, which is considered to show a lower flow value than the plain mortar. Figure 6 shows pictures that compare flows of SiO_2-coated carbon fiber mortar, uncoated carbon fiber mortar, and plain mortar, respectively. The uncoated carbon fiber mortar was not sufficiently mixed, and some fibers were exposed to the surface. When the reinforced fibers are uniformly dispersed as the flow value increases, it may be evaluated that the flow value of a mortar increases accordingly. As a consequence, the optimum dispersibility and workability could be obtained. In dry mixing, fiber balls and maldistribution of fibers would occur, and even in wet mixing, there was a tendency to make smooth dispersibility difficult; entanglement between each fiber could easily occur due to the increased amount of mixed fibers, by thus affecting workability adversely.

3.2.2. Unit Weight of Mortar. Figure 7 shows the test results of unit weight of SiO_2-coated carbon fiber mortar and uncoated carbon fiber mortar with different fiber lengths and fiber volume fractions compared to plain mortar. As shown in Figure 7, regardless of whether the fibers were coated, variation in the unit weight was slight in fiber lengths of 6 mm and 12 mm but tended to decrease significantly as the fiber volume fractions increased. Compared to plain mortar, the unit weight was significantly reduced. This is due to the difference in the density of cement and carbon fiber, and it is thought that the unit weight is reduced due to the

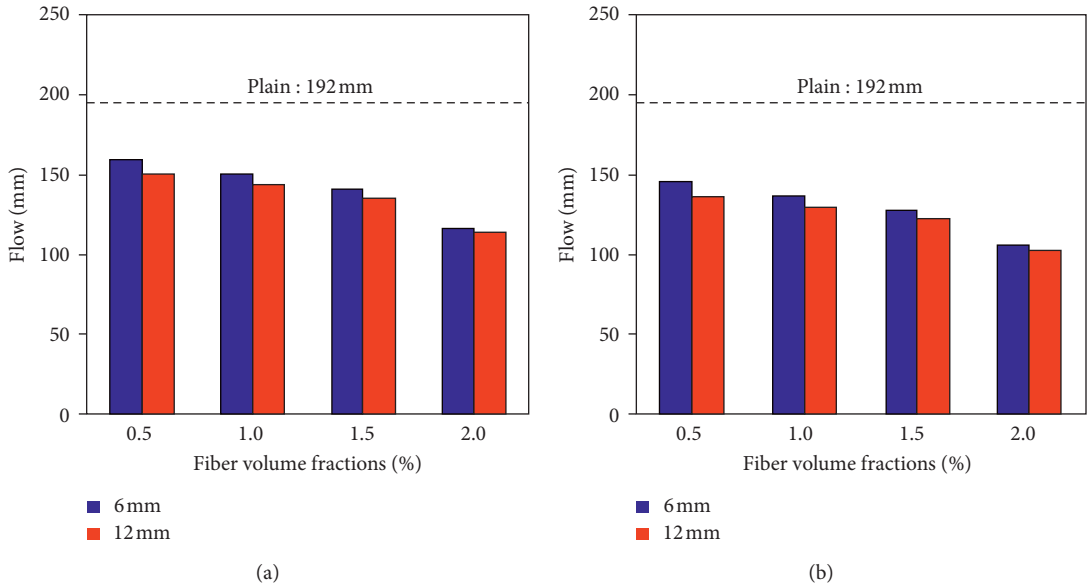

Figure 5: Flow test results with different fiber lengths and fiber volume fractions: (a) SiO_2-coated carbon fiber and (b) uncoated carbon fiber.

Figure 6: Flow test of mortar samples: (a) SiO_2-coated carbon fiber mortar, (b) uncoated carbon fiber mortar, and (c) plain mortar.

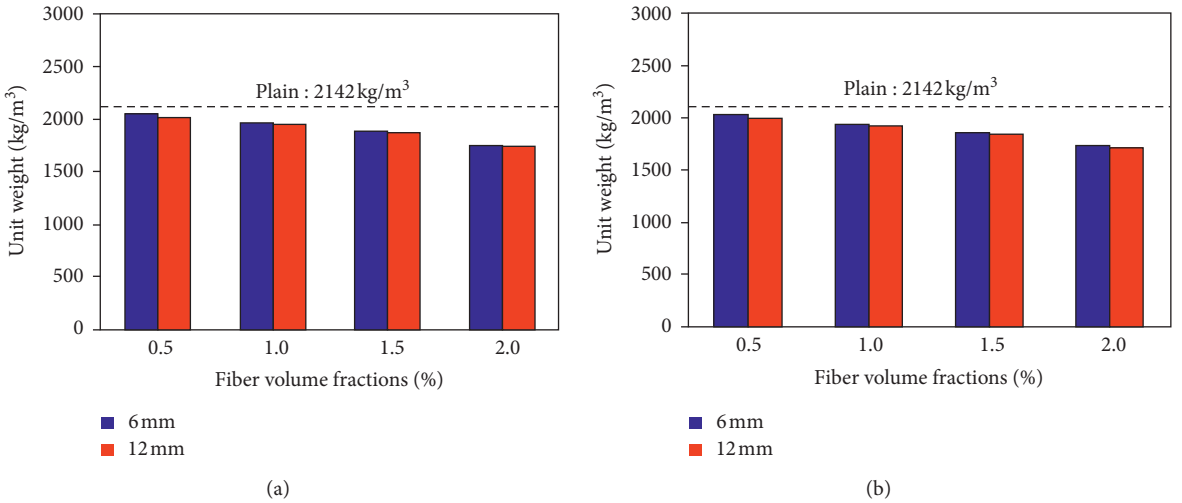

Figure 7: Unit weight test results with different fiber lengths and fiber volume fractions: (a) SiO_2-coated carbon fiber and (b) uncoated carbon fiber.

large amount of incorporated carbon fibers with a relatively smaller density than cement. Regardless of whether the fibers were coated or not, the unit weight of carbon fiber mortar could be reduced by about 4 ~ 5% as fiber volume fractions increased and by about 18 ~ 20% of plain mortar.

3.2.3. Air Content of Mortar. Figure 8 shows the test results of air content of SiO_2-coated carbon fiber mortar and uncoated carbon fiber mortar with different fiber lengths and fiber volume fractions compared to plain mortar. As shown in Figure 8, regardless of whether the fibers were coated or not,

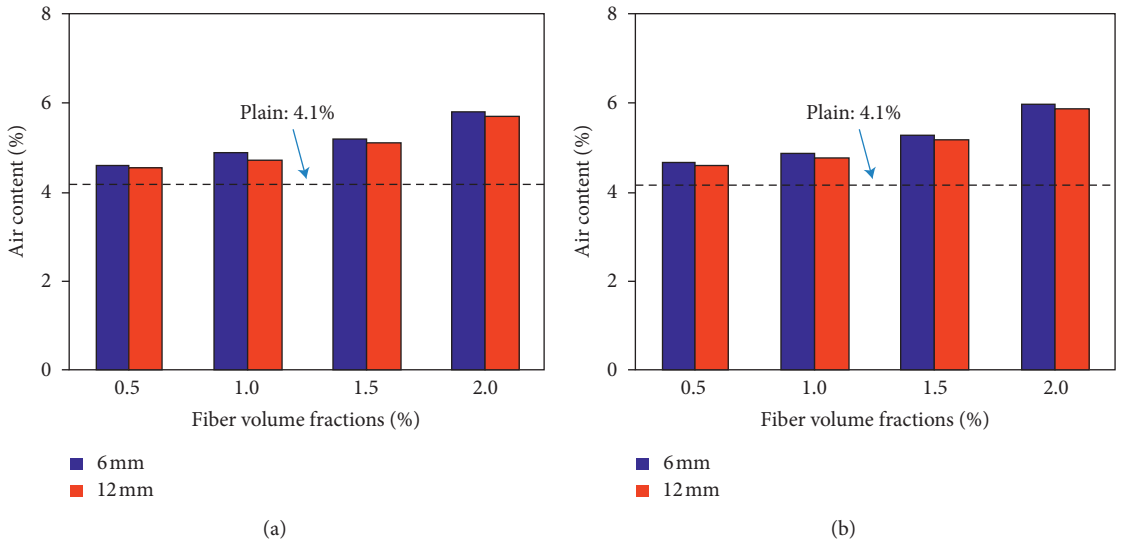

Figure 8: Air content test results with fiber lengths and fiber volume fractions: (a) SiO_2-coated carbon fiber and (b) uncoated carbon fiber.

variation in the air content was slight when the lengths of fibers were 6 mm and 12 mm but tended to increase a little as the fiber volume fractions increased. Compared to plain mortar, air content increased for both. The test results estimated that the effect on the air content in the case of carbon fiber mortar was not so much, and the air content did not vary significantly in line with the increasing rate of fiber mixture.

3.3. Properties of Hardened Mortar

3.3.1. Properties of the Compressive Strength. Figure 9 shows the test results of the compressive strength of SiO_2-coated CFRM composite specimens and uncoated CFRM composite specimens with different fiber lengths and fiber volume fractions compared to plain mortar specimens. The compressive strength of plain mortar specimens at 28 days of age was measured to be 30.6 MPa in average. As shown in Figure 9(a), the compressive strength was reduced compared to plain mortar specimens, except for the CFRM composite specimens with 0.5% of fibers and SiO_2-coated carbon fiber. Whether or not fibers were coated, the compressive strength of the CFRM composite specimens showed an overall decrease in strength as the fiber volume fractions increased. This is thought to be caused by the carbon fiber, and the strength of which is lowered because the interfacial bonding force between fibers and matrix in the mortar was weakened after hardening due to the nonhydrophilic material on the surface of carbon fibers. These results were also reported in the previous studies [34, 35], which revealed that the dispersibility of fibers decreased and more agglomeration was caused since the fiber volume fractions become higher from a certain amount, which resulted in decrease of the compressive strength. As the flow value decreased due to fiber volume fractions, the quality of material that could affect the compressive strength was uneven and, as a consequence, the compressive strength decreased accordingly. Regardless of whether the fibers were coated or not, the compressive strength tended to decrease rapidly due to high fiber volume fractions when fibers were mixed in the ratio of 1.5% and 2.0%. In the event fibers were mixed with 2.0%, particularly, it was difficult to uniformly disperse the fibers in cement matrix. Moreover, fiber balls occurred and the compressive strength was rapidly reduced due to insufficient dispersion. When the lengths of fibers are 6 mm and 12 mm, and they are mixed at 0.5% and 1.0%, the compressive strength was almost the same or slightly different, but when mixed at 2.0%, the compressive strength of fibers was reduced drastically by approximately 29.7 ~ 55.3% more than plain mortar specimens. Meanwhile, the use of 12 mm fibers was seen to be more efficient than that of 6 mm ones. Therefore, in case of the CFRM composite specimens, 0.5% and 1.0% are considered to be the most appropriate fiber volume fractions in terms of securing the compressive strength while maintaining the maximum workability. Concerning the tendency for the compressive strength to decrease rapidly due to high fiber volume fractions, it is required to conduct further studies to improve the strength.

3.3.2. Properties of the Flexural Strength. Figure 10 shows the test results of the flexural strength of SiO_2-coated CFRM composite specimens and uncoated CFRM composite specimens with different fiber lengths and fiber volume fractions compared to plain mortar specimens. The flexural strength of plain mortar specimens at 28 days of age was measured to be 3.1 MPa in average. As shown in Figure 10, the flexural strength of SiO_2-coated CFRM composite specimens demonstrated fairly higher value compared to the plain mortar specimen in all types except for uncoated CFRM composite specimens mixed with fibers of 6 mm length and in the ratio of 0.5%. In particular, the SiO_2-coated CFRM composite specimens with fiber length of 12 mm and mixture of 1.5% had the highest flexural strength of about 4.9 MPa. It was analyzed that the flexural strength increased by 10.4% and 58.1%, respectively, compared to uncoated

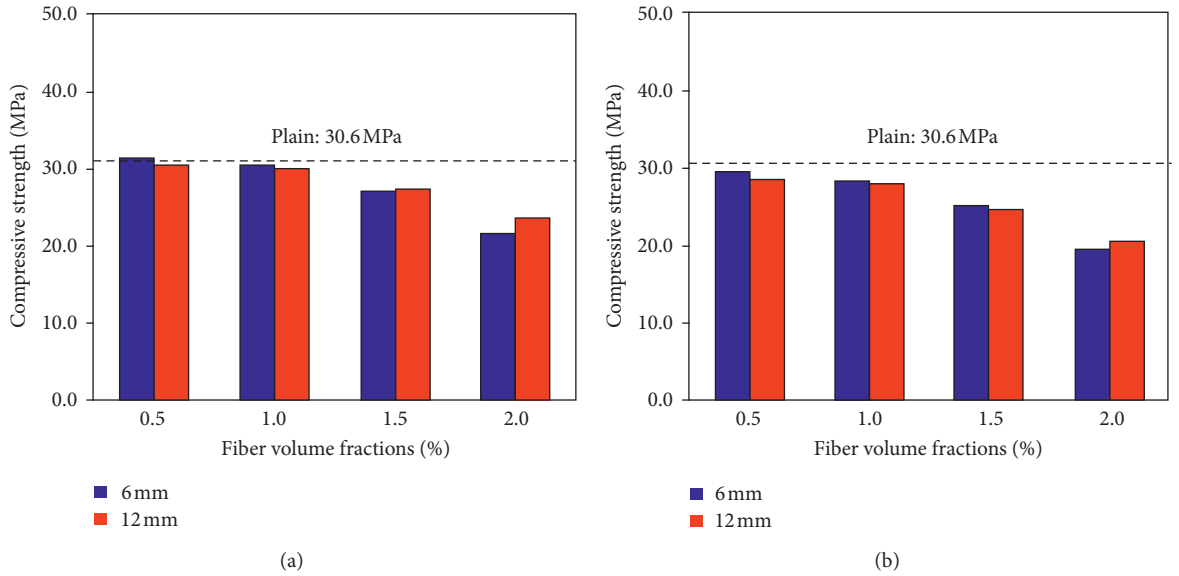

Figure 9: Relationships between compressive strengths of the CFRM composite specimens with different fiber lengths and fiber volume fractions: (a) SiO_2-coated carbon fiber and (b) uncoated carbon fiber.

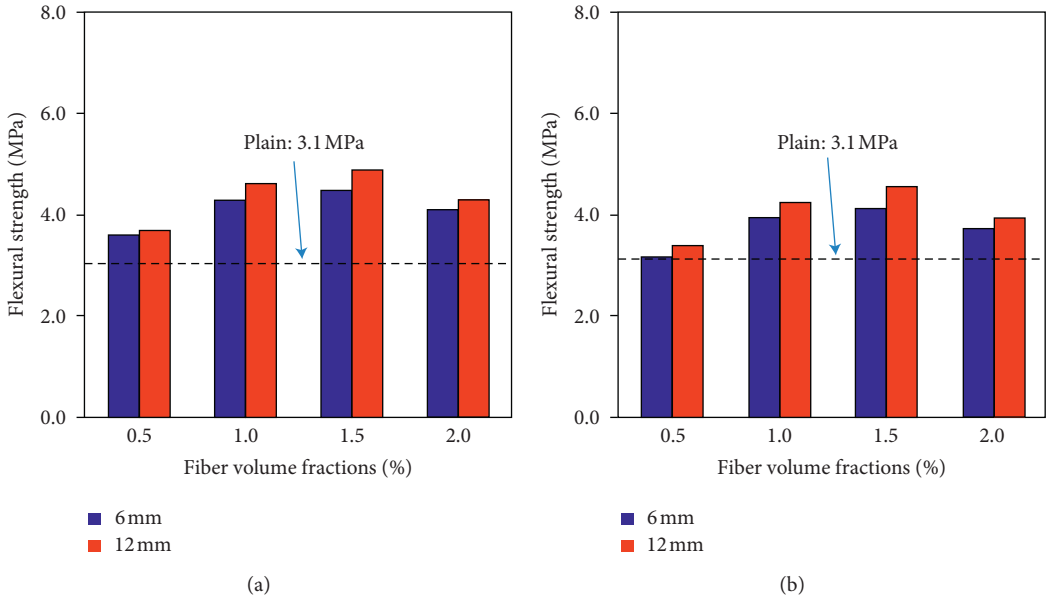

Figure 10: Relationships between flexural strengths of CFRM composite specimens with different fiber lengths and fiber volume fractions: (a) SiO_2-coated carbon fiber and (b) uncoated carbon fiber.

CFRM composite specimens and plain mortar specimens. These results are judged to be because added fibers have a bridging effect to prevent the growth of cracks and improve the flexural strength through redistribution of stress. The flexural strength improved until the fiber volume fractions reached up to 1.5%, but the increasing effect would not be so great if the fiber volume fractions were greater than that. Actually, however, it was laid bare that the fibers with a length of 6 mm and mixing ratio of 2.0% had the least flexural strength because dispersibility and finishing performance were not favorable due to the high fiber volume fractions. Moreover, when the length of the fiber was 6 mm, it could be confirmed that the flexural strength was lower than that of 12 mm. This is thought to be due to the bridging action between the fibers that could not be obtained sufficiently because the length of the fibers was reduced by 50% compared to the 12 mm fibers.

3.3.3. Relationship between the Compressive and Flexural Strengths. Table 5 summarizes the test data results of the compressive and flexural strengths of SiO_2-coated CFRM composite specimens, uncoated CFRM composite specimens, and plain mortar specimens. For SiO_2-coated CFRM

Table 5: Results of strength tests with different fiber lengths and fiber volume fractions.

Type of mortar	Fiber volume fractions (%, in vol)	Fiber lengths (mm)	Mortar strength (MPa)		f_c/f_r
			f_c	f_r	
SiO_2-coated carbon fiber (CFRM)	0.5	6	31.4	3.6	8.7
		12	30.4	3.7	8.2
	1.0	6	30.5	4.3	7.1
		12	30.0	4.6	6.5
	1.5	6	27.1	4.5	6.0
		12	27.3	4.9	5.6
	2.0	6	21.6	4.1	5.3
		12	23.6	4.3	5.5
Uncoated carbon fiber (CFRM)	0.5	6	29.6	3.2	9.3
		12	28.6	3.4	8.4
	1.0	6	28.5	3.9	7.3
		12	28.0	4.2	6.7
	1.5	6	25.3	4.1	6.2
		12	24.8	4.5	5.5
	2.0	6	19.7	3.7	5.3
		12	20.7	3.9	5.2
Plain mortar	—	—	30.6	3.1	9.9

f_c is the average of the compressive strength measured at 28 days, and f_r is the average of the flexural strength measured at 28 days.

composite specimens at 28 days of age, the ratio of the flexural strength to the compressive strength was within the range of 1/5.3 ~ 1/8.7. On the other hand, the ratio of uncoated CFRM composite specimens was shown to be in the range of 1/5.2 to 1/9.3, indicating that the flexural strength increased a little compared to the 1/9.9 level of the plain mortar specimen. These results are assumed to be because the mixed fibers prevented crack propagation due to the bridging role and the flexural strength was improved through redistribution of stress. Regardless of whether the fibers were coated or not, the flexural strength was improved when fibers were mixed up at 1.5%, but the increasing effect was not so great when more fibers were mixed. In case of uncoated CFRM composite specimens having a fiber length of 6 mm and a mixture of 2.0%, it can be seen that the flexural strength was the lowest because of poor dispersion and finishing performance caused by high mixing ratio.

3.3.4. Flexural Stress-Displacement Relationship Curves. Figure 11 shows the flexural stress-displacement relationship curves of a representative specimen based on a three-point loading test. In case of plain mortar specimens, the flexural stress increased linearly, and there was little displacement after reaching the maximum stress due to rapid brittle fracture at the same time as the flexural crack occurred. On the other hand, the CFRM composite specimens showed a behavior in which the stress decreased after arriving at the maximum stress, displacement increased to a certain extent, and then the descending slope fell down gradually, while displacement increased. In case of uncoated CFRM composite specimens, it can be seen that the displacement is subject to stress up to 1.7 mm, and the displacement of SiO_2-coated CFRM composite specimens was found to resist up to 2.0 mm due to ductile properties. Therefore, the amount of displacement increased in the flexural stress and the

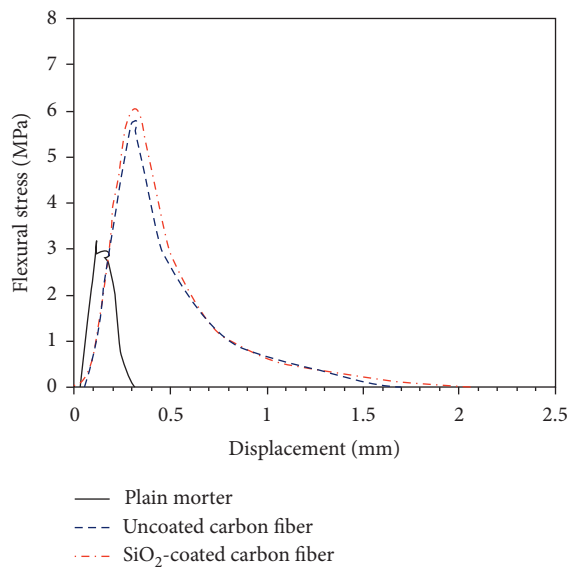

Figure 11: Flexural stress-displacement relationship curves.

displacement curve was found to be the largest for SiO_2-coated CFRM composite specimens in the order of SiO_2-coated CFRM composite specimens > uncoated CFRM composite specimens > plain mortar specimens.

3.4. SEM Observation. Figure 12 shows the microstructure of the fiber surface observed by using SEM after the strength test of SiO_2-coated CFRM composite specimens and uncoated CFRM composite specimens. In general, the bond performance of reinforced fibers is affected by the interfacial bonding force between fibers and cement matrix. Therefore, to improve the interface bonding force between the fibers and matrix in the cement composites, sizing treatment of

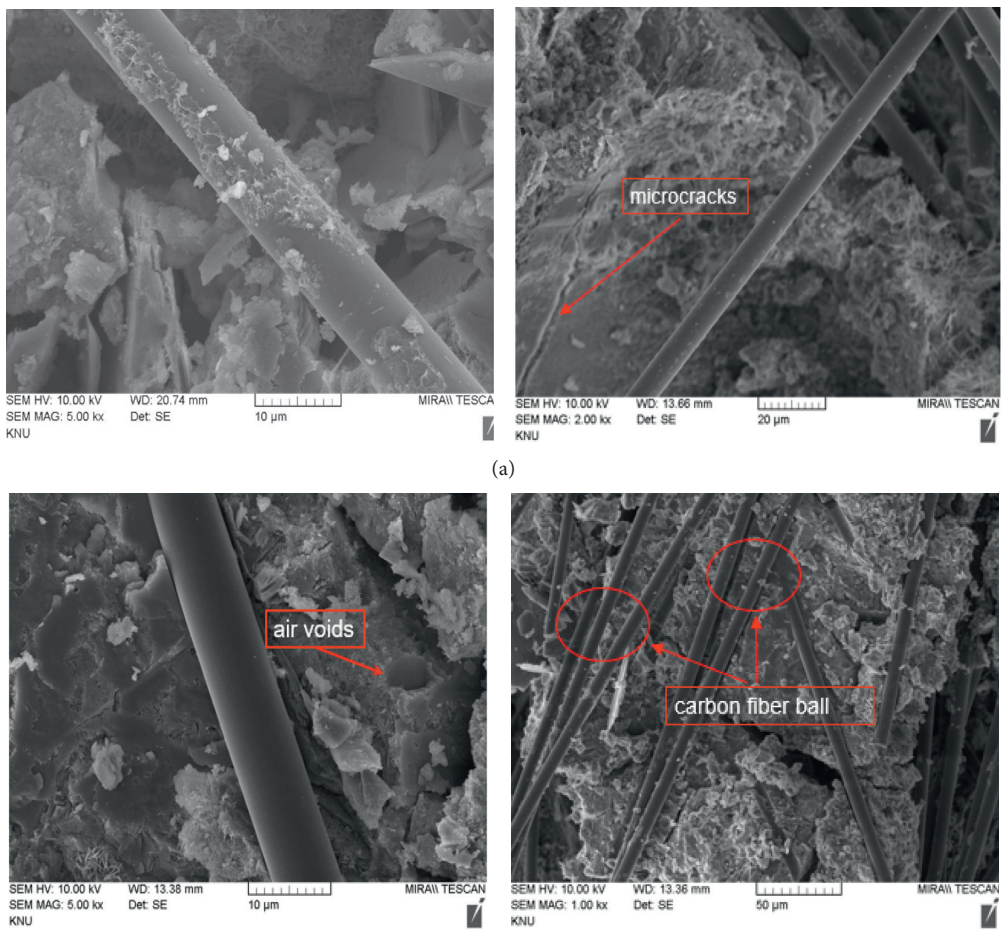

Figure 12: SEM images of CFRM composite specimens after strength tests (5000 or 1000 times): (a) SiO_2-coated carbon fiber and (b) uncoated carbon fiber.

carbon fibers is performed. If the interfacial bonding force is large, the bond performance is excellent, whereas the bond performance is poor, if the interfacial bonding force is small. It is reported that the thickness between fibers and cement matrix interface is about 10 to 50 μm, and this interface thickness is known to affect strength and durability [36, 37]. As revealed in Figure 12(a), it can be seen that, in case of the SiO_2-coated CFRM composite specimens, large and small C-S-H gels are uniformly distributed in a rough shape on the surface of fibers, and almost no pores can be observed. However, microcracks are shown to be occasionally occurring, though. It is thus made clear that the interfacial bonding force between fibers and matrix was improved owing to formation and increase of the cement hydration product. On the other hand, it was observed from Figure 12(b) that the fiber surface of uncoated CFRM composite specimens looked very clean and quite smooth and that a number of pores were formed. This is because the cement hydration product is difficult to crystallize and has a low affinity, so the interfacial bonding force between fibers and cement matrix is low. It appears therefore that fiber balls have occurred. As such, the SiO_2-coated CFRM composite specimens showed better interfacial bonding force than the uncoated CFRM composite specimens owing to the improved interfacial bonding force between fibers and cement matrix.

4. Conclusions

In the present study, carbon fibers coated with SiO_2 as cement-reinforcing materials were manufactured, and the mechanical properties of SiO_2-coated CFRM composites and uncoated CFRM composites with different fiber lengths and fiber volume fractions were compared and analyzed. The outcomes of the study may be summarized as follows:

(1) The target flow value of plain mortar was satisfactory, but the flow values of SiO_2-coated carbon fiber mortar and uncoated carbon fiber mortar decreased significantly as fiber volume fractions increased. In this regard, there is a need for a means to insure fluidity with increasing carbon fiber volume fractions. In addition, compared to plain mortar, the unit weight decreased by about 1820% as the fiber volume fractions increased, while the air content increased a little bit.

(2) Regardless of whether the fibers were coated, the compressive strength of CFRM composite specimens decreased somewhat compared to plain mortar specimens, and there was a strong tendency that the more the fiber volume fractions increased, the more the compressive strength decreased. In particular, when the fiber length was 6 mm and mixed at 2.0%, the compressive strength was significantly reduced.

(3) The flexural strength of SiO_2-coated CFRM composite specimens was higher than that of uncoated CFRM composite specimens and plain mortar specimens by 10.4% and 58.1%, respectively. Particularly, when the fiber length was 12 mm and mixed at 1.5 %, the highest flexural strength could be obtained.

(4) The ratio of the flexural strength to the compressive strength is approximately 1/5.3 ~ 1/8.7 and 1/5.2 ~ 1/9.3 for SiO_2-coated CFRM composite specimens and uncoated CFRM composite specimens, respectively, confirming that the flexural strength increased significantly compared to the 1/9.9 level of plain mortar specimens.

(5) The SEM observation result showed that, in case of SiO_2-coated CFRM composite specimens, a number of crystals of the cement hydration product were formed on the surface of the carbon fiber, which pushed the interfacial bonding force higher than that of the uncoated CFRM composite specimens.

Data Availability

The data used to support the findings of this study are available from the corresponding author upon request.

Conflicts of Interest

The authors declare that there are no conflicts of interest regarding the publication of this paper.

Acknowledgments

This research was supported by the Basic Science Research Program through the National Research Foundation of Korea (NRF) funded by the Ministry of Education (grant no. NRF-2018R1A6A1A03025542).

References

[1] A. Abrishambaf, M. Pimentel, and S. Nunes, "Influence of fibre orientation on the tensile behaviour of ultra-high performance fibre reinforced cementitious composites," *Cement and Concrete Research*, vol. 97, pp. 28–40, 2017.

[2] D. j. Kim, A. E. Naaman, and S. EL-Tawil, "Comparative flexural behavior of four fiber reinforced cementitious composites," *Cement and Concrete Composites*, vol. 30, no. 10, pp. 917–928, 2008.

[3] G. H. Heo, J. G. Park, and C. G. Kim, "Evaluating the resistance performance of the VAEPC and the PAFRC composites against a low-velocity impact in varying temperature," *Advances in Civil Engineering*, vol. 2020, Article ID 7901512, 15 pages, 2020.

[4] L. Lavagna, S. Musso, G. Ferro, and M. Pavese, "Cement-based composites containing functionalized carbon fibers," *Cement and Concrete Composites*, vol. 88, pp. 165–171, 2018.

[5] L. Sun, Q. Hao, J. Zhao, D. Wu, and F. Yang, "Stress strain behavior of hybrid steel-PVA fiber reinforced cementitious composites under uniaxial compression," *Construction and Building Materials*, vol. 188, pp. 349–360, 2018.

[6] S.-T. Kang, Y. Lee, Y.-D. Park, and J.-K. Kim, "Tensile fracture properties of an ultra high performance fiber reinforced concrete (UHPFRC) with steel fiber," *Composite Structures*, vol. 92, no. 1, pp. 61–71, 2010.

[7] A. M. Brandt, "Fibre reinforced cement-based (FRC) composites after over 40 years of development in building and civil engineering," *Composite Structures*, vol. 86, no. 13, pp. 3–9, 2008.

[8] H. Li, R. Mu, L. Qing, H. Chen, and Y. Ma, "The influence of fiber orientation on bleeding of steel fiber reinforced cementitious composites," *Cement and Concrete Composites*, vol. 92, pp. 125–134, 2018.

[9] K. Hannawi, H. Bian, W. P. Agbodjan, and B. Raghavan, "Effect of different types of fibers on the microstructure and the mechanical behavior of Ultra-High Performance Fiber-Reinforced Concretes," *Composites Part B: Engineering*, vol. 86, pp. 214–220, 2016.

[10] M. Cao, Y. Mao, M. Khan, W. Si, and S. Shen, "Different testing methods for assessing the synthetic fiber distribution in cement-based composites," *Construction and Building Materials*, vol. 184, pp. 128–142, 2018.

[11] A. Bentur and S. Mindess, *Fibre Reinforced Cementitious Composites*, Elsevier Applied Science, London, UK, 1990.

[12] A. Bhutta, M. Farooq, C. Zanotti, and N. Banthia, "Pull-out behavior of different fibers in geopolymer mortars: effects of alkaline solution concentration and curing," *Materials and Structures*, vol. 50, no. 1, pp. 1–13, 2017.

[13] ACI Committee 544, *Fibre Reinforced Concrete*, Vol. SP-81, America Concrete Institute, Farmington Hills, MI, USA, 1984.

[14] A. E. Naaman, "Toughness, ductility, surface energy and deflection-hardening FRC composites," in *Proceedings of the JCI International Workshop on Ductile Fiber-Reinforced Cementitious Composites (DFRCC), Application and Evaluation*, Japan Concrete Institute, Tokyo, Japan, pp. 33–57, October 2002.

[15] D. L. Naik, A. Sharma, R. R. Chada, R. Kiran, and T. Sirotiak, "Modified pullout test for indirect characterization of natural fiber and cementitious matrix interface properties," *Construction and Building Materials*, vol. 208, pp. 381–393, 2019.

[16] D.-Y. Yoo, J.-J. Park, S.-W. Kim, and Y.-S. Yoon, "Combined effect of expansive and shrinkage-reducing admixtures on the properties of ultra high performance fiber-reinforced concrete," *Journal of Composite Materials*, vol. 48, no. 16, pp. 1981–1991, 2014.

[17] W. Zemei, K. K. Henri, and S. Caijun, "Effect of nano-SiO_2 particles and curing time on development of fiber-matrix bond properties and microstructure of ultra-high strength concrete," *Cement Concrete Research*, vol. 95, pp. 247–256, 2017.

[18] Z. Rong, W. Sun, H. Xiao, and G. Jiang, "Effects of nano-SiO_2 particles on the mechanical and microstructural properties of ultra-high performance cementitious composites," *Cement and Concrete Composites*, vol. 56, pp. 25–31, 2015.

[19] A. Bhutta, P. H. R. Borges, C. Zanotti, M. Farooq, and N. Banthia, "Flexural behavior of geopolymer composites

reinforced with steel and polypropylene macro fibers," *Cement and Concrete Composites*, vol. 80, pp. 31–40, 2017.

[20] J. P. Won, B. T. Hong, T. J. Choi, S. J. Lee, and J. W. Kang, "Flexural behavior of amorphous micro-steel fibre-reinforced cement composites," *Composites Structure*, vol. 94, pp. 1443–1449, Elsevier, Amsterdam, Netherlands, 2012.

[21] B. Gao, R. Zhang, M. He et al., "Interfacial microstructure and mechanical properties of carbon fiber composites by fiber surface modification with poly (amidoamine)/polyhedral oligomeric silsesquioxane," *Composites Part A: Applied Science and Manufacturing*, vol. 90, pp. 653–661, 2016.

[22] H. Yao, X. Sui, Z. Zhao et al., "Optimization of interfacial microstructure and mechanical properties of carbon fiber/epoxy composites via carbon nanotube sizing," *Applied Surface Science*, vol. 347, pp. 583–590, 2015.

[23] G. A. Galhano, L. F. Valandro, R. M. de Melo, R. Scotti, and M. A. Bottino, "Evaluation of the flexural strength of carbon fiber-, quartz fiber-, and glass fiber-based posts," *Journal of Endodontics*, vol. 31, no. 3, pp. 209–211, 2005.

[24] J. Sun, F. Zhao, Y. Yao, X. Liu, Z. Jin, and Y. Huang, "A two-step method for high efficient and continuous carbon fiber treatment with enhanced fiber strength and interfacial adhesion," *Materials Letters*, vol. 196, no. 1, pp. 46–49, 2017.

[25] J. Sun, F. Zhao, Y. Yao, Z. Jin, X. Liu, and Y. Huang, "High efficient and continuous surface modification of carbon fibers with improved tensile strength and interfacial adhesion," *Applied Surface Science*, vol. 412, no. 1, pp. 424–435, 2017.

[26] X. Fu, W. Lu, and D. D. L. Chung, "Improving the tensile properties of carbon fiber reinforced cement by ozone treatment of the fiber," *Cement and Concrete Research*, vol. 26, no. 10, pp. 1485–1488, 1996.

[27] W. Chuang, J. G. Sheng, L. B. Liang et al., "Dispersion of carbon fibers and conductivity of carbon fiber-reinforced cement-based composites," *Ceramics International*, vol. 43, no. 17, pp. 15122–15132, 2017.

[28] R. Liu, H. G. Xiao, H. Li et al., "Effects of nano-SiO_2 on the permeability-related properties of cement-based composites with different water/cement ratios," *Journal of Materials Science*, vol. 53, no. 13, pp. 4974–4986, 2018.

[29] T. Sugama, L. E. Kukacka, N. Carciello, and D. Stathopoulos, "Interfacial reactions between oxidized carbon fibers and cements," *Cement and Concrete Research*, vol. 19, no. 3, pp. 355–365, 1989.

[30] M. Balapour, A. Joshaghani, and F. Althoey, "Nano-SiO_2 contribution to mechanical, durability, fresh and microstructural characteristics of concrete: a review," *Construction and Building Materials*, vol. 181, pp. 27–41, 2018.

[31] M. Lu, H. Xiao, M. Liu, X. Li, H. Li, and L. Sun, "Improved interfacial strength of SiO_2 coated carbon fiber in cement matrix," *Cement and Concrete Composites*, vol. 91, pp. 21–28, 2018.

[32] G.-H. Heo, K.-C. Song, J.-G. Park, J.-H. Park, and H.-M. Jun, "Effect of mechanical properties of SiO_2 coated carbon fiber reinforced mortar composites," *Journal of the Korea Concrete Institute*, vol. 32, no. 1, pp. 65–76, 2020.

[33] KS L ISO 679, *Methods of Testing Cements-Determination of Strength*, Korean Standards Association, Seoul, Republic of Korea, 2016.

[34] M. Boulfiza, N. Banthia, and K. Sakai, "Application of continuum damage mechanics to carbon fiber-reinforced cement composites," *ACI Materials Journal*, vol. 97, no. 3, pp. 245–253, 2000.

[35] S. Y. Lee and Y. D. Park, "Mechanical properties of high strength carbon fiber reinforced cement composites," *RIST Report*, vol. 8, no. 2, pp. 321–330, 1994.

[36] K. L. Scrivener, A. K. Crumbie, and P. Laugesen, "The interfacial transition zone (ITZ) between cement paste and aggregate in concrete," *Interface Science*, vol. 12, no. 4, pp. 411–421, 2004.

[37] P. K. Metha, *Concrete-Structure, Properties, and Materials*, Prentice-Hall, Upper Saddle River, NJ, USA, 1986.

Hindawi
Advances in Civil Engineering
Volume 2020, Article ID 8836516, 13 pages
https://doi.org/10.1155/2020/8836516

Research Article

Seismic Behavior Analysis of Damaged Steel Fiber-Reinforced High-Strength Concrete Frame Joints Strengthened by FRP

Wang Tingyan,[1,2] **Zhou Yun**,[1] **and Zhang Junwei**[3]

[1]*School of Civil Engineering, Guangzhou University, Guangzhou 510006, China*
[2]*North China University of Water Resources and Electric Power, Zhengzhou 450045, China*
[3]*Henan Agricultural University, Zhengzhou 450002, China*

Correspondence should be addressed to Wang Tingyan; 124466715@qq.com

Received 8 April 2020; Revised 20 June 2020; Accepted 21 September 2020; Published 8 October 2020

Academic Editor: Peng Zhang

In this paper, the seismic behavior of fiber-reinforced polymer (FRP) strengthened and unstrengthened steel fiber-reinforced high-strength concrete frame joints under low cyclic loading was tested. Then, the nonlinear finite element program was used to simulate the seismic behavior of FRP strengthened and unstrengthened steel fiber-reinforced high-strength concrete frame joints under low cyclic repeated load. The influence of FRP bond direction on the seismic behavior of steel fiber-reinforced high-strength concrete frame joints was studied. Through the comparison of the test values and numerical simulation values of the hysteretic curve, skeleton curve, energy dissipation capacity, displacement ductility, bearing capacity degradation, stiffness degradation, and other performance indexes of frame joints, the rule was obtained. The results showed that the 45° bonding direction of carbon fiber cloth is better than the 0° bonding direction, and the digital simulation results are in good agreement with the test results. Therefore, the constitutive model, element, end constraint, and loading method used in the finite element numerical simulation of this paper were reasonable, which can provide reference for the similar research in the future.

1. Introduction

Frame joint is an important and key part of frame structure. A node is not only the pivot of transferring and distributing internal force but also plays an important role in the whole structure without collapse. Once the frame joint is destroyed, it is easy to cause the collapse of the whole structure. In the high-strength concrete frame structure, although the high-strength concrete can greatly improve the bearing capacity of the concrete structure, it cannot significantly improve the crack resistance and ductility of the concrete structure. Many earthquake disasters at home and abroad show that, under the action of earthquake, the joint area is still the most vulnerable part of the high-strength concrete frame structure, and its damage often leads to the collapse of the whole building structure [1]. Therefore, to improve the ductility of joints and avoid joint failure is the goal of our seismic design [2, 3].

The mechanical properties of concrete, such as tension, bending, shear, and torsion, can be significantly improved by adding fiber into concrete. Fiber can also significantly improve the ductility, toughness, energy consumption, and other deformation properties of concrete. Especially in the high-strength concrete structure, the interface bonding performance between the high-strength concrete and the steel fiber is better, and the steel fiber distribution in the high-strength concrete can play a more active role. Therefore, adding steel fiber into high-strength concrete frame joints is an effective measure to improve the mechanical properties of frame joints, improve the reinforcement crowding, and reduce the construction difficulty. Therefore, adding steel fiber into the joints of high-strength concrete frame should play a positive role in improving the seismic performance of the joints [4, 5].

Although steel fiber can improve the ductility and stress of high-strength reinforced concrete frame joints, steel

fiber-reinforced high-strength concrete frame joints are still unable to avoid damage in the midium and large earthquakes. After the earthquake, the steel fiber-reinforced high-strength concrete frame joints still need to be strengthened [6, 7]. Fiber-reinforced polymer (FRP) reinforcement technology, as a newly developed reinforcement method with high-performance materials, has attracted great attention at home and abroad due to its advantages of convenient construction, high strength and efficiency, and good durability [8, 9]. Therefore, this paper uses FRP to strengthen the damaged steel fiber-reinforced high-strength concrete frame joints. In this paper, the seismic behavior of damaged SFRHC frame joints strengthened by FRP under low cycle repeated load is studied by experiment and numerical simulation. The influence of the FRP bonding direction on the seismic behavior of frame joints is analyzed, and some valuable conclusions are obtained.

2. The Experimental Conditions

2.1. Design of the Model. The frame joint model adopted the side joint between the end column of the middle story and the frame beam. The size and reinforcement drawing, designed according to the Code for Design of Concrete Structures (GB50010-2010), are shown in Figure 1 [10]. The steel fiber used for experiment was ingot milling fiber (AMI04-32-600) with the volume ratio of 1.0%, length diameter ratio of 35~40, equivalent diameter of 0.94 mm, tensile strength ≥700 MPa, and adulteration range of 125 mm and 50 mm, respectively, in the beam end and two sides of the pillar end at the core area. The cement used was 42.5 # high-strength Portland cement. The maximum particle size of the stone was 20 mm. The fineness modulus of medium-coarse sand was 2.91, and the aggregate gradation was fair. The concrete strength was C60. The water reducer was a JKH-1 highly efficient powder water reducer (FDN) with a reducing rate of 18%~25%.

The fiber-reinforced polymer used in this test was carbon fiber-reinforced polymer (CFRP). The measured elastic modulus of the CFRP sheet was 234 GPa, the tensile strength was 2645.84 MPa, the thickness was 0.167 mm, and the elongation was 1.08%. The measured mechanical properties of reinforcement and concrete are shown in Tables 1 and 2.

2.2. Strengthening Scheme. The schematic diagram of the frame joint strengthened by the carbon fiber sheet is shown in Figure 2. Low cyclic loading was applied to simulate the earthquake load that damages the model of steel fiber-reinforced high-strength concrete frame joints. The FRP sheet was used to reinforce the joint. The strengthening scheme was shown in Table 3.

The cracks on the surface of the concrete are located, the width is measured, and they are repaired. The small independent chinks with the width ≤0.2 mm should be repaired with a repair adhesive of good permeability and, then, sealed. For large independent and penetrating cracks, the periphery should be sealed first. Then, the high-strength repair adhesive could be applied. For a dormant crack of a width ≥0.5 mm, the method was to fill up the crack. First, a U-shape groove is chiseled along the crack with a concrete cutting disc. Then, the crack is cleaned with acetone, the grout nipple is pasted, and the crack is filled up with a sealant. Under the sustained compression made by the air compressor, the structural repair adhesive was injected into the cracks. The nooks of the beams were beveled by the structural adhesive. The surface was burnished with the sander when the adhesive was solidified.

Next, the damaged joints were reinforced by CFRP. The concrete surface was polished until the tectorium was removed and the smooth structure interface appears. Intensively mixed fat material was, then, spread on the concrete surface evenly with a brush, which should not be too thin. The processed fiber sheet was pasted to the due position and rolled with the special roller along the stress direction for several times till the connection resin was extruded from the fiber. By this, the bubble was squeezed out so that the fiber sheet was pressed closely to the concrete surface. Then, the impregnating resin was applied to the surface of the fiber sheet. The process mentioned above was repeated to paste more pieces of fiber sheet. The CFRP sheet, made by hand and by impregnating the substrate with fiber, was homemade CFRP.

2.3. Loading Scheme. The experiment applied a multichannel electrohydraulic servodynamic fatigue test system to conduct low cyclic loading. The pillar end would endure axial load from a 2000 kN oil jack fixed on the heavy frame. First, the pillar top was put under the axial load from the oil jack. When the axial compression ratio reaches the predesigned 0.3, it was kept unchanged during the experiment. Then, low cyclic loading was applied by using the electrohydraulic servo actuator. The first two cycles load with control force, of which the first cycle loads to 75% of the yield load calculated value so as to simulate the stress condition in normal occasions. Since the key part of the study lied in the phase of plastic deformation, in the second cycle, the model was loaded directly to the yielded state. Displacement control was, then, used for loading. Staged loading was adopted according to the multiple of the displacement of the pillar end in the yielded state. At each displacement level, recycling was performed twice until the maximum load value of the nth cycle was lower than 85% of the highest load value when the model was damaged.

3. Finite Element Analysis Model

3.1. Constitutive Structure Relation of Materials. The axial compressive stress-strain curve of high-strength concrete used the Code for Design of Concrete Structures (GB 50010-2010) [10]. The tensile stress-strain relationship of high-strength concrete is described as follows: upper period as line and lower period as index. The elastic modulus before crack was the same as that of the initial elastic modulus after crack, and the concrete was considered as nonbrittle material. That was to say, the concrete tensile strength of the crack did not decline to zero immediately, but declined with the widening

of the crack. For high-strength concrete, the parameter of the calculation formula was from reference [11, 12].

At the yielding period, the reinforcement's stress had a small change, but strain increased dramatically, and the stress-strain curve was a $0.01E$ slope line, where E was the elastic modulus of reinforcement. After the plastic hinge to form, the ultimate deformation of the plastic area concrete would seldom exceed 0.006, so the deformation of reinforcement had a small change at the hardening period, and the stress-strain curve was a $0.01E$ slope line, taking $E' = 0.01E$ [13]. As metal material, steel fiber took the ideal elastoplasticity stress-strain relationship as reinforcement. The damage of steel fiber concrete was mainly because of the pulling out of steel fiber from the concrete, not because of the broken of the steel fiber; therefore, the tensile stress was taken when steel fiber was pulling out as the tensile strength of steel fiber, and in this paper, it was taken as 250 MPa [14].

3.2. Concrete Failure Criterion and the Crack Treatment. The concrete failure criterion took the William–Warnke model with five parameters, and the formula was $(F/f_c) - S \geq 0$. In this formula, F was the function of the main stress σ_1, σ_2, and σ_3, S was the destroying section of the main stress, and the five parameters, f_t, f_c, f_{cb}, f_1, and f_2, were uniaxial tensile strength, axial compressive strength, equal pressure biaxial compressive strength, biaxial compressive strength under hydrostatic pressure, and multiaxial compressive strength under ambient pressure, respectively. Also, the ANSYS method was used, when the ambient pressure was small, the failure surface could be made certain by two parameters f_t and f_c, and the other three parameters were $f_{cb} = 1.2f_c$, $f_1 = 1.45f_c$, and $f_2 = 1.725f_c$ [15].

In analysis, the dispersion crack model was used to treat the frame joint cracking process. After cracks emerge, subsequent loading would produce sliding or shearing on the crack surface. In analysis, a split plane shear transfer coefficient (β_t) when the crack opens and split plane transfer coefficient (β_c) were introduced to simulate the loss of the concrete shearing capacity. β_t had a great influence on the calculation result when the crack emerges, and generally, it was between 0.3~0.5. The β_t value of the shear member was small, the β_t value of the flexural member was large, and the frame node was the shear member, so the β_t value was small, and in this paper, $\beta_t = 0.3$. β_c had a little influence on the result of the monotonic loading load-carrying specimen, and generally, it was between 0.9~1.0, and in this paper, $\beta_c = 0.9$. For not considering the concrete crush, it was hard to simulate the concrete failure process, and the normal failure surface would cause the premature crush invalidation. Therefore, this paper used the expanded crush plane to consider the restriction effect of the steel fiber to the concrete, and the axis compressive strength parameter of the failure criterion was $1.2 \cdot f_c \sim 2 \cdot f_c$.

3.3. Element Choosing. Reinforcement used Link 8, and concrete used Solid 65. The FRP sheet used shell 41. The steel fibers were large in number, and also, they distribute in chaos, so it was impossible to model the role of each single steel fiber. Therefore, we take the steel fibers as distributing microreinforcements. They distribute into the concrete Solid 65 evenly according to volume ratio, and together with concrete, they compose an integral model, that is, steel fiber was distributed along with the axes of the coordinates, and in each direction, the volume ratio was distributed according to the unit side length ratio; also, the influence of the steel fiber distribution effective coefficient and orientation coefficient is considered. Moreover, the steel fiber tensile strength was the tensile strength when steel fiber was pulling out, so there was no need to consider the bond-slip between the steel fiber and the concrete. For the concrete and reinforcement, the discrete model was used for modeling. The bond-slip between the two uses Combin 39 to simulate, and the bond-slip constitutive construction relation uses the four line segment model advised by the CEB-FIPMC90 in reference [16].

For concrete and the CFRP sheet, the discrete model was used for modeling. The bond-slip between the two used Combin 39 to simulate. As the plane was perpendicular to the fiber direction of slip, the loading process did not occur, so in the analysis, it could correspond to nodes in the direction of coupled degrees of freedom, and it only needed to consider the vertical slip to the FRP and the slip along the fiber direction. The bond-slip curve between concrete and fiber cloth was based on the formula given in [17, 18]. For the transversal U-shaped wrapped FRP sheet, it was assumed that the relative slip concrete was mainly along the beam height direction with respect to the FRP sheet and the joint of concrete and FRP sheet node displacement coupling in the other two directions.

3.4. Element Birth and Death. If materials need to be added or deleted in the structure during the finite element analysis, the life and death option of the element could be used to kill or activate the element. The element being killed was not to delete the element from the model, but to multiply the corresponding position in the overall stiffness matrix by a tiny factor, so that the element can be ignored, but the element still exists. The element activation was not to add elements to the model, but to reactivate the previously killed elements, that is, the corresponding position in the overall stiffness matrix was not multiplied by a small factor, at this time, the element attributes such as mass and stiffness will restore their original values, but there is no strain value [19, 20].

Since the reinforcement is based on the cracks of the frame joints, although the cracks had been repaired before reinforcement, there were still microcracks in the concrete. If the influence of the existing microcracks was not considered in the finite element analysis, the rigidity of the structure would be too large, which is inconsistent with the test results. Therefore, in the finite element analysis, the method of element birth and death was used to consider the influence of the existing microcracks. The CFRP element was killed in the load step before the cracking of the specimen, and the stress of the joint was analyzed according to that of the unreinforced frame. The CFRP element was reactivated in the load step after the crack is generated, and it was involved in the stress work.

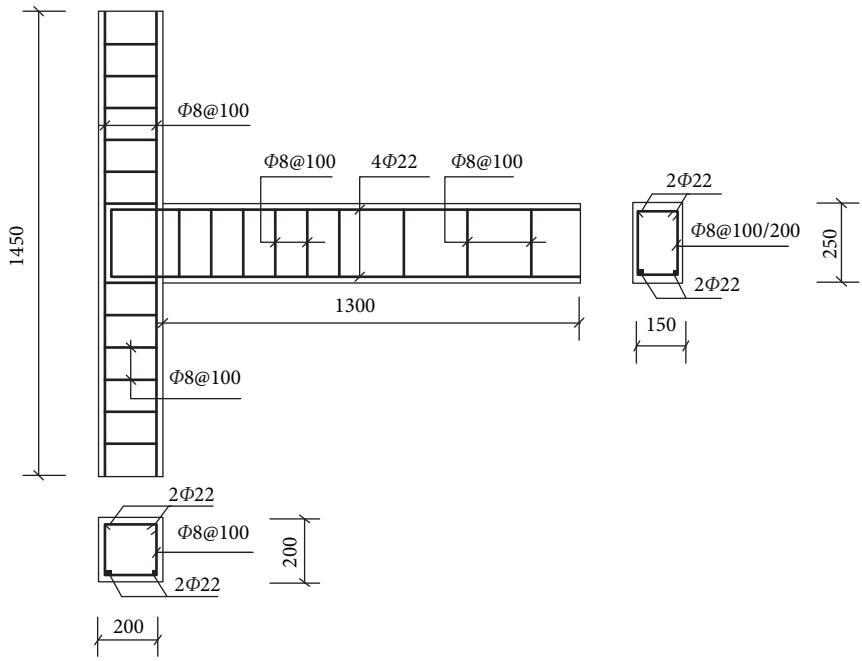

Figure 1: The sizes and reinforcements of the specimen (unit: mm).

Table 1: Mechanical performance index of the steel bar.

Rebar grade	Diameter (mm)	Yield strength (MPa)	Modulus of elasticity (GPa)
HPB235	8	312.87	203
HPB335	22	373.68	203

Table 2: Mechanical performance index of concrete.

Model	Concrete type	Concrete strength			Modulus of elasticity (GPa)
		Cube strength (MPa)	Axial compressive strength (MPa)	Tensile strength (MPa)	
1	HSC	62.73	57.07	4.32	40.48
	FHSC	64.43	58.56	4.61	41.09
2	HSC	58.64	50.88	3.91	40.75
	FHSC	65.20	50.36	4.43	37.38

HSC: high-strength concrete; FHSC: steel fiber high-strength concrete.

3.5. Mesh Partition. When we perform analysis by taking the whole model of joints, the size and the shape of the element mesh will both influence the analysis results. If the meshes were divided too meticulously, it will cause the instability of numerical calculation, and if the meshes were divided too coarsely, it will influence precision. Only the right meshes can get the convergence. By comparison, in this paper, mesh partition is performed by 5 cm, and the corresponding mesh partition needs to satisfy certain geometry topology rule. As it was necessary to consider the thickness of the protective layer of the beam and the column, in this paper, besides 5.0 cm, there were also 3.5 cm and 4.0 cm. The finite element model is shown in Figure 3.

3.6. Boundary Conditions and Load Application. In order to simulate the form of joint destruction under the low cycle loading, we supplied the X-direction the two lateral surfaces of the upper and lower end of the column translation displacement constraint, supplied X, Y, Z three directions translation displacement constraints at the lower end of the column, supplied Y axial force at the column top end, and supplied Y reversed force or displacement at the beam ends. In the nonlinear analysis, by defining load step and load substep, we divided the load into a series of load increments. To solve by finite element, we made a series of linear approaches in the load increments to achieve balance. Considering the nonlinear influence of steel fiber concrete, we adopt the

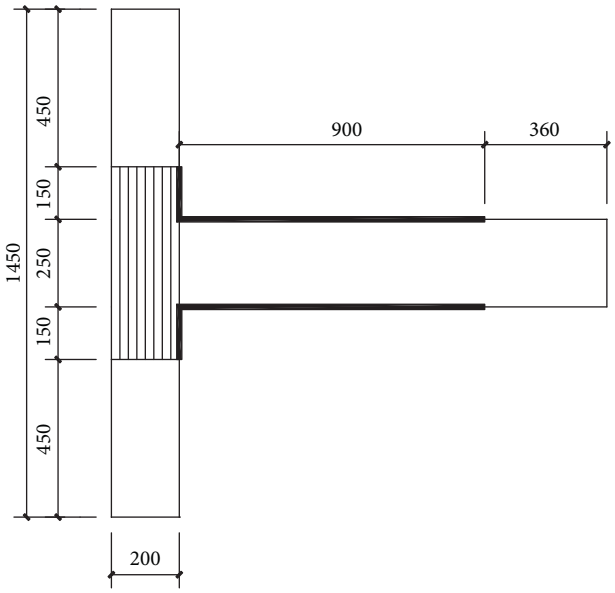

Figure 2: Sticking method and the range of CFRP (unit: mm).

Table 3: Strengthening scheme of the joints.

Model	Strengthening scheme of the damaged model
1	Treat the crack; paste one piece of FRP at the angle of 45° across another piece in the core area; and paste two pieces of FRP at the beam.
2	Treat the crack; paste two pieces of FRP vertically at the angle of 0° in the core area; and paste two pieces of FRP at the beam.

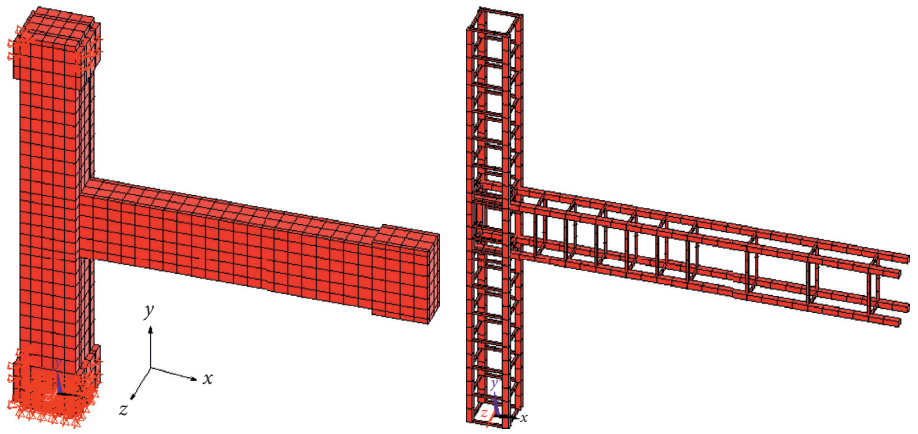

Figure 3: Finite element model of frame exterior joints.

Newton–Raphson method doing nonlinear iteration. The displacement convergence criterion was used, and the convergence precision was 1%. In order to improve the convergence of nonlinear analysis, adaptive descend gene, linear searching, forecasting, and dichotomy were used in this paper.

4. Findings and Discussion

Table 4 shows the comparative result of the damaged frame joints reinforced by FRP. According to the ratio of the experimental results and the analysis results, the average value of the yield load was 1.011, the standard deviation of the yield load was 0.043, and the coefficient of variation of the yield load was 0.042. The average value of the yield displacement was 1.049, the standard deviation of the yield displacement was 0.064, and the coefficient of variation of the yield displacement was 0.061. The average value of the ultimate load was 0.963, the standard deviation of the ultimate load was 0.087, and the coefficient of variation of the ultimate load was 0.091. The average value of the ultimate displacement was 1.066, the standard deviation of the ultimate displacement was 0.074, and the coefficient of variation of the ultimate displacement was 0.069. Thus, it showed that the analysis results and the experimental results match well.

According to the analysis results, the yield load of reinforced model 1 was 1.12 times of that before. The yield displacement of reinforced model 1 was 1.34 times of that before. The ultimate load of reinforced model 1 was 1.39 times of that before. The ultimate displacement of reinforced model 1 was 2.09 times of that before. Model 2 also presents a similar result. The yield load of reinforced model 2 was 1.26 times of that before. The yield displacement of reinforced model 2 was 2.13 times of that before. The ultimate load of reinforced model 2 was 1.37 times of that before. The ultimate displacement of reinforced model 2 was 1.63 times of that before. Thus, the yield load, yield displacement, ultimate load, and ultimate displacement are improved and all reach the original condition, which can meet the standard of seismic appraisal.

The major problem of reinforced model 1 was the crazing of the concrete along the margin of fiber sheet, while the problem of model 2 after strengthening was the rip of fiber sheet in the core area. Although the ultimate load of the two models was similar, the ultimate displacement of reinforced model 1 was larger than that of model 2 mainly because of the mechanical behavior and fiber direction of the fiber sheet. Model 2 with the fiber sheet pasted at 0° vertically in the core area only provides vertical constraint, while model 1 with the cross fiber sheet enhances both vertical and horizontal deformation capability of the core area concrete.

4.1. Hysteretic Curve and Skeleton Curve. The hysteretic curve and skeleton curve of the damaged frame joints model strengthened by FRP are shown in Figures 4–11. The skeleton curve of the concrete joint specimen could be obtained by connecting each load drop point of the load-displacement hysteretic curve, that is, the envelope line of the peak point of each stage of the load-displacement hysteretic curve. The load-displacement curve of the joint under the same loading was similar, which reflects the relationship between the loading and deformation of the joint, and was an important basis for the seismic performance analysis of the joint. The result showed that compared with the original model, the hysteretic curve of damaged joint model strengthened by FRP was fuller. Meanwhile, the ultimate load, ultimate displacement, and times of circulation all increased to some degree. The coverage of the skeleton curve enlarged, which met the standard of the seismic appraisal. For example, compared with original model 1, reinforced model 1 had a fuller hysteretic curve and more circulation times, whose ultimate load and ultimate displacement were 1.39 and 2.09 times, respectively, of that before. For reinforced model 2, the hysteretic curve was also fuller. The ultimate load and ultimate displacement were 1.37 and 1.63 times, respectively, of that before, while the circulation times remained the same.

Compared with reinforced model 2, reinforced model 1 had a fuller hysteretic curve, larger coverage of the skeleton curve and more circulation times. The ultimate load of model 1 was 0.95 times of model 2, and the ultimate displacement was 1.02 times of model 2. The result indicated that the cross fiber sheet at the angle of 45° exerts stronger constraint on the core area concrete than the vertical fiber sheet. The shear capacity and the deformation capacity of the joint core area were enhanced; thus, the energy dissipation capacity was improved.

4.2. Energy Dissipation Capacity. The energy dissipation capacity was the area surrounded by the load-deformation hysteretic curve. The energy dissipation capacity of damaged frame joints mode l reinforced by FRP is shown in Table 5. The result showed that, after reinforcement, the energy dissipation capacity of the model reaches the original level which meets the standard of seismic appraisal. For example, the dissipation energy and strain energy of reinforced model 1 were 4.58 times and 2.98 times of that before, respectively. The ratio of dissipation energy and strain energy was 1.53 times of that before. The dissipation energy and strain energy of reinforced model 2 were 2.13 times and 1.65 times of that before, respectively. The ratio of dissipation energy and strain energy was 1.30 times of that before.

The dissipation energy and strain energy of reinforced model 2 were 0.86 times of that of model 1. The ratio of dissipation energy and strain energy of model 2 and model 1 was the same. The result indicates that the cross fiber sheet at the angle of 45° exerts stronger constraint on the core area concrete than the vertical fiber sheet and, thus, enhances the energy dissipation capacity.

4.3. Displacement Ductility. The displacement ductility ratio was defined as the ultimate displacement divided by the yield displacement. The displacement ductility ratio of damaged

Table 4: Result of the experiment and analysis.

Model	YS		US		Condition	Means	AR/BR			
	Load (kN)	Displacement (mm)	Load (kN)	Displacement (mm)			YS load	YS displacement	US load	US displacement
1	36.00	8.98	47.39	17.89	BR	Experiment	1.01	1.56	1.12	2.34
	36.52	14.03	53.07	41.91	AR					
	34.04	10.37	40.27	19.92	BR	Analysis	1.12	1.34	1.39	2.09
	38.04	13.86	56.10	41.67	AR					
2	30.06	7.40	47.44	25.14	BR	Experiment	1.20	2.18	1.19	1.39
	35.98	16.14	56.66	35.05	AR					
	30.06	7.69	42.98	24.98	BR	Analysis	1.26	2.13	1.37	1.63
	37.96	16.36	58.88	40.72	AR					

YS- yield state, US- ultimate state, BR- before reinforcement, AR- after reinforcement.

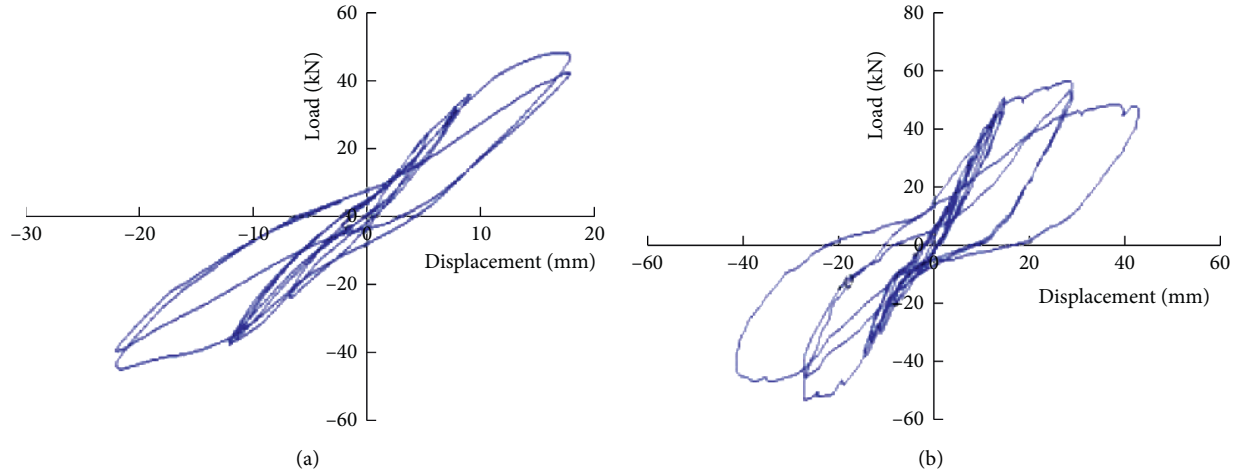

Figure 4: Comparison of the hysteretic curves of model 1 (experimental results): (a) before reinforcement; (b) after reinforcement.

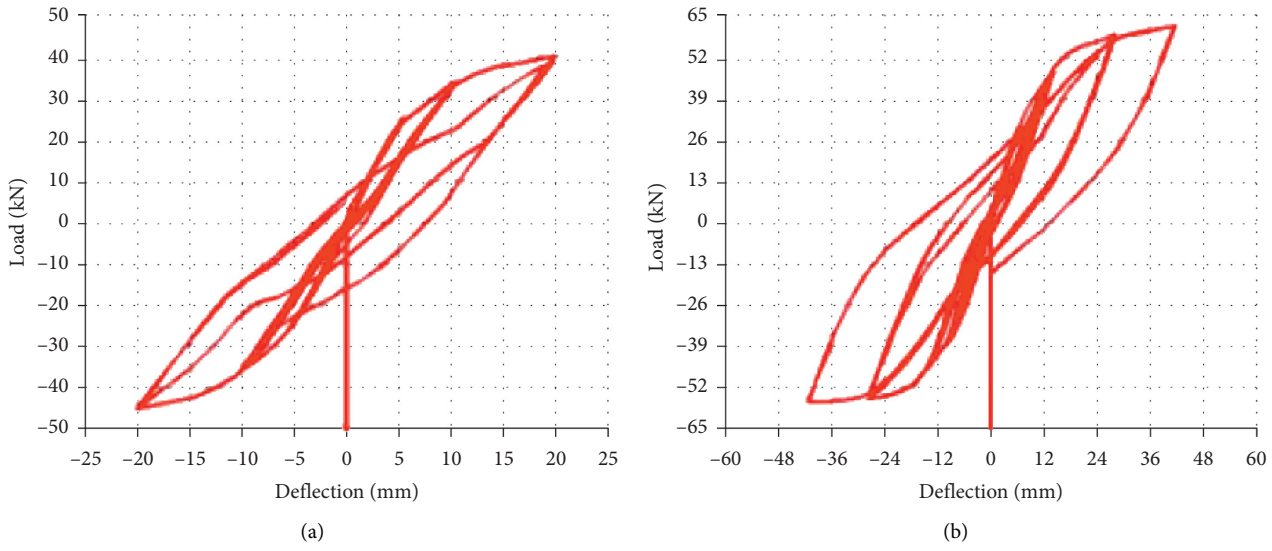

Figure 5: Comparison of the hysteretic curves of model 1 (analysis results): (a) before reinforcement; (b) after reinforcement.

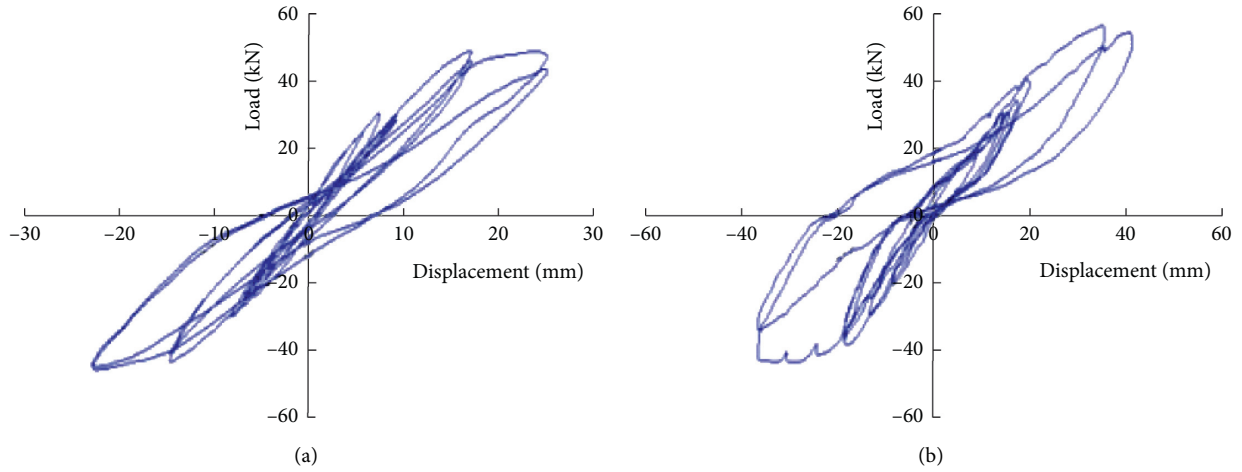

Figure 6: Comparison of the hysteretic curves of model 2 (experimental results): (a) before reinforcement; (b) after reinforcement.

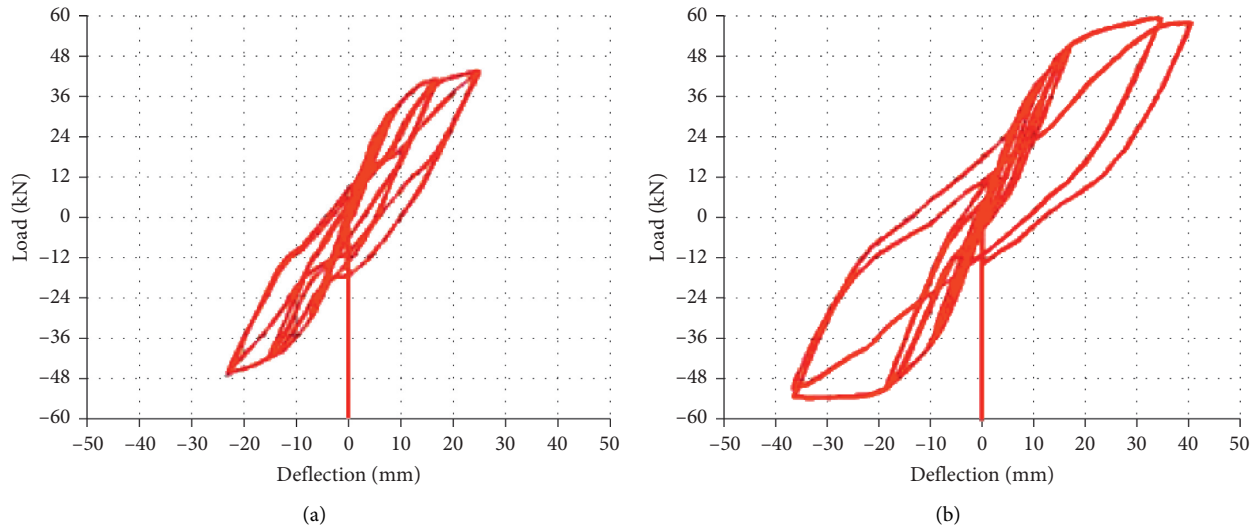

Figure 7: Comparison of the hysteretic curves of model 2 (analysis results): (a) before reinforcement; (b) after reinforcement.

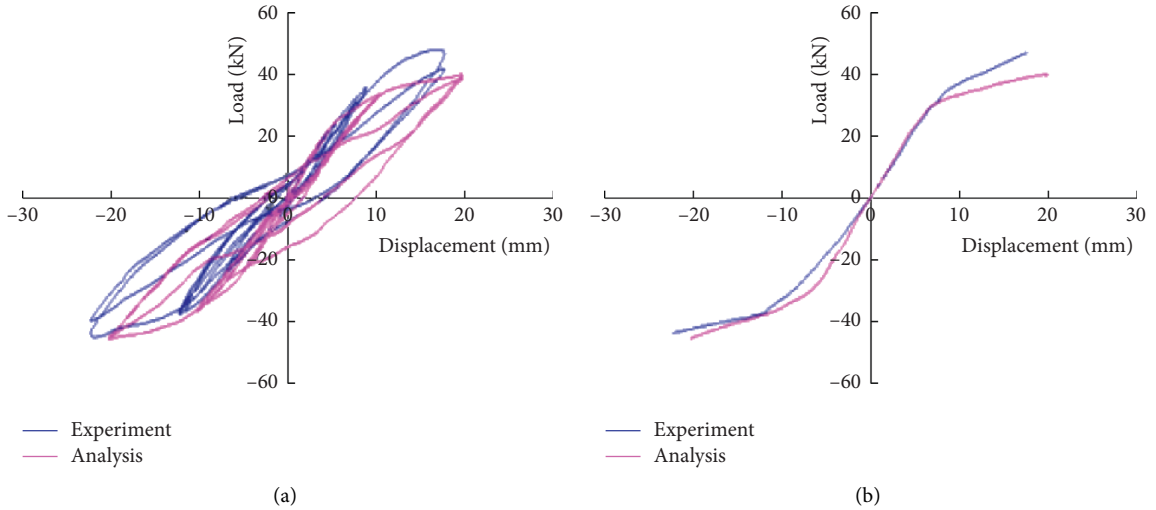

Figure 8: Comparison of the hysteretic curves and skeleton curve of model 1 (before): (a) hysteretic reinforcement; (b) skeleton reinforcement.

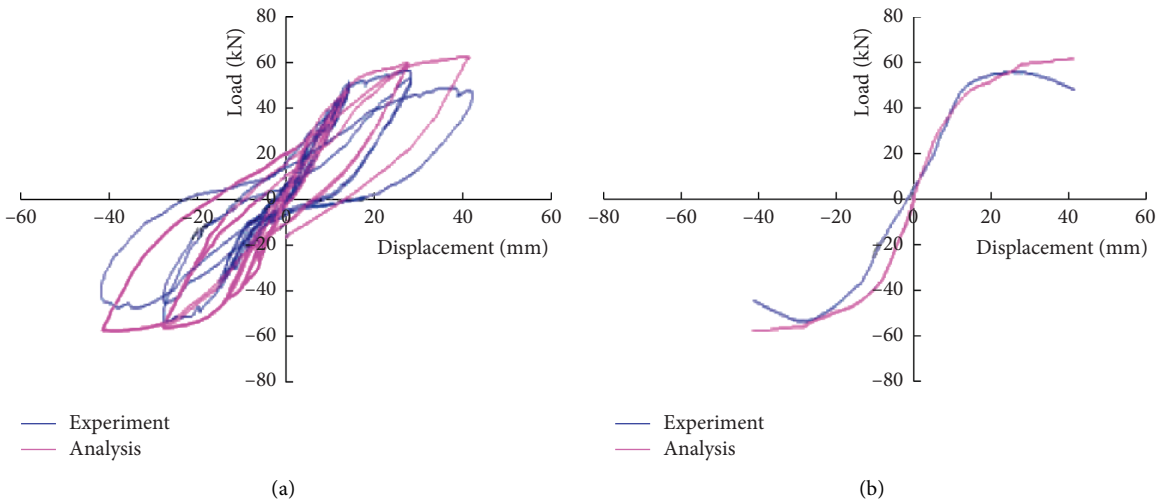

Figure 9: Comparison of the hysteretic curves and skeleton curve of model 1 (after): (a) hysteretic reinforcement; (b) skeleton reinforcement.

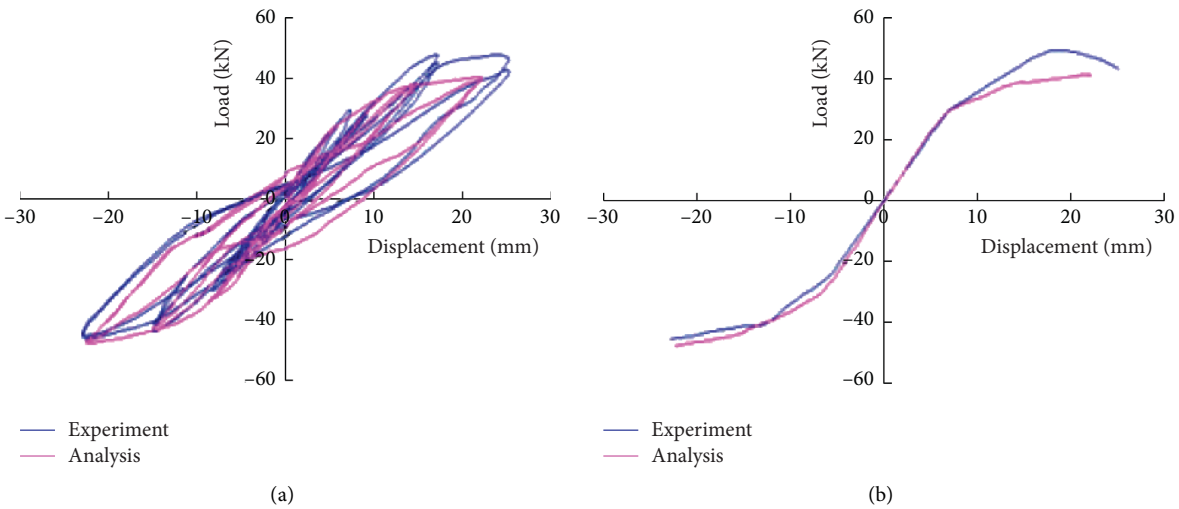

Figure 10: Comparison of the hysteretic curves and skeleton curve of model 2 (before): (a) hysteretic reinforcement; (b) skeleton reinforcement.

frame joints reinforced by FRP is shown in Table 6. The results showed that, for model 1, the yield displacement, ultimate displacement, and displacement ductility ratio after reinforcement were 1.34 times, 2.09 times, and 1.57 times of that before reinforcement, respectively. For model 2, the yield displacement, ultimate displacement, and displacement ductility ratio after reinforcement were 2.13 times, 1.63 times, and 0.77 times of that before reinforcement, respectively. The result showed that the displacement ductility of the model with the cross fiber sheet at the angle of 45° meets the standard of seismic appraisal, but the model with the fiber sheet at the angle of 0° proves a bad displacement ductility.

4.4. Bearing Capacity Degeneration. The reduction coefficient of bearing capacity was expressed by the ratio of the peak value of the second cycle load to the peak value of the first cycle load. The bearing capacity reduction coefficient of the damaged frame joints reinforced by FRP is shown in Table 7. The result showed that different methods of reinforcement barely lead to any differences of the bearing capacity reduction. For example, when displacement was Δy, the bearing capacity reduction coefficient of model 1 was 0.97 times of that before, while the number of model 2 was 1.00. When the displacement was $2\Delta y$, the bearing capacity reduction coefficient of model 1 was 0.98 times of that before, while that of model 2 was 0.98. When the

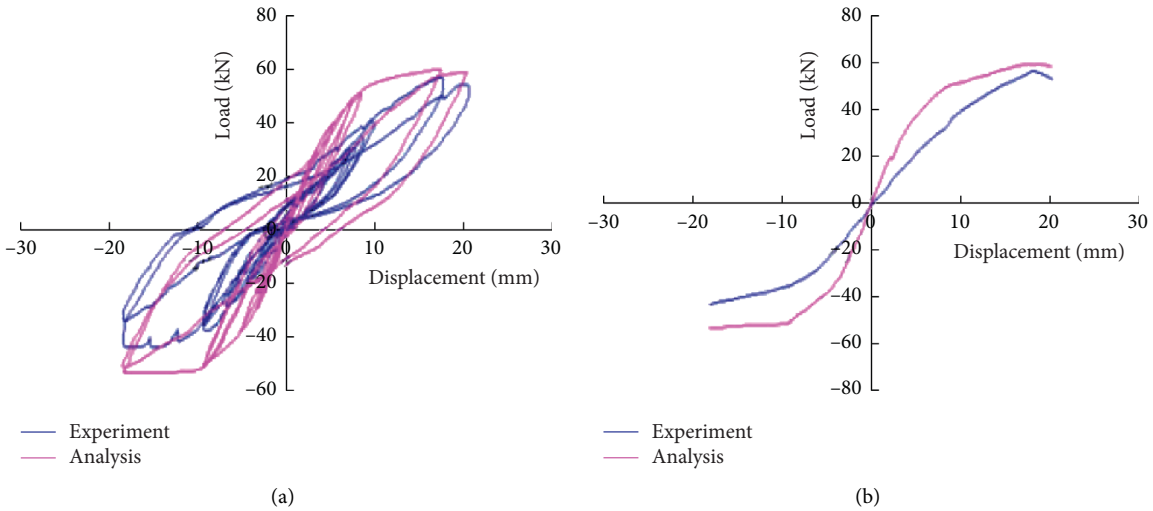

Figure 11: Comparison of the hysteretic curves and skeleton curve of model 2 (after): (a) hysteretic reinforcement; (b) skeleton reinforcement.

Table 5: The energy dissipation capacity of joints.

Model	DE (kN·mm)	SE (kN·mm)	DE/SE	Condition	Means	AR/BR		
						DE	SE	DE/SE
1	1344.1	3394.2	0.4	BR	Experiment	3.86	2.61	1.48
	5194.7	8870.9	0.59	AR				
	1184.3	3504.0	0.34	BR	Analysis	4.58	2.98	1.53
	5424.0	10438.2	0.52	AR				
2	2160.7	5314.9	0.41	BR	Experiment	1.93	1.42	1.34
	4161.1	7559.1	0.55	AR				
	2175.9	5424.0	0.4	BR	Analysis	2.13	1.65	1.30
	4643.0	8948.9	0.52	AR				

DE- dissipation energy; SE- strain energy.

Table 6: Displacement ductility of joints.

Model	YD (mm)	UD (mm)	DDR	Condition	Means	AR/BR		
						YD	UD	DDR
1	8.98	17.89	1.99	BR	Experiment	1.56	2.34	1.50
	14.03	41.91	2.99	AR				
	10.37	19.92	1.92	BR	Analysis	1.34	2.09	1.57
	13.86	41.67	3.01	AR				
2	7.40	25.14	3.40	BR	Experiment	2.18	1.39	0.64
	16.14	35.05	2.17	AR				
	7.69	24.98	3.25	BR	Analysis	2.13	1.63	0.77
	16.36	40.72	2.49	AR				

YD- yield displacement; UD- ultimate displacement; DDR- displacement ductility ratio.

displacement was $3\Delta y$, Model 2 was damaged, which was reinforced. From this, we see that the bearing capacity reduction of the models after the reinforcement was worse than before.

Table 7: Comparison of bearing capacity reduction coefficient of joints.

Model	YL (kN)	UL (kN)	Δy	$2\Delta y$	$3\Delta y$	Condition	Means	AR/BR			
								YL	UL	Δy	$2\Delta y$
1	36.00	47.39	0.969	0.901	—	BR	Experiment	1.01	1.12	0.97	1.03
	36.52	53.07	0.937	0.930	—	AR					
	34.04	40.27	0.996	0.969	—	BR	Analysis	1.12	1.39	0.97	0.98
	38.04	56.10	0.967	0.946	—	AR					
2	30.06	47.44	0.949	0.950	0.909	BR	Experiment	1.20	1.19	1.01	1.01
	35.98	56.66	0.963	0.957	—	AR					
	30.06	42.98	0.993	0.977	0.982	BR	Analysis	1.26	1.37	1.00	0.98
	37.96	58.88	0.994	0.956	—	AR					

YL- yield load; UL- ultimate load.

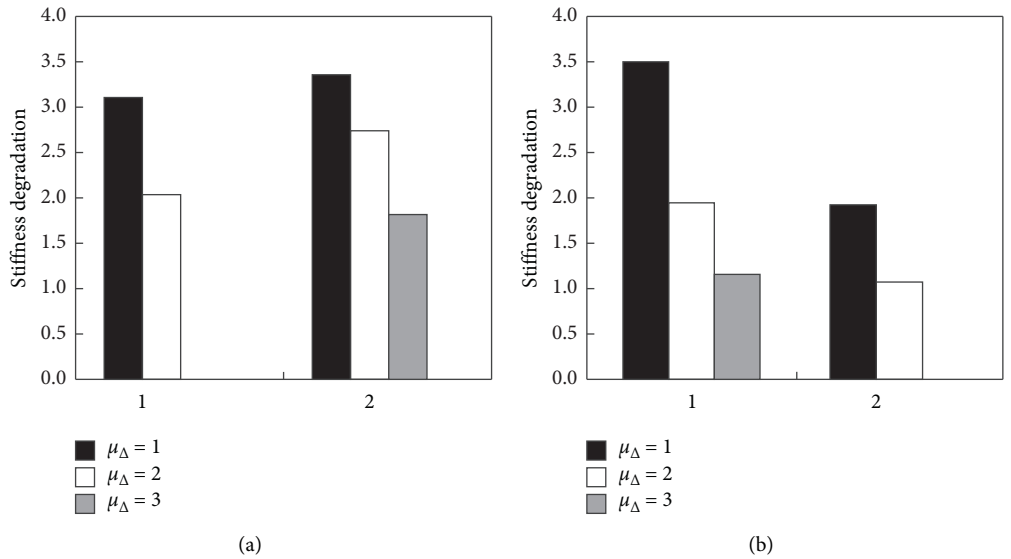

Figure 12: Stiffness comparison of joints (experimental results): (a) before reinforcement; (b) after reinforcement.

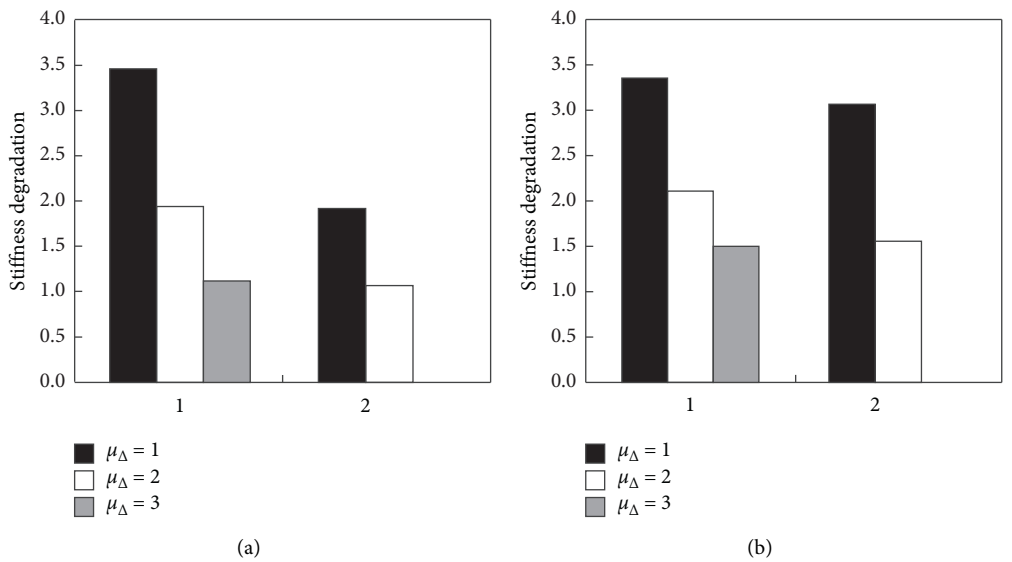

Figure 13: Stiffness comparison of joints (analysis results): (a) before reinforcement; (b) after reinforcement.

4.5. Stiffness Degradation. In this paper, the stiffness used for stiffness degradation was loop stiffness. It was calculated by the displacement corresponding to the peak load ratio of each loading cycle. The loop and linear stiffness of the damaged frame joint model reinforced by FRP are shown in Figures 12~13. At every ductility factor, the stiffness of model 2 was lower than that of model 1, and the circulation times of model 2 were fewer than those of model 1. The result indicated that the stiffness of the reinforced model with the cross fiber sheet at the angle of 45° meets the standard of seismic appraisal, but the model with the fiber sheet at the angle of 0° degenerates fast.

5. Conclusions

Based on the seismic performance test and finite element analysis of damaged steel fiber-reinforced high-strength concrete frame joints strengthened by FRP under low cyclic repeated load, the following conclusions are drawn:

Pasting the carbon fiber sheet at the angle of 45° in the core area after crack treatment can lead to better reinforcement performance than at 0°.

Although these two methods exert a little influence on the degradation of bearing capacity, the pasted fiber sheet increases the constraint of the core area concrete so that the bearing capacity, as well as the energy dissipation capacity, of the model was enhanced.

The strengthening method of pasting the carbon fiber sheet at 45° in the joint core area prevents the rigidity degeneration and improves the displacement ductility of the model. On the contrary, the method of pasting the carbon fiber sheet at 0° speeds up the rigidity degeneration and reduces the displacement ductility.

The finite element analysis result proves the rationality of the element type, material constitutive relation, and failure criterion used in the finite element analysis.

Data Availability

The data used in this study can be obtained from the corresponding author on request.

Conflicts of Interest

The authors declare no conflicts of interest.

Acknowledgments

The authors sincerely thank Professor Gao Danying of Zhengzhou University for the guidance and help. The research presented in this paper was supported by the National Natural Science Foundation of China (No. 50678159).

References

[1] M. J. Shannag, N. Abu-Dyya, and G. Abu-Farsakh, "Lateral load response of high performance fiber reinforced concrete beam-column joints," *Construction and Building Materials*, vol. 19, no. 7, pp. 500–508, 2005.

[2] M. Gencoqlu, "The effects of stirrups and the extents of regions used SFRC in exterior beam-column joints," *Structural Engineering and Mechanics*, vol. 27, no. 2, pp. 223–241, 2007.

[3] B. S. Hamad and C. D. B. Abs, "Effect of fiber-reinforced polymer confinement on bond strength of hooked bars in high-strength concrete," *ACI Structural Journal*, vol. 106, no. 6, pp. 831–839, 2009.

[4] D. Gao and J. Zhang, "Experimental investigation on seismic behavior of steel fiber reinforced high-strength concrete frame exterior joints," *Industrial Construction*, vol. 42, no. 5, pp. 84–89 + 28, 2012.

[5] J. Zhang and T. Wang, "Experimental investigation on seismic behavior of high-strength concrete frame exterior joints partially reinforced by steel fiber," *Concrete*, no. 7, pp. 13–16, 2011.

[6] T. Wang and J. Zhang, "The seismic behavior of steel fiber reinforced high-strength concrete frame joints," *Disaster Advances*, vol. 5, no. 4, pp. 1418–1423, 2012.

[7] T. Y. Wang, J. W. Zhang, and D. Y. Gao, "The seismic behavior of high-strength concrete frame joints," *Applied Mechanics and Materials*, vol. 238, pp. 838–843, 2012.

[8] J. Zhang, X. Tian, T. Wang, and D. Gao, "Influence of FRP material types on seismic behavior of FRP reinforced damaged steel fiber reinforced high-strength concrete frame exterior joints," *Concrete*, vol. 9, no. 8, pp. 24–28, 2013.

[9] A. Bousselham, "State of research on seismic retrofit of RC beam-column joints with externally bonded FRP," *Journal of Composites for Construction*, vol. 14, no. 1, pp. 49–61, 2010.

[10] National Standards of the People's Republic of China, *Code for Design of Concrete Structures (GB50010-2010)*, China Architecture& Building Press, Beijing, China, 2010.

[11] G. Zhenhai, "Strength and deformation of concrete," *Journal of Tongji University*, vol. 25, no. 3, pp. 255–261, 1997, in Chinese.

[12] Z. Yang and C. Wu, "Analysis on the seismic performance of RC frame beam-column joints strengthened by sprayed FRP," *Applied Mechanics and Materials*, vol. 578-579, pp. 835–838, 2014.

[13] Z. P. Liu, *Nonlinear Numerical Simulation of Pre-Stressed Concrete and Reinforced Concrete Beam Based on ANSYS*, Xinjiang Agricultural University, Xinjiang, China, 2007.

[14] G. Zhao, S. Peng, and C. Huang, *Steel Fiber Reinforced Concrete Structures*, ROC Military Academy, Kaohsiung, Taiwan, China, 1999.

[15] S. Moaveni, *Finite Element Analysis: Theory and Application with ANSYS*, Minnesota State University, Mankato, China, Fourth edition, 2015.

[16] B.-J Si, Z.-G. Sun, Q.-H. Ai, and D. Wang, "Sensitive analysis and model modification for finite element analysis of R/C bridge piers under cyclic loading," *Engineering Mechanics*, vol. 26, no. 1, pp. 174–180 + 186, 2009.

[17] L. De Lorenzis, B. Miller, and A. Nanni, "Bond of fiber-reinforced polymer laminates to concrete," *ACI Materials Journal*, vol. 98, no. 3, pp. 256–264, 2001.

[18] K. T. Lau, P. K. Dutta, L. M. Zhou, and D. Hui, "Mechanics of bonds in an FRP bonded concrete beam," *Composites Part B: Engineering*, vol. 32, no. 6, pp. 491–502, 2001.

[19] S. Peng, C. Xu, M. Lu, and J. Yang, "Experimental research and finite element analysis on seismic behavior of CFRP-strengthened seismic-damaged composite steel-concrete frame columns," *Engineering Structures*, vol. 155, pp. 50–60, 2018.

[20] H. T. Liu and T. Y. Wang, "Experimental study and finite element analysis of the seismic behaviors for steel fiber reinforced high-strength concrete frame exterior joints," *Advanced Materials Research*, vol. 295–297, pp. 1499–1504, 2011.

Hindawi
Advances in Civil Engineering
Volume 2020, Article ID 8839386, 11 pages
https://doi.org/10.1155/2020/8839386

Research Article

Research on the Corrosion Damage Mechanism of Concrete in Two Freeze–Thaw Environments

Xianhua Yao,[1] Min Zhang,[1] Junfeng Guan ,[1] Lielie Li ,[1] Weifeng Bai,[2] and Zepeng Liu[1]

[1]*School of Civil Engineering and Communication, North China University of Water Resources and Electric Power, Zhengzhou 450045, China*
[2]*School of Water Conservancy, North China University of Water Resources and Electric Power, Zhengzhou 450045, China*

Correspondence should be addressed to Junfeng Guan; shuaipipi88@126.com and Lielie Li; 13370912@qq.com

Received 21 August 2020; Revised 13 September 2020; Accepted 21 September 2020; Published 8 October 2020

Academic Editor: Yifeng Ling

This study aims to investigate the effects of two freeze–thaw environments (i.e., maintenance freeze-thaw (MFT) environment and immersion freeze-thaw (IFT) environment) on the durability performance, deterioration rules, and mechanisms of concrete. In MFT, the concrete specimens were firstly cured in the standard curing environment (temperature, 20 ± 3, humidity, not less than 95%, and ages, 28 d) and then were carried out in freeze–thaw environment, while in IFT, the concrete specimens were firstly cured in the salt ($NaHCO_3$, NaCl, and Na_2SO_4) immersion environment for 90 d and then were carried out in freeze–thaw environment. In this study, the damage features, relative dynamic elastic modulus, mass changes, and erosion-resistance coefficient of concrete have been measured. Thereafter, using the scanning electron microscopy (SEM) and the mercury intrusion porosimetry (MIP), the air-void structure parameters and the microstructures have been measured, respectively. The results show that the relative dynamic elastic modulus and the erosion-resistance coefficient of the compressive strength of the concrete in the IFT environment are, respectively, 14.3% and 21.0% higher than those of the concrete in the MFT environment. In addition, the results of the microstructure analyses show that the corrosion damages of the concrete are mainly caused by the combined action of the corrosion products of ettringite and freeze–thaw environment. However, the damage to the concrete in the MFT environment is more serious than that in the IFT environment. The results of the MIP analysis show that the harmful pore value for the concrete in the MFT environment is almost two times larger than that for the concrete in the IFT environment.

1. Introduction

Many earlier studies investigated the damage to concrete caused by freeze-thaw cycles [1, 2]. Ma et al. [3] showed that the frost resistance of high-performance concrete blended with 20 wt% fly ash (FA) and 0.1% polypropylene fiber was superior when subjected to rapid freeze-thaw cycles. Zhou and Qiao [4] observed that when a concrete material was subjected to rapidly repeated freeze-thaw cycles, the energy-based approach was more sensitive and effective than the elastic modulus-based approach in evaluating the deterioration of the concrete material over time and capturing the accumulative material degradation. Liu et al. [5] found that the addition of FA in ordinary concrete reduced the formation of gypsum and prevented the decalcification of calcium silicate hydrate (C-S-H) when subjected to sodium sulfate attack. Zhang et al. [6] found that an excessive number of nano-SiO2 particles could have an adverse effect on the durability of the concrete. Forgeron [7] and Trottier [8] found that the mechanical properties of concrete under the combined action of the fatigue load and the freeze-thaw cycles were equivalent or even better than when only the fatigue load was applied. Diao et al. [9] reported that with the increase in the number of freeze-thaw cycles, the compressive strength of concrete decreased when subjected to alternating actions of the freeze-thaw cycles and seawater immersion. Gong et al. [10] developed a comprehensive hydraulic pressure model that can be applied to different cases, such as different saturation degrees and cooling rates. Diao et al. [11] found that when subjected to the freeze-thaw

cycles and mixed corrosion, the loading capacity of reinforced concrete beams decreased by 4%. Amini and Tehrani [12] developed quantitative damage models to predict the mass loss and the compressive strength loss due to the combined effect of saltwater and water flow on the deterioration of concrete subjected to freeze-thaw cycles. Richardson et al. [13] found that rubber crumb was effective in providing freeze-thaw protection. Yuan et al. [14] observed that the extent of concrete damage increased gradually from surface to complete disintegration of the interior concrete after 30 freeze-thaw cycles. Wang et al. [15] found that the freezing temperature was independent of the freeze-thaw cycles; however, thawing temperature changed with the number of freeze-thaw cycles. Shang et al. [16] found that the loss of the compressive strength and the tensile strength of concrete was more evident than those of the dynamic modulus of elasticity and the weight loss after the concrete was subjected to the freeze-thaw cycles. Ranz et al. [17] developed a nondestructive methodology that can be used as an alternative method to evaluate the damage in cementitious materials when subjected to freeze-thaw cycles. Li et al. [18] found that air content can delay the time for concrete to reach a critical degree of saturation; however, this did not prevent the damage to concrete caused by the freeze-thaw cycles. Richardson et al. [19] observed that fibers had the ability to entrain air, which might contribute to the improvement in freeze-thaw durability. Zhang et al. [20–22] showed that nano-SiO_2, nano-$CaCO_3$, and ground-granulated blast-furnace slag could strengthen mechanical performance of concrete. Li et al. [23] found that the deterioration of concrete under the freeze-thaw plus dry-wet conditions was significantly higher than that under the dry-wet plus freeze-thaw conditions and much higher than that under one of these two conditions only. Su and Wang [24] studied the corrosion damage properties of concrete subjected to multi-salt soaking, freeze-thaw, and dry-wet cycles. Yao et al. [25, 26] investigated the microscopic mechanism of concrete using multiple admixtures under the common action of multisalt soaking, wetting-drying, and freeze-thaw cycles.

Researchers have also carried out studies on the influences of different freeze–thaw environments on concrete. Shi et al. [27] found that with the increase in the freeze–thaw cycles the concrete elastic moduli at the upper-limit temperature were decreasing due to the accumulated damage caused by the freeze–thaw cycle action of different temperature ranges. Under different freeze–thaw media, Yin et al. [28] showed that the concrete in 3.5wt% NaCl solution was much worse than that in water, and the degree of deterioration of the mass loss rate, relative dynamic elastic modulus, average compressive strength, and porosity of CT scanning images of the recycled aggregate pervious concrete increased with the increasing number of freeze–thaw cycles. In the investigation of the difference between the effects of the water-resistant freeze–thaw and the salt–freeze–thaw cycles on ordinary concrete, Xu et al. [29] found that there was a multiplier relationship between the two, and the multiplier value had nothing to do with the concrete mix ratio, strength grade, and stone powder content. By analyzing the mechanical properties of concrete subjected to freeze–thaw cycles in three solutions (i.e., water, 3.5 wt% NaCl, and aircraft deicing fluid), Zhao et al. [30] found that the damage to the concrete in 3.5 wt% NaCl solution was much worse than that in water, and there was only limited damage to the concrete in the aircraft deicing fluid. Through a study of the effects of different freezing and thawing methods on the fracture of concrete with double-k, Hu et al. [31] found that there were similarities in the influence of different freeze–thaw methods on the concrete.

However, most of these earlier studies focused on the damage to concrete under a water freeze-thaw environment or a sulfate attack environment. Even for the studies on the effects of different freeze–thaw environments on the mechanical properties and microstructures of concrete, the methods used in most of these studies were freezing and thawing concrete in water, or in a single salt (e.g., NaCl) solution. They did not investigate freezing and thawing concrete in a multisalt (NaCl, Na_2SO_4, and $NaHCO_3$) solution. Therefore, it is necessary to investigate the durability performance and deterioration rules and mechanisms of concrete in different freeze–thaw environments, including the multisalt freeze–thaw environments.

In real-life practical engineering, the corrosive failure mechanisms of concrete are different in different parts of China. For instance, in the cold saline-alkali corrosive areas in Western China, concrete may encounter two situations. One is for the concrete to be subjected to the composite salt freeze-thaw cycles after a certain standard curing period (usually not more than 28 days and the concrete specimens were in water only). The other is for the concrete to be subjected to the multisalt freeze-thaw cycles after a certain period of erosion (generally 1–5 months and the concrete specimens were in the multisalt solution) caused by the multisalt (e.g., NaCl, Na_2SO_4, and $NaHCO_3$) [32]. In real-life practical engineering, the corrosive failure mechanism of concrete is different in the two situations above. However, there are only a few reports on the physical properties, chemical changes, mechanical performances, and microcrack evolution process of concrete subjected to freeze-thaw cycles and multisalt solution attack. Therefore, in the cold and saline-alkali corrosive areas of Western China, a study on the effects of freeze-thaw cycles and multisalt erosion on concrete has important scientific research significance and practical engineering value.

In this study, in view of the multisalt solution attack environment in the cold region in western China and the actual situation of Dexiang Expressway Project in Delingha City, Qinghai Province, the effects of two freeze-thaw environments (i.e., MFT and IFT) on the durability performance, deterioration rules, and mechanisms of concrete have been investigated using the concrete mix ratio provided by the site so as to develop theories for the actual project and experimental basis.

2. Experimental Materials and Concrete Specimens

2.1. Materials. In this study, PO 42.5 portland cement (provided by Qinghai Province Cement Co., Ltd, China) has

been used for the preparation of the concrete specimens. The concrete specimens have been prepared by replacing a part of FA (provided by Qinghai Province Datong Co., Ltd., China) and slag (provided by Qinghai Province Jintuo Co., Ltd., China). The chemical composition, physical and mechanical properties, and mineral compositions of the materials used are shown in Tables 1–5.

The reactive sand used in this study has the mud concentration of 0.8%, apparent density of 2650 kg/m^3, bulk density of 1470 kg/m^3, and fineness modulus of 2.6. The sand, provided by the manufacturer Qinghai Province, China, has been classified as a type of medium sand. The coarse aggregate used in this study was provided by the manufacturer Qinghai Province, China, has a continuous grade of 5–20 mm, the apparent density of 2520 kg/m^3, and bulk density of 1350 kg/m^3. The high-range water reducer used in this study was produced by Shanxi Province Chemical Co., Ltd. It has a naphthalene-type superplasticizer with a water reduction of greater than 20%. The content of Na_2SO_4 was less than 2%, and the content of chloride ions in water was less than 0.01%.

2.2. Concrete Specimens. The environment of the Dexiang Highway Project is a corrosive salt marsh environment. The salt marsh contains many types of corrosive ions (i.e., Cl^-, HCO_3^-, and SO_4^{2-}), which affect the durability of concrete negatively. Therefore, the soil samples in the area have been analyzed chemically. The artificial multi-salt consists of $NaHCO_3$, NaCl, Na_2SO_4, and H_2O, and the chemical reagents proportions are shown in Table 6. The mix proportion for the concrete specimens has been designed according to the practical engineering requirements of concrete. The mix proportion is shown in Table 7.

Then, the materials, such as cement, FA, SG, sand, gravel, and water-reducing agent, were dry mixed in a blender for 1 min. Thereafter, water was added, and the mixture was blended for 3 min. The concrete specimens of two sizes (100 mm × 100 mm × 100 mm and 100 mm × 100 mm × 400 mm) were produced. The 100 mm concrete cubes were used to measure the reduction in compressive strength and concrete mass and 100 mm × 100 mm × 400 mm prisms were used to measure the relative dynamic elastic modulus and microstructure. Each concrete specimen was placed in a mold and cured for 24 h. The concrete specimens were then divided into two groups. After demolding, one group was placed into water of (20 ± 3)°C for 28 d standard curing. The other group, also demolded, was placed into multisalt water for 90 d curing.

2.3. Experimental Program. In general, the damage mechanism and the reaction outcomes of concrete subjected to freeze-thaw cycles and multisalt solution attack are different. The internal structure of the concrete tends to be denser after the multisalt solution attack, as compared to the concrete after being subjected to the freeze-thaw cycles. Therefore, in order to investigate this difference, experiments have been carried out with the concrete specimens in the MFT and IFT environments, and the results are shown in experiment in the MFT environment and experiment in the IFT environment.

Table 1: Chemical composition of main raw materials (in percentage).

Material	SiO_2	Al_2O_3	Fe_2O_3	CaO	MgO	Na_2O	K_2O
PO 42.5	23.46	3.88	3.32	66.82	1.32	0.42	0.78
FA	55.31	26.83	5.65	5.88	2.56	1.98	1.79
Slag	47.33	6.43	1.12	40.23	3.21	0.77	0.91

Experiment in the MFT Environment. After immersing the concrete specimens in pure water of (20 ± 3)°C for 24 days, the specimens were immersed in the multisalt solution of (20 ± 3)°C for 4 days and subjected to 150 freeze-thaw cycles and multisalt solution attack. The mass change, compressive strength, and relative dynamic elastic modulus of the concrete specimens have been determined at 0, 25, 50, 75, 100, 125, and 150 cycles. Using the scanning electron microscopy (SEM) and mercury intrusion porosimetry (MIP), the microstructure of the concrete has been evaluated.

Experiment in the IFT Environment. This group of concrete specimens was exposed to the multisalt solution for 90 days and then subjected to 150 freeze-thaw cycles and multisalt solution attack. The mass change, compressive strength, and relative dynamic elastic modulus of concrete specimens have been determined at 0, 25, 50, 75, 100, 125, and 150 cycles. Using the scanning electron microscopy (SEM) and mercury intrusion porosimetry (MIP), the microstructure of the concrete has been evaluated.

In this study, the Standard for Test Methods of Long-Term Performance and Durability of Ordinary Concrete (GB/T 50082-2009) has been used as a guide. The concrete specimens of the sizes 100 mm × 100 mm × 100 mm and 100 mm × 100 mm × 400 mm have been prepared for the freeze-thaw test. During the test, the central temperature of the specimens was controlled, and they were changed between −15 ± 2°C and 6 ± 2°C. The deicer solution level was 20 mm higher than the top of the specimens. Each freeze-thaw cycle lasted for nearly 2 h, and the thawing time was approximately 2 h. The freeze-thaw test was stopped when the mass loss (W_n) reached 5% or the relative dynamic elastic modulus (E_r) decreased to 60%. At that point, the number of freeze-thaw cycles is considered as the maximum number of freeze-thaw cycles, n. The mass loss, W_n, is then calculated after n freeze-thaw cycles as follows:

$$W_n = \frac{G_0 - G_n}{G_0} \times 100\%, \quad (1)$$

where (G_0) is the original mass before the start of the freeze-thaw cycles, and (G_n) is the mass after n freeze-thaw cycles.

The relative dynamic elastic modulus, E_r, is calculated as follows:

$$E_r = \frac{E_n}{E_0} = \frac{f_n^2}{f_0^2} \times 100\% E_r, \quad (2)$$

where E_0 is the original relative dynamic elastic modulus of the concrete specimens, E_n is the relative dynamic elastic

Table 2: Basic physical and mechanical properties of cement.

Cement	Specific surface area ($m^2 \cdot kg^{-1}$)	Initial setting time	Final setting time	Compression strength (MPa)	
		Min	Min	3 d	28
PO 42.5	344	240	315	24.1	49.3

Table 3: Mineral composition of main raw materials (in percentage).

Material	C3S	C2S	C3A	C4AF	f-CaO
PO 42.5	55.7	22.09	5.12	16.79	0.29

Table 4: Basic physical and mechanical properties of FA (in percentage).

Material	Fineness (45 μm)	Water demand ratio	SO_3	Loss
FA	10.8	94	0.67	1.66

modulus of the concrete specimens after n freeze-thaw cycles, f_0^2 is the original frequency of the concrete specimens, and f_n^2 is the frequency of the concrete specimens after n freeze-thaw cycles. Further, the compression strength of the concrete specimens has been evaluated.

The erosion-resistance coefficient, K_c, of the specimens can be calculated as follows:

$$K_c = \frac{f_c}{f_s}, \tag{3}$$

where f_c is the compression strength of the concrete specimens subjected to n freeze-thaw cycles and the multisalt solution attack, and f_s is the original compression strength of the concrete specimens immersed in the multisalt solution before the start of the freeze-thaw cycles.

3. Experimental Results and Discussion

3.1. Visual Inspection. As shown in Figures 1 and 2 and Table 8, the degree of damage of the concrete specimens after being subjected to freeze-thaw cycles is different in different experiments. With the increase in the number of freeze-thaw cycles, the degree of damage of concrete increases gradually. After being subjected to the maximum number of freeze-thaw cycles in the IFT environment, which is 125, a large number of stones in the concrete specimen are exposed or at one end of the concrete specimen, they are even peeled. Comparing to that in the IFT environment, the damage of the concrete specimens in the MFT environment is more serious. The whole surface of the concrete specimen fell off. Moreover, when the number of freeze-thaw cycles reaches 100 times, the degree of damage of the concrete specimen is 125 times of that in the IFT environment. This is an indication that the MFT environment is more destructive to concrete than the IFT environment.

3.2. Mass Change. Figure 3 shows that the mass loss of the concrete specimen increases with increasing the number of freeze-thaw cycles. Before 75 freeze-thaw cycles, the mass loss of the concrete specimen in the IFT environment is slightly higher than that in the MFT environment. However, after 75 freeze-thaw cycles, due to the peeling of the concrete specimen in the MFT environment, the mass loss of the concrete specimen in the MFT environment is higher than that in the IFT environment. This is an indication that the rate mass loss of the concrete specimen in the MFT environment is faster after 75 freeze-thaw cycles.

3.3. Relative Dynamic Elastic Modulus. Figure 4 shows the variations of E_r of the concrete specimens subjected to the freeze-thaw cycles and the multisalt solution attack. Before 75 freeze–thaw cycles, E_r of the concrete specimen in the MFT environment is slightly higher than that in the IFT environment. That is to say, the MFT case showed better frost resistance in the first several cycles the IFT. However, the results show that in the latter stage of the concrete degradation, the decrease in E_r in the MFT environment is significantly larger than that in the IFT environment. This is an indication that the deterioration of concrete subjected to freeze-thaw cycles and the multisalt solution attack is faster due to the salt crystallization. For instance, in Figure 4, E_r for the concrete specimens in the MFT environment decreases by 48.7% after 100 freeze-thaw cycles. On the other hand, E_r for the concrete specimens in the IFT environment decreases by 44.2% after 125 freeze-thaw cycles. Hence, E_r for the concrete specimen in the MFT environment decreases by 4.5% more than that in the IFT environment. From the downward trend (Figure 4), when the number of freeze-thaw cycles increases from 75 to 100, E_r of the concrete specimen in the MFT environment decreases from 87.6% to 51.3% (a decrease of 36.3%). This sharp downward trend is an indication of brittle damage characteristics. By contrast, when the freeze-thaw cycles increases from 75 to 100, E_r of the concrete specimen in the IFT environment decreases from 75.7% to 61.4% (a decrease of 14.3%). So, the decrease in E_r of the concrete specimen in the IFT environment is slower than that in the MFT environment. Comparing with the damage caused by the freeze-thaw cycles, the damage to the concrete specimen by the salt solution attack is less. Therefore, the damage to concrete in the IFT environment is generally less than that in the MFT environment.

3.4. Erosion-Resistance Coefficients. Figure 5 shows the variations of K_c of the concrete specimens subjected to the freeze-thaw cycles and the multisalt solution attack. As shown in the figure, for the concrete specimens in the MFT environment, there is slight corrosion. In the initial stage, K_c of the concrete specimen increases with increasing the number of freeze–thaw cycles, which is known as the

Table 5: Basic physical properties of slag (in percentage).

Material	Specific surface area ($m^2 \cdot kg^{-1}$)	Loss	SO_3	Water demand ratio	Activity index	
					7 d	28 d
Slag	405	0.17	0.11	97	76	103

Table 6: Proportion of chemical reagents in multisalt. Unit: g/L.

$NaHCO_3$	NaCl	Na_2SO_4
0.54	31.01	3.55

Table 7: Mix proportion for concrete specimens (grade C30). Unit: kg/m^3.

Cement	Sand	Gravel (5–20 mm)	Water	Water reducing agent	Fly ash	Slag
262	767	1103	170	5.23	87	87

corrosion strengthening stage. This stage is followed by a stabilizing stage. Comparing with the concrete specimens in the IFT environment, the damage to the concrete specimens in the MFT environment is more seriously after 25 freeze-thaw cycles. K_c of the concrete specimens in the MFT environment decreases sharply from 25 to 50 freeze-thaw cycles and then decreases gradually as the freeze-thaw cycles increase. For example, K_c of the concrete specimens in the MFT environment is reduced by 59% after 150 freeze-thaw cycles, whereas for the concrete specimens in the IFT environment is reduced by 38%. Hence, the reduction in K_c of the concrete specimens in the MFT environment is 21% more than that in the IFT environment. From the results of the mass loss, E_r and K_c of the concrete specimens, they all show that the degree of damage of the concrete specimens in the MFT environment is more serious than that in the IFT environment. Therefore, when concrete is to be subjected to freeze-thaw cycles and multisalt solution attack, it is recommended to place concrete in a multisalt erosion environment for three months prior to freezing.

3.5. Analysis of Microstructure of Concrete Specimens

3.5.1. Analysis of Microstructure Using SEM and EDS. Figure 6 shows the SEM images of the deteriorated part of the concrete specimen in the IFT environment subjected to the multisalt solution attack and freeze-thaw cycles from 0 to 125. Figure 6(a) shows the microstructure of the concrete specimen attacked by the multisalt solution after 90 days. Before the 90 days, there were no freeze-thaw cycles, and the concrete microstructure is quite compact. As shown in Figure 6(a), the corrosion products of ettringite are formed inside the concrete; however, there are no microcracks. This may be attributed to the corrosion products of ettringite integrate with the concrete. Figure 6(c) shows the microstructure of the concrete in the IFT environment. It can be seen that there are several microcracks and the maximum width of the microcracks is approximately 0.8 μm. With the increase in the freeze-thaw cycles, for the concrete specimen in the IFT environment, the maximum width of the microcracks increases gradually, and large pores have a loose structure (Figure 6(e)).

Figure 7 shows the microstructure of the concrete specimen in the MFT environment. Before the freeze-thaw cycles, the SEM microscopic analysis shows that the concrete microstructure is quite compact because of the C-S-H dispersed well in the concrete (Figure 7(a)). After 25 freeze-thaw cycles, there are several voids in the concrete, as shown in Figure 7(b). With the increase in the freeze-thaw cycles, several corrosion products formed as indicated by the arrows in Figure 7(c). With the further increase in the freeze-thaw cycles, the voids became larger; thus, more corrosion products entered the interior of the concrete (Figure 7(d)). Therefore, they interacted and promoted each other. The maximum width of some microcracks is approximately 3.0 mm (Figure 7(e)), which is wider than that for the concrete specimen in the IFT environment.

The reason for the wider microcracks in the concrete specimen in the IFT environment may be attributed to the immersion of the concrete specimen in the multisalt solution for a long time before freezing. The advantage is that the chloride ions in the multisalt solution have strong penetration ability; they enter into the concrete to reduce the freezing point, prevent the invasion of sulfate ions, and reduce the corrosion production of ettringite, thereby improving its corrosion resistance performance. The disadvantage is that the concrete specimen in the IFT environment is easily eroded when subjected to the multisalt solution attack after demolition. However, the concrete specimen in the MFT environment has been immersed in the multisalt solution for only 28 days before freezing. In the MFT case, before 75 freeze–thaw cycles, due to the filling of corrosive products in a short period of time, the strength of concrete will increase; however, with the increase of corrosive ion concentration, especially sulfate ion concentration, excessive ettringite which are corrosive products will expand inside the concrete. When the expansion stress exceeds the tensile strength of concrete, the concrete will be damaged. In contrast, in the IFT case, before 75 freeze–thaw cycles, due to the filling of corrosive products in the curing time (90 d), corrosive products are integrated with the concrete [25], there are relatively few pores in concrete, and no more corrosive products enter the concrete; therefore, the damage is less. Therefore, the damage to the concrete specimen subjected to the freeze-thaw cycles is more serious than that subjected to the multisalt solution attack. In general, the degree of damage of the concrete specimen in the IFT environment is smaller than that in the MFT environment.

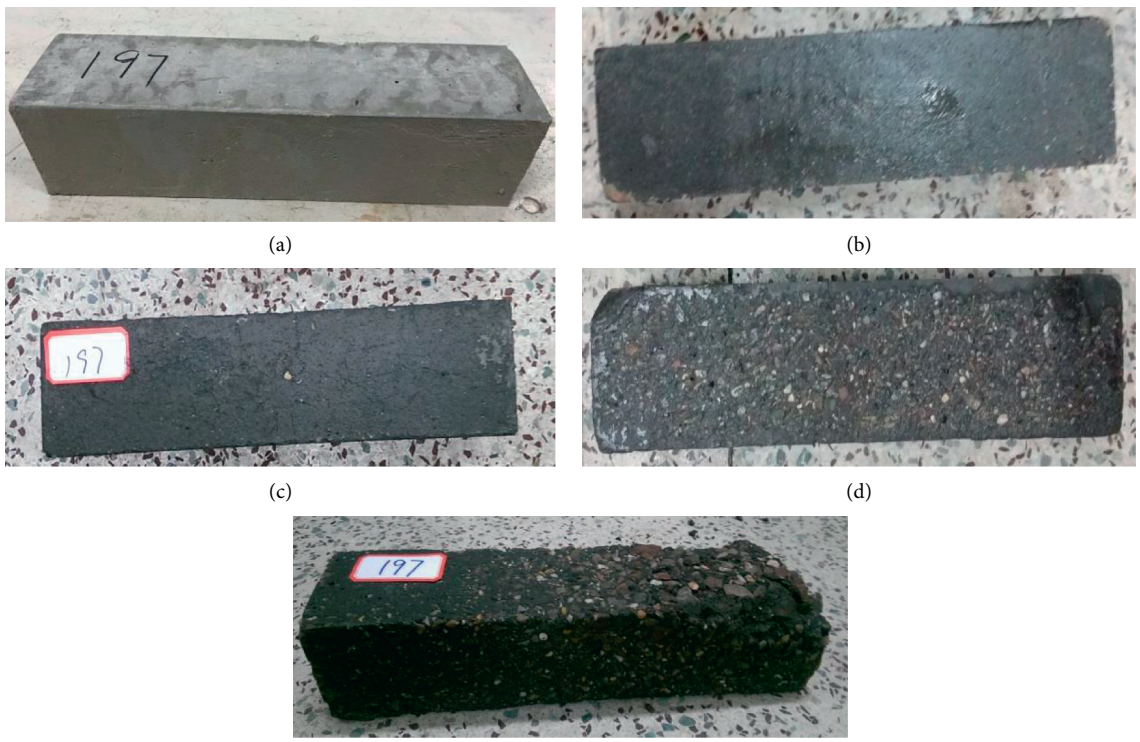

(a) (b) (c) (d) (e)

Figure 1: Typical failure modes of the concrete in the IFT environment. (a) 0 freeze-thaw cycles; (b) 25 freeze-thaw cycles; (c) 50 freeze-thaw cycles; (d) 75 freeze-thaw cycles; and (e) 125 freeze-thaw cycles.

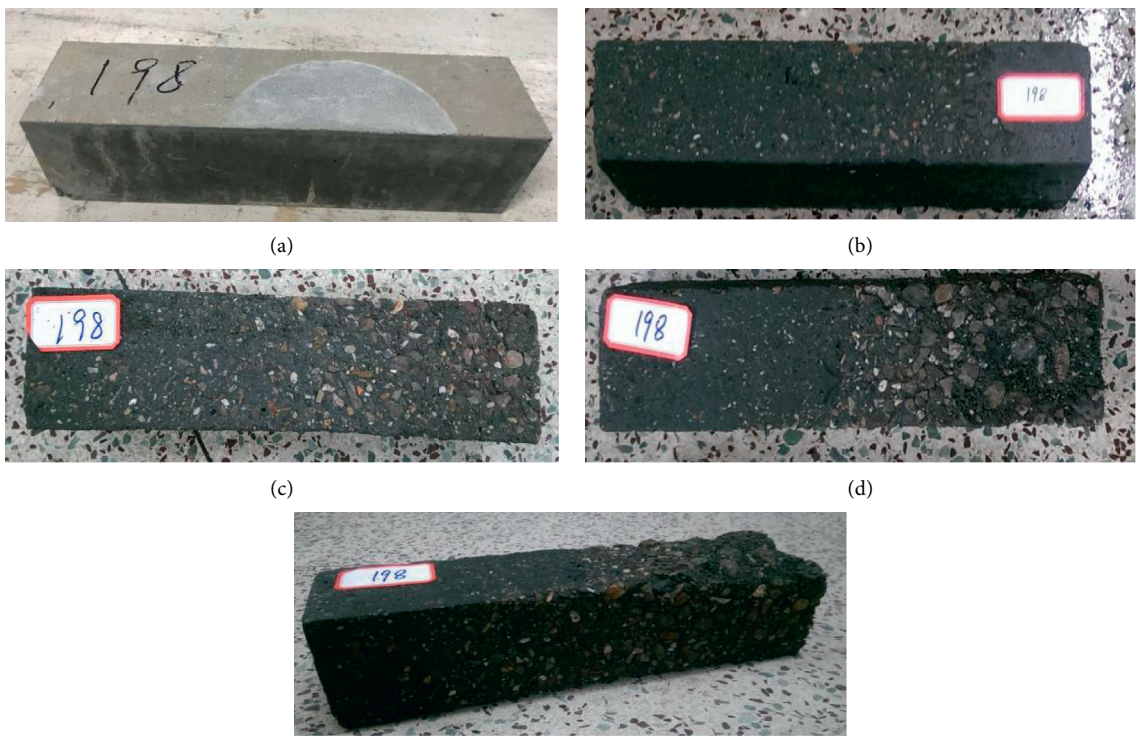

(a) (b) (c) (d) (e)

Figure 2: Typical failure modes of the concrete in the MFT environment. (a) 0 freeze-thaw cycles; (b) 25 freeze-thaw cycles; (c) 50 freeze-thaw cycles; (d) 75 freeze-thaw cycles; and (e) 100 freeze-thaw cycles.

Table 8: Visual assessment[a] of specimens' deterioration in concrete specimens.

Environment	Freeze–thaw cycles					
	0	25	50	75	100	125
IFT	0	1	2	3	b	4
MFT	0	1	3	4	5	—

[a]Deterioration scale; b: no test was carried out due to damaged experimental apparatus; 0: no visible deterioration; 1: some deterioration at corners; 2: deterioration at corners and cracking along the edges; 3: bulge of surfaces; 4: extensive spalling; and 5: complete damage.

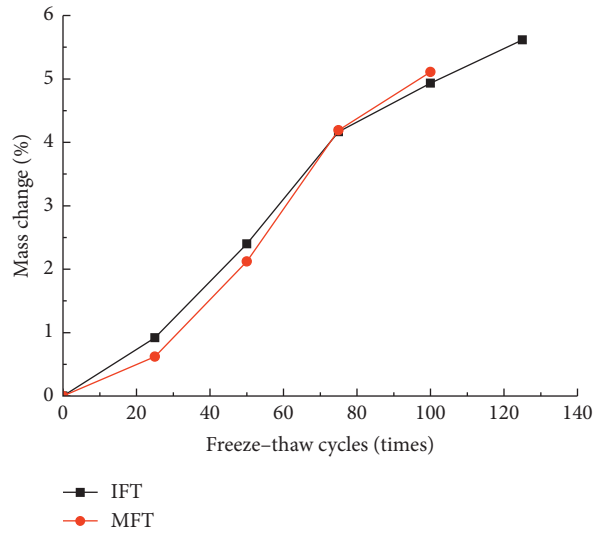

Figure 3: Variations of relative mass change of concrete specimens with freeze–thaw cycles in IFT and MFT environments.

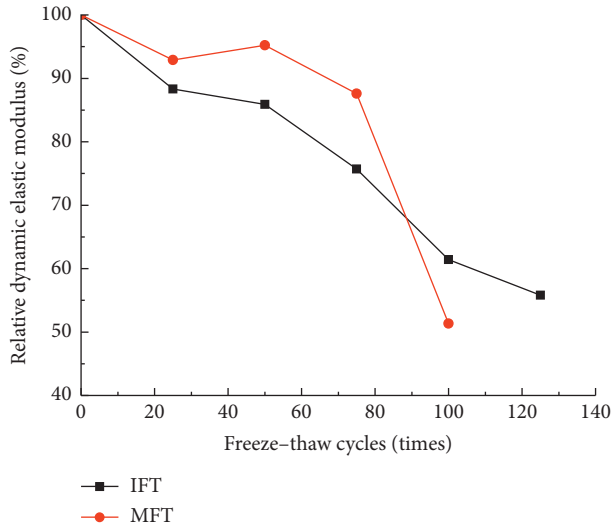

Figure 4: Variations of relative dynamic elastic modulus of concrete specimens with freeze–thaw cycles in IFT and MFT environments.

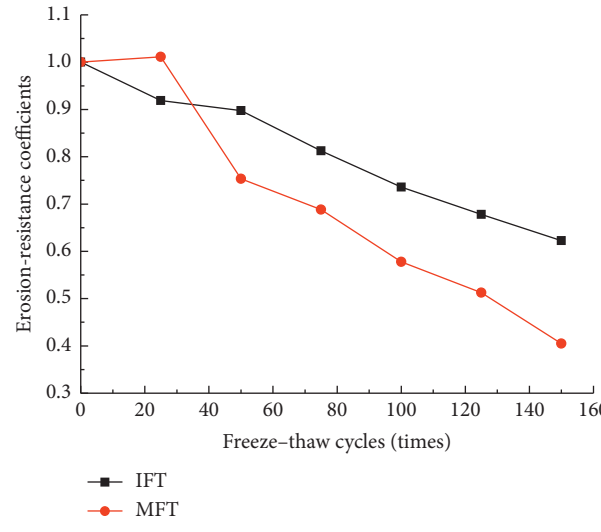

Figure 5: Variations of erosion-resistance coefficient of concrete specimens with freeze–thaw cycles in IFT and MFT environments.

3.5.2. Analysis of Microstructure Using MIP. Since pore structure directly affects the performance and durability of concrete, it is an important part of microstructure of concrete [33]. Figure 8 and Table 9 show that the internal pore size of the concrete specimen has changed significantly after two freeze-thaw environments, in both MFT and IFT. The average pore size, most probable pore size, median pore

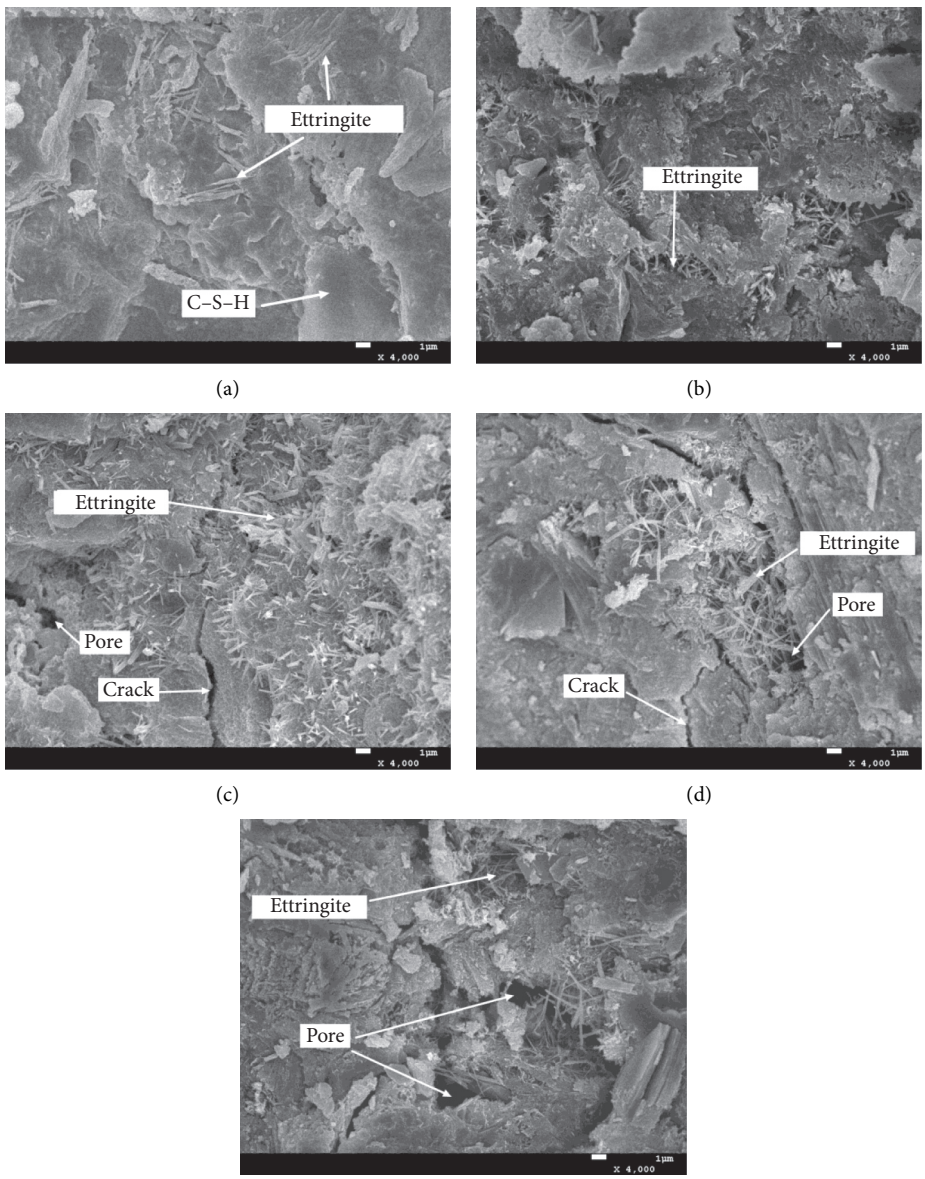

Figure 6: Microstructure of the concrete in the IFT environment. (a) 0 freeze-thaw cycles; (b) 25 freeze-thaw cycles; (c) 50 freeze-thaw cycles; (d) 75 freeze-thaw cycles; and (e) 125 freeze-thaw cycles.

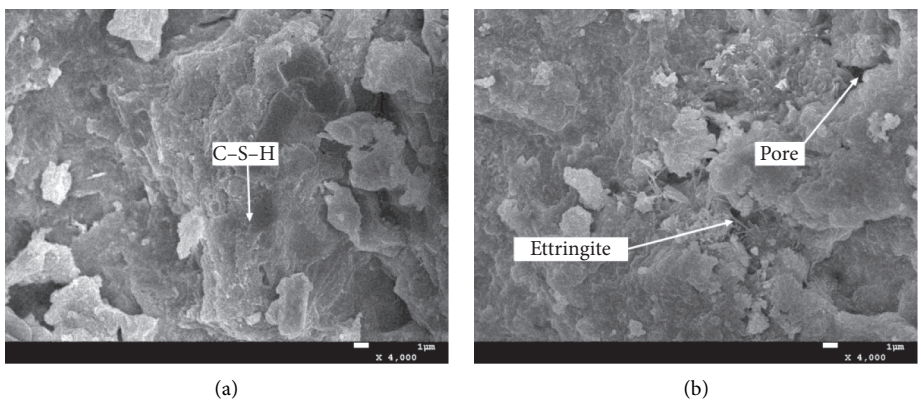

Figure 7: Continued.

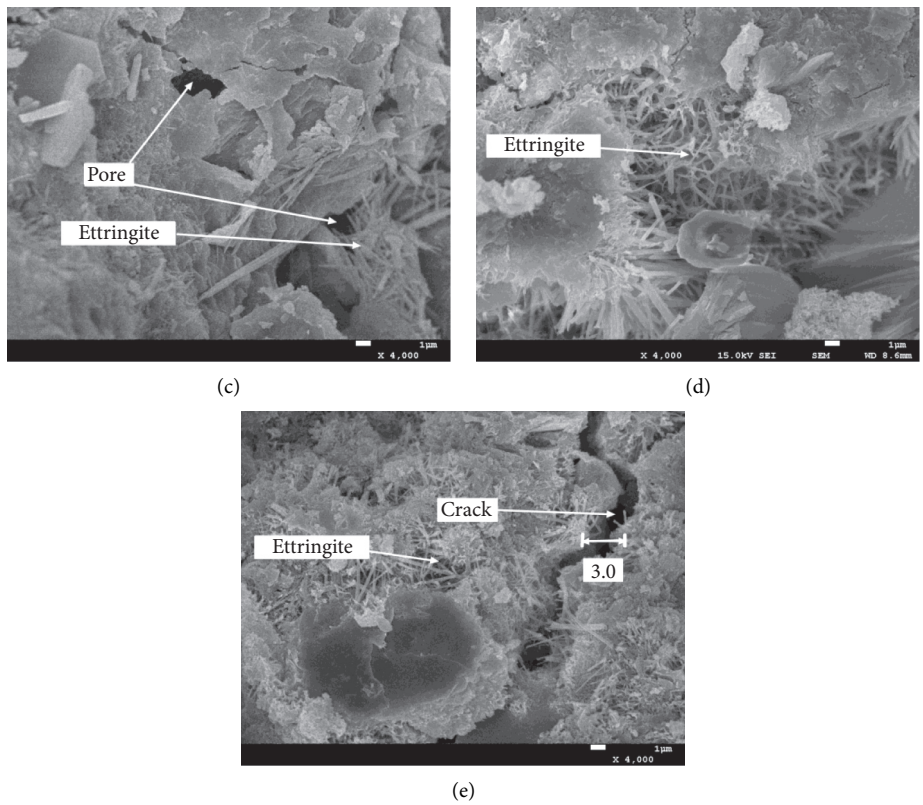

Figure 7: Microstructure of the concrete in the MFT environment. (a) 0 freeze-thaw cycles; (b) 25 freeze-thaw cycles; (c) 50 freeze-thaw cycles; (d) 75 freeze-thaw cycles; and (e) 100 freeze-thaw cycles.

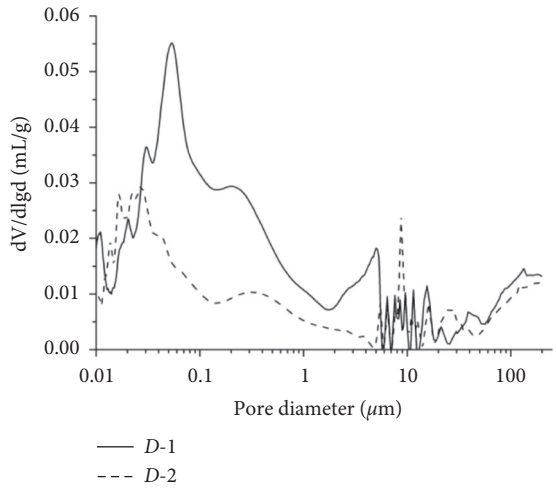

Figure 8: Pore size distributions of sample *D*-1 and *D*-2.

size, porosity, and total pore volume of the concrete specimen in the IFT environment subjected to 100 freeze-thaw cycles are all smaller than those of the concrete specimen in the MFT environment subjected to 125 freeze-thaw cycles. Wu et al. [34] found that, based on the classification of the pore size of concrete, smaller than 50 nm is harmless pore, equals 50–100 nm is harmful pore, and bigger than 100 nm is much harmful pore; the pore size distributions of the concrete specimens in the IFT and MFT environments are shown in Table 9.

From the overall pore size distribution, the proportions of the pore within the sizes of $d \leq 50$ nm, $50\text{ nm} \leq d \leq 100$ nm, and $d \geq 100$ nm for the concrete specimen in the MFT environment are 32.0%, 16.2%, and 51.8%, respectively, whereas for the concrete specimen in the IFT environment are 45.3%, 9.2%, and 45.5%, respectively. Although the

Table 9: Pore size distributions of concrete specimens in IFT and MFT environments.

Specimen	Mean pore D (nm)	Mode pore D (nm)	Median pore D (nm)	Total porosity (by volume) (%)	Total pore volume (10^{-2}·ml·g^{-1})	Pore volume (%)		
						$d \le 50$ nm	50 nm $\le d \le$ 100 nm	$d \ge 100$ nm
D-1	35.5	53.9	113.0	16.7	8.1	32.0	16.2	51.8
D-2	24.6	27.4	68.3	10.9	4.7	45.3	9.2	45.5

D-1 is the specimen of concrete in the MFT environment subjected to 100 freeze-thaw cycles, and D-2 is the specimen of concrete in the IFT environment subjected to 125 freeze-thaw cycles.

proportion of the pores within the size ($d \ge 100$ nm) for the concrete specimen in the MFT environment is similar to that for the concrete specimen in the IFT environment, the average pore size, median pore size, and porosity for the concrete specimen in the MFT environment are 1.44, 1.65, and 1.53 higher than that for the concrete specimen in the IFT environment, respectively. This is an indication that the damage to the concrete specimen in the MFT environment is more serious than that to the concrete specimen in the IFT environment. For the most probable aperture and total pore volume of the two concrete specimens, the difference is larger, where the value for the concrete specimen in the MFT environment is almost twice as large as for the concrete specimen in the IFT environment (Table 9). In summary, the deterioration process of concrete is the process of increasing the number of macropores, decreasing the number of micropores, and gradual expansion of microcracks.

4. Conclusions

This study investigates the damage to concrete subjected to the two freeze–thaw environments (i.e., maintenance freeze-thaw environment and immersion freeze-thaw environment) attack. The conclusions are as follows.

On the basis of the erosion-resistance coefficients, mass change, relative dynamic elastic modulus, and microstructure of the concrete, the damage to the concrete in the MFT environment is more serious than that in the IFT environment.

After 150 freeze-thaw cycles, the erosion-resistance coefficient of the concrete in the MFT environment decreases by 59%, whereas that of the concrete in the IFT environment decreases by 38%. The decrease in the erosion-resistance coefficient of the concrete in the MFT environment is therefore 21% more than that of the concrete in the IFT environment.

The analyses of the microstructure of concrete show that, under the action of various environmental factors, the corrosion damage to concrete is caused by the accumulated damage caused by pore development, microcrack development, and penetration.

Data Availability

The data used to support the findings of this study are included in the article.

Conflicts of Interest

The authors declare that they have no conflicts of interest regarding the publication of this paper.

Acknowledgments

The authors would like to express their gratitude to the National Natural Science Foundation of China (51779095 and 51679092) and the Science Technology Innovation Talents in Universities of Henan Province (20HASTIT013).

References

[1] P. Zhang, Q.-F. Li, J. Wang, Y. Shi, and Y.-F. Ling, "Effect of PVA fiber on durability of cementitious composite containing nano-SiO_2," *Nanotechnology Reviews*, vol. 8, no. 1, pp. 116–127, 2019.

[2] P. Zhang, Y. Zheng, K. Wang, and J. Zhang, "A review on properties of fresh and hardened geopolymer mortar," *Composites Part B: Engineering*, vol. 152, pp. 79–95, 2018.

[3] H. Ma, H. Yu, C. Li, Y. Tan, W. Cao, and B. Da, "Freeze-thaw damage to high-performance concrete with synthetic fibre and fly ash due to ethylene glycol deicer," *Construction and Building Materials*, vol. 187, no. 187, pp. 197–204, 2018.

[4] Z. Zhou and P. Qiao, "Durability of ultra-high performance concrete in tension under cold weather conditions," *Cement and Concrete Composites*, vol. 94, no. 94, pp. 94–106, 2018.

[5] K. W. Liu, D. S. Sun, A. G. Wang, G. Zhang, and J. Tang, "Long-term performance of blended cement paste containing fly ash against sodium sulfate attack," *Journal of Materials in Civil Engineering*, vol. 30, no. 12, pp. 1–10, Article ID 04018309, 2018.

[6] P. Zhang, Q. F. Li, Y. Z. Chen, Y. Shi, and Y.-F. Ling, "Durability of steel fiber-reinforced concrete containing SiO_2 nano-particles," *Materials*, vol. 12, no. 13, pp. 1–18, Article ID 2184, 2019.

[7] D. P. Forgeron and J. F. Trottier, "Evaluating the effects of simultaneous freezing and thawing and flexural fatigue loading cycles on the fracture properties of FRC," in *High Performance Structures and Materials Proceedings No. 2*, W. P. De Wilde and C. A. Brebbia, Eds., WIT Press, Chilworth, SO, USA, 2004.

[8] J. F. Trottier and D. P. Forgeron, "Cumulative effects of flexural fatigue loading and freezing and thawing cycles on the flexural toughness of fiber reinforced concrete," in *Concrete under Severe Conditons Proceedings No. 3*, N. Banthia, K. Sakai, and O. E. Gjφrv, Eds., Routledge Press, Abingdon, UK, 2011.

[9] B. Diao, J. Zhang, Y. H. Ye, and S. Cheng, "Effects of freeze-thaw cycles and seawater corrosion on the behavior of reinforced air-entrained concrete beams with persistent loads," *Journal of Cold Regions Engineering*, vol. 27, no. 1, pp. 44–53, 2013.

[10] F. Y. Gong, E. Sicat, D. W. Zhang, and T. Ueda, "Stress analysis for concrete materials under multiple freeze-thaw cycles," *Journal of Advanced Concrete Technology*, vol. 13, no. 3, pp. 124–134, 2015.

[11] B. Diao, Y. Sun, S. H. Cheng, and Y. Ye, "Effects of mixed corrosion, freeze-thaw cycles, and persistent loads on

behavior of reinforced concrete beams," *Journal of Cold Regions Engineering*, vol. 25, no. 1, pp. 37–52, 2011.

[12] B. Amini and S. S. Tehrani, "Combined effects of saltwater and water flow on deterioration of concrete under freeze-thaw cycles," *Journal of Cold Regions Engineering*, vol. 25, no. 4, pp. 145–161, 2011.

[13] A. E. Richardson, K. A. Coventry, and G. Ward, "Freeze/thaw protection of concrete with optimum rubber crumb content," *Journal of Cleaner Production*, vol. 23, no. 1, pp. 96–103, 2012.

[14] J. Yuan, Y. Liu, H. Li, and B. Zhang, "Experimental investigation of the variation of concrete pores under the action of freeze-thaw cycles by using X-Ray CT," *Advances in Materials Science and Engineering*, vol. 2014, Article ID 571357, 11 pages, 2014.

[15] Z. Wang, Q. Zeng, Y. Wu, L. Wang, Y. Yao, and K. Li, "Relative humidity and deterioration of concrete under freeze-thaw load," *Construction and Building Materials*, vol. 62, pp. 18–27, 2014.

[16] H. S. Shang, T. H. Yi, and Y. P. Song, "Behavior of plain concrete of a high water-cement ratio after freeze-thaw cycles," *Materials*, vol. 5, no. 9, pp. 1698–1707, 2012.

[17] J. Ranz, S. Aparicio, H. Romero, M. Casati, M. Molero, and M. González, "Monitoring of freeze-thaw cycles in concrete using embedded sensors and ultrasonic imaging," *Sensors*, vol. 14, no. 2, pp. 2280–2304, 2014.

[18] W. T. Li, M. Pour-Ghaz, J. Castro, and J. Weiss, "Water absorption and critical degree of saturation relating to freeze-thaw damage in concrete pavement joints," *Journal of Materials in Civil Engineering*, vol. 24, no. 3, pp. 299–307, 2012.

[19] A. E. Richardson, K. A. Coventry, and S. Wilkinson, "Freeze/thaw durability of concrete with synthetic fibre additions," *Cold Regions Science and Technology*, vol. 83-84, no. 83, pp. 49–56, 2012.

[20] P. Zhang, Y. Zheng, K. Wang, and K. Zhang, "Combined influence of nano-$CaCO_3$ and polyvinyl alcohol fibers on fresh and mechanical performance of concrete incorporating fly ash," *Structural Concrete*, vol. 21, no. 2, pp. 724–734, 2019.

[21] P. Zhang, Z. Gao, J. Wang, J. Guo, S. Hu, and Y. Ling, "Properties of fresh and hardened fly ash/slag based geopolymer concrete: a review," *Journal of Cleaner Production*, vol. 270, Article ID 122389, 2020.

[22] P. Zhang, K. Wang, J. Wang, J. Guo, S. Hu, and Y. Ling, "Mechanical properties and prediction of fracture parameters of geopolymer/alkali-activated mortar modified with PVA fiber and nano-SiO_2," *Ceramics International*, vol. 46, no. 12, pp. 20027–20037, 2020.

[23] G. F. Li and X. D. Shen, "A study of the durability of aeolian sand powder concrete under the coupling effects of freeze-–thaw and dry–wet conditions," *JOM*, vol. 71, no. 6, pp. 1962–1974, 2019.

[24] X. P. Su and Q. Wang, "Corrosion damage of concrete under multi-salt soaking, freezing-thawing and dry-wet cycles," *Journal of Jilin University (Engineering and Technology Edition)*, vol. 1, no. 1, pp. 112–120, 2015, (in Chinese).

[25] X. H. Yao, Z. J. Feng, F. C. Wang et al., "Property of multiple admixture concrete in multi-salt soaking under wetting-drying and freezing-thawing cycles," *Acta Compositae Sinica*, vol. 35, no. 3, pp. 690–698, 2018, (in Chinese).

[26] X. H. Yao, Z. J. Feng, F. C. Wang et al., "Experiment on erosion-resistance of highway bridge pile foundation material under salt marshes environment," *Journal of Chang'an University (Natural Science Edition)*, vol. 38, no. 1, pp. 49–58, 2018, (in Chinese).

[27] X. D. Shi, Y. Q. Li, L. Qian et al., "Experimental Study on elastic modulus of concrete undergoing freeze-thaw cycle action with different ultralow temperature ranges," *Engineering Mechanics*, vol. 36, no. 8, pp. 106–113, 2019, (in Chinese).

[28] Z. G. Yin, K. Zhang, W. Fan et al., "Experimental study on the durability of recycled aggregate pervious concrete under different freeze-thaw media conditions," *Bulletin of the Chinese Ceramic Society*, vol. 38, no. 7, pp. 2137–2143, 2019, (in Chinese).

[29] G. Xu, C. Gong, J. Liu et al., "Correlation between water freeze-thaw resistance and salt freeze-thaw cycle of concrete," *Journal of Building Materials*, vol. 1–10, 2020 (in Chinese).

[30] Y. R. Zhao, X. Q. Fan, L. Q. Wang et al., "Attenuation model of mechanical properties of concrete under different freezing and thawing," *Acta Materiae Compositae Sinica*, vol. 34, no. 2, pp. 463–470, 2017, (in Chinese).

[31] S. W. Hu and Y. Wang, "Experimental study on double-K fracture toughness of concrete in different freezing and thawing modes," *Hydro-Science and Engineering*, vol. 2, pp. 90–96, 2018, (in Chinese).

[32] X. H. Yao, *Mechanics Properties and Safety Evaluation of Highway Bridge Pile in Alpine Salt marshes*, Chang'an University, Xi'an, China, 2018, (in Chinese).

[33] Y. Xiong, D. Wu, and F. A. Liu, "Experimental study on realkalization repair of concrete compressive strength after high-temperature based on microstructure analysis," *Engineering Mechanics*, vol. 6, no. 6, pp. 205–211, 2013, (in Chinese).

[34] Z. W. Wu and H. Z Lian, *High Performance Concrete*, China Railway Publishing House, Beijing, China, 1999, (in Chinese).

Hindawi
Advances in Civil Engineering
Volume 2020, Article ID 8856327, 16 pages
https://doi.org/10.1155/2020/8856327

Research Article

Parametric Analysis on Seismic Performance of Hybrid Precast Concrete Beam-Column Joint

H.-K. Choi

Department Fire and Disaster Prevention Engineering, Kyungnam University, Changwon, Gyeongsangnam-Do, Republic of Korea

Correspondence should be addressed to H.-K. Choi; chk7796@kyungnam.ac.kr

Received 3 March 2020; Revised 29 July 2020; Accepted 25 August 2020; Published 29 September 2020

Academic Editor: Grzegorz Golewski

In this paper, a nonlinear finite element (FE) analysis of high-performance hybrid system (HPHS) beam-column connections is presented. The detailed experimental results of the ten half-scale hybrid connections with limited seismic detailing have been discussed in a different paper. However, due to the inherent complexity of HPHS beam-column joints and the unique features of the tested specimens, the experimental study was not comprehensive enough. The new connection (HPHS) detail suggested in this study is characterized by ductile connection, steel connectors, and engineered cementitious composite (ECC) which is a kind of high-performance fiber reinforced cement composite with multiple fine cracks (HPFRCCs). Therefore, in this paper, FE analysis results are compared with experimental results from the cycle tests of the two specimens (RC and PC) to assess model accuracy, and detailed model descriptions are presented, including the determination of stiffness and strength. The critical parameters influencing the joint's behavior are the axial load on column, beam connection steel plate length, inner bolt stress contribution, and plastic hinge area.

1. Introduction

Precast concrete has not been used widely as a framing system for buildings located in several seismic regions. Precast concrete joints between the prefabricated members have some issues. Connections, in particular beam-to-column connections, are the vital part of precast concrete construction. To satisfy the structural requirements of the overall frame, each connection must have the ability to transfer vertical shear, transverse horizontal shear, axial tension and compression, and occasionally bending moment and torsion between one precast component and another, safely. The transfer of forces between the components and eventually the behavior of frames are governed by the characteristics of the connections. However, in practice, the behavior of precast connections is not well established and not fully understood to fulfill the requirements needed in the design and construction development of precast technology [1–3].

Current technology is widely available to satisfy the growing demand required of engineers to provide communities with superior levels of structural performance during an earthquake. As more advances are made in seismic engineering, the available technology becomes more cost-competitive when compared to traditional construction practice: further financial benefits can be associated with the improved response of the system considering the seismic risk applied over the working life of the structure. High performing systems will be designed to operate more efficiently as they are tuned to their direct application. As a result, the seismic demand imposed onto a structure (maximum displacements and accelerations) can be significantly reduced, thereby reducing material costs and construction time. However, in developing this new technology, design recommendations are required to ensure the technology is appropriately utilized.

This paper focuses on understanding the behavior of the HPHS (high-performance hybrid system) under seismic action. The validity of the HPHC system was demonstrated by a series of experimental tests, which proved the system has good performance under lateral loading. For application of the HPHS to the real structure, the seismic performance of single connections for several primary variables has to be

assessed. In this study, parametric study for the HPHS connection was carried out based on test and FEM analysis. Investigated parameters include (1) axial load on column, (2) beam connection steel plate length, (3) inner bolt stress contribution, and (4) plastic hinge area. Therefore, this paper is aimed at developing and calibrating a nonlinear FE model and further uses it to investigate the behavior of HPHS by varying the main control parameters [4].

2. Previous Development Connection and Test Results

The new connection detail suggested in this study is characterized by ductile connection, steel connectors, and engineered cementitious composite (ECC) which is a kind of high-performance fiber reinforced cement composite with multiple fine cracks (HPFRCCs) and used in order to improve the constructability of joint and efficiently transfer stress between discontinued precast members. Making steel connector consists of bolting steel tubes and steel plates which are usually placed inside the precast column and beam and casting the ECC to some parts of the beam and joint in the field (refer to Figures 1, and 2) [1–3].

The dimensions and details of reinforcements of the specimens are shown in Figure 3, and the other experimental parameters are listed in Tables 1 and 2. Stress discontinuity between the members associated with the steel connectors and the ECC was not observed, and the load was effectively transferred to the beam and joint. The connection detail developed and suggested in this study which has elastic joint and steel plate connector satisfied the requirement prescribed in the ACI structural guideline and thus was verified to provide excellent seismic performance (refer to Figure 4) [1–3].

3. Analytical Model

The proposed connection system (HPHS) has various types of structural elements such as concrete, steel plate, and ECC. It is very difficult to investigate design variable experiment, so nonlinear finite element analysis was conducted based on the experimental results. To improve understanding of the proposed connection system of local stress-strain behavior and joint strength in the vicinity of beam-to-column connection, a total of three concrete models were adopted and analyzed. These innovative high-performance hybrid systems (HPHSs) make use of steel, bolt sections, and ECC into the beam-column joint region to facilitate the connection of precast elements. In the experimental study, two cast-in-place and ten PC specimens, whose connection configurations slightly differed from each other, were tested. However, due to unique features of the tested specimens and material heterogeneity, it was difficult to understand the complex seismic behavior of beam-column connections. Furthermore, the effect of several influencing parameters such as flexural strength ratio and axial load cannot be varied in a limited number of experiments. The ABAQUS (ABAQUS version 6.6-1, 2006) finite element code was used to analyze the proposed precast beam-column connections. These

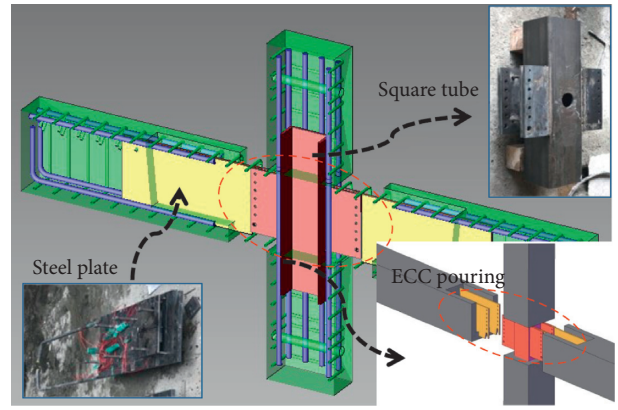

Figure 1: Description of development of precast concrete beam-to-column connection.

numerical models consisted of a combination of elements, springs, and constraint conditions. Amongst these were refined 2D plane stress elements incorporating the full nonlinear material/geometric properties, contact elements, surface interaction with friction, constraint conditions using equation points, concrete crack conditions, and elastic foundation springs. These advanced modeling methods were intended to provide a detailed and accurate understanding of the overall behavior of the connections, including the stress distributions on the contact surfaces in spite of the high computational cost typically associated with this type of data [4, 5].

3.1. Material Properties. The longitudinal reinforcement of the beam and column was deformed bars of yield strength 437 MPa and 508 MPa, while the beam stirrups and column transverse ties were applied with yield strength 475 MPa and 400 MPa. The slump value of the concrete mix was 75 ± 25 mm. The average compressive strength of concrete calculated using the cylinder tests was found to be 27.5 MPa (joint area ECC = 40.5 MPa). Steel connector, used in the construction of the specimens, was confirmed to be SS400. Average values of steel section properties were obtained from the samples of tensile coupon tests. However, for the wide range of parametric study, proposed equations were used and compared with test results. Used stress-strain models of concrete were the modified Kent–Park model and Collins model accounting for the confinement effect of steel tube embedded in the column. Additionally, the concrete damaged plasticity model was provided by ABAQUS; it needs the true stress-logarithmic stress-strain relation for tension and compression. Therefore, in this research, an equivalent uniaxial constitutive model for concrete in tension suggested by Torres [6] was used. It is also shown in Figure 5. The steel material properties for the steel plate and column tube were modeled after SS400 with fully nonlinear isotropic characteristics. For the same reason of concrete, steel was modeled to simplified hardening material as shown in Figures 6 and 7. The stress-strain curve of reinforcements was also determined by the test. However, the flexural moment ratio is an important variable for the design of

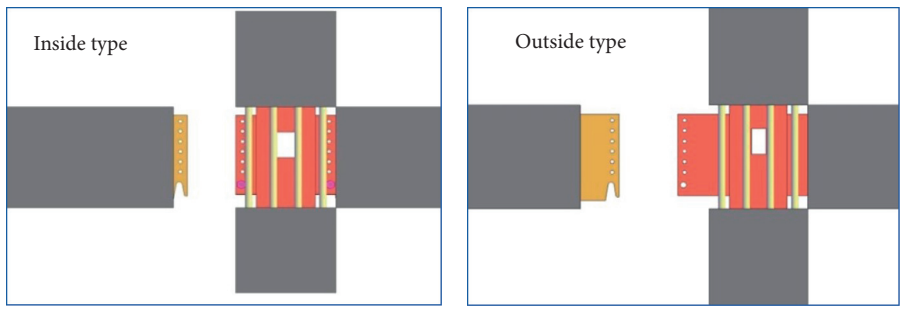

Figure 2: Proposed connection type. (a) Inside connection. (b) Outside connection.

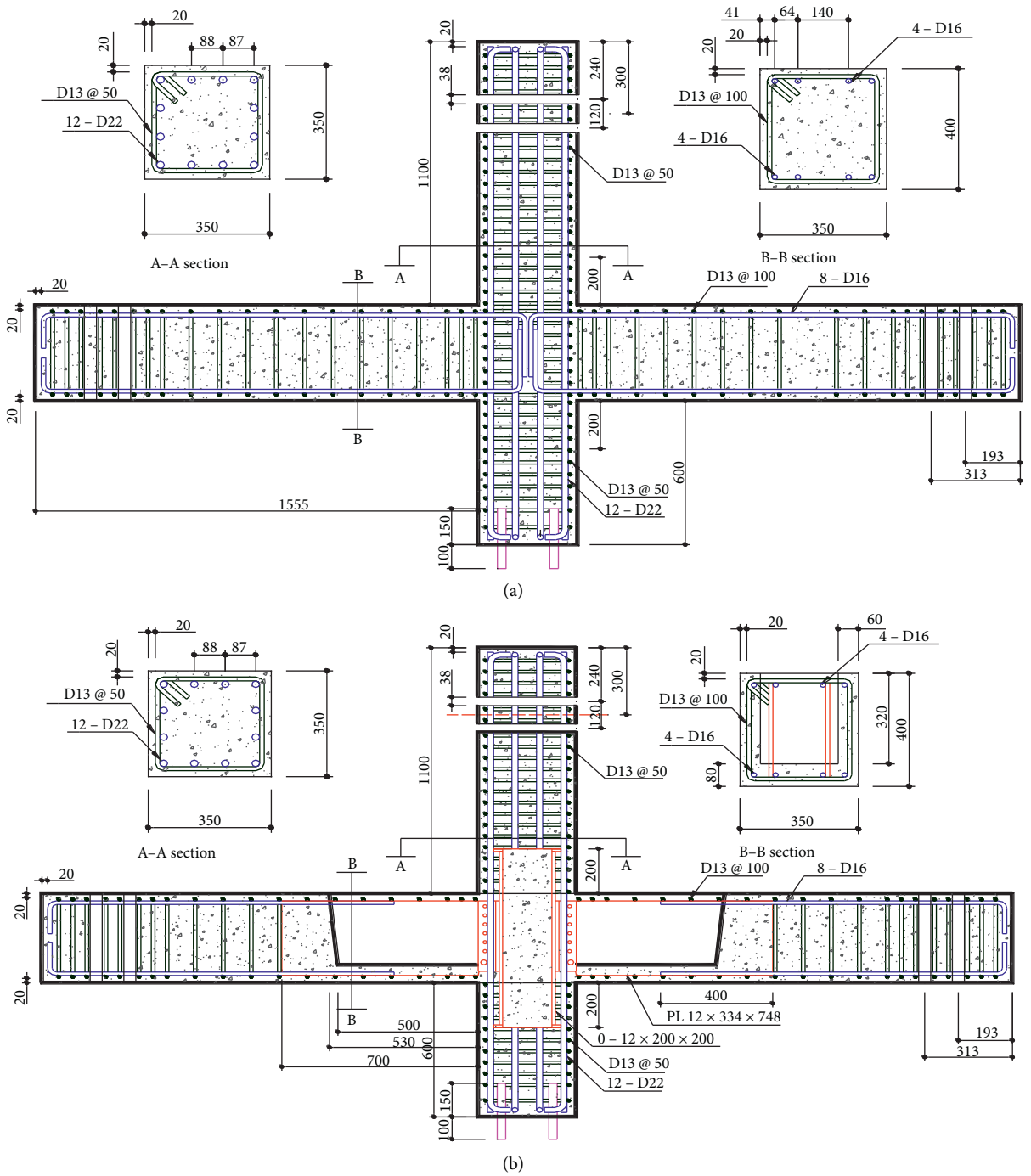

Figure 3: Details of specimens. (a) RC-control. (b) PC-I50-0.2.

Table 1: Details of test specimen and material properties.

Specimens	Connection method (axial force)	Hoop bar of joint area	ECC area (mm)	Column size (mm)	Beam size (mm)	Column						
						Reinforcing bar (upper and lower)			Hoop			
						f_{cy} (MPa)	ρ_c	n_c	f_{hy} (MPa)	ρ_h	s_h (mm)	n_b
RC-control	Cast-in-place (0.1)	O	—	350×350	350×400	508	0.038	12-D22	475	0.011	50	D13
PC-I50-0.2	Inside connection (0.2)	*X*	500 (1.4 d)									

Specimens	Beam							f'_c (MPa)							
	Reinforcing bar (upper and lower)			Stirrup											
	f_{by} (MPa)	ρ_{bu}, ρ_{bl}	n_b	f_{sy} (MPa)	ρ_s	s_b (mm)	n_s	PC member	ECC member	$(\sum M_c / \sum M_b)$	v_{j1} (kN)	v_{j2} (kN)	v_{jby} (kN)	(v_{j1}/v_{jby})	(v_{j2}/v_{jby})
RC-control	437	0.012	8-D16	475	0.014	100	D13	27.5	—	1.6	1,056	792	629	1.68	1.53
PC-I50-0.2	461	0.016	8-D19					27.5	40.5	1.6	1,286	965	628	2.04	1.53

f_{cy}, f_{hy}, f_{by}, and f_{sy}: yield strength of column bar, hoop, beam bar, and beam stirrup, respectively; ρ_c, ρ_h, ρ_{bu}, ρ_{bl}, and ρ_s: ratio of column bar, hoop, upper beam bar and lower beam bar, and stirrup, respectively; n_c, n_h, n_b, and n_s: size of column bar, hoop, beam bar, and stirrup, respectively; f'_c: compressive strength of concrete and ECC; v_{j1} and v_{j2}: type 1 and type 2 shear strength of joint predicted by ACI 318-05; v_{jby}: joint shear strength when beam bar yields.

Table 2: Test results.

Specimen		P_y (kN)	P_{max} (kN)	P_f (kN)	δ_y (%)	δ_{max} (%)	δ_f (%)	u [−]	M_n (kN. m)	M_{uj} (kN. m)	M_{peak} (kN. m)	v_n (kN)	v_u (kN)	v_{peak} (kN. m)	(v_{peak}/v_u)
RC-control	Pos	89	119	114	1.5	3.5	4.25	2.3	125	285	206	792	540	572	1.06
	Neg	95	127	120	1.9	3.5	4.25	1.8			219			611	1.13
PC-I50-0.2	Pos	111	148	114	1.3	3.5	4.25	2.7	125	346	255	964	583	711	1.22
	Neg	124	166	110	1.3	3.5	4.25	2.7			286			798	1.36

All estimates associated with moment and shear are computed based on actual material properties. P_y: moment at first yield of top bar (measured); P_{max}: peak load (measured); P_f: failure load (measured); δ_y: yield displacement (measured); δ_{max}: peak displacement (measured); δ_f: failure displacement (measured); u: ductility (δ_{max}/δ_y); M_n: nominal moment; M_{uj}: moment corresponding to v_n (computed); M_{peak}: peak moment (measured); v_n: nominal joint shear capacity (computed); v_u: joint shear demand (computed); v_{peak}: joint shear at M_{peak}.

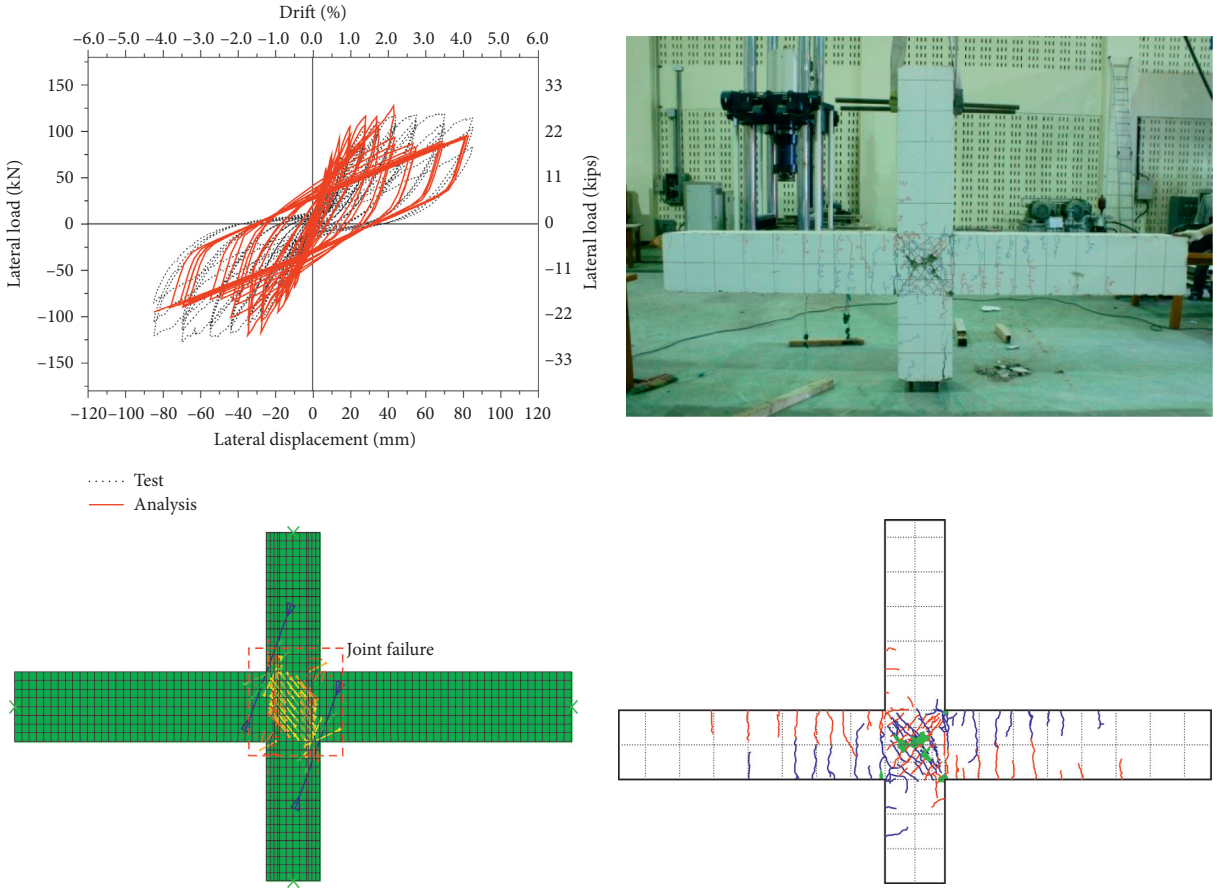

(a)

Figure 4: Continued.

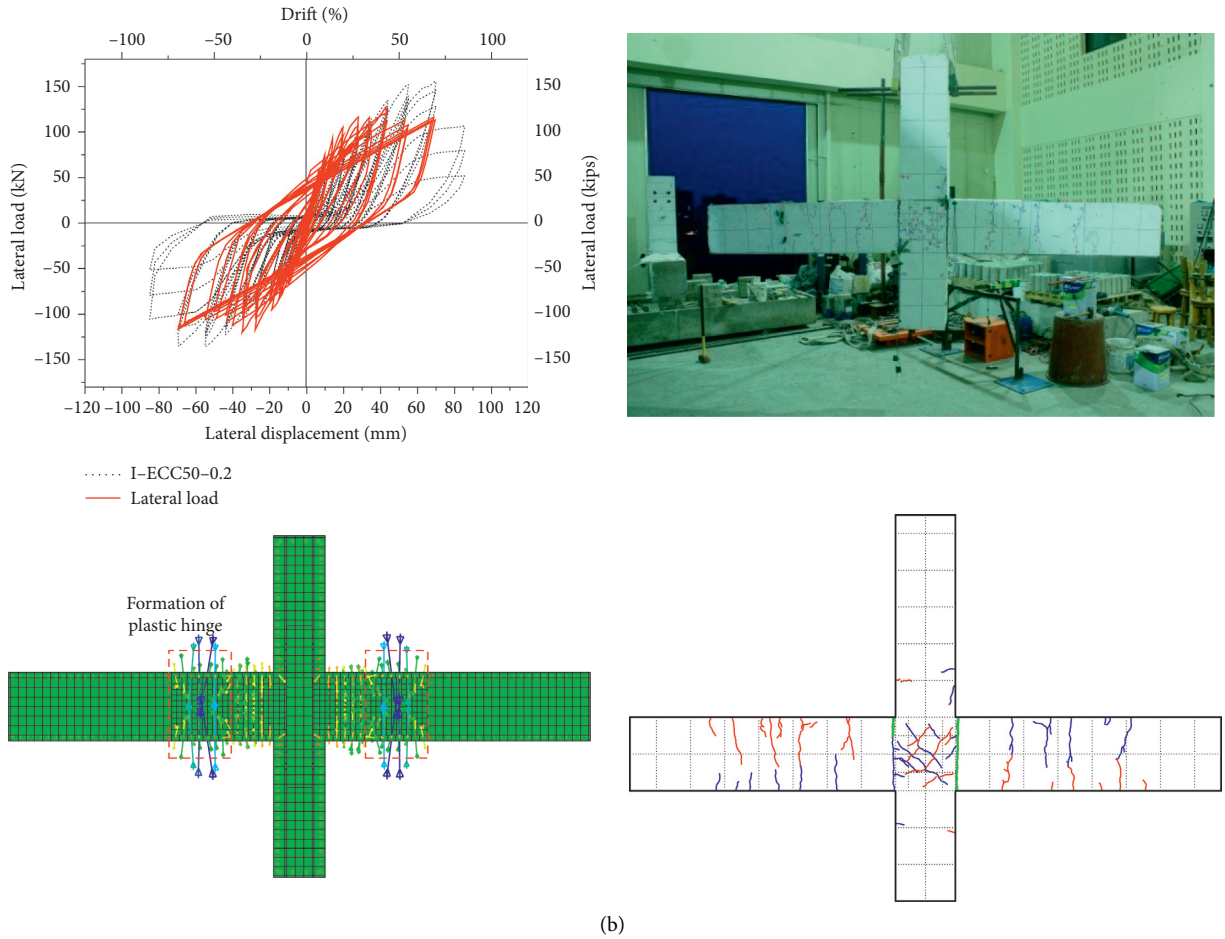

Figure 4: Test and analysis results. (a) RC-control. (b) PC-I50-0.2.

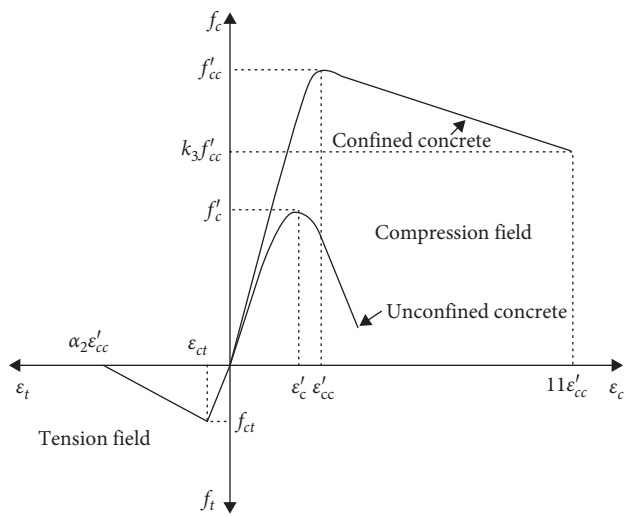

Figure 5: Stress-strain curve of concrete in uniaxial stress state.

moment frame, and stress-strain relation for other reinforcements would be needed. Therefore, we also use the stress-strain relation for various diameter of reinforcements (refer to Figure 6). Table 3 indicates the material input codes of the concrete damage plasticity for ABAQUS.

The last set of material properties is ECC in compression and tension. As previously discussed, ECC has very large capacity in tension. Using stress-strain data from the test, equivalent perfectly plastic material behavior was used for material modeling in tension (refer to Figure 8). And available test data were used for compression.

3.2. Finite Element Modeling. In the present study, the specimens were analyzed using the ABAQUS software. Two-dimensional (2D) plane stress elements were applied to simulate the concrete and steel plates, while reinforcing bars were modeled as truss elements. In material modeling, the concrete models were based on nonlinear fracture mechanisms to account for cracking, and plasticity models were used for the concrete in compression and steel reinforcement. The ABAQUS (ABAQUS version 6.10-1, 2010) finite element code was used to analyze the effect of variables of the proposed connection system (refer to Figure 9).

Generally, in the composite structure, there are many problems with contact area of concrete and steel. Therefore, all interfaces between two contact surfaces were constrained with each other. The general contact formulation used in ABAQUS involves a master-slave algorithm. This formulation considers the hard contact for normal direction of

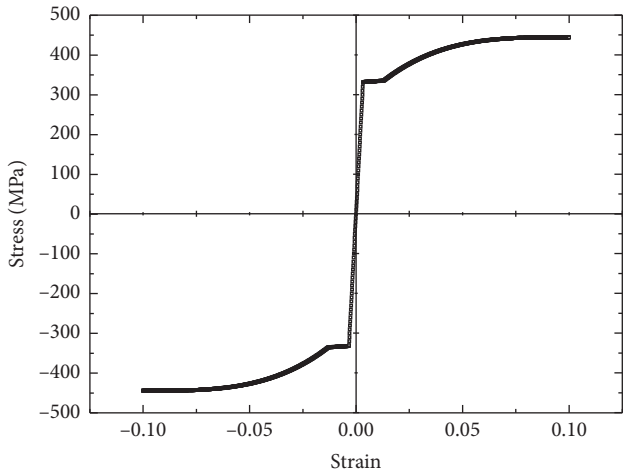

Figure 6: Stress-strain curve of steel in uniaxial stress state.

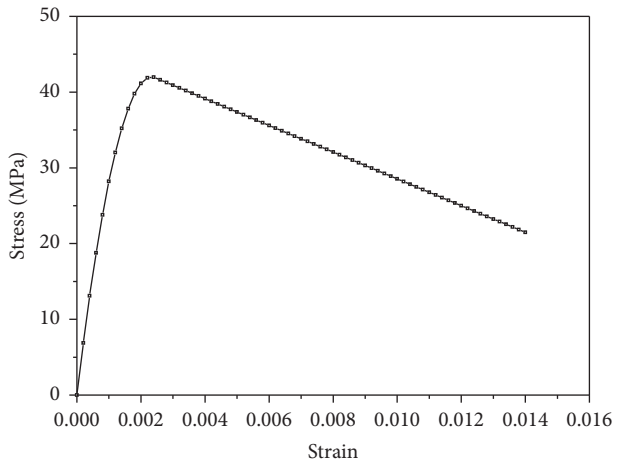

Figure 7: Stress-strain curve for confined concrete.

Table 3: ABAQUS input values for confined concrete.

Plastic stress (MPa)	Plastic strain	Compression damage
28.21	0	0
32.03	0.000110	0.01
35.23	0.000221	0.02
39.80	0.000493	0.05
41.92	0.000834	0.1
41.99	0.001032	0.15
41.29	0.001450	0.2
39.89	0.002287	0.5
21.22	0.01331	0.9

each surface and frictional contact behavior for tangential direction. Surface interactions and constrained area are shown in Figure 10. Boundary conditions for generated model are shown in Figure 11. Bottom of the column was supported by pin, and the end of the beam was supported through roller condition. These boundary conditions were determined from the test assumptions. The beam end was restrained only in roller, and the bottom of the column was restrained with a hinge. The FE models were loaded in two steps. Axial load was applied in first step at the column, and

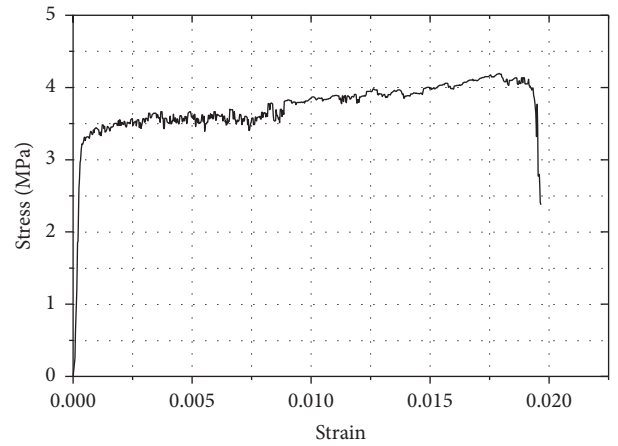

Figure 8: Stress-strain curve for ECC in uniaxial stress state in tension.

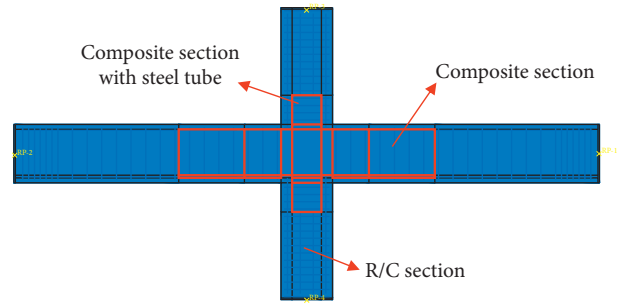

Figure 9: Partitioned 2D models for proposed connection system (hybrid connection).

lateral load was applied to the same location in second step, cyclically. Cyclic load was applied by displacement control, and this is shown in Figure 12.

3.3. FE Analysis Results. To verify the finite element model, the analytical results were compared with the experimental results. The specimens were modeled with a truss elements and the remaining plane stress 2D elements. Concrete was modeled using 2D plane stress elements which were isoparametric elements. On the other hand, the reinforcing steel bars were modeled as two-node truss elements. At the joint core region, the area of truss elements close to the boundary was increased appropriately to simulate their corresponding steel area contributions. The beam bottom bars were discontinued at the face of the column. Steel plates, which were used for the connection at the joint, extended inside the beam at one side and abutted with the column face on the other side. These plates were simulated as 2D plane stress elements. These elements were assigned with steel plate thickness and its material properties. The concrete on the front and rear side of these elements was neglected in the analysis as it was filled up after the connections were fastened. Four rows of 2D elements at the bottom of the joint were treated as being connected by the steel plates, and their equivalent area was transferred to the column main bars and transverse links.

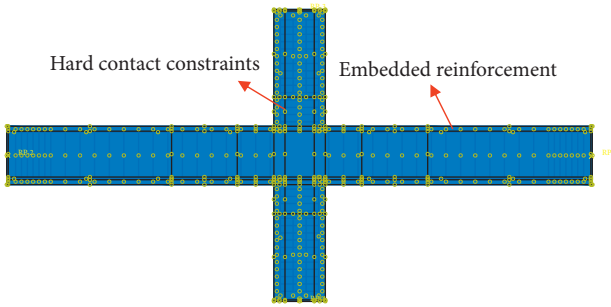

Figure 10: Constrained model.

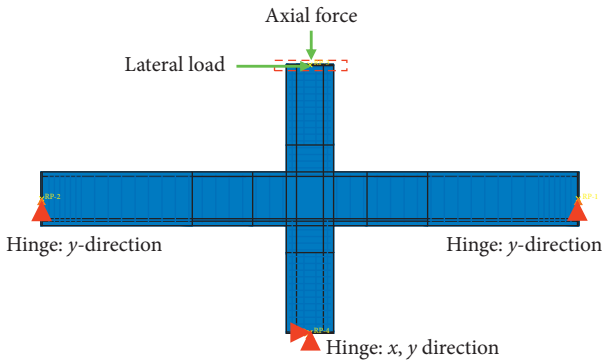

Figure 11: Boundary condition.

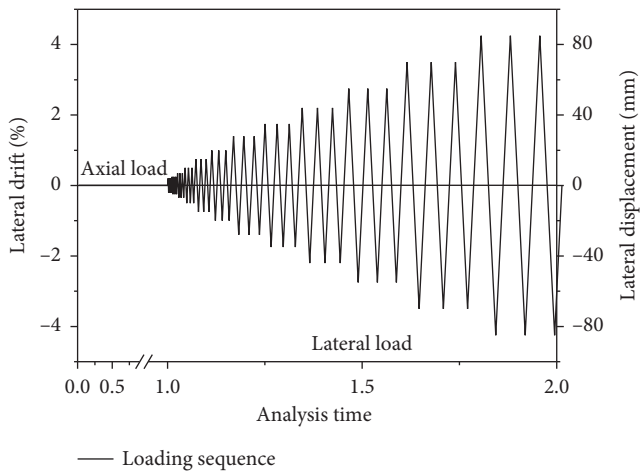

Figure 12: Loading sequence.

The predicted and observed responses of the specimens are presented in Figure 13. From Figure 13(a) of specimen RC-control, it can be seen that the analytical model seemed to have predicted a good response with respect to the experimental observations. Although the displacements of the analytical model for a few initial cycles were slightly higher, the later cycles' predicted results were in good agreement with the experimental counterparts. Specimen RC-control achieved a displacement ductility factor (μ) of about 2.8, and pinching was observed in the loops. The loops were thin and quite similar to the experimental results. A large deformation of the joint core was observed at this stage. Figure 13(b) shows the analytical and experimental results comparison for specimen PC-I50-0.2. From the experimental results, it was seen that the specimen exhibited a large initial displacement for many cycles. The specimen achieved good energy dissipation till μ of approximately of 2.8. The global deformed shape of the specimen corresponding to μ of 1.5 is given in Figure 13(b). A moderate deformation of the joint core and upper and lower parts of the column was seen from the figure. Specimen I-ECC25 reached μ of approximately 2.9, slightly lesser when compared to its experimental values. Although the experimental loops showed large initial displacements, their analytical counterparts always depicted steady displacements throughout. This may be due to the fact that the connections might have had some initial gaps in the steel connector, where the nuts and bolts were fastened, which might have slipped after the application of load leading to large initial displacements.

Comparison of the analytical and experimental results of all the specimens showed that the lateral load-displacement hysteresis loops obtained from the FE analyses were quite similar to the experimental observations. Besides, the failure modes and the ultimate ductility capacities correlated well with the experimental results. The FE analyses also showed that results of the deformations and cracking patterns matched well with the experimental observations. From the aforementioned observations and predictions of both the global and local behaviors using the FE analysis, the use of FE modeling techniques can, therefore, be further extended to study the joint performance by varying different parameters.

4. Parametric Studies

4.1. Influence of Axial Loads on Behavior of Beam-Column Joints. Axial loading is a critical parameter in the studies of beam-column joints, but its effect on seismic behavior of beam-column joints has not been fully understood. Previous investigations have shown that axial force is beneficial to the joint shear resistance [3]. Since the neutral axis depth in the column increases with axial compression load, a larger portion of the bond forces from the beam bars can be assumed to be transferred to the diagonal strut. Therefore, the concrete contribution to the joint shear resistance will be increased. In [7], the authors experimentally investigated two nonductile interior beam-column joints with different axial loading levels. However, both of these specimens failed due to the pullout of the embedded beam bottom bars instead of joint shear failure.

Lin and Restreop's investigations [8] showed that axial compression in excess of $0.3f'_cA$ became detrimental to the joints. In a study conducted by Fu et al. [9], it was pointed out that if the shear was small, the increase of axial loads was favorable to the joints, whereas for high shears, the increase of axial loads was unfavorable. Li et al. [10] found that for a rectangle joint, an axial load less than $0.4f'_cA_g$ was beneficial to the joint, while the axial compression load ranging between zero to $0.2f'_cA_g$ enhanced the joint's performance for deep wall-like column joints.

In this study, the influence of axial loading on the seismic behavior of hybrid-steel concrete joints is investigated. Axial load was applied in first step at the column, and lateral load

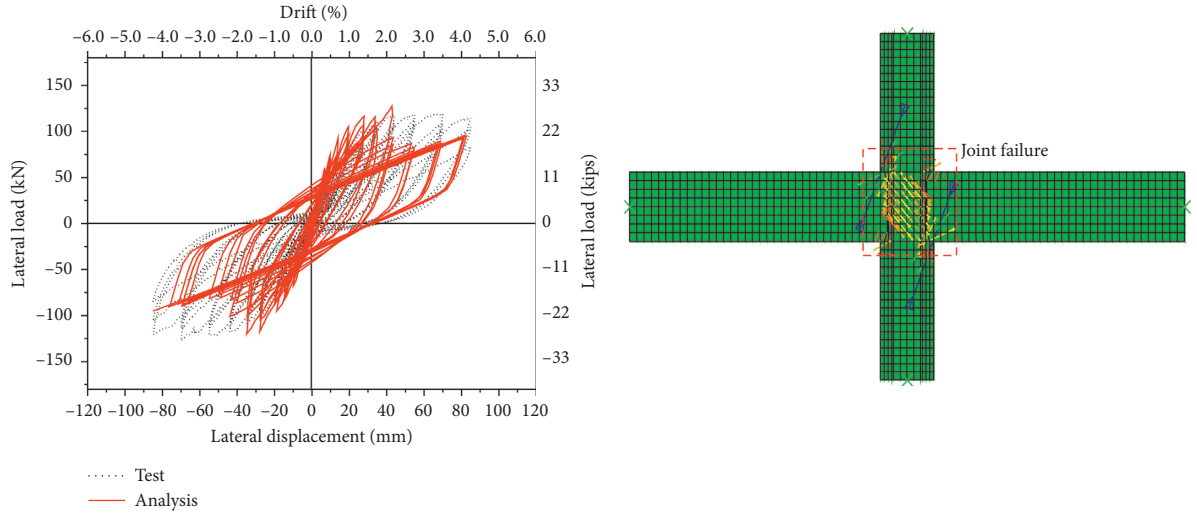

(a)

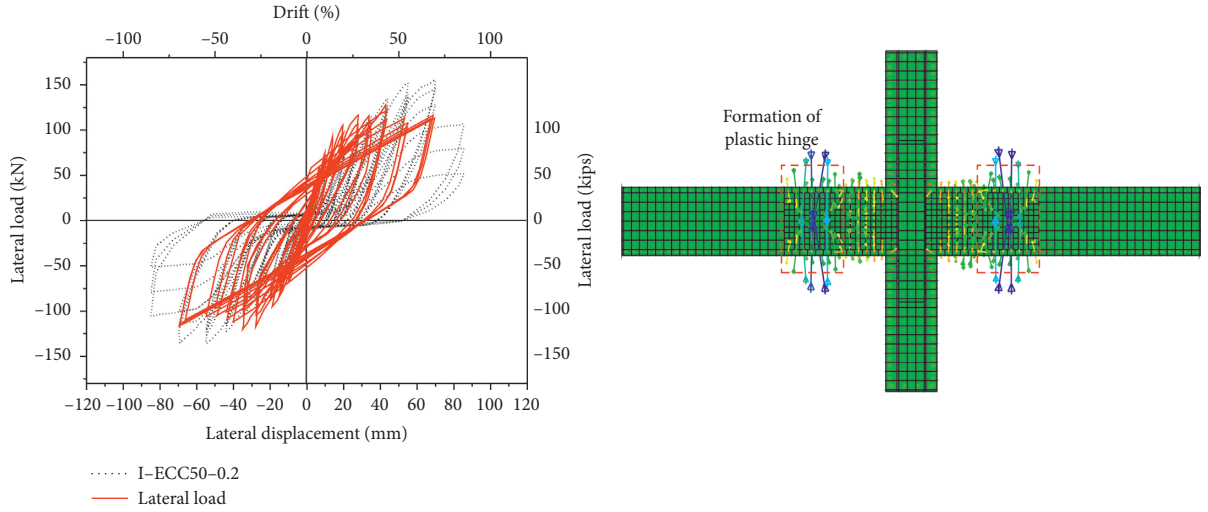

(b)

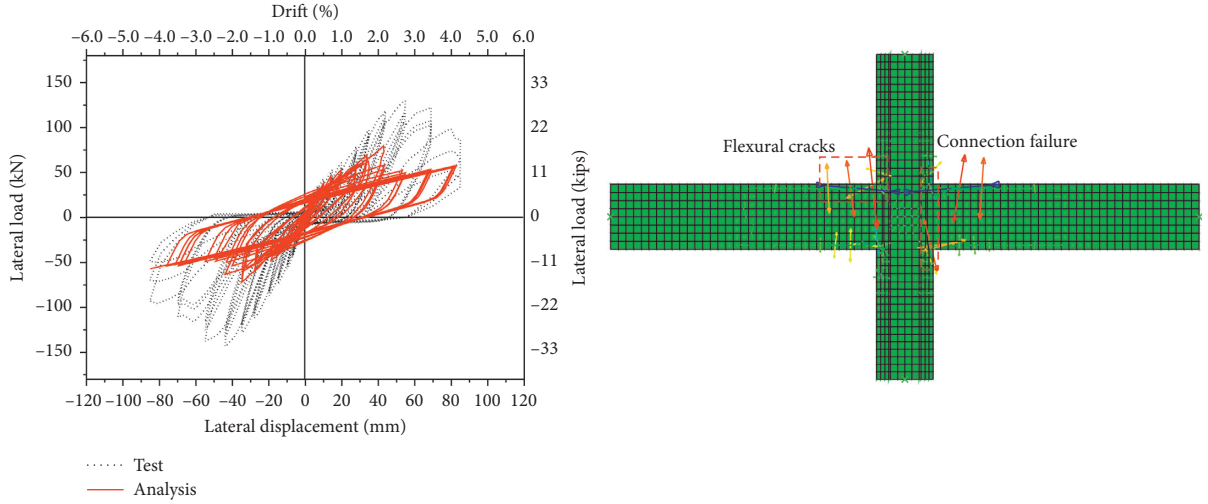

(c)

Figure 13: Continued.

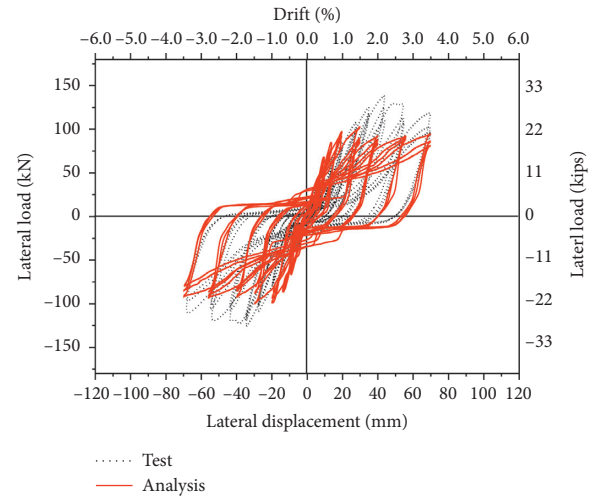

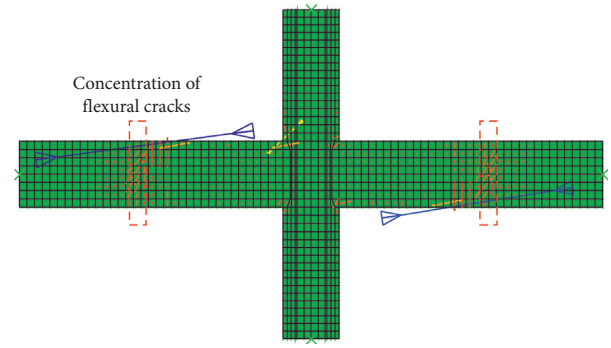

(d)

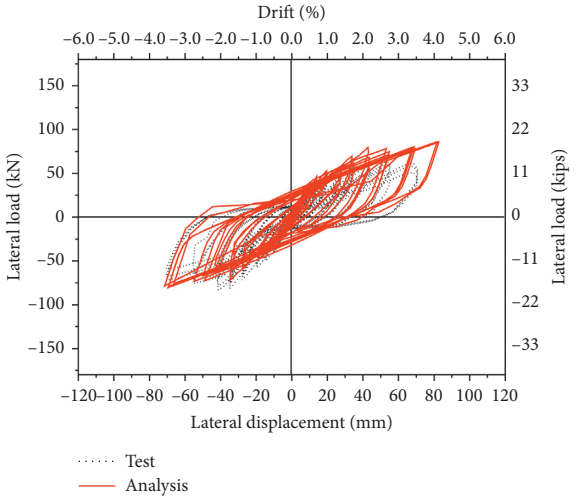

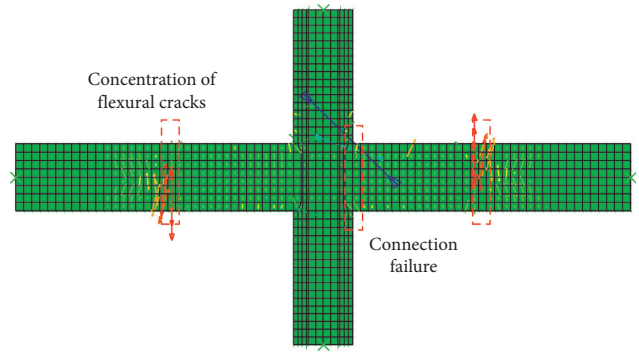

(e)

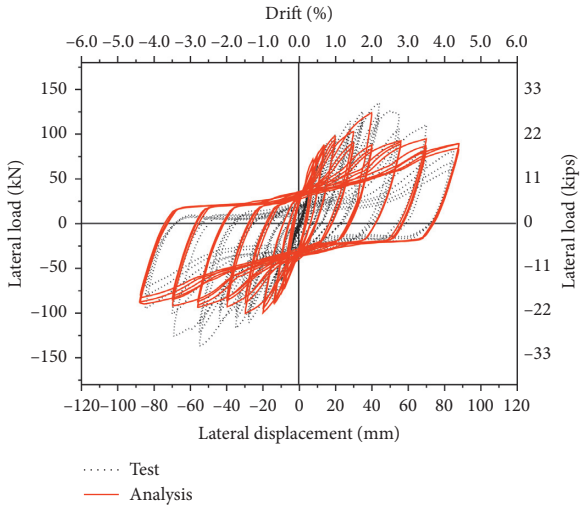

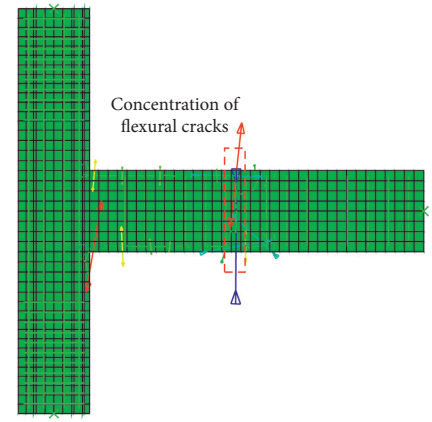

(f)

Figure 13: Predicted story shear forces versus horizontal displacement and crack pattern. (a) RC-control. (b) PC-I50-0.2. (c) PC-50H-0.1. (d) PC-I25H-0.1. (e) PC-O50-H-0.1. (f) PC-O25-H-0.1 (exterior).

was applied to the same location in second step, cyclically. The same loading histories as those used in the analysis of specimens without axial loading were applied, and the story shear force versus horizontal displacement plots corresponding to different axial load levels were plotted for specimen PC-I50-0.2. It can be seen that Specimen inter series attained an optimum value of ultimate story shear when axial load ratio was $(N/A_g f'_c) = 0.2$. Therefore, the analysis results suggested that the axial load $(N/A_g f'_c) \leq 0.3$ was beneficial to the joints' performance. However, the axial load ratio $(N/A_g f'_c) > 0.3$ was found to be detrimental as it reduces the story shear and energy dissipation of the joint (refer to Figure 14).

4.2. Formation of Plastic Hinge. When designing the reinforced concrete frame, the most important design consideration is the moment strength ratio of beam and column and plastic hinge location. Furthermore, steel plates would be a very important design parameter because this parameter determines the strength and stiffness of beams.

The moment strength ratio is defined as the ratio of the sum of the nominal moment strengths of the column above and below the joint to the sum of the nominal moment strengths of all the beams in one plane framing into the joint. Theoretically, a moment strength ratio greater than one should cause the plastic hinges to form in the beams and not in the column. However, ACI318 Building Code [2] and ASCE-ACI Committee 352 recommend the moment strength ratio to be greater than or equal to 1.2 and 1.4, respectively. For the beam failure of proposed connection, specimens were designed to have the moment strength ratio as 1.6. For designing the proposed connection system more economically, plate length and thickness should be examined widely. Therefore, in this section, FE models were investigated. Investigated range of connection detail was determined according to the moment strength ratio of 1 to 1.6.

As a result of finite element analysis, the capacity of beam-to-column joint specimen could be determined by the strength of beam for most cases. However, the failure mode of the beam-to-column specimen for the case of moment capacity ratio 1 had shown beam-joint failure. Other test specimens which have a moment strength capacity of 1.2 ~ 1.6 have shown beam failure mode. As the moment capacity ratio increased, the plastic hinge location moved to the outside of the joint. And cracks were more concentrated to plastic hinge. It is shown in Figures 15 and 16.

Strain distribution is very important information for plastic hinge location; from the strain information of FEA results, plastic hinge location was clearly observed. All specimens have experienced yielding of reinforcements. However, decreasing the moment strength ratio decreases the stress in plastic hinge region. At low level of moment strength ratio, yielding of reinforcement was shown latterly, than other cases of specimens. It is shown in Figure 17. Furthermore, to verify the contribution of steel plate and to locate the plastic hinge region, more FE analyses were performed. As described above, the stiffness of the beam

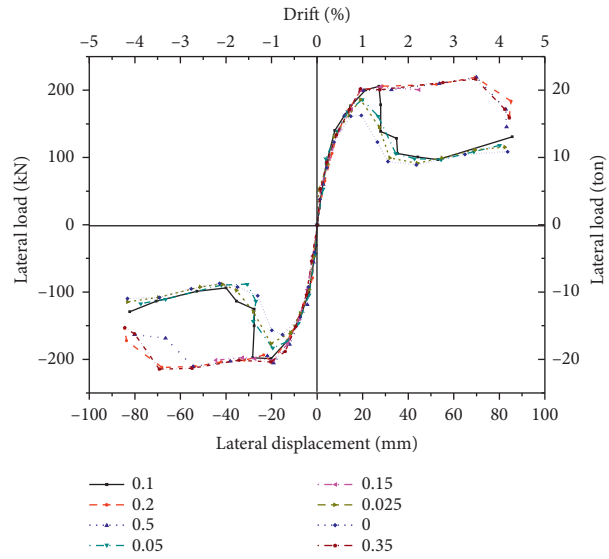

Figure 14: Load-displacement predictions under different axial loading levels (specimen PC-I50-0.2).

section is the main parameter for locating plastic hinge region. As a result of FE analysis, the crack pattern of each FE model, which has different lengths of connecting plate, is clearly different. The location of plastic hinge was determined by the length of plates clearly. This is shown in Figure 18.

5. Design Consideration

To determine the moment capacity of bolt connection, the strain distribution of bolts and connecting plates should be investigated. Because bolt strain cannot be measured from the test, 3D finite element analysis was performed. Because too many components were needed to compensate details of the proposed connection system, analysis was performed in monotonic loading, only. The finite element model consisted of 3 parts: concrete parts, steel parts, and reinforcement. For the reality of finite element modeling, each part was modeled separately. And reinforcements were embedded in concrete components. These models are illustrated in Figure 19. Boundary conditions and other restraints are made with the same method of 2D finite element analysis.

As a result of finite element analysis, stress contour and strain field were provided. Especially, stress and strain of bolts components were investigated for the distribution of resultants forces for connecting area. The stress distribution is illustrated in Figure 20. In the connecting area, most of stress was concentrated in end of the plate. Because stress was flowing along the normal direction of contact area, stress concentration of concrete was shown at the end part of the steel plate. However, concrete of the column remained in elastic range. For locating the plastic hinge of beam elements, the stress distribution of reinforcements was investigated. Basically, stress was concentrated at the end of the steel plate. Therefore, using the proposed connection system, plastic hinge could be controlled by the plate length. This is shown in Figure 21. For the design purposes, stress

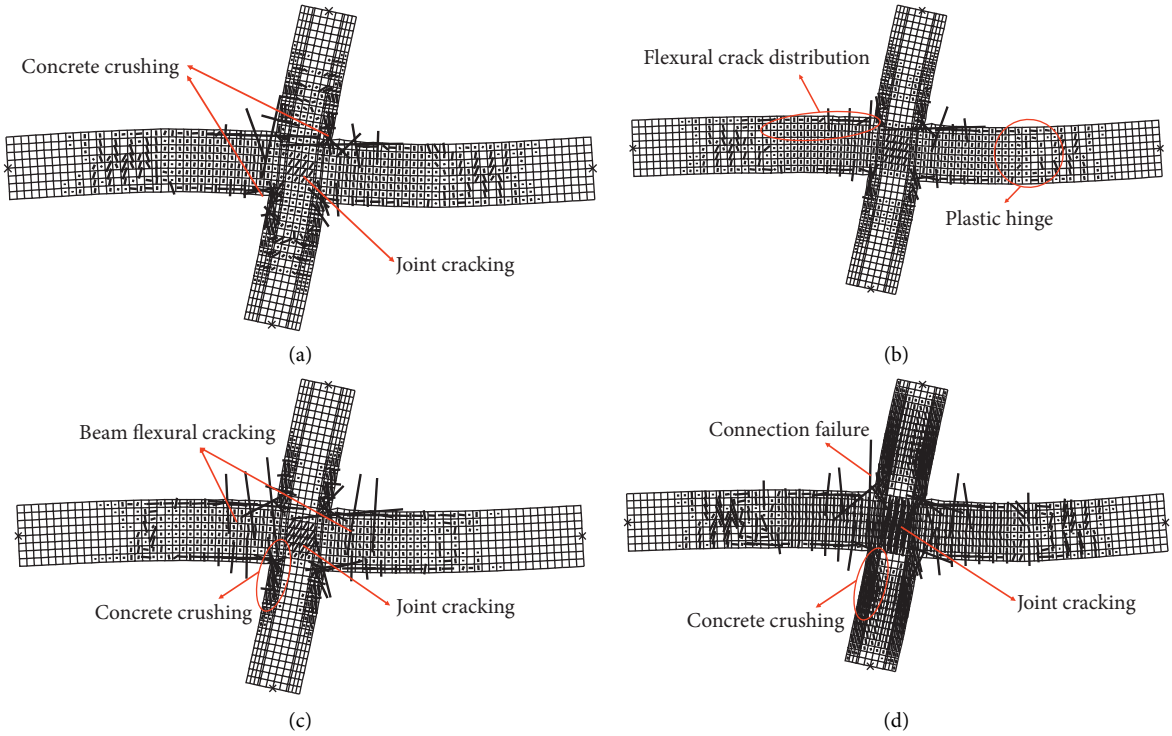

Figure 15: Crack pattern by axial load (specimen PC-I50-0.2). (a) Axial load ratio of 0.1. (b) Axial load ratio of 0.2. (c) Axial load ratio of 0.3. (d) Axial load ratio of 0.5.

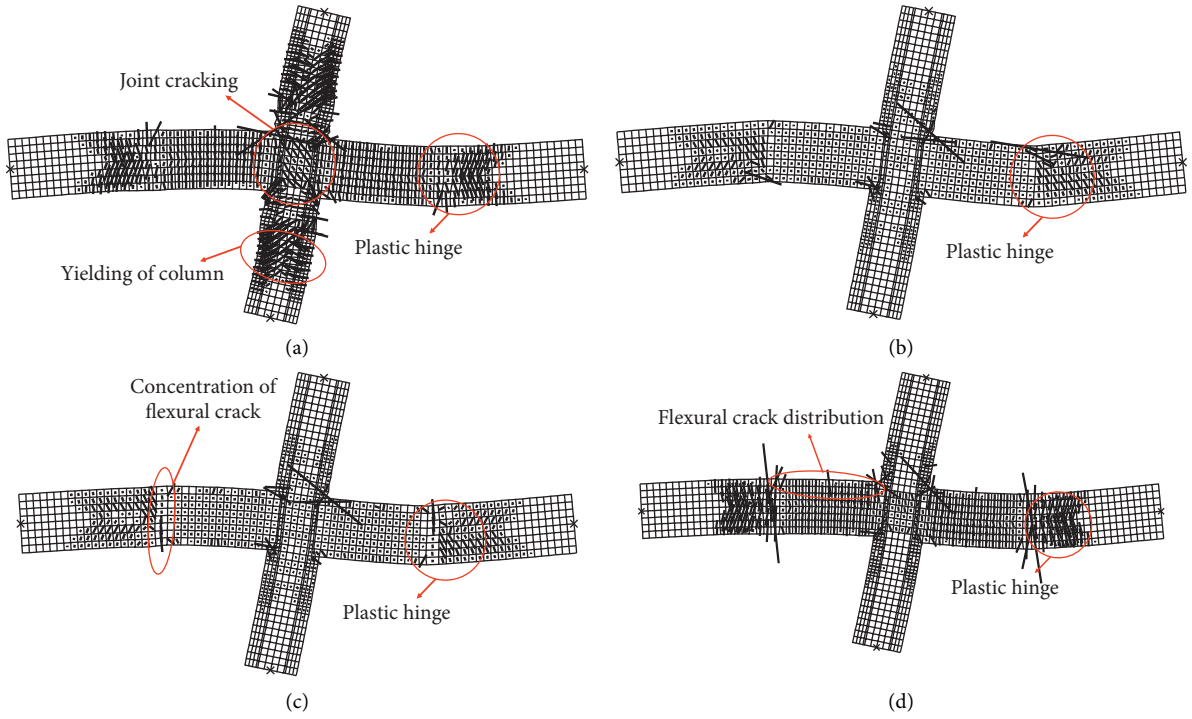

Figure 16: Crack pattern according to moment strength ratio (specimen PC-I50-0.2). (a) Moment strength ratio of 1.0. (b) Moment strength ratio of 1.2. (c) Moment strength ratio of 1.4. (d) Moment strength ratio of 1.6.

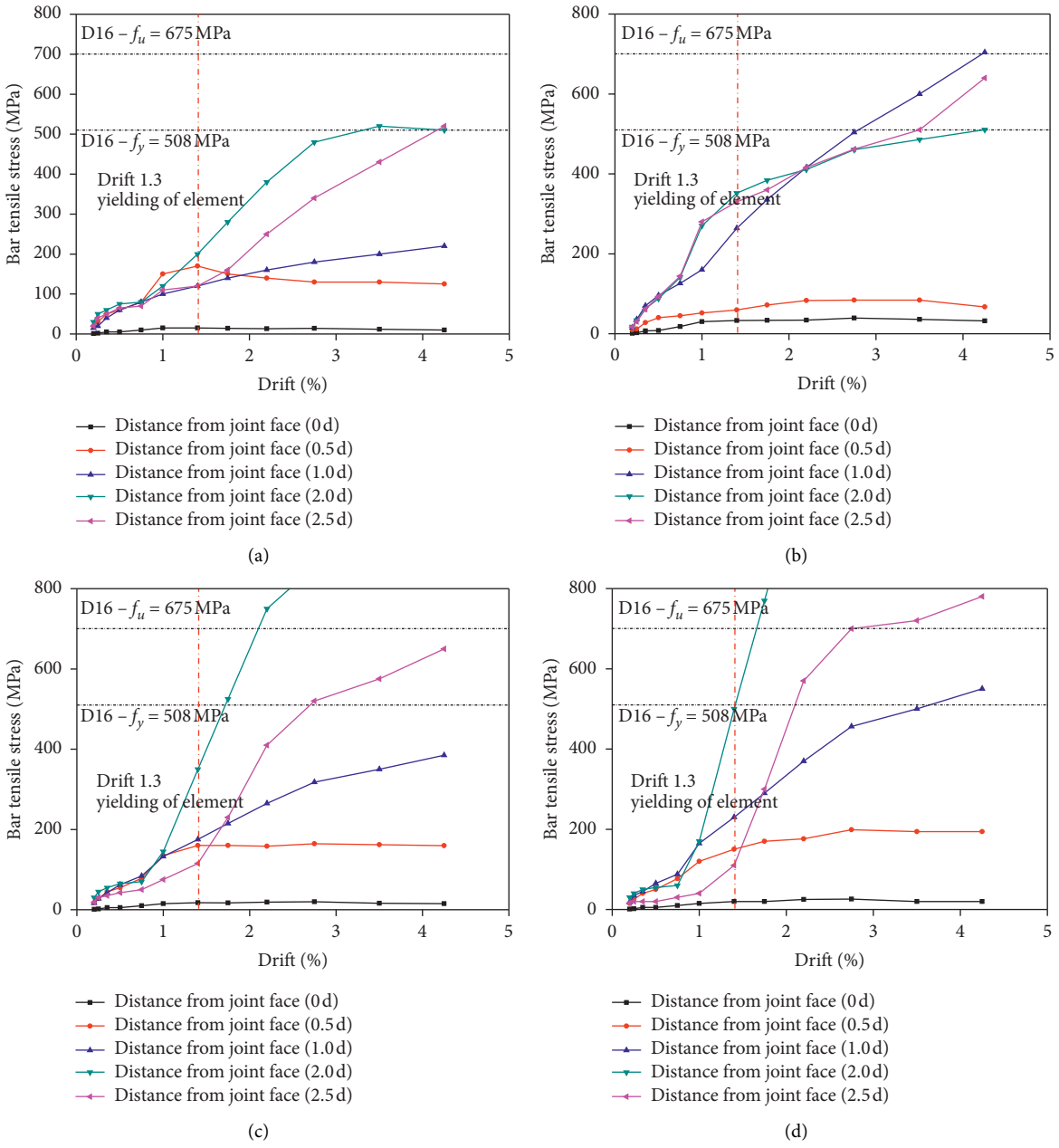

Figure 17: Stress distribution according to moment strength ratio (specimen PC-I50-0.2). (a) Moment strength ratio of 1.0. (b) Moment strength ratio of 1.2. (c) Moment strength ratio of 1.4. (d) Moment strength ratio of 1.6.

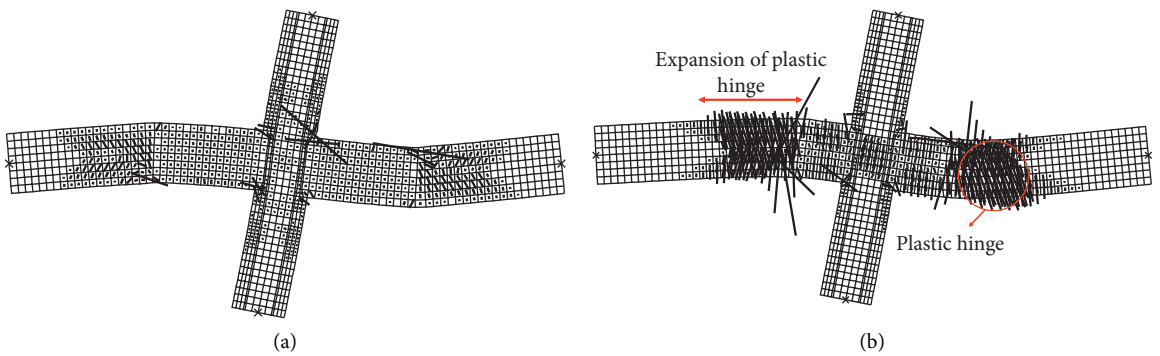

Figure 18: Plastic hinge location according to plate length. (a) Tested length. (b) Half of tested length.

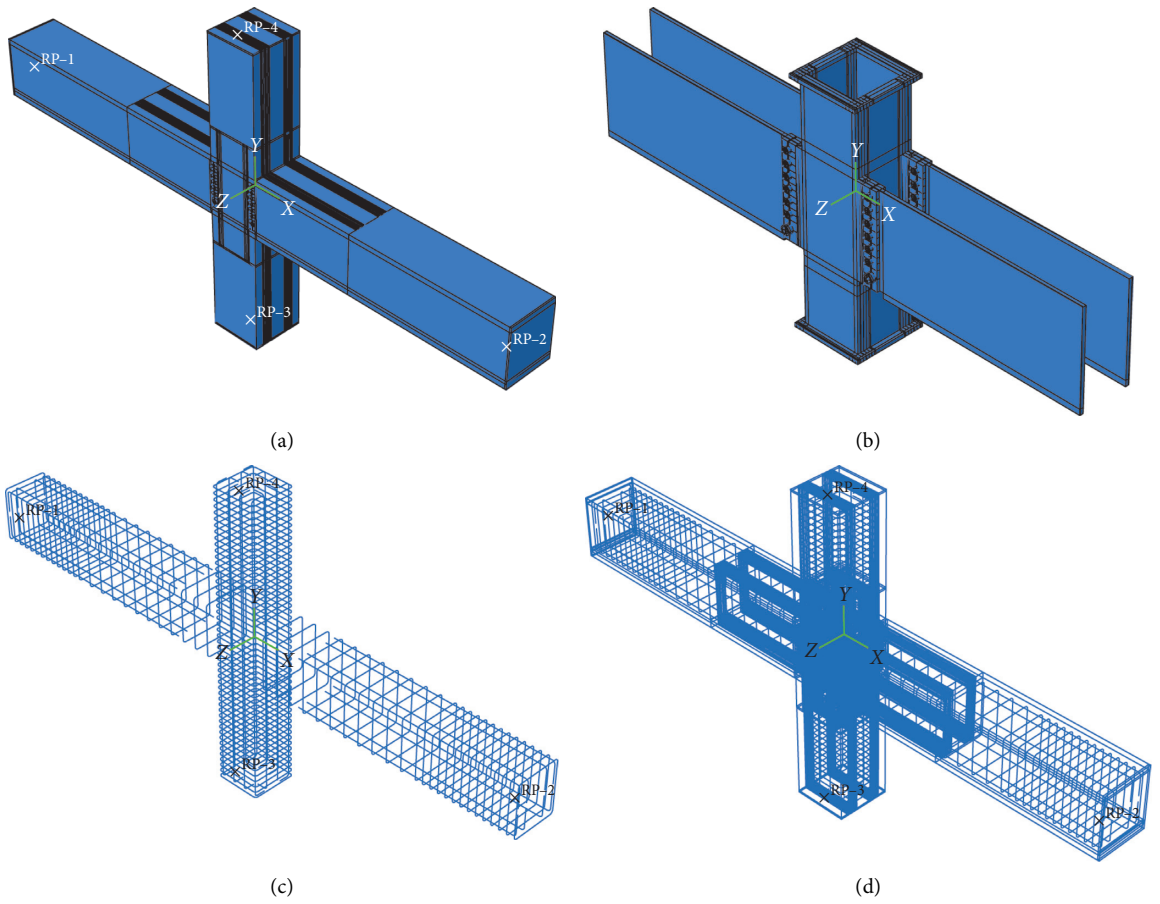

Figure 19: Finite element modeling (embedded components). (a) Concrete part. (b) Steel plate part. (c) Reinforcement part. (d) Total modeling.

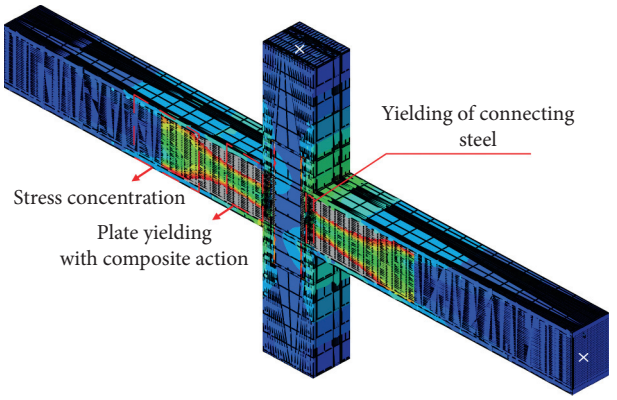

Figure 20: Stress distribution of total model.

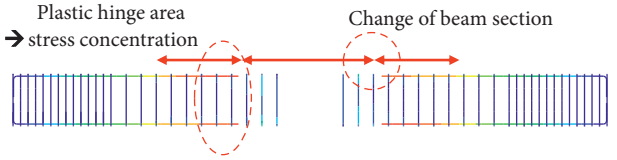

Figure 21: Stress distribution of reinforcements.

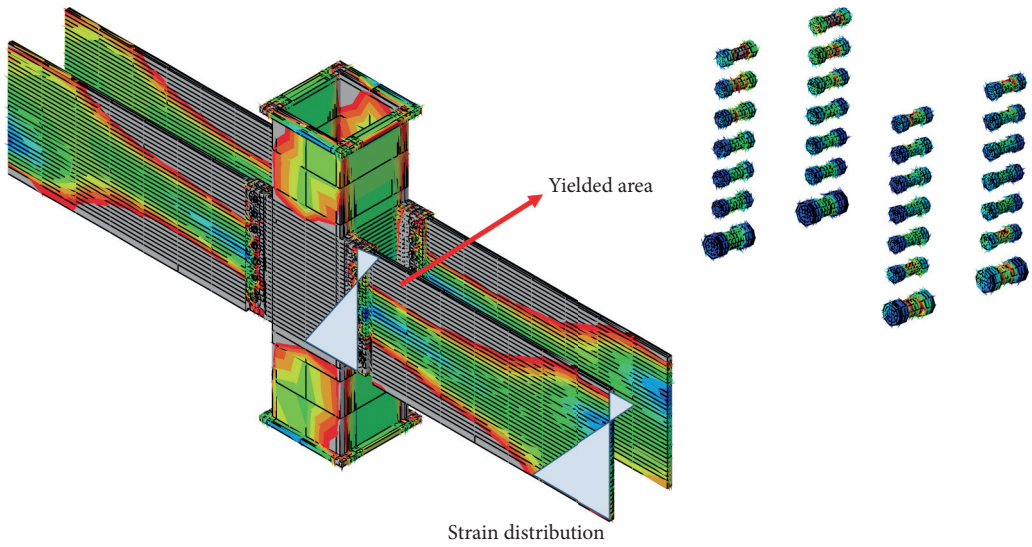

Figure 22: Stress distribution. (a) Steel plates. (b) Connection bolts.

Table 4: Stress distribution and resultant force results.

Element ID	Stress type	Strain compatibility		FEM	
		Stress (MPa)	Resultant force (kN)	Stress (MPa)	Resultant force (kN)
El. 1	Tension	400	624	368	574
El. 2	Tension	280	302	253	272
El. 3	Tension	180	151	150	125
El. 4	Tension	90	76	65	54
El. 5	Compression	92	77	113	94
El. 6	Compression	200	73	253	92
Cc	Compression	30	770	36	720

distribution of connecting steel plate would be needed. Using the information of stress distribution at the center of bolt element, which was described in this section, resultant force could be calculated. This is also shown in Figure 22.

Neutral axis was formed at the third bolt from the compressive extreme fiber. Because stiffness could be increased with the composite action at compressive area, compressive stress area was bigger than tensile one. Provided stress is shown in Table 4.

6. Conclusion

FE models used in this study well predict the behavior of test specimens. However, the initial stiffness problems encountered by the embedded truss model should be solved for the more wide parametric study such as serviceability check in design process.

According to the parametric study, the effect of axial load was investigated. There is a reduction in story shear and ultimate number of cycles after enhancement in axial load ratio beyond 0.3 (i.e., $(N/A_g f_c') > 0.3$). Therefore, the analysis results suggested that the axial load $(N/A_g f_c') > 0.3$ was beneficial to the joint's performance. However, the axial load ratio $(N/A_g f_c') > 0.3$ was found to be detrimental as it reduces the story shear and energy dissipation of the joint.

Plastic hinge region is very important design criteria for frame action. From the result of the parametric study, plastic hinge location is determined by the moment strength ratio and plate length. Generally, plastic hinge was formed far from the column face with the increase of moment strength ratio. It was clarified by investigating the stress distribution of reinforcement. For low value of moment strength ratio, reinforcement is hard to yield and plastic hinge cannot be formed easily, in the area of plate installed area. However, the length of plates is an important parameter for location of plastic hinge. Investigation from the test and FE model revealed that plastic hinge occurred at the end of steel plates. Therefore, using the proposed connecting system, plastic hinge location can be controlled by the designers.

Complicated 3D model for the proposed connecting system would be used for design strength calculation for connection. The stress distribution of bolt elements is similar to the stress distribution resulted from strain compatibility

methods. Therefore, the proposed connection can be designed using conventional design methods.

Data Availability

The data used to support the findings of this study are included within the article. Any additional data related to the paper may be requested from the corresponding author.

Conflicts of Interest

The author declares that there are no conflicts of interest.

Acknowledgments

This study was supported by Kyungnam University Foundation Grant, 2016.

References

[1] H.-K. Choi, Y.-C. Choi, and C.-S. Choi, "Development and testing of precast concrete beam-to-column connections," *Engineering Structures*, vol. 56, pp. 1820–1835, 2013.

[2] H.-K. Choi, Y.-C. Choi, and C.-S. Choi, "Hysteretic behavior and seismic resistant capacity of precast concrete beam-to-column connections," *Journal of the Earthquake Engineering Society of Korea*, vol. 14, no. 4, pp. 61–71, 2010.

[3] C.-S. Choi, S.-H. Kim, Y.-C. Choi, and H.-K. Choi, "Analytical study on hybrid precast concrete beam-column connections," *Journal of the Korea Concrete Institute*, vol. 25, no. 6, pp. 631–639, 2013.

[4] S. A. Kulkarni, B. Li, and W. K. Yip, "Finite element analysis of precast hybrid-steel concrete connections under cyclic loading," *Journal of Constructional Steel Research*, vol. 64, no. 2, pp. 190–201, 2008.

[5] J. Hu, "Design and modeling for smart PR-CFT connection systems," in *Smart Connection Systems*Taylor & Francis Group, Milton, England, 2015.

[6] L. Torres, F. López-Almansa, and L. M. Bozzo, "Tension-stiffening model for cracked flexural concrete members," *ASCE*, vol. 130, no. 8, pp. 1242–1251, 2004.

[7] M. Attila B, S. P. Pessiki, R. N. White, and P. Gergely, "Implications of experiments on the seismic behavior of gravity load designed RC beam-to-column connections," *Earthquake Spectra*, vol. 12, no. 2, pp. 185–198, 1996.

[8] C. M. Lin and J. I. Restreop, "Seismic behaviour and design of reinforced concrete interior beam-column joints," *Bulletin of the New Zealand for Society Earthquake Engineering*, vol. 35, no. 2, pp. 108–128, 2002.

[9] J. P. Fu, T. Chen, Z. Wang, and S. Bai, "Effect of axial load ratio on seismic behaviour of interior beam-column joints," in *Proceedings of the 12WCEE 2000*, pp. 1–5, Auckland, New Zeland, February 2000.

[10] B. Li and C. L. Leong, "Experimental and numerical investigations of the seismic behavior of high-strength concrete beam-column joints with column axial load," *ASCE*, vol. 141, no. 9, pp. 1842–1853, 2004.

Hindawi
Advances in Civil Engineering
Volume 2020, Article ID 8821132, 11 pages
https://doi.org/10.1155/2020/8821132

Research Article

Fatigue Characteristics of Prestressed Concrete Beam under Freezing and Thawing Cycles

Yuanxun Zheng,[1] Lei Yang,[1] Pan Guo ,[1,2] and Peibing Yang[1]

[1]*School of Water Conservancy Science and Engineering, Zhengzhou University, Zhengzhou, Henan 450001, China*
[2]*School of Civil Engineering, Zhengzhou University, Zhengzhou, Henan 450001, China*

Correspondence should be addressed to Pan Guo; 77741289@qq.com

Received 6 July 2020; Revised 31 July 2020; Accepted 23 August 2020; Published 4 September 2020

Academic Editor: Yifeng Ling

In order to reveal the influence of freezing and thawing on fatigue properties of the prestressed concrete beam, a kind of novel freeze-thaw test method for large concrete structure components was proposed, and the freeze-thaw experiments and fatigue failure test of prestressed concrete hollow beams were performed in this paper. Firstly, the compressive strength and dynamic elastic modulus of standard specimens subjected to different numbers of freeze-thaw cycles (0, 50, 75, and 100) were determined. Then, the static and dynamic experiments were performed for prestressed concrete beams under different freeze-thaw cycles. Depending on the static failure test results, the fatigue load for the prestressed concrete beam model was carried out, the fatigue tests for prestressed concrete beam under freezing and thawing cycles were done, and the influence of fatigue loading times on dynamic and static characteristics of prestressed concrete beam was also studied. Finally, the relation between fatigue characteristics and numbers of freeze-thaw cycles was established, and the fatigue life prediction formulas of prestressed concrete beams under freeze-thaw cycles were developed. The research shows that the freezing and thawing cycles had obvious influence on fatigue life, and the freezing and thawing cycles should be taken into account for life prediction and quality evaluation of prestressed concrete beams.

1. Introduction

Because of excellent crack resistance and spanning performance, prestressed concrete structures have been applied extensively in single building structures, highway bridges, offshore, chemical building docks, airports, large tonnage, and other special complex structures. However, prestressed concrete structures inevitably suffer from excessive erosion from the natural environment. In cold climates with greatly contrasting temperatures, concrete bridge structures often experience freeze-thaw damage, which results in the decreased durability of bridges as time progresses, which may eventually lead to the attenuation of the service life of the bridge. Bridge structure disease and collapse accidents have happened caused by freeze-thaw damage in recent decades. Because prestressed concrete bridges have been widely used and assume a vital role in traffic engineering operations, it is critical to strengthen the freeze-thaw durability of prestressed concrete structures.

Several studies have focused on the frost-resisting performance of prestressed concrete structures. The main theories and academic hypotheses on the mechanisms of concrete freezing and thawing damage are the theory of ice crystal formation, hydrostatic pressure hypothesis, osmotic pressure hypothesis, Litvan freeze-thaw damage theory, critical saturated degree theory, etc. [1]. The most acceptable theories are hydrostatic pressure hypothesis and osmotic pressure hypothesis [2, 3]. He et al. [4] studied the influence of different factors on the temperature field distribution of the slurry in the low-temperature freeze-thaw cycle. The results indicated that several factors such as adding fine aggregate, reducing water-to-cement ratio, and low water content could improve the freeze-thaw cycles resistance of cement-based materials to a certain extent.

Studies have shown that the frost-resisting performance was related to internal pores, water saturation degree, and concrete strength. Hua et al. [5] divided cement mortar specimens into cement mortar and rubber particles, which were, respectively, represented by RSS and CR parameters. Typical correlation method and Szpilman correlation method were used in the analysis. The statistical analysis shows that CR has a high correlation with the residual strength of specimens after freeze-thaw cycle. Jin and Zhao [6] used hydraulic servo test system to test different intermediate stress ratios of 100 mm concrete under triaxial compression. The results show that the triaxial compressive strength is greater than the biaxial compressive strength and uniaxial compressive strength after the same rapid freeze-thaw cycle.

Vesa [7] has statistically studied the deterioration of concrete due to frost action in nonsaline and saline environments. The most significant variables affecting freezing-thawing durability of concrete were calculated statistically and the estimated response surface profile was obtained. The water-cement ratio and air content of concrete are the main factors affecting the internal and surface damage of concrete under freezing-thawing load. On the other hand, Zhao et al. [8] studied the influence of basalt fiber and freeze-thaw cycle on the impact failure mechanism of concrete by means of the concrete beam falling ball impact test. In the early stage of freeze-thaw, the impact energy loss was the fastest and the largest, indicating that freeze-thaw cycle would cause damage and defects to the fiber/matrix interface, thus gradually losing the strengthening effect of three-dimensional fiber system. The experimental study provides a new way to understand the influence of fiber and freeze-thaw cycle on the impact resistance of concrete.

Wu et al. [9] conducted freeze-thaw cycle tests on forty-eight 300 mm cubes of compound concrete and seventy-two 100 mm cubes of FC or demolished concrete, respectively, and determined the compressive failure strength and splitting failure strength of freeze-thaw specimens. With the increase of freeze-thaw cycles, the tensile splitting strength of composite concrete decreases faster than that of FC, while the decline trend of compressive strength is not very obvious. Rui et al. [10] studied the matching of pervious concrete with different matrix types, pore system characteristics, and fiber reinforcement characteristics. The influence of matrix, pore system characteristics, and fiber reinforcement on the freeze-thaw durability of pervious concrete is investigated and potential freeze-thaw failure mechanisms are discussed. Ababneh and Xi [11] proposed an ultrasonic wave model that evaluates concrete salt-freezing damage using pulse velocity and resonant frequency, and the degree of freeze-thaw damage was obtained. Wu et al. [12] regarded mass loss as the variable representing the degree of concrete freeze-thaw damage and proposed a mass loss model. Zhao et al. [13], based on the horizontal strain field on the specimen's surface, a damage degree factor, and a localization factor, proposed to describe the bending damage and failure characteristics of the specimens, with a further analysis of the effect of the fiber content and freeze-thaw cycles on the characteristics. The experimental results show that the failure process can be divided into three stages: the microfracture dispersion, the macrocrack selection, and the main crack propagation. However, Boyd et al. [14] studied the influence of freeze-thaw metamorphism on the tensile fatigue life of aerated concrete at the initial stage of metamorphism. The results indicated that even though the ultimate static tensile strength of the specimens did not vary significantly due to the freeze-thaw cycles, the residual fatigue properties were degraded. Cho [15] described freeze-thaw damage of concrete using strain change and established a limit function relation between residual strain and the experimental results, and an equivalent plastic strain and its limit state function were established. Peng et al. [16] studied the effect of freeze-thaw cycles on interfacial bonding between concrete and ordinary concrete, high-strength concrete, and additional freeze-resistant concrete by pull-out tests. It is found that the freeze-thaw cycle results in a significant decrease in the compressive strength of ordinary concrete, while the strength of high-strength concrete and concrete mixed with water-reducing agent and air-entraining agent does not. Guo et al. [17] conducted rapid freezing-thawing cycle tests of 0.4, 0.5, and 0.6 water-cement ratios (W/C), respectively, in 0% (water), 1%, and 5% Na_2SO_4 solutions to study the sulfate freezing-thawing cycle performance of ordinary concrete. The results show that, due to the coupling effect of freeze-thaw cycle and sulfate corrosion, the damage of concrete freeze-thaw cycle in Na_2SO_4 solution is greater than that in tap water. Vesikarle [18] obtained the number of frost resistance cycles of concrete by rapid freezing and thawing test cycles, and the service life of concrete was proposed by concrete freeze-thaw cycles fixed in the actual environment every year. Chen et al. [19] conducted experimental research on the degradation of compressive strength of concrete under compressive load and freeze-thaw cycle. The results showed that, based on the degradation model, the freeze-thaw cycle failure evolution model of concrete surface under compression load was established. Wang et al. [20] investigated the loss of shear strength and the mechanism of degradation caused by freeze-thaw cycles through shear tests on the cement-sandstone bonding interface and the material itself. The results show that the shear strength decreases linearly with the increase of freeze-thaw cycles and increases linearly with the increase of normal stress.

In order to effectively evaluate the mechanical properties of concrete after seawater freezing-thawing and seawater erosion, Zhang et al. [21] conducted mechanical properties tests of concrete after seawater freezing-thawing and seawater erosion based on large static and dynamic stiffness servo press. The experimental results show that the compressive strength and elastic modulus of concrete axis gradually decrease and the tensile and compressive meridians of strength criterion gradually shrink with the increase of the cycles of dry and wet cycle and freeze-thaw cycle. Sinha et al. [22] proposed a concrete "deformation uniqueness" in the study of structure fatigue. Matapob [23] described two typical problems of concrete flexural members under repeated load: (1) the influence of steel structure on the strength of flexural reinforced concrete members, crack

formation, and stiffness; (2) some problems on the calculation theory of the fatigue structure of reinforced concrete. Schläfli and Brühwiler [24] conducted a fatigue test on 27 reinforced concrete decks to study the relationship between midspan deflection, concrete strain, and the number of action cycles. Aas-Jakobsen and Lenschow [25] proposed a universal fatigue strength formula for concrete. Furthermore, Tepfers and Kutti [26] perfected the universal fatigue strength formula by a series of tests, and the coefficients were obtained. Zhao [27] performed a test on 16 slabs and analyzed the influence of reinforcement ratio, number of fatigue cycles, and performance of fatigue cycle on fatigue crack, deformation, failure mode, and fatigue resistance capacity of normal section of reinforced concrete slab. Normal section and crack calculation methods for reinforced concrete slab were proposed under fatigue load. Zhao [28] systematically described the fatigue deformation of reinforced concrete and crack and proposed normal section and oblique section fatigue strength models for reinforced concrete and prestressed concrete.

Reinforced concrete tends to suffer internal damage under fatigue actions; that is, it is a period during which fatigue crack brings out, extends, and makes structure broken. The biggest difference between fatigue damage and normal damage is the cumulative fatigue damage period experienced as the load cycles increase. Cheng and Shen [29] pointed out that fatigue lifetime consists of three consecutive stages: fatigue crack formation, fatigue crack propagation, and fatigue damage. Fatigue damage models can be roughly divided into three categories. The first category does not consider the actual performance degradation mechanism for an S-N curve or a similar figure. The second category indicates residual strength. The residual stiffness model of the third category is a damage development model. Yi et al. [30] used linear elastic fracture mechanics to obtain the rotational stiffness expression of the crack section of a concrete member, based on the dynamic test data for four prestressed concrete hollow slabs and their damage performance. Yeo et al. [31] estimated the extent of damage by the static response data of structure. Vestroni and Capecchi [32] identified the damage of structures based on available beam frequency data.

Standard plain concrete or ordinary small reinforced concrete member is gradually becoming the main focus in freeze-thaw and fatigue tests of concrete. Fu [33] performed a fatigue experiment on beams with 0.515 m length which have experienced freeze-thaw erosion, studied component failure mechanism for different freeze-thaw cycles, and discussed the influence of prestressed concrete on freeze-thaw resisting damage as well as the relationship between prestress level, freeze-thaw cycles, and fatigue performance. Lu et al. [34] showed that, for the concrete specimens after exposure to only freeze-thaw cycling or to a combination of freeze-thaw cycles and fatigue loading, with the increase of freezing and thawing cycles, the specimen masses firstly increase and then decrease, whereas the relative dynamical elastic modulus gradually decreases. In addition, Shi et al. [35] points out that the reliability results are in good agreement with the percentile rank method. Furthermore, Liu et al. [36] performed a fatigue test after the prestressed concrete beams experienced several freeze-thaw cycles and analyzed attenuation law of structure stiffness under fatigue cumulative damage, which states that the greater the number of freeze-thaw cycles is, the more severely beams bend downwards.

To sum up, most of the literatures at home and abroad mainly focus on freeze-thaw cyclic corrosion test or fatigue test on standard ordinary concrete members or ordinary small reinforced concrete members. However, there are few researches on freeze-thaw test and fatigue failure test of prestressed concrete hollow beams with large concrete components. In view of this, a new freeze-thaw test method for large concrete members is presented in this paper, and the freeze-thaw test and fatigue failure test for prestressed concrete hollow beams are carried out. Finally, the relationship between fatigue characteristics and the number of freeze-thaw cycles is established, and the fatigue life prediction formula of prestressed concrete beams under freeze-thaw cycles is established. The freeze-thaw cycle has obvious influence on the fatigue life, so it should be considered in the life prediction and quality evaluation of prestressed concrete beams.

2. Freeze-Thaw Test

2.1. Model Design and Construction. Prestressed concrete hollow beams with concrete grade C50 were used in the test. The mixing proportion of the mixture is shown in Table 1.

The prestressed concrete hollow beam was designed using a 1×7 stranded wire with ultimate tensile strength of 1860 MPa, diameter of 12.7 mm, and calculating area of 98.7 mm^2. The regular reinforcement consists of a longitudinal bar, stirrup, and bearing rod with a diameter of 6 mm. Table 2 summarizes the mechanical property of the regular reinforcement.

The length of the prestressed concrete beam was 2 m with 320 mm height and 500 mm width, while its inner hollow part is 220 mm high and 400 mm wide. There were three prestressed stranded wires in the bottom flange and 16 evenly spaced (100 mm) stirrups in the midspan of the beam. The spacing between the other four stirrups was relatively narrow (50 mm). Figure 1 illustrates the beam section and reinforcement.

2.2. Freeze-Thaw Test and Test Data. Three groups of prestressed concrete beams and C50 concrete cubes were used in the freeze-thaw test. The numbers of freeze-thaw cycles were 50, 75, and 100, respectively. Moreover, an NM-4 A nonmetal ultrasonic detector was used to detect the relative dynamic modulus of elasticity of C50 concrete cubes after the freeze-thaw test. Equations (1) and (2) give the formula of relative dynamic modulus of elasticity [11]:

$$E_d = \frac{(1+v)(1+2v)\rho V^2}{1-v} = \frac{(1+v)(1+2v)\rho L^2}{(1-v)t^2}, \quad (1)$$

$$E_{\mathrm{rd}} = \frac{E_{dt}}{E_{d0}} = \frac{V_t^2}{V_0^2} = \left(\frac{T_0}{T_t}\right)^2, \quad (2)$$

where E_d is the dynamic modulus of elasticity, v is Poisson's ratio, ρ is the concrete density (kg/cm^3), L is the length of

Table 1: Concrete mixing proportion.

Cement	Fly ash	River sand	Macadam	Polycarboxylic acid type water-reducer	Water
450	50	722	1035	5	160

Table 2: Ordinary steel mechanical property.

Reinforcement	Tensile strength design value (MPa)	Compressive strength design value (MPa)	Elastic modulus (ep)
Φ6	330	330	2.0×10^5

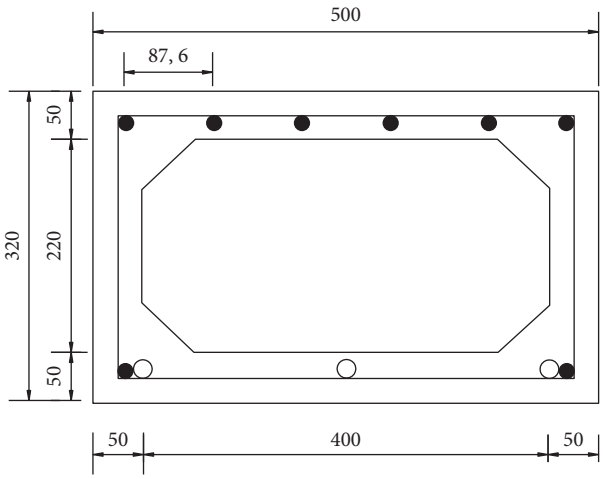

Figure 1: Beam section and reinforcement (unit: mm).

component (m), t is the propagation time of ultrasonic testing (μs), E_{rd} is the relative dynamic modulus of elasticity, T_0 is the propagation time of ultrasonic testing in concrete cube before erosion, and T_t is the propagation time of ultrasonic testing in concrete cube after erosion. During the erosion process, Poisson's ratio v of concrete is insensitive and changes slightly.

Pressure testing machine was used to test the compressive strength of C50 concrete cubes, which is computed by the following equation [37]:

$$f_c = 0.95\frac{F}{A}, \tag{3}$$

where f_c is the compressive strength of concrete cube, F is the failure load, and A is the pressure-bearing area.

Tables 3 and 4 summarize the relative dynamic elastic modulus and compressive strength data, respectively.

According to Table 3, the relative dynamic elastic modulus of the same C50 concrete reduced as the number of freeze-thaw cycles increased, and the speed of ultrasonic wave through C50 concrete reduced. The internal parts of the concrete begin to experience gradual increase in damage as freeze-thaw cycles increase.

3. Fatigue Load Experiment

3.1. Static Load Test. Static load test was performed before fatigue load experiment to determine the ultimate bearing capacity of prestressed concrete beam. Based on the ultimate bearing capacity, the fatigue stress ratio was determined as 0.8 [38]. Figures 2 and 3 illustrate the schematic of static load test and actual device, respectively.

Prestressed concrete hollow slab shows large deformation, and the upper concrete is nearly broken when the static load is 200 kN. The static load changes slowly on the specimen when it is 200–245 kN. But when the load is up to 245 kN, the specimen is completely crushed, and the displacement of midspan part changes acutely. In view of the experiment phenomenon and the related strain deflection data, the ultimate limit fracture of the test beam is $P_{max} = 200$ kN.

3.2. Fatigue Cycle Test. Fatigue load experiments were performed on beams that experienced 0, 50, 75, and 100 freeze-thaw cycles. Figure 2 illustrates the load method, while Table 5 summarizes the fatigue limit load and load frequency.

The fatigue test was performed using a hydraulic fatigue testing machine. The dynamic performance tests were carried out after 5.0×10^5 fatigue load times. The appearance and development of crack were observed continually, and the component was considered as failure and the test was stopped when the crack width was up to 0.2 mm. As shown in Figures 4 and 5, the electronic strain gauges and vibration pickups were used to collect test data.

3.3. Data and Analysis of Fatigue Test Results

3.3.1. Numbers of Failure Fatigue Load Actions and Cracking Load Actions. As the freeze-thaw cycles increased, the crack width was up to 0.2 mm and the test was stopped. The numbers of failure fatigue load and cracking load actions differed when four groups of prestressed concrete beams cracked. Figures 6 and 7 illustrate the numbers of cracking load actions and failure fatigue load actions, respectively.

In Figure 6, the number of cracking load actions decreased as the freeze-thaw cycles increased. Comparing 50 freeze-thaw cycles with 75 freeze-thaw cycles, the number of cracking load actions decreased slowly, while the number of cracking load actions of beams that experienced 100 freeze-thaw cycles decreased rapidly.

These phenomena indicate that the beams cracked before the freeze-thaw cycles increased such that the crack resistance of the beams decreased very rapidly after relative multiple freeze-thaw cycles equal to the number of failure fatigue load actions. In Figure 7, the increase in freeze-thaw

Table 3: Relative dynamic elastic modulus of concrete cubes experiencing different freeze-thaw cycles.

Number of freeze-thaw cycles	Relative dynamic elastic modulus (%)
0	100
50	87.1
75	84.9
100	78.6

Table 4: Average compressive strength of concrete cubes experiencing different freeze-thaw cycles.

Number of freeze-thaw cycles	Average fracture load (kN)	Average compressive strength ($\overline{f}_{cu}$)
0	553.600	52.59
50	482.000	45.79
75	471.300	44.77
100	455.500	43.27

cycles led to a decrease in the fatigue life. The cracking load action has a similar degradation rule.

3.3.2. Data of Static Load after Fatigue Action. Freeze-thaw cycles are a variable of fatigue loading causing accumulated damage. Static and dynamic load tests after 5.0×10^5 fatigue load actions are means of monitoring the beam performance. A fatigue experiment was carried out for four groups of prestressed concrete beams, where the numbers of loading actions are 0, 5.0×10^5, and 1.0×10^6. A level 3 loading test was then performed, where the loads are 5 ton, 10 ton, and 15 ton. Figure 8 illustrates the midspan compressive strain for different freeze-thaw cycles before fatigue action, while Figure 9 illustrates the midspan tensile strain for different freeze-thaw cycles before fatigue action. Figure 10 illustrates the midspan displacement for different freeze-thaw cycles before fatigue action.

Figure 8 illustrates that the force made frost heave cracks close gradually in the compressive zone as the freeze-thaw cycles increased, thereby resulting in an increase in the concrete compressive strain. Comparing the results of 0, 50, and 100 freeze-thaw cycles with 50, 75, and 100 freeze-thaw cycles, the increase in freeze-thaw cycles accelerated the increase in compressive strain of concrete at the upper flange plate of the beam.

In Figure 9, compared with beam that never suffered freeze-thaw cycles, tensile strain increment of the beam's lower flange plate that suffered different freeze-thaw cycles is little. The results of 50 and 75 freeze-thaw cycles have same parts, and the results of 100 freeze-thaw cycles are evident. But range ability is not rapid as compressive strain. Meanwhile, the expansion coefficients of concrete and steel are similar. Hence, the influence of freeze-thaw actions on cementing action between prestressed wire and concrete is insignificant.

Data acquisition and data processing were carried out after every 5.0×10^5 fatigue action cycles. The same-level load (15 tons) was selected to observe the change in the strain of

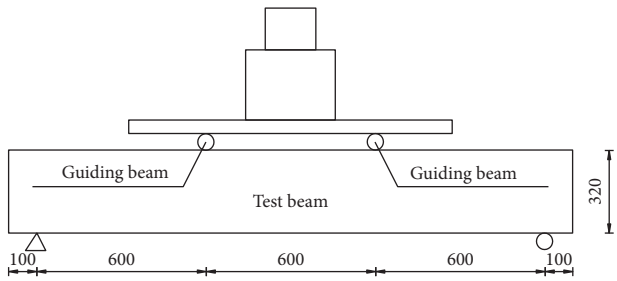

Figure 2: Schematic diagram of static load (unit: mm).

Figure 3: Loading equipment and methods of static load.

Table 5: Fatigue limit load and load frequency.

Specimen number	Maximum fatigue load F'_{max} (kN)	Minimum fatigue load F'_{min} (kN)	Frequency (Hz)
D-0	160	60	5
D-50	160	60	5
D-75	160	60	5
D-100	160	60	5

beam. The beams used in all the tests below suffered different freeze-thaw cycles and then suffered fatigue action. Figure 11 illustrates the midspan strain of the beam's upper flange plate, whereas Figure 12 illustrates the change in midspan tensile strain of the beam's lower flange plate. Moreover, Figure 13 illustrates the change in midspan displacement of the beam's lower flange plate, whereas Figure 14 illustrates the change in compressive strain of the beam's upper 1/4 part. In addition, Figure 15 illustrates the change in tensile strain of the lower 1/4 part of the beam, whereas Figure 16 illustrates the change in the midspan displacement of the lower 1/4 flange plate of the beam.

From Figures 11–15, the following can be observed: (1) The strain and displacement of prestressed concrete beams that experienced freeze-thaw cycles were larger in comparison with the prestressed concrete beams that did not experience freeze-thaw cycles. In this situation, the change in compressive strain of the midspan part of the beam is evident. The compressive strain increased as the freeze-thaw cycles increased such that the compressive strain increased rapidly for 50 freeze-thaw cycles. This tendency is mainly reflected in the static load test on the test beams with different freeze-thaw cycles (50, 75, and 100 times). The

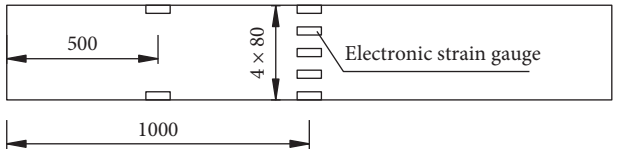

Figure 4: Longitudinal view of the electronic strain gauge location (unit: mm).

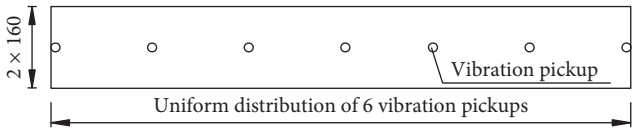

Figure 5: Location of vibration pickup in top area (unit: mm).

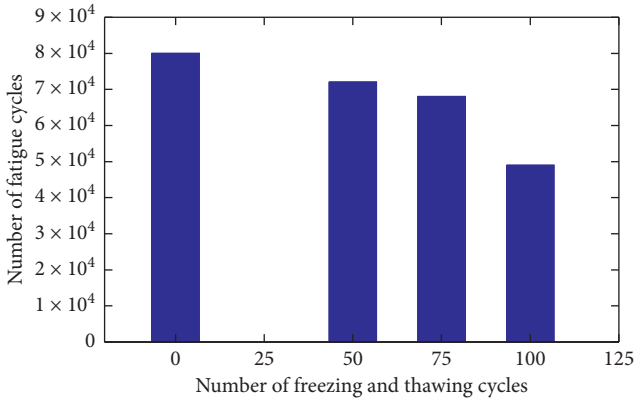

Figure 6: Fatigue loading times of beams with different freeze-thaw cycles.

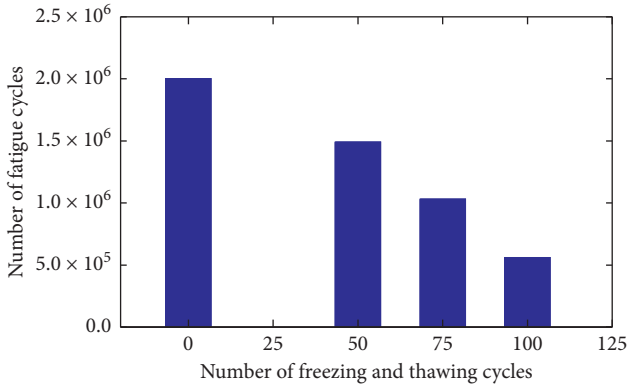

Figure 7: Fatigue loading times of beams with different freeze-thaw cycles.

different freeze-thaw cycles the beam suffers, the more the number of freeze-thaw cycles is and the bigger the compressive strain is. Moreover, the compressive strain increases considerably as the freeze-thaw cycles increase similar to midspan displacement. Thus, the compressive strain of the beam's upper flange plate increased as the number of freeze-thaw cycles increased. For 5.0×10^5 fatigue loading actions, the strain increases rapidly as the beam suffers 100 freeze-

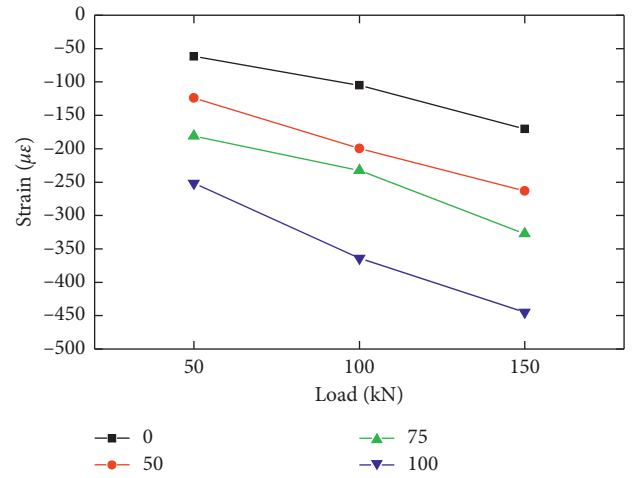

Figure 8: Compressive strain at the top of the test beam under three-stage loading for different freeze-thaw cycles before fatigue.

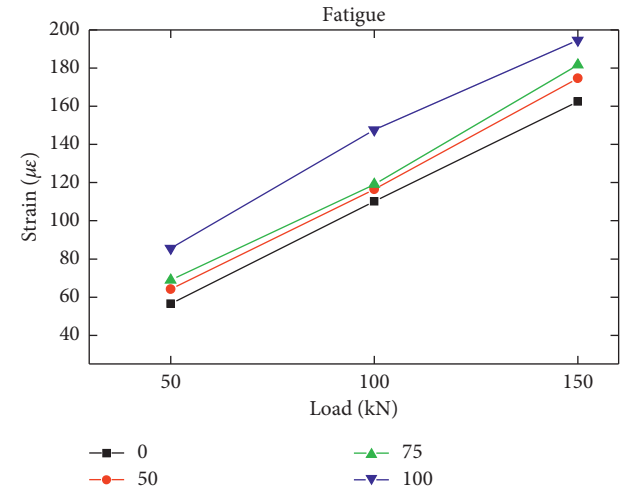

Figure 9: Different freeze-thaw cycles before fatigue test load under tensile strain beam span.

thaw cycles. This may be due to the development of cracks or concrete failure. (2) Considering the tensile strain in the midspan and 1/4 bottom part of the beam, the bottom strain of four groups of beams increases slightly. In Figure 12, when fatigue loading actions reach 1.0×10^6 times, the difference that freeze-thaw cycles lead to is evident compared with the midspan tensile strain. Thus, the change rule of tensile strain of the beam's 1/4 parts is not evident. (3) In Figures 13 and 16, the beam displacement increased as the freeze-thaw cycles increased, thereby indicating that the influence of freeze-thaw cycles on the bending performance of beam is high. For example, the midspan displacement of the test beams with the same fatigue times increases gradually with the increase of freeze-thaw times.

To study the influence of freeze-thaw cycles on strain and displacement of beam comprehensively, four groups of beams were prepared as a test object, based on the condition that the smallest number of fatigue failure loads is 5.0×10^5. To study the compressive strain at the top midspan of the

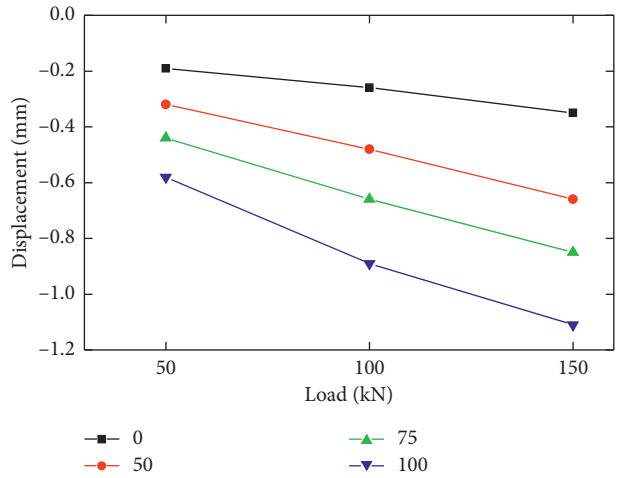

Figure 10: Midspan displacement under three-stage load of test beam for different freeze-thaw cycles before fatigue.

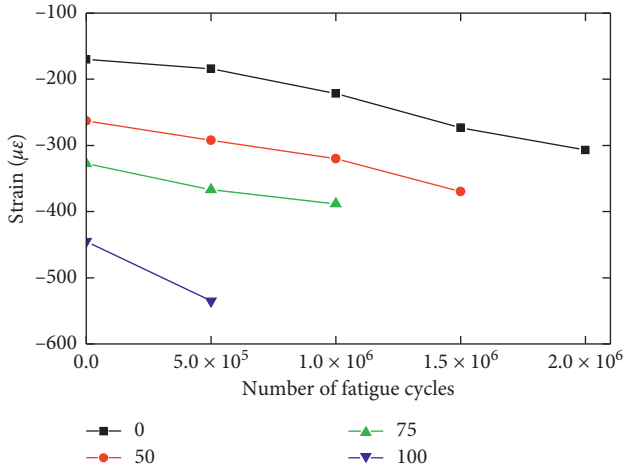

Figure 11: Compressive strain at the top of the span under fatigue action of test beams for different freeze-thaw cycles.

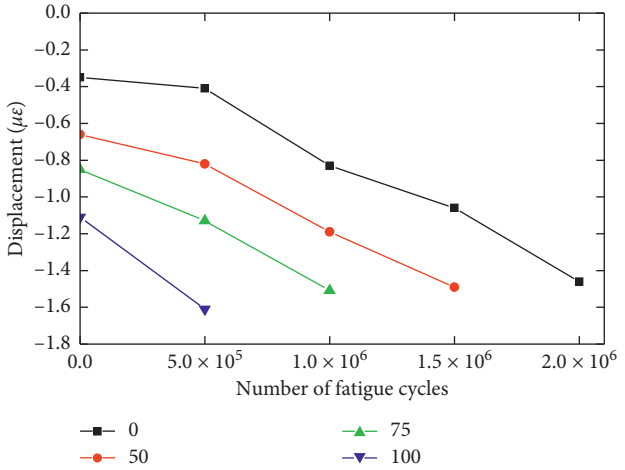

Figure 13: Midspan displacement of test beams subjected to fatigue for different freeze-thaw cycles.

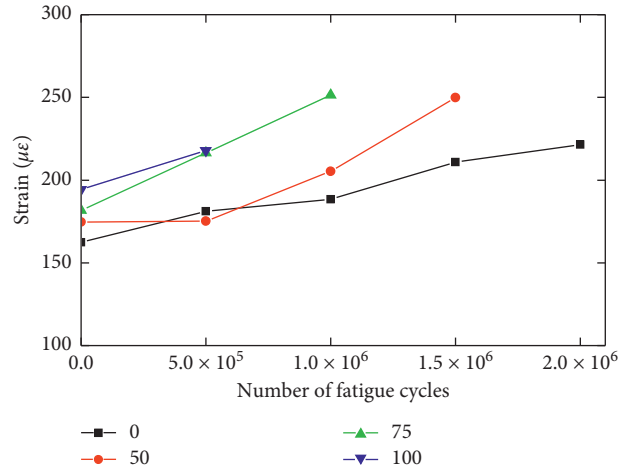

Figure 12: Tensile strain at the bottom of the span under fatigue action of test beams for different freeze-thaw cycles.

beam and displacement at the bottom midspan of the beam, the number of fatigue loading actions of beam ranges from 0 to 5.0×10^5. Figure 17 illustrates the percentage of increase of compressive strain at the top midspan of the beam, while Figure 18 illustrates the percentage of increase of displacement at the bottom midspan of the beam.

In Figure 17, an expression could be obtained using the number of freeze-thaw cycles N and percentage of increase Y as follows:

50–75 freeze-thaw cycles: $Y_2 = 0.000383539N$.

75–100 freeze-thaw cycles: $Y_3 = 0.003262578N$.

In Figure 18, an expression could be obtained using the number of freeze-thaw cycles N and percentage of increase Y as follows:

50–75 freeze-thaw cycles: $Y = 0.319714795N$

75–100 freeze-thaw cycles: $Y = 0.43727398N$

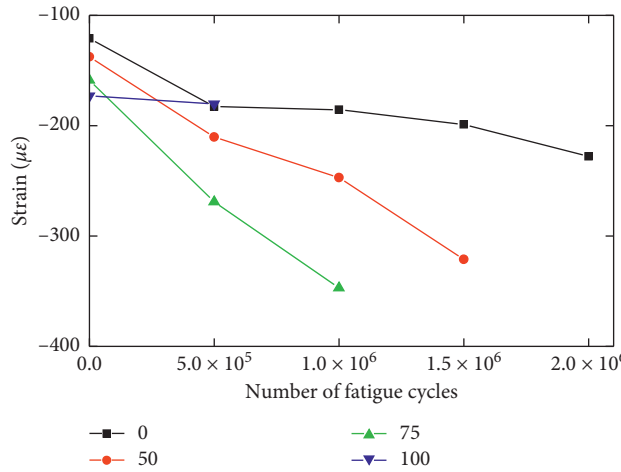

Figure 14: Compressive strain at the top of 1/4 test beams for different freeze-thaw cycles.

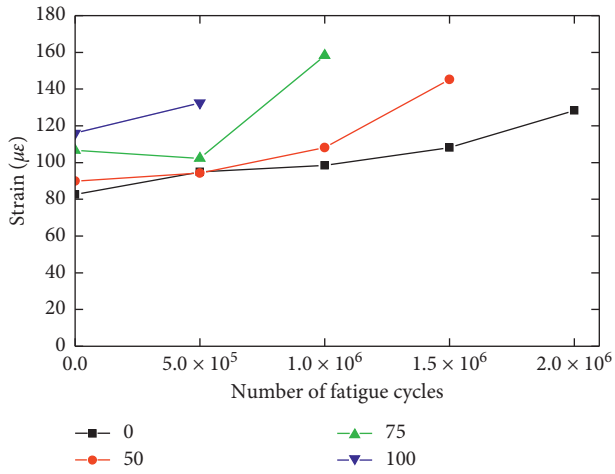

Figure 15: Tensile strain at the bottom of 1/4 test beams subjected to fatigue for different freeze-thaw cycles.

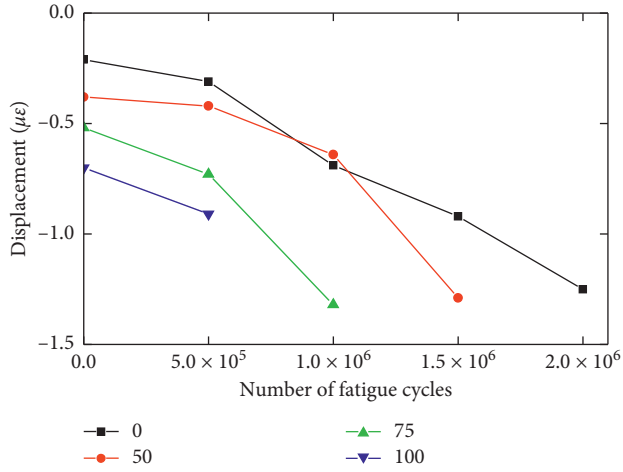

Figure 16: 1/4 displacement of test beams subjected to fatigue for different freeze-thaw cycles.

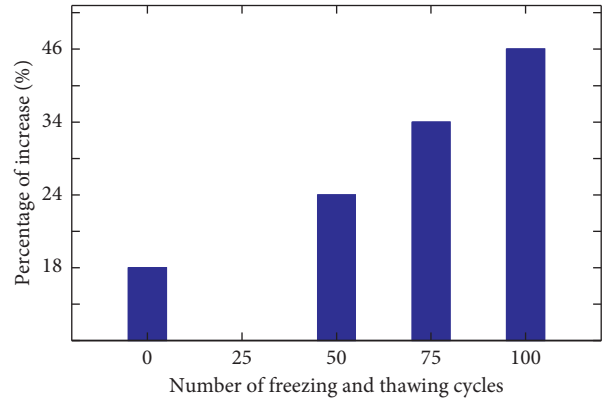

Figure 17: Percentage of increase of compressive strain of test beam from 0 to 5.0×10^5 times for different freeze-thaw cycles.

In Figures 17 and 18, the two groups of histograms show an increasing trend. The slope of the expression increased and indicated that the beam's compressive strain increased significantly as the freeze-thaw cycles increased. This proves that the failure of the upper parts of the beam develops rapidly with the increase in freeze-thaw cycles under the same fatigue actions, the midspan displacement significantly increases, and downwarping occurs increasingly quickly. These are similar to the situation where the amount of failure fatigue load and the amount of cracking load decrease.

3.3.3. Dynamic Load Results after Fatigue Load. The dynamic load test includes a frequency test and dynamic displacement test, daubing the yellow grease on the bottom of vibratory sensors. The vibratory sensors were placed in a similar way to that in Figure 5, and the results are illustrated in Figure 19. Strain and displacement were measured in the same manner. Moreover, an ultrasonic acquiring instrument with a collecting frequency of 50 Hz was used in the displacement test, where the test probes were placed at the bottom and center of the beam. Then, a signal acquiring instrument that was developed by Beijing Oriental Institute

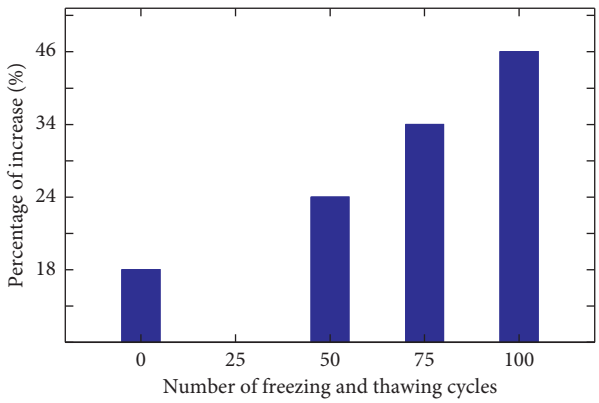

Figure 18: Percentage of increase of displacement test beam from 0 to 5.0×10^5 times for different freeze-thaw cycles.

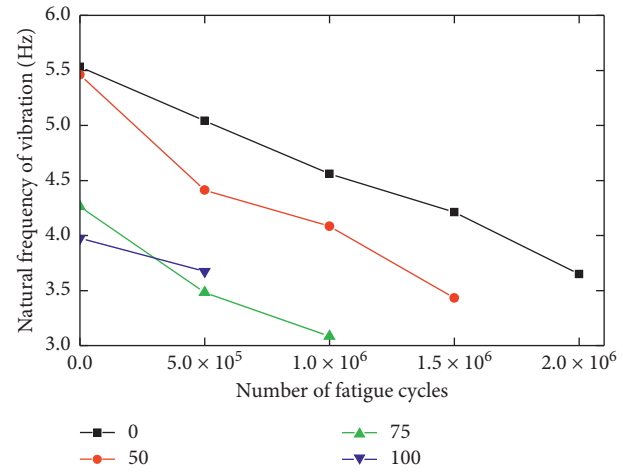

Figure 19: Fundamental frequency value of different freeze-thaw cycle test beams under fatigue action.

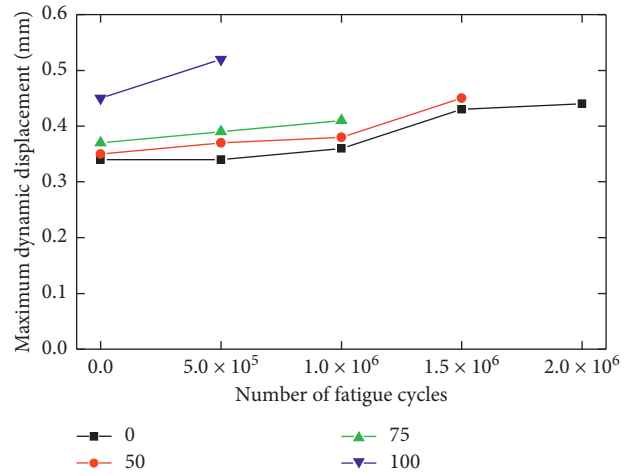

Figure 20: Peak value of dynamic displacement wave under fatigue action of test beams for different freeze-thaw cycles.

of Technology was used to capture vibration and noise. The test was then performed under fatigue loading actions, and the results are illustrated in Figure 20.

The natural frequency decreased as the fatigue loading actions increased and decreased as the freeze-thaw cycles increased. In Figure 20, the crest value of dynamic displacement increased after experiencing frost erosion and after fatigue action for the same freeze-thaw cycles.

4. Conclusions

(1) As the freeze-thaw cycles increase, the time point of crack failure of prestressed concrete beams crack after freeze-thaw cycles under fatigue actions is earlier than that of the beam without freeze-thaw cycles. Furthermore, the speed of development of the beam's fatigue cracks is faster than that in the beam that never suffered frost erosion.

(2) As the freeze-thaw cycles increase for the same number of fatigue loading actions, the compressive strain at the upper flange plate and the tensile strain at the lower flange plate of the beam increase. Moreover, as the number of freeze-thaw cycles increases further, this tendency increases faster. The change in the compressive strain at the upper flange plate is significant. However, the change in tensile strain is insignificant before 1.0×10^6 fatigue actions and gradually becomes significant after 1.0×10^6 fatigue actions.

(3) The beam's midspan displacement increases during this process. Thus, freeze-thaw cycles have an influence on the blending resistance performance of the test beam and accelerate the decrease in the stiffness of the beam.

(4) Based on the strain and displacement histograms and by fitting linear formula, we can see that, with an increase in freeze-thaw cycles under the same fatigue loading action, the compressive strain at the upper flange plate and displacement of midspan tend to increase. The compressive strain progressively increases, which proves that the modulus of elasticity decreases after the freeze-thaw cycles. Although the freeze-thaw cycles accelerate the degree of deflection, the increasing speed of displacement is lower than the increasing speed of compressive strain. Thus, the prestressed concrete beam's health decreases.

(5) Depending on the data of the beam natural frequency test, the natural frequency of the beams decreases as the freeze-thaw cycles increase, as damage occurs in the beam's internal parts when stiffness decreases during the frost period. Meanwhile, cracks occur in the beam under fatigue loading actions. These cracks develop further, thereby leading to a decrease in the bearing capacity and stiffness of the beam. Thus, the natural frequency decreases.

Data Availability

The data used to support the findings of this study are included within the article.

Conflicts of Interest

The authors declare that they have no conflicts of interest.

Acknowledgments

This work was supported by the Natural Science Foundation of Henan (Grant No. 51508114), Science and Technology Program of the Communications Department of Henan Province (Grant No. 2014K37-2), Foundation Sponsored by Program for Science and Technology Innovation Talents in Universities of Henan Province (Grant No. 16HASTIT012), and Outstanding Young Talent Research Fund of Zhengzhou University (Grant No. 4). The authors acknowledge the test field support of the Communications Department of Henan Province and also acknowledge the advice and support of Dr. Pan Ernian of the University of Akron.

References

[1] X. Liu and G. Tang, "Research on prediction method of concrete freeze-haw durability under field environment," *Chinese Journal of Rock and Mechanics and Engineering*, vol. 26, no. 12, pp. 2412–2419, 2007.

[2] T. C. PoWers, "A working hypothesis for further studies of frost resistance," *Journal of the American Concrete Institute*, vol. 16, no. 4, pp. 245–272, 1945.

[3] T. C. PoWers and H. El Muthra, "Theory of volume change in hardened portland cement paste during freezing," *Highway Research Board*, vol. 32, pp. 85–21, 1953.

[4] B. He, MingjunXie, Z. Jiang, C. Zhang, and XinpingZhu, "Temperature field distribution and microstructure of cement-based materials under cryogenic freeze-thaw cycles," *Construction and Building Materials*, vol. 234, pp. 1–14, 2020.

[5] L. Hua, "A potential damage mechanism of rubberized cement under freeze-thaw cycle," *Construction and Building Materials*, vol. 252, pp. 1–12, 2020.

[6] W. Jin and Y. Zhao, "*The Durability of Concrete Structure*," Science Press, Beijing, China, 2002.

[7] V. Penttala, "Surface and internal deterioration of concrete due to saline and non-saline freeze-thaw loads," *Cement and Concrete Research*, vol. 36, no. 5, pp. 921–928, 2006.

[8] Y.-R. Zhao, L. Wang, Z.-K. Lei, X.-F. Han, and Y.-M. Xing, "Experimental study on dynamic mechanical properties of the basalt fiber reinforced concrete after the freeze-thaw based on the digital image correlation method," *Construction and Building Materials*, vol. 147, pp. 194–202, 2017.

[9] B. Wu and Z. Li, "Mechanical properties of compound concrete containing demolished concrete lumps after freeze-thaw cycles," *Construction and Building Materials*, vol. 155, pp. 187–199, 2017.

[10] R. Zhong and K. Wille, "Influence of matrix and pore system characteristics on the durability of pervious concrete," *Construction and Building Materials*, vol. 162, pp. 132–141, 2018.

[11] A. N. Ababneh and Y. Xi, "Evaluation of environmental degradation of concrete in cold regions," in *Proceedings of the 13th International Conference on Cold Regions Engineering*, American Society of Civil Engineers, Orono, ME, USA, pp. 1–10, July 2006.

[12] Q. Wu, H. Yu, and X. Chen, "A Service life prediction method of concretes based on mass loss rate: establishment and narration of mathematical model," in *Proceedings of the 10th International Conference of Chinese Transportation Professionals*, American Society of Civil Engineers, Beijing, China, pp. 3253–3260, August 2010.

[13] Y.-R. Zhao, L. Wang, Z.-K. Lei, X.-F. Han, and J.-N. Shi, "Study on bending damage and failure of basalt fiber reinforced concrete under freeze-thaw cycles," *Construction and Building Materials*, vol. 163, pp. 460–470, 2018.

[14] A. J. Boyd and A. Leone, "Effect of freeze-thaw cycling on fatigue behaviour in concrete," *Materials Science and Engineering*, vol. 652, pp. 1–6, 2019.

[15] T. Cho, "Prediction of cyclic freeze-thaw damage in concrete structures based on response surface method," *Construction and Building Materials*, vol. 21, no. 12, pp. 2031–2040, 2007.

[16] H. Peng, F. Asce, J. Yu, and J. Zhang, "Experimental investigation of bond between near-surface-mounted cfrp strips and concrete under freeze-thawing cycling," *American Society of Civil Engineers*, vol. 32, no. 1, Article ID 4018125, 2019.

[17] Li Guo, D. U. Jian Min, X. S. Wu, and K. Yang, "Resistance of concrete to Na_2SO_4 freeze-thaw cycles and failure mechanism analysis," *Key Engineering Materials*, vol. 711, pp. 335–342, 2016.

[18] E. Vesikarle, "*Service Life Design of Concrete Structure with Regard to Frost Resistance of Concrete*," pp. 215–228, Nordic Concrete Research, Oslo, Norway, 2018.

[19] S. Chen, X. Song, and X. Liu, "Compressive strength degradation and evolution of failure surfaces in compressively preloaded concrete under freeze-thaw cycles," *Materials Research Innovations*, vol. 19, pp. 433–437, 2015.

[20] W. Wang, X. Yang, S. Huang, D. Yin, and G. Liu, "Experimental study on the shear behavior of the bonding interface between sandstone and cement mortar under freeze-thaw," *Rock Mechanics and Rock Engineering*, vol. 53, no. 2, pp. 881–907, 2019.

[21] F. Zhang, S. Li, J. Ye, and S. Li, "Evolution model of concrete failure surface under coupling effect of seawater freeze-thaw and erosion," *Journal of Southeast University(English Edition)*, vol. 27, no. 2, pp. 206–209, 2011.

[22] B. P. Sinha, K. H. Gcrstlc, and L. G. Tulin, "Stress-strain relations for concrete under cyclic loading," *ACI Journal*, vol. 61, no. 2, pp. 195–211, 2014.

[23] И. А. Matapob, "*Performance Research of Reinforced Concrete Flexural Members Performance Study*," Beijing: Science Press, Beijing, China, 1964.

[24] M. Schläfli and E. Brühwiler, "Fatigue of existing reinforced concrete bridge deck slabs," *Engineering Structures*, vol. 20, no. 11, pp. 991–998, 1998.

[25] K. Aas-Jakobsen and R. Lenschow, "Behavior of reinforced columns subjected to fatigue loading," *Journal of the American Concrete Institute*, vol. 70, no. 3, pp. 199–206, 1973.

[26] R. Tepfers and T. Kutti, "Fatigue strength of plan, ordinary, and lightweight concrete," *Journal of the American Concrete Institute*, vol. 76, no. 5, pp. 199–206, 1979.

[27] S. Zhao, "Experimental study on fatigue behaviors of reinforced concrete plates," *Journal of Basic Science and Engineering*, vol. 7, no. 3, pp. 289–297, 1999.

[28] G. Zhao, *High Reinforced Concrete Structural Study*, China Electric Power Press, Beijing, China, 1999.

[29] Yi Cheng and S. Shen, "The fatigue crack propagation laws and their application in the research on fatigue property of concrete," *Journal of Harbin University of Civil Engineering & Architecture*, vol. 33, no. 5, pp. 20–24, 2000, in Chinese.

[30] W. Yi, C. Wang, and P. Shen, "Actual vibration test examples of concrete structures and their analysis," *Journal of Hunan University*, vol. 22, no. 3, pp. 96–103, 1995.

[31] I. Yeo, S. Shin, H. S. Lee, and S.-P. Chang, "Statistical damage assessment of framed structures from static responses," *Journal of Engineering Mechanics*, vol. 126, no. 4, pp. 414–421, 2000.

[32] F. Vestroni and D. Capecchi, "Damage detection in beam structures based on frequency measurements," *Journal of Engineering Mechanics*, vol. 126, no. 7, pp. 761–768, 2000.

[33] K.. Fu, "The fatigue properties of prestressed concrete structure in an erosion environment with fatigue subjoining freezing-thawing circle," , Master thesis, Zhenjiang:Faculty of Civil Engineering and Mechanics, Zhenjiang, China, 2008.

[34] J. Lu, L. Tian, L. Tong, and K. Zhu, "Dynamic properties of concrete subjected to combined action of fatigue load and freeze-thaw cycles," *Journal of Biomechanical Science and Engineering*, vol. 26, no. 5, pp. 1055–1066, 2018.

[35] K. Shi, Y. Zhang, X. Wang, and Y. Dai, "Analysis of reliability of pre-stressed concrete fatigue system in freezing and thawing environment based on Monte Carlo method," *Journal of Jiangsu University of Science and Technology (Natural Science Edition)*, vol. 32, no. 5, pp. 740–745, 2018.

[36] R. Liu, Y. Zhang, and Y. Chen, "Fatigue damage model of prestressed concrete beams suffered freeze–thawing," *Journal Of Jiangsu University (Natural Science Edition)*, vol. 33, no. 1, pp. 115–119, 2012.

[37] "Standard for test methods for physical and mechanical properties of concrete," 2019.

[38] X. Zhao, X. Wang, Z. Wu, and Z. Zhu, "Fatigue behavior and failure mechanism of basalt FRP composites under long-term cyclic loads," *International Journal of Fatigue*, vol. 88, pp. 58–67, 2016.

Hindawi
Advances in Civil Engineering
Volume 2020, Article ID 8847494, 12 pages
https://doi.org/10.1155/2020/8847494

Research Article

Statistical Characteristics of Polymer Grouting Material Microstructure

Juan Wang,[1,2] **Xun Li**,[2] **Hongyuan Fang**,[2] **Juan Zhang**,[1] **and Jinping Li**[1]

[1]*CCCC First Highway Consultants Co., Ltd., State Key Laboratory of Road Engineering Safety and Health in Cold and High-Altitude Regions, Xi'an, Shaanxi 710075, China*
[2]*School of Water Conservancy Engineering, Zhengzhou University, Zhengzhou 450001, China*

Correspondence should be addressed to Xun Li; lixun_zzu@163.com and Hongyuan Fang; fanghongyuan@zzu.edu.cn

Received 5 June 2020; Revised 15 July 2020; Accepted 5 August 2020; Published 30 August 2020

Academic Editor: Grzegorz Golewski

The two-component foaming polyurethane is a kind of grouting material that has recently been widely used in engineering structural repair. Its physical and mechanical properties are closely related to its microstructure. Therefore, the qualitative and quantitative analysis of polymer microstructure has always been a research hotspot. The statistical characteristics of polymer grouting material microstructure are investigated by six groups of specimens with different densities, and the density varies from 0.1 to 0.6 g/cm^3. The microstructure morphology of polymer was observed and described by scanning electron microscopy (SEM), and the microstructure feature parameters were extracted and calculated by image processing technology. The quantitative analysis of section cell roundness distribution, cell diameter distribution, and polymer porosity shows that low-density polymer materials have anisotropy. While the density exceeds 0.3 g/cm^3, the cell structure tends to be spherical. The section cell diameters obey a normal distribution, and when the density increases, the cell diameter decreases. The porosity of the polymer has a linear negative correlation with the density. The polymer matrix has a density of 1.21 g/cm^3. The microstructural information obtained in this study will help establish a cell-based model to explain the mechanical response of rigid polymer foams.

1. Introduction

Nonwater reacted polymer grouting materials produced via a two-component polyurethane foam are a new kind of grouting materials [1]. Under grouting pressure, the polymer material reacts chemically, expands in volume, and rapidly solidifies [2]. This material has a good compressive strength [3], relatively high tensile strength [4], and good water impermeability [5]. It has been widely used in foundation reinforcement, void filling, antiseepage plugging, and other repair projects [6–9].

With the increase in engineering applications, the engineering properties of polymer grouting materials have also received extensive attention. In recent years, the research on the engineering properties of rigid polyurethane (RPU) has mainly focused on the relationship between material density, cellular microstructure, and physicomechanical properties. Hawkins et al. [10] studied the relationship between cell morphology, density, and mechanical properties in different positions of polyurethane samples with three mold sizes. The results showed that there is a relationship between cellular morphology and compression modulus and collapse stress in foamed plastics. And the shape and direction of cell not only affect the failure mechanism, but also affect the mechanical data. The authors of [11–14] studied the stress-strain behavior, microstructure characteristics, fatigue behaviour, and failure mode of RPU grouting materials under uniaxial compression, dynamic compression, and cyclic loading. Studies have shown that RPU grout materials with different densities show elastoplastic or atypical brittle characteristic; the main mechanical properties increase with increasing of density. In addition, the compressive failure of the material was caused by a yielding of the cell edges, and the manifestation of the microscopic fatigue failure was the expansion of the cracks in the cell walls and buckling of the cell edges. Ridha et al. [15] conducted experiments on the

tensile properties of RPU materials, studied their microstructure characteristics, such as the size and geometric composition of the cells and struts, and defined the cell edges. The results showed that the cells were elongated under a tensile load; therefore, the material exhibited anisotropy, and the flexure of the struts at the cell edges were the main mechanism controlling the deformation and failure. Zheng et al. [16] conducted a study on RPU grouting materials through three-point bending load and uniaxial compression tests and analyzed the mechanical behavior using a cell structure model. The results showed that the bending and compressive strengths of the polymer increased with the increase in density. In addition, with the increase in the density, the cell size decreased, and the degree of edge and corner polymerization between the cells decreased. Therefore, the antidamage ability of the cell was enhanced and the compression strength finally increased. Wu and He et al. [17, 18] studied the failure of RPU foam under a high temperature and vibration, and the degree of damage after treatment was evaluated through its tensile properties. The results showed that the tensile strength decreases with the increase in vibration amplitude and time, and the vibration failure of RPU foam was mainly due to the existence of microcracks in the cell structure. With the increasing heat-treating temperature, the stress concentration in the RPU foam increased, and the tensile strength and modulus decreased due to the comprehensive effect of cell wall degradation and the generation of new defects.

The microimages of polyurethane polymers directly reflect many characteristics of the cellular structure. Through image analysis, many characteristics of the cell structure can be measured and characterized. According to the different image types, the image analysis and characterization methods of cell structure can be divided into 2D image analysis method and 3D image analysis method [19, 20]. The comparison between the two methods is shown in Table 1.

Two-dimensional image analysis methods include microimage acquisition and computer image analysis methods. The 2D image of the cell structure is usually obtained by optical microscope (OM) [21–23] or scanning electron microscope (SEM) [24, 25]. The objective magnification of SEM can be changed from 10 times to more than 300,000 times. It can be used to detect small structural characteristics of foam, such as structural defects that damage the foam of samples [17, 18]. Computer image analysis method consists of image processing technology and image analysis technology [26]. Image processing technology corrects the blurring and other defects in the cell structure image and strengthens the cell information, so as to achieve the basic goal of correction and improvement of image quality. Image graying and threshold segmentation are common methods in 2D image processing. Computer image analysis technology refers to the extraction, description, and recognition of the characteristics (porosity, cross-section size, and cross-section shape of the cell) in the cell structure image based on a certain algorithm. However, the 2D image of cellular structure is a cross-section image of 3D structure, so the cell structure characteristics reflected in 2D images are not directly equivalent to the actual size of the feature in three-dimensional space. Therefore, it is necessary to transform the features of 2D cell structure image into the actual 3D cell structure parameters according to the principles of solid geometry and statistics [27, 28].

In the same way, the 3D image analysis method needs to acquire the micro 3D structure image and carry out the computer 3D image processing. The 3D cell structure image needs to be obtained by 3D imaging methods, including optical tomography(OT) [29], laser confocal microscopy (LCM) [30], magnetic resonance imaging (MRI) [31, 32], X-ray computerized tomography (X-CT) [30, 33], and so on. On the basis of complex 3D image processing algorithm, three-dimensional cell structure analysis and characterization of foam materials can be made by using a professional 3D image processing toolkit. Watershed segmentation and minimum intensity pixelization-based method are two commonly used algorithms for computer 3D image processing [34, 35]. 3D images can reflect the cell morphology of foam plastics in three dimensions, and the cell structure information is much richer than 2D images. However, at present, this technology needs to be improved. The acquisition of 3D image is too expensive, and the processing is complex and time-consuming, so it has not reached the stage of extensive practical application.

In this study, the microstructure of polymer grouting materials was observed and described by SEM, and the geometric characteristics of the size and shape of the cells under different densities were statistically analyzed with image processing technology. The quantitative relationship between geometric parameters such as cell content and size to polymer density are established. The purpose of this work is to provide a strategy for the research on the structure and performance of polymer grouting materials and suggest a potential method to study the mechanical properties and strength mechanism of polymer.

2. Statistics of Polymer Microstructure Characteristics

2.1. Test Overview. The two-component foaming polyurethane is primarily composed of polyols and isocyanates. The raw materials (Wanhua Energysav Science & Technology Group Co., Ltd., Yantai, Shandong, China) for the test are shown in Figure 1. Specimen casting, density measurement, and microstructure observation were carried out on the basis of the current standard GB/T 8813-2008 [36], GB/T 6343-2009 [37], and GB/T 12811-1991 [38]. The test mold adopts a split central cylinder with an inner diameter of 50 mm and a height of 600 mm, and the wall thickness is 10 mm. The one-step mechanical pouring foaming process was used. The two components, called white and black materials, were mixed evenly and quickly into the mold at room temperature (ambient temperature 15°C–20°C). After mixing, the two materials reacted violently and foamed rapidly, and the mold space was quickly filled. After 30 min, the specimen was removed from the mold after forming, and after standing for 3 h, the specimen was cut into a cylinder with a height of 100 mm. The weight of each specimen was taken and

Table 1: Comparison of 2D and 3D image analysis methods.

Image analysis method	Image acquisition method	Computer image analysis method (software packages and algorithms)	Characteristic
2D	OM SEM	Adobe Photoshop Matlab ImageJ Image-Pro plus Image graying Threshold segmentation	Flexibility Simple operation Wide amplification range High resolution Simple and fast target information processing and extraction 2D to 3D conversion required
3D	X-CT MRI OT LCM	Mavi Avizo Aphelion 3D Watershed segmentation Minimum intensity pixelization-based method	Rich information of 3D structure More information can be extracted No damage to the interior of the target test piece High cost of image acquisition Complex processing

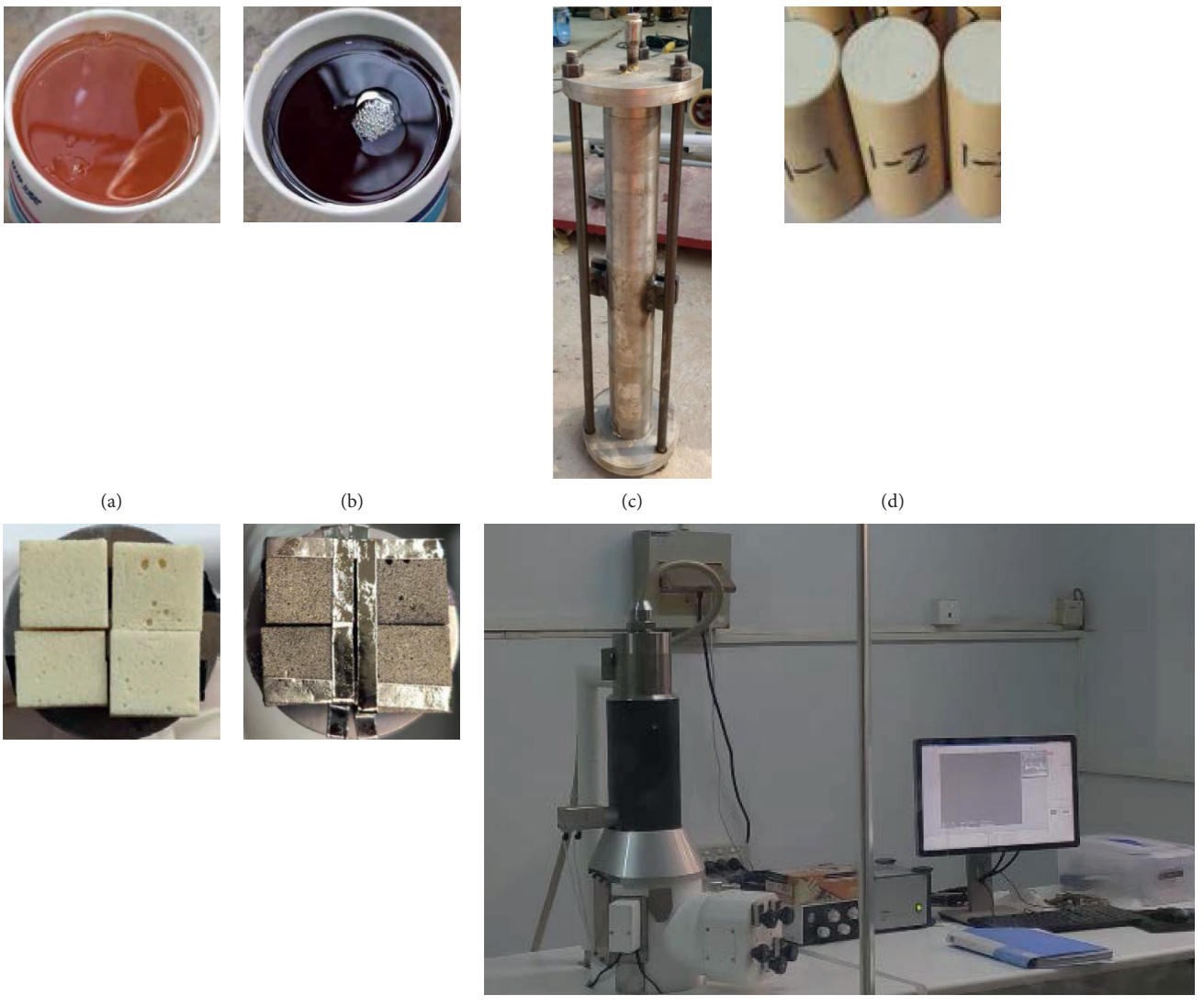

(a) (b) (c) (d)

(e) (f) (g)

Figure 1: Raw material, sample preparation, and the primary instrument. (a) Material A; (b) material B; (c) grouting forming polymer; (d) specimen of polymer; (e) observation sample; (f) target section spraying gold; (g) SEM.

recorded, its actual density was calculated, and the specimens whose density met the requirements were numbered. To analyze the microstructure morphology and statistical characteristics of the polymer grouting materials, six groups of densities were designed, which were 0.1, 0.2, 0.3, 0.4, 0.5, and 0.6 g/cm^3. The measured densities were 0.11, 0.25, 0.31, 0.40, 0.51, and 0.56 g/cm^3, respectively.

The microstructure of the polymer samples was observed by SEM. The samples used for the SEM test were processed as follows. A cylindrical core sample was taken along the center of the specimen with a core drilling machine (round drill bit, outer diameter 38 mm, inner diameter 2.8 mm) and then cut to a thickness of 20 mm on a machine tool. To improve its conductivity, the target section of the sample was sprayed with gold prior to the observation. A scanning electron microscope (KYKY-EM6200, Beijing Zhongke Science and Technology Co., Ltd., Beijing, China) was used to observe the section of the sample, and structure images of the cells were taken.

2.2. Microstructure Feature Extraction

2.2.1. Microstructure Variables. The polymer grouting material has a kind of cell structure, whose internal feature parameters mainly include cell shape [34], cell size [39], cell size distribution [25], and cell content [10]. The parameters of roundness, cell diameter, and porosity are often used to measure the above geometric characteristics. The definition and calculation formula of each variable are as follows.

(1) Section roundness (n) is the percentage of the ratio of 4π times the area to the perimeter square [27], represented in (1). The section roundness indicates the degree to which each cell section tends to be round. The percentage is closer to 100%, and the shape of the cell section is closer to be a circle; that is, when $n = 100\%$, the cell section is circular.

$$n = \frac{4\pi \cdot s}{c^2} \times 100\%, \tag{1}$$

where c is the perimeter of the cell section, and s is the area of the cell section.

(2) Section cell diameter (d) is the calculated size of a single cell in the cross-section. Each cell is equivalent to a circle, and the cell size is represented by the equivalent diameter of the circle. The length of the line segment passing through the centroid of the cell was measured every 2°, and then the average value, which is recorded as the cell diameter, is calculated.

Section average cell diameter ($\overline{d}$) is the arithmetic mean of all cell diameters in the statistical section, represented as

$$\overline{d} = \frac{\sum n_i d_i}{\sum n_i}. \tag{2}$$

In this formula, d_i is a possible value of the cell section diameter, and n_i is the number of cells with a cell diameter of d_i.

Standard deviation of section cell diameter (S) is the distribution of the diameter of the cells in the statistical section, represented as

$$S = \sqrt{\frac{1}{N-1}\sum_{i=1}^{N}\left(d_i - \overline{d}\right)^2}, \tag{3}$$

where N is the total number of cells in the sample, d_i is the diameter of any cell section, and $\overline{d}$ is the section average cell diameter.

It is assumed that the cell is spherical and disordered. When the number of cells on the SEM image tends to infinity, there is also a quantitative relationship between the section average cell area and the average cell diameter. As shown in Figure 2, when a 2D image plane passes through a cell, the distance from the cross-section to the center of the cell is random, and the section area of the cell changes accordingly.

When the number of cells passing through the two-dimensional image plane is large, the average cross-sectional area of cells ($\overline{A}$) tends to a fixed value related to the cell diameter (D) [11], which is shown as follows:

$$\overline{A} = \int_0^R A\frac{dx}{R} = \frac{1}{R}\int_0^R \pi\left(R^2 - x^2\right)dx = \frac{2}{3}\pi R^2 = \frac{\pi}{6}D^2. \tag{4}$$

The cell diameter (D) can also be expressed by the average cell cross-sectional area ($\overline{A}$):

$$D = \left(\frac{6}{\pi}\right)^{1/2}\overline{A}^{1/2} = 1.382\overline{A}^{1/2}, \tag{5}$$

where A is the area of any cell section, x is the distance from the section to the cell center, and R is the cell diameter.

The formula for calculating the standard deviation of cell diameter can be obtained by the differential equation (5):

$$S_D = \left(\frac{6}{\pi}\right)^{1/2}(\overline{A})^{-1/2}S_A = 1.382\,(\overline{A})^{-1/2}S_A, \tag{6}$$

where S_D is the standard deviation of cell diameter and S_A is the standard deviation of the sectional area of the cell.

(3) Porosity (f) is the ratio of the gas phase volume to the total volume, represented as

$$f = \frac{V_s}{V_f}. \tag{7}$$

In this formula, V_s is the volume of the gas phase, and V_f is the total volume of the polymer.

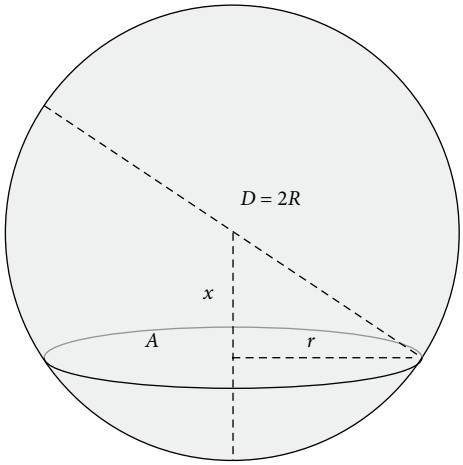

Figure 2: Method of converting 2D area measured from SEM image to 3D diameter of a foam cell in a RPU specimen.

It is difficult to directly measure the volume of the gas phase; therefore, the gas phase is determined according to the basic equation (8) of quantitative metallography [40].

$$V_V = A_A = L_L. \tag{8}$$

In this formula, V_V is the volume fraction of the measured phase, A_A is the area fraction of the measured phase, and L_L is the line segment fraction of the measured phase.

2.2.2. Analysis of the Structural Variables of Polymer Grouting Materials. Image processing technology was used to preprocess the SEM image. According to the definition of the microstructure variables, relevant geometric parameters in the image are extracted and the distribution characteristics are analyzed. The main steps are as follows.

(1) Image preprocessing: The noncell information pixels on the picture are cut out, and the image with the largest size range is used. The size of the cropped image is approximately 4 mm × 4 mm, and each image can contain hundreds of cells, as shown in Figures 3(a) and 3(b).

(2) Image reconstruction: Under the principle of image fidelity, the cells in the SEM image are filled with black by ImageJ software. Then, the filled SEM image is binarized to obtain black cells in a white background through MATLAB software, so that the target cells are highlighted (none of the above operations change the image pixel density). The reconstructed SEM image is shown in Figure 3(c).

(3) Boundary processing: First, the incomplete cells at the edges of the picture are removed. Some of the cells in the material's microstructure will be in contact with each other, and the smaller the density is, the more obvious this phenomenon is; therefore, the boundaries need to be processed. Based on the original image, the cells that touch each other are segmented by the Split Objects function of the Image-Pro Plus software. The SEM image of the edge cell removal and the contact cell segmentation is shown in Figure 3(d).

(4) Microstructure variable statistics: A pixel analysis is performed on the image obtained from steps 2 and 3 by the Image-Pro Plus software. The porosity is obtained from the reconstructed image, and the other structural variable values are calculated from the removed and segmented image. All measured samples are counted, the microstructure variables of the polymers are calculated, and their distribution characteristics are analyzed.

3. Results and Discussion

3.1. Microstructure of Polymers. The formation of cells in polyurethane polymer materials is mainly described by the foaming process. Generally, the foaming process is divided into three stages: the nucleation of small bubbles in the liquid polymer, growth of small bubbles to a predetermined volume, and stabilization of the cell structure [24]. After curing, the polyurethane polymer material can be prepared. Figure 4 shows the microstructure of polymers with different magnification at different densities. Figures 4(a), 4(d), 4(g), 4(j), 4(m), and 4(p) are SEM images of the polyurethane polymer materials at approximately 20 times magnification for six groups of densities. It can be seen that, on the microscopic scale, the material is composed of closely contacted and closed cells. The difference in the material density is mainly due to the structural characteristics of the cells, except for the density of the polymer matrix material. As the density increases, the shapes of the polymer cells tend to change from polygons to ellipses and circles, the cell diameter decreases, the cell spacing increases, and the porosity decreases.

For 0.11 g/cm^3 SEM image, in Figure 4(b) (magnified 100 times), the cell diameter is generally greater than 150 μm, the cell structure is irregular and nonuniform, and the cell cross-section is generally hexagonal. The contact surface (face) between each cell is large, and the faces with a thin film means that the cells have a high closed cell ratio. The strut is between two adjacent faces. The vertex is at strut intersection. Most of the matrix material is concentrated on the struts and vertices that make up the cell frame. In Figure 4(c) (magnified 200 times), the faces are generally greater than 50 μm, and the face shape is oval. There are usually twelve faces in the cell, which means that the cell is a dodecahedron. There are many triangle cut struts, and the struts are long and thin. It can be seen that struts play a major supporting role. Under load, struts will buckle and faces will crack [13].

For 0.25 g/cm^3 SEM image, in Figure 4(e) (magnified 100 times), the cell diameter is generally greater than 120 μm, and the cell structure is an ellipse with large ellipticity. The number of intracellular faces slightly decreased, and the face is relatively large. In Figure 4(f) (magnified 200 times), the faces are generally greater than 40 μm, and the face shape is round or oval. The number of intracellular faces decreased. The struts become thicker and shorter, and the triangle cut strut reduction.

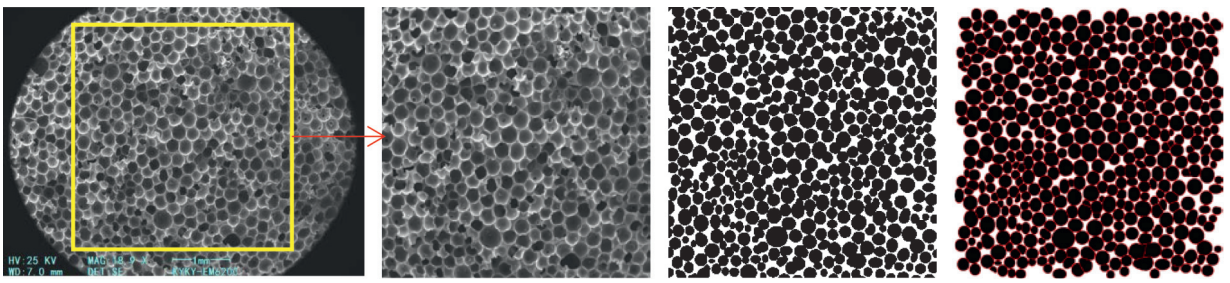

(a) (b) (c) (d)

Figure 3: SEM image processing steps for the polyurethane polymer microstructure. (a) Raw SEM image; (b) cropped image; (c) reconstructed image; (d) removed and segmented image.

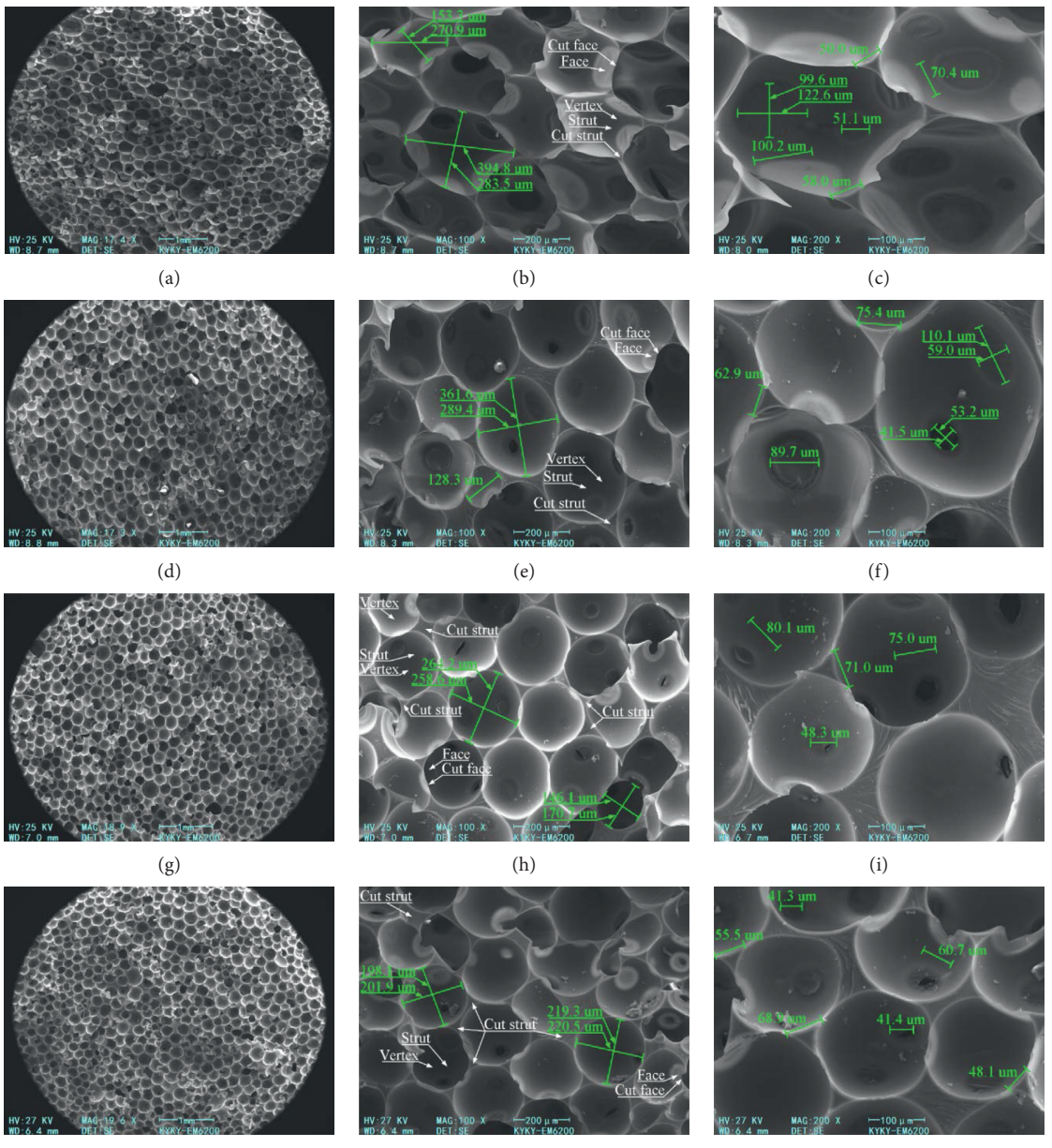

(a) (b) (c)

(d) (e) (f)

(g) (h) (i)

(j) (k) (l)

Figure 4: Continued.

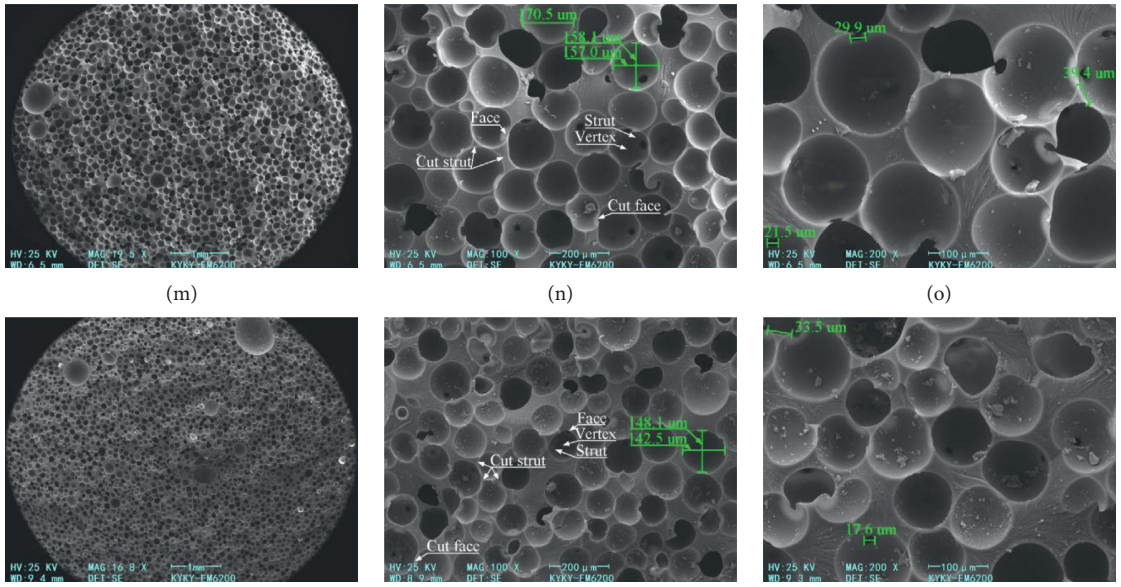

Figure 4: Microstructure of polymers at different densities. (a) 0.11 g/cm^3; (b) detail of (a); (c) detail of (b); (d) 0.25 g/cm^3; (e) detail of (d); (f) detail of (e); (g) 0.31 g/cm^3; (h) detail of (g); (i) detail of (h); (j) 0.40 g/cm^3; (k) detail of (j); (l) detail of (k); (m) 0.51 g/cm^3; (n) detail of (m); (o) detail of (n); (p) 0.56 g/cm^3; (q) detail of (p); (r) detail of (q).

For 0.31 g/cm^3 SEM image, in Figure 4(h) (magnified 100 times), the cell diameter is generally less than 260 μm, and the cell shape is circular or elliptical. The face is relatively small. The cells basically meet the closest packing. In Figure 4(i) (magnified 200 times), the faces are usually less than 50 μm, and the shape of the face tends to be circular. The number of triangle cut struts further reduces, the polygonal cut strut increases, and the length of strut is reduced.

For 0.40 g/cm^3 SEM image, in Figure 4(k) (magnified 100 times), the cell diameter is generally less than 220 μm, and the cell shape is an ellipse with very small ellipticity. Some adjacent cells do not contact each other and there are a lot of matrix materials between them, and the number of face further reduced. In Figure 4(l) (magnified 200 times), the faces are usually less than 40 μm, and the faces are with a thin film. The part of the adjacent triangular cut struts merges, and the struts are wide and short.

For 0.51 g/cm^3 SEM image, in Figure 4(n) (magnified 100 times), the cell diameter of the specimen is generally less than 180 μm, and the cell shape is round or oval with a small ellipticity. The face is extremely small. The matrix material of adjacent cells increased. In Figure 4(o) (magnified 200 times), the faces are usually less than 30 μm, and the number of intracellular faces decreased significantly. The cut strut of triangle is obviously reduced.

For 0.56 g/cm^3 SEM image, in Figure 4(q) (magnified 100 times), the cell diameter of the specimen is generally less than 150 μm, and the cell shape is basically round. There are almost no windows mean cells do not touch. There are a lot of matrix materials between cells. In Figure 4(r) (magnified 200 times), the faces are usually less than 20 μm. There are almost no triangle cut struts. It can be seen that the strength of polymer increases with the increase of matrix material content and cell spacing [16].

3.2. Statistical Analysis of the Polymer Cell Geometry. By observing the SEM morphology of the polyurethane polymer material, an intuitive understanding of the cell structure of the polymer is obtained, which provides a basis for determining the geometric characteristics of the cell. The statistical results of the roundness distribution, cell diameter distribution, and porosity are as follows.

3.2.1. Section Roundness Distribution. Figure 5 is a section cell roundness distribution diagram for polyurethane polymer samples of each density. It can be seen from Figure 4 that, for low-density materials, the section cells with a roundness between 90% and 100% account for only 50% to 70% of the total cells, and there are a few cells with a section roundness less than 75%. The reason for this phenomenon is that the cells squeeze each other due to the increase in cell diameter, and the shape tends to be an ellipsoid or an irregular polyhedron. When the density of the polymer is higher than 0.3 g/cm^3, the proportion of cells with a section roundness of 90% to 100% is higher than 80%, and the section roundness of most of the cells is higher than 75%. Therefore, with the increase in density, the shape of the polymer cells tends to be round.

As shown in Table 2, the statistical parameters of the section roundness of the cells at each density is further calculated. It can be seen that as the density of the polymer increases, the average value of the section roundness of the cells increases. By comparing the average values and median of the section roundness at each density, it can be seen that the anisotropy of the cells in the specimen is not serious, especially that the high-density specimen is basically close to the ball, which may be related to the location of the sample in

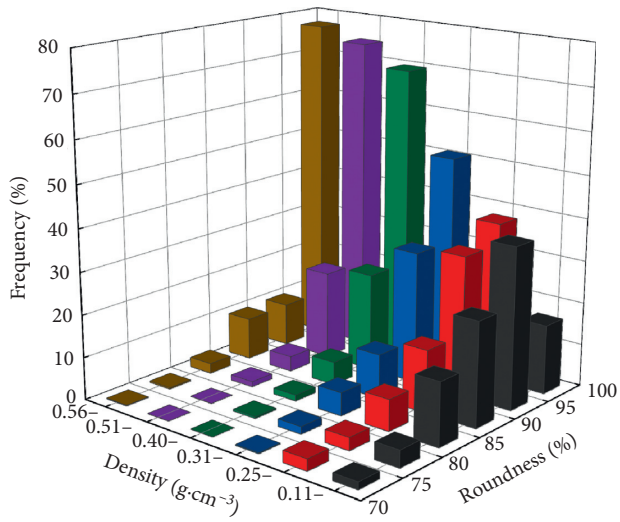

Figure 5: Section cell roundness distribution of polyurethane polymer samples of various densities.

Table 2: Summary of the statistical parameters of the section cell roundness.

Density (g/cm^3)	Average (%)	Standard deviation	Minimum (%)	Median (%)	Maximum (%)
0.11	89.58	5.86	68.23	90.81	98.99
0.25	91.43	6.70	60.68	93.75	99.81
0.31	93.53	4.96	65.16	95.23	100
0.40	95.66	3.48	76.36	96.71	99.84
0.51	95.76	2.86	81.73	96.25	100
0.56	95.90	3.93	73.37	96.70	100

the specimen [10], so it is appropriate to use the average sphere size to characterize the cell size in (4). When the density exceeds 0.3 g/cm^3, the section roundness of the cells approaches 100%, and this result indicates that the shape of the cells is closer to a sphere, and the macroscopic performance is close to isotropic.

3.2.2. Cell Diameter Distribution. Figure 6 is a section cell diameter distribution chart for the polyurethane polymer specimens with different densities. It can be seen from Figures 6(a)–6(f) that the section cell diameter distribution of each density specimen basically follows the normal distribution. As the density of the specimen increases, the length and endpoint of the section cell diameter distribution interval decreases. Figure 7 shows a summary of the section cell diameter distribution. It can be seen from Figure 7 that as the density of the specimen increases, the overall size of the section cell diameter decreases, and the degree of dispersion of the section cell diameter distribution also decreases. And the average section cell diameter and standard deviation of the specimens at each density are negatively correlated with the density.

As shown in Table 3, the statistical parameters of the section cell diameter distribution of the cells at each density is further calculated. With the increase of density, the statistical parameters tend to decrease.

According to (5), the average section cell area measured by the computer two-dimensional image analysis software Image-Pro Plus is transformed into the cell diameter. According to (6), the standard deviation of the cell cross-section area is converted into the standard deviation of the cell diameter. In this way, the measured two-dimensional area can be transformed from SEM image to three-dimensional cell diameter and distribution. The average cell diameter, standard deviation, and density of the polymer materials were fitted, and it is found that they have a basically linear relationship. Figure 8 is a fitting graph of each cell diameter parameter and density.

As shown in Figure 8(a), a linear fitting of the average cell diameter and density can be obtained as follows:

$$D = -371.19\rho + 323.29, \tag{9}$$

where D is the average cell diameter, and ρ is the polymer density.

As shown in Figure 8(b), a linear fitting of the standard deviation and density of the cell diameter distribution can be obtained as follows:

$$S_D = -172.22\rho + 143.93, \tag{10}$$

where S_D is the standard deviation of the cell diameter distribution, and ρ is the polymer density.

The quantification of cell size is helpful to understand the influence of microstructure on the mechanical properties of

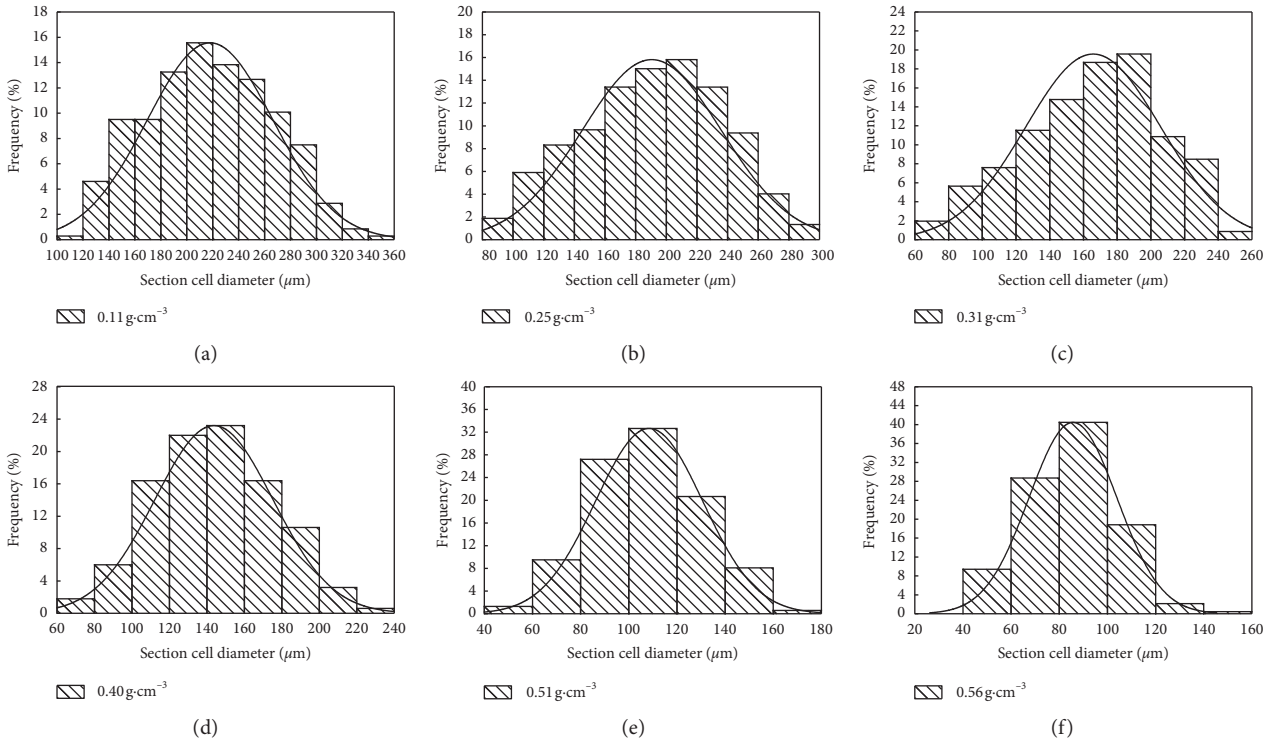

Figure 6: Section cell diameter distribution of polyurethane polymer samples. (a) 0.11 g/cm^3; (b) 0.25 g/cm^3; (c) 0.31 g/cm^3; (d) 0.40 g/cm^3; (e) 0.51 g/cm^3; (f) 0.56 g/cm^3.

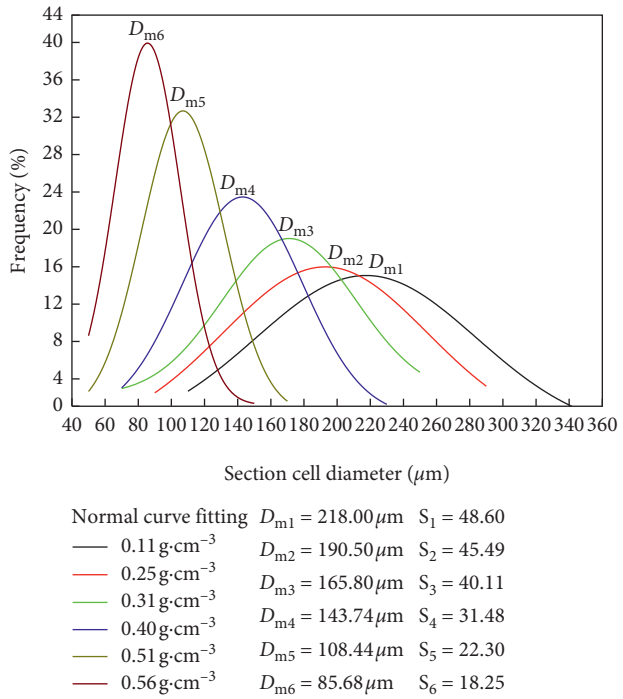

Figure 7: Summary of the section cell diameter distribution (D_{m1}–D_{m6} are the average section cell diameters, and S_1–S_6 are the standard deviations).

materials. When the cell size is large, the compressive property of the material is mainly determined by the strut. According to the previous studies, the critical cell size of the turning point which defines the influence of cell size on compressive strength increases with the increase of density. The results show that the cell size of 0.60 g/cm^3

Table 3: Summary of the statistical parameters of the section cell diameter distribution.

Density (g/cm^3)	Average (μm)	Standard deviation	Minimum (μm)	Median (μm)	Maximum (μm)
0.11	218.00	48.60	111.05	215.39	350.56
0.25	190.50	45.49	92.44	190.98	286.29
0.31	165.80	40.11	70.75	170.85	253.20
0.40	143.74	31.48	64.26	144.11	230.41
0.51	108.44	22.30	50.76	109.31	178.38
0.56	85.68	18.25	42.54	85.92	147.25

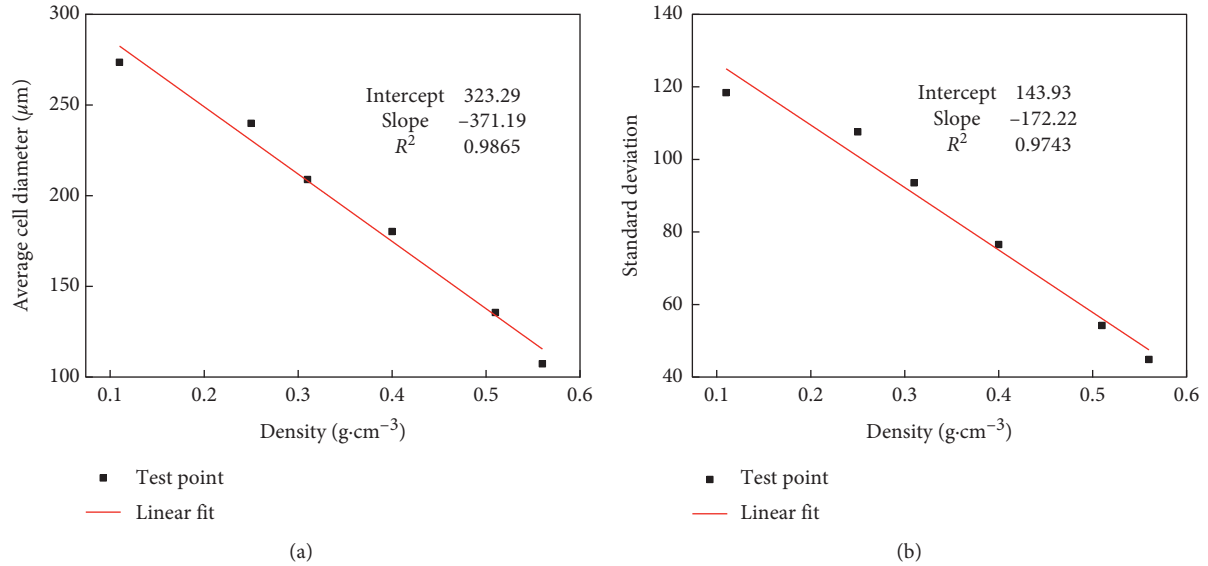

Figure 8: Relationship between cell diameter and density. (a) Relationship between average cell diameter and density; (b) relationship between standard deviation and density.

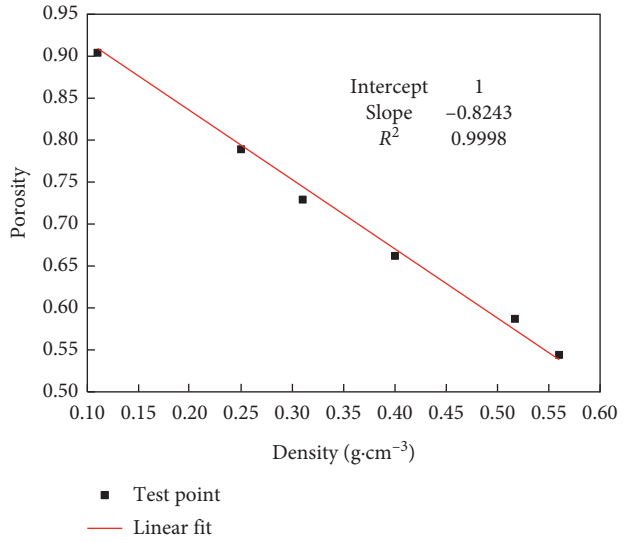

Figure 9: Relationship between porosity and density.

specimen is more than 60 μm, which is larger than the critical cell size [41]. Therefore, it can be inferred that the compression failure of materials is caused by the yielding of struts [11].

3.2.3. Polymer Porosity. The density of the polyurethane polymer material is obviously related to the polymer porosity and density of the matrix. As shown in Figure 9, as the density increases, the polymer porosity decreases.

A linear fit of the porosity and density of the polymer yields the following relationship:

$$f = -0.8243\rho + 1. \quad (11)$$

In this formula, f is the porosity, and ρ is the polymer density.

According to (11), when the porosity is 0, the polymer matrix density is 1.21 g/cm^3. It is basically consistent with the description in literature [42] that the matrix density of rigid polyurethane foam is about 1.2 g/cm^3.

4. Conclusions

In this study, micromorphology SEM images of the specimens were observed, and feature parameters were counted. The microstructural information obtained in this study will help establish a cell-based model to explain the mechanical response of rigid polymer foams. The main results and conclusions are as follows:

(1) The cells of the low-density polymer material are deformed due to the mutual extrusion of the cells, which are irregular polyhedrons or ellipsoids. Therefore, low-density polymer materials have anisotropy. As the density increases and exceeds 0.3 g/cm^3, the cell structure tends to be spherical, and the polymer materials are close to isotropic.

(2) The section cell diameters in the same specimen obey a normal distribution, and the section average cell diameter, standard deviation, the length and endpoint of the section cell diameter distribution interval decrease as the density of the specimen increases. The cell diameter and standard deviation have linear negative correlations with the density.

(3) The porosity of the polymer has a linear negative correlation with the density. The polymer matrix has a density of 1.21 g/cm^3.

Data Availability

The data used in the paper are available from the authors upon request.

Conflicts of Interest

The authors declare that there are no conflicts of interest regarding the publication of this paper.

Acknowledgments

The authors would like to acknowledge the financial support received from the National Key Research and Development Program of China (no. 2018YFC1508401) and the Open Fund Project of State Key Laboratory of Road Engineering Safety and Health in Cold and High-Altitude Regions of China (no. YGY2017KYPT-03).

References

[1] H. Liu, F. Wang, M. Shi, and W. Tian, "Mechanical behavior of polyurethane polymer materials under triaxial cyclic loading: a particle flow code approach," *Journal of Wuhan University of Technology*, vol. 33, no. 4, pp. 980–986, 2018.

[2] M. Hao, F. Wang, X. Li, B. Zhang, and Y. Zhong, "Numerical and experimental studies of diffusion law of grouting with expansible polymer," *Journal of Materials in Civil Engineering*, vol. 30, no. 2, 2018.

[3] M. Shi, F. Wang, and J. Luo, "Compressive strength of polymer grouting material at different temperatures," *Journal of Wuhan University of Technology*, vol. 25, no. 6, pp. 962–965, 2010.

[4] M. Shi, *Research on polymer grouting material properties and directional fracturing grouting mechanism for dykes and dams*, PhD Thesis, Dalian University of Technology, Dalian, China, 2010.

[5] N. Rana and R. Nair, "Performance of polyurethane grouting to handle heavy seepage in tunnels," in *Proceedings of the Conference on Recent Advances in Rock Engineering (RARE)*, Bengaluru, India, 2016.

[6] O. Buzzi, S. Fityus, Y. Sasaki, and S. Sloan, "Structure and properties of expanding polyurethane foam in the context of foundation remediation in expansive soil," *Mechanics of Materials*, vol. 40, no. 12, pp. 1012–1021, 2008.

[7] H. Fang, B. Li, F. Wang, Y. Wang, and C. Cui, "The mechanical behaviour of drainage pipeline under traffic load before and after polymer grouting trenchless repairing," *Tunnelling and Underground Space Technology*, vol. 74, pp. 185–194, 2018.

[8] H. Fang, Y. Su, X. Du, F. Wang, and B. Li, "Experimental and numerical investigation on repairing effect of polymer grouting for settlement of high-speed railway unballasted track," *Applied Sciences*, vol. 9, p. 21, 2019.

[9] C. Guo, B. Sun, D. Hu, F. Wang, M. Shi, and X. Li, "A field experimental study on the diffusion behavior of expanding polymer grouting material in soil," *Soil Mechanics and Foundation Engineering*, vol. 56, no. 3, pp. 171–177, 2019.

[10] M. C. Hawkins, B. O'Toole, and D. Jackovich, "Cell morphology and mechanical properties of rigid polyurethane foam," *Journal of Cellular Plastics*, vol. 41, no. 3, pp. 267–285, 2005.

[11] Y. Wei, F. Wang, X. Gao, and Y. Zhong, "Microstructure and fatigue performance of polyurethane grout materials under compression," *Journal of Materials in Civil Engineering*, vol. 29, no. 9, 2017.

[12] L. Shi and Z.-M. Li, "Morphology development of high-density rigid polyurethane foam upon compression by on-line scanning electronic microscope," *Journal of Applied Polymer Science*, vol. 105, no. 4, pp. 2008–2011, 2007.

[13] K. Liu, W. Liang, F. Ren, J. Ren, F. Wang, and H. Ding, "The study on compressive mechanical properties of rigid polyurethane grout materials with different densities," *Construction and Building Materials*, vol. 206, pp. 270–278, 2019.

[14] E. Linul, D. A. Şerban, L. Marsavina, and T. Sadowski, "Assessment of collapse diagrams of rigid polyurethane foams under dynamic loading conditions," *Archives of Civil and Mechanical Engineering*, vol. 17, no. 3, pp. 457–466, 2017.

[15] M. Ridha and V. P. W. Shim, "Microstructure and tensile mechanical properties of anisotropic rigid polyurethane foam," *Experimental Mechanics*, vol. 48, no. 6, pp. 763–776, 2008.

[16] X. Zheng, "Study on relationship between density and mechanical behavior of high polymer grouting materials," *Journal of Wuhan University of Technology*, vol. 36, no. 4, pp. 44–47, 2014.

[17] J. Wu, Y. He, and Z. Yu, "Failure mechanism of rigid polyurethane foam under high temperature vibration condition by experimental and finite element method," *Journal of Applied Polymer Science*, vol. 137, no. 6, 2019.

[18] Y. He, J. Wu, D. Qiu, and Z. Yu, "Experimental and numerical analyses of thermal failure of rigid polyurethane foam," *Materials Chemistry and Physics*, vol. 233, pp. 378–389, 2019.

[19] K. Mader, R. Mokso, C. Raufaste et al., "Quantitative 3D characterization of cellular materials: segmentation and morphology of foam," *Colloids and Surfaces A: Physicochemical and Engineering Aspects*, vol. 415, pp. 230–238, 2012.

[20] S. Pérez-Tamarit, E. Solórzano, A. Hilger, I. Manke, and M. A. Rodríguez-Pérez, "Multi-scale tomographic analysis of polymeric foams: a detailed study of the cellular structure," *European Polymer Journal*, vol. 109, pp. 169–178, 2018.

[21] Z. Zakaria, Z. Mohamad Ariff, and A. Abu Bakar, "Monitoring deformation mechanism of foam cells in polyethylene foams via optical microscopy: effect of density and microstructure," *Journal of Cellular Plastics*, vol. 54, no. 6, pp. 957–976, 2018.

[22] C. Yang, Z.-H. Zhuang, and Z.-G. Yang, "Pulverized polyurethane foam particles reinforced rigid polyurethane foam and phenolic foam," *Journal of Applied Polymer Science*, vol. 131, no. 1, 2014.

[23] E. Esmaeilnezhad, M. Rezaei, and M. K. Razavi, "The effect of alternative blowing agents on microstructure and mechanical characteristics of rigid polyurethane foam," *Iranian Polymer Journal*, vol. 18, no. 7, pp. 569–579, 2009.

[24] J. R. Dawson and J. B. Shortall, "The microstructure of rigid polyurethane foams," *Journal of Materials Science*, vol. 17, no. 1, pp. 220–224, 1982.

[25] J. Reignier, P. Alcouffe, F. Mechin, and F. Fenouillot, "The morphology of rigid polyurethane foam matrix and its evolution with time during foaming - new insight by cryogenic scanning electron microscopy," *Journal of Colloid and Interface Science*, vol. 552, pp. 153–165, 2019.

[26] J. Pinto, E. Solórzano, M. A. Rodriguez-Perez, and J. A. de Saja, "Characterization of the cellular structure based on user-interactive image analysis procedures," *Journal of Cellular Plastics*, vol. 49, no. 6, pp. 555–575, 2013.

[27] K. M. Lewis, I. Kijak, K. B. Reuter, and J. B. Szabat, "An image analysis method for cell-size and cell-size distribution measurement in rigid foams," *Journal of Cellular Plastics*, vol. 32, no. 3, pp. 235–259, 1996.

[28] D. L. Sahagian and A. A. Proussevitch, "3D particle size distributions from 2D observations: stereology for natural applications," *Journal of Volcanology and Geothermal Research*, vol. 84, no. 3, pp. 173–196, 1998.

[29] R. Garcia-Gonzales, C. Monnereau, J. F. Thovert, P. M. Adler, and M. Vigners-Adler, "Conductivity of real foams," *Colloids and Surfaces A: Physicochemical and Engineering Aspects*, vol. 151, no. 3, pp. 497–503, 1999.

[30] F. De Pascalis, M. Nacucchi, M. Scatto, and R. Albertoni, "Quantitative characterisation of low-density, high performance polymeric foams using high resolution X-ray computed tomography and laser confocal microscopy," *NDT & E International*, vol. 83, pp. 123–133, 2016.

[31] G. Ovarlez, K. Krishan, and S. Cohen-Addad, "Investigation of shear banding in three-dimensional foams," *Europhysics Letters*, vol. 91, no. 6, Article ID 68005, 2010.

[32] J. Braun, M. O. Klein, J. Bernarding, M. B. Leitner, and H. D. Mika, "Non-destructive, three-dimensional monitoring of water absorption in polyurethane foams using magnetic resonance imaging," *Polymer Testing*, vol. 22, no. 7, pp. 761–767, 2003.

[33] M. Marvi-Mashhadi, C. S. Lopes, and J. Llorca, "Modelling of the mechanical behavior of polyurethane foams by means of micromechanical characterization and computational homogenization," *International Journal of Solids and Structures*, vol. 146, pp. 154–166, 2018.

[34] M. D. Montminy, *Complete structural characterization of foam using 3D images*, PhD Thesis, University of Minnesota, Ann Arbor, MI, USA, 2001.

[35] M. D. Montminy, A. R. Tannenbaum, and C. W. Macosko, "The 3D structure of real polymer foams," *Journal of Colloid and Interface Science*, vol. 280, no. 1, pp. 202–211, 2004.

[36] General Administration of Quality Supervision, "Inspection and quarantine of the People's Republic of China, standardization administration of the People's Republic of China," *Rigid Cellular Plastics-Determination of Compression Properties*, Standards Press of China, China, 2008.

[37] General Administration of Quality Supervision, "Inspection and quarantine of the People's Republic of China and standardization administration of the People's Republic of China," *Cellular Plastics and Rubbers-Determination of Apparent Density*, Standards Press of China, China, 2009.

[38] General Administration of Quality Supervision, "Inspection and quarantine of the People's Republic of China," *Test Method for Average Cell Size of Rigid Cellular Plastics*, Standards Press of China, China, 1991.

[39] J. Xu, T. Wu, J. W. Zhang, H. Chen, W. Sun, and C. Peng, "Microstructure measurement and microgeometric Packing characterization of rigid polyurethane foam defects," *Cellular Polymers*, vol. 36, no. 4, pp. 183–204, 2017.

[40] M. B. Rhodes and B. Khaykin, "Foam characterization and quantitative stereology," *Langmuir*, vol. 2, no. 5, pp. 643–649, 1986.

[41] G. F. Smits, "Effect of cellsize reduction on polyurethane foam physical properties," *Journal of Thermal Insulation and Building Envelopes*, vol. 17, no. 4, pp. 309–329, 1994.

[42] L. J. Gibson and M. F. Ashby, "The mechanics of three-dimensional cellular materials," *Proceedings of the Royal Society of London. A. Mathematical and Physical Sciences*, vol. 382, no. 1782, pp. 43–59, 1982.

Hindawi
Advances in Civil Engineering
Volume 2020, Article ID 8897621, 10 pages
https://doi.org/10.1155/2020/8897621

Research Article

Numerical Analysis on the Bending Performance of Prestressed Superposing-Poured Composite Beams

Jianmin Wang,[1,2] **Chengfeng Zhu**,[1] **Ziqiang Xiao**,[1] **Qijun Zhao**,[1] **and Junzhe Liu**[3]

[1]*School of Civil and Environmental Engineering, Ningbo University, Ningbo 315211, China*
[2]*Key Laboratory of Impact and Safety Engineering, Ministry of Education, Ningbo University, Ningbo 315211, China*
[3]*School of Architecture Engineering, Qingdao Agricultural University, Qingdao 266109, China*

Correspondence should be addressed to Jianmin Wang; wangjianmin@nbu.edu.cn and Junzhe Liu; liujunzhe@nbu.edu.cn

Received 6 June 2020; Revised 20 July 2020; Accepted 10 August 2020; Published 29 August 2020

Academic Editor: Peng Zhang

Aiming at the bending performance of the prestressed superposing-poured concrete beam, the numerical simulation on the composite beams poured with the normal weight concrete (NWC) superposed on the fibred ceramsite lightweight aggregate concrete (LWAC) was conducted. Three kinds of prestressing schemes, straight linear prestressing force, curved prestressing force not across the casting interface, and curved prestressing force across the casting interface, were simulated for comparison, and the influence of the casting interval time was also considered. Results indicate that the stiffness of the superposing-poured beam can be effectively strengthened by considered schemes of the prestressing force; in addition, there are certain increases on the ultimate load except imposing the straight linear prestressing force. As the curved prestressing force is imposed across the casting interface, the maximal interlayer slip of the casting interfacial transition zone (C-ITZ) approximately equals to that without the prestressing force. The scalar stiffness degradation (SDEG) of the C-ITZ for the casting interval time being 14 days is obvious because of the weakening on the bonding performance of the C-ITZ. Comparatively, the SDEG variation of the C-ITZ in the model with the curved prestressing force across the casting interface is smoother and smaller on the whole than the other two prestressed schemes for the case of the casting interval time being 14 days.

1. Introduction

Ceramsite lightweight aggregate concrete (LWAC) possesses the merit with higher strength relative to lighter density, which benefits from the ceramsite characterizing lighter apparent density and rough surface with many small opening holes. The density of LWAC is lighter than that of the normal weight concrete (NWC) for about 25%–30%. In addition, LWAC shows good performance such as the thermal insulation [1–3]. The developing of the prefabricated building technology puts forward higher requirements to the composite concrete members and the functionally graded concrete (FGC) members. Generally, the composite concrete members are composed of the precast and the cast in-situ components. For the composite concrete and FGC, the interfacial bonding performance is prominent to guarantee the integration and compatibility of whole members. Lightweight aggregate can effectively improve the microstructure of the interface in concrete and make the interfacial transition zone (ITZ) more compact because of its own morphological structure and apparent pores [4]. Akmaluddin and Murtiadi [5] discussed the connection behaviour of the composite concrete precast column and the sandwich beam under the static loading. Campi and Monetto [6, 7] proposed a closed solution of two-layer beams considering the interlayer slip, in which a linear and nonproportional law relating interfacial shear tractions and slips was chosen to describe the interfacial behaviour. Iskhakov et al. [8, 9] studied the mechanical property of prestressed composite beams and proposed a new concept that considers the interlayer deformation of concrete in the tension and compression zones. Ji et al. [10] analyzed the change rule of the midspan deflection of prestressed reactive powder concrete (RPC) and the NWC composite beams

considering the influence of the prestressing degree, the RPC height, and the NC strength; the higher the prestressing degree is, the longer the elastic stage before crack is, and the faster the stiffness in strengthening stage after the yielding decreases. Study indicates that the application of prestressing can improve the rigidity of composite beams and reduce the cracks [11, 12]. Wu et al. [13] studied the failure mechanism, flexural capacity, short-term stiffness, and crack distribution of U-shaped and inverted T-shaped prestressed composite beams and pointed out that composite beams with natural rough surface can be analyzed as whole beams not considering the relative slip. Li and Ji [14] analyzed the developing law of the crack during the loading of prestressed composite beams considering different prestressing degrees and prefabricated component heights. Li et al. [15] studied the interfacial bonding performance of the prestressed composite beams with different stirrup spaces and pointed out that the smaller the stirrup spacing is, the less possible the bonding slip occurs on the casting interface.

The related research are mainly focused on the overall performance of composite members composed of NWC without prestressing or only with straight linear prestressing force. Moreover, different casting interval times are necessary to suit the constructional variety of the superposing-poured composite members. The imposing of the prestressing force can effectively increase the stiffness of the concrete beams. Because of the existing of the casting interfacial transition zone (C-ITZ) in the superposed composite beams, the mechanism and performance of the composite beams after exerting the prestressing force is complicated. Besides, the arrangement of the prestressed bars and the casting interval time are great importance to the performance of the composite beams [16]. In this paper, the numerical simulation was conducted on the mechanical performance of the composite beams poured with the NWC superposed on the ceramsite LWAC. Different arrangement ways of prestressed bars and casting interval times were specially discussed on the influence of the overall performance of the superposing-poured beams.

2. Simulation Modelling

2.1. Modelling Scheme. The simulation analysis is based on the bending experiment of the simplified supported superposing-poured beams composed of the ceramsite LWAC and NWC. The precast ceramsite LWAC component at the bottom of the beam mainly bears the tensile force under the experimental load, and the NWC is casted on the LWAC component late. The detailed parameters of the superposing-poured beams are shown in Figure 1, in which the sectional casting height are determined according to the neutral axis in the section of the composite beams. The description on the prestressing schemes and the casting interval time are listed in Table 1. There are eight superposing-poured beam models designed for simulation, in which six models are prestressed superposing-poured beams, and the other two ordinary beams models are based on the experiment used for comparison. The grades of the longitudinal bars and the stirrups bars are HRB400 and HRB300, respectively. The prestressing bars are 1860 grade 1×7 stranded wire, and the prestressing force is 30 kN.

2.2. Material Constitutive Relationship in the Model. The concrete damaged plasticity model (CDP) is used to simulate the mechanical properties of superposing-poured concrete beams in this paper. It describes the inelastic performance of concrete based on the isotropic damage elasticity together with the isotropic stretching and compression damage plasticity. Besides, the CDP model can effectively simulate the dynamic and static mechanical behaviour of the concrete [17, 18]. The mix ratio of the two kinds of concrete in the experimental members B1-1 and B1-2 are listed in Table 2, and the basic mechanical properties of the concrete and reinforced bars are listed in Tables 3 and 4.

The C-ITZ is a typical part zone in the composite beams, which has significant influence on the overall performance of the composite beams. The mechanical property of the C-ITZ is related to the treatment method of the casting interface, the casting interval time, two kinds of concrete materials, and so on. The manual chiselling method was adopted to handle the casting interface in the referring experiment [19]. The cohesive element is used in the model to simulate the C-ITZ in the superposing-poured beam model. The basic mechanical parameters of the cohesive element listed in Table 5 are determined according to the experimental data [16] and the relevant formula [20, 21].

2.3. Model Building. In the model, the concrete and reinforced bars are modelled using the solid element and link element, respectively. Among them, the reduced integral element C3D8R is assigned to simulate the concrete, and the T3D2 truss element is assigned to simulate the reinforced bars in the model. The C-ITZ between the LWAC and NWC in the stack-poured beams are simulated by the cohesive elements. The local rigid bodies are modelled at the loading point and bearings to avoid the stress concentration during the simulation. The boundary constraints and loading scheme are shown in Figure 1 and are identical to the experiment [19].

The application of the prestressing force in the model is realized by the cooling method in the temperature field corresponding to the initial state. In the subsequent analysis step, the prestressing strand shrinks as the temperature reduces to generate the pretension force. The temperature cooling value is determined according to the following formula [22]:

$$\Delta T = \frac{F}{\alpha E A} = \frac{\sigma}{\alpha E}, \tag{1}$$

in which F is the prestressing force, σ is the prestressing stress, A is the cross-sectional area, E is the elastic modulus, and α is the linear expansion coefficient.

3. Simulation Results

3.1. Modelling Verification. The effectiveness of the modelling was first verified by comparing the simulation results of B1-1 and B1-2 with that of the experiment. The load-midspan deflection is shown in Figure 2. The modelling

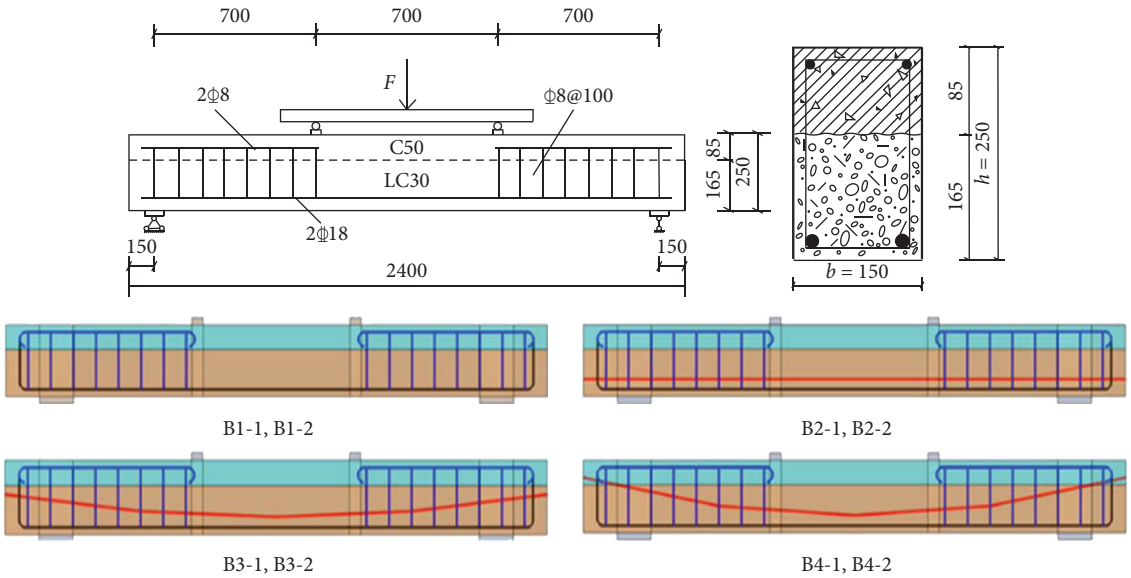

Figure 1: Scheme of the superposing-poured beam model.

Table 1: Description of the superposing-poured beam model.

Model no.	Prestressing schemes	Casting interval time
B1-1*	Superposing-poured beams no prestress	45 minutes
B1-2*		14 days
B2-1	Superposing-poured beams with straight linear prestressed bars	45 minutes
B2-2		14 days
B3-1	Superposing-poured beams with curved prestressed bars not across the casting interface	45 minutes
B3-2		14 days
B4-1	Superposing-poured beams with curved prestressed bars across the casting interface	45 minutes
B4-2		14 days

*For modelling comparison based on the experiment.

Table 2: Mix ratio of LWAC and NWC of the experiment [19].

Concrete	(kg/m^3)						Reinforcement ratio (%)
	Ceramsite	Crushed stone	Sand	Cement	Fly ash	Water	
LC30	820	—	510	440	80	237	1.52
C40	—	1180	580	400	80	200	

Table 3: Mechanical parameters of the concrete from the experiment [19].

Concrete	f_{cu} (MPa)	f_{ck} (MPa)	f_t (MPa)	E_c (MPa)	Density (kg/m^3)
LWAC/LC30	36.2	32.0	3.2	2.55×10^4	1740
NWC/C50	56.1	47.4	4.3	3.55×10^4	2400

Table 4: Mechanical parameters of reinforced bars [16].

Types of bars	Diameter (mm)	Yielding strength (MPa)	Ultimate strength (MPa)
Stirrups	8	364.8	564
Hanger bars	8	364.8	564
Longitudinal bars	20	455.1	580
Prestressing bars*	9.5	1395	1860

*Referring to the code for design of concrete structures (GB 50010-2010).

Table 5: Parameters of the cohesive element to simulate the C-ITZ.

Casting interval time	Modulus E (GPa)	Density ρ (kg/m^3)	Elastic stiffness K_n (N/mm^3)	Cohesion strength σ_n (MPa)	Fracture energy G_f (N/mm)
45 minutes	23	2100	10^6	3.2	0.033
14 days	23	2100	10^6	2.0	0.027

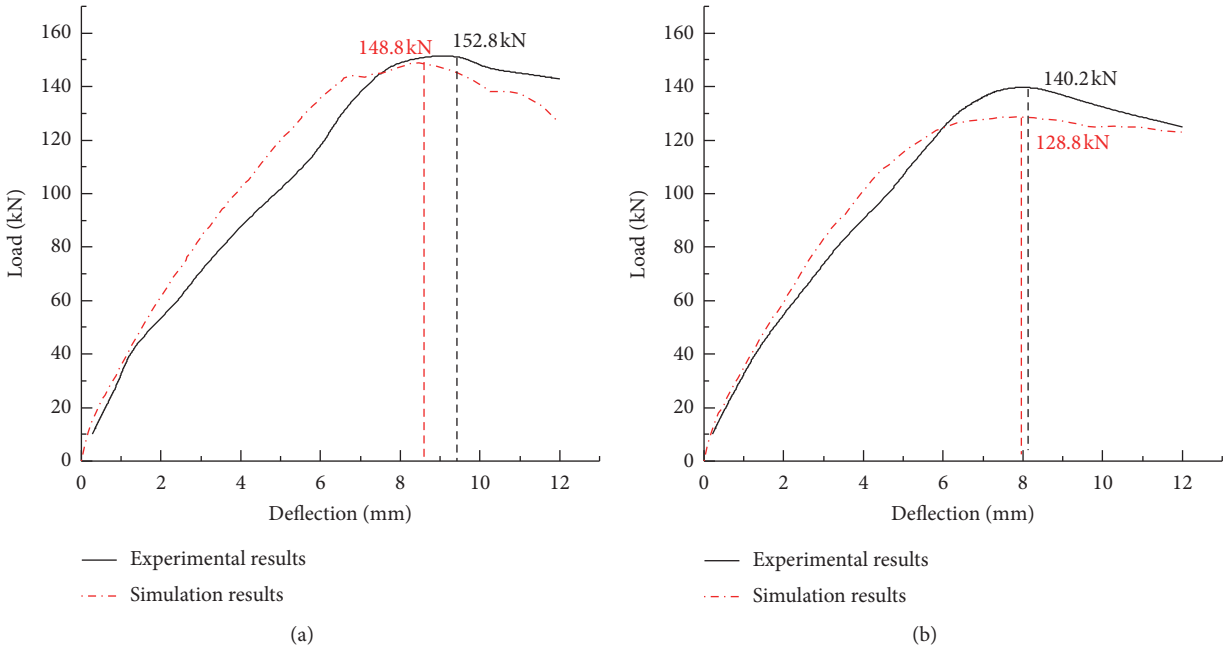

Figure 2: Load-deflection relationship of B1-1 and B1-2. (a) B1-1. (b) B1-2.

results fit well with that from the experiment before the yielding except that the deflection is a little smaller than that of the experiment. This difference becomes obvious during the loading late stage. It is mainly because of the typical influence of the generation of macrocracks in the experiment members as the load increases. Besides, the yielding loads are a little lower than that of the experiment. Considering the variation of the casting interval times, the ultimate load of model B1-2 is lower than that of B1-1 whether from the experiment or from the simulation. It is because the bonding performance of C-ITZ in the superposing-poured beams is weakened as the casting interval time increases. The emerging and developing of the cracks in the model can be represented by the compressive and tensile damage factors of the concrete element, which are shown in Figure 3. The cracks distribution result from the simulation coincides well with that of the experimental result.

At the loading beginning stage, the vertical bending cracks first emerge in the midspan bottom bending zone. The bending cracks develop upward with the loading. At the same time, diagonal cracks also emerge near both two foot bearings and incline upward to the loading points. One important characteristic is that most cracks have a brief stop as they develop close to the C-ITZ. This can be verified both by the experimental and the simulating results. Subsequently, only some cracks develop across the C-ITZ as the load continually increases. Finally, the beam failures due to the yielding of the longitudinal reinforcement and the concrete crack are at the top of the midspan.

In addition, the simulation on the prestressing is verified by comparing the simulation results of B2-1, B3-1, and B4-1 with results from the corresponding calculation method and design codes. The prestressing effect can be represented by the equivalent load method: The effect of straight linear prestressing and curved prestressing are equivalent to the pure bending and uniformly distributed load, respectively. Due to a certain difference existing in the elastic module between LWAC and NWC, the ceramsite LWAC is first converted into NWC by the equivalent section converting method. The inverse arch deflections of the superposing-poured beam model are calculated according to the bending-moment-area method. At the same time, the inverse arch deflections of the straight prestressing and the curved prestressing are calculated [23, 24]:

$$f_Z = \frac{N_{po} e L^2}{8 E_c I_o}, \qquad f_Q = \frac{5 N_{po} e L^2}{48 E_c I_o}, \tag{2}$$

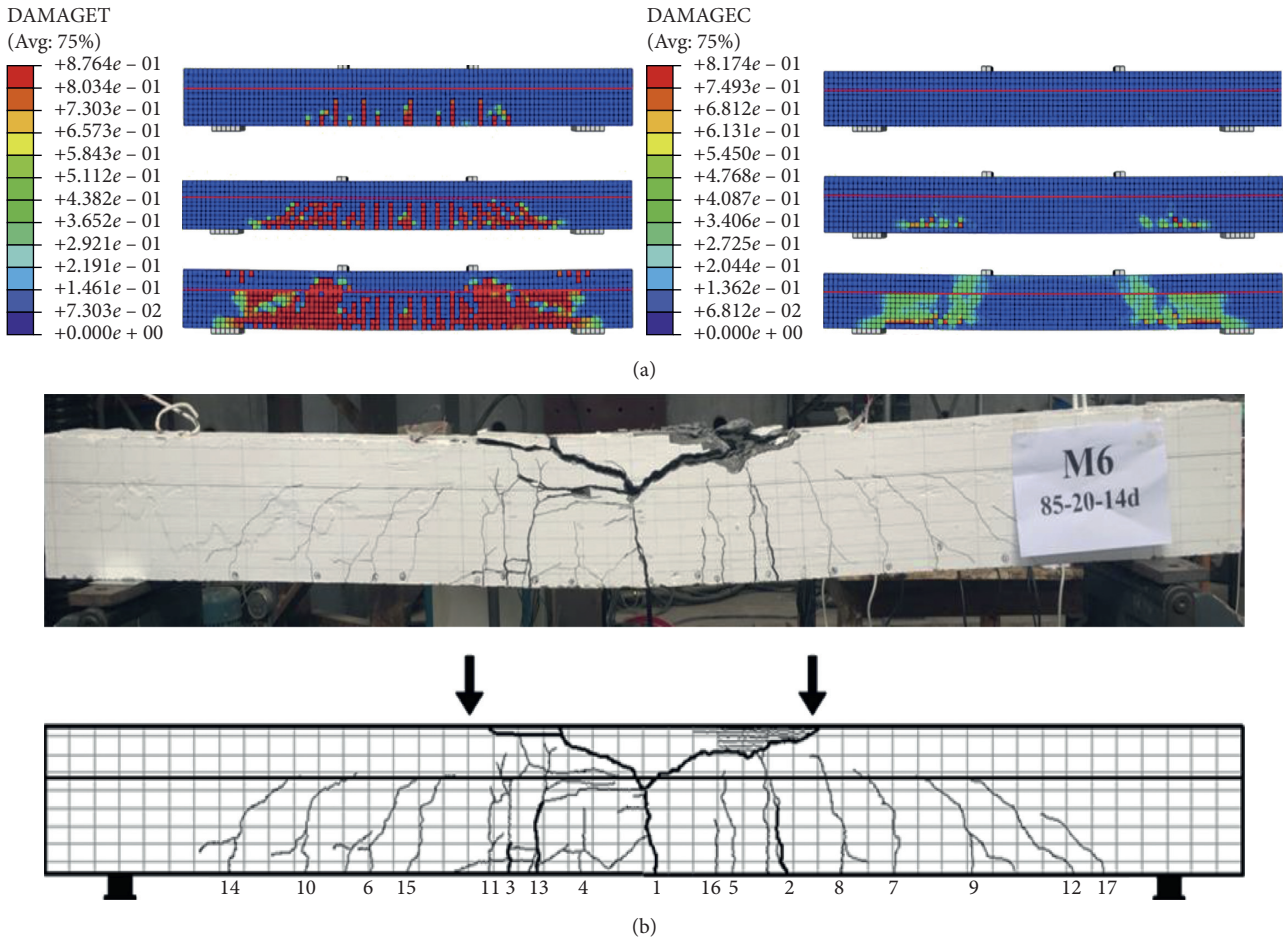

Figure 3: Comparison of cracks distribution of B1-2. (a) The tensile and compressive damage nephogram from the simulation.(b) Experimental beam.

where N_{po} is the effective prestressing force, e is the eccentricity from the center of prestressed bars to the neutral axis of the converted section, L is the span length, E_c is the elastic modulus, and I_o is the inertial moment of the converted section.

The comparison of the results is listed in Table 6. The simulation results are close to that from the referring calculation method and design codes on the whole. Compared with the bending-moment-area method and ACI318-99, it is shown that the result from GB50010-2002 is more reliable due to the stiffness reduction during calculating.

3.2. Load-Deflection Relationship. The load-deflection curves of the superposing-poured beams are shown in Figure 4. Compared with B1-1 and B1-2 without the prestressing force, the midspan deflections of beams with different arrangement modes of prestressed bars are all lower before the yielding load. In addition, there are observable increases on the ultimate loads of beams with prestressed bars except that of B2-1 and B2-2. Compared with the straight linear prestressing scheme at the bottom of the beam, the increases on the ultimate loads of beams with curved prestressed bars are more obvious for different casting interval times.

The simulation results are listed in Table 7. For B2-1 and B2-2 exerting the straight linear prestressing force at the bottom of beams, there is no obvious increasing on the ultimate load compared with B1-1 and B1-2, respectively. But the midspan deflection is clearly smaller than that of B1-1 and B1-2, respectively. The reduction of the deflection is about 23% and 19.9% that of B1-1 and B1-2, respectively. At the same time, the induced inverted arch deflection at the midspan are largest among the three kinds of prestressing schemes.

For the scheme with curved prestressed bars not across the C-ITZ, the ultimate load of B3-1 is clearly increased about 8.7% compared with B1-1 while the deflection is reduced about 8.0%. Comparatively, the ultimate load of B3-2 is increased about 12.5% compared with that of B1-2 with the midspan deflection reduced about 7.0%. It is due to the weakening of the bonding performance of the C-ITZ in the superposing-poured beams, which has significant influence on the deformation of the beam as the load increases. Because the bonding shear performance of the C-ITZ in the superposing-poured beams decreases quickly as the casting interval time increases, and the remaining shear strength

Table 6: Comparison of the inverse arch deflections of the prestressing force.

Model no.	Simulation results	Moment-area method		GB50010-2010		ACI318-99	
	f (mm)	f_1 (mm)	f_1/f	f_2 (mm)	f_2/f	f_3 (mm)	f_3/f
B2-1	0.192	0.184	0.958	0.216	1.125	0.184	0.958
B3-1	0.177	0.158	0.893	0.223	1.260	0.189	1.068
B4-1	0.179	0.174	0.972	0.246	1.374	0.209	1.168

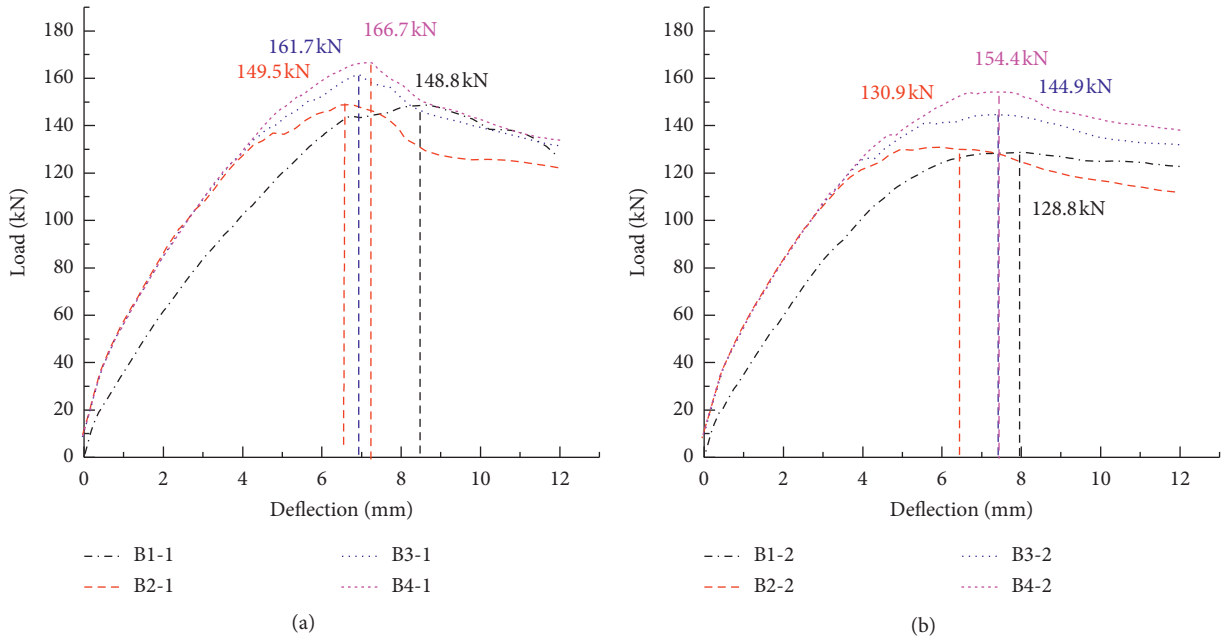

Figure 4: Load-deflection curves of the beam model. (a) 45 minutes casting interval time. (b) 14 days casting interval time.

Table 7: Simulation results of the model.

Model	Inverse arch deflection, f (mm)	Ultimate loads (kN)	Deflection (mm)
B1-1	—	148.8	8.61
B2-1	0.192	149.5	6.63
B3-1	0.177	161.7	6.92
B4-1	0.179	166.7	7.12
B1-2	—	128.8	7.99
B2-2	0.191	130.9	6.40
B3-2	0.179	144.9	7.43
B4-2	0.184	154.4	7.42

with the casting interval time being 14 days is about 40% that casting at the same time [24].

As the curved prestressed bars in the superposing-poured beam models are located across the C-ITZ for the model B4-1 and B4-2, the increase extent of the ultimate loads is 12.0% and 19.9%, respectively, compared with B1-1 and B1-2. At the same time, the midspan deflections are similar to that of B3-1 and B3-2, respectively.

3.3. Relative Slip in the C-ITZ. The cohesive element are adopted to simulate the performance of C-ITZ in the superposing-poured beams. The relative longitudinal slip of the C-ITZ outside the loading point is extracted as shown in Figure 5 for discussion. Whether there is or no prestressing force, the relative slip of C-ITZ in the beam that the casting interval time is 45 minutes is much smaller than that with the casting interval time being 14 days as the load increases. The final maximal relative slip value for all models is listed in Table 8.

For B2-1 and B2-2 exerted the straight linear prestressing force, the final relative slip value is 1.8 times and 2.05 times as large as that of B1-1 and B1-2, respectively, and the relative slip in the C-ITZ both of B1-2 and B2-2 characterizes continual and accelerated increasing with regards to the loading until the final failure.

As imposed, the curved prestressing force with the casting interval time being 45 minutes, the overall variation

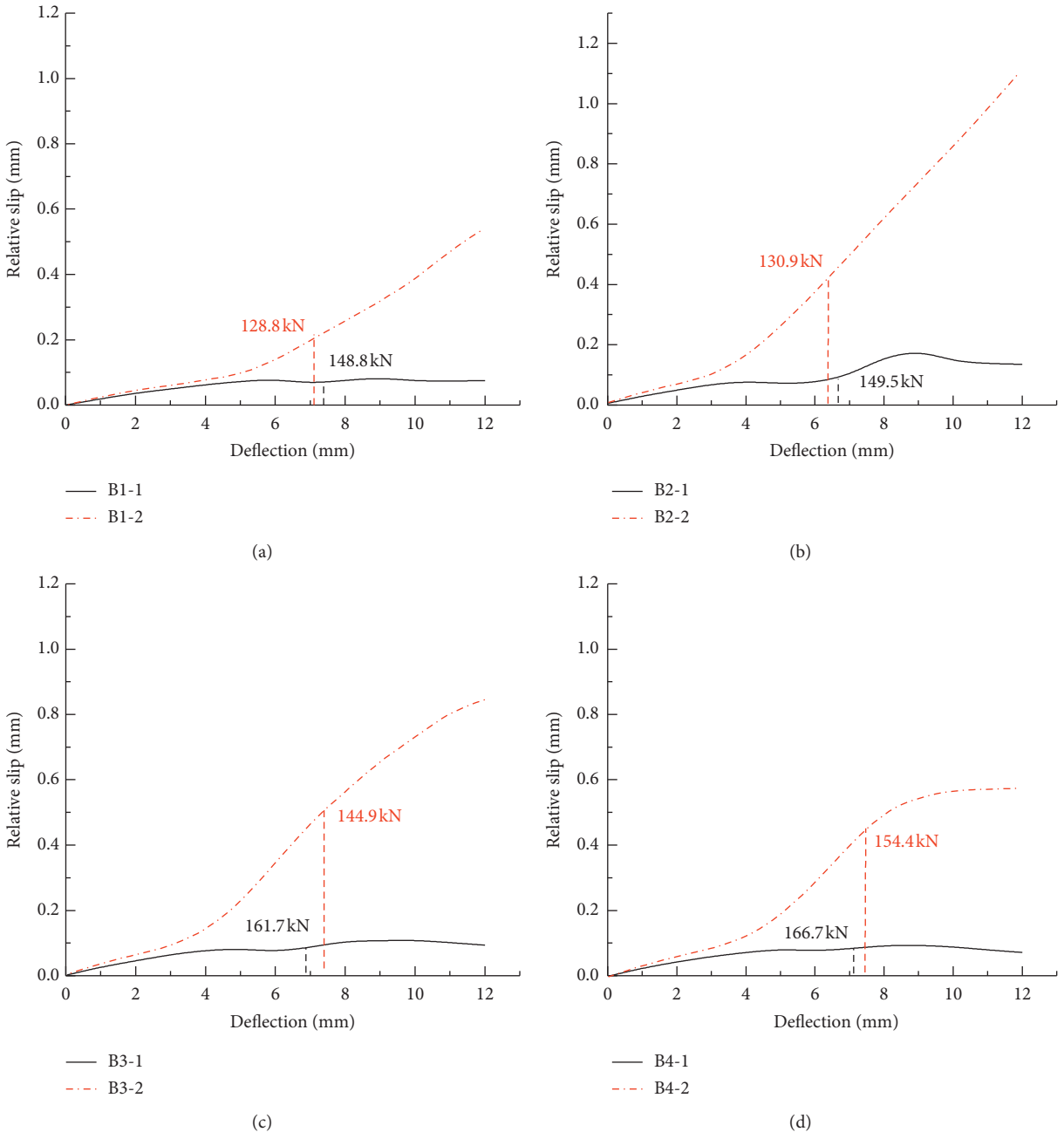

Figure 5: Relative slip of the C-ITZ. (a) B1-1and B1-2. (b) B2-1 and B2-2. (c) B3-1and B3-2. (d) B4-1 and B4-2.

Table 8: Maximal relative slip in C-ITZ.

Model no.	Relative slip (mm)
B1-1	0.075
B2-1	0.135
B3-1	0.094
B4-1	0.072
B1-2	0.542
B2-2	1.114
B3-2	0.846
B4-2	0.574

of the relative slip with regard to the loading for B3-1 and B4-1 is similar to that of B1-1. The final maximal relative slip of B3-1 is about 125% that of B1-1. Comparatively, this value of B4-1 is almost similar to that of B1-1. For the casting interval time being 14 days with the curved prestressing force, a significant characteristic for the variation relation of the relative slip with the loading is that the increase of the relative slip eases up after yielding both for B3-2 and B4-2. The possible reason is that the moment distribution generated by the curved prestressing force in the beam is similar to that from the experimental load. After the yielding of the

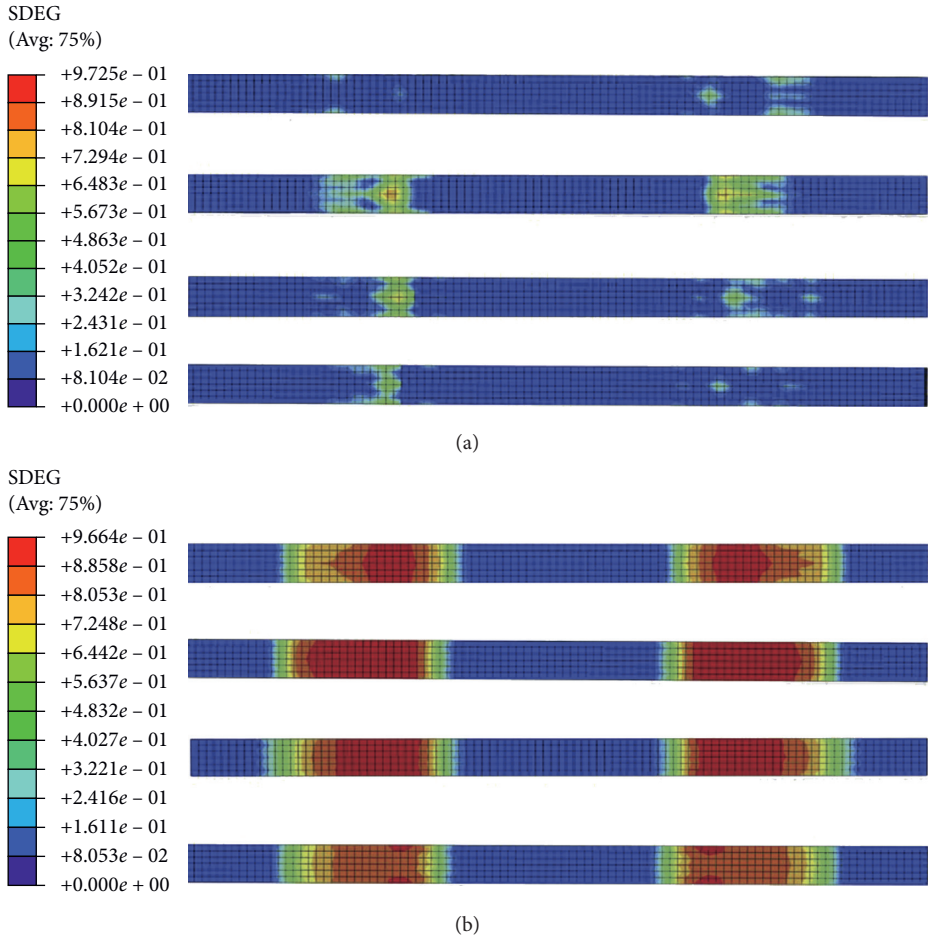

Figure 6: SDEG distribution of C-ITZ at the ultimate load state. (a) B1-1, B2-1, B3-1, and B4-1. (b) B1-2, B2-2, B3-2, and B4-2.

longitudinal bars, the existing of the curved prestressing force effectively slow down the developing of the relative slip in the C-ITZ. Finally, the maximal relative slip value of B3-2 is about 156% that of B1-2. Comparatively, the maximal relative slip value of B4-2 is almost similar to that of B1-2.

3.4. Stiffness Degradation of the C-ITZ. The key for superposing-poured beams to perform with well-collaborative behaviour is whether there is excellent working compatibility and adhesion in the C-ITZ. The performance of the C-ITZ is influenced by the constructional method of the casting interface, the difference in the elastic module and strengths between the two kinds of concretes together with the casting interval time, and so on. The scalar stiffness degradation (SDEG) of the cohesive elements in the modelling can be extracted to symbolically characterize the damage variation in the C-ITZ. SDEG equaling 0 indicates that there is no damage, and SDEG equaling 1 means the cohesive elements are in full failure. The SDEG diagrams of cohesive elements to simulate the C-ITZ in the modelling at the ultimate load state are shown in Figure 6. The mainly prominent region is located in the shear span near the loading point. For cases of the casting interval time being 45 minutes, there is a larger region with higher SDEG values emerged in B2-1 compared with B1-1, B3-1, and B4-1. The possible reason is the arrangement of the curved prestressing force in B3-1 and B4-1 approximate the bending moment diagrams under the designed load, which make the coordinated performance of the superposing-poured beam model better than that of B2-1.

Compared with the situation of the casting interval time being 45 minutes, the region with higher SDEG values are more obvious for all beam models with the casting interval time being 14 days. It is due to that the bonding shear strength of the C-ITZ decreases to 40% with the casting interval time being 45 minutes. Results indicate that the distribution range and the SDEG values of B4-2 are generally similar to that of B1-2 from Figure 6(b). In addition, the distribution of SDEG values in B4-2 is smoother than that in B1-2. Comparatively, the area range with higher SDEG values in B3-2 and B2-2 are larger, especially for B2-2. Similarly, the SDEG values of B2-2 are generally larger than that in B3-2 and B4-2.

The SDEG variation of the C-ITZ corresponding to the loading is shown in Figure 7, in which the data are extracted and averaged from the SDEG distribution area with relatively higher values. The increase of SDEG in B2-1 is much larger than that of B1-1, B3-1, and B4-1 for cases with the casting interval time being 45 minutes. Comparatively, the

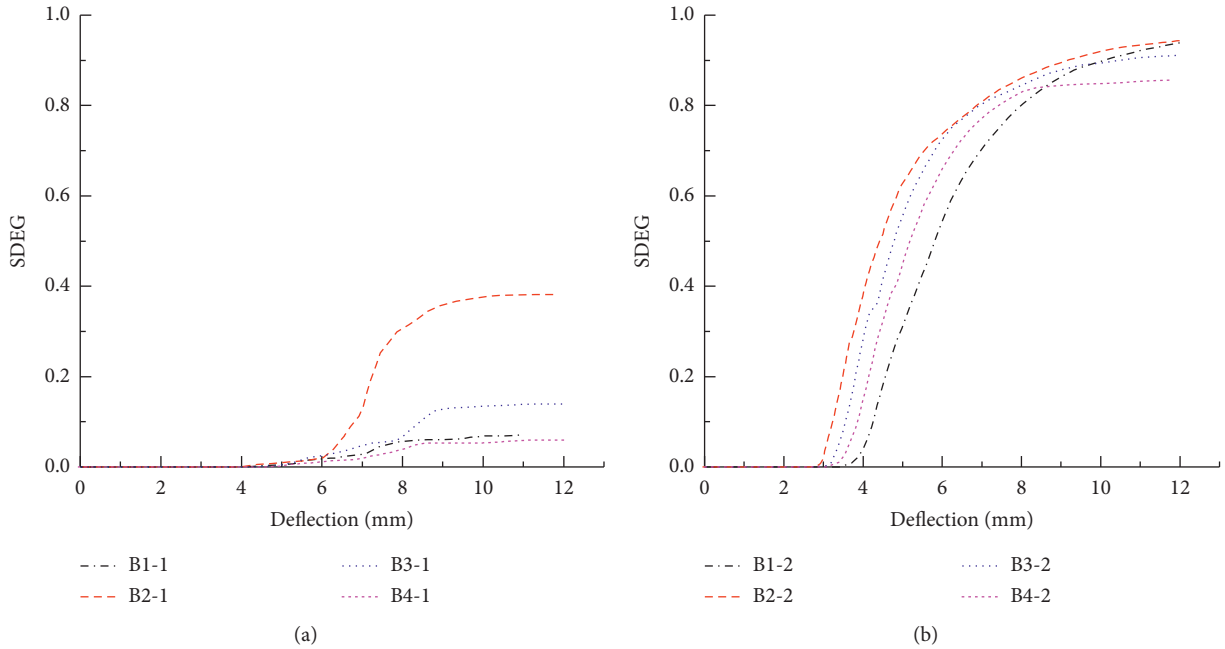

Figure 7: SDEG curves of stack-poured beams. (a) 45 minutes casting interval time. (b) 14 days casting interval time.

Table 9: Slipping loads and ultimate loads of beam models.

Model no.	Slipping load (kN)	Ultimate load (kN)	Ratio L_R (%)
B1-1	108.2	148.8	72.7
B2-1	129.1	149.5	86.4
B3-1	134.5	161.7	83.2
B4-1	142.5	166.7	85.5
B1-2	91.6	128.8	70.7
B2-2	101.5	130.9	77.5
B3-2	108.4	144.9	74.8
B4-2	111.3	154.4	72.1

SDEG variation of B4-1 with regard to the loading is similar to that of B1-1.

For the casting interval time being 14 days, the variation of the SDEG of B2-2, B3-2, and B4-2 with regard to the loading are similar. The midspan deflection of B2-2, B3-2, and B4-2 as the SDEG begin to increase clearly is smaller than that of B1-2 due to the effect of the inverse arch from the prestress. Comparatively, the SDEG of B4-2 changes smoothly, and it is smaller than that of B2-2 and B3-2 on the whole.

The slipping load of the beam model is defined here as the load when the SDEG value of the C-ITZ is not zero and begins to change obviously. The slipping load of all beam models is listed in Table 9 together with the ratio of the slipping load to the ultimate load L_R. After exerting the prestressing force, the slipping loads and the ratio L_R all increase for all beam models. As the casting interval time changes from 45 minutes to 14 days, the slipping load all decrease whether there is or no prestressing force. In addition, the ratio L_R also decreases. For both two casting interval time cases, the increased degree of the slipping load and the ultimate load for the curved prestressing force across the casting interface are larger than that of the other two considered schemes of the prestressing force.

4. Conclusions

The bending performance of the superposing-poured composite concrete beams was analyzed considering the influence with different prestressing schemes and different casting interval times.

(1) For the schemes imposing the straight linear prestressing force, the stiffness of the superposing-poured beam can be effectively strengthened, but there is little influence on the ultimate load. Comparatively, with the curved prestressing force imposed, there is observable increase on the ultimate load of the superposing-poured beam at the time of the stiffness effectively strengthened.

(2) The relative slip of the C-ITZ is obvious as the casting interval time changes from 45 minutes to 14 days because of the weakening on the bonding performance of the C-ITZ. Imposing the straight linear prestressing force further obviously increases the relative slip. Comparatively, the variation relationship of the relative slip with regards to the loading as imposing the curved prestressing force across the C-ITZ is more rational, which eases up after the yielding load of the beam. And the final maximal relative slip is similar to that with no prestressing force whether the casting interval time is 45 minutes or 14 days.

(3) When the casting interval time changes from 45 minutes to 14 days, the region with higher SDEG value at the ultimate state expands obviously whether there is or no prestressing force imposed. As imposed the straight linear prestress or the curved prestress but not across the casting interface, the region with higher SDEG value in the C-ITZ is larger

than that with no prestress. Comparatively, when the curved prestressed bars are arranged across the C-ITZ, the region with higher SDEG value is similar to that with no the prestress; and the distribution of the SDEG are relatively uniform.

It is shown that more rational effect and performance can be obtained with the curved prestressing force across the casting interface exerted in the composite beams if it is practicable in the real construction. There is important influence on the mechanical performance of the superposing-poured composite beams as imposing the prestressing force. The possible interlayer slip and the stiffness degradation in the casting interfacial zone need further experimental analysis based on the numerical simulation.

Data Availability

The data used to support the findings of this study are available from the corresponding author upon request.

Conflicts of Interest

The authors declare that there are no conflicts of interest regarding the publication of this paper.

Acknowledgments

This work was supported by the National Natural Science Foundation of China (Nos. 51878360 and 51778302), Natural Science Foundation of Zhejiang Province (LY18E080008), and Ningbo Science and Technology Project (202002N3117).

References

[1] S. H. Dong, W. C. Yang, Y. Ge et al., "Mechanical properties of concrete containing ceramsite sand," in *Proceedings of the Fifth International Conference on Transportation Engineering*, pp. 1259–1265, Dalian, China, 2015.

[2] Q. X. Wang, Y. X. Shi, J. B. Shi et al., "An experimental study on thermal conductivity of ceramsite cellular concrete," in *Proceedings of the International Conference On Structural*, pp. 64–69, Atlantis Press, Dalian, China, 2015.

[3] X. Zhang, D. Deng, and J. Yang, "Mechanical properties and conversion relations of strength indexes for stone/sand-lightweight aggregate concrete," *Advances in Materials Science and Engineering*, vol. 2018, Article ID 5402953, 12 pages, 2018.

[4] P. Vargas, O. Restrepo-Baena, and J. I. Tobón, "Microstructural analysis of interfacial transition zone (ITZ) and its impact on the compressive strength of lightweight concretes," *Construction and Building Materials*, vol. 137, pp. 381–389, 2017.

[5] Akmaluddin and S. Murtiadi, "Hybrid precast concrete column and sandwich concrete beam under static loading," *Procedia Engineering*, vol. 54, pp. 286–298, 2013.

[6] F. Campi and I. Monetto, "Numerical analysis of two-layer beams with interlayer slip and step-wise linear interface law," *Engineering Structures*, vol. 144, pp. 201–209, 2017.

[7] F. Campi and I. Monetto, "Analytical solutions of two-layer beams with interlayer slip and bi-linear interface law," *International Journal of Solids and Structures*, vol. 50, no. 5, pp. 687–698, 2013.

[8] I. Iskhakov and Y. Ribakov, "A design method for two-layer beams consisting of normal and fibered high strength concrete," *Materials & Design*, vol. 28, no. 5, pp. 1672–1677, 2007.

[9] I. Iskhakov, Y. Ribakov, K. Holschemacher et al., "Experimental investigation of full scale two-layer reinforced concrete beams," *Mechanics of Composite Materials & Structures*, vol. 21, no. 4, pp. 273–283, 2014.

[10] W. Y. Ji, W. W. Li, M. L. Guo et al., "Experimentation and calculation methods of prestressed RPC-NC composite beam deflection," *Journal of Jilin University (Engineering and Technology Edition)*, vol. 48, no. 1, pp. 129–136, 2018.

[11] C. J. Zeng, *Experimental Study on Bending Behavior and Design Methods of Prestressed Concrete Composite Beams*, Hunan University, Changsha, China, 2005.

[12] X. G. Wang, L. Qiao, and Z. D. Shang, "Experimental study on flexural behavior of partially pre-stressed concrete composite beams subjected to service load," *Journal of Liaoning Technical University (Natural Science)*, vol. 27, no. 1, pp. 69–72, 2008.

[13] F. B. Wu, H. L. Huang, X. H. Zhou et al., "Experimental study on flexural behavior of prestressed precast component composite beams," *Journal of Building Structures*, vol. 32, no. 5, pp. 107–115, 2011.

[14] W. W. Li and W. Y. Ji, "Experimental study of cracks in prestressed RPC-NC composite beams," *Bridge Construction*, vol. 47, no. 1, pp. 59–64, 2017.

[15] S. Q. Li, W. W. Wang, S. Wan et al., "Experimental study on bond behavior of interface between old and new concrete composite beam under pre-stressing forces," *Engineering Mechanics*, vol. 26, no. 6, pp. 141–146, 2009.

[16] A. Q. Liu, Y. M. Wang, J. M. Wang et al., "Experiment on the bonding performance of fibred ceramsite aggregate concrete and normal concrete," *Journal of Ningbo University (NSEE)*, vol. 29, no. 4, pp. 92–95, 2016.

[17] P. Grassl, D. Grégoire, L. Rojas Solano, and G. Pijaudier-Cabot, "Meso-scale modelling of the size effect on the fracture process zone of concrete," *International Journal of Solids and Structures*, vol. 49, no. 13, pp. 1818–1827, 2012.

[18] T. Yu, J. G. Teng, Y. L. Wong, and S. L. Dong, "Finite element modeling of confined concrete-II: plastic-damage model," *Engineering Structures*, vol. 32, no. 3, pp. 680–691, 2010.

[19] A. Q. Liu, *Experimental Study on Bonding Behavior of Fiber Ceramsite Concrete Composite Members*, Ningbo University, Ningbo, China, 2017.

[20] L. G. Huang, *The Analysis of Cohesive Zone Model and User-Defined Subroutine Development in Finite Element Method*, Zhengzhou University, Zhengzhou, China, 2010.

[21] J. F. Kou, F. Xu, J. P. Guo et al., "Damage laws of cohesive zone model and selection of the parameters," *Journal of Mechanical Strength*, vol. 33, no. 5, pp. 714–718, 2011.

[22] L. He and J. L. Wang, "Method of equivalent load and temperature reduction on prestressing tendon for effective prestress simulation," *Journal of Highway and Transportation Research and Development*, vol. 32, no. 11, pp. 75–80, 2015.

[23] L. M. Zhang, S. B. Zhao, and C. K. Huang, "Experimentation and calculation of deflection of prestressed high-performance concrete beams," *Journal of Dalian University of Technology*, vol. 45, no. 1, pp. 96–101, 2005.

[24] Y. T. Zhang, Y. Z. Sun, and Z. Z. Zhang, "Study on deflection calculation of prestressed reinforced concrete beams," *Journal of Huazhong University of Science and Technology (Urban Science Edition)*, vol. 23, no. 4, pp. 27–30, 2006.

Hindawi
Advances in Civil Engineering
Volume 2020, Article ID 8887112, 10 pages
https://doi.org/10.1155/2020/8887112

Research Article

Similar Materials and Engineering Application of Cemented Sand and Gravel Dam Model

Qihui Chai,[1,2] Zongkun Li,[1] Juan Wang,[1] Zelin Ding,[2] and Meiju Jiao[1]

[1]*School of Water Conservancy Engineering, Zhengzhou University, Zhengzhou 450001, China*
[2]*School of Water Resources, North China University of Water Resources and Electric Power, Zhengzhou 450045, China*

Correspondence should be addressed to Juan Wang; wangjuan@zzu.edu.cn

Received 6 March 2020; Revised 17 June 2020; Accepted 30 June 2020; Published 18 August 2020

Academic Editor: Yifeng Ling

This paper takes the cemented sand and gravel dam (CSGD) in Shoukoubao reservoir as the prototype to introduce in detail the similarity principle of model test and describe the selection steps of materials for CSG model. It has developed similar materials for CSGD model by mixing coarse sand, barite powder, gypsum powder, cement, and iron powder so as to provide reference for CSGD model test in the future. The dam model test has studied the stress distribution and displacement deformation of the dam during construction and normal operation, in order to provide experimental support for the study of failure mechanism of the CSGD and facilitate the design and construction of dams of this kind. The stress level of the body and the foundation of the model dam varied from 1/9 to 1/17 of the designed compressive strength of dam material. The results showed that CSGD is a safe new type of dams.

1. Introduction

Reservoir dams are the basis and carrier of water conservancy and hydropower development. They play an irreplaceable role in the comprehensive utilization of water and hydropower resources. They have increasingly important role in supporting the sustainable development of China's social economy [1]. According to the first national water resources census, which was carried out from 2010 to 2012, China had 98,002 reservoir dams. Among the 3,000 dams that had collapsed in China, 98% were earth-rock dams. Earth-rock dams are easily overtopped, which leads to dam breaking. By contrast, concrete dams are expensive to build with overly high material stress. Therefore, it is necessary to find an inexpensive solution so as to build a new type of dams that will not collapse even if overtopped. Such a solution should not only apply to new dams but also become a new technical support for strengthening existing dams. Cemented sand and gravel dam (CSGD) is developed based on two construction techniques: roller compacted concrete dam (RCCD) and concrete face rockfill dam (CFRD) [2]. This new type of dam is formed between RCCD and CFRD. Its section in the main body is basically symmetrical, which is made of cementitious materials, water, and riverbed gravel or excavation materials [3]. After cementitious materials and water are added to gravel or excavation materials, efficient earth-rock transport machinery and compaction machinery are used to shape the materials into CSGDs [4].

As a new model, CSGD is still evolving, and the research on dam safety is not systematic enough. According to statistics, since the 1980s, dozens of CSGDs have been built abroad, and relevant engineering exploration and practice have been carried out in Japan, Greece, Dominica, Philippines, Pakistan, Turkey, and other countries

[5]. The application of CSGD in China began in 2004 in the upstream overflow cofferdam project of Daotang Reservoir in Guizhou Province. In this project, CSGD was adopted in China for the first time. The height of the cofferdam is 7 m. Since then, CSGD technology was used in temporary construction such as downstream cofferdam of Jiemian Hydropower Station, upstream cofferdam of Hongkou Hydropower Station, and upstream cofferdam of Gongguoqiao Hydropower Station. On October 14, 2018, the filling of CSGDs was completed in Shoukoubao, Shanxi Province, with the maximum dam height of 61.6 m. On June 7, 2019, the CSGD project of Jinjigou in Yingshan County of Sichuan Province was completed, with the maximum dam height of 33 m, indicating that this dam type began to be applied in permanent projects.

The common methods of CSGD stress analysis include theoretical analysis, practical observation, numerical simulation, and model test [6–9]. It is very difficult to describe the failure process of CSGD with theoretical analysis of a single mathematical model [10]. The actual observation method is affected by many factors. It is hard to reproduce complex working conditions without perfect computational constitutive model for numerical analysis and practical engineering [11]. Compared with other research methods, physical model test has the advantage that the test conditions can be manually controlled and changed [12]. Therefore, physical model test is an effective method to study the stress distribution of CSGD [13], in which similar material selection is the most important part [14, 15]. The model test data of cemented sand gravel is relatively scarce, and there are few reports on similar materials.

2. Research Status of CSG Model Similar Materials

Choosing the right and reasonable similar materials is key to accurately simulating the engineering prototype [14]. As modern testing technology and simulation theory keep developing, studies on model materials deepen and new model testing technologies (such as geomechanical model and centrifugal simulation technology) are successfully applied, and the research range of hydraulic structure model test further expands [15–18]. At present, the mainstream similar materials used for model tests in China are as follows: (1) MIB materials of high bulk density, low elastic modulus, and low strength, developed by Han Boli of Wuhan University [19, 20]; (2) NIOS materials developed by Li Zhongkui of Tsinghua University [21, 22]; and (3) iron barites sand cementation material (IBSCM) developed by Wang Hanpeng of Shandong University [23]. Organic materials such as oil, rosin, and alcohol and inorganic materials such as gypsum, water, and cement are used as binders for model materials [24]; copper powder, iron powder, iron concentrate powder, bentonite, sand, or diatomite are used as filling materials [25]; glycerol, rosin, alcohol, cooked starch slurry, and gypsum are used as additives [26]. Hydraulic structure model test has been developing in a more comprehensive way. However, as CSGD only has a short history and unique dam material properties, only a few research works at home and aboard have covered this material. The centrifuge modeling test was carried out by Chen Jiaojiao of Hohai University [27] to investigate the deformation of the dam model, while the materials used in the experiment to cast dam were consistent with the actual projects. There are many mechanical properties tests of cemented sand and gravel dam building materials in the existing research [10, 28, 29], but the research on similar materials for model test of CSG dam is still not enough.

3. CSG Similar Material Simulation Test

3.1. Similarity Theory. The similarity theory is used to reveal the inherent relationship between similar physical phenomena and explore the fixed ratio between the physical quantities of the same name, and it is applied to scientific experiments and engineering and technical practice. Generally, the model test should satisfy the needs for geometric similarity and physical and mechanical similarity [30, 31]:

$$\text{geometric similarity scale:} \begin{cases} \text{length similarity constant } C_L = \dfrac{L_p}{L_m}, \\ \text{angular similarity constant } C_\theta = \dfrac{\theta_p}{\theta_m}, \end{cases}$$

$$\text{Physical similarity scale:}\begin{cases}\text{stress similarity constant } C_\sigma = \dfrac{\sigma_p}{\sigma_m},\\ \text{displacement similarity constant } C_\delta = \dfrac{\delta_p}{\delta_m},\\ \text{Poisson}'\text{s ratio similarity constant } C_\mu = \dfrac{\mu_p}{\mu_m};\\ \text{density similarity constant } C_\rho = \dfrac{\rho_p}{\rho_m},\\ \text{strain similarity constant } C_\varepsilon = \dfrac{\varepsilon_p}{\varepsilon_m},\\ \text{elastic modulus similarity constant } C_E = \dfrac{E_p}{E_m},\\ \text{volumetric force similarity constant } C_X = \dfrac{X_p}{X_m},\\ \text{bulk density similarity constant } C_\gamma = \dfrac{\gamma_p}{\gamma_m},\end{cases} \tag{1}$$

where C is the similarity scale; p is the prototype physical quantity; m is the model physical quantity; L is the length; θ is the angular displacement;σ is the stress; δ is the displacement; μ is Poisson's ratio; ρ is the density; ε is the strain; E is the elastic modulus; X is the volumetric force; and γ is the bulk density.

3.2. Similarity Relation. According to the equilibrium, geometric and physical equation, and boundary conditions of the similarity theory, the main loads for CSGD come from water pressure, uplift pressure, and dam body weight. Specifically, water pressure and uplift pressure act in the form of surface force, and gravity acts in the form of volume force. Then, based on dimensional analysis, similarity relation of CSGD model test can be obtained [32, 33]:

$$\begin{cases} C_\mu = C_\varepsilon = 1;\\ C_\gamma = C_\rho,\\ C_\sigma = C_\gamma C_L = C_E C_\varepsilon,\\ C_\varepsilon = \dfrac{C_\gamma C_L}{C_E},\\ C_\delta = \dfrac{C_\gamma C_L^2}{C_E},\\ C_F = C_\gamma C_L^3 = C_E C_L^2. \end{cases} \tag{2}$$

where $C_\mu\, C_\gamma$, C_ρ, C_σ, C_L, $C_\varepsilon, C_E, C_\delta, C_F$ refer to the above-mentioned terms.

As $C_\gamma = 1$, then

$$\begin{aligned} C_E &= C_L,\\ C_F &= C_L^3. \end{aligned} \tag{3}$$

Because the aforementioned conditions are interrelated, the model has great difficulties in fully satisfying all of them. Based on the key points and characteristics of the research content, the model test can only satisfy the main similarity relationships and becomes basically similar to the prototype. Then, the test results are analyzed and selected.

3.3. Selection of Similar Materials. In general, the following requirements should be satisfied for selecting material similar to that of the model [34]: (1) According to the formula in the similarity theory, the bulk density of the model material should be the same as that of the prototype material. That is to say, when $C_\gamma = 1$, the conversion between the physical parameters of the model and the prototype can be greatly simplified, and the effects of the gravity stress field can be better reflected. (2) The main physical and mechanical properties of the model material are equivalent to or close to the prototype material parameters after similar conversion. (3) The model material has good workability, which creates feasible conditions for molding, construction, and repair. (4) The physical, mechanical, chemical, and thermal properties of the model materials are stable and are less affected by the changes of time, temperature, and humidity.

In this test for the target, gravity similarity ratio $C_\gamma = 1$, and geometric similarity ratio $C_L = 100$. Given mechanical parameters and target similarity ratio of CSGD, the target parameters for preparing similar materials can be obtained, as shown in Table 1.

Based on the existing research results, the mechanical properties of SCG material have been simulated. In that test, coarse sand is chosen to simulate the prototype coarse

Table 1: Physicomechanical target parameters of the material.

Parameters	Bulk density (kN/m³)	Elastic modulus (MPa)	Compressive strength (MPa)	Internal friction angle φ (°)	Cohesion, c (kPa)	Poisson's ratio (μ)
Prototype material (Shoukoubao dam)	22.8–26.3	4500–5200	8.2–15.1	28–38	476–710	0.2
Model material (conversion value)	22.8–26.3	45–52	0.08–0.15	28–38	4.76–7.1	0.2

aggregate, barite powder, as filler to simulate the prototype fine aggregate, and gypsum powder and cement, as cementitious materials. The strength of the material is controlled through changing the amount of gypsum and the ratio of water to gypsum. The elastic modulus of the material is changed by the amount of cement, and the bulk density of the model material is changed by choosing iron powder as the admixture. The excess water in the model material evaporates during the drying process, forming many tiny pores inside the gypsum block. This is the basis for simulating the pore characteristics of the prototype material.

3.4. Mix Design and Result Analysis. The four-factor and four-level orthogonal method was adopted for testing the model material test. Four factors were set up, namely, A, B, C, and D. Factor A refers to the ratio of iron powder content to total material content (%); factor B, the ratio of gypsum content to total material content (%); factor C, gypsum content/cement content; and factor D, coarse sand content/barite powder. In the process of mixing material, water is added in different stages (water consumption is determined by plasticity and fluidity of similar materials in the mixing process). Orthogonal design is detailed in Table 2.

In the model material test, 16 groups of orthogonal mixing schemes and 144 forming specimens were designed. In addition, the mechanical parameters of the model material were tested systematically and comprehensively. The results showed that when the iron powder content was 10%, gypsum content was 20%, gypsum : cement = 2 : 1, coarse sand : barite powder = 3 : 1, and the material parameters of the model were closest to the test target value. The specific values and the test process are shown in Table 3 and Figure 1, respectively.

4. Model Test of CSG Dam Body

4.1. Model Scale Design. This dam model test took the prototype design of CSGD of Shoukoubao reservoir in Shanxi Province as a reference and carried out a generalized simulation, which is located in the upper reaches of Heishui River, with a geographic location of 113°40′e and 40°25′n, about 10 km northwest of Yanggao County. Shoukoubao reservoir was started in April 2014 and was awarded as Technical Demonstration Project for Dam Construction with Cemented Granular Materials by General Institute of Water Conservancy and Hydropower Planning and Design, Ministry of Water Resources, in September 2017. The parameters of the prototype dam body are as follows: the maximum dam height was 61.6 m, the width of the dam top was 6 m, and the upstream and downstream slopes were 1 : 0.6. Cementitious materials are made of 50 kg/m^3 of cement material and 40 kg/m^3 of fly ash. The bulk density of the dam body was 23.5 kN/m^3, the elastic modulus is 4.8 GPa, and Poisson's ratio is 0.20; the bulk density of the dam foundation was 20.2 kN/m^3, with 7 GPa of elastic modulus and 0.24 of Poisson's ratio. Based on the measurement requirements of model tests and engineering conditions, the dam foundation depth was simulated at 50 m in depth, about 0.8 H. The upstream simulation range was 30 m, about 0.5 H, and the downstream simulation range was 150 m, around 2.4 H (H is dam height). Model dam parameters were as follows: dam was 61.6 cm in height, and dam crest was 6 cm in width. In addition, both upstream and downstream slopes were 1 : 0.6. Dam foundation was simulated as 50 cm in depth. Upstream simulation range was 30 cm, while downstream simulation range was 150 cm. Then, the coordinates were set, with dam heel as the origin. According to the similarity relation, the similarity constants are shown in Table 4.

4.2. Modeling. Modeling includes the building of model groove and dam foundation, as well as dam body concreting and splicing. Dam body concreting and splicing should be carried out after model groove and dam foundation are built. The processes are introduced in detail [35–39] below.

(1) Preparation: coarse sand, barite powder, gypsum powder, cement, and iron powder were prepared in different masses, which were estimated based on the model size and the abovementioned mix ratio of model materials.

(2) Mixing: firstly, coarse sand, barite powder, and iron powder were weighed and poured into the mixing tank which mixed them evenly into aggregate. Secondly, gypsum powder and cement were added to the aggregate. Thirdly, a shovel was used to stir the mixed materials by lifting and dropping them 10–15 times, during which water was added. Water amount must be strictly controlled to prevent segregation. After fully mixing, the material was in a plastic state with fluidity. Finally, the material was poured into the preassembled mold to solidify.

(3) Drying and demolding: mold filled with material was carefully moved to the drying chamber. A far infrared heating plate of 20 × 30 cm was used to bake the mold for 7 days. The temperature was strictly

Table 2: Orthogonal design of similar materials.

Group	Factor A Iron powder content (%)	Factor B Gypsum content (%)	Factor C Gypsum : cement	Factor D Coarse sand : barite powder
1	5	10	1 : 1	1 : 1
2	10	15	2 : 1	2 : 1
3	15	20	3 : 1	3 : 1
4	20	25	4 : 1	4 : 1

Table 3: Physicomechanical test parameters of the material.

Parameters	Bulk density (kN/m^3)	Elastic modulus (MPa)	Compressive strength (MPa)	Internal friction angle (°)	Cohesion (kPa)	Poisson's ratio
Prototype material (Shoukoubao dam)	22.8–26.3	4500–5200	8.2–15.1	28–38	476–710	0.2
Model material (test value)	23.5	46.02	0.11	32	5.12	0.2

Figure 1: Model similar material testing process.

Table 4: Model similarity parameter table.

Similarity constant	C_L	C_μ	C_γ	C_ε	C_f	C_c	C_σ	C_E	C_δ	C_F
Value	100	1	1	1	1	1	100	100	100	100^3

Note. The meaning of each symbol is as mentioned above.

controlled between 40°C and 45°C to ensure the mold was heated evenly as too high temperature will lead to dehydration and powdery surface. What is more, if the temperature becomes too high, strength and elastic modulus of the newly formed blank will be reduced significantly, which will affect the measurement results. After drying, the blank can be demolded.

(4) Polishing and molding: after demolding, the blank was larger than the dam model, and its surface was attached with a hard shell (consisting of oil, dust, etc.). Therefore, it needs to be polished manually or mechanically before connecting with the dam foundation. The surface smoothness of the model was corrected repeatedly with the prefabricated sample. The accuracy was controlled at ±3 mm to ensure the accuracy of the subsequent loading measurement. The fabrication of dam body mold is shown in Figure 2.

4.3. The Model Measurement System and Loading. The measurement system in the dam model test comprised strain measurement and displacement measurements. The strains and displacement of the dam body surface were monitored with resistance strain gauges and displacement digital display instruments, respectively. Three rows of strain measuring points, numbered 1–9, 10–18, and 19–23, were arranged at the dam bottom, 1/3 dam height and 1 cm near the dam bottom, respectively. The same measuring points were also arranged on the back of the model at the same time as objects of reference. Each measuring point was equipped with a strain gauge rosette containing three resistors at 45° relative orientations, and a compensator was set up to eliminate the temperature effect. Vertical displacement sensors whose numbers were No. 1, No. 3, No. 5, and No. 7, respectively, and horizontal displacement sensors whose numbers were No. 2, No. 4, No. 6, and No. 8, respectively, were installed on the dam crest on the downstream face, at 2/3 dam height, 1/3 dam

Figure 2: Dam body molds.

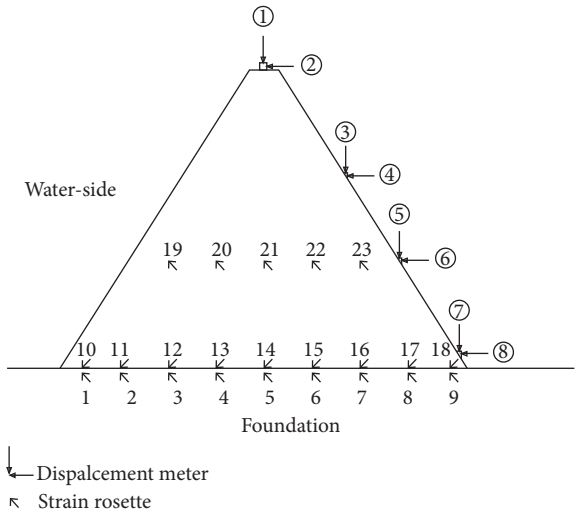

Figure 3: Measurement system.

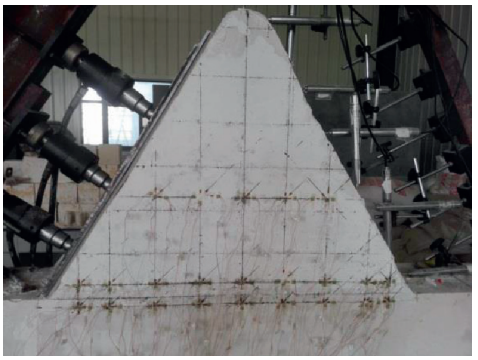

Figure 4: Loading system.

height, and the toe of the dam, respectively, as shown in Figure 3.

This test simulated the water pressure and the self-weight of the dam as main loads, without considering the seepage field and the seismic load. Among the loads considered, the upstream normal water level was taken as the water pressure, and the self-weight was simulated by ensuring that the prototype material had the same volume density as the dam material [40]. Three jacks were used to act vertically on the steel plate, which was flat against the dam surface to transform the point loads of the jacks into the surface load on the upstream face of the dam, as shown in Figure 4.

4.4. Test Results and Analysis. The dam model test contained two periods: the construction simulation and the normal operation simulation. During the construction period, the dam was divided into four layers and placed layer by layer to monitor the stress of the dam foundation and body, considering only the dam gravity. As the water pressure was an additional factor during the normal operation period, the dam layers during the construction period were closely bonded with polymer cementing materials (model 1#), and the whole load was applied to measure the stress and displacement of the dam foundation and the dam body. In addition, a comparison model (model 2#) was made using overall pouring to verify the data. The stress value was positive in compression and negative in tension, the horizontal displacement was positive downstream, and the vertical displacement was positive upstream [41].

4.4.1. Stress Measurement during Construction. The dam stress during the construction period was obtained after the measured data were processed based on the measurement scale of the model, as shown in Figure 5.

The test results show the following: (1) during the construction period, the stress of dam foundation, dam bottom, and dam center was very small. The maximum stress of the dam was found in the middle of the dam bottom, which was less than 0.6 MPa, about 1/14–1/25 of the designed compressive strength of the dam material. (2) The stress of the dam body and the foundation increased as the construction height rose. For the dam body, the stress was identified as compressive stress. Tensile stress appeared near the toe and heel of the dam, but the value was very small. (3) At different elevations, the stress was distributed symmetrically around the axis of the dam. The reasons were analyzed by simulating the construction process of CSGD. The construction period is only affected by the gravity of the dam body. It turned out that the construction period was only affected by the self-weight of the dam body, while the profile of the dam body was designed to be symmetrical and the stress was uniform. As a result, only compressive stress was generated

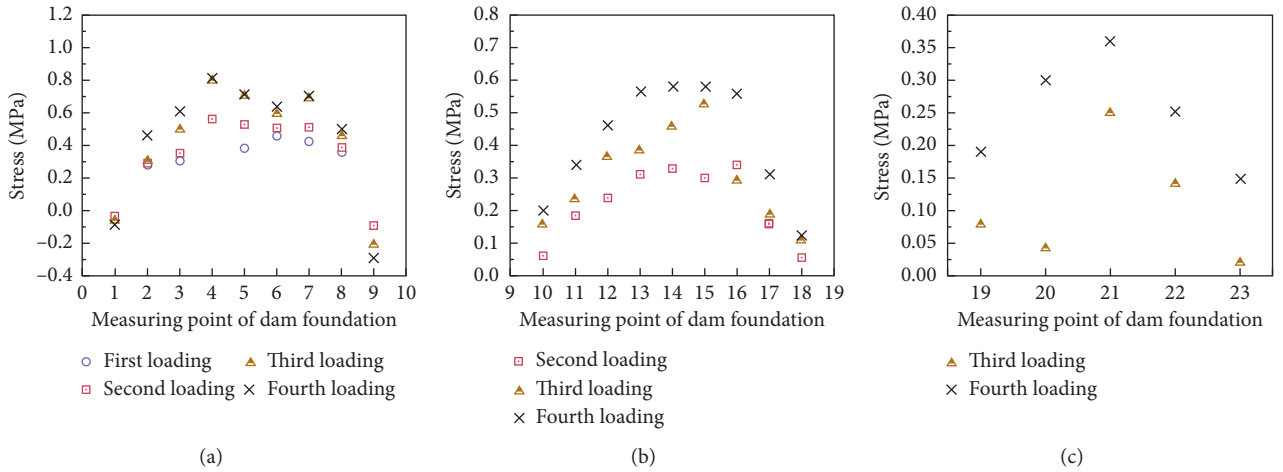

Figure 5: Stress survey map during construction period.

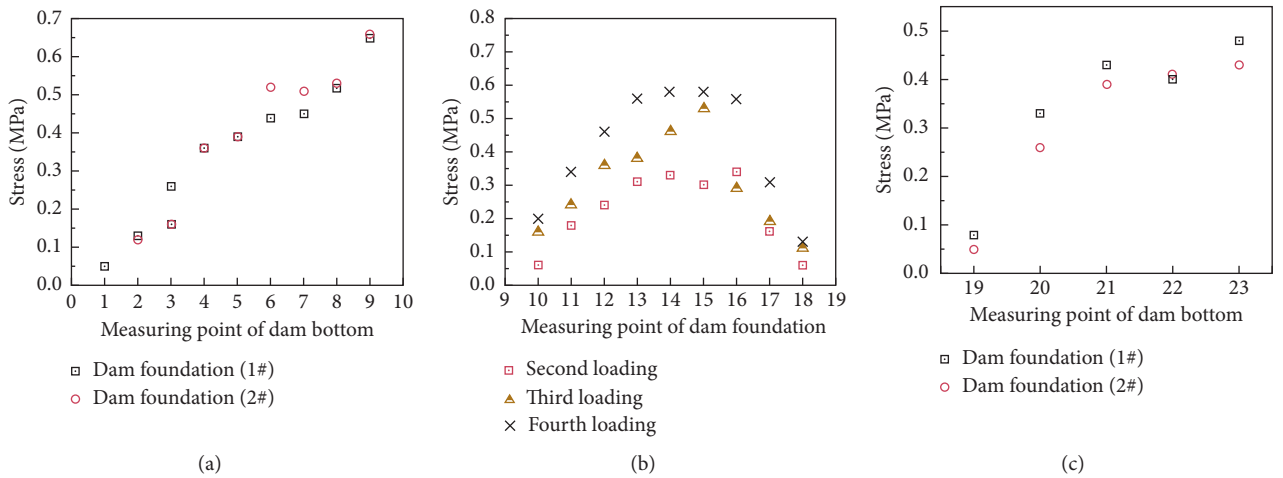

Figure 6: Stress survey map during normal operation period.

inside the dam body. The gravity of the dam body caused slight settlement deformation of the dam foundation, and the created tensile stress appeared near the toe and heel of the dam, which were both within the allowable range [42].

4.4.2. Stress Measurements and Displacement Measurements during Normal Operations. The measured data were processed according to the measurement scale of the model. The stress of the dam body in the normal operation period was obtained by excluding the data of the self-weight influence on the dam body and dam foundation in the process of layered loading, keeping only the data of the dam body under water load, as shown in Figure 6 (1#: cemented dam body, 2#: overall pouring). The dam displacement during the normal operation period is presented in Figure 7.

The test results indicate the following: (1) The slight and consistently distributed differences of stress between consolidated model (1#) and overall casting model (2#)

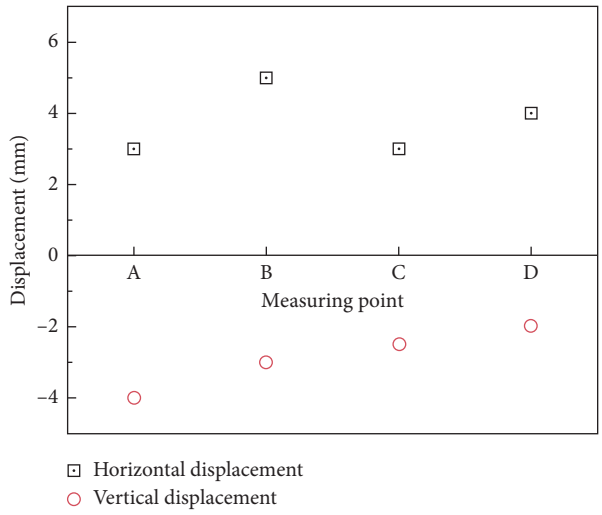

Figure 7: Displacement survey map during normal operation period.

under normal operation show that the impact of the layered and graded loading simulation construction on dam body and foundation is rational. (2) Compressive stress, the stress undertaken by the foundation and the body of the model dam, generally peaks when measured at the bottom of the dam and reaches the maximum level (less than 0.9 MPa) in the downstream of the dam bottom, ranging from 1/9 to 1/17 of the designed compressive strength of dam material. (3) The stress distribution of dam foundation and dam body under operation is totally different from that under construction. The stress distribution increases gradually from upstream to downstream at the same elevation, while the stress distribution of dam body decreases gradually from bottom to top if measured at different elevations. The analysis shows that self-weight and water load, vertical to the upstream surface, are the main sources of stress compressing the dam body. Meanwhile, the section of the dam is designed to be symmetrical, so the stress is distributed evenly as the self-weight of the dam body counteracts the tensile stress on the dam heel from the water load [43].

The distribution law of displacement: Under the pressure of water load and self-weight, the whole dam body deforms horizontally towards the downstream, with the maximum deformation at 2/3 height of the dam; vertically, the dam has settlement deformation with the maximum deformation at 0.65% of the dam height at the top of the dam.

The stress level of the body and the foundation of the model dam are too low under the two abovementioned construction conditions where the potential of material strength cannot be fully realized, and the section design can be further optimized. When operating normally, the deformation of dam body is even slighter than that of dams built with similar materials. Therefore, CSGD proved to be a safe new type of dams [44].

5. Conclusions

This paper takes CSGD in Shoukoubao, Shanxi Province, as a prototype to introduce in detail the similarity principle of model test and describe the selection steps of CSG model. The material similar to the one used in CSG dam for the model has been developed as a mix of coarse sand, barite powder, gypsum powder, cement, and iron powder. The model-based tests of dam body have studied the two working conditions of construction and normal operation. The main conclusions obtained were as follows:

(1) As the results of extensive experiments show, the physical and mechanical parameters of the model material are the closest to the target value of the prototype when the iron powder content is 10%, gypsum content is 20%, gypsum: cement = 2 : 1, and coarse sand: barite powder = 3 : 1.

(2) The maximum stress of dam body, found at the center of the bottom during construction, is about 1/14–1/25 of the designed compressive strength of dam body material, distributed symmetrically on both sides of the axis of the dam. When operating, the stresses of the foundation and the body of the model dam are compressive stresses which generally peak when measured at the bottom of the dam and reach the maximum level in the downstream of the dam bottom, ranging from 1/9 to 1/17 of the designed compressive strength of the dam material.

(3) The stress distribution increases gradually from upstream to downstream at the same elevation, while the stress distribution of dam body decreases gradually from bottom to top if measured at different elevations. Under the pressure of water load and self-weight, the whole dam body deforms horizontally towards the downstream, with the maximum deformation at 2/3 height of the dam; vertically, the dam suffers settlement deformation with the maximum deformation at 0.65% of the dam height at the top of the dam.

(4) The stress level of the body and the foundation of the model dam are too low under the abovementioned two construction conditions where the potential of material strength cannot be fully realized and the section design can be further optimized. Therefore, CSGD proved to be a safe new type of dams. In addition, taking the nature of discreteness of CSG material into consideration, further research should be conducted to solve issues including upgrading simulation when selecting model materials and the method to load the internal seepage field in the process of dam model experiment.

Data Availability

The data used to support this study are included within the article.

Conflicts of Interest

The authors declare that there are no conflicts of interest regarding the publication of this paper.

Acknowledgments

The authors would like to acknowledge the financial support received from the National Key Research and Development Program of China (2018YFC0406803) and Foundation for University Key Teacher by Henan Province of China (2019GGJS009).

References

[1] P. Londe and M. Lino, "The faced symmetrical Hard-fill dam: a new concept for RCC," *International Water Power & Dam Construction*, vol. 44, no. 2, pp. 19–24, 1992.

[2] J. S. Jia, F. L. Ma, X. Y. Li et al., "Study on material characteristics of cemented sand-gravel dam and engineering application," *Journal of Hydraulic Engineering*, vol. 37, no. 5, pp. 578–582, 2006.

[3] M. A. Stevens and J. Linard, "The safest dam," *Journal of Hydraulic Engineering*, vol. 128, no. 2, pp. 139–142, 2002.

[4] J. S. Jia, N. Liu, C. Y. Zheng et al., "Research on progress and engineering application of cemented granular material dam," *Journal of Hydraulic Engineering*, vol. 47, no. 3, pp. 315–323, 2016.

[5] J. M. Peter, "Hardfill and the ultimate dam," *Hydro Review Worldwide*, vol. 6, no. 11, pp. 26–29, 2004.

[6] S. Batmaz, "Cindere dam-107m high roller compacted Hardfill dam (RCHD) in Turkey," in *Proceedings of the 4th International Symposium on Roller Compacted Concrete Dams*, pp. 121–126, Madrid, Spain, 2003.

[7] T. Hirose, T. Fujisawa, H. Yoshida et al., "Concept of CSG and its material properties," in *Proceedings of the 4th International Symposium on Roller Compacted Concrete Dams*, pp. 465–473, Madrid. Spain, 2003.

[8] T. Fujisawa, A. Nakamura, H. Kawasaki et al., "Material properties of CSG for the seismic design of trapezoid-shaped CSG dam," in *Proceedings of the 13th World Conference on Earthquake Engineering*, pp. 391–394, Vancouver, Canada, 2004.

[9] L. Kongsukprasert, F. Tatsuoka, and M. Tateyama, "Several factors affecting the strength and deformation characteristics of cement-mixed gravel," *Soils and Foundations*, vol. 45, no. 3, pp. 107–124, 2004.

[10] T. N. Lohani, L. Kongsukprasert, K. Watanabe, and F. Tatsuoka, "Strength and deformation properties of compacted cement-mixed gravel evaluated by triaxial compression tests," *Soils and Foundations*, vol. 44, no. 5, pp. 95–108, 2004.

[11] L. Kongsukprasert, Y. Sano, and F. Tatsuoka, "Compaetion-indueed anisotropy in the strength and deformation characteristics of cemen-mixed gravelly soils," *Soil Stress-Strain Behavior: measurement, Modeling and Analysis*, pp. 479–490, Springer, Dordrecht, Netherlands, 2006.

[12] P. J. Mason, R. A. N. Hughes, and J. D. Molyneux, "The design and construction of a faced symmetrical Hardfill dam," *International Journal on Hydropower and Dams*, vol. 15, no. 3, pp. 90–94, 2008.

[13] Z. Tokmechi, "Structural safety studies of Klahir dam in Iran," *Middle-East Journal of Scientific Research*, vol. 6, no. 5, pp. 500–504, 2010.

[14] M. Q. Sun, S. F. Yang, and Q. Q. Tian, "Summary of research on mechanical properties, durability and dam type of cemented sand and gravel material," *Yellow River*, vol. 7, pp. 83–85, 2016.

[15] Q. H. Chai, M. Q. Sun, and S. F. Yang, "Study on influencing factors of compressive strength of cemented sand and gravel materials," *Yellow River*, vol. 7, pp. 86–88, 2016.

[16] H. C. Yang, *Structural Design and Engineering Application of Cemented Sand and Gravel Dam*, China Institute of Water Resources and Hydropower Research, Beijing, China, 2013.

[17] Z. J. Yue, *The Working Characteristics of Cemented Sand and Gravel Dam on Different Foundation*, Wuhan University, Wuhan, China, 2005.

[18] H. B. Nie, J. H. Dong, and L. Zhang, "Study on destroy mode and stability of Hardfill dam under different foundation conditions," *Journal of Sichuan University (Engineering Science Edition)*, vol. 47, no. S1, pp. 36–40, 2015.

[19] B. L. Han, Y. H. Gu, and M. X. Song, "Study on triaxial stress characteristics of several model materials," *Engineering Journal of Wuhan University*, vol. 1, no. 1, pp. 3–11, 1984.

[20] B. L. Han, X. L. Chen, Y. L. Song et al., "Research on similar material of rock mass," *Engineering Journal of Wuhan University*, vol. 30, no. 2, pp. 6–9, 1997.

[21] F. P. Ma, Z. K. Li, and G. F. Luo, "NIOS model material and its use in geomechanical similarity model test," *Journal of Hydroelectric Engineering*, vol. 23, no. 1, pp. 48–51, 2004.

[22] Q. Y. Zhang, S. C. Li, and Y. Y. Jiao, *Rock Mass Numerical Analysis Method and Geomechanics Model Test Principle and Engineering Application*, China Water Power Press, Beijing, China, 2005.

[23] H. P. Wang, S. C. Li, Q. Y. Zhang et al., "Development of a new geomechanical similar material," *Chinese Journal of Rock Mechanics and Engineering*, vol. 25, no. 9, pp. 1842–1847, 2006.

[24] J. Y. Chen, L. Zhang, and Y. Chen, "Failure model test on deep anti-sliding stability of Wudu RCC gravity dam," *Chinese Journal of Rock Mechanics and Engineering*, vol. 26, no. 10, pp. 2097–2103, 2007.

[25] B. Q. Yang, L. Zhang, J. Y. Chen et al., "Experimental study of 3D geomechanical model for global stability of Xiaowan high arch dam," *Chinese Journal of Rock Mechanics and Engineering*, vol. 29, no. 10, pp. 2086–2093, 2010.

[26] Z. L. Ding, L. Zhang, X. L. Yao et al., "Failure experimental study on stability of high arch dam on complex foundation," *Journal of Sichuan University (Engineering Science Edition)*, vol. 42, no. 6, pp. 25–30, 2010.

[27] J. Chen, X. Cai, E. Lale, J. Yang, and G. Cusatis, "Centrifuge modeling testing and multiscale analysis of cemented sand and gravel (CSG) dams," *Construction and Building Materials*, vol. 223, pp. 605–615, 2019.

[28] X. Cai, Y. L. Wu, H. X. Li et al., "Constitutive equation for CSG materials," *Chinese Journal of Geotechnical Engineering*, vol. 32, no. 9, pp. 1340–1344, 2010.

[29] X. Cai, J. Yang, X. W. Guo et al., "A new type of nonlinear K-G-D constitutive model for CSG material," *Journal of Hohai University(Natural Sciences)*, vol. 42, no. 6, pp. 41-42, 2014.

[30] Z. L. Ding, L. Zhang, Y. Chen et al., "3D geo-mechanical model failure test on stability against deep sliding of gravity dam," *Journal of Hydraulic Engineering*, vol. 42, no. 4, pp. 499–504, 2011.

[31] K. Xiong, Y. L. He, and W. Wu, "Study on structure failure test of hardfill dam," *Journal of Hydraulic Engineering*, vol. 43, no. 10, pp. 1214–1222, 2012.

[32] Z. L. Ding, S. F. Yang, and M. Q. Sun, "Model test of cemented sand and gravel dam," *Yellow River*, vol. 38, no. 9, pp. 92–95, 2016.

[33] X. T. Cui, Z. D. Zhang, and S. Fan, "Research on mechanical model test materials Based on the similar theory," *Pearl River*, vol. 40, no. 5, pp. 82–86, 2019.

[34] X. Y. Geng and Z. X. Zhang, "Study on preparation methods for similar materials of sandstone," *Chinese Journal of Underground Space and Engineering*, vol. 11, no. 1, pp. 23–28, 2015.

[35] Z. V. Chen, J. Wu, J. R. Zhang et al., "Preparation of similar materials of the surrounding rock in model test," *Modern Tunnelling Technology*, vol. 55, no. S2, pp. 102–107, 2018.

[36] Y. Q. Yang, T. N. Xue, T. C. Li et al., "Comparison research on materials similar to bolt in model test," *Mining Research and Development*, vol. 38, no. 8, pp. 81–83, 2018.

[37] J. Yao, J. Li, and X. Huang, "Experimental study on mia proportion of similar material for weathered mudstone," *Modern Tunnelling Technology*, vol. 55, no. 2, pp. 1069–1079, 2018.

[38] S. L. He, X. Huang, and Z. X. Zhang, "Study on the mechanical properties of gypsum specimens," *Chinese Journal of Underground Space and Engineering*, vol. 12, no. 1, pp. 49–55, 2016.

[39] J. Y. Dong, J. H. Yang, G. X. Yang et al., "Research on similar material proportioning test of model test based on orthogonal design," *Journal of China Coal Society*, vol. 37, no. 1, pp. 44–49, 2012.

[40] X. Yang, D. L. Su, B. Zhou et al., "Experiment study on similarity ratio of similar material for model test on red-bed soft rock," *Rock and Soil Mechanics*, vol. 37, no. 8, pp. 2231–2237, 2016.

[41] X. L. Zhang, "Test research on construction technique parameters of cemented sand and gravel dam at the Datong Shoukoupu Reservoir," *Shanxi Hydrotechnics*, vol. 11, no. 4, pp. 103–105, 2015.

[42] J. H. Cao, "Test and analysis of shear strength of contact surface of cemented sand and gravel cushion in Shoukoubu reservoir's Dam," *Shanxi Hydrotechnics*, vol. 8, no. 3, pp. 77–79, 2017.

[43] J. Y. Yang, H. Y. Yan, and J. Y. Wang, "Design of cemented sand and gravel dam of Shoukoupu Reservoir," *Technical Progress in Construction and Operation Management of High Dams-CHINCOLD Collected Papers of the 2014 Annual Academic Conference*, pp. 561–568, Yellow River Water Conservancy Press, Zhengzhou, China, 2014.

[44] W. J. Song, "Experimental study on cemented sand and gravel dam construction in Shoukoubao Reservoir," *China Water Power & Electrification*, vol. 1, no. 1, pp. 49–51, 2017.

Hindawi
Advances in Civil Engineering
Volume 2020, Article ID 8836284, 13 pages
https://doi.org/10.1155/2020/8836284

Research Article

Calculation on Bending Stiffness of RC Short Beam Strengthened by CFRP

Wang Tingyan,[1,2] **Zhou Yun**,[1] **and Zhang Junwei**[3]

[1]*School of Civil Engineering, Guangzhou University, Guangzhou 510006, China*
[2]*North China University of Water Resources and Electric Power, Zhengzhou 450045, China*
[3]*Henan Agricultural University, Zhengzhou 450002, China*

Correspondence should be addressed to Wang Tingyan; 124466715@qq.com

Received 25 April 2020; Revised 20 June 2020; Accepted 9 July 2020; Published 8 August 2020

Academic Editor: Peng Zhang

Based on the bending tests of seven reinforced concrete (RC) short beams strengthened with carbon fiber reinforced polymer (CFRP), the bending stiffness curves of the whole process of the short beams strengthened with CFRP were obtained. The variation law of bending stiffness curve of short beam in the whole loading process was analyzed. Based on the reasonable calculation assumption, the calculation method of flexural rigidity of short reinforced concrete beams strengthened with CFRP sheets in the whole loading process was put forward. The comparison between the calculated value and the test value of bending stiffness showed that the calculation method of bending stiffness was reasonable and had high calculation accuracy. This calculation method can be used not only in the calculation of flexural rigidity of short reinforced concrete beams strengthened with CFRP sheets but also in the calculation of flexural rigidity of ordinary short reinforced concrete beams. The calculation method in this paper can provide a theoretical basis for the deformation calculation of reinforced concrete short beams strengthened with CFRP sheets.

1. Introduction

In China, a large number of structural engineering has been damaged or destroyed due to the damage of natural disasters such as earthquake, the increase of service load, the long construction time, or the lower original design standard. It is necessary to reinforce and reconstruct the existing engineering structure. In the existing engineering structure, there is a kind of simply supported beam whose span height ratio is between 2 and 5, which is called short beam. Short beam is a common horizontal component in the existing engineering structure. It is not only widely used in construction engineering but also widely used in hydraulic engineering, port engineering, railway, highway, municipal engineering, and other fields [1]. Because of the small span height ratio, the short beam has a large bearing capacity. The failure of reinforced concrete short beam belongs to bad brittle failure. In order to improve the ductility and bearing capacity of reinforced concrete short beams, it can be realized by adding a certain amount of short fiber or by fiber reinforced polymer (FRP) reinforcement. Steel fiber, polypropylene fiber, and polyvinyl alcohol fiber are the short fibers to be added. This method is often used in new structure [2–4]. FRP is more suitable for the reinforcement of existing reinforced concrete structures. Among the commonly used FRP materials, the CFRP material has the best performance and is most commonly used in structural strengthening [5].

Scholars at home and abroad have done a lot of experimental and theoretical research on the flexural behavior of reinforced concrete shallow beams strengthened with FRP materials and achieved many research results [6–10]. There are many research studies on the calculation method of bearing capacity of beams strengthened with CFRP in the existing literature [11–15]. There are few studies on the stiffness of beams strengthened with CFRP in the existing literature [16–18]. In the existing literature, the research object of flexural rigidity is mostly reinforced concrete

shallow beam [19–21]. The stiffness analysis method is often used in the existing literature [22]. The obtained stiffness calculation formula is cumbersome or needs to be discussed [23–25]. The stress stage of the existing literature is the stage before the steel bars yield, and the stiffness after the steel bars yield has not been studied. In view of the importance of beam stiffness to deformation calculation and the lack of current research, based on the effective moment of inertia method, this paper further discusses the calculation method of short-term stiffness of reinforced concrete short beams strengthened with carbon fiber reinforced plastic sheets in the whole loading process.

In order to study the flexural rigidity of short RC beams strengthened with CFRP sheets, the flexural rigidity expression consistent with that of ordinary reinforced concrete beams is established. In this paper, the influence of CFRP layers, concrete strength grade, and longitudinal reinforcement ratio on the flexural rigidity of reinforced concrete short beams is studied through 7 members. In this paper, the calculation formula of flexural rigidity for short reinforced concrete beams strengthened with CFRP sheets and ordinary short reinforced concrete beams is put forward.

2. Experimental Program

Seven beams were designed in this experiment. The cross section of the beams was 150 mm in width and 500 mm in height. The clear span was 2000 mm with the span ratio of 4. The geometrical dimensions and reinforcement of the beams are shown in Figure 1. One beam was an ordinary RC short beam without CFRP sheets and the rest were RC short beams with CFRP sheets. As shown in Figure 2, CFRP sheets were pasted on the beam bottom to improve bending strength, and two strips of CFRP sheet with 100 mm width were set up in the bending shear zone of each side to prevent the occurrence of stripping at the ends. The detailed design parameters of beams are shown in Table 1. The measured elastic modulus of CFRP sheet was 246 GPa, the tensile strength was 3512 MPa, the thickness was 0.167 mm, and the elongation was 1.71%. The measured mechanical properties of concrete and reinforcement are shown in Tables 2 and 3.

A monotone static loading test was carried out for all beams. The concrete strain, deflection, inclination, and bearing capacity of beams are measured. The arrangement of test loading and measuring equipment is shown in Figure 3. The concrete strains in the compression zone, tension zone, and beam height range of the pure bending span were measured using the strain gauges of π shape. Strain-type displacement sensors were arranged in the upper part of the support, the lower part of the loading point, and the middle of the span to measure the deflection. Ten inclinometers were placed at 25 mm intervals on the top of the beam to measure the rotation angle of the top of the beam. All test data were collected by a data acquisition instrument.

The cracking load, yield load, and ultimate load of 7 test pieces measured in the test are listed in Table 4. The failure modes of CFRP strengthened beams include three modes: first tensile failure of CFRP, first crushing failure of concrete, and almost simultaneous boundary failure of both. The specific failure modes are also listed in Table 4.

The values of curvature and stiffness for the pure bending section of beam under different bending moments were calculated by equations (1) and (2). All bending moment-curvature curves and bending moment-stiffness curves are drawn in Figures 4–10.

$$\phi = \frac{1}{\rho} = \frac{\left(\overline{\varepsilon}_c + \overline{\varepsilon}_s\right)}{h}, \tag{1}$$

$$B = EI = \frac{M}{\phi}, \tag{2}$$

where ρ is the radius of curvature; $\overline{\varepsilon}_c$ is the average concrete strain in the compression zone of pure bending section; $\overline{\varepsilon}_s$ is average concrete strain in the tension zone of pure bending section; h is the average distance between strain gauge in the compression zone and the tension zone of the pure bending section; E is the elastic modulus of concrete; I is inertia moment of beam; and M is the bending moment of the midspan section.

The general characteristics of bending moment-curvature and bending moment-stiffness curves are shown in Figures 11 and 12, respectively. Curves are divided into three stages by the cracking moment, yielding moment, and ultimate bending moment:

(1) Stage of precracking of concrete: the curvature is linear, and linear slope is a maximum value. The stiffness is a constant value in general. However, the measured bending stiffness changes greatly because of the small curvature in this stage, which is affected by the precision of π strain gauge, and there will be small fluctuation in curvature. From formula (2), it can be seen that the small fluctuation of curvature will cause great fluctuation in bending stiffness. Therefore, the bending stiffness value close to the cracking load should be taken as the fixed value in this stage as far as possible.

(2) Stage of concrete cracking to the yield-steel: the curvature is approximately linear, the slope decreases, and the stiffness decreases sharply. A nonlinear regulation is presented in this stage.

(3) Stage of the yield-steel to the ultimate bearing state: the curvature is also approximately linear, and the slope and stiffness continuously decrease. A nonlinear change regulation is also presented in this stage.

3. Calculation of Bending Stiffness

3.1. Calculation Assumption. There are three assumptions for the calculation of bending stiffness:

The concrete is elastic in the precracking stage.

In the stage of concrete cracking to the yield-steel, the compressive strain of concrete is smaller than the peak strain. Concrete is assumed as a linear elastic material,

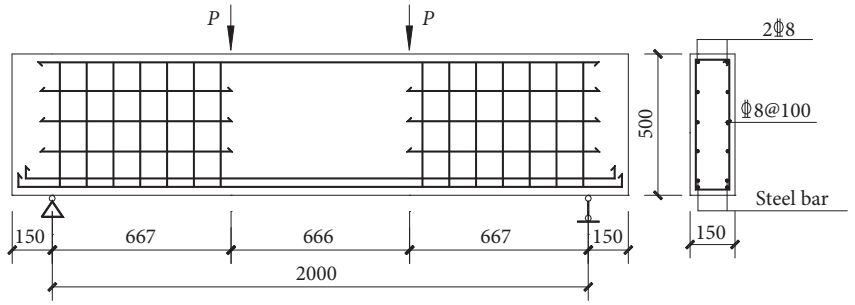

Figure 1: Specimen size and reinforcement drawing (unit: mm).

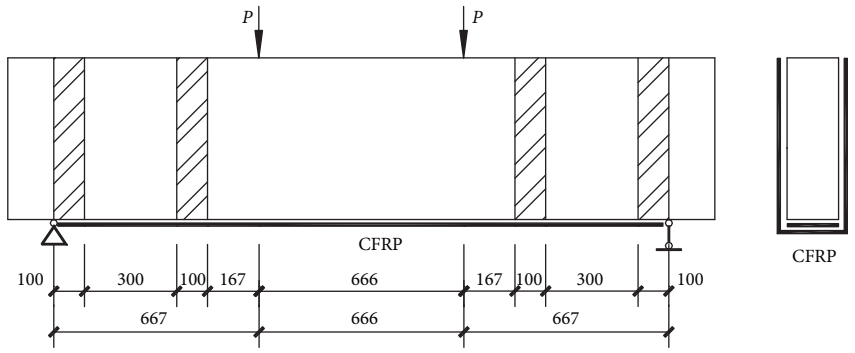

Figure 2: Specimen reinforcement (unit: mm).

Table 1: Design parameters of the specimen.

No.	Beams ID	CFRP sheet layers	Concrete strength	Reinforcement ratio (%)
1	B-0-30-4	0	C30	0.42
2	B-1-30-4	1	C30	0.42
3	B-2-30-4	2	C30	0.42
4	B-1-20-4	1	C20	0.42
5	B-1-40-4	1	C40	0.42
6	B-1-30-6	1	C30	0.60
7	B-1-30-8	1	C30	0.82

Table 2: Mechanical performance index of concrete.

Beams ID	Concrete strength			Modulus of elasticity (MPa)
	Cube strength (MPa)	Axial compressive strength (MPa)	Tensile strength (MPa)	
B-0-30-4	32.95	22.67	1.72	16073.9
B-1-30-4	38.11	32.62	2.40	23023.6
B-2-30-4	36.38	29.63	2.11	20325.7
B-1-20-4	35.60	26.67	2.06	19490.8
B-1-40-4	43.85	38.37	2.69	24078.7
B-1-30-6	35.49	21.91	1.82	20898.2
B-1-30-8	32.18	23.59	2.00	16495.0

Table 3: Mechanical performance index of steel bar.

Rebar grade	Diameter (mm)	Yield strength (MPa)	Tensile strength (MPa)	Modulus of elasticity (GPa)
HRB400	8	418	642	200
	10	411	641	200
	12	520	616	200
	14	421	543	200

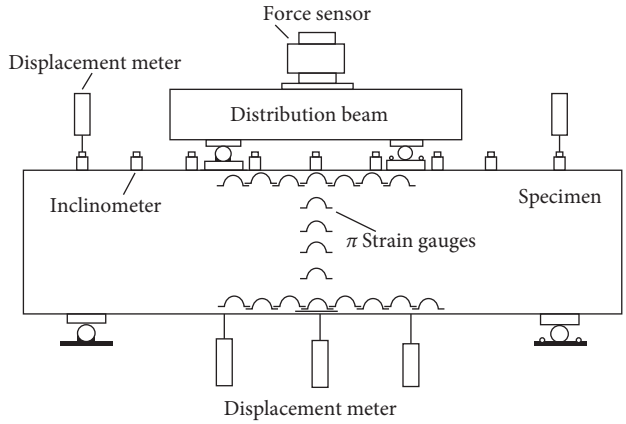

Figure 3: Layout of test measuring equipment (unit: mm).

Table 4: Main test results of the specimen.

Beams ID	Cracking load (kN)	Yield load (kN)	Ultimate load (kN)	Failure mode
B-0-30-4	66.5	153.0	223.0	Failure mode of suitable reinforced beam
B-1-30-4	100.0	188.9	282.0	CFRP sheet pulled
B-2-30-4	98.0	190.3	355.0	Boundary failure
B-1-20-4	83.0	154.4	283.0	CFRP sheet pulled
B-1-40-4	115.0	170.5	303.0	CFRP sheet pulled
B-1-30-6	82.5	294.8	358.9	Concrete crushed
B-1-30-8	92.0	325.0	371.4	Concrete crushed

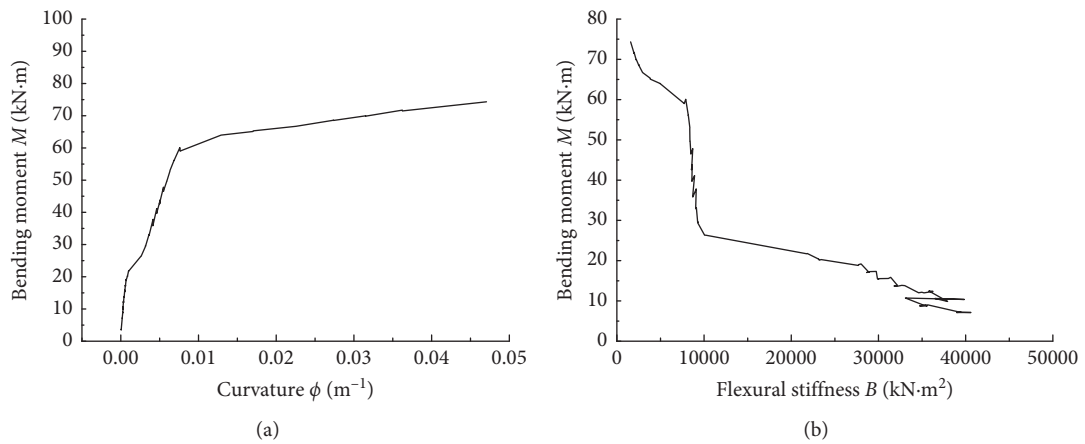

Figure 4: B-0-30-4. (a) Bending moment-curvature curve. (b) Bending moment-stiffness curve.

and the tensile steel bar is still elastic. The stress-strain relationship conforms to Hooke's law. The average strain of the beam section is assumed to be in line with the plane section assumption. The correction coefficient of internal force arm is taken into account for the short beam, and the calculation method is conformed to reference [16]. The resistance to tension of concrete in the tensile zone of cracking section is ignored.

The basic assumption in the stage of the steel yield to the ultimate bearing state is in accordance to reference [16].

3.2. Calculation of the Precracking Stage. In this stage, as the concrete has not cracked yet, the steel bar and CFRP sheet can be equivalent to concrete according to the elastic theory.

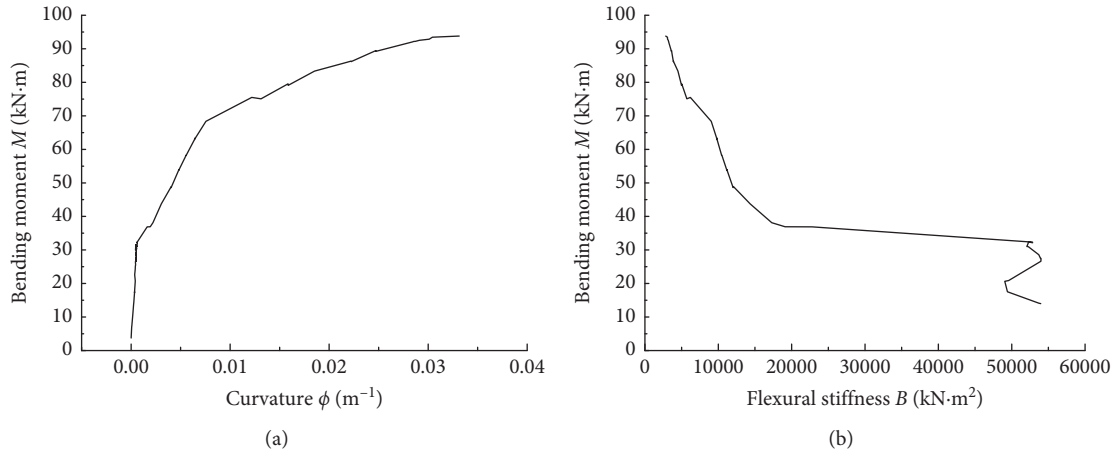

Figure 5: B-1-30-4. (a) Bending moment-curvature curve. (b) Bending moment-stiffness curve.

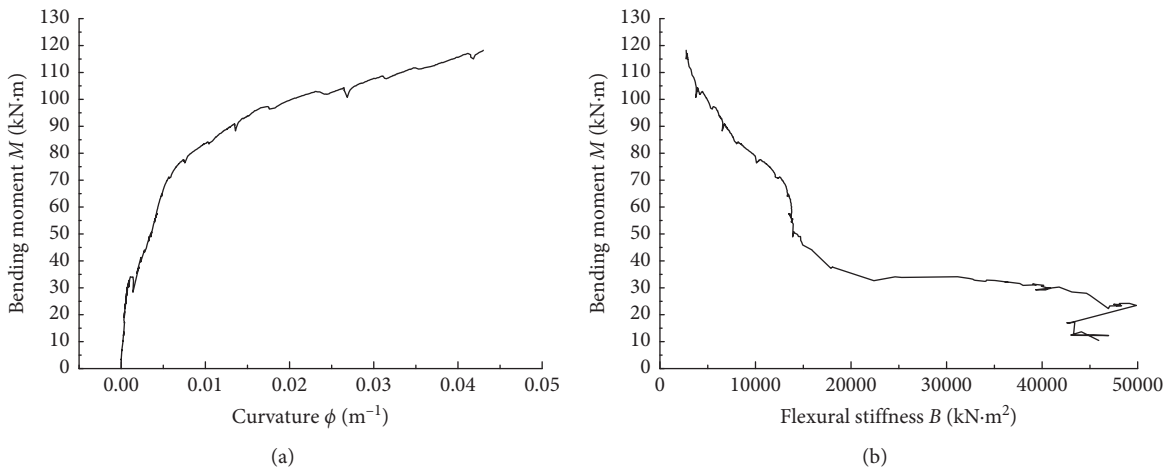

Figure 6: B-2-30-4. (a) Bending moment-curvature curve. (b) Bending moment-stiffness curve.

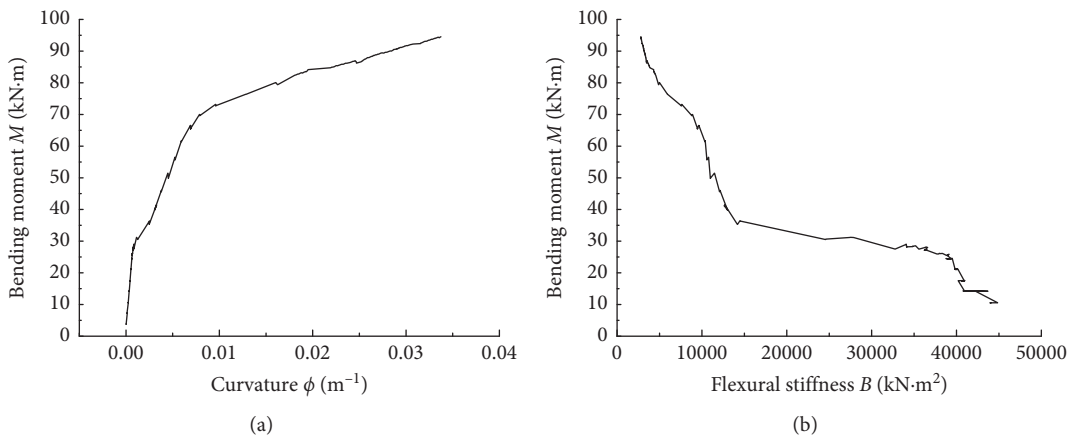

Figure 7: B-1-20-4. (a) Bending moment-curvature curve. (b) Bending moment-stiffness curve.

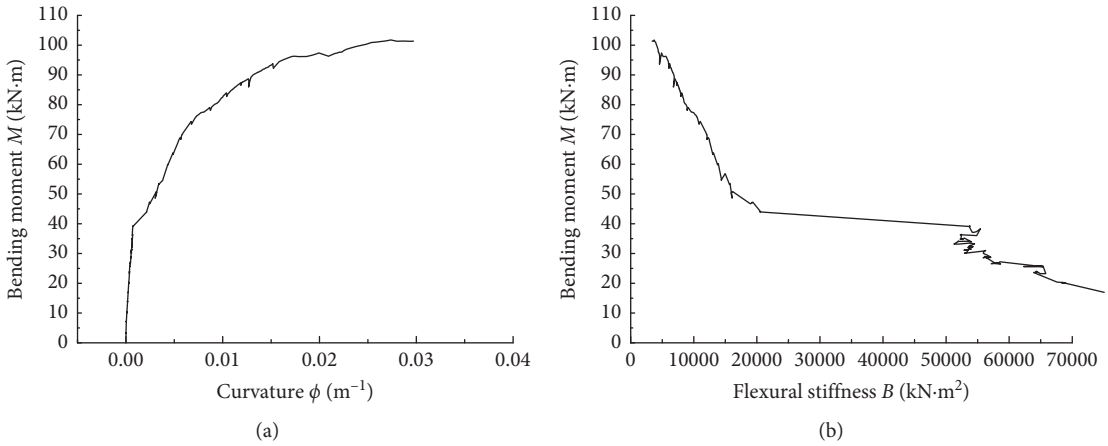

Figure 8: B-1-40-4. (a) Bending moment-curvature curve. (b) Bending moment-stiffness curve.

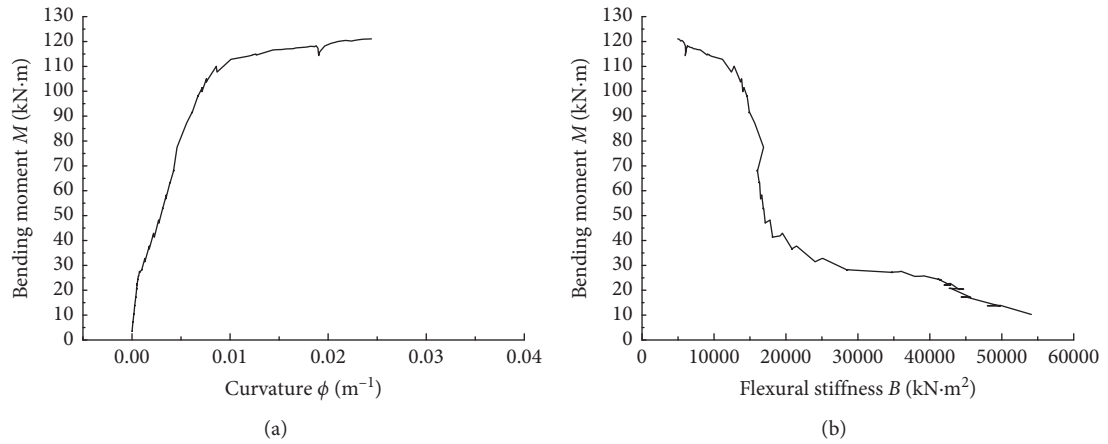

Figure 9: B-1-30-6. (a) Bending moment-curvature curve. (b) Bending moment-stiffness curve.

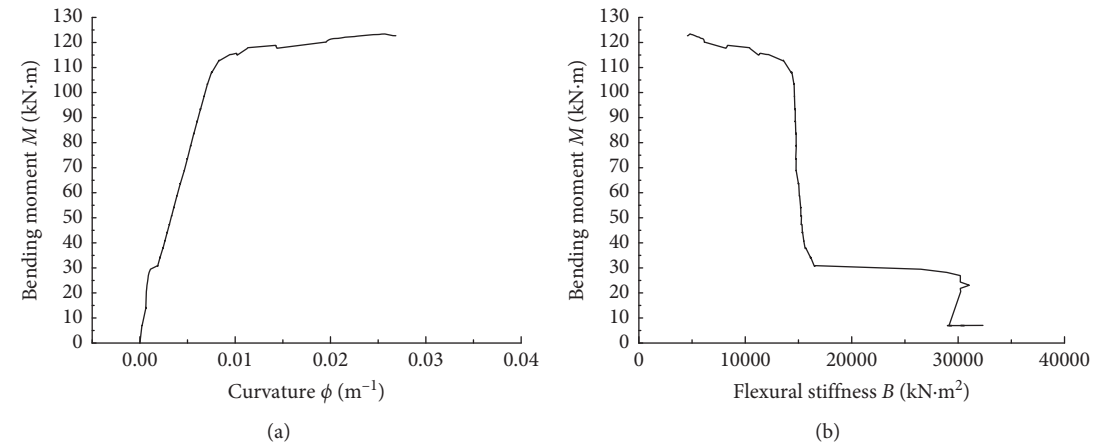

Figure 10: B-1-30-8. (a) Bending moment-curvature curve. (b) Bending moment-stiffness curve.

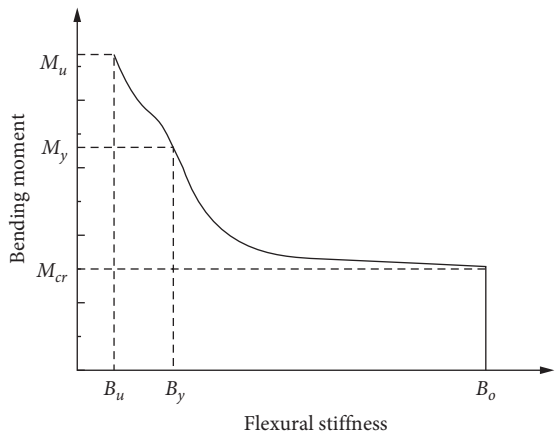

Figure 11: Characteristics of moment-stiffness curve.

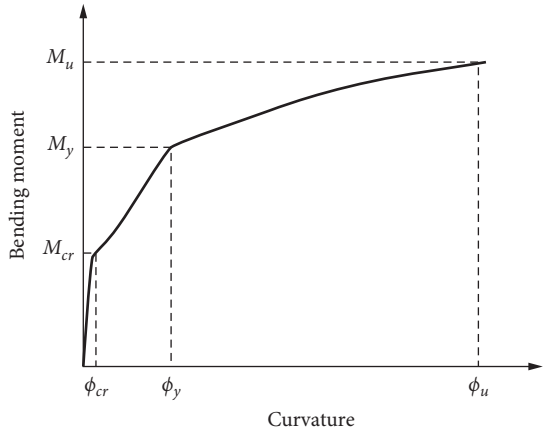

Figure 12: Characteristics of moment-curvature curve.

So, the calculation equations of parameters for beam section are established.

The height of neutral axis from the edge of concrete in the compressive zone x_0 and the inertia moment of section I_0 can be calculated by the following two equations:

$$x_0 = \frac{(bh^2/2) + (\alpha_E - 1)A_s h_0 + \alpha_f A_f h}{bh + (\alpha_E - 1)A_s + \alpha_f A_f}, \tag{3}$$

$$I_0 = \frac{bx_0^3}{3} + \frac{b(h - x_0)^3}{3} + (\alpha_E - 1)A_s(h_0 - x_0)^2 + \alpha_f A_f (h - x_0)^2, \tag{4}$$

where b, h, and h_0 are beam width, height, and the distance from the joint action point of tensile steel bars to the compression edge of the beam, respectively. A_s and A_f are section areas of tensile steel bar and CFRP sheet, respectively. α_E is the ratio of elastic modulus of steel bar to the elastic modulus of concrete (E_s/E_c). α_f is the ratio of elastic modulus of CFRP sheet to the elastic modulus of concrete (E_f/E_c). E_s, E_c, and E_f are elastic moduli of steel bar, concrete, and CFRP sheet, respectively. I_0 is the inertia moment of the uncracked beam section.

Thus, the bending stiffness B_0 of the uncracked beam section is calculated using the following equation:

$$B = B_0 = E_c I_0. \tag{5}$$

The cracking moment is calculated using the following equation:

$$M_{\mathrm{cr}} = \frac{\gamma_m f_t I_0}{(h - x_0)}, \tag{6}$$

where f_t is tensile strength of concrete and γ_m is the plastic coefficient of section resistance moment. The value of γ_m is 1.75, referring to the ordinary RC beam.

3.3. Calculation of Concrete Cracking to the Yield-Steel. It is assumed that the concrete in the compression zone is a linear elastic material, and the cross-sectional force diagram at this stage is shown in Figure 13. C is the resultant force of compression concrete. σ_s and A_s are tensile stress and area of steel bars, respectively. σ_f and A_{fe} are the tensile stress and effective area of CFRP sheets. A_{fe} is the actual area of the CFRP sheet multiplied by the thickness reduction coefficient K_m. The value of K_m is determined according to Chinese specification GB50367-2013 [26].

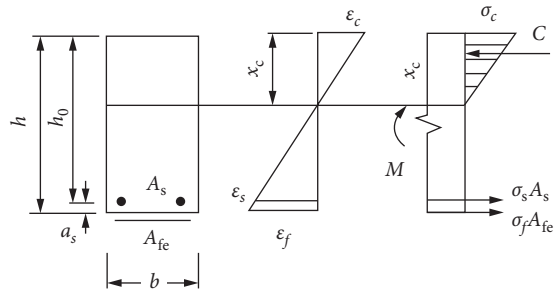

Figure 13: Cross-sectional diagram of force.

When the tensile steel yields, equations (7) and (8) can be obtained according to the equilibrium condition of the force.

$$f_y A_s + \sigma_f A_{fe} - \frac{1}{2} b x_c \sigma_c = 0, \tag{7}$$

$$E_s \varepsilon_y A_s + E_f \varepsilon_f A_{fe} - \frac{1}{2} b x_c E_c \varepsilon_c = 0, \tag{8}$$

where f_y, σ_c, and x_c are yield strengths of steel bar, compressive stress of concrete, and height of the concrete compression zone, respectively.

The yield strain ε_y of steel bar is known from $\varepsilon_y = (f_y/E_s)$. As shown in equations (9) and (10), the concrete strain ε_c and CFRP sheet strain ε_f can be obtained from the similar triangle relation of strain.

$$\varepsilon_c = \frac{\varepsilon_y x_c}{h_0 - x_c}, \tag{9}$$

$$\varepsilon_f = \frac{\varepsilon_y (h - x_c)}{h_0 - x_c}. \tag{10}$$

Equations (9) and (10) are substituted into equation (8) to obtain the following equation:

$$E_s \varepsilon_y A_s + E_f \frac{\varepsilon_y (h - x_c)}{h_0 - x_c} A_{fe} - \frac{1}{2} b x_c E_c \frac{\varepsilon_y x_c}{h_0 - x_c} = 0. \tag{11}$$

The height of the compression zone x_c can be obtained by solving equation (11), and then the yield bending moment is obtained as follows:

$$M_y = E_s \varepsilon_y A_s \alpha_d \left(h_0 - \frac{x_c}{3}\right) + E_f \varepsilon_f A_f \alpha_d \left(h - \frac{x_c}{3}\right). \tag{12}$$

When the steel yields, the inertia moment of the cracked section I_{cr} can be calculated by the following equation:

$$I_{cr} = \frac{1}{3} b x_c^3 + (\alpha_E - 1) A_s (h_0 - x_c)^2 + \alpha_f A_f (h - x_c)^2. \tag{13}$$

The inertia moment of the cracked section I_{cr} is the minimum inertia moment of each section along the component axis. The stiffness of the cracked section is calculated using the following equation:

$$B_{cr} = E_c I_{cr}. \tag{14}$$

In this stage, the value of average section stiffness B is a value between B_0 and B_{cr}, which decreases with the increase of bending moment.

For the ordinary RC beam, according to the United States code ACI318-05 [27], the effective stiffness of the beam section B_{eff} in normal service stage is calculated using the following equation:

$$B_{eff} = E_c I_{eff} = \left(\frac{M_{cr}}{M}\right)^3 E_c I_0 + \left[1 - \left(\frac{M_{cr}}{M}\right)^3 E_c I_{cr}\right]. \tag{15}$$

According to the test data of bending moment-bending stiffness curve in this experiment, the equation of bending stiffness for RC short beams strengthened by CFRP sheet is obtained using the nonlinear regression method.

$$B = \left(\frac{M_{cr}}{M}\right)^4 B_0 + \left[1 - \left(\frac{M_{cr}}{M}\right)^4 B_{cr}\right]. \tag{16}$$

When the bending moment M is the yield bending moment M_y, the calculated yield stiffness B_y of the beam is calculated using the following equation:

$$B_y = \left(\frac{M_{cr}}{M_y}\right)^4 B_0 + \left[1 - \left(\frac{M_{cr}}{M_y}\right)^4 B_{cr}\right]. \tag{17}$$

3.4. Calculation of Longitudinal Bars after Yielding. Two bending failure modes as breakage of CFRP sheet and crushing of concrete are observed in this experiment. Two theoretical equations for calculating the bending capacity M_u in corresponding failure modes have been established in literature [16]. The calculation method in this paper is the same as that in reference [16]. Equations (18) and (19) are calculation equations of section curvature ϕ_u, respectively.

For the breakage of CFRP sheet:

$$\phi_u = \frac{(0.9\varepsilon_{fu}/(h - x_c))}{\alpha_d}. \tag{18}$$

For the crushing of concrete:

$$\phi_u = \frac{(\varepsilon_{cu}/x_c)}{\alpha_d}. \tag{19}$$

In the ultimate bearing state, the bending stiffness B_u is calculated using the following equation:

Table 5: Experimental and calculated values of cracking moment, yield moment, and ultimate moment of member (unit: kN·m).

Beam ID	M_{cr}			M_y			M_u		
	Exp.	Cal.	Ratio	Exp.	Cal.	Ratio	Exp.	Cal.	Ratio
B-0-30-4	22.17	21.24	1.044	50.99	152.51	0.971	74.33	71.73	1.036
B-1-30-4	33.33	28.91	1.153	62.95	59.77	1.053	94.00	95.62	0.983
B-2-30-4	32.67	26.13	1.250	63.42	65.97	0.961	118.33	114.24	1.036
B-1-20-4	27.67	25.27	1.095	51.47	59.41	0.866	94.33	93.59	1.008
B-1-40-4	38.33	32.25	1.188	56.82	59.89	0.949	101.00	97.93	1.031
B-1-30-6	27.50	22.98	1.196	98.26	102.86	0.955	119.63	120.48	0.993
B-1-30-8	30.67	27.63	1.110	108.33	107.53	1.008	123.80	128.48	0.964
Mean value	30.33	26.34	1.148	70.32	86.85	0.966	103.63	103.15	1.007
Mean-square deviation	5.17	3.69	0.070	23.23	35.69	0.057	17.91	19.27	0.029
Coefficient of variation	0.17	0.14	0.061	0.33	0.41	0.059	0.17	0.19	0.028

M_{cr} denotes cracking moment. M_y denotes yield moment. M_u denotes ultimate moment.

Table 6: Experimental and calculated values of cracking curvature, yield curvature, and ultimate curvature of members.

Beam ID	ϕ_{cr}			ϕ_y			ϕ_u		
	Exp.	Cal.	Ratio	Exp.	Cal.	Ratio	Exp.	Cal.	Ratio
B-0-30-4	9.98	8.94	1.116	0.592	0.553	1.071	4.965	4.363	1.138
B-1-30-4	6.71	7.45	0.900	0.640	0.532	1.203	3.313	3.328	0.995
B-2-30-4	8.82	7.70	1.144	0.568	0.593	0.958	4.302	3.556	1.210
B-1-20-4	7.52	7.66	0.982	0.453	0.578	0.784	3.367	3.391	0.993
B-1-40-4	7.29	8.10	0.900	0.401	0.468	0.857	2.970	3.308	0.898
B-1-30-6	7.68	7.50	1.024	0.673	0.833	0.808	2.442	2.976	0.821
B-1-30-8	10.60	11.10	0.955	0.753	0.783	0.962	2.686	2.971	0.904
Mean value	8.37	8.35	1.003	0.580	0.62	0.949	3.44	3.41	0.994
Mean-square deviation	1.47	1.32	0.098	0.120	0.14	0.150	0.90	0.47	0.138
Coefficient of variation	0.18	0.16	0.097	0.210	0.22	0.158	0.26	0.14	0.139

ϕ_{cr} is cracking curvature. ϕ_y is yield curvature. ϕ_u is ultimate curvature.

Table 7: Experimental and calculated values of cracking stiffness, yield stiffness, and ultimate stiffness of members.

Beam ID	B_0			B_y			B_u		
	Exp.	Cal.	Ratio	Exp.	Cal.	Ratio	Exp.	Cal.	Ratio
B-0-30-4	2.22	2.38	0.933	0.86	0.95	0.906	1.50	1.64	0.915
B-1-30-4	4.97	3.88	1.281	0.98	1.12	0.879	2.84	2.87	0.990
B-2-30-4	3.71	3.39	1.094	1.12	1.11	1.009	2.75	3.21	0.857
B-1-20-4	3.68	3.30	1.115	1.14	1.03	1.107	2.80	2.76	1.014
B-1-40-4	5.26	3.98	1.322	1.42	1.28	1.109	3.40	2.96	1.149
B-1-30-6	3.58	3.06	1.170	1.46	1.23	1.187	4.90	4.05	1.210
B-1-30-8	2.89	2.49	1.161	1.44	1.37	1.051	4.61	4.32	1.067
Mean value	3.76	3.21	1.154	1.20	1.16	1.035	3.26	3.12	1.029
Mean-square deviation	1.07	0.62	0.128	0.24	0.15	0.112	1.17	0.89	0.124
Coefficient of variation	0.28	0.19	0.111	0.20	0.13	0.108	0.36	0.28	0.121

B_0 is cracking stiffness. B_y is yield stiffness. B_u is ultimate stiffness.

$$B_u = \frac{M_u}{\phi_u}. \tag{20}$$

At this stage, the value of bending stiffness B of the beam section is a value between B_y and B_u and decreases with the increase of bending moment. According to the experimental data of bending moment-bending stiffness, the nonlinear regression method is adopted to obtain the calculation equation of bending stiffness of RC beams reinforced by CFRP sheet in the stage of yield-steel to the ultimate bearing state.

$$B = \frac{B_y + \left(B_u - B_y\right)\left(M - M_y\right)^{0.7}}{\left(M_u - M_y\right)^{0.7}}. \tag{21}$$

When the bending moment M is equal to the yield bending moment M_u, the bending stiffness of the beam is calculated using the following equation:

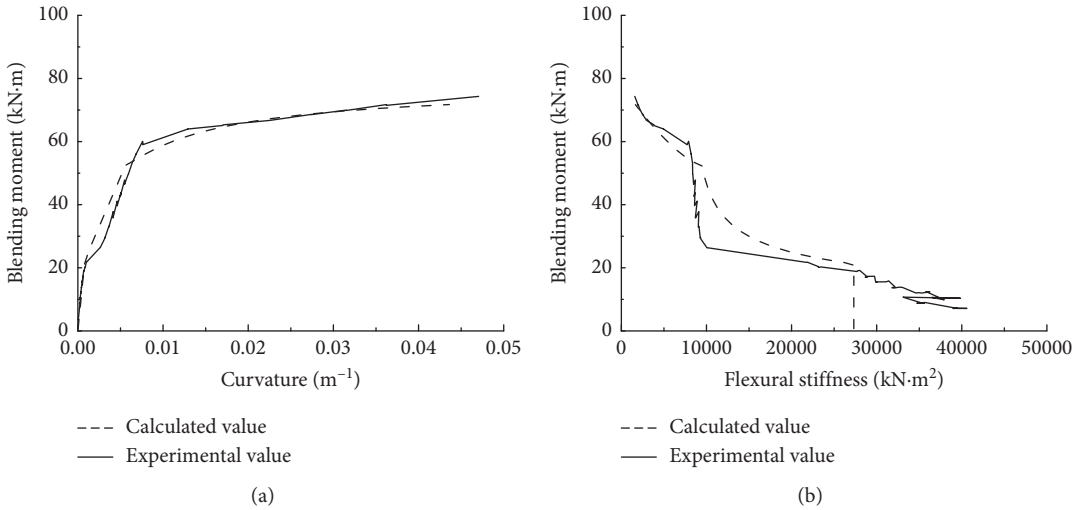

Figure 14: Beam B-0-30-4. (a) Bending moment-curvature curve. (b) Bending moment-stiffness curve.

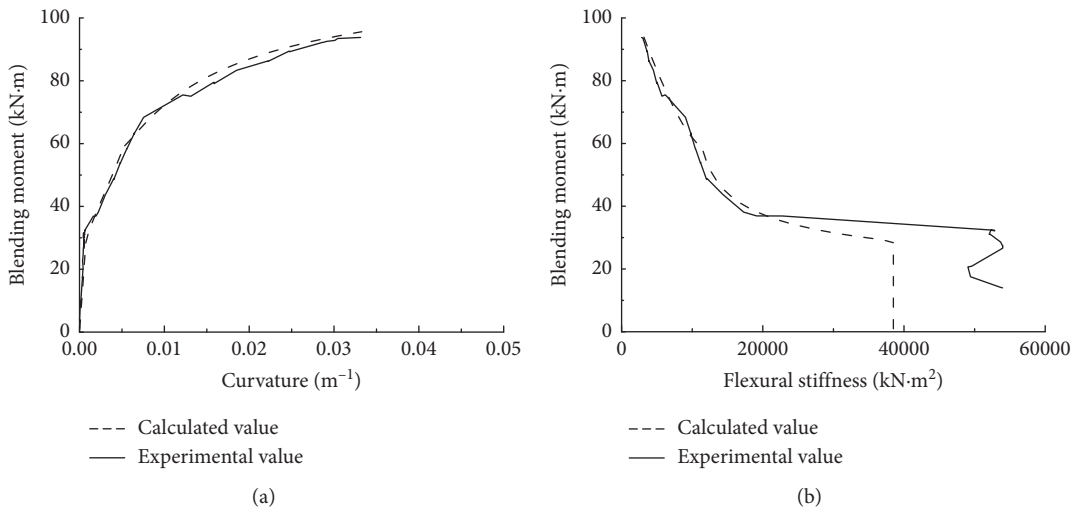

Figure 15: Beam B-1-30-4. (a) Bending moment-curvature curve. (b) Bending moment-stiffness curve.

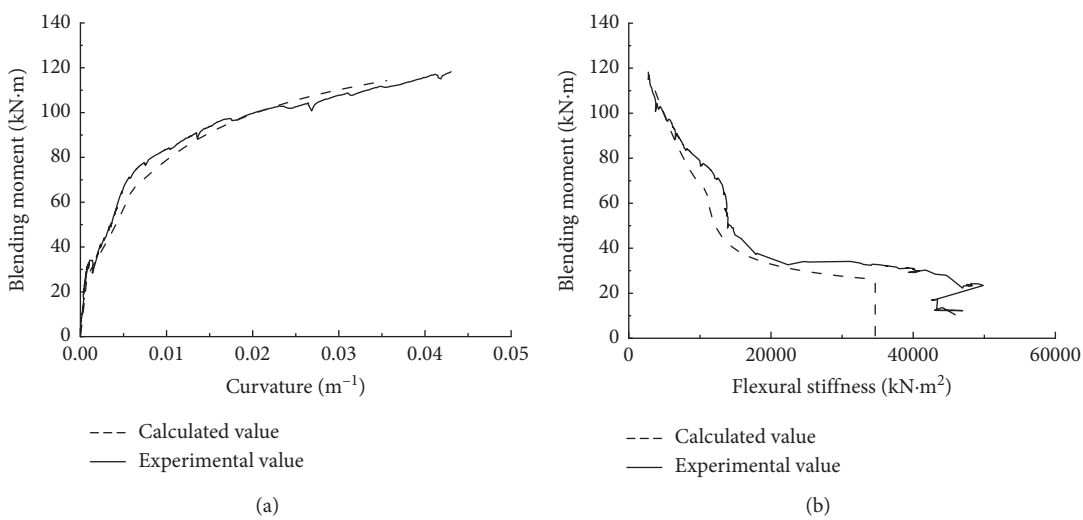

Figure 16: Beam B-2-30-4. (a) Bending moment-curvature curve. (b) Bending moment-stiffness curve.

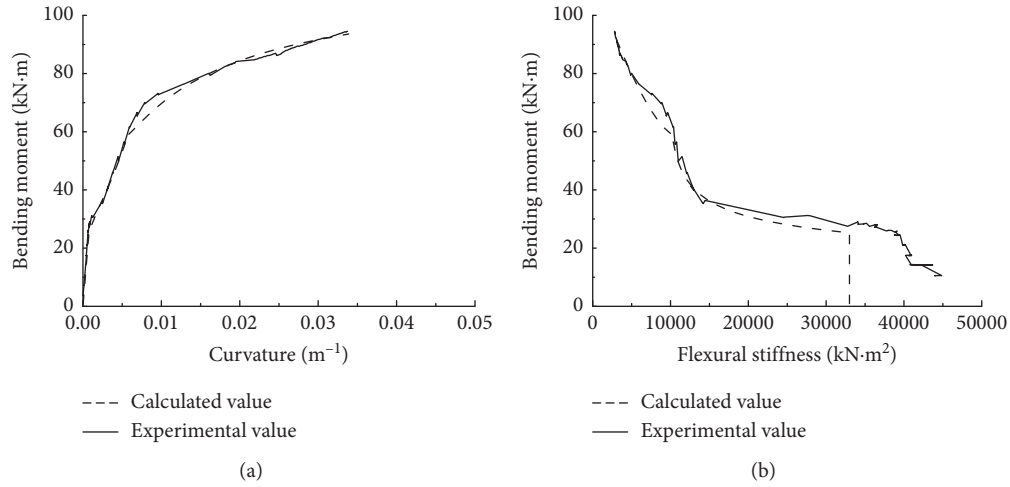

Figure 17: Beam B-1-20-4. (a) Bending moment-curvature curve. (b) Bending moment-stiffness curve.

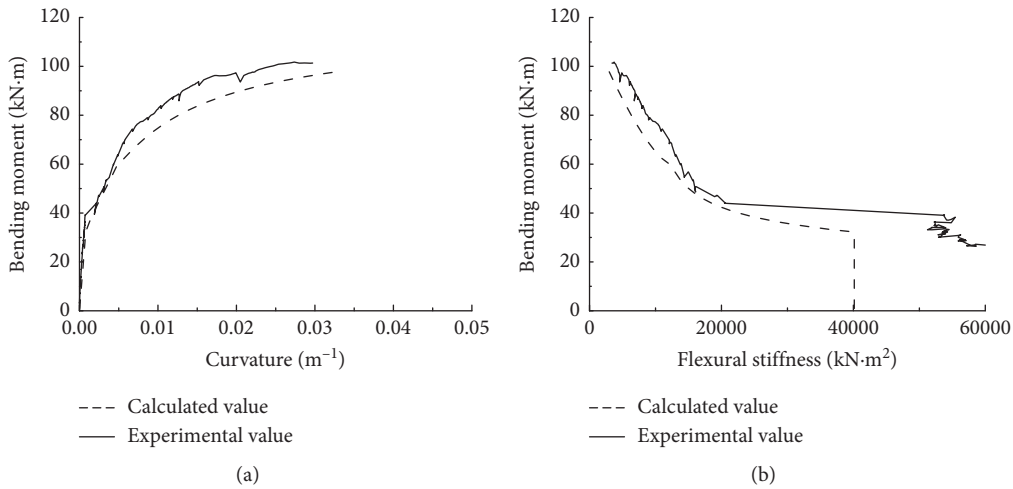

Figure 18: Beam B-1-40-4. (a) Bending moment-curvature curve. (b) Bending moment-stiffness curve.

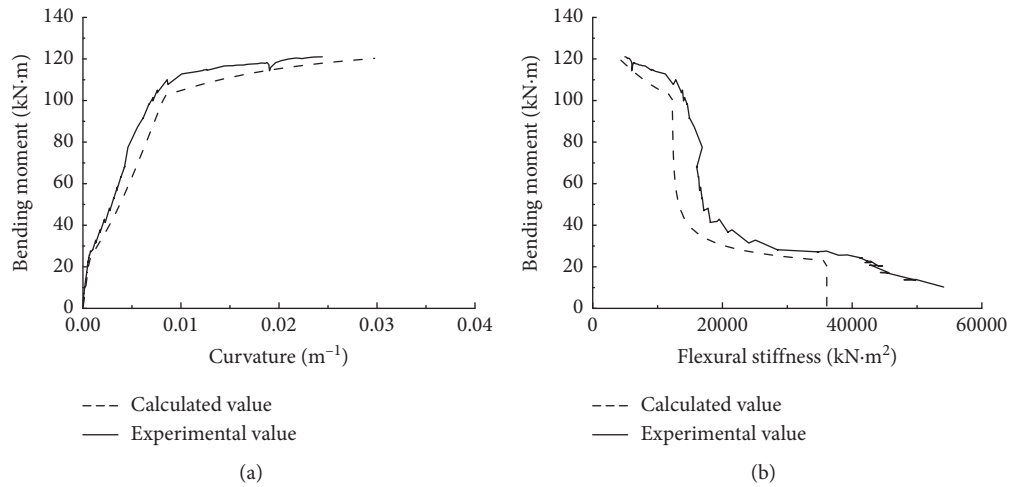

Figure 19: Beam B-1-30-6. (a) Bending moment-curvature curve. (b) Bending moment-stiffness curve.

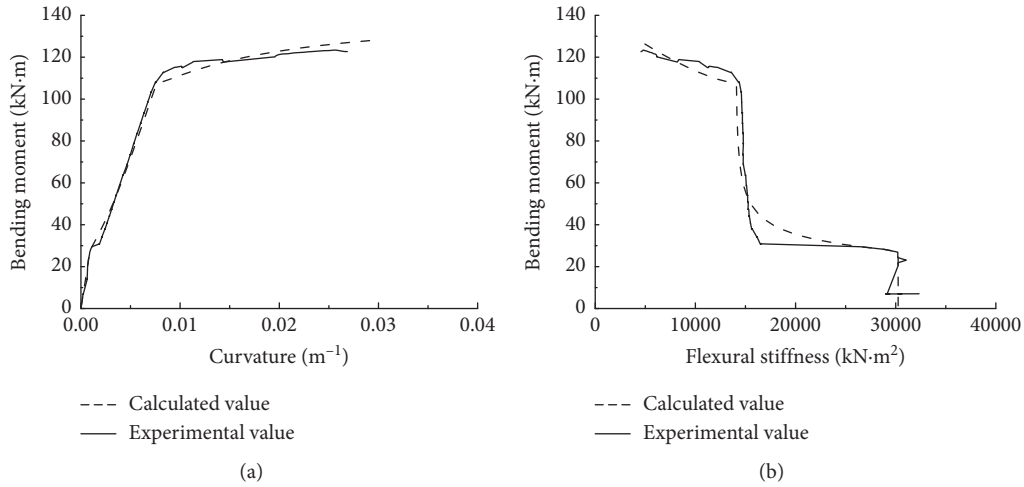

Figure 20: Beam B-1-30-8. (a) Bending moment-curvature curve. (b) Bending moment-stiffness curve.

$$B = B_u. \tag{22}$$

4. Comparison of Calculated and Experimental Data

The test and calculated values of cracking, yield, and ultimate bending moment are shown in Table 5. The ratio in the table is the calculated value divided by the test value. The average values of the ratio of cracking, yield, and ultimate bending moment are 1.148, 0.996, and 1.007, respectively. The coefficient of variation of the ratio of cracking, yield, and ultimate bending moment is 0.061, 0.059, and 0.028, respectively.

The test and calculated values of cracking, yield, and ultimate curvature are shown in Table 6. The ratio in the table is the calculated value divided by the test value. The average values of the ratio of cracking, yield, and ultimate curvature are 1.003, 0.949, and 0.994, respectively. The coefficients of variation of the ratio of cracking, yield, and ultimate curvature are 0.097, 0.158, and 0.139, respectively.

The test and calculated values of cracking, yield, and ultimate bending stiffness are shown in Table 7. The ratio in the table is the calculated value divided by the test value. The average values of the ratio of cracking, yield, and ultimate flexural rigidity are 1.154, 1.035, and 1.029, respectively. The coefficient of variation of the ratio of cracking, yield, and ultimate flexural rigidity is 0.111, 0.108, and 0.121, respectively.

The bending moment-curvature curve and bending moment-flexural rigidity curve are shown in Figures 14–20. It can be seen from the figures that the dotted line is the calculated value and the solid line is the test value. Except for the difference between the calculated value and the test value at the cracking moment, the calculated value and the test value at the rest of the moment are basically consistent.

The comparison between Tables 5–7 and Figures 14–20 shows that the bending rigidity calculation method proposed in this paper is reasonable, with high calculation accuracy, and is suitable for the bending rigidity calculation of reinforced concrete short beams strengthened with carbon fiber sheet.

5. Conclusions

Based on the experiment of flexural performance of short reinforced concrete beams strengthened with CFRP sheets, the calculation method of flexural rigidity of short beams in the whole loading process was proposed. The calculated flexural rigidity value was compared with the experimental value, and the following conclusions are drawn:

The characteristics of the bending moment-curvature curve and the bending moment-stiffness curve of the pure bending section in the span of 7 specimens were obtained. The curve of flexural stiffness was divided into three sections by cracking load and yield load. The bending stiffness curve after cracking moment was nonlinear.

According to the characteristics of the three stress stages, the reasonable calculation assumption was adopted. Based on the effective moment of inertia method, the calculation formula of flexural rigidity of reinforced concrete short beams strengthened with CFRP sheets was proposed. The formula was applicable to both short beams strengthened by CFRP and ordinary reinforced concrete beams without reinforcement, and the calculation accuracy was high.

The calculation method of flexural rigidity proposed in this paper can provide theoretical basis for the calculation of the corner of the reinforced concrete short beam strengthened by CFRP and also provide data support and reference for other research studies in the future.

Data Availability

The data used to support the findings of the study are available from the corresponding author upon request.

Conflicts of Interest

The authors declare that they have no conflicts of interest.

Authors' Contributions

Wang Tingyan did the whole experiment and wrote the article, Zhang Junwei calculated the data, and Zhou Yun revised the article. All authors have read and agreed to the published version of the manuscript.

Acknowledgments

This study was supported by the National Natural Science Foundation of China (No. 50579068 and 51708514).

References

[1] T. Wang and J. Zhang, "Experimental study on the flexural performance of reinforced concrete short beams strengthened by CFRP sheets," *Building Structure*, vol. 50, no. 2, pp. 76–81, 2020, in Chinese.

[2] P. Zhang, Y. Zheng, K. Wang, and K. Zhang, "Combined influence of nano-CaCO3 and polyvinyl alcohol fibers on fresh and mechanical performance of concrete incorporating fly ash," *Structural Concrete*, vol. 21, no. 2, pp. 724–734, 2020.

[3] P. Zhang, Y. Ling, J. Wang, and Y. Shi, "Bending resistance of PVA fiber reinforced cementitious composites containing nano-SiO_2," *Nanotechnology Reviews*, vol. 8, no. 1, pp. 690–698, 2019.

[4] P. Zhang, L. Kang, J. Wang, J. Guo, S. Hu, and Y. Ling, "Mechanical properties and explosive spalling behavior of steel-fiber-reinforced concrete exposed to high temperature-a review," *Applied Sciences*, vol. 10, no. 7, pp. 1–21, 2020.

[5] X. Chen, *Guide for the Design and Construction of Fiber Reinforced Plastics in Civil Engineering*, pp. 1–4, China Architecture & Building Press, Beijing, China, 2009, in Chinese.

[6] S. Shang, H. Peng, H. Tong, and L. Zhang, "Study of strengthening reinforced concrete beam using prestressed carbon fiber sheet," *Journal of Building Structures*, vol. 24, no. 5, pp. 24–30, 2003.

[7] L. Bu, L. Song, and C. Shi, "Experimental and theoretical study on flexural behavior of RC beams strengthened with carbon fiber plates (CFP)," *Journal of Building Structures*, vol. 28, no. 1, pp. 72–79, 2007.

[8] J. Yang, G. Xiong, Z. Yan et al., "Experimental study on flexural strength of hybrid CF/SGF composite strengthening concrete beams," *China Civil Engineering Journal*, vol. 37, no. 7, pp. 18–22, 2004.

[9] Y. Yang, Q. Yue, and L. Ye, "Calculation for flexural debonding bearing capacity of RC beams strengthened with carbon fiber sheets," *China Civil Engineering Journal*, vol. 37, no. 2, pp. 23–32, 2004.

[10] M. R. Esfahani, M. R. Kianoush, and A. R. Tajari, "Flexural behaviour of reinforced concrete beams strengthened by CFRP sheets," *Engineering Structures*, vol. 29, no. 10, pp. 2428–2444, 2007.

[11] L. I. Xiang and X. GU, "Bending bearing capacity of low strength reinforced concrete beams strengthened with carbon fiber composite sheets," *China Civil Engineering Journal*, vol. 45, no. 1, pp. 23–29, 2012, in Chinese.

[12] D. Gao, Pu Zhang, and C. Zhang, "Flexural performance of reinforced concrete one-way slabs strengthened with fiber reinforced polymer sheets," *Journal of Building Structures*, vol. 36, no. 7, pp. 51–58, 2015, in Chinese.

[13] Q. Kong and L. Liu, "Experimental investigation of RC beam strengthened with CFRP," *Journal of Zhengzhou University (Engineering Science)*, vol. 25, no. 4, pp. 24–27, 2004.

[14] W. Zhang, X. Wang, and X. Gu, "Flexural behavior of corroded reinforced concrete beams strengthened with carbon fiber composite sheets," *China Civil Engineering Journal*, vol. 43, no. 6, pp. 34–41, 2010.

[15] W. Zheng, W. Chen, and M. Wang, "Experimental study on flexural behavior of concrete beams strengthened with CFRP sheets bonded with an inorganic matrix," *China Civil Engineering Journal*, vol. 43, no. 4, pp. 37–45, 2010, in Chinese.

[16] D. Gao, T. Wang, and Y. He, "Flexural test and calculation on capacity of reinforced concrete short beam strengthened by CFRP sheets," *Journal of Building Structures*, vol. 38, no. 11, pp. 122–131, 2017.

[17] R. Z. Al-Rousan and M. A. Issa, "Flexural behavior of RC beams externally strengthened with CFRP composites exposed to severe environment conditions," *KSCE Journal of Civil Engineering*, vol. 21, pp. 2300–2309, 2017.

[18] G. Spadea, F. Bencardino, and R. N. Swamy, "Structural behavior of composite RC beams with externally bonded CFRP," *Journal of Composites for Construction*, vol. 2, no. 3, pp. 132–137, 1998.

[19] X. Chen, H. Li, and X. Zhu, "Experimental and theoretical research on short-term stiffness of reinforced concrete beams strengthened with FRP sheets," *Journal of Building Structures*, vol. 39, no. 1, pp. 146–152, 2018.

[20] D. Gao, D. Fang, and Y. Zhu, "Flexural property and calculation method of one-way reinforced concrete slabs externally prestressed with unbonded FRP tendons," *Journal of Basic Science & Engineering*, vol. 23, no. 1, pp. 115–126, 2015, in Chinese.

[21] X. Wang, X. Gu, and W. Zhang, "Flexural stiffness of corroded reinforced concrete beams strengthened with carbon fiber composite sheets," *Journal of Building Structures*, vol. 30, no. 5, pp. 169–176, 2009, in Chinese.

[22] Y. Yang and Q. Yue, "Calculation of sectional stiffness of RC beams strengthened with carbon fiber sheet," *Industrial Construction*, vol. 31, no. 9, pp. 1–4, 2001.

[23] M. Yang and S. Wang, "Calculation of bending stiffness of reinforced concrete beams strengthened with carbon fiber sheets," *Building Science*, vol. 21, no. 4, pp. 34–37, 2005.

[24] G. E. Chao, *Calculation of Bending Stiffness of Reinforced Concrete Beams Strengthened with Carbon Fiber Sheets*, pp. 66–68, Kunming University of Science & Technology, Kunming, China, 2012, in Chinese.

[25] P. Zhang, H. Zhu, S. Meng, and G. Wu, "Calculation of sectional stiffness and deflection of FRP sheets strengthened reinforced concrete beams," *Journal of Building Structures*, vol. 32, no. 4, pp. 87–94, 2011, in Chinese.

[26] National Standards of the People's Republic of China, *Code for Design of Strengthening Concrete Structure (GB50367-2013)*, China Architecture& Building Press, Beijing, China, 2013, in Chinese.

[27] American Concrete Institute Committee: Building Code Requirements for Structural Concrete (ACI318-05).

Hindawi
Advances in Civil Engineering
Volume 2020, Article ID 8853442, 9 pages
https://doi.org/10.1155/2020/8853442

Research Article

Experimental Evaluation of the Influence of Early Disturbance on the Performance of Basalt Fiber Concrete

Zhe Huang, Yan Li, Yichen Liu, Fengjie Cai, and Tianyu Liang

School of Highway, Chang'an University, Xi'an 710064, China

Correspondence should be addressed to Yan Li; liyan@chd.edu.cn

Received 27 May 2020; Revised 10 July 2020; Accepted 14 July 2020; Published 31 July 2020

Academic Editor: Peng Zhang

By applying early disturbance to the concrete, the influence of the disturbance on the macroscopic mechanical properties of basalt fiber concrete during the period from the initial setting to the final setting is explored, and the influence mechanism is revealed. Also, the influence of this disturbance on the process of sulfate erosion of concrete is evaluated by the sulfate erosion test and by the ultrasonic data acquisition of its damage process. The experimental results show that the flexural strength of basalt fiber concrete is increased after the concrete has been disturbed in the early stage of condensation but is decreased in the middle stage of condensation and is not affected in the later stage. When the condensation and hardening processes are disturbed, damage is caused inside the concrete, which is greater with the increase in the condensation degree until the penetration resistance reaches about 15 MPa, which then is more and more reduced. The durability of basalt fiber concrete is reduced by disturbance, which has a significant effect on it when the penetration resistance is between 7 MPa and 16 MPa.

1. Introduction

Concrete materials demonstrate excellent compressive performance, but the tensile strength is only 1/10 of its compressive strength, which is unfavorable to the concrete in the tensile zone of the structure [1–3]. Addition of fiber can much improve this defect. There are many kinds of fibers often used in concretes, such as steel fiber, carbon fiber, glass fiber, cellulose fiber, polypropylene fiber, and polyvinyl acetate (PVA) fiber [4, 5]. The addition of fiber can improve the strength and durability of concrete, prolong its service life, and adapt to complex environment [6–8]. In the early stage of condensation and hardening, since the cement hydration process has not been completed, the strength and bonding properties of concrete continue to change with the age of it, and the structural properties of concrete also keep changing. Therefore, the concrete structure in the early age is essentially different from that in the normal use stage [9, 10]. As a heterogeneous mixed material, the performance of hardened concrete depends on its early microstructure formation process [11]. In order to ensure the overall progress and continuity of the project, blasting excavation and impact piling are often carried out in parallel with the concrete pouring construction, resulting in inevitable construction vibration around the concrete structure, and we call it disturbance [12, 13]. Before the concrete is finally set, its internal microstructure has not been fully formed, and the concrete is very sensitive to the influence of external disturbances. Disturbance causes tensile stress inside the concrete, resulting in microcracks that cannot be closed [14, 15]. The presence of these microcracks will provide an intrusive channel for corrosive media, which not only directly affects the aesthetics of building decoration but affects the durability and working life. Compared with ordinary concrete, the tensile strength and ultimate elongation of fiber concrete are improved [16, 17]. Studies show that addition of fibers significantly improves the early plastic cracking, antiabrasion, and impact resistance of mortar and concrete [18]. Fiber has a significant effect on the crack resistance of cement concrete. The chaotic support system formed by the fibers in concrete produces an effective reinforcement effect, which greatly improves the crack resistance of concrete [19].

Basalt fiber is a new type of concrete reinforced material. It has the advantages of high cost performance, high tensile

strength, anticorrosion, high temperature resistance, and good crack resistance, which make it an ideal substitute for other fiber materials [20–22]. At present, the research on basalt fiber in the field of civil engineering is mainly focused on the mechanical properties of basalt fiber concrete, but the influence of disturbance on basalt fiber concrete is rarely studied [23]. Therefore, systematic research on the impact of disturbance on the performance of early basalt concrete is of important theoretical and practical value to the analysis and control of early disturbance safety during the construction period of fiber-reinforced concrete structures.

2. Test Materials and Methods

2.1. Test Material and Specimen Preparation

2.1.1. Test Material. The cement used in the test was P•O 42.5R cement, and the performance indices are shown in Table 1. Natural river sand was adopted as fine aggregate, whose fineness modulus was 2.9, and apparent density was 2650 kg/m^3. Crushed limestone was taken as coarse aggregate, which was continuously graded from 5 to 25 mm, with an apparent density of 2690 kg/m^3. The physical and mechanical property indices of basalt fiber used are shown in Table 2. When preparing concrete, in order to save cement, improve the workability of the mixture, or reduce the water-cement ratio to increase the concrete strength level, a certain amount of water-reducing agent is often added. Polycarboxylic acid water-reducing agent was used as the water-reducing agent, whose water-reducing rate was 25% (mass fraction).

2.1.2. Mix Ratio Determination and Specimen Preparation. Volume method and mass method are often employed to determine the concrete mix ratio, among which the volume method is the most common [24]. In order to make concrete meet the requirements of strength grade, workability, durability, and economic application, the concrete mix ratio should be designed with careful selection of raw materials according to specific requirements and reasonable determination of the proportion of each component [25]. The strength grade of the concrete used in this test was C40, and according to the information provided by the manufacturer, the dosage of water-reducing agent was 4% of the cementing material. According to the mix ratio experiment, the specific proportion is shown in Table 3. The slump of the newly mixed concrete measured 130–150 mm.

There are generally two preparation processes for basalt fiber concrete: the direct fiber incorporation method and the pretreatment fiber incorporation method. Studies have shown that the incorporation of basalt fibers will have a greater impact on the internal structure of concrete [26]. The mechanical properties of the pretreatment fiber incorporation method are significantly higher than the direct fiber incorporation method. The former can make the fibers well dispersed in the concrete, enhance the adhesion between the fibers and the concrete, and thus improve the performance of the concrete matrix, so the pretreatment fiber incorporation method is used. In the experiment, stones and sand were first put in order and mixed dry for 60 s; then, cement and water were added and mixed for 30 s. At the same time, the fiber was evenly spread into the mixer, and then, the weighing water reducer was added and mixed for 2 min. The fresh concrete is mixed evenly, without segregation and bleeding, and the workability is good. Put the fresh concrete into the mold and use a shovel to insert the mold when entering the mold. After entering the mold, smoothen the surface with a shovel and vibrate on the shaker for 5 s to make the concrete fully dense.

This experiment formed two kinds of specimens of different sizes: a cube specimen of 100 mm × 100 mm × 100 mm for the compressive strength test and sulfate corrosion durability test and a prism specimen of 100 mm × 100 mm × 400 mm for the flexural strength test and ultrasonic testing.

2.2. Test Process and Method

2.2.1. Determination of Condensation Time. Since the research object was the concrete which was between the initial setting and the final setting and did not totally meet hardening standards, the initial setting and final setting of the concrete needed to be measured and analyzed before the disturbance test started. The setting time of concrete was measured by the method of penetration resistance, referring to the setting time test in GBT50080-2016 [27], and the penetration resistance was calculated as follows:

$$f_{\mathrm{PR}} = \frac{P}{A}, \tag{1}$$

where f_{PR} is the penetration resistance, MPa; P is the penetration pressure, N; and A is the stylus area, mm^2; calculation was accurate to 0.1 MPa.

Setting time was determined by the drawing fitting method. With the penetration resistance as the ordinate and time as the abscissa (accurate to 1 min), the relationship between penetration resistance and time was plotted. After two straight lines parallel to the abscissa with 3.5 MPa and 28 MPa were drawn, the abscissa of the two intersections that intersected the curve showed the initial and final setting times of the concrete mixture.

2.2.2. Disturbance Test and Ultrasonic Testing. When concrete is between the initial setting stage and the final setting stage, the disturbance has the greatest impact on its performance. Therefore, the disturbed period was determined between the initial and the final setting stages [28]. According to the influence of different disturbance forms on concrete performance in the actual project and the relevant literature [29–32], the DC-1000-15 horizontal electric vibration table was selected to provide the disturbance, with the frequency being 15 Hz, the maximum vibration speed 37.7 cm/s, the amplitude 4 mm, and the vibration forms sinusoidal vibration. The vibration started from the initial setting of cement mortar and was distributed in the whole process of cement mortar condensation. The vibration duration of each group was 40 min.

Table 1: Chemical composition and properties of P•O 42.5R cement.

Initial setting time (h/min)	Final setting time (h/min)	Stability (mm)		Flexural strength (3 d) (MPa)		Compressive strength (3 d) (MPa)	
		Standard	Test	Standard	Test	Standard	Test
2/45	3/51	≤5.0	0.5	≥21.0	30.6	≥42.5	54.6

Table 2: Physical and mechanical properties of basalt fiber.

Length/mm	Density (kg/m^3)	Tensile modulus (GPa)	Tensile strength (MPa)	Elongation at break (%)
18	2650	93–110	4150–4800	3.1

Table 3: Concrete mix ratio (kg/m^3).

Cement	Sand	Gravel	Water	Water-cement ratio	Sand rate	Water-reducing agent
420	760	1040	176	0.42	0.42	16.8

After curing for 7 d and 28 d, the disturbed specimens were subjected to ultrasonic nondestructive testing by an NM-4A nonmetal ultrasonic detection analyzer to detect whether the defects in the concrete were increased due to disturbance, as shown in Figure 1. The test principle was that when the wave transmits in concrete, it will encounter various medium defects and its transmission direction and path will inevitably change, so the energy of the wave at the defects will be attenuated. As sound time, amplitude, and frequency change, velocity, time, and amplitude change too [33]. After mold removal, the specimens were cured in water for 7 d and 28 d, and then, they were, respectively, conducted ultrasonic testing. Before the test, the specimens were kept dry to avoid the influence of water content on the test results. The average value of three measured data of a sample was taken to be compared with that of the undisturbed sample, and then, the damage degree was calculated [34].

2.2.3. Concrete Compression and Flexural Test. Considering the limitations of a single evaluation method, the influence of early disturbance on the macroscopic mechanical properties of concrete was comprehensively evaluated by indices such as compressive strength, flexural strength, and damage degree. When the test piece reached the age of 28 d, its surface was wiped clean and dry so that compression and flexural tests referring to GBT50080-2016 could be carried out. When compressive strength of concrete was being measured, the loading speed during the test operation was set 0.5–0.8 MPa per second in order to make the data reliable. A 100 kN universal material testing machine was used as the flexural test equipment. When the test was being conducted, the side of the test piece was used as the load-bearing surface. The descending speed of the press head was controlled to 0.5 mm per minute when loading.

2.2.4. Sulfate Corrosion Test. The properties and microstructure of concrete are the direct factors affecting the durability of structural engineering, and the erosion of concrete by sulfate is one of the important factors causing the damage and destruction to concrete [35]. Early disturbed concrete will inevitably be exposed to sulfate erosion environment in the service process. Therefore, the early disturbed concrete after being hardened was subjected to the dry-wet cycle sulfate erosion test to explore the deterioration degree of the disturbed concrete by sulfate erosion with measurement of mass change rate and ultrasonic testing. The test was conducted with reference to GBT 50082-2009 "sulfate dry-wet cycle test" [36]. Considering the effect of concentration on the erosion mechanism and according to the related literature, sodium sulfate solution was used as the erosion medium in this experiment, with the solution mass fraction being 7% [37–40]. When reaching 2 d before the predetermined age, the specimen was taken out of the standard curing box, wiped until its surface was dry, and put into the oven. After being dried, the specimen was cooled to room temperature in a dry environment and then put into the sulfate dry-wet cycling machine for test. After this test, the mass of each sample was detected, and ultrasonic detection was conducted every ten cycles.

3. Analysis of Test Results

3.1. Concrete Setting Time. The development of concrete penetration resistance was first studied, and the condensation and hardening processes were divided into three stages. It was defined that when the penetration resistance was 0~3.5 MPa, the concrete was in the initial stage of condensation and hardening; when the penetration resistance value was 3.5~28 MPa, the concrete was in the intermediate stage of condensation and hardening; and when the penetration resistance was greater than 28 MPa, the concrete was in the later stage of condensation and hardening. The resulting data are shown in Figure 2.

The fitting function equation is

$$y = 0.0173 \times 1.0125^{x}. \quad (2)$$

According to the method of setting time fitting, the initial setting time of basalt fiber concrete was 430 min and the final setting time was 640 min. After the initial setting time had been determined, vibration was carried out, which started exactly from it. The two specimens were, respectively,

(a) (b)

Figure 1: NM-4A nonmetal ultrasonic detection analyzer.

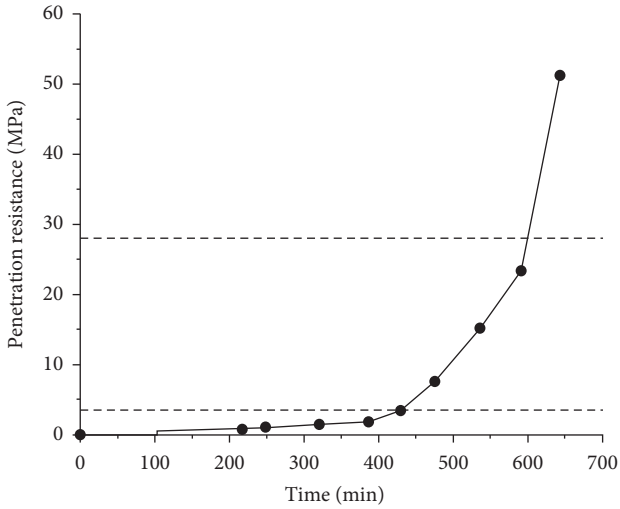

Figure 2: Curve of penetration resistance-time.

disturbed at different time periods until all the specimens were completely disturbed.

3.2. Influence of Disturbance on the Strength of Basalt Fiber Concrete

3.2.1. Influence of Disturbance on the Flexural Strength of Basalt Fiber Concrete. Twelve specimens were prepared by five perturbations between the initial setting and the final setting of concrete. They were divided into six groups, two for each group, and numbered, respectively. The flexural test data of basalt fiber concrete and plain concrete are shown in Tables 4 and 5.

It can be seen from Figure 3 that the flexural strength of basalt fiber concrete has been significantly improved by disturbing the concrete specimen before the initial setting of cement mortar. As the concrete hardens, the disturbance has a significant negative effect on the basalt fiber flexural strength. Since the setting time is about 400 min, the disturbance makes the flexural strength of the fiber concrete decrease significantly. When the penetration resistance is 7.4 MPa, the basalt fiber concrete is vibrated, and its flexural strength reaches the lowest. Therefore, it can be seen that the flexural strength of basalt fiber concrete can be significantly improved by disturbing the concrete before the initial setting. After the initial setting, the flexural strength of basalt fiber concrete is greatly reduced by disturbance. When basalt fiber concrete is disturbed near the final setting, the effect of the compressive strength decreases gradually. In addition, the flexural strength of basalt fiber concrete is slightly higher than that of plain concrete.

This phenomenon is closely related to the bond degree of aggregate, fiber, and gelling material. After the initial setting, the bonds between the materials have been formed, which make the concrete lose its plasticity, but vibrance will disturb the newly formed bonds and separate them. Therefore, after the disturbance, the condensation continues to be not much affected. As a result, during the disturbed time, the flexural strength loss is small. With the development of condensation and hardening, more and more connection bonds are formed, so the damage grows greater after the disturbance is caused. In the later stage of condensation, due to the formation of the bonds, the plastic loss reaches a certain stage, and the impact of the compressive strength decreases gradually.

3.2.2. Influence of Disturbance on the Compressive Strength of Basalt Fiber Concrete. The test process was the same as above. The basalt fiber concrete and plain concrete compressive test data are shown in Tables 6 and 7.

Tables 6 and 7 can be used to make a broken line graph, as shown in Figure 4.

As can be seen from Figure 4, the compressive strength of basalt fiber concrete and plain concrete first increases and then decreases with the increase in penetration resistance after disturbance, and the compressive strength increases most obviously before condensation. This is because in the early stage of condensation, the connection between the aggregate and cementitious material has not yet been formed and is in a separated state, and the fiber concrete is in the plastic stage. Disturbance makes the fiber, coarse and fine aggregates, and cementitious material fully combined so that the various interfaces in the later stage of condensation and hardening are fully combined, thereby enhancing the compressive strength.

Table 4: Flexural data of basalt fiber concrete.

Number	Maximum force (kN)	Flexural strength (MPa)	Average (MPa)	Vibration time (min)	Penetration resistance (MPa)
G0-1	14.910	6.150	6.301	0	0
G0-2	15.670	6.452			
G1-1	15.692	8.062	8.011	40	1.82
G1-2	17.020	7.959			
G2-1	14.010	6.305	5.911	40	3.4
G2-2	12.260	5.517			
G3-1	10.240	5.608	5.432	40	7.6
G3-2	13.900	5.256			
G4-1	12.450	5.603	5.736	40	15.27
G4-2	13.040	5.868			
G5-1	18.020	6.509	6.399	40	23.4
G5-2	16.200	6.290			

Table 5: Flexural data of plain concrete.

Penetration resistance (MPa)	Vibration time (min)	Number	Flexural strength (MPa)	Average (MPa)
0	0	A0-1	5.278	5.558
		A0-2	6.838	
1.82	40	A1-1	6.858	6.377
		A1-2	5.895	
3.4	40	A2-1	4.514	4.723
		A2-2	4.932	
7.6	40	A3-1	4.740	5.116
		A3-2	5.492	
15.27	40	A4-1	6.467	6.253
		A4-2	6.039	
23.4	40	A5-1	5.371	5.043
		A5-2	4.715	

According to Tables 4 and 5, graphs can be drawn, as shown in Figure 3.

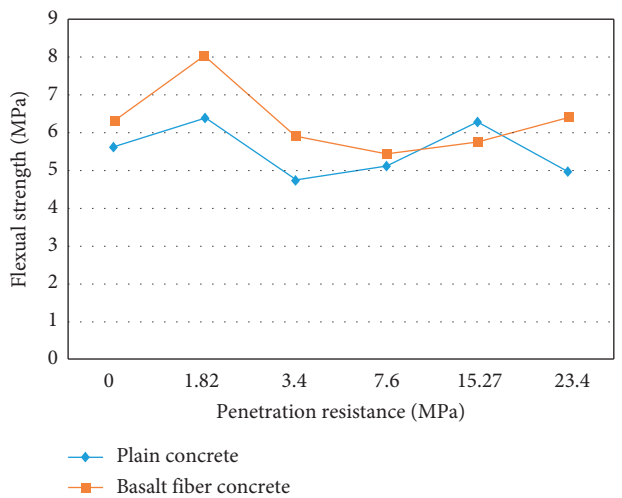

Figure 3: Comparison of flexural strength of plain concrete and basalt fiber concrete.

When the penetration resistance is 7~16 MPa, the disturbance has a negative effect on the flexural strength of the two kinds of concrete, while the fiber concrete is less affected. The influence of disturbance on the compressive strength of basalt fiber concrete and plain concrete is reduced when the final setting is near. The influence trend of disturbance on the two kinds of concrete is basically the same.

3.3. Influence of Disturbance on Internal Damage of Basalt Fiber Concrete. There is a certain correlation between ultrasonic wave velocity and concrete strength, which can be used to reflect the internal microscopic damage of concrete. In order to quantitatively analyze the internal damage of concrete, the relative value of ultrasonic wave velocity attenuation is defined as concrete damage degree D [41], and D is calculated as follows:

$$D = 1 - \left(\frac{V_t}{V_0}\right)^2, \tag{3}$$

where V_t is the ultrasonic wave velocity of disturbed concrete, km/s, and V_0 is the ultrasonic wave velocity of undisturbed concrete, km/s.

The graphs of ultrasonic data are shown in Figures 5 and 6.

As shown in the figures, disturbance at any time during the whole coagulation process causes damage, but the damage degree is different at different periods. At the initial stage of condensation, the basalt fiber concrete is in the plastic stage, and not so many connection bonds are formed. The connection between basalt fiber, aggregate, and cementitious material is damaged by disturbance. However,

Table 6: Compressive data of basalt fiber concrete.

Number	Compressive strength (MPa)	Average (MPa)	Vibration time (min)	Penetration resistance (MPa)
G0-1	36.332	36.513	0	0
G0-2	36.684			
G1-1	37.410	37.421	40	1.82
G1-2	37.432			
G2-1	38.124	36.885	40	3.4
G2-2	36.656			
G3-1	35.162	34.752	40	7.6
G3-2	34.332			
G4-1	35.940	35.491	40	15.27
G4-2	35.042			
G5-1	37.854	36.024	40	23.4
G5-2	36.624			

Table 7: Compressive data of plain concrete.

Penetration resistance (MPa)	Vibration time (min)	Number	Compressive strength (MPa)	Average (MPa)
0	0	A0-1	35.361	35.129
		A0-2	34.897	
1.82	40	A1-1	36.213	37.079
		A1-2	37.945	
3.4	40	A2-1	36.676	36.431
		A2-2	36.185	
7.6	40	A3-1	33.294	34.585
		A3-2	35.875	
15.27	40	A4-1	34.070	33.856
		A4-2	33.641	
23.4	40	A5-1	34.723	34.959
		A5-2	35.194	

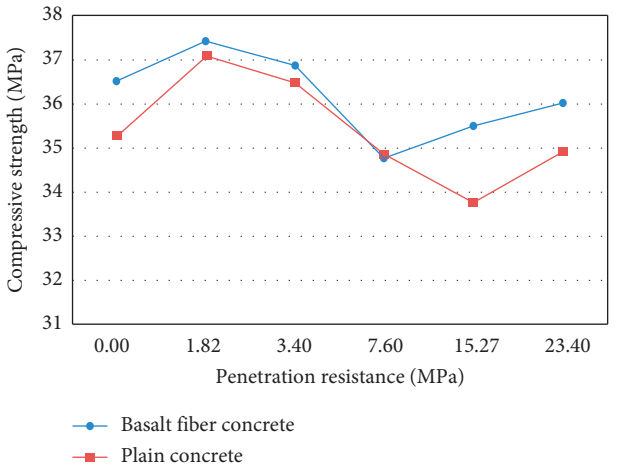

Figure 4: Comparison of compressive strength of plain concrete and of basalt fiber concrete.

after disturbance is stopped, the basalt fiber concrete is still in the plastic stage or has just lost its plasticity, which can be reformed later. When the penetration resistance reaches 3.4 MPa, which marks the initial setting, the concrete is disturbed to minimize the damage. The disturbance in the middle stage of condensation has the greatest damage to concrete. Because the connection between the materials is smaller at this time and the connection is more and more difficult to form after the disturbance is stopped, the influence of the disturbance increases. As the condensation progresses, the plastic phase is nearing its end and brittleness appears. The bonds between aggregate, cementitious material, and fiber are great, and the influence of disturbance on concrete decreases gradually in the late stage of condensation. It can be seen from the graphs that the damage degree of basalt fiber concrete cured for 7 d is obviously higher than that cured for 28 d.

3.4. Influence of Disturbance on Durability of Basalt Fiber Concrete. Ultrasonic detection and mass loss measurement were performed after cyclic immersion of sulfate solution. The mass change rate is used to measure the quality change in corroded concrete. The mass change rate is defined as the ratio of the mass change in the disturbed concrete specimen when it is eroded to a certain age to the mass before erosion, which is calculated according to the following formula, and the test data obtained are shown in Figures 7 and 8:

$$K_m = \frac{(m_n - m_0)}{m_0}, \tag{4}$$

where K_m is the mass change rate of the specimen after n days of erosion, %; m_0 is the mass of specimen before

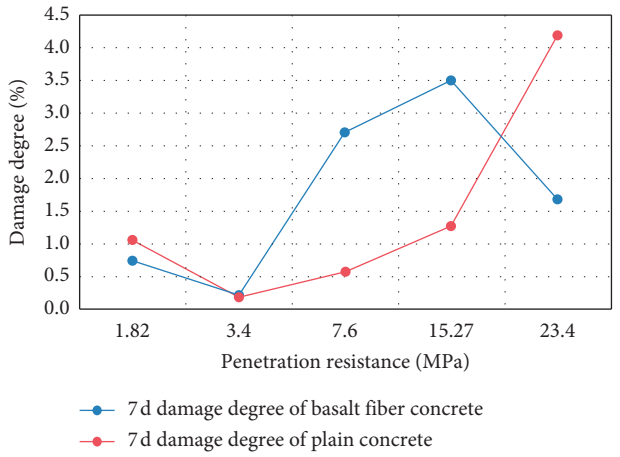

Figure 5: Damage degree of basalt fiber concrete and plain concrete for 7 d.

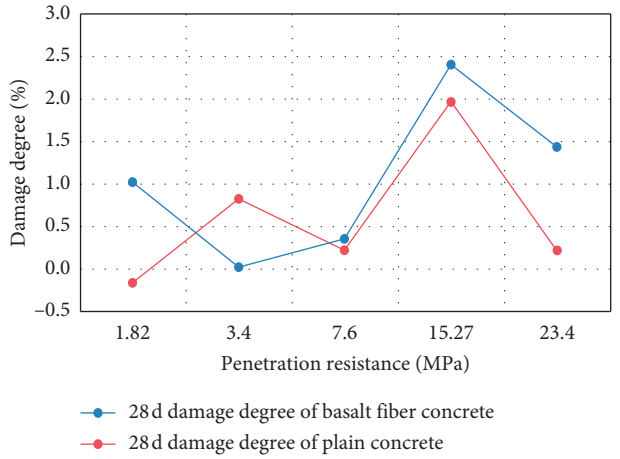

Figure 6: Damage degree of basalt fiber concrete and plain concrete for 28 d.

erosion, kg; and m_n is the mass of the specimen after n days of erosion, kg.

As can be seen from Figure 7, with the increase in cycle times, the damage caused by basalt fiber concrete also increases, and the damage of disturbed specimens is greater than that of undisturbed specimens. On the whole, the internal defects and damage are greatest after disturbing the basalt fiber concrete in the middle stage of condensation and soaking it in sulfate solution. This is because in the beginning, the components in the basalt fiber concrete react with the sulfate and produce condensate, which increases the mass of the specimen. After the cycle of soaking, the fiber concrete is eroded and starts to peel off, so the mass becomes smaller. Before and after the initial setting and the final setting, the quality of the specimens changes slowly and the durability is not affected. When the penetration resistance is between 7 and 15 MPa, the quality of basalt fiber concrete varies greatly, and the corrosion resistance decreases obviously.

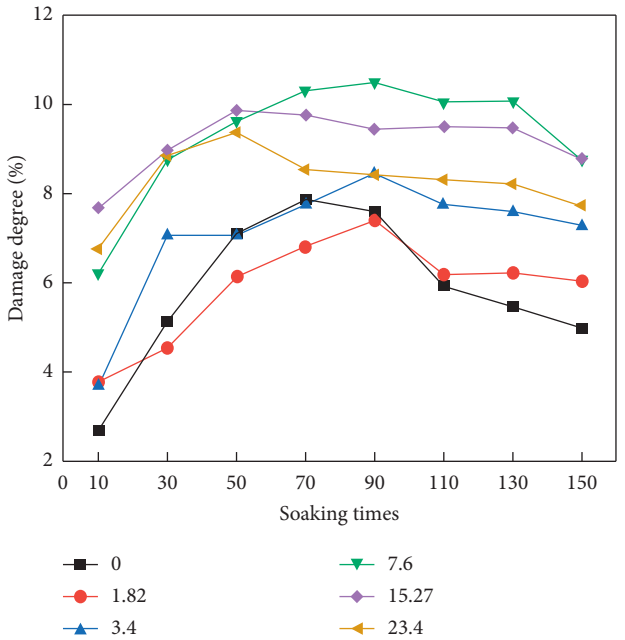

Figure 7: Basalt fiber concrete resistance to sulfate corrosion.

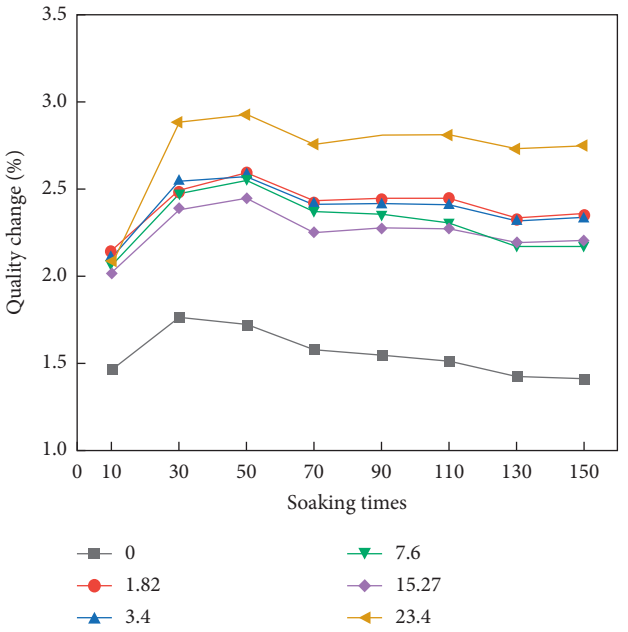

Figure 8: Quality change.

4. Conclusions

By disturbing the basalt fiber concrete and investigating the influence of basalt fiber on the macroscopic mechanical properties of the disturbed concrete, this paper establishes the relationship between the microscopic strengthening mechanism and the macroscopic mechanical properties of basalt fiber concrete. The main conclusions are as follows:

(1) A variety of comparative tests show that the mechanical and antidisturbance properties of basalt fiber concrete are superior to that of plain concrete. This finding can be used in engineering practice to increase the safety and stability of concrete by adding basalt fiber.

(2) The flexural strength of basalt fiber concrete is about 21% lower, and its compressive strength is about 5% lower than that of undisturbed specimens when the concrete is disturbed in the middle stage of condensation. During the period of condensation, the bending strength and compressive strength first increase and then decrease with time. In addition, the flexural strength of basalt fiber concrete is greatly improved due to the disturbance from the early stage of condensation to the initial setting, but the disturbance has little effect on the compressive strength of the basalt fiber concrete.

(3) In the early stage of condensation, the internal damage of basalt fiber concrete is relatively small and the damage degree is small too. In the middle stage of condensation, the damage degree of basalt fiber first increases and then decreases, and the damage degree caused by the disturbance after the final setting is quite small.

(4) The durability of basalt fiber concrete is reduced by disturbance. Before and after the initial setting and the final setting, the quality of the specimens changes slowly and the durability is not affected. When the penetration resistance is between 7 and 15 MPa, the quality of basalt fiber concrete varies greatly, and the corrosion resistance decreases obviously.

Data Availability

The data used to support the findings of this study are available from the corresponding author upon request.

Conflicts of Interest

The authors declare that there are no conflicts of interest.

Acknowledgments

This study was supported by the China Postdoctoral Science Foundation (no. 2017M620434), Shaanxi Postdoctoral Grant Program (no. 2017BSHYDZZ17), and the Special Fund for Basic Scientific Research of Central College of Chang'an University (no. 310821173501). The authors gratefully acknowledge their financial support.

References

[1] Y. L. Hu and P. W. Gao, "Study on mechanical properties of rubber concrete with different substitution rates," *Journal of Building Materials*, vol. 1, pp. 85–92, 2020.

[2] W. Li and J. Xu, "Mechanical properties of basalt fiber reinforced geopolymeric concrete under impact loading," *Materials Science and Engineering: A*, vol. 505, no. 1-2, pp. 178–186, 2009.

[3] H. Y. Zhou and H. Y. Liu, "Study on the mechanism of fatigue compressive damage of concrete and its size effect," *Concrete*, vol. 12, pp. 1–5, 2019.

[4] P. Zhang and Q.-f. Li, "Effect of polypropylene fiber on durability of concrete composite containing fly ash and silica fume," *Composites Part B: Engineering*, vol. 45, no. 1, pp. 1587–1594, 2013.

[5] A. Babar and A. Q. Liaqat, "Influence of glass fibers on mechanical and durability performance of concrete with recycled aggregates," *Construction and Building Materials*, vol. 228, 2019.

[6] P. Zhang, Q. Li, J. Wang, Y. Shi, Y. Zheng, and Y. Ling, "Effect of nano-particle on durability of polyvinyl alcohol fiber reinforced cementitious composite," *Science of Advanced Materials*, vol. 12, no. 2, pp. 249–262, 2020.

[7] G. W. Li, "Application of basalt fiber in hydraulic erosion resistant high-performance concrete," *Concrete*, vol. 11, pp. 77–79, 2008.

[8] Y. F. Ling, P. Zhang, and J. Wang, "Effect of sand size on mechanical performance of cement-based composite containing PVA fibers and nano-SiO_2," *Materials*, vol. 13, no. 2, pp. 1–14, 2020.

[9] H. M. Pan and Q. X. Zhao, "Progress in the study of early age concrete," *Bulletin of the Chinese Ceramic Society*, vol. 1, pp. 64–70, 2017.

[10] E. R. Grist, K. A. Paine, A. Heath, J. Norman, and H. Pinder, "Structural and durability properties of hydraulic lime-pozzolan concretes," *Cement and Concrete Composites*, vol. 62, pp. 212–223, 2015.

[11] S.-H. Han, W.-S. Park, and E.-I. Yang, "Evaluation of concrete durability due to carbonation in harbor concrete structures," *Construction and Building Materials*, vol. 48, pp. 1045–1049, 2013.

[12] N. H. P. Para and P. T. Haybale, "Early-strength development of blended concrete under different curing conditions," *Emerging Materials Research*, vol. 9, no. 1, pp. 59–64, 2020.

[13] P. Zhang, Q. F. Li, and Y. Z. Chen, "Durability of steel fiber-reinforced concrete containing SiO_2 nano-particles," *Materials*, vol. 12, no. 13, 2019.

[14] W. Shen, C. Zhang, X. Li, H. Shi, G. Wang, and X. Tian, "Low carbon concrete prepared with scattering-filling coarse aggregate process," *International Journal of Concrete Structures and Materials*, vol. 8, no. 4, pp. 309–313, 2014.

[15] Y. H. Man and B. K. Sung, "Effects of concrete strength on structural behavior of holed-incrementally prestressed concrete (H-IPC) girder," *Advances in Concrete Construction*, vol. 3, no. 2, pp. 113–126, 2015.

[16] G. B. Juma and A. R. Yousif, "Size effect on the shear failure of high-strength concrete beams reinforced with basalt FRP bars and stirrups," *Construction and Building Materials*, vol. 209, pp. 77–94, 2019.

[17] J. Krassowska and M. Kosior-Kazberuk, "Experimental investigation of shear behavior of two-span fiber reinforced concrete beams," *Archives of Civil Engineering*, vol. 65, no. 2, pp. 35–55, 2019.

[18] B. Laurence, B. Estelle, and S. Michel, "Physicochemical characterisations of the bitumen–aggregate interface to get a better understanding of stripping phenomena," *Road Materials and Pavement Design*, vol. 14, no. 2, pp. 384–403, 2013.

[19] M. Peng and H. X. Huang, "Experimental study on basic mechanical properties of basalt fiber concrete," *Concrete*, vol. 1, pp. 74-75, 2012.

[20] L. F. Zhang and Y. L. Yin, "Permanent deformation of asphalt pavement under horizontal moving load," *Bulletin of the Chinese Ceramic Society*, vol. 11, pp. 2834–2837, 2014.

[21] Y. H. Pi, Y. Li, Y. Pi, X. Y. Tan, and M. He, "Wetting model of asphalt on the aggregate surface and its effect factors," *Advances in Materials Science and Engineering*, vol. 2019, Article ID 4126464, 7 pages, 2019.

[22] J. L. Song and L. He, "BFRP bars as an alternative reinforcement of concrete structures-compatibility and adhesion issues," *Advanced Materials Research*, vol. 3903, pp. 233–241, 2015.

[23] T. Y. Liu and P. W. J. Zhang, "Compressive strength prediction of PVA fiber-reinforced cementitious composites containing nano-SiO_2 using BP neural network," *Materials*, vol. 13, no. 3, pp. 1–25, 2020.

[24] B. M. Wang and N. Tu, "Research progress of concrete mix design methods at home and abroad," *Ready-Mixed Concrete*, vol. 12, pp. 27–30, 2010.

[25] M. Cherrak, A. Bali, and K. Silhadi, "Concrete mix design containing calcareous tuffs as a partial sand substitution," *Construction and Building Materials*, vol. 47, pp. 318–323, 2013.

[26] Y. Wang, T. Zhang, C. Yan et al., "Effect of different loading systems on acousto-ultrasonic characteristics of concrete under axial compression," *Materials Testing*, vol. 61, no. 6, pp. 591–599, 2019.

[27] GBT50080-2016, *Standard for Test Method of Performance on Ordinary Fresh Concrete*, National Standards of the People's Republic of China, Beijing, China, 2016.

[28] S. Liu, J. Zhu, S. Seraj, R. Cano, and M. Juenger, "Monitoring setting and hardening process of mortar and concrete using ultrasonic shear waves," *Construction and Building Materials*, vol. 72, no. 72, pp. 248–255, 2014.

[29] J.M. Hu and J.Q Zhang, "Water transport in organic coatings: Fick diffusion process," *Journal of Chinese Corrosion and Protection*, vol. 22, no. 5, pp. 311–315, 2002.

[30] Z. W. Jiang and X. Xiao, "Study on the influence of vehicle-bridge coupling vibration on the early performance of concrete," *Concrete World*, vol. 1, pp. 88–95, 2015.

[31] D. G. Manning, *Effects of Traffic-Induced Vibrations on Bridge-Deck Repairs*, Transportation Research Board, National Academy of Sciences, Washington, DC, USA, 1981.

[32] J. J. Wei, J. X. Xing, and Z. Fu, "The influence of bridge vibration caused by driving load on the performance of repaired concrete," *Journal of Southeast University*, vol. 40, no. 5, pp. 1057–1060, 2010.

[33] D. S. Ye and S. P. Shang, "Study on the influence of train vibration on the construction of railway bridge," *Highway*, vol. 9, pp. 20–24, 2001.

[34] N. Sabbağ and O. Uyanık, "Prediction of reinforced concrete strength by ultrasonic velocities," *Journal of Applied Geophysics*, vol. 141, pp. 13–23, 2017.

[35] D. H. Deng and Z. Q. Liu, "Research progress on sulfate crystal destruction theory," *Journal of the Chinese Ceramic Society*, vol. 40, no. 2, pp. 175–185, 2012.

[36] GBT 50082-2009, *Standard for Test Methods of Long-Term Performance and Durability of Ordinary Concrete*, National Standards of the People's Republic of China, Beijing, China, 2009.

[37] F. G. Leng, X. X. Ma, and G. F. Tian, "Test method for sulfate resistance of concrete," *Journal of Southeast University (Natural Science Edition)*, vol. 27, no. s2, pp. 45–48, 2006.

[38] K. N. Jallad, M. Santhanam, and M. D. Cohen, "Stability and reactivity of thaumasite at different pH levels," *Cement and Concrete Research*, vol. 33, no. 3, pp. 433–437, 2003.

[39] Q. X. Zhao, D. H. Li, and G. L. Yan, "Resistance to sulfate corrosion of damaged concrete," *Journal of the Chinese Ceramic Society*, vol. 40, no. 2, pp. 217–220, 2012.

[40] C. Ferraris, P. Stutzman, M. Peltz, and J. Winpigler, "Developing a more rapid test to assess sulfate resistance of hydraulic cements," *Journal of Research of the National Institute of Standards and Technology*, vol. 110, no. 5, pp. 529–540, 2005.

[41] S. P. Chen and J. W. Wang, "Research on damage model of fiber concrete in freeze-thaw environment," *Concrete*, vol. 10, pp. 58–61, 2017.

Hindawi
Advances in Civil Engineering
Volume 2020, Article ID 8824308, 16 pages
https://doi.org/10.1155/2020/8824308

Research Article

Shear Strength Prediction for SFRC Shear Wall with CFST Columns by Softened Strut and Tie Model

Peibo You,[1,2] **Shuaiqi Song**,[1] **Haiyang Zhang**,[3] **Lijuan Zhang**,[4] **Ke Shi**,[5] **and Yi Wang**[1]

[1]*School of Civil and Transportation Engineering, Henan University of Urban Construction, Pingdingshan 467000, China*
[2]*School of Civil Engineering, Zhengzhou University, Zhengzhou 450001, China*
[3]*Henan Joywin Engineering Testing Technology Co., Ltd., Zhengzhou 450000, China*
[4]*School of Mechanics and Safety Engineering, Zhengzhou University, Zhengzhou 450001, China*
[5]*School of Civil Engineering, Zhengzhou University of Aeronautics, Zhengzhou 450001, China*

Correspondence should be addressed to Peibo You; 382618232@qq.com

Received 5 May 2020; Revised 11 June 2020; Accepted 17 June 2020; Published 29 July 2020

Academic Editor: Peng Zhang

The steel fiber reinforced concrete (SFRC) shear wall with concrete filled steel tube (CFST) columns is an innovative composite structure. In order to calculate the shear strength of SFRC shear wall with CFST columns, the softened strut and tie model (SSTM) of SFRC shear wall with CFST columns was proposed based on the analysis of shear mechanism of SFRC shear wall with CFST columns. The SSTM was composed of diagonal, horizontal, and vertical mechanisms, in which the contributions of concrete, reinforcement, and steel fiber to the shear strength of SFRC web of shear wall were identified. The shear capacities of 24 shear walls were calculated and compared with the available test results, and reasonable agreement was obtained. The results also showed that the steel fibers distributed randomly in concrete could be treated as longitudinal and transverse reinforcement in the shear strength analysis of SFRC web, and the SSTM was reasonable and useful to analyze and predict the shear strength of SFRC shear wall with CFST columns.

1. Introduction

Reinforced concrete (RC) shear wall system is a common one to resist lateral force, which has been widely used in the regions of high seismic activity in the past decade. However, due to low tensile strength and large brittleness of normal-strength concrete, the ductility, energy dissipation, and load bearing capacities of RC shear wall are poor. In particular, the transverse dimension of shear wall can be decreased with the application of high strength concrete, but its brittleness increases inevitably. Correspondingly, the higher requirement for the seismic performance of shear wall especially with high strength concrete (HSC) would be put forward. In order to improve the seismic performance of shear wall, the use of RC shear wall with concrete filled steel tube (CFST) columns and steel fiber reinforced concrete (SFRC) shear wall has attracted the interest of structural engineers in recent years.

First, theoretical analysis and experimental study [1–4] show that the CFST columns serving as boundary members can provide the effective constraint to reinforced high strength concrete (RHSC) wall, restrain the cracking development, and also bear part of transverse load after the RHSC wall deteriorates gradually, indicating that the RHSC shear wall with CFST columns can form double-channel seismic line and have favorable seismic performance. Secondly, the application of SFRC is a good way to enhance the seismic behavior of conventional shear wall structure, especially the RHSC shear wall [5]. Several researchers [6–10] have conducted the experiments on the seismic performance of SFRC shear wall. In these experiments, the SFRC shear walls were subjected to reversed cyclic loading. As expected, because SFRC has good properties, such as stretching, shear resistance, cracking resistance, toughness [11], fire resistance, durability [12, 13], and earthquake resistance, it can remarkably improve the seismic behavior of RC shear wall

and reduce the phenomenon of reinforcement congestion and construction difficulty. The load bearing capacity, ductility, and energy dissipation capacities of SFRC shear walls increase with the increasing of steel fiber volume fraction.

In this study, an innovative composite shear wall referred to as SFRC shear wall with CFST columns is introduced, which consists of SFRC web and CFST boundary elements. In this new composite shear wall, SFRC web can mainly improve the ductility and energy dissipation capacities, CFST boundary elements can enhance the load bearing capacity. This kind of composite shear wall will adequately make use of the advantages of SFRC shear wall and CFST columns. In order to more fully understand the seismic behavior of this structure form, six SFRC shear wall with CFST column specimens were tested under constant axial force and reversed cyclic loading. The failure mode of shear wall specimens was analyzed, and the influencing factors, such as the steel fiber volume fraction and concrete strength on the shear strength of shear wall specimens, were studied. Since the load transferring mechanism of shear walls under the combined action of compression, bending, and shearing is very complicated, the researches on the load bearing mechanism and the calculation methods for shear capacity of shear walls are relatively few. In addition, the only existing calculation methods for shear capacity proposed are mostly semiempirical relations based on the experimental results and are lacking in the reasonable theoretical model. Furthermore, the analysis and calculations are not very accurate.

The softened strut and tie model (SSTM) for determining the shear strengths of RC members failing in diagonal compressions was proposed by Hwang and Lee, which originated from the strut and tie concept, considered the compression softening characteristics of concrete, and was derived to satisfy equilibrium, compatibility, and constitutive laws of cracked reinforced concrete [14–19]. The SSTM has been used in shear strength prediction of various kinds of concrete members and the accuracy has been checked by comparing calculated shear strengths with experimental data reported in the previous literature [20–24].

In this paper, the SSTM of SFRC shear wall with CFST columns was proposed based on the analysis for its shear mechanism, in which the steel fibers distributed randomly in concrete were equivalent to the longitudinal and transverse reinforcements. Furthermore, a new calculation method based on the SSTM for the shear strength of SFRC shear wall with CFST columns, RC shear wall with CFST columns, and SFRC shear wall was established. Finally, the shear capacities of 24 low-rise shear walls were calculated and the calculated values showed a reasonable agreement with the available experimental results [2, 4, 9, 10].

2. General Test Situation

2.1. Specimen Details. The dimensions and configurations of the shear wall specimens are shown in Figure 1. Each specimen mainly consists of five parts: one SFRC web in the centre, two CFST columns which are located in the right and left sides of middle SFRC web, and two RC beams which are located in the top and bottom sides of middle SFRC web. In order to ensure the reliable connections between the CFST columns and the shear wall web, the U-shaped connectors [25] with the same space as the horizontal reinforcing bars are also welded to the wall of steel tubes. The photos of completed steel frame and U-shaped connector are shown in Figures 2(a) and 2(b), respectively.

The side length and height of the square CFST columns were 120 mm and 750 mm, respectively. The steel plates for hollow sections of square CFST columns and U-shaped connectors were made by cold-formed steel tubes with the thickness of 3 mm and 2 mm, respectively. The strength grade of reinforcement was HRB400, and the grade of steel plates was Q235B based on the Chinese code. The material properties of steel bar and plate are listed in Table 1. The steel fiber is hooked at both ends with length of 35 mm, diameter of 0.55 mm, and aspect ratio of 64.

The test parameters included steel fiber volume fraction ρ_{sf} (0, 0.5%, 1.0%, and 1.5%) and concrete strength grade (CF40, CF60, and CF80). According to the test parameters, six shear wall specimens were cast, tested, and numbered as SS-1.0-00-C60, SS-1.0-05-CF60, SS-1.0-10-CF60, SS-1.0-15-CF60, SS-1.0-10-CF40, and SS-1.0-10-CF80. In the serial number of specimens, the first part SS represents that steel tube and steel fiber; the second part 1.0 refers to the shear span ratio of 1.0, the third part represents the steel fiber volume fraction of the web in shear wall, and the fourth part represents the concrete, in which C represents plain concrete, whilst CF represents SFRC, and the following number denotes target concrete strength of shear wall specimen. The summary of information of each shear wall specimen is listed in Table 2. The mechanical properties of the harden concrete used in the shear wall of all specimens are also listed in Table 2. All the harden concretes reached its target compressive strength.

2.2. Test Scheme. In the test, the load exerted on the specimens included horizontal and vertical one, and the test setup is shown in Figure 3. The horizontal load was cyclic one and applied by an electrohydraulic servo control actuator on the top beam of specimen; the axial compressive force was kept constant and applied by hydraulic Jack. The target axial compression ratio, n, was taken as 0.2 for all specimens. The rolling support between hydraulic Jack and vertical reaction steel frame assured the smooth horizontal slipping of specimens. Rotation control mode was adopted and the typical rotation controlled loading history is shown in Figure 4. A nominal yield rotation angle (θ_{ym}) was designated to 0.0025 rad according to the research in literature [1], which was corresponding to a nominal yield lateral displacement (Δ_{ym}) at the loading point, $\Delta_{ym} = \theta_{ym} \times 750\ \text{mm} = 1.875\ \text{mm}$. Before θ_{ym}, the rotation levels of $0.5\theta_{ym}$ and $0.75\theta_{ym}$ were imposed. Hereafter, the rotation increment was 0.0025 rad for each rotation level and three cycles were imposed at each rotation level. The tests were conducted under the rotation controlled cyclic loading until the axial compressive force could not be maintained or the lateral force degraded below 85% of peak lateral load.

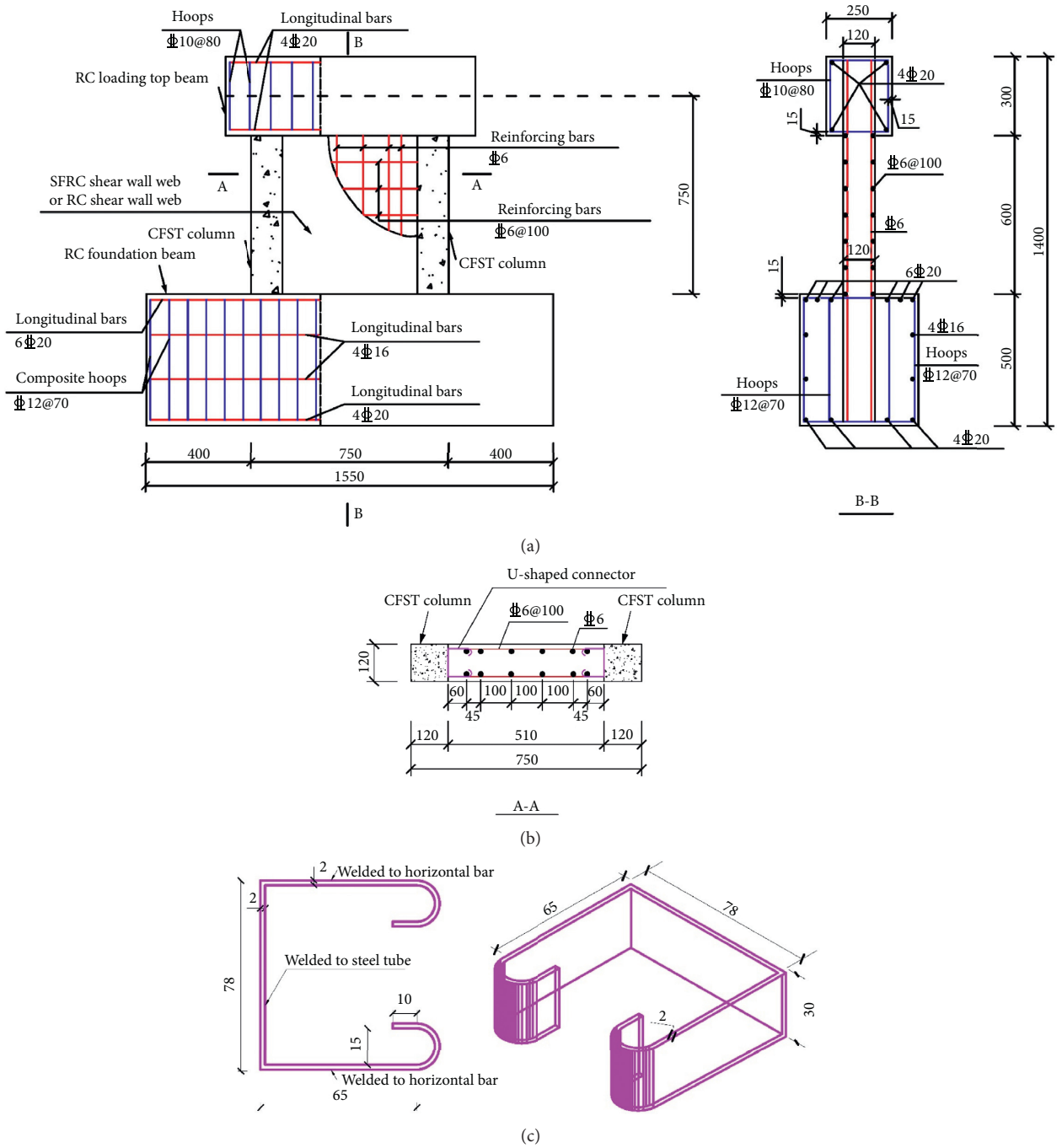

Figure 1: Specimen configuration (unit: mm). (a) Elevation. (b) A-A section. (c) One-dimensional and three-dimensional graph of U-shaped connector.

2.3. Failure Process. The whole process from the initiation to failure of specimens was observed. During the initial loading period, the inclined cracks gradually appeared and constantly extended under cyclic lateral loading. Then several pairs of visible intercrossing diagonal cracks developed approximately along the diagonal directions of the web in shear wall, the horizontal reinforcing bars in the web of the shear wall yielded successively with the loading, and the diagonal strut mechanism in the web of the shear wall was formed. Hereafter, new cracks seldom occurred and the width of the diagonal cracks at the middle part of the web in shear wall increased rapidly with further loading. The web of the shear wall began to fail in diagonal compression, the concrete in the web was crushed and spalled, and the web lost bearing capacity gradually. Upon further cycles, slight local buckling was observed at the bottom of CFST columns and plastic hinges were formed. Finally, the lateral load rapidly dropped to about 85% of the peak lateral load and the specimen failed. All specimens mainly exhibited a typical diagonal cracking pattern during the test process and

(a) (b)

Figure 2: Steel frame and U-shaped connector. (a) Steel frame. (b) U-shaped connector.

Table 1: Material properties of steel plate and bar.

Type	Yield strength f_y (N/mm^2)	Ultimate strength f_u (N/mm^2)	Elastic modulus E_s (N/mm^2)
3 mm plate	307.67	392.00	1.98×10^5
2 mm plate	236.67	323.20	1.88×10^5
C 6 bar	369.17	521.60	1.85×10^5

Table 2: Summary of specimen information.

Identification number	ρ_{sf} (%)	Columns f_c (MPa)	Columns f_t (MPa)	Web f_c (MPa)	Web f_{ft} (MPa)	$V_{jh,test}$ (kN)
SS-1.0-00-C60	0	55.9	2.76	56.3	2.81	902
SS-1.0-05-CF60	0.5	55.5	2.73	55.2	3.67	948
SS-1.0-10-CF60	1.0	55.5	2.74	55.1	6.15	1005
SS-1.0-15-CF60	1.5	56.0	2.77	56.5	7.88	1048
SS-1.0-10-CF40	1.0	38.1	2.15	38.3	3.78	810
SS-1.0-10-CF80	1.0	64.6	3.96	65.6	6.84	1107

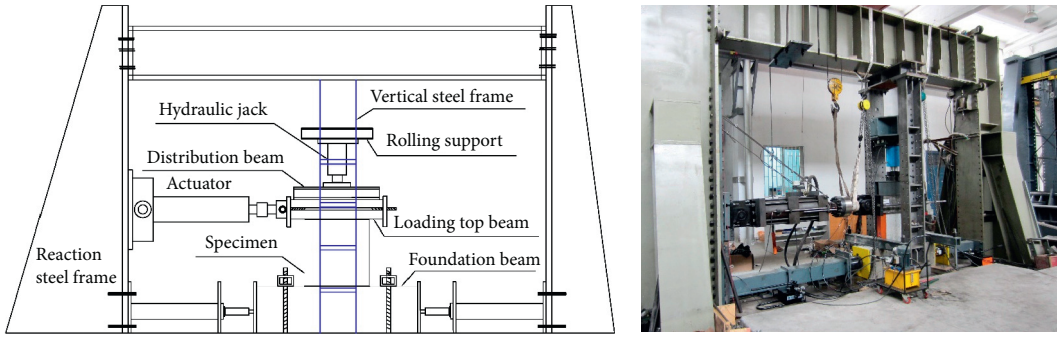

(a) (b)

Figure 3: Test set-up. (a) Schematic view. (b) Test scene.

showed a shear-dominant failure mode. The failure pattern and crack distribution at the peak lateral load and ultimate state (the lateral force degraded to 85% of the peak lateral load) of all tested specimens are shown in Figure 5.

During the test process, the connections between the CFST columns and web were reliable and no significant separation at the interface occurred, which indicated that the performance of the U-shaped connector designed was effective. Moreover, no evident local buckling on the CFST columns of the SFRC shear wall specimens was observed at the ultimate state. The SFRC shear wall specimens had smaller destruction compared with that without steel fibers, which indicated that the SFRC shear wall specimens had the better repairability.

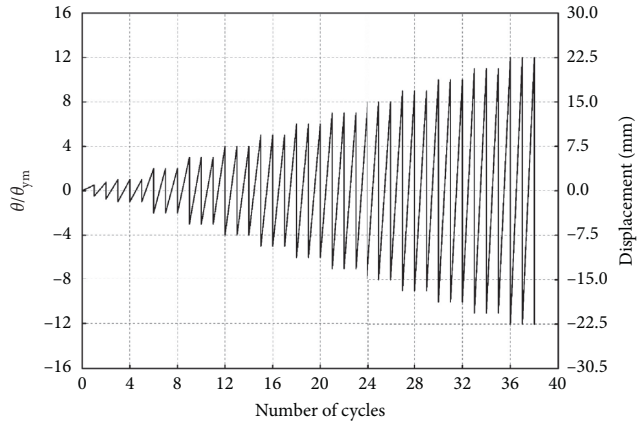

Figure 4: Loading history.

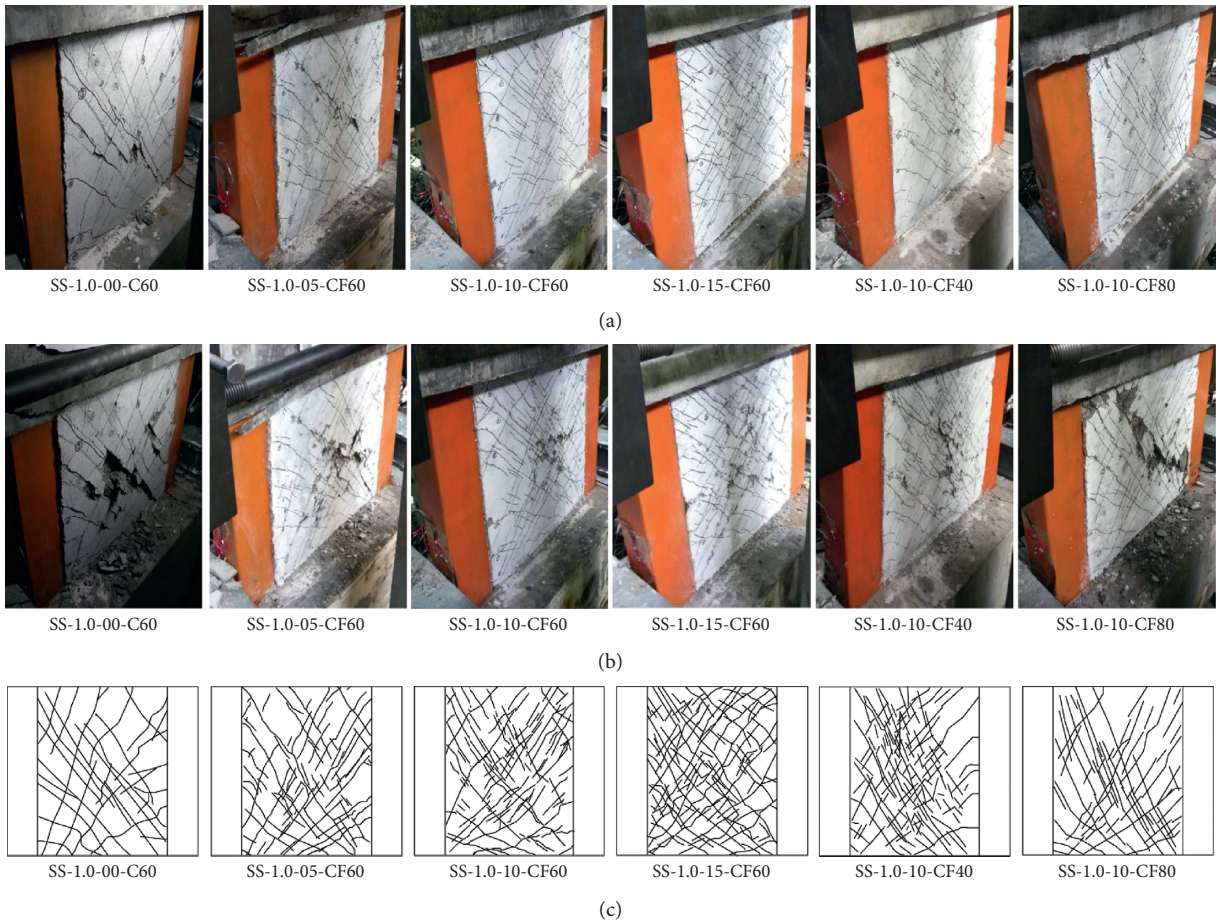

Figure 5: Failure pattern and crack distribution of shear wall specimens. (a) Failure pattern at peak state. (b) Failure pattern at ultimate state. (c) Schematic view of crack distribution.

2.4. Influence Factors. The shear capacities of all specimens are listed in Table 2. It can be seen from Table 2 that the shear performance of specimens is improved obviously with the increase of steel fiber volume fraction from 0% to 1.5%. Compared with the specimen SS-1.0-00-C60, the shear capacity of specimen SS-1.0-05-CF60, SS-1.0-10-CF60, and SS-1.0-15-CF60 is increased by 5.10%, 11.42%, and 16.19%, respectively. In addition, steel fiber could effectively control the crack width and improve the distribution shape of cracks in the web of shear wall. The cracks became much thinner, denser, of more quantity, and wider distribution with the increase of steel fiber volume fraction, whilst the crushing and spalling of concrete were also reduced. For instance, the maximum crack width of RC shear wall specimen numbered

SS-1.0-00-C60 was 2.0 mm at the peak load, whilst the maximum crack width of SFRC shear wall specimen numbered SS-1.0-05-CF60, SS-1.0-10-CF60, and SS-1.0-15-CF60 was 1.6 mm, 1.2 mm, and 1.0 mm, respectively. The maximum crack width decreased significantly with the increase of steel fiber volume fraction; the similar results were reported in the literature [9, 10].

Furthermore, it can be seen from Table 2 that the shear performance of specimens is improved obviously with the enhancing of concrete strength from CF40 to CF80. Compared with the specimen SS-1.0-10-CF40, the shear capacity of SS-1.0-10-CF60 and SS-1.0-10-CF80 is increased by 24.07% and 36.67%, respectively. And as shown in Figure 5, the SFRC shear wall specimens with different concrete strength had the similar failure appearance at the peak and ultimate state under the condition of the same steel fiber volume fraction. It can be seen that the lateral load of SFRC shear wall specimen with higher strength concrete deteriorated more obviously after the peak load, the crushing, and spalling of concrete were more serious at the ultimate state, especially for the specimen SS-1.0-00-CF80.

3. Shear Resisting Mechanism of SFRC Shear Wall with CFST Columns

It was observed in the test that the failing process of SFRC shear wall with CFST columns can be divided into two stages: at early loading stage, the all bending moments acted on the SFRC shear wall with CFST columns were carried by the CFST columns, nearly all the horizontal shear forces were carried by the web, and the axial forces were shared by the CFST columns and web; at medium and late loading stage, the concrete in the web continuously cracked, resulting in a decrease of the stiffness, and the shear forces gradually transferred from the web to CFST columns. Therefore, the calculation method for shear strength of SFRC shear wall with CFST columns can be defined as

$$V_{\mathrm{jh,calc}} = V_{\mathrm{jh}} + V_{\mathrm{col}}, \tag{1}$$

where $V_{\mathrm{jh,calc}}$ is the calculated value for shear strength of SFRC shear wall with CFST columns; V_{jh} is the shear strength of web; and V_{col} is the shear strength of CFST columns.

The shear strength of CFST columns can be defined as [4]

$$V_{\mathrm{col}} = \alpha_{\mathrm{v}} \cdot A_{\mathrm{sc}} \cdot \tau_{\mathrm{scy}}, \tag{2}$$

where α_{v} is the calculation coefficient for shear capacity, $\alpha_{\mathrm{v}} = 0.97 + 0.2\mathrm{In}(\xi)$, ξ is the confinement factor, $\xi = \alpha_{\mathrm{s}} f_{\mathrm{y}}/f_{\mathrm{c}}$, f_{y} is the yield strength of steel tube, f_{c} is the axial compressive strength of concrete, α_{s} is the steel ratio of CFST column, $\alpha_{\mathrm{s}} = A_{\mathrm{s}}'/A_{\mathrm{c}}'$, A_{s}' and A_{c}' are the cross-sectional areas of steel tube and concrete, respectively, A_{sc} is the total cross-sectional area of CFST column, and τ_{scy} is the shear yield limit, $\tau_{\mathrm{scy}} = (0.422 + 0.313\alpha_{\mathrm{s}}^{2.33})\ \xi^{0.134}\ (1.14 + 1.02\xi)\ f_{\mathrm{c}}$.

The load transferring mechanism of SFRC web under the combined action of compression, bending, and shearing is very complicated, which is similar to RC web in the literature [2, 3]. In the SSTM, the shear strength of the web is assumed to be that of concrete compressive struts, and the concrete in the web can continue to withstand shear force after the tension ties yield. Therefore, the main characteristic of web failure is that the concrete in the web reaches its compressive strength and is crushed and spalled. For diagonal compression failure, the shear strength of the web is defined as the concrete compressive stress on the nodal zone as the concrete reaches its capacity. The concrete bearing capacity is the summation of compressions from the concrete compressive struts in the diagonal, horizontal, and vertical mechanisms [14–19]. Hence, three strut and tie load paths are proposed to simulate the force transfer within the web, including the diagonal, horizontal, and vertical mechanisms, as shown in Figure 6.

The concrete in the web is subjected to the compression force; thus the diagonal compressive strut is formed, as shown in Figure 6(a). Due to the higher tensile strength of SFRC, the diagonal tension forces in the web are mainly carried by the SFRC before the cracking of concrete, the action of reinforcing bars is much smaller at this time. The initial inclined cracks in the web occur when the diagonal tension force is greater than the tensile strength of concrete. After the initial cracking of concrete, the diagonal tension forces in the web are mainly carried by the horizontal and vertical ties. The horizontal ties are composed of horizontal reinforcing bars and steel fibers as shown in Figure 6(b), whilst the vertical ties are composed of vertical reinforcing bars and steel fibers as shown in Figure 6(c). In summary, the reinforcing bars and steel fibers are subjected to tension and the concrete acts as compressive struts after the development of the first cracking pattern in the web; thus a strut and tie action is formed.

The diagonal mechanism (Figure 6(a)) is a single SFRC diagonal compression strut whose angle of inclination θ is defined as

$$\theta = \tan^{-1}\left(\frac{H}{l}\right), \tag{3}$$

where H is the distance from the lateral force loading point to the shear wall base; l is internal lever arm of the vertical shear couple, $l = 0.8l_{\mathrm{w}}$; and l_{w} is the length of the entire web in the direction of the applied lateral force.

The effective area of the SFRC diagonal compression strut A_{str} is defined as

$$A_{\mathrm{str}} = \alpha_{\mathrm{s}} \times b_{\mathrm{s}}, \tag{4}$$

where a_{s} is the depth of diagonal strut and b_{s} is the width of diagonal strut that can be taken as the width of the web t_{w}.

The depth of the diagonal strut a_{s} depends on its end condition provided by the compression zone at the base of the web. It can be intuitively assumed that

$$\alpha_{\mathrm{s}} = \alpha_{\mathrm{w}}, \tag{5}$$

where a_{w} is the depth of the compression zone at the base of the web, which can be approximately determined by [15]

$$\alpha_{\mathrm{w}} = \left(0.25 + 0.85\frac{N'}{A_{\mathrm{w}} f_{\mathrm{c}}'}\right) l_{\mathrm{w}}, \tag{6}$$

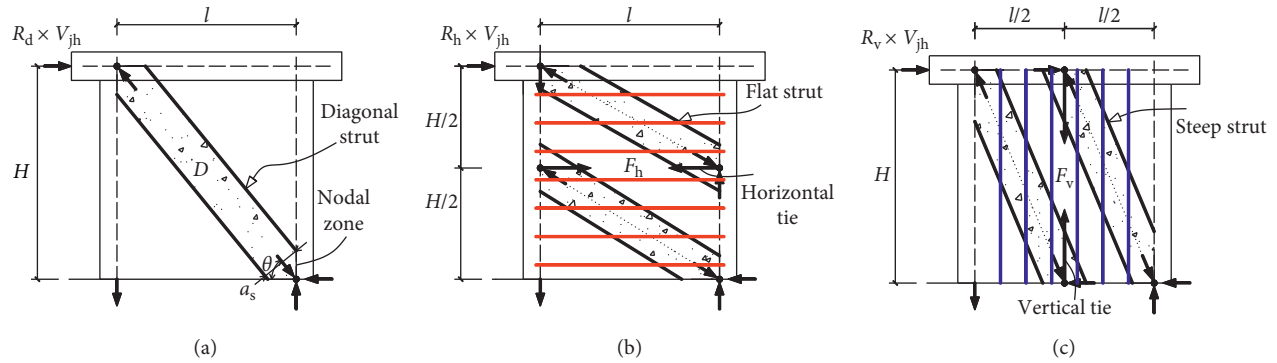

Figure 6: Shear resisting mechanisms of web. (a) Diagonal. (b) Horizontal. (c) Vertical.

where N' is the axial compressive force for the web; A_w is the cross-sectional area of the web, $A_w = t_w \times l_w$; and f_c' is the compressive strength of a standard concrete cylinder (MPa).

The axial compressive force for the web N' can be calculated as

$$N' = \frac{0.85E_c t_w l_w}{0.85E_c t_w l_w + 2E_s' A_s' + 2E_c' A_c'} N, \tag{7}$$

where N is the axial compressive force for the shear wall specimen; E_c is the elastic modulus of web concrete; 0.85 is the reduction coefficient of axial compressive stiffness for web concrete [4]; E_s' is the elastic modulus of steel tube; and E_c' is the elastic modulus of concrete inside the steel tube.

The horizontal mechanism (Figure 6(b)) includes one horizontal tie and two flat struts. Since steel fiber improves the tensile strength of the concrete, which makes the performance of SFRC shear wall different from that of RC shear wall. The horizontal tie is made up of the horizontal reinforcing bars and steel fibers and can be described as the following:

$$F_h = F_{s,h} + F_{sf,h}, \tag{8}$$

where F_h is the tension force in the horizontal tie; $F_{s,h}$ is the tension force of horizontal reinforcing bars, $F_{s,h} = A_{s,h} \times f_{s,h}$; $A_{s,h}$ is the sectional area of horizontal reinforcing bars; $f_{s,h}$ is the tensile strength of horizontal reinforcement; $F_{sf,h}$ is the tension force of horizontal steel fibers, $F_{sf,h} = A_{sf,h} \times f_{sf}$; $A_{sf,h}$ is the sectional area of horizontal steel fibers; and f_{sf} is the tensile strength of steel fiber.

The experimental results indicated that the horizontal reinforcing bars in the web did not fully yield when the web damaged, so the effective coefficient for shear resistance of horizontal reinforcement, η_1, is introduced. Thus $F_{s,h}$ can be defined as $F_{s,h} = \eta_1 \times A_{s,h} \times f_{s,h}$, where η_1 is taken as 0.75 based on the analysis for the test results in the literature [15].

For simplicity, the steel fibers randomly distributed in the three dimensions of the web can be equivalent to horizontal and vertical microreinforcing bars, as shown in Figure 7. Thus, the sectional area of horizontal steel fibers, $A_{sf,h}$, can be defined as

$$A_{sf,h} = n_{sf} A_{sf}, \tag{9}$$

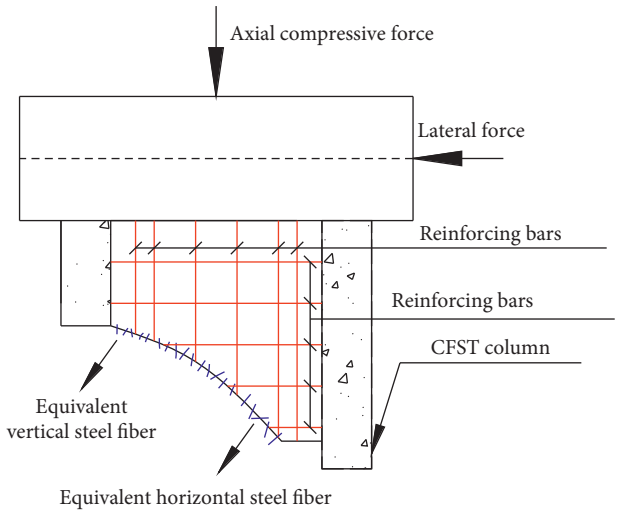

Figure 7: Steel fiber ties.

where A_{sf} is the cross-sectional area of a single steel fiber and n_{sf} is the equivalent steel fiber number, which can be calculated as

$$n_{sf} = \eta_2 \rho_{sf} \frac{t_w \quad H}{A_{sf} \sin \theta}, \tag{10}$$

where ρ_{sf} is the steel fiber volume fraction and η_2 is the equivalent coefficient, which can be approximately designated as 0.41 according to the study in the literature [26].

The sectional area of horizontal steel fibers, $A_{sf,h}$, can be determined as

$$A_{sf,h} = \frac{0.41\rho_{sf} t_w H}{\sin \theta}. \tag{11}$$

The vertical mechanism (Figure 6(c)) is composed of one vertical tie and two steep struts. Similar to the horizontal tie, the vertical tie includes the vertical reinforcing bars and steel fibers within the web and can be described as the following:

$$F_v = F_{s,v} + F_{sf,v}, \tag{12}$$

where F_v is the tension force in the vertical tie; $F_{s,v}$ is the tension force of vertical reinforcing bars, $F_{s,v} = A_{s,v} \times f_{s,v}$; $A_{s,v}$ is the sectional area of vertical reinforcing bars; $f_{s,v}$ is the tensile strength of vertical reinforcement; $F_{sf,v}$ is the tension force of

vertical steel fibers, $F_{sf,v} = A_{sf,v} \times f_{sf}$; $A_{sf,v}$ is the sectional area of vertical steel fibers; and $A_{sf,v} = 0.41\rho_{sf}t_w l_w/\cos\theta$ based on the above analysis.

The research in literature [15] shows that the vertical reinforcing bars are not fully effective in constituting the vertical tie, and the effective coefficient for shear resistance of vertical reinforcing bars, η_3, is introduced. Thus, $F_{s,v}$ can be defined as $F_{s,v} = \eta_3 \times A_{s,v} \times f_{s,v}$, where η_3 is taken as 0.8 [15].

4. Calculation Method for Shear Strength of SFRC Shear Wall with CFST Columns

The SSTM is used to determine the shear strength of web failing in diagonal compression.

4.1. Equilibrium Conditions. Based on the proposed strut and tie model for a web of shear wall, the horizontal and vertical shear forces can be calculated as follows:

$$V_{jh} = D\cos\theta + F_h + F_v\cot\theta, \tag{13}$$

$$V_{jv} = D\sin\theta + F_v + F_h\tan\theta, \tag{14}$$

where V_{jh} is the horizontal shear force; V_{jv} is the vertical shear force; and D is the compression force in SFRC diagonal strut. The details of force diagram are shown in Figure 8.

The ratios of the horizontal shear V_{jh} assigned among the three resisting mechanisms can be defined as [15]

$$D\cos\theta\colon F_h\colon F_v\cot\theta = R_d\colon R_h\colon R_v, \tag{15}$$

where R_d, R_h, and R_v are the web shear ratios resisted by the diagonal, horizontal, and vertical mechanisms, respectively, which can be defined as the following [15]:

$$R_d = \frac{(1-\gamma_h)(1-\gamma_v)}{1-\gamma_h\gamma_v}, \tag{16}$$

$$R_h = \frac{\gamma_h(1-\gamma_v)}{1-\gamma_h\gamma_v}, \tag{17}$$

$$R_v = \frac{\gamma_v(1-\gamma_h)}{1-\gamma_h\gamma_v}, \tag{18}$$

where γ_h is the fraction of horizontal shear transferred by the horizontal tie in the absence of the vertical tie and γ_v is the fraction of vertical shear carried by the vertical tie in the absence of the horizontal tie. The values of γ_h and γ_v can be obtained as [27]

$$\gamma_h = \frac{2\tan\theta - 1}{3}, \quad \text{for } 0 \le \gamma_h \le 1, \tag{19}$$

$$\gamma_h = \frac{2\tan\theta - 1}{3}, \quad \text{for } 0 \le \gamma_h \le 1. \tag{20}$$

By solving (13)–(15), the values of D, F_h, and F_v can be obtained as

$$D = \frac{1}{\cos\theta} \times \left(\frac{R_d}{R_d + R_h + R_v}\right) \times V_{jh}, \tag{21}$$

$$F_h = \left(\frac{R_h}{R_d + R_h + R_v}\right) \times V_{jh}, \tag{22}$$

$$F_v = \frac{1}{\cot\theta} \times \left(\frac{R_v}{R_d + R_h + R_v}\right) \times V_{jh}. \tag{23}$$

To check whether the web of shear wall reached failure strength, the bearing pressure on the nodal zone (Figure 6), where the compressive forces from the diagonal, flat, and steep struts intersect (Figure 8), must be checked. The maximum compressive stress $\sigma_{d,max}$ acting on the nodal zone can be calculated as

$$\sigma_{d,\max} = \frac{1}{A_{str}}\left[D + \frac{F_h}{\cos\theta}\left(1 - \frac{\sin^2\theta}{2}\right) + \frac{F_v}{\sin\theta}\left(1 - \frac{\cos^2\theta}{2}\right)\right]. \tag{24}$$

4.2. Constitutive Laws. The softened stress-strain relation of cracked SFRC concrete can be represented as the following [28]:

$$\sigma_d = \zeta f_c'\left[2\left(\frac{\varepsilon_d}{\zeta\varepsilon_0}\right) - \left(\frac{\varepsilon_d}{\zeta\varepsilon_0}\right)^2\right], \quad \text{for } \frac{\varepsilon_d}{\zeta\varepsilon_0} \le 1, \tag{25}$$

where σ_d is the average principal stress of concrete in the d-direction; ζ is the softening coefficient; ε_d is the average principal strain in the d-direction; and ε_0 is the concrete cylinder strain corresponding to the cylinder strength f_c', which can be defined approximately as [29]

$$\varepsilon_0 = -0.002 - 0.001\left(\frac{f_c' - 20}{80}\right), \quad \text{for } 20\,\text{MPa} \le f_c' \le 100\,\text{MPa}. \tag{26}$$

The softening coefficient ζ can be calculated as [28]

$$\zeta = \frac{5.8}{\sqrt{f_c'}}\ \frac{1}{\sqrt{1 + 400\varepsilon_r}} \le \frac{0.9}{\sqrt{1 + 400\varepsilon_r}}, \tag{27}$$

where ε_r is the average principal strain in the r-direction.

Whether the shear strength of the web of shear wall reaches the compressive stress, the strain of the concrete diagonal strut can be conformed by the following formula:

$$\sigma_d = \zeta f_c', \tag{28}$$

$$\varepsilon_d = \zeta\varepsilon_0. \tag{29}$$

The stress-strain relation of reinforcing bar can be described as

$$\begin{cases} f_s = E_s\varepsilon_s, & \varepsilon_s < \varepsilon_y, \\ f_s = f_y, & \varepsilon_s \ge \varepsilon_y, \end{cases} \tag{30}$$

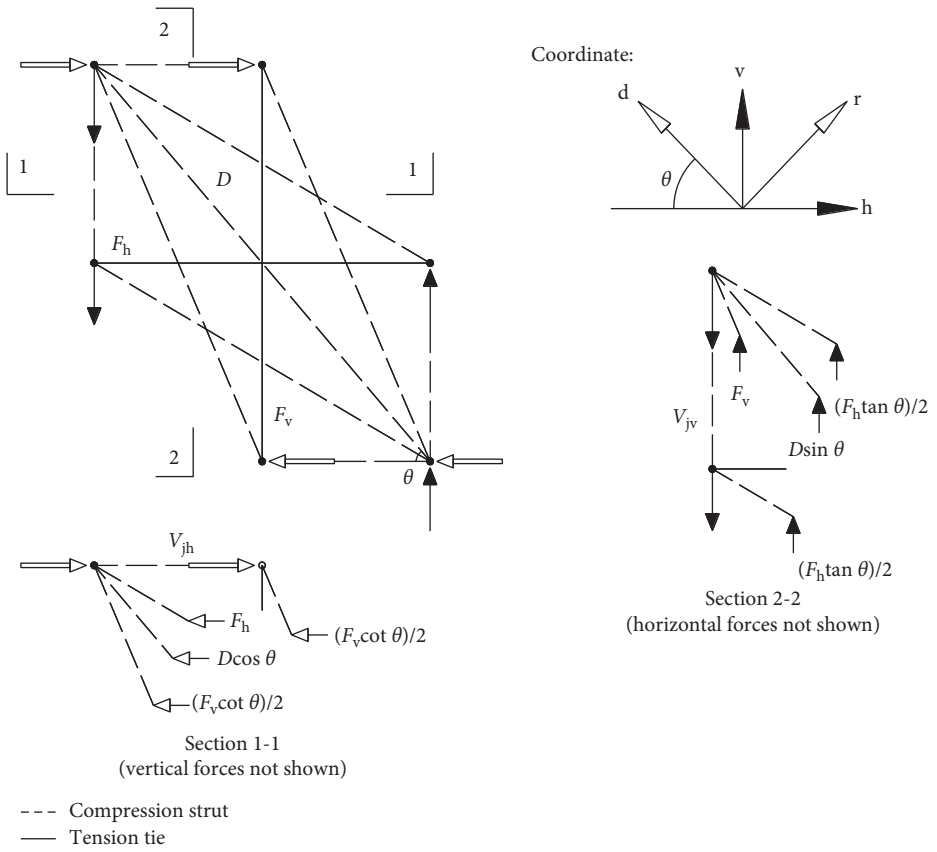

Figure 8: Strut and tie model for the web of shear wall.

where E_s is the elastic modulus of reinforcing bars; f_y is the yield strength of reinforcing bars; and f_s and ε_s are the stress and strain in mild steel, respectively. f_s becomes $f_{s,h}$ or $f_{s,v}$, E_s becomes $E_{s,h}$ or $E_{s,v}$, ε_s becomes $\varepsilon_{s,h}$ or $\varepsilon_{s,v}$, and f_y becomes f_{yh} or f_{yv} when equation (30) is applied to horizontal or vertical reinforcing bars, respectively.

The stress-strain relation of steel fiber can be expressed as

$$f_{sf} = E_{sf}\varepsilon_{sf}, \tag{31}$$

where E_{sf} is the elastic modulus of steel fiber and f_{sf} and ε_{sf} are the stress and strain of steel fiber, respectively.

The experiment results show that steel fibers are usually pulled out from concrete rather than broken due to their good tensile strength. Thus, the shear resistant action of the steel fiber depends on the bond strength between steel fiber and concrete. The stress of steel fiber, f_{sf}, should satisfy the relationship as the following:

$$A_{sf} f_{sf} \le \lambda_{sf} A_{spf} \tau_{sf,max}, \tag{32}$$

where $\tau_{sf,max}$ is the maximum bond strength between steel fiber and concrete, $\tau_{sf,max} = 2.5 f_{ct}$ [30]; f_{ct} is the matrix tensile strength of SFRC; λ_{sf} is the influence coefficient of steel fiber type; the values of λ_{sf} for long straight, wave-shaped, and hooked steel fibers are 0.5, 0.75, and 1.0, respectively; A_{spf} is the surface area of steel fiber, $A_{spf} = \pi d_{sf}\ l_{sfo}$; d_{sf} is the nominal diameter of steel fiber; l_{sfo} is the effective anchorage length of steel fiber, $l_{sfo} = 0.25 l_{sf}$; and l_{sf} is the length of steel fiber.

By adopting equation (33), the stress of steel fiber f_{sf} can be defined as

$$f_{sf} \le \lambda_{sf}\left(\frac{l_{sf}}{d_{sf}}\right)\tau_{sf,max}. \tag{33}$$

The relationship between forces and strains of the tension ties becomes

$$F_h = F_{s,h} + F_{sf,h} = 0.75 A_{s,h} E_{s,h} \varepsilon_{s,h} + \frac{0.41 \rho_{sf} t_w H E_{sf} \varepsilon_{sf,h}}{\sin \theta} \le F_{yh}, \tag{34}$$

$$F_v = F_{s,v} + F_{sf,v} = 0.8 A_{s,v} E_{s,v} \varepsilon_{s,v} + \frac{0.41 \rho_{sf} t_w l_w E_{sf} \varepsilon_{sf,v}}{\cos \theta} \le F_{yv}, \tag{35}$$

$$\begin{aligned} \varepsilon_{s,h} &= \varepsilon_{sf,h} = \varepsilon_h, \\ \varepsilon_{s,v} &= \varepsilon_{sf,v} = \varepsilon_v, \end{aligned} \tag{36}$$

where $\varepsilon_{s,h}$ and $\varepsilon_{sf,h}$ are the strains of the reinforcing bars and the steel fibers in the h-direction, respectively; $\varepsilon_{s,v}$ and $\varepsilon_{sf,v}$ are the strains of the reinforcing bars and the steel fibers in the v-direction, respectively; ε_h and ε_v are the average normal strains in the h- and v-directions, respectively; and F_{yh} and

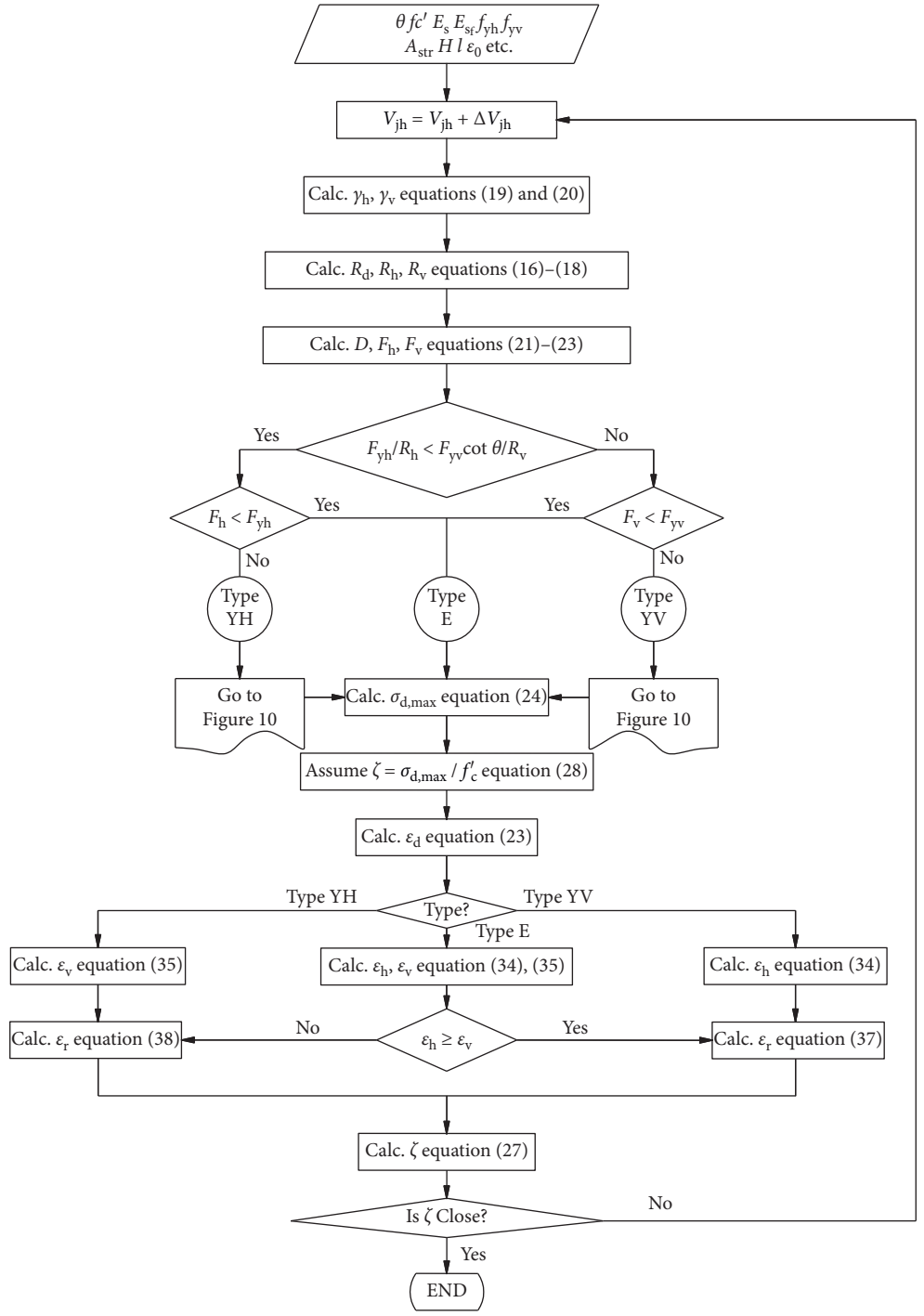

Figure 9: Flow chart showing efficient algorithm.

F_{yv} are the yielding forces of the horizontal and vertical ties, respectively.

4.3. Compatibility Condition. The compatibility conditions adopted herein are given as the following [31]:

$$\varepsilon_r = \varepsilon_h + (\varepsilon_h - \varepsilon_d)\cot^2\theta, \tag{37}$$

$$\varepsilon_r = \varepsilon_v + (\varepsilon_v - \varepsilon_d)\tan^2\theta. \tag{38}$$

4.4. Solution Procedures. The solution procedures are proposed [15, 19], as shown in Figures 9 and 10. The algorithm in Figure 9 starts with a selection of the horizontal shear V_{jh} and consists of three major steps. Firstly, $\sigma_{d,max}$ is calculated by employing the equilibrium equations. By assuming the strength of the concrete strut is reached, an initial value of the softening coefficient ζ is obtained through $\zeta = \sigma_{d,max}/f'_c$. Secondly, the strains of the struts and ties are calculated by applying the corresponding constitutive laws. Finally, the

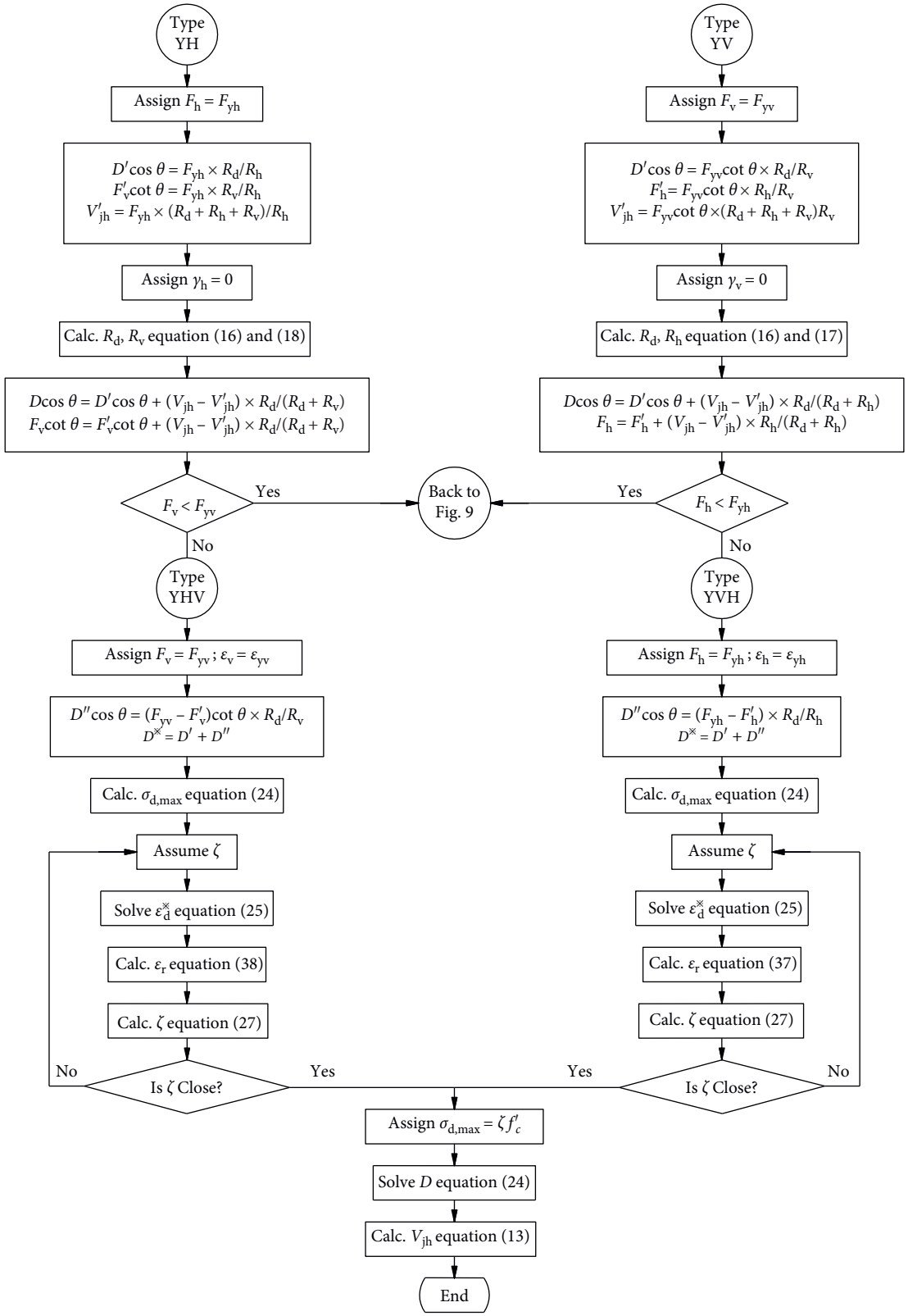

Figure 10: Algorithm for postyielding cases.

Table 3: Calculation type.

Type	Type E	Type YH	Type YV	Type YHV	Type YVH
Condition	$F_h < F_{yh}$ and $F_v < F_{yv}$	$F_h = F_{yh}$ and $F_v < F_{yv}$	$F_h < F_{yh}$ and $F_v = F_{yv}$	$F_h = F_{yh}$ and then $F_v = F_{yv}$	$F_v = F_{yv}$ and then $F_h = F_{yh}$

Table 4: Experimental verification.

Specimen	Web f_c (MPa)	Columns f_c (MPa)	H (mm)	$t_w \times l_w$ (mm)	$a \times t$ (mm)	n	Horizontal reinforcement	f_{yh} (MPa)	Vertical reinforcement	f_{yv} (MPa)	Steel fiber		$V_{jh,test}$ (kN)	$V_{jh,calc}$ (kN)	$V_{jh,test}/V_{jh,calc}$
											l_{sf}/d_{sf}	ρ_{sf} (%)			
SS-1.0-00-C60	56.3	55.9	750	120 × 510	120 × 3.0	0.2	C6@100	369.17	12 C 6	369.17	—	—	902	848	1.06
SS-1.0-05-CF60	55.2	55.5	750	120 × 510	120 × 3.0	0.2	C6@100	369.17	12 C 6	369.17	64	0.5	948	896	1.06
SS-1.0-10-CF60	55.1	55.5	750	120 × 510	120 × 3.0	0.2	C6@100	369.17	12 C 6	369.17	64	1.0	1005	931	1.08
SS-1.0-15-CF60	56.5	56.0	750	120 × 510	120 × 3.0	0.2	C6@100	369.17	12 C 6	369.17	64	1.5	1048	947	1.11
SS-1.0-10-CF40	38.3	38.1	750	120 × 510	120 × 3.0	0.2	C6@100	369.17	12 C 6	369.17	64	1.0	810	795	1.02
SS-1.0-10-CF80	65.6	64.6	750	120 × 510	120 × 3.0	0.2	C6@100	369.17	12 C 6	369.17	64	1.0	1107	1008	1.10
SW1.0-2 [2]	42.14	42.14	740	140 × 460	159 × 3.7	0.35	A6@120	478.73	A4@80	683.17	—	—	872.09	974	0.90
CFST-S-S1 [4]	39.71	39.71	920	85 × 860	120 × 3.0	0.31	A6@120	397	A6@120	397	—	—	770.6	786	0.98
CFST-S-S2 [4]	39.71	39.71	920	85 × 860	120 × 3.0	0.62	A6@120	397	A6@120	397	—	—	891.4	826	1.08
CFST-S-L1 [4]	39.71	39.71	920	85 × 1320	120 × 3.0	0.31	A6@120	397	A6@120	397	—	—	991	1044	0.95
CFST-S-L2 [4]	39.71	39.71	920	85 × 1320	120 × 3.0	0.62	A6@120	397	A6@120	397	—	—	1265	1091	1.16
CFST-C-S1 [4]	39.71	39.71	920	85 × 860	140 × 2.0	0.29	A6@120	397	A6@120	397	—	—	788.5	792	1.00
CFST-C-S2 [4]	39.71	39.71	920	85 × 860	140 × 2.0	0.58	A6@120	397	A6@120	397	—	—	895.1	834	1.07
CFST-C-L1 [4]	39.71	39.71	920	85 × 1320	140 × 2.0	0.29	A6@120	397	A6@120	397	—	—	987.5	1053	0.94
CFST-C-L2 [4]	39.71	39.71	920	85 × 1320	140 × 2.0	0.58	A6@120	397	A6@120	397	—	—	1225	1100	1.11
SW-05-40 [9]	21.2	—	900	—	—	0.1	A8@150	340	6 B 14	373.5	57	0.5	730	608	1.20
SW-10-40 [9]	26.8	—	900	—	—	0.1	A8@150	340	6 B 14	373.5	57	1.0	745	730	1.02
SW-15-40 [9]	25.1	—	900	—	—	0.1	A8@150	340	6 B 14	373.5	57	1.5	770	748	1.03
SW-20-40 [9]	26.9	—	900	—	—	0.1	A8@150	340	6 B 14	373.5	57	2.0	808	792	1.02
SW-10-30 [9]	17.8	—	900	—	—	0.1	A8@150	340	6 B 14	373.5	57	1.0	730	586	1.25
FSW1 [10]	36	—	600	—	—	0.09	6A6.5	310	6A6.5	310	64	1.0	335	431	0.78
FSW2 [10]	33.5	—	600	—	—	0.09	6A6.5	310	6A6.5	310	64	1.5	330	436	0.76

Table 4: Continued.

Specimen	Web f_c (MPa)	Columns f_c (MPa)	H (mm)	$t_w \times l_w$ (mm)	$a \times t$ (mm)	n	Horizontal reinforcement	f_{yh} (MPa)	Vertical reinforcement	f_{yv} (MPa)	Steel fiber l_{sf}/d_{sf}	Steel fiber ρ_{sf} (%)	$V_{jh,test}$ (kN)	$V_{jh,calc}$ (kN)	$V_{jh,test}/V_{jh,calc}$
FSW3 [10]	35	—	600	—	—	0.09	6A6.5	310	6A6.5	310	64	2.0	340	465	0.73
FSW4 [10]	34.5	—	600	—	—	0.09	6A6.5	310	8A6.5	310	64	1.0	330	430	0.77
Total 24, average 1.01, COV 0.14.															

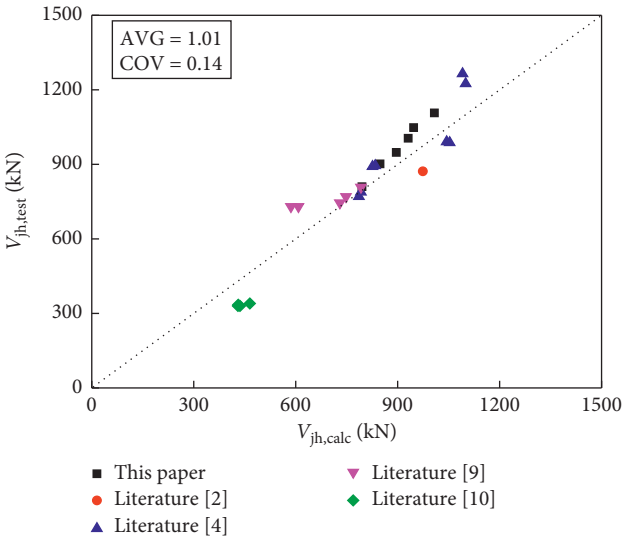

Figure 11: Correlation of experimental and predicted wall shear strengths.

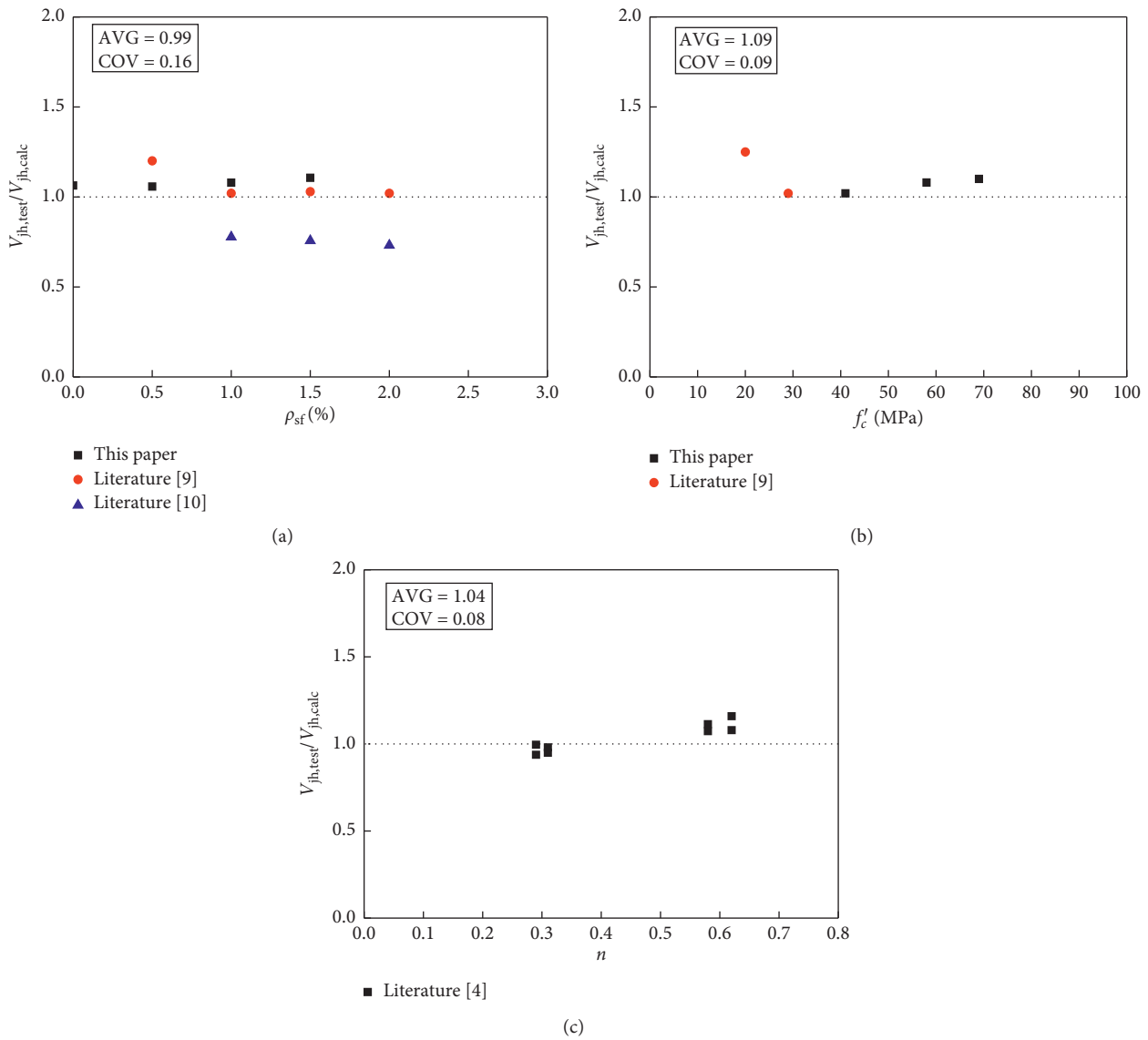

Figure 12: Effects on shear strength predictions. (a) Effect of steel fiber volume fraction on shear strength predictions. (b) Effect of concrete strength on shear strength predictions. (c) Effect of axial compression ratio on shear strength predictions.

average principal strain in the r-direction ε_r is calculated with the aid of the compatibility equation. Then, a new value of ζ is calculated by using the softening theoretical formula. If the assumed ζ value is close to the new ζ, the V_{jh} selected is the shear strength of the web, otherwise back to the iterations.

Furthermore, the procedure in Figure 9 is categorized into five types according to varied yielding conditions of the ties [15, 19], as shown in Table 3. Figure 10 presents the force redistribution of the web shears after the yielding of the horizontal tie.

5. Experimental Verification

Although the experimental design parameters of SFRC shear wall specimens, RC shear wall with CFST columns specimens, and SFRC shear wall with CFST columns specimens were different, the failure processes of shear wall specimens in this paper and the literature [2, 4, 9, 10] are similar. Based on the experimental results, the failure process generally could be divided into four stages: initial cracking stage, main diagonal cracks forming stage, limit stage, and failure stage. The web of shear wall was separated into a series of diagonal compression rhombic blocks by the intercrossing inclined cracks under gradually increasing lateral load. As the lateral load increased continuously, the concrete rhombic blocks reached ultimate compressive strength and the concrete in the web was crushed and spalled, resulting in obvious shear-dominant failure mode for the shear wall specimens in this paper and the literature [2, 4, 9, 10]. The existence of steel tubes and steel fibers cannot change the ultimate failure mode of shear wall specimens. Therefore, the model presented in this paper can be used to calculate the shear strength of the abovementioned three types of shear walls failing in diagonal compressions in theory.

A total of 24 test specimens [2, 4, 9, 10] and their results (Table 4) are used to verify the proposed method, including 6 SFRC shear wall with CFST columns specimens in this paper, 9 RC shear wall with CFST columns specimens, and 9 SFRC shear wall specimens in the available literature [2, 4, 9, 10]. The test specimens selected cover a wide range of structure forms, geometry, loading, steel tube, steel fiber, and reinforcement detailing, as summarized in Table 4. The test specimens considered herein have three major common features: (1) all walls showed a web shear-dominant failure mode; (2) they were one-story isolated walls; (3) all contained both horizontal and vertical reinforcement uniformly distributed basically throughout the web.

In Figure 11, the experimental shear strengths from 24 walls are compared to their shear strengths predicted by the method presented in this paper. The relationship between the prismatic strength f_c and the cylinder strength f'_c is obtained from literature [32]. The last column of Table 4 lists the values of $V_{jh,test}/V_{jh,calc}$ ratios to indicate the precision of the proposed model. Figure 11 shows satisfactory results for the comparison of the measured and predicted strengths. The average strength ratio ($V_{jh,test}/V_{jh,calc}$) is 1.01 with a coefficient of variation (COV) of 0.14 (Table 4). It is concluded that the proposed model can accurately predict the shear strengths of the shear walls mentioned above.

Figure 12 shows the effects of steel fiber volume fraction, concrete strength, and axial compression ratio on the shear strength predictions of the proposed method. The steel fiber volume fraction, concrete strength, and axial compression ratio are not observed to have significant influences on the strength ratio ($V_{jh,test}/V_{jh,calc}$), indicating that the main factors which affect the shear wall bearing capacity are reflected in the proposed model.

6. Conclusions

This paper introduces the tests for an innovative composite shear wall named SFRC shear wall with CFST columns and presents a proposal for determining the shear strength of the shear wall. The proposed SSTM is derived from the concept of struts and ties and satisfies equilibrium, compatibility, and constitutive laws of cracked SFRC. Based on the test results in this paper and available literature and their comparison with the proposed model, the following conclusions can be drawn:

(1) All the SFRC shear wall with CFST columns specimens showed a shear-dominant failure mode in the current tests, and all specimens mainly exhibited a typical diagonal cracking pattern during the testing process. Steel fiber could effectively control the crack width and improve the distribution shape of cracks in the web of shear wall.

(2) The shear mechanism of SFRC shear wall with CFST columns can be described by the SSTM, which consists of diagonal, horizontal, and vertical mechanisms.

(3) The steel fibers distributed randomly in concrete can be treated as longitudinal and transverse reinforcement in the shear strength analysis of SFRC shear wall with CFST columns. And the contribution of steel fiber to the wall shear strength is identified.

(4) Examination of existing experimental data indicated that the proposed model is capable of predicting the shear strengths of SFRC shear wall with CFST columns, RC shear wall with CFST columns, and SFRC shear walls for diagonal compression failures.

Data Availability

The data used to support the findings of this study are available from the corresponding author upon request.

Conflicts of Interest

The authors declare that there are no conflicts of interest regarding the publication of this paper.

Acknowledgments

The authors wish to thank Mr. Ji-Yu Tang of Zhengzhou University and Mr. Hong-Bo Han of Jinan DOCER Test

Machine Technology Co., Ltd. for their assistance in the test programme. The research reported in the paper is part of the Project 51708514 supported by the National Natural Science Foundation of China and Key Scientific Research Projects of Colleges and Universities of Henan Provincial Department of Education (19A560005). Their financial support is highly appreciated.

References

[1] H.-S. Hu, J.-G. Nie, J.-S. Fan, M.-X. Tao, Y.-H. Wang, and S.-Y. Li, "Seismic behavior of CFST-enhanced steel plate-reinforced concrete shear walls," *Journal of Constructional Steel Research*, vol. 119, pp. 176–189, 2016.

[2] Y. Yang and W. Cao, "Seismic performance of shear wall with CFST columns and encased steel truss," *Journal of Asian Architecture and Building Engineering*, vol. 15, no. 3, pp. 613–618, 2016.

[3] L.-H. Han, W. Li, and Y.-F. Yang, "Seismic behaviour of concrete-filled steel tubular frame to RC shear wall high-rise mixed structures," *Journal of Constructional Steel Research*, vol. 65, no. 5, pp. 1249–1260, 2009.

[4] F.-Y. Liao, L.-H. Han, and Z. Tao, "Seismic behaviour of circular CFST columns and RC shear wall mixed structures: Experiments," *Journal of Constructional Steel Research*, vol. 65, no. 8-9, pp. 1582–1596, 2009.

[5] P. Zhang, S. Han, S. Ng, and X.-H. Wang, "Fiber-reinforced concrete with application in civil engineering," *Advances in Civil Engineering*, vol. 2018, Article ID 1698905, 4 pages, 2018.

[6] J. Zhao and H. Dun, "A restoring force model for steel fiber reinforced concrete shear walls," *Engineering Structures*, vol. 75, pp. 469–476, 2014.

[7] T. Dun, S. Kang, and O. Kim, "Earthquake resistance of structural walls confined by conventional tie hoops and steel fiber reinforced concrete," *Earthquakes and Structures*, vol. 7, no. 5, pp. 843–859, 2014.

[8] W. G. Lim, S. W. Kang, and H. D. Yun, "Shear behavior of squat steel fiber reinforced concrete (SFRC) shear walls with vertical slits," *Applied Mechanics and Materials*, vol. 372, pp. 207–210, 2013.

[9] J. Zhao, D. Y. Gao, and X. L. Du, "Seismic behavior of steel fiber reinforced concrete low-rise shear wall," *Journal of Earthquake Engineering and Engineering Vibration*, vol. 29, no. 4, pp. 103–108, 2009.

[10] X. R. Tang, Y. S. Jiang, and D. J. Ding, "Application of the theory of softened truss to low-rise steel fiber high strength concrete shear walls," *Journal of Building Structures*, vol. 14, no. 2, pp. 2–11, 1993.

[11] P. Zhang, Y.-n. Zhao, C.-h. Liu, P. Wang, and T.-h. Zhang, "Combined effect of nano-SiO_2 particles and steel fibers on flexural properties of concrete composite containing fly ash," *Science and Engineering of Composite Materials*, vol. 21, no. 4, pp. 597–605, 2014.

[12] D. Gao, L. Zhang, J. Zhao, and P. You, "Durability of steel fibre-reinforced recycled coarse aggregate concrete," *Construction and Building Materials*, vol. 232, Article ID 117119, 2020.

[13] P. Zhang, Q. F. Li, Y. Z. Chen, Y. Shi, and Y. F. Ling, "Durability of steel fiber-reinforced concrete containing SiO_2 nano-particles," *Materials*, vol. 12, no. 13, pp. 1–18, 2019.

[14] S.-J. Hwang and H.-J. Lee, "Strength prediction for discontinuity regions by softened strut-and-tie model," *Journal of Structural Engineering*, vol. 128, no. 12, pp. 1519–1526, 2002.

[15] S.-J. Hwang, W.-H. Fang, H.-J. Lee, and H.-W. Yu, "Analytical model for predicting shear strengthof squat walls," *Journal of Structural Engineering*, vol. 127, no. 1, pp. 43–50, 2001.

[16] S. J. Hwang, W. Y. Lu, and H. J. Lee, "Shear strength prediction for deep beams," *ACI Structural Journal*, vol. 97, no. 3, pp. 367–376, 2000.

[17] S. J. Hwang, W. Y. Lu, and H. J. Lee, "Shear strength prediction for reinforced concrete corbels," *ACI Structural Journal*, vol. 97, no. 4, pp. 543–552, 2000.

[18] S. J. Hwang and H. J. Lee, "Analytical model for predicting shear strengths of interior reinforced concrete beam-column joints for seismic resistance," *ACI Structural Journal*, vol. 97, no. 1, pp. 35–44, 2000.

[19] S. J. Hwang and H. J. Lee, "Analytical model for predicting shear strengths of exterior reinforced concrete beam-column joints for seismic resistance," *ACI Structural Journal*, vol. 96, no. 5, pp. 846–857, 1999.

[20] Y. Okahashi and C. P. Pantelides, "Strut-and-tie model for interior RC beam-column joints with substandard details retrofitted with CFRP jackets," *Composite Structures*, vol. 165, pp. 1–8, 2017.

[21] D. Y. Gao, K. Shi, and S. B. Zhao, "Calculation method for shear capacity of steel fiber reinforced concrete beam-column joints based on softened strut-and-tie model," *Journal of Building Structures*, vol. 47, no. 9, pp. 101–109, 2014.

[22] X. W. Liang, J. L. Che, P. H. Yang et al., "Seismic behavior of high-strength concrete structural walls with edge columns," *ACI Structural Journal*, vol. 110, no. 6, pp. 953–963, 2013.

[23] S. Sasmal and K. Ramanjaneyulu, "Evaluation of strength hierarchy of beam-column joints of existing RC structures under seismic type loading," *Journal of Earthquake Engineering*, vol. 16, no. 6, pp. 897–915, 2012.

[24] W.-Y. Lu, "Shear strength prediction for steel reinforced concrete deep beams," *Journal of Constructional Steel Research*, vol. 62, no. 10, pp. 933–942, 2006.

[25] M.-G. Vetr, N. Mohamad Shirali, and A. Ghamari, "Seismic resistance of hybrid shear wall (HSW) systems," *Journal of Constructional Steel Research*, vol. 116, pp. 247–270, 2016.

[26] S. A. Al-Ta and N. S. H. Al-Husaini, "Softened truss model theory for the analysis of fibre reinforced concrete deep beams and corbels-E," *AL-Rafdain Engineering Journal (AREJ)*, vol. 22, no. 4, pp. 12–23, 2014.

[27] K. Schäfer, "Strut-and-tie models for the design of structural concrete," *Notes of Workshop*, Department of Civil Engineering, National Cheng Kung University, Tainan, Taiwan, 1996.

[28] L.-X. B. Zhang and T. T. C. Hsu, "Behavior and analysis of 100 MPa concrete membrane elements," *Journal of Structural Engineering*, vol. 124, no. 1, pp. 24–34, 1998.

[29] S. J. Foster and R. I. Gilbert, "The design of nonflexural members with normal and high-strength concrete," *ACI Structural Journal*, vol. 93, no. 1, pp. 3–10, 1996.

[30] J. Y. L. Voo and S. J. Foster, *Variable Engagement Model for Fibre Reinforced Concrete in Tension*, The University of New South Wales, Sydney, Australia, 2003.

[31] T. T. C. Hsu, *Unified Theory of Reinforced Concrete*, CRC Press, Boca Raton, FL, USA, 1993.

[32] P. Zhang, S. Fu, K. Zhang, and T. Zhang, "Mechanical properties of polyvinyl alcohol fiber-reinforced concrete composite containing fly ash and nano-SiO_2," *Science of Advanced Materials*, vol. 10, no. 6, pp. 769–778, 2018.

Hindawi
Advances in Civil Engineering
Volume 2020, Article ID 8834507, 11 pages
https://doi.org/10.1155/2020/8834507

Research Article

Effect of Surface Shape and Content of Steel Fiber on Mechanical Properties of Concrete

Lijuan Zhang,[1] **Jun Zhao**,[1] **Cunyuan Fan**,[2] **and Zhi Wang**[1]

[1]*School of Mechanics and Safety Engineering, Zhengzhou University, No. 100 Science Avenue, Zhengzhou 450001, Henan, China*
[2]*School of Civil Engineering, Zhengzhou University, No. 100 Science Avenue, Zhengzhou 450001, Henan, China*

Correspondence should be addressed to Lijuan Zhang; floycn526@163.com

Received 24 May 2020; Revised 22 June 2020; Accepted 27 June 2020; Published 21 July 2020

Academic Editor: Grzegorz Golewski

Steel fiber reinforced concrete (SFRC) has gained popularity in the last decades attributed to the improvement of brittleness and low tensile strength of concrete. This study investigates the effect of three shapes of steel fibers (straight, hooked end, and corrugated) with four contents (0.5%, 1%, 1.5%, and 2%) on the mechanical properties (compression, splitting tension, shear, and flexure) of concrete. Thirteen groups of concrete were prepared and investigated experimentally. Test results indicated that steel fiber had significant reinforcement on mechanical properties of concrete. When the steel fiber content increases from 0.5% to 2.0%, the compressive strengths increase about 4–24%, splitting tensile strengths increase about 33–122%, shear strengths increase about 31–79%, and flexural strengths increase about 25–111%. Corrugated steel fiber has the best reinforced effect on strength of SFRC, hooked end steel fiber takes the second place, and straight steel fiber is the least. Calculated formulas of compressive, splitting tensile, shear, and flexural strengths were established with consideration of the bonding properties between concrete and steel fiber. Influence factors of steel fiber (α_f) and concrete matrix strength (α_c) were put forward and determined by regression analysis of experimental data. Calculated results agree well with the experimental results.

1. Introduction

Concrete is the largest amount and the most widely used material; its tensile strength is significantly lower than its compressive strength. Synthetic, glass, basalt, carbon, PVA, and steel fiber have been used in concrete to make up for the low tensile strength of concrete [1]. Fiber can notably enhance mechanical performance of concrete [2–4]. Compared with other fibers, steel fiber has many advantages, such as high stiffness and elasticity modulus and tensile strength. Steel fiber reinforced concrete (SFRC) has excellent tensile and flexural property [5, 6], which has been widely used as structural material. In order to improve the reinforced effect of steel fiber, the reinforced mechanism of steel fiber on concrete had been researched widely [7, 8]. Reinforced effect of steel fiber is mainly affected by fiber content, type, geometry, and strength of concrete matrix [9]. When the concrete matrix is fixed, the fiber content, type, and geometry are the main influence factors [10, 11].

It is generally acknowledged that the mechanical property of SFRC increases with the rising of steel fiber content. However, some studies suggest that steel fiber does not significantly affect the compressive strength [3]. The axial compressive strength almost keeps unchanged when the volume fraction of steel fiber is larger than 1.0% [12]. Other studies suggest that compressive strength increases by 25% with the volume fraction of steel fiber increasing from 0.5% to 1.5% for the moderately high strength concrete [13]. Some literatures have proved that steel fiber added in concrete increases the compressive strength of concrete by about 4–19% [14, 15]. Steel fiber in concrete significantly increases the split tensile and flexural strength of concrete [12]. Split tensile strength of SFRC is higher about 11–54% than the reference mixture. Besides, flexural strengths of SFRC are higher by 3–81% than reference mixture. In addition, the increase ratio of flexural strength is higher than that of the split tensile and compressive strength [16]. Shear strength increases by 44% for the steel fiber volume fraction

of 0.5% and 65% for the volume ratio of 1% [17]. The shear strength of SFRC exhibits a linear increase with the amount of steel fiber crossing the shear crack interface [18]. It can be seen that even if the content of steel fiber is the same, steel fiber still has different reinforced effect on different mechanical property. In a word, the reinforced effect of steel fiber on concrete strength still has not uniform answer.

According to manufacturing form, steel fiber is usually classified into three main shapes (straight form, hooked ends form, and corrugated form) [11, 19]. Different steel fiber shapes have different effect on the mechanical performance of concrete due to the different bond property. However, some researchers suggest that steel fiber shape almost has no influence on compressive strength [12] or the compressive performance is insignificantly affected by the length and type of fiber [20]. The compressive strength and the elastic modulus of SFRC were developed with hooked end steel fiber [21]. The compressive strength is improved by twisted steel fiber compared to short straight steel fiber, but the improvement is relatively insignificant compared to what is observed for the tensile and flexural performance [22]. The tensile strength is improved by using the deformed steel fiber, as compared to that with the short straight steel fiber [23]. The specimens with 2% of twisted steel fiber exhibit a tensile strength which is approximately 32% higher than those with 2% of short straight steel fiber. Previous research has showed that corrugated and hooked fiber significantly improved the bond properties by three to seven times when compared to those with straight fiber [24, 25]. It can be concluded that even if the content of steel fiber is the same, the different shape steel fiber has different effect on concrete mechanical property.

Although much work has been done about SFRC, there still exists unsolved problem:

(i) Although the reinforced effect of steel fiber on compressive strength is much less than that on tensile strength, shear strength, and flexural strength, the increase ratio of compressive strength still can reach 25% for low or moderately high strength (≤60 MPa) concrete. Some literature studies suggest that steel fiber shape almost has no influence on compressive strength; others indicate that compressive strength can be improved by steel fiber no matter what type steel fiber is. There are still many different conclusions about the reinforced effect of steel fiber on compressive strength, so the reinforced effect of steel fiber with different content and type on compressive strength should be studied further.

(ii) Splitting tensile, flexure, and shear strength of SFRC increase with the rising of steel fiber content; some researchers suggest that concrete strength will no longer increase when steel fiber content exceeds a certain value, which means that there exists the most economical steel fiber content for certain strength. But there is no final word on the most economical content of steel fiber.

(iii) The shape of steel fiber has significantly influence on the enhancement effect of splitting tensile, flexure, and shear strength of SFRC. At the same time, the reinforced effect of different shapes on various mechanical properties of concrete is also different. So, there is the best shape of steel fiber which can achieve the best enhancement effect on one kind of mechanical property of content.

How to determine the optimal content and shape of steel fiber is an important problem. This would help improve the utilization rate of steel fiber and reduce the cost of SFRC.

In this research, the impact of steel fiber shape and content on the reinforced effect of concrete will be monitored and analyzed through the compressive, splitting tensile, shear, and flexural experiments. Three shapes (straight, hooked end, and corrugated) of steel fiber were used to research the influence on the mechanical performance of concrete with different volume fractions (0, 0.5%, 1%, 1.5%, and 2%). Based on the test result, calculation model of compressive, splitting tensile, shear, and flexural strength of SFRC were put forward.

2. Experiment Investigation

2.1. Materials. Portland cement (P. O. 42.5) conforming to GB 175 [26] was used in all mixes; properties of the cement are shown in Table 1. The coarse aggregate was crushed limestone with continuous grading of particle sizes from 4.75 mm to 20 mm. Fine aggregate was river sand with a fineness modulus of 2.7. Properties of all aggregates used in the test are shown in Table 2 according to the Chinese Standard GB/T 14685 [27]. Three shapes of steel fiber, namely, straight (ST-F), hooked end (HE-F), and corrugated (CO-F) were used in tests. Geometry and mechanical characteristics of steel fiber are listed in Table 3. Four different volume fractions of steel fiber were developed to cover the majority of practically used fractions range: 0.5%, 1.0%, 1.5%, and 2%.

2.2. Mix Proportion. Three shapes of steel fiber and four steel fiber volume fractions (V_f = 0.5%, 1.0%, 1.5%, and 2%) were chosen as test parameters. Steel fiber volume fraction (V_f) was defined as the absolute volume of steel fiber in 1 m^3 concrete. Water-cement ratio was taken as 0.55. The mixture proportion design method conformed to the Chinese Standards JGJ 55-2011 [28] and JG/T 472-2015 [29]. The target slump was taken as 180 mm. The sand ratio of plain concrete was taken as 42%. In order to ensure the working performance of concrete, the sand rate increases by 1% when the steel fiber volume fraction increases by 1%. Details of mixture proportion designs are listed in Table 4. PC represents plain concrete for comparison; letters represent the type of steel fiber; numbers represent the steel fiber volume fraction (%), such as ST-F0.5; it means that straight steel fiber and steel fiber volume fraction is 0.5%.

Table 1: Physical and mechanical properties of cement.

Type	Specific gravity (kg/m^3)	Surface area (m^2/kg) %	Standard consistency	Stability	Setting time (min)		Compressive strength (MPa)		Flexural strength (MPa)	
					Initial	Final	3 d	28 d	3 d	28 d
P. O. 42.5	3100	352	24.7	Eligibility	175	220	23.5	45	5.6	8.5

Table 2: Physical properties of the coarse and fine aggregate.

Aggregate type	Apparent density (kg/m^3)	Loose packing density (kg/m^3)	Dry-rodded density (kg/m^3)	Water absorption (wt %)	Crush index (%)	Void ratio (%)
Coarse aggregate	2814	1568	1630	1.40	8.8	44.3
Fine aggregate	2556	1611	1486	0.56	—	—

Table 3: Geometry and mechanical characteristics of steel fibers.

	ST-F	HE-F	CO-F
Fiber shape	Straight	Hooked end	Corrugated
Mean length (l_f), mm	32.34	32.19	32.27
Mean diameter (d_f), mm	1.036	0.993	1.215
Aspect ratio (l_f/d_f)	31.21	32.41	26.56
Density (g/cm^3)	7.9	7.9	7.9
Elastic modulus (GPa)	200	200	200
Tensile strength (MPa)	500	380	500

Table 4: Mixture proportions (kg/m^3).

Mixture number	Water	Cement	Sand	Stone	Steel fiber
PC	264	480	716.5	989.5	0
ST-F0.5	264	480	727.8	965.8	39
ST-F1	264	480	739.2	942.3	78
ST-F1.5	264	480	750.5	917.3	117
ST-F2	264	480	761.9	895.1	156
HE-F0.5	264	480	727.8	965.8	39
HE-F1	264	480	739.2	942.3	78
HE-F1.5	264	480	750.5	917.3	117
HE-F2	264	480	761.9	895.1	156
CO-F0.5	264	480	727.8	965.8	39
CO-F1	264	480	739.2	942.3	78
CO-F1.5	264	480	750.5	917.3	117
CO-F2	264	480	761.9	895.1	156

2.3. Test Specimen. The cubic specimens with side length of 150 mm were cast for the compressive strength (f_{cu}, f_{fcu}) and splitting tensile strength (f_{ts}, f_{fts}) test, the prism specimens of 100 mm × 100 mm × 300 mm were cast for shear strength (f_v, f_{fv}) test, the prism specimens of 100 mm × 100 mm × 400 mm were cast for flexural strength (f_{tm}, f_{ftm}) test, and three specimens were prepared for each group. To distinguish the concrete with and without steel fiber, f_{cu}, f_{ts}, f_v, and f_{tm} are used to represent the mechanical performance indexes of the plain concrete; f_{fcu}, f_{fts}, f_{fv}, and f_{ftm} are used to represent the mechanical performance indexes of SFRC.

A multifunction mixer was used to prepare the concrete. Mixing process of concrete included three steps: firstly, all aggregate and cement were put into a forced concrete mixer to mix for about 2 minutes; secondly, the water was added and mixed continuously for 2 minutes; finally, steel fiber was sprinkled evenly and then mixed for another 3 minutes. Fresh concrete was put rapidly into the moulds which were brushed oil in advance. Specimens were vibrated for 20 seconds. After 24 hours of curing in air, specimens were carefully demoulded and placed in a curing room at approximately 95% RH and 20°C.

2.4. Test Method. All the tests were conducted at the age of 28 days. The compressive strength and splitting tensile strength test were performed according to GB/T50081 [30] and were carried on a servohydraulic closed-loop testing machine with capacity of 3000 kN at the loading rate of 0.6 MPa/s and 0.06 MPa/s, respectively. Test setup of splitting tensile test is shown in Figure 1.

One steel bearing plate and one plywood bearing strip were placed between specimen and the top and bottom pressure plate, respectively. The section of bearing plate is part of circle radius of 75 mm; thickness is 20 mm. The section of bearing strip is 20 mm × 4 mm. The bearing plate and bearing strip should align with the center line of the top and bottom surface of specimen. The splitting tensile strength of the specimen was calculated as follows:

$$f_{fts} = 0.637\frac{F}{A}, \quad (1)$$

where f_{fts} is the splitting tensile strength, MPa; F is the maximum applied load indicated by the testing machine, N; A is the area of splitting surface, mm^2.

The shear test was also carried on a servohydraulic closed-loop testing machine with capacity of 3000 kN at the loading rate of 0.06 MPa/s; the test setup is shown in Figure 2.

The load was recorded with a load transducer. The ultimate shear strength was calculated as follows:

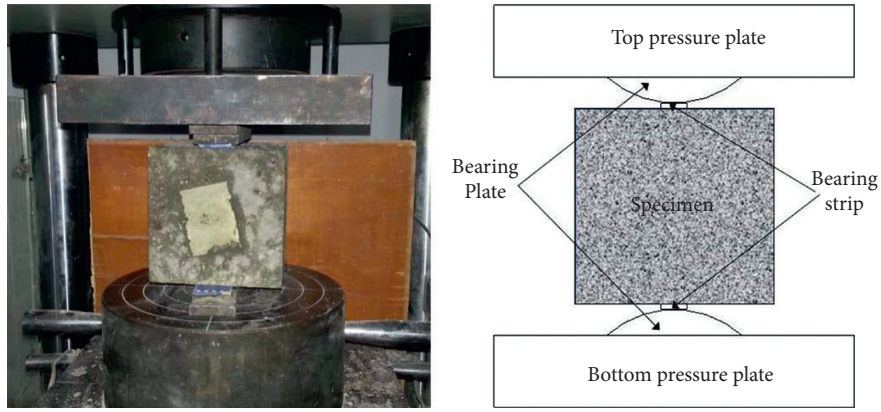

Figure 1: Test setup of splitting tensile strength.

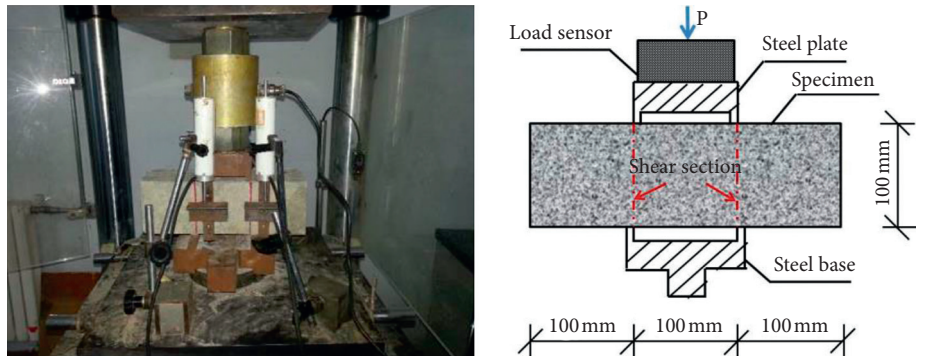

Figure 2: Test setup of shear strength.

$$f_{\mathrm{fv}} = \frac{F}{2b_{\mathrm{eff}}d_{\mathrm{eff}}}, \tag{2}$$

where f_{fv} is the ultimate shear strength; F is the maximum applied load indicated by the testing machine; b_{eff} is the effective width of the specimen (the average value of the width of the two shear sections), and d_{eff} is its effective depth (the average value of the depth of the two shear sections).

Flexural tests were carried on a MTS810 testing machine with capacity of 500 kN with displacement control at a rate of 0.1 mm/min, according to ASTM C1609 (using beam with third-point loading) [31]. The test setup is shown in Figure 3.

The specimens were normally rotated an angle of 90° from the casting position to eliminate the eccentricity effect from the roughness of the surface. Calculate the flexural strength of the specimen as follows:

$$f_{\mathrm{ftm}} = \frac{Fl}{bh^2}, \tag{3}$$

where f_{ftm} is flexural strength, MPa; F is the maximum applied load indicated by the testing machine, N; b and h are the average width and height of specimen, mm; l is the span length of test specimen, mm.

At least, three specimens in each group were tested and their mean values were taken as the test results. Test results of f_{fcu}, f_{fts}, f_{fv}, and f_{ftm} are listed in Table 5.

3. Test Results and Discussion

3.1. Compressive Strength. Relationship between compressive strength (f_{fcu}), compressive strength reinforced ratio ($f_{\mathrm{fcu}}/f_{\mathrm{cu}}$), and steel fiber volume fraction (V_{f}) with the different steel fiber shape are shown in Figure 4.

In general, f_{fcu} increased continuously as V_{f} increased from 0 to 2%. However, the increasing trend has slight difference with the different steel fiber shape. When $V_{\mathrm{f}} \leq 1\%$, the $f_{\mathrm{fcu}}/f_{\mathrm{cu}}$ of ST-F and HE-F was slightly bigger than that of CO-F. But, when V_{f} reached 2%, $f_{\mathrm{fcu}}/f_{\mathrm{cu}}$ of CO-F reached its maximum value 1.24, which was higher than $f_{\mathrm{fcu}}/f_{\mathrm{cu}}$ of ST-F and HE-F. It indicated that ST-F and HE-F had better strength reinforcement when V_{f} was below 1%, while CO-F had better strength reinforcement when V_{f} was above 1%. Although different steel fiber shape has reinforced effect on compressive strength of concrete, the increment is limited and the maximum value of $f_{\mathrm{fcu}}/f_{\mathrm{cu}}$ is 1.24.

The steel fiber can limit the lateral expansion and restrain the crack propagation of concrete under compressive load, which can delay the damage of concrete and enhance the compressive performance. The reinforced effect is decided by the bonding performance between steel fiber and concrete. The bonding force is affected by the surface shape of steel fiber. So, the different surface shape has the different effect on the compressive strength of concrete.

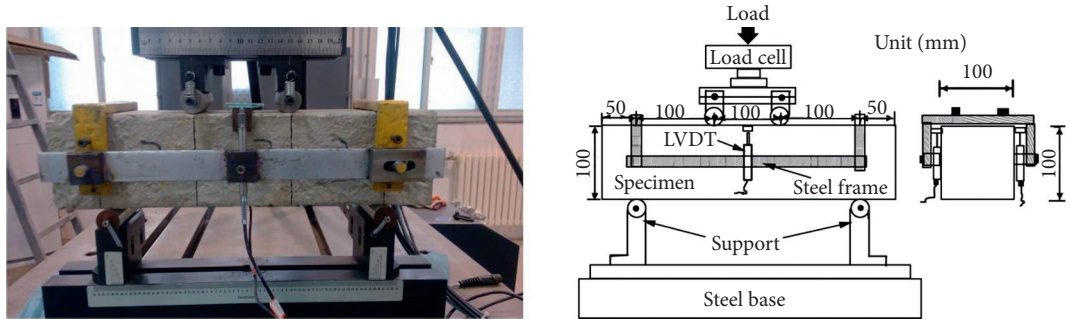

Figure 3: Test setup of flexural strength.

Table 5: Test results of mechanics strength (MPa).

Mixture number	f_{fcu}	f_{fts}	f_{fv}	f_{ftm}
PC	34.6	3.15	6.85	4.32
ST-F0.5	36	4.19	9.39	5.40
ST-F1	38.8	4.45	10.20	6.25
ST-F1.5	38.1	4.89	11.06	7.39
ST-F2	40.8	5.34	12.25	7.95
HE-F0.5	38.2	4.28	10.01	6.09
HE-F1	38.1	5.20	11.00	7.26
HE-F1.5	40.3	5.81	12.21	7.55
HE-F2	41.6	6.41	11.38	8.68
CO-F0.5	35	4.64	9.80	6.58
CO-F1	37.7	5.30	10.08	7.35
CO-F1.5	40.1	6.55	12.01	8.51
CO-F2	42.9	7.00	11.12	9.11

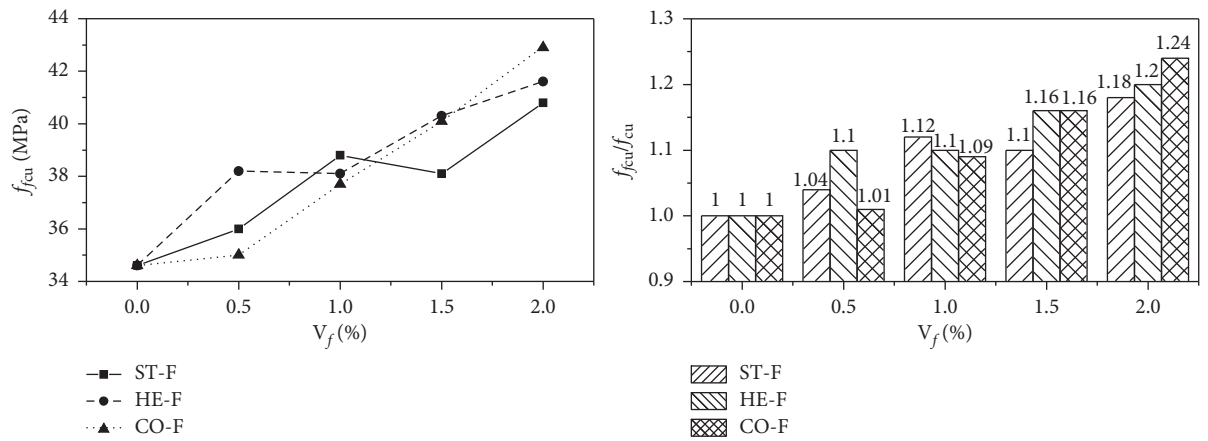

Figure 4: Relationship between f_{fcu}, f_{fcu}/f_{cu}, and V_f.

3.2. Tensile Strength. Relationship between splitting tensile strength (f_{fts}), splitting tensile strength reinforced ratio (f_{fts}/f_{ts}), and steel fiber volume fraction (V_f) with the different steel fiber shape is shown in Figure 5. f_{fts} increased continuously as V_f increased from 0 to 2%. When $V_f \leq 0.5\%$, ST-F and HE-F have a similar reinforced effect on concrete; CO-F has a slighter better reinforced effect than them. When $V_f \geq 0.5\%$, CO-F still has the best reinforced effect and HE-F takes the second place. When $V_f = 2\%$, f_{fts}/f_{ts} of CO-F is 2.22, f_{fts}/f_{ts} of HE-F is 2.03, and f_{fts}/f_{ts} of ST-F is only 1.7. As shown in 3, these three types of steel fibers have similar length and diameter; the only difference is the surface shape. With the same steel fiber content, the reinforced effect can be improved dramatically by changing the surface shape of steel fiber.

Test results proved that CO-F had the best reinforced effect on f_{fts}. This is because the surface of CO-F is the shape of corrugate and it can provide higher interface bonding force than ST-F and HE-F. Similarly, HE-F with the hooked form at both ends can provide better interface bonding force than ST-F with straight surface. ST-F has the smallest reinforced effect on f_{fts} because its surface is smooth and can not provide the mechanical occlusive force. It can be seen that because the surface shape of steel fiber has important

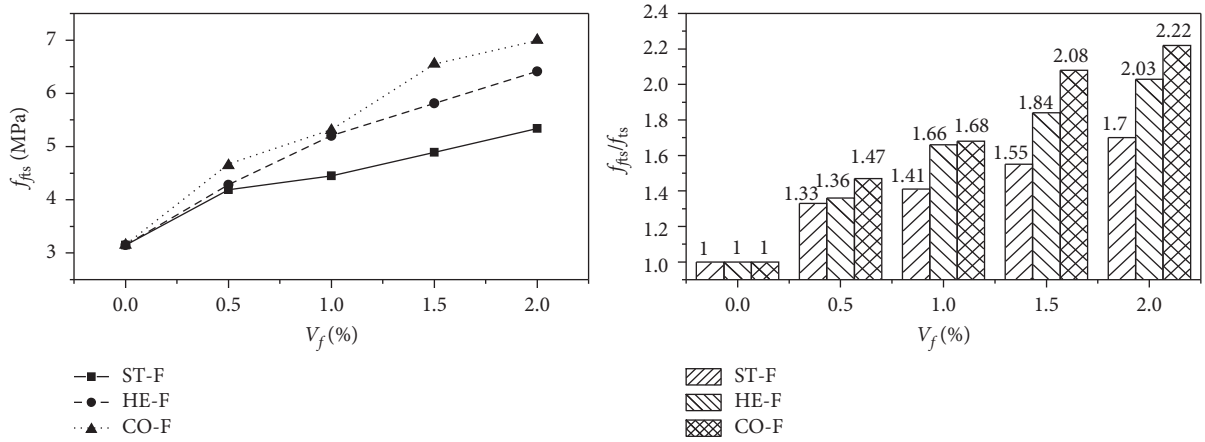

Figure 5: Relationship between f_{fts}, f_{fts}/f_{ts}, and V_f.

effect on the interface bonding force between concrete and steel fiber, the surface shape of steel fiber obviously affects the reinforced effect on the splitting tensile strength of concrete. In order to increase the reinforcement of steel fiber on concrete, the rough surface of steel fiber is the best choice.

3.3. Shear Strength. Relationship between shear strength (f_{fv}), shear strength reinforced ratio (f_{fv}/f_v), and steel fiber volume fraction (V_f) with the different steel fiber shape is shown in Figure 6. When V_f increases from 0 to 0.5%, f_{fv} increases rapidly. When $V_f = 0.5\%$, $f_{fv}/f_v = 1.37$ for ST-F, $f_{fv}/f_v = 1.46$ for HE-F, and $f_{fv}/f_v = 1.43$ for CO-F. Whatever the steel fiber shape is, f_{fv} increases about 40% when V_f increases from 0 to 0.5%. When V_f increases from 0.5 to 1.5%, f_{fv} still increases with the increase of V_f, but the growth ratio is slowing down. When V_f is more than 1.5%, f_{fv} of ST-F continuously increases while f_{fv} decreases with the increase of V_f for HE-F and CO-F.

This result indicates that too much steel fiber can cause shear strength reduction. The reason lies in two aspects. One is that the compressive strength of concrete matrix is not high; it leads steel fiber which is pulled out from concrete matrix before concrete failure because of the low bond force between concrete and steel fiber. And steel fiber cannot give full play when the steel fiber volume fraction is big. Some literature gave a similar result: to improve the shear strength, the first way consists in the increase of the compressive strength of the concrete; the second way is obtained with the addition of fiber [14]. The other reason is that higher V_f may more easily cause the uneven distribution of steel fiber; the uneven distribution of steel fiber leads to the lower bonding force between some steel fiber and concrete and also produces some weakened region. An optimum steel fiber content exists for a given concrete, beyond which the reinforcing effect of steel fiber on the shear strength becomes weakened with increase of steel fiber content. This result is slightly different to many previous literatures which proved that direct shear capacity of SFRC is clearly related to the amount of fiber [15].

3.4. Flexural Strength. Relationship between flexural strength (f_{ftm}), flexural strength reinforced ratio (f_{ftm}/f_{tm}), and steel fiber volume fraction (V_f) with the different steel fiber shape is shown in Figure 7.f_{ftm} increased continuously as V_f increased from 0 to 2%. Whatever the shapes of steel fiber are, the three trend lines are nearly straight upward; this indicates that f_{ftm} is all nearly a linear function of V_f. However, the slopes of three lines are different, the slope of CO-F is the biggest, and the slope of ST-F is the least. This means that when V_f is fixed, the enhancement effect is different with the different shape of steel fiber. CO-F is the best and HE-F takes the second place. It can be attributed to the bond strength of the matrix and steel fiber. The deformed shape provides better bond property than the straight fiber.

When V_f reaches its maximum value 2%, f_{ftm}/f_{tm} of CO-F is 2.11 and f_{ftm}/f_{tm} of HE-F is 2.01; this means that f_{ftm} of concrete in corrugated and hooked steel fiber doubles the value of plain concrete. f_{ftm}/f_{tm} of ST-F is the least, which is 1.84. This proved that steel fiber has excellent enhancement effect on flexural strength. Previous research suggested that the limited volume fraction of HE-F is 1.5% for the economical and efficient use of steel fiber on flexural performance [11]. However, test results of this paper indicated that flexural strength still increased with V_f, even if $V_f \geq 1.5\%$. This may be because the concrete matrix strength in this test is only about 40 MPa. The flexural failure is attributable mostly to pull-out rather than rupture of the steel fiber. The flexural strength of the SFRC increased with the increase of fiber content, which is closely related to the number of steel fibers that provide a bridging action. Then, steel fiber of deformed shape can play more important role than that with straight shape.

4. Strength Calculation Model

The above result analysis proved that steel fiber can improve f_{fcu}, f_{fts}, f_{fv}, and f_{ftm} of concrete obviously with the increasing of V_f. When V_f is fixed, the reinforcement ratio mainly is influenced by the interface bonding force between concrete and steel fiber. The interface bonding force mainly consists of three parts: chemical cementation force, frictional

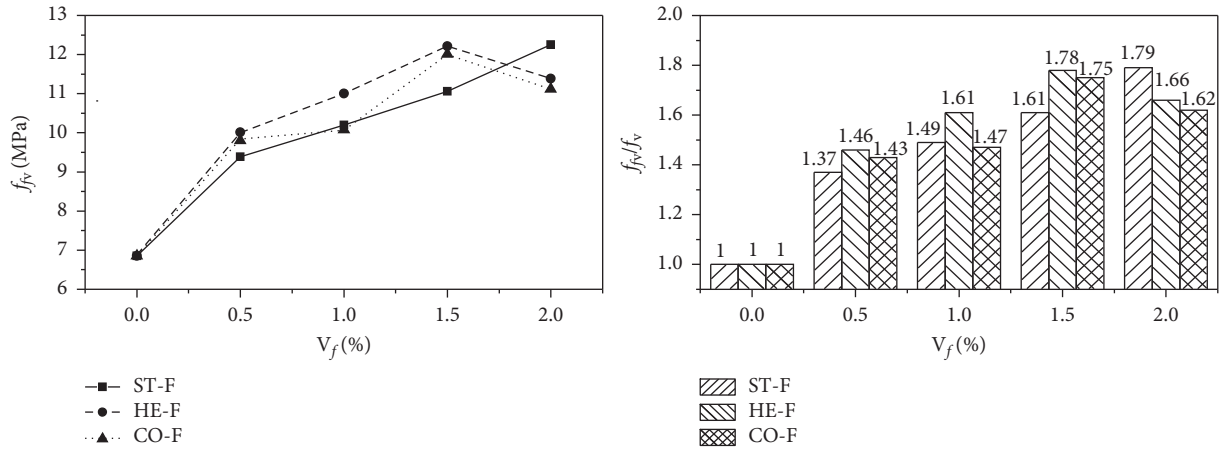

Figure 6: Relationship between f_{fv}, f_{fv}/f_v, and V_f.

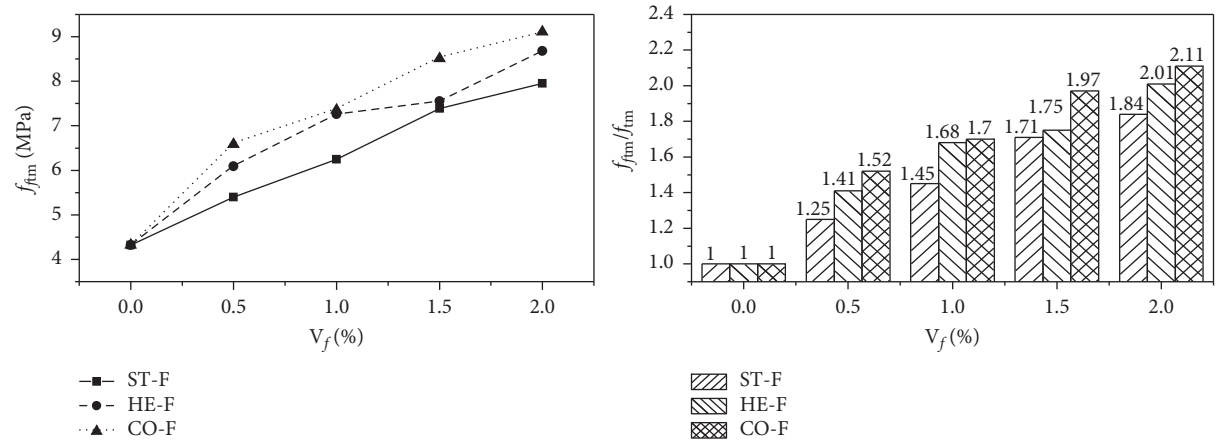

Figure 7: Relationship between f_{ftm}, f_{ftm}/f_{tm}, and V_f.

resistance, and mechanical interaction force. Chemical cementation force is mainly influenced by the strength of concrete matrix (f_{cu}). Frictional resistance is mainly affected by surface area and roughness. Mechanical occlusal force is mainly affected by the surface dents of steel fiber. Thus, the important enhancement factors of ffcu, f_{fts}, f_{fv}, and f_{ftm} are concrete matrices (f_{cu}), aspect ratio (l_f/d_f), content (V_f), and shape and surface dents of steel fiber.

4.1. Effect of Steel Fiber. Based on the above analysis, reinforcement ratio of f_{fcu} is influenced by content, aspect ratio, and shape of steel fiber; it can be expressed as follows:

$$\frac{f_{fcu}}{f_{cu}} = 1 + \alpha_f \lambda_f, \tag{4}$$

where f_{fcu} is the compressive strength of SFRC; f_{cu} is the compressive strength of plain concrete; α_f is the influence coefficient of steel fiber shape, which is related to the geometric and surface shape of steel fiber; λ_f is the characteristic coefficient of steel fiber, $\lambda_f = V_f\, l_f/d_f$.

α_f of these three shapes steel fiber can be obtained through the regression analysis of experiment data in this paper and relative research literature [13, 16, 32–35] based on (4). The relationship between f_{fcu}/f_{cu} and λ_f is shown in Figure 8.

As shown in Figure 8, although the length and aspect ratio of steel fiber from different literature are different, the reinforcement ratio of f_{fcu} had a linear relationship with λ_f when the surface shape of steel fiber is the same. Value of α_f can be obtained through regression analysis: $\alpha_f = 0.21$ for ST-F; $\alpha_f = 0.27$ for HE-F; $\alpha_f = 0.4$ for CO-F. α_f of CO-F is the biggest; this is because corrugated surface not only can increase the surface roughness, but also can provide mechanical interaction force. α_f of HE-F is in the second place; hooks at the end of steel fiber can increase part of the frictional resistance. Adding surface roughness or uneven of steel fiber can improve its enhancement effect obviously under the condition of keeping content of steel fiber.

4.2. Effect of Concrete Matrix. Concrete matrix also plays an important role in bonding strength, so it significantly affects

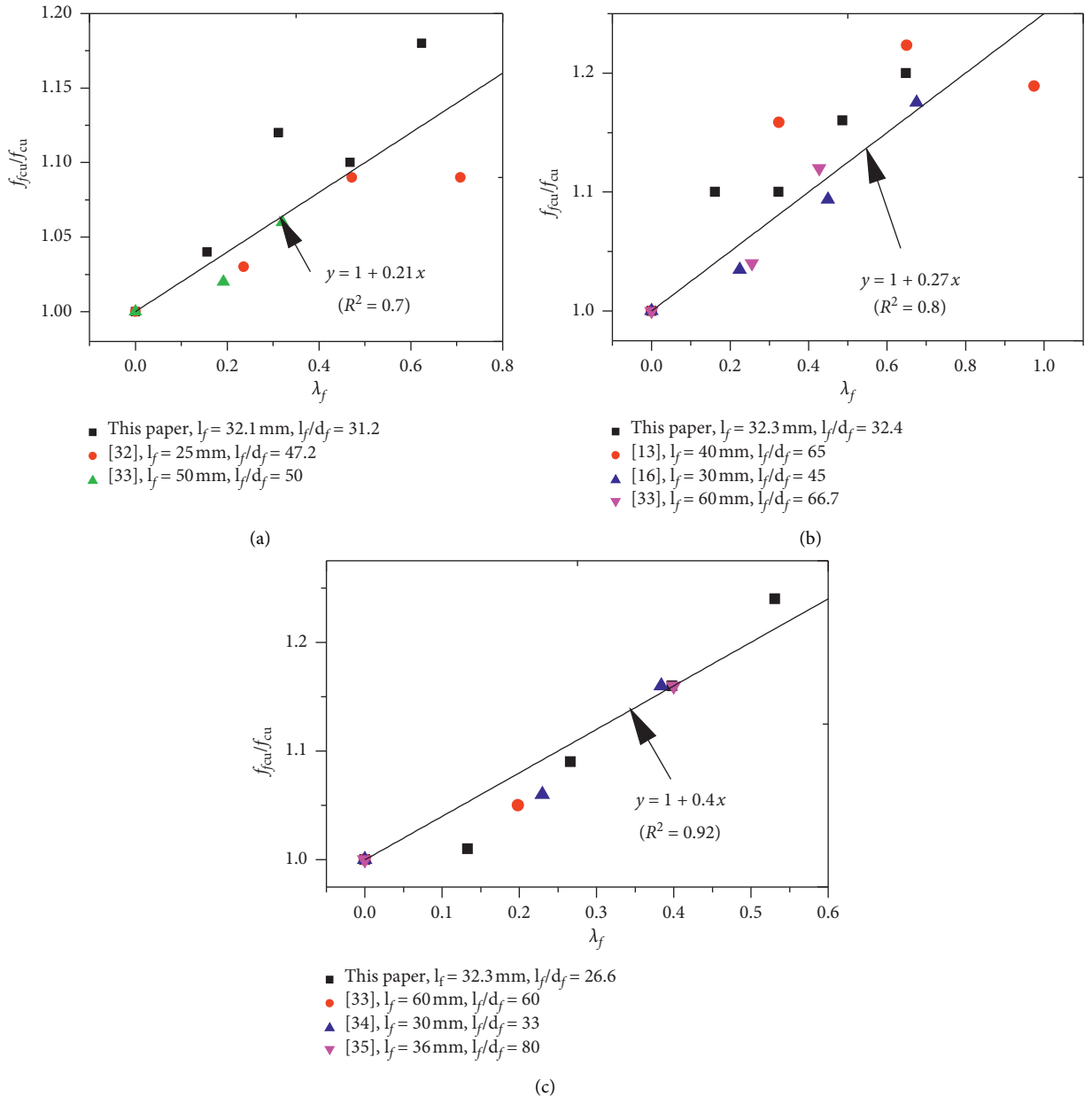

Figure 8: Relationship between f_{fcu}/f_{cu} and λ_f (a) ST-F, (b) HE-F, and (c) CO-F.

the reinforcement ratio of f_{fts}, f_{fv}, and f_{ftm}. The reinforcement ratio of f_{fts}, f_{fv}, and f_{ftm} can be expressed as follows:

$$R_f = 1 + \alpha_f \alpha_c \lambda_f, \tag{5}$$

where R_f is strength reinforced ratio of SFRC; it can represent f_{fts}/f_{ts}, f_{fv}/f_v, or f_{ftm}/f_{tm}; α_c is the influence coefficient of concrete matrix, which is related to compressive strength of concrete matrix.

α_c can be obtained through the regression analysis of experiment data in this paper and previous literature [13, 16, 21, 32–36] based on equation (5). According to equation (4), α_f is known: $\alpha_f = 0.21$ for ST-F; $\alpha_f = 0.27$ for HE-F; $\alpha_f = 0.4$ for CO-F. The relationship between R_f and $\alpha_f\lambda_f$ is shown in Figure 9.

As shown in Figure 9, although the length and aspect ratio of steel fiber from different literature are different and R_f represents different strength reinforcement rates, such as f_{fts}/f_{ts}, f_{fv}/f_v, or f_{ftm}/f_{tm}, R_f showed a linear relationship with $\alpha_f\lambda_f$. This indicates that the reinforced effect of concrete matrix on the strength of SFRC is linear when eliminating the effect of steel fiber. As shown in Figure 9, the value of α_c can be obtained through linear regression with the experiment data, $\alpha_c = 4.86$ and $R^2 = 0.87$. This shows that the correlation between R_f and $\alpha_f\lambda_f$ is fairly good. Since the compressive strength of plain concrete in this test is fixed ($f_{cu} = 34.6$ MPa), the value of α_c could change with the changing of f_{cu}. The relationship between f_{cu} and α_c should be studied further for high strength concrete.

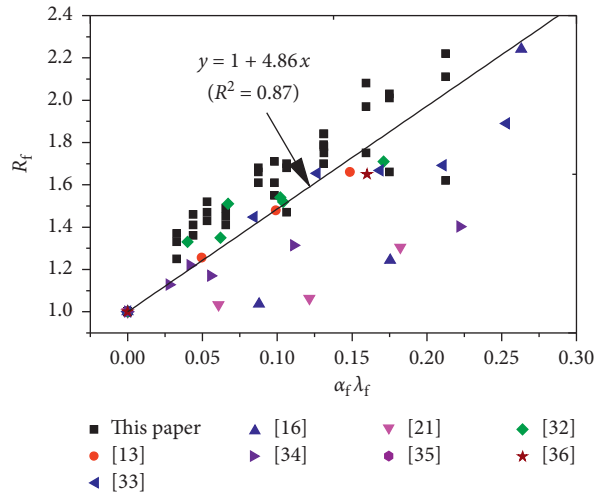

Figure 9: Relationship between R_f and $\alpha_f\lambda_f$.

Table 6: Calculated results and the comparison between calculated results and test results of mechanics strength.

Mixture number	f_{fcu}		f_{fts}		f_{fv}		f_{ftm}	
	Cal (MPa)	C/T	Cal (MPa)	C/T	Cal (MPa)	C/T	Cal (MPa)	C/T
PC	34.6	1	3.15	1.00	6.85	1	4.32	1.00
ST-F0.5	35.7	0.99	3.65	0.87	7.94	0.85	5.01	0.93
ST-F1	36.9	0.95	4.15	0.93	9.03	0.89	5.70	0.91
ST-F1.5	38.0	1.00	4.66	0.95	10.12	0.92	6.38	0.86
ST-F2	39.1	0.96	5.16	0.97	11.21	0.92	7.07	0.89
HE-F0.5	36.1	0.95	3.82	0.89	8.32	0.83	5.24	0.86
HE-F1	37.6	0.99	4.49	0.86	9.76	0.89	6.16	0.85
HE-F1.5	39.1	0.97	5.16	0.89	11.22	0.92	7.08	0.94
HE-F2	40.7	0.98	5.83	0.91	12.68	1.11	7.99	0.92
CO-F0.5	36.4	1.04	3.96	0.85	8.62	0.88	5.44	0.83
CO-F1	38.3	1.02	4.78	0.90	10.39	1.03	6.55	0.89
CO-F1.5	40.1	1.00	5.59	0.85	12.16	1.01	7.67	0.90
CO-F2	42.0	0.98	6.40	0.91	13.92	1.25	8.78	0.96

Note that Cal stands for the calculated result and C/T stands for the ratio of the calculated result with test result.

4.3. Formula Validation. Above is the main analysis of the enhancement effect of steel fiber. In order to verify the correctness of the equations (4) and (5) and regression coefficient of α_f and α_c, the strength calculation method of f_{fcu}, f_{fts}, f_{fv}, and f_{ftm} can be put forward based on equations (4) and (5):

$$f_{fcu} = f_{cu} \times (1 + \alpha_f\lambda_f), \tag{6}$$

$$f_{fts} = f_{ts} \times (1 + \alpha_f\alpha_c\lambda_f), \tag{7}$$

$$f_{fv} = f_{v} \times (1 + \alpha_f\alpha_c\lambda_f), \tag{8}$$

$$f_{ftm} = f_{tm} \times (1 + \alpha_f\alpha_c\lambda_f), \tag{9}$$

where $\alpha_f = 0.21$ for ST-F; $\alpha_f = 0.27$ for HE-F; $\alpha_f = 0.4$ for CO-F; $\alpha_c = 4.86$; $\lambda_f = V_f l_f/d_f$. Putting the test data of f_{cu} in (6), f_{ts} in (7), f_v in (8), and f_{tm} in (9), the calculated value of f_{fcu}, f_{fts}, f_{fv}, and f_{ftm} and the ratio of calculated value to test value are put into Table 6.

The ratio of calculated value to test value of f_{fcu} varies from 0.95 to 1.04; this indicates that calculated value of f_{fcu} coincides with test value quite well. The ratio of calculated value to test value of f_{fts} and f_{ftm} varies from 0.85 to 1. Although the calculated value is slightly less than test value, the calculated value is still close to the test value. Except CO-F2, the ratio of calculated value to test value of f_{fv} varies from 0.83 to 1.11; the calculated value is also close to the test value. According to the previous analysis, when V_f is larger than 1.5%, the enhancement effect of steel fiber becomes weak, but in the calculation of equation (8) this can not reflect this character, so when V_f is 2%, the calculated value is larger than the test value. Further research should be taken for SFRC with steel fiber volume fraction that is above 2%.

5. Conclusions

The general objective of this research project was to evaluate the effect of steel fiber shape and content on the mechanical property of SFRC and the calculation method of reinforced effect of steel fiber with different shape and content on compressive strength, splitting strength, shear strength, and flexural strength. The main conclusions are as follows:

(1) Expecting that shear strength gets its maximum value at steel fiber volume ratio which is 1.5%, compressive strength, splitting strength, and flexural strength all express linear increase trend with the increasing of steel fiber volume ratio from 0 to 2%.

(2)When the steel fiber content is fixed, CO-F has the best reinforced effect on compressive strength, splitting strength, shear strength, and flexural strength of SFRC; HE-F takes the second place and ST-F is the least.

(3) In order to increase the reinforcement of steel fiber on concrete, the steel fiber has rough surface which is the best choice. At least, interface bonding force should be increased as far as possible.

(4) Two influence factors α_f and α_c were put forward and their value was obtained by regression analysis of experiment data. The proposed calculated formulas for compressive strength, splitting tensile strength, shear strength, and flexural strength of SFRC have good agreement with the experimental results.

(5) When steel fiber volume fraction is larger than 2%, the reinforced effect of steel fiber on shear strength needs to be studied further. Relationship between f_{cu} and α_c should also be researched further for high strength concrete ($f_{cu} \geq 60$ MPa).

Data Availability

The experimental data used to support the findings of this study are included within the article.

Conflicts of Interest

The authors declare that there are no conflicts of interest regarding the publication of this paper.

Acknowledgments

This research was supported by China National Natural Science Foundation Youth Fund Project (51808509), Innovation Team Development Plan of China's Ministry of Education (IRT_16R67), Key Scientific Research Projects of Colleges and Universities of Henan Provincial Department of Education (19A560005) and Thousand Talents Plan in Henan Province (ZYQR201912029).

References

[1] P. Zhang, S. Fu, K. Zhang, and T. Zhang, "Mechanical properties of polyvinyl alcohol fiber-reinforced concrete composite containing fly ash and nano-SiO_2," *Science of Advanced Materials*, vol. 10, no. 6, pp. 769–778, 2018.

[2] D. Niu, L. Jiang, M. Bai, and Y. Miao, "Study of the performance of steel fiber reinforced concrete to water and salt freezing condition," *Materials & Design*, vol. 44, pp. 267–273, 2013.

[3] P. Zhang, Q.-F. Li, J. Wang, Y. Shi, and Y.-F. Ling, "Effect of PVA fiber on durability of cementitious composite containing nano-SiO_2," *Nanotechnology Reviews*, vol. 8, no. 1, pp. 116–127, 2019.

[4] F. Bencardino, L. Rizzuti, G. Spadea, and R. N. Swamy, "Stress-strain behavior of steel fiber-reinforced concrete in compression," *Journal of Materials in Civil Engineering*, vol. 20, no. 3, pp. 255–263, 2008.

[5] L. Carabba, M. Santandrea, C. Carloni, S. Manzi, and M. C. Bignozzi, "Steel fiber reinforced geopolymer matrix (S-FRGM) composites applied to reinforced concrete structures for strengthening applications: a preliminary study," *Composites Part B: Engineering*, vol. 128, pp. 83–90, 2017.

[6] M. T. Kazemi, H. Golsorkhtabar, M. H. A. Beygi, and M. Gholamitabar, "Fracture properties of steel fiber reinforced high strength concrete using work of fracture and size effect methods," *Construction and Building Materials*, vol. 142, pp. 482–489, 2017.

[7] S. Tayfur, N. Alver, S. Abdi, S. Saatcı, and A. Ghiami, "Characterization of concrete matrix/steel fiber de-bonding in an SFRC beam: principal component analysis and *k*-mean algorithm for clustering AE data," *Engineering Fracture Mechanics*, vol. 194, pp. 73–85, 2018.

[8] P. Zhang, Q. F. Li, Y. Z. Chen, Y. Shi, and Y. F. Ling, "Durability of steel fiber-reinforced concrete containing SiO_2 nano-particles," *Materials*, vol. 12, no. 13, pp. 1–18, 2019.

[9] H. Wu, G. M. Ren, Q. Fang, and J. Z. Liu, "Effects of steel fiber content and type on dynamic tensile mechanical properties of UHPCC," *Construction and Building Materials*, vol. 173, pp. 251–261, 2018.

[10] A. Khabaz, "Analysis of sliding mechanism of straight steel fibers in concrete and determine the effect of friction," *Archives of Civil and Mechanical Engineering*, vol. 17, no. 3, pp. 599–608, 2017.

[11] A. Khabaz, "Monitoring of impact of hooked ends on mechanical behavior of steel fiber in concrete," *Construction and Building Materials*, vol. 113, pp. 857–863, 2016.

[12] G. M. Ren, H. Wu, Q. Fang, and J. Z. Liu, "Effects of steel fiber content and type on static mechanical properties of UHPCC," *Construction and Building Materials*, vol. 163, pp. 826–839, 2018.

[13] W. Abbass, M. I. Khan, and S. Mourad, "Evaluation of mechanical properties of steel fiber reinforced concrete with different strengths of concrete," *Construction and Building Materials*, vol. 168, pp. 556–569, 2018.

[14] S.-J. Jang and H.-D. Yun, "Combined effects of steel fiber and coarse aggregate size on the compressive and flexural toughness of high-strength concrete," *Composite Structures*, vol. 185, pp. 203–211, 2018.

[15] E. Güneyisi, M. Gesoğlu, A. O. M. Akoi, and K. Mermerdaş, "Combined effect of steel fiber and metakaolin incorporation on mechanical properties of concrete," *Composites Part B: Engineering*, vol. 56, pp. 83–91, 2014.

[16] Ş. Yazıcı, G. İnan, and V. Tabak, "Effect of aspect ratio and volume fraction of steel fiber on the mechanical properties of SFRC," *Construction and Building Materials*, vol. 21, no. 6, pp. 1250–1253, 2007.

[17] B. Boulekbache, M. Hamrat, M. Chemrouk, and S. Amziane, "Influence of yield stress and compressive strength on direct shear behaviour of steel fibre-reinforced concrete," *Construction and Building Materials*, vol. 27, no. 1, pp. 6–14, 2012.

[18] T. Soetens and S. Matthys, "Shear-stress transfer across a crack in steel fibre-reinforced concrete," *Cement and Concrete Composites*, vol. 82, pp. 1–13, 2017.

[19] A. Khabaz, "Performance evaluation of corrugated steel fiber in cementitious matrix," *Construction and Building Materials*, vol. 128, pp. 373–383, 2016.

[20] D.-Y. Yoo and Y.-S. Yoon, "Structural performance of ultra-high-performance concrete beams with different steel fibers," *Engineering Structures*, vol. 102, pp. 409–423, 2015.
[21] S.-C. Lee, J.-H. Oh, and J.-Y. Cho, "Compressive behavior of fiber-reinforced concrete with end-hooked steel fibers," *Materials*, vol. 8, no. 4, pp. 1442–1458, 2015.
[22] D.-Y. Yoo, S.-T. Kang, and Y.-S. Yoon, "Effect of fiber length and placement method on flexural behavior, tension-softening curve, and fiber distribution characteristics of UHPFRC," *Construction and Building Materials*, vol. 64, pp. 67–81, 2014.
[23] K. Wille, D. J. Kim, and A. E. Naaman, "Strain-hardening UHP-FRC with low fiber contents," *Materials and Structures*, vol. 44, no. 3, pp. 583–598, 2011.
[24] Z. Wu, K. H. Khayat, and C. Shi, "How do fiber shape and matrix composition affect fiber pullout behavior and flexural properties of UHPC?" *Cement and Concrete Composites*, vol. 90, pp. 193–201, 2018.
[25] P. Zhang, Y. Ling, J. Wang, and Y. Shi, "Bending resistance of PVA fiber reinforced cementitious composites containing nano-SiO_2," *Nanotechnology Reviews*, vol. 8, no. 1, pp. 690–698, 2019.
[26] S. A. C. Aqsiq, *Common Portland Cement*, GB/175-2007, Beijing, China, 2007.
[27] S. A. C. Aqsiq, *Pebble and Crushed Stone for Construction*, GB/T 14685, Beijing, China, 2011.
[28] Mohurd, *Specification for Mix Proportion Design of Ordinary Concrete*, JGJ 55-2011, China Architecture & Building Press, Beijing, China, 2011.
[29] Mohurd, *Steel Fiber Reinfroced Concrete*, JG/T 472-2015, Beijing, China, 2015.
[30] Aqsiq, *Standard for Test Method of Mechanical Properties on Ordinary Concrete*, GB/T50081, Beijing, China, 2002.
[31] ASTM, *Standard Test Method for Flexural Performance of Fiber-Reinforced Concrete (Using Beam With Third-Point Loading)*, C1609, Beijing, China, 2012.
[32] G. Appa Rao and A. Sreenivasa Rao, "Toughness indices of steel fiber reinforced concrete under mode II loading," *Materials and Structures*, vol. 42, no. 9, pp. 1173–1184, 2009.
[33] M. N. Soutsos, T. T. Le, and A. P. Lampropoulos, "Flexural performance of fibre reinforced concrete made with steel and synthetic fibres," *Construction and Building Materials*, vol. 36, pp. 704–710, 2012.
[34] Y. Zhang, Z. Li, X. Liu et al., "Experiment on tension-compression ratio of steel fiber reinforced concrete," *Journal of Jiangsu University (Natural Science Edition)*, vol. 38, no. 6, pp. 719–723, 2017.
[35] R. Perumal, "Correlation of compressive strength and other engineering properties of high-performance steel fiber-–reinforced concrete," *Journal of Materials in Civil Engineering*, vol. 271 pages, 2015.
[36] F. Hasan-Nattaj and M. Nematzadeh, "The effect of forta-ferro and steel fibers on mechanical properties of high-strength concrete with and without silica fume and nano-silica," *Construction and Building Materials*, vol. 137, pp. 557–572, 2017.

Hindawi
Advances in Civil Engineering
Volume 2020, Article ID 8879746, 17 pages
https://doi.org/10.1155/2020/8879746

Research Article

Experimental Study on Fatigue Performance of Negative Bending Moment of Steel-Concrete Continuous Composite Box Girder

Pu Gao,[1] Kuan Li,[2] and Yuanxun Zheng[2]

[1]*Technology Center, China Construction Sixth Engineering Division Corp. Ltd., Tianjin 300451, China*
[2]*School of Water Conservancy Science and Engineering, Zhengzhou University, Zhengzhou, Henan 450001, China*

Correspondence should be addressed to Yuanxun Zheng; yxzheng@zzu.edu.cn

Received 3 May 2020; Revised 30 May 2020; Accepted 15 June 2020; Published 9 July 2020

Academic Editor: Grzegorz Golewski

The experimental work presents results on the fatigue performance of composite beams in the negative moment region and the changes of stiffness and deformation of composite beams under repeated loads; fatigue tests were carried out on two double-layer composite beams. The fatigue performance of composite beams with different reinforcement ratios under complete shear connection and the variation of deflection, strain of the reinforcement, strain of steel beam, and crack growth under fatigue load were obtained. The results showed that the fatigue resistance performance of concrete slab with low reinforcement ratio was much lower than that of concrete slab with high reinforcement ratio whereas, under the fatigue load, the stress of the welding nail in the negative moment region was small and the slip was almost negligible. The degradation of stiffness and the development of cracks were mainly due to the degradation of bond-slip between the concrete and reinforcement. The fatigue failure mode was the fracture of the upper reinforcement in negative moment region. The results obtained in this study are helpful in the design of composite beam.

1. Introduction

Steel-concrete composite beam is a kind of flexural structure which connects steel beam and concrete slab as a whole. It can make full use of the material properties of steel and concrete and has significant advantages as small structural height, light weight, high bearing capacity, large stiffness, and good comprehensive benefits [1–3]. However, in the process of use, the negative bending moment exists at the fulcrum in the continuous composite beam bridge, when concrete slab is under tension, steel beam bottom plate and web are under compression, the performance of the two materials is not effectively achieved, and concrete slab in most cases is unfavorable under tensile condition [4–6]. Concrete with low tensile strength will crack when the load is very small. After cracking, the section stiffness of negative moment region decreases, and the concrete slab and steel beam have a relative slip, which leads to the redistribution of the internal force of the structure and affects the mechanical performance of the whole composite beam. The mechanical properties of the negative moment region of the concrete slab after cracking are complicated and must be studied through experiments.

The control area of the continuous composite beam is the negative moment region. The crack of concrete in negative bending area, the stress of reinforcement in concrete slab, and the buckling and fatigue of steel beam are the research emphases of continuous composite beam. In recent years, researchers have done considerable experiments on the static properties of steel-concrete composite beams. Barnard and Johnson [7] and Mallick and Chattopadhyay [8] showed that as long as secondary failure could be avoided, it was feasible to design most continuous composite beams according to the simplified plastic method. Hamada and Longworth [9] conducted tests on three continuous composite beams with two equal spans; their study showed that the failure mode was based on the crushing of concrete in the positive moment region or the local buckling of steel beam flange in the negative moment region, the ultimate load of continuous composite beams could be accurately calculated,

and the amount of longitudinal reinforcement was the main factor influencing the failure mode in the negative moment region. Johnson et al. [10, 11] conducted tests on three-span continuous composite beams; their results indicated that the design of continuous composite beams is often controlled by the yield and cracking of materials under the service load. Johnson and May [12, 13] studied the vertical shear capacity of continuous composite beams through experiments, respectively, including the shear distribution of concrete slabs and steel beams. The results showed that the concrete slab can withstand about 20% of the total shear capacity in ordinary continuous composite beams and can even withstand 50% of the total shear capacity in slim sections. Johnson [14] conducted experimental studies on the shear strength and flexural stiffness of continuous composite beams, believing that the shear stiffness of sections is proportional to the number of shear joints, and shear connectivity is an important parameter in the design of continuous composite beams. Grant et al. [15] made a theoretical and experimental study on the influence of shear connection on the mechanical properties of continuous composite beams and concluded that the reduction of shear connection could greatly affect the bearing capacity of beams. Gautam [16] considered that shear nails, as a component of steel-concrete composite structure, play an important role in the performance of composite structure. Therefore, the influence of group columns on simply supported continuous box girder was studied, and the experimental results displayed that the higher the shear connectivity, the smaller the maximum slip value.

In recent years, the fatigue performances of steel-concrete composite beams have also been studied experimentally. Liao [17] obtained that the fatigue life of the welding nails was mainly controlled by the stress amplitude and not affected by the maximum stress. The strength of concrete has little influence on the fatigue life of welding nails. Fatigue load test of composite beams was carried out by Yen et al. [18]; and the test results revealed that it was recommended to use complete shear connection to avoid excessive deformation of composite beams under fatigue load. The type of reinforcement had significant effect on the fatigue performance of the beam. The composite beams with fine steel hinge lines displayed better fatigue resistance than the composite beams with reinforcement. Considering the particularity of composite beams connected by partial shear force, the corresponding experimental studies were conducted by Geattesco et al. [19]; and the test results showed that the European code 3 tended to be conservative when evaluating the fatigue life of internal bolts of composite beams, and the fatigue performance of internal bolts of beams was better than that of internal bolts of specimens under the same conditions. Youn et al. [20] conducted static loading and fatigue loading tests on the 1 : 5 composite bridge model, and the test results showed that when the load was applied to the middle of the bridge panel, the static strength and fatigue strength of the bolt were higher than those when the load was applied near the support. Johnson [21] summarized many representative research results and the latest provisions of several internationally popular codes, adopted the European code model, and suggested that the fatigue life of composite beams should be calculated as follows:$\log NK + 5.5\log\Delta\tau = 16.4$.

In the review of both domestic and foreign literature, most studies mainly focused on the stiffness degradation caused by the sliding of welding nails under repeated loads and the fatigue failure of welding nails [22, 23] but there were few studies on the crack development of concrete bridge slab after cracking and the failure pattern of bridge slab caused by reinforcement fracture. The mechanism of stiffness degradation and fatigue failure of composite beams connected by complete shear force under repeated loads was rarely studied. In this paper, through the design of two reverse-loading simply supported composite beams, the mechanical behavior of the negative moment region of double-layer composite beams with different reinforcement ratios under monotone and repeated loads was studied. The crack development of concrete slab in negative moment region, the change of sectional stress of composite beam, the change of midspan deflection of composite beam, and the fatigue failure pattern were observed, and the results provided a reference for the design of composite beam.

2. Experimental Model Design

2.1. Experimental Beam Design. In order to make the test model truly reflect the stress characteristics of the actual composite beam bridge, this study simplified the scale of a continuous composite beam bridge and designed the test beam model in accordance with the principle that the relative height of the neutral axis remained unchanged, the structural stiffness was equivalent, and the shear connection degree was the same. The design parameters and loading mode of the test beam are shown in Table 1. The total length of the composite beam was 5.5 m, the distance between two supports was 4.9 m, the beam height was 0.55 m, and the beam width was 1.4 m. The transverse and longitudinal sections of the test beam are shown in Figures 1 and 2.

2.2. Design of Welding Nail Connector. In order to effectively combine concrete and steel, a certain number of welding nail connectors were arranged on the floor of the steel beam to strengthen the connection between steel and concrete, as shown in Figure 3. The floor concrete was 95 mm thick, the top layer was covered with reinforcing mesh, the longitudinal steel bar had a diameter of 8 mm and a spacing of 70 mm, and the transverse steel bar had a diameter of 6 mm and a spacing of 90 mm. The concrete structure of base plate is shown in Figure 4. The welding nail connectors were arranged in a continuous manner, as shown in Figure 5.

2.3. Design of Bridge Deck. The PLG-1 and PLG-2 test beams used ordinary reinforced concrete bridge decks. In order to study the influence of different reinforcement ratio on the mechanical properties of composite beams, concrete slabs with the reinforcement ratio of 0.86% and 1.72% were used, respectively. The reinforcement structure is shown in Figure 6.

Table 1: Parameters of composite beam specimens.

Specimen no.	Section form	Layout of upper flange welding nails	Number of upper flange welding nails	Reinforcement ratio of concrete slab (%)	Measured compressive strength of concrete (MPa)	Loading method
PLG-1	Double-layer concrete	Continuous arrangement	176	1.76	59.05	Repeated loading
PLG-2	Double-layer concrete	Continuous arrangement	176	0.88	60.18	Repeated loading

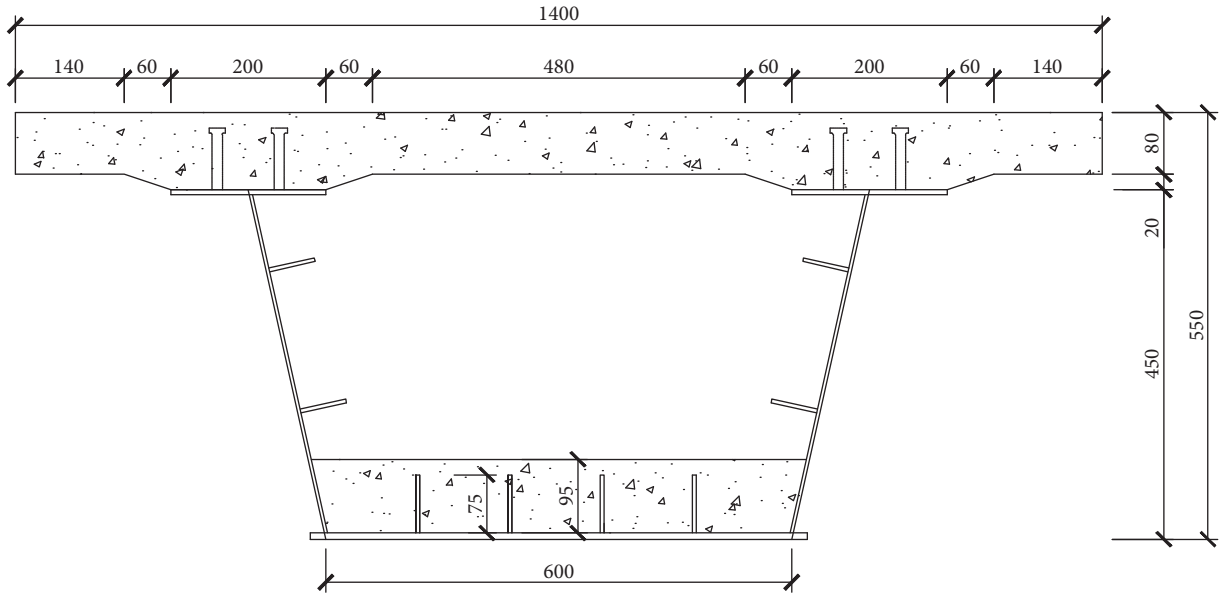

Figure 1: Cross section of test beam (unit: mm).

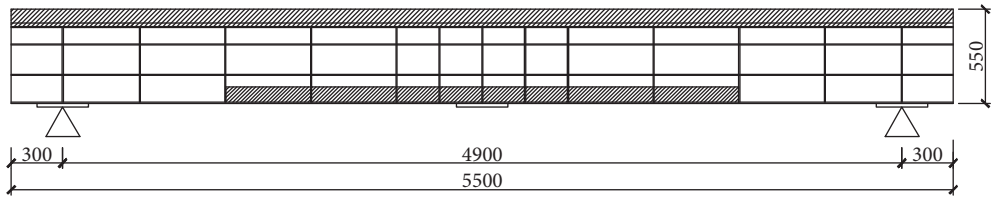

Figure 2: Longitudinal section of test beam (unit: mm).

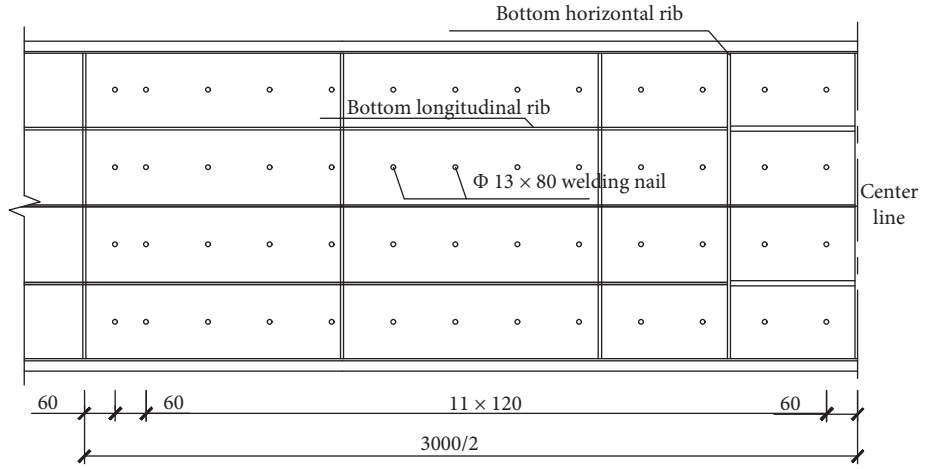

Figure 3: Layout of welding nails on the bottom plate (unit: mm).

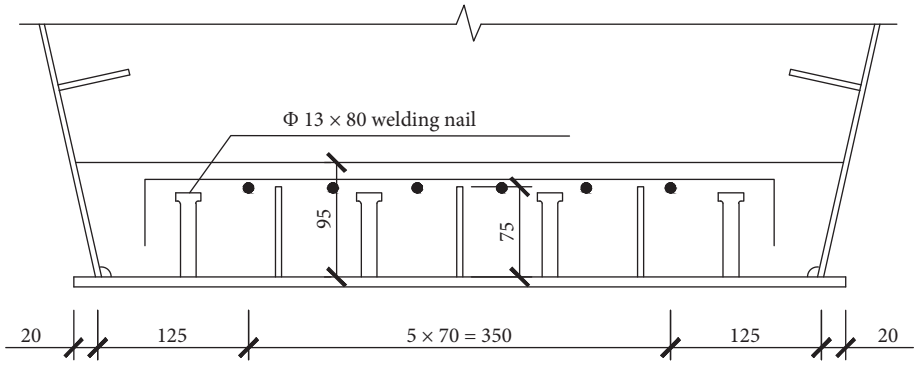

Figure 4: Concrete structure of base plate (unit: mm).

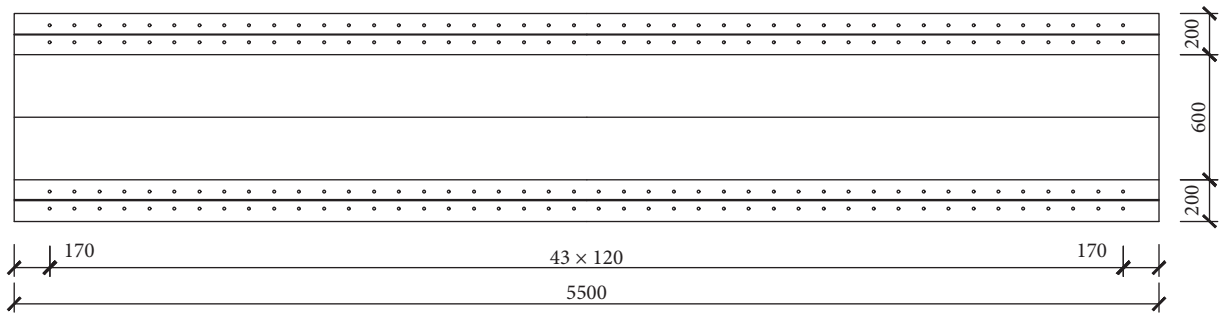

Figure 5: Layout of welding nails on the upper flange (unit: mm).

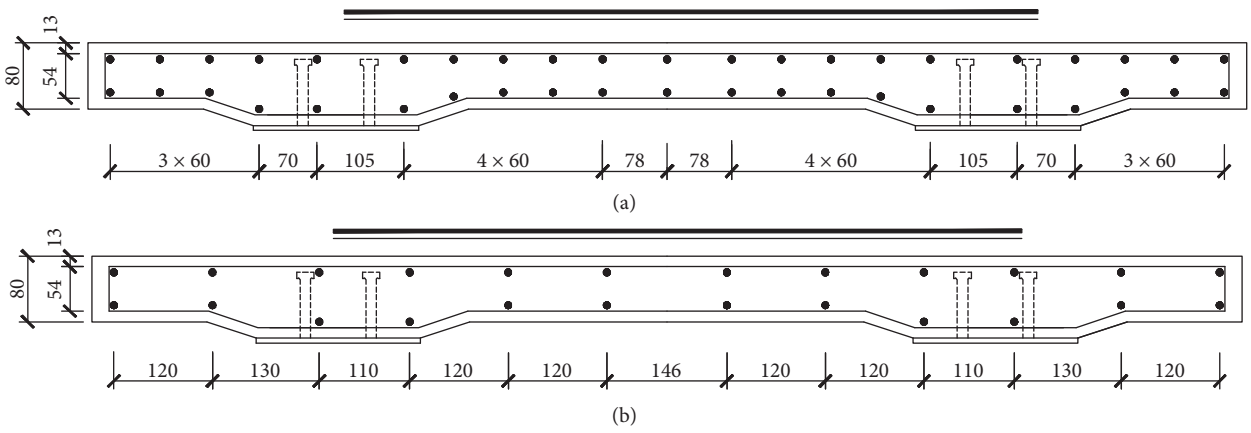

Figure 6: Structure of ordinary reinforcement in concrete slabs (unit: mm). (a) PLG-1: reinforcement ratio 1.72%. (b) PLG-2: reinforcement ratio 0.86%.

2.4. Basic Mechanical Properties of Concrete. The concrete was all commercial concrete, according to the test method in *GB/T 50081-2002 Standard for Testing Methods of Mechanical Properties of Ordinary Concrete*; the compressive strength, tensile strength, and elastic modulus of concrete cubes with ages of 7 days and 28 days were tested. The specimen size used in the compressive strength and tensile strength tests was 150 mm × 150 mm × 150 mm, and the size of the specimen used in the elastic modulus test was 150 mm × 150 mm × 300 mm. The basic mechanical properties of concrete at 7 days and 28 days are shown in Table 2.

2.5. Experimental Scheme Design

2.5.1. Loading System. This test was performed in the laboratory of the Institute of Structural Engineering and Disaster Prevention of Tongji University. The loading

Table 2: Basic mechanical properties of concrete at 7 days and 28 days.

Age/day	Test type	Specimen number	Measured value (MPa)	Use value (MPa)
7	Compressive strength	1	46.23	46.93
		2	49.38	
		3	45.19	
	Tensile strength	1	2.76	3.08
		2	3.01	
		3	3.47	
	Elastic modulus	1	32800	35300
		2	38900	
		3	34100	
28	Compressive strength	1	52.26	56.42
		2	56.1	
		3	60.89	
	Tensile strength	1	3.52	3.68
		2	3.83	
		3	3.7	
	Elastic modulus	1	36500	40500
		2	43900	
		3	41100	

equipment used was the PMS-500 fatigue tester. The maximum load was 1000 kN and the maximum frequency was 10 Hz. The loading method of simply supported composite test beam with negative moment is shown in Figure 7. Due to the test site and loading method, the test beam was hoisted in the opposite direction, with the concrete slab facing down and the bottom plate facing up. Repeated loads were placed in the middle of the beam span by the distribution beam; the loading diagram is shown in Figure 8.

2.5.2. Loading Procedure. According to the results of the Liu [24] static load test, the upper limit of the load of PLG-1 was 490 kN and the lower limit was 225 kN. In order to prevent the cracks from appearing too wide during the entire test, the initial load limit of the fatigue test piece PLG-2 was 190 kN, and the variable load method was used gradually to increase the maximum load limit and load amplitude.

PLG-1 was loaded in two ways, static and dynamic. The static load was divided into 10 levels, with the maximum load being 490 kN and the load of each level being 49 kN. The upper and lower limits of the dynamic load were 225 kN–490 kN, with 4 Hz loading frequency. The specific loading process was as follows: before the dynamic load was applied, three static loads were applied to make the concrete slab crack, so as to simulate the cracked working state of the bridge deck. The dynamic load was stopped every 250,000 cycles, and a static load was applied after each stop to measure strain and deflection and observe cracks. After 2 million dynamic loads, the test beam had not been damaged, the upper limit load and the stress amplitude will be increased, and the observation will be stopped every 250,000 cycles until the final failure.

PLG-2 adopted the method of variable amplitude loading because the reinforcement ratio was small, the stress of the steel bar under the same load was also large, and the cracks appeared earlier. Therefore, the load was gradually increased by increasing the upper limit of the load and the load amplitude. The static load was divided into 10 levels,

Figure 7: Test beam loading site.

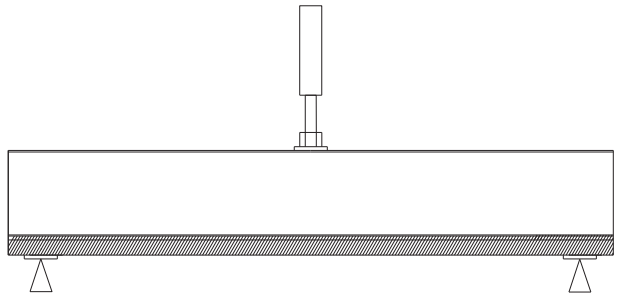

Figure 8: Schematic diagram of test beam loading.

190 kN as maximum load, and the load of each level was 19 kN. The upper and lower limits of the dynamic load were 90 kN–190 kN, with the loading frequency being 4 Hz. The specific loading process was as follows: before the dynamic load was applied, three static loads were applied to make the concrete slab crack, so as to simulate the cracked working state of the bridge deck. The dynamic load was stopped every 200,000 cycles, and a static load was applied after each stop to measure strain and deflection and observe cracks. After 1

million dynamic loads, the load upper limit and load amplitude were gradually increased, and the observation stopped at every 250,000 times until the load fails. The loading scheme is shown in Table 3.

3. Layout of Measuring Points

3.1. Layout of Displacement Meter. Figures 9 and 10 show the layout of the combined test beam displacement meter and the micrometer. P was the deflection displacement meter for measuring the vertical displacement of the whole beam, with an accuracy of 0.01 mm, arranged on the top surface of the concrete beam. *S* was the dial indicator for measuring slip.

3.2. Layout of Strain Measuring Points. The measuring points of the upper flange were arranged on the bottom of the upper flange and the outside of the box girder. There were strain gauges inside and outside of the web, and the measurement results were checked with each other. The measuring points of the steel beam bottom plate were arranged on the outer side of the bottom, while there were no measuring points on the inner side of the steel beam bottom plate box. Figure 11 shows the layout of the steel beam strain gauge.

PLG-1 was arranged with 5 measuring points at the midspan section, 1 time the beam height, 2 times the beam height, and 3 measuring points at the height of 0.5 times beam height, respectively, at the front and back, a total of 21 measuring points. PLG-2 was equipped with 4 measuring points at each of the 5 sections, with a total of 20 measuring points. Figures 12 and 13 show the measuring points of reinforcement in the concrete bridge panel.

4. Test Results and Analysis

4.1. Failure Process and Shape of Test Beam. The loading failure process of the test beams PLG-1 and PLG-2 was roughly the same. During the experiment, there was no obvious slip occurring in both specimens, and the slip measured in static loading was less than 0.02 mm. The concrete slab and the steel flange were always tightly combined and no separation was seen.

In the initial stage of static load loading, the top surface of the concrete slab was pulled apart and cracked. With the increase of load, the distribution range of cracks in the concrete slab increased and the crack width increased. After the first stop under the dynamic load, the crack development range and crack width increased obviously. The main cracks had basically all appeared after the completion of the first dynamic load. In the subsequent fatigue loading, the cracks expanded along the original direction, the width gradually increased with fatigue loading, and the number remained basically unchanged. In the last static test, the width of the crack reached 0.29 mm, which was about 24% more than before the fatigue loading. Before 750,000 cycles, there was no significant change in deflection. When the static load test was performed after 1 million cycles, the deflection increased significantly compared to before fatigue loading, and the deflection increased by about 17%. During the loading process, the position of the neutral axis across the midsection had not changed, which means that there was no reduction in stiffness caused by slippage, and the steel beams and steel bars had not reached yield.

After the fatigue failure stopped, the reinforcement at the crack section was observed to be completely fractured. The failure modes of the fractured reinforcement can be divided into two types. The first type was typical fatigue fracture. The second type was the damage caused by the cracks that made the reinforcement enter the plastic phase. The cross section was characterized by uneven stubble and obvious necking. Until the final stage of loading, no bending and shear failure occurred in the shear nails, and no compression failure occurred in the concrete near the shear nails. The failure of PLG-1 is shown in Figure 14.

At the initial stage of PLG-2 loading, the cracks developed to about 0.21 mm at 200 kN. Due to the low load amplitude, the number and spacing of cracks became stable around 600,000 cycles. After loading for 1 million cycles, the crack width increased to 0.27 mm and the crack width increased by 29%. After 1 million cycles, the maximum crack width also began to increase due to the increase of stress amplitude, and the crack width increased to 0.31 mm for 1.5 million cycles. There was no significant increase in deflection before 1 million cycles, and it was destroyed after loading 1.65 million cycles. During the 1.5 million shutdown tests, no sudden change in the strain of the steel bars and beams was found.

When the static load before fatigue loading was completed, it was seen that the neutral axis of the midspan section after cracking has been lowered to 150 mm above the bottom surface, between the first state and the second state. Before 1 million cycles, the position of the neutral axis across the midsection had not changed, indicating that there was no decrease in stiffness due to slippage and that the steel beams and reinforcement did not yield. When the load reached 1 million cycles, the neutral axis position dropped to about 200 mm, indicating that the bonding and slip performance of the reinforcement weakened and the section stiffness decreased. When loaded to about 1.62 million cycles, an opening crack of about 3 mm appeared. Fatigue fracture of some reinforcement had occurred at the crack, and the connection between the concrete slab and the steel flange was still intact. At this time, the load was continued without stopping, and the crack developed rapidly. As the cracks developed, the tension released by the concrete slab was shared by the remaining ordinary reinforcement and the upper flange of the steel beam. The ordinary reinforcement in concrete slab was first tensioned to yield and the displacement amplitude increased obviously. Then the reinforcement in the concrete slab at the centerline broke, followed by the flange crack on the steel beam, and the cracks gradually spread to the web of the steel beam and stopped at 1.65 million cycles.

After the shutdown, it was observed that the reinforcement was completely broken at the crack section, and the fracture form of the broken reinforcement was the same as PLG-1. Until the final stage of loading, there was no bending and shear failure of the shear nails, and there was no compression failure of the concrete near the shear nails. The damage of PLG-2 is shown in Figure 15.

Table 3: Test load.

Specimen		PLG-1	PLG-2 (0–1×10^6 cycles)	PLG-2 (1×10^6–1.5×10^6 cycles)	PLG-2 (after 1.5×10^6 cycles)
Load (kN)	Upper limit	490	190	300	380
	Lower limit	225	90	90	130
	Amplitude	265	100	210	250

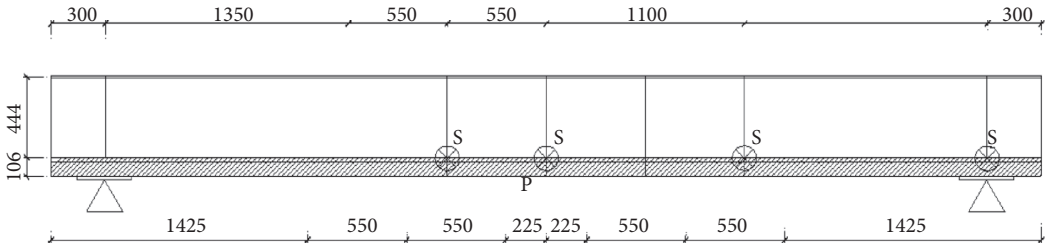

Figure 9: Layout on the left (unit: mm).

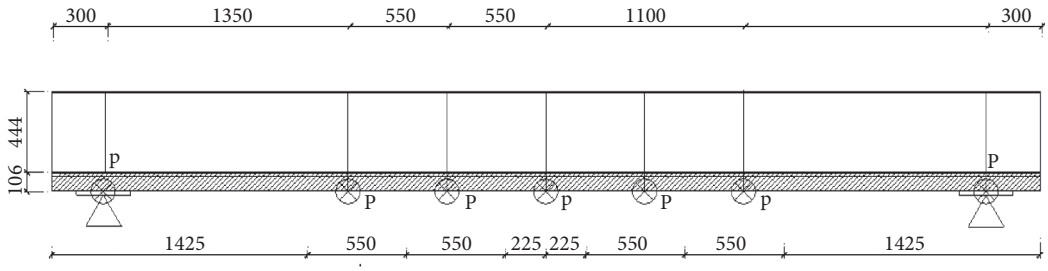

Figure 10: Layout on the right (unit: mm).

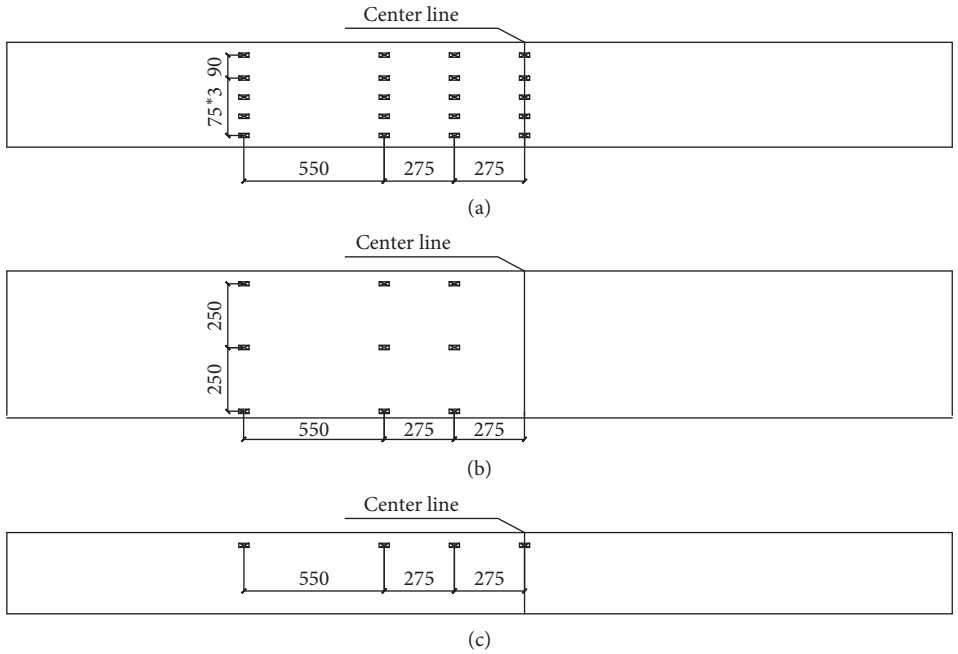

Figure 11: Layout of measuring points of steel beam (unit: mm). (a) Layout of inner and outer webs. (b) Layout of outside of base plate. (c) Layout of lower side of upper flange.

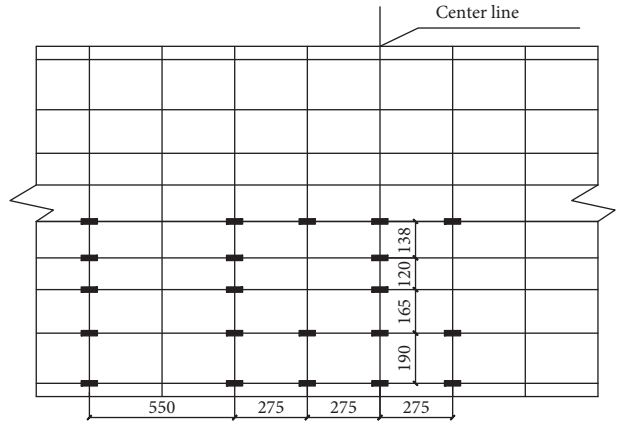

Figure 12: Layout of PLG-1 reinforcement measuring point (unit: mm).

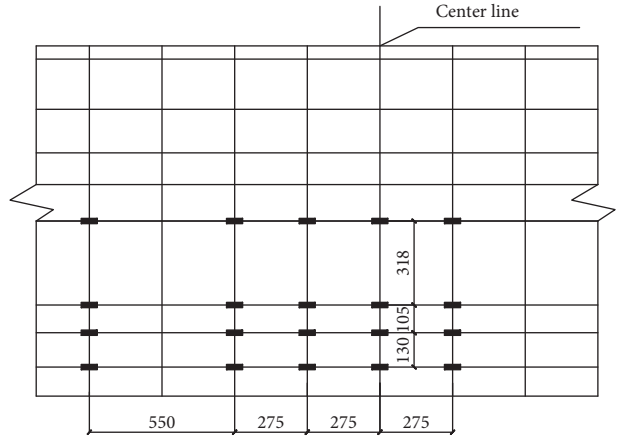

Figure 13: Layout of PLG-2 reinforcement measuring point (unit: mm).

4.2. Cracks in Concrete Slab

4.2.1. PLG-1. After the initial static load of PLG-1, the cracks were mainly concentrated in the range of 2.5 times the beam height on both sides of the center line. The maximum crack width was 0.25 mm, and the main through crack distance was about 14 cm. After 250,000 cycles, the crack expanded to 3.5 times the beam height on both sides of the centerline, and the maximum width of the crack reached 0.26 mm. After 500,000 cycles, 750,000 cycles, and 1 million cycles, the range of crack distribution and the maximum crack width changed little, which was the penetration and widening of the original crack. Before fatigue failure, the maximum crack width increased by about 24%. The crack width information of the test beam is summarized in Table 4. Figures 16 and 17 show the crack distribution diagram of PLG-1 concrete slab and the photos of the crack with the maximum width.

4.2.2. PLG-2. After the initial static load, five cracks appeared within a range of 1 time the beam height from the centerline, and the maximum width of the initial crack was 0.21 mm. After 200,000 cycles, several new cracks appeared, and the cracks were mainly concentrated within the double beam height on both sides of the middle fulcrum. After 400,000 cycles, several new cracks appeared within the original cracks. After 600,000 cycles, the number and length of cracks had developed greatly. The cracks were mainly concentrated in the range of 2.5 times the beam height on both sides of the middle fulcrum, and many cracks penetrated the plate width. After 800,000 cycles and 1 million cycles, the range of crack distribution and the maximum crack width changed little, basically the penetration and widening of the original cracks. When the load did not increase, the crack width increased by 29% after 1 million cycles. After increasing the upper limit of the load and the amplitude of the load, during the 1.25 million shutdown observations, several through cracks appeared, and the main cracks were concentrated within 3.5 times the beam height on both sides of the center line. After 1.5 million cycles, the distribution range and length of the cracks were similar to those after 1.25 million cycles, and some cracks had developed. The crack width information of the test beam is summarized in Table 5. Figures 18 and 19 show the crack distribution diagram of PLG-2 concrete slab and the photos of the crack with the maximum width.

(a) (b) (c)

Figure 14: Failure mode of PLG-1. (a) Global failure of composite beam. (b) Failure of reinforcement. (c) Failure of steel beam.

(a) (b) (c)

Figure 15: Failure mode of PLG-2. (a) Global failure of composite beam. (b) Crack of concrete slab. (c) Failure of concrete slab.

Table 4: Cracks of concrete slab of PLG-1 (unit: mm).

PLG-1	Before the dynamic load	Before the dynamic load	After 250,000 cycles	After 250,000 cycles	After 250,000 cycles	After 1 million cycles
Static load (kN)	380	490	490	490	490	490
Crack width	0.22	0.25	0.26	0.27	0.29	0.31

4.3. Load-Displacement Curve

4.3.1. PLG-1. Before the dynamic load was applied, the static load was applied to the test beam first. The static load was divided into ten levels; each level was 49 kN. The load-displacement curve under static load of PLG-1 is shown in Figure 20. It can be seen from the figure that the concrete cracked when the displacement was small, the cracking load was approximately 100 kN. After cracking, the slope of the load-displacement curve decreased, indicating that the stiffness of the test beam decreases gradually. The static loading before fatigue loading reached a maximum displacement of about 7.0 mm at 500 kN.

As can be seen from Figure 21, the load-displacement curves of PLG-1 in static load test after each fatigue load showed a linear relationship. Before the occurrence of fatigue failure, the midspan deflection did not change significantly under the same static load, within 1 mm. It was shown that there is no significant stiffness decrease of PLG-1 test beam before fatigue failure.

4.3.2. PLG-2. Before dynamic load was applied, static load was applied to the test beam. There were ten stages of static load, each of which is 20 kN. The load-displacement curve under static load is shown in Figure 22. It can be seen that concrete cracks occurred when the displacement was very small, and the cracking load was about 48 kN, which decreased by 52% compared with PLG-1. The static loading before fatigue loading reached a maximum displacement of about 2.5 mm at 200 kN.

As can be seen from Figure 23, the load-displacement curves of PLG-2 in static load test after each fatigue load showed a linear relationship. Under the same static load, the deflection in the span did not change much. The static test displacement after 1 million times increased by 1.6% compared with the deflection before dynamic loading, but the deflection after 1.25 million times increased by 46% and the deflection after 1.5 million times increased by 60%, indicating that the stiffness of the beam decreased significantly shortly before fatigue failure. Compared with PLG-1, the stiffness of PLG-2 under fatigue load decreased more significantly before fatigue failure.

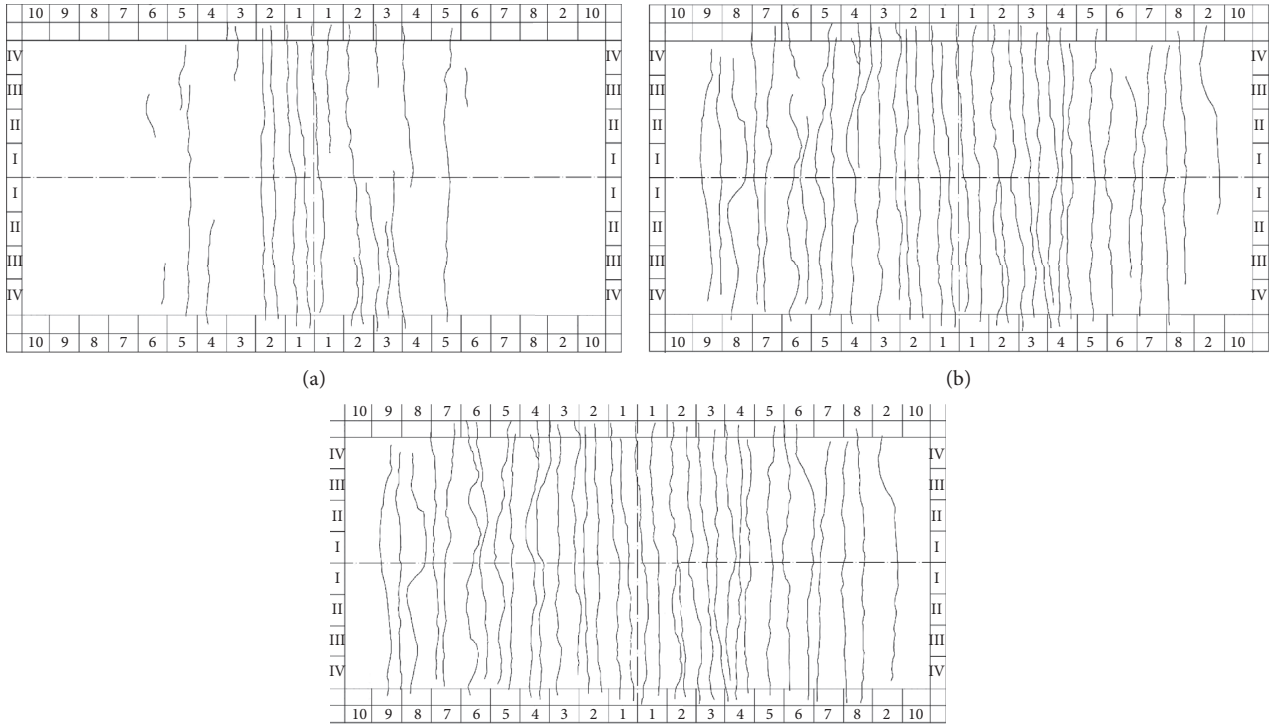

Figure 16: Distribution of cracks in the concrete slab of PLG-1. (a) 380 kN. (b) After 250,000 cycles. (c) After 1 million cycles.

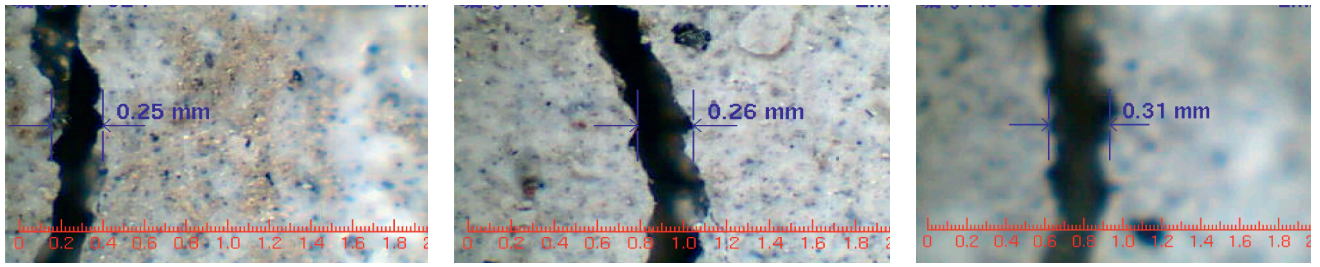

Figure 17: The largest crack in the concrete slab of PLG-1. (a) 380 kN. (b) After 250,000 cycles. (c) After 1 million cycles.

Table 5: Cracks of concrete slab of PLG-2 (unit: mm).

PLG-2	Before the dynamic load	After 200,000 cycles	After 400,000 cycles	After 600,000 cycles	After 800,000 cycles	After 1 million cycles	After 1.25 million cycles	After 1.5 million cycles
Static load (kN)	190	190	190	190	190	190	300	380
Crack width	0.21	0.23	0.25	0.26	0.27	0.27	0.29	0.32

4.4. Reinforcement Strain of Concrete Slab. The strain of upper reinforcement at the center line of PLG-1 and PLG-2 was selected for analysis. Figure 24 shows the midspan reinforcement strain of PLG-1 after 1 million dynamic loaded. It can be seen that the reinforcement strain at the top of the web was larger than that at the other positions, indicating a shear lag effect existence, but the effect was not obvious. Figure 25 shows the strain of the midspan reinforcement of PLG-2 after 1.25 million dynamic loaded, and it was not found that the strain of the web reinforcement was

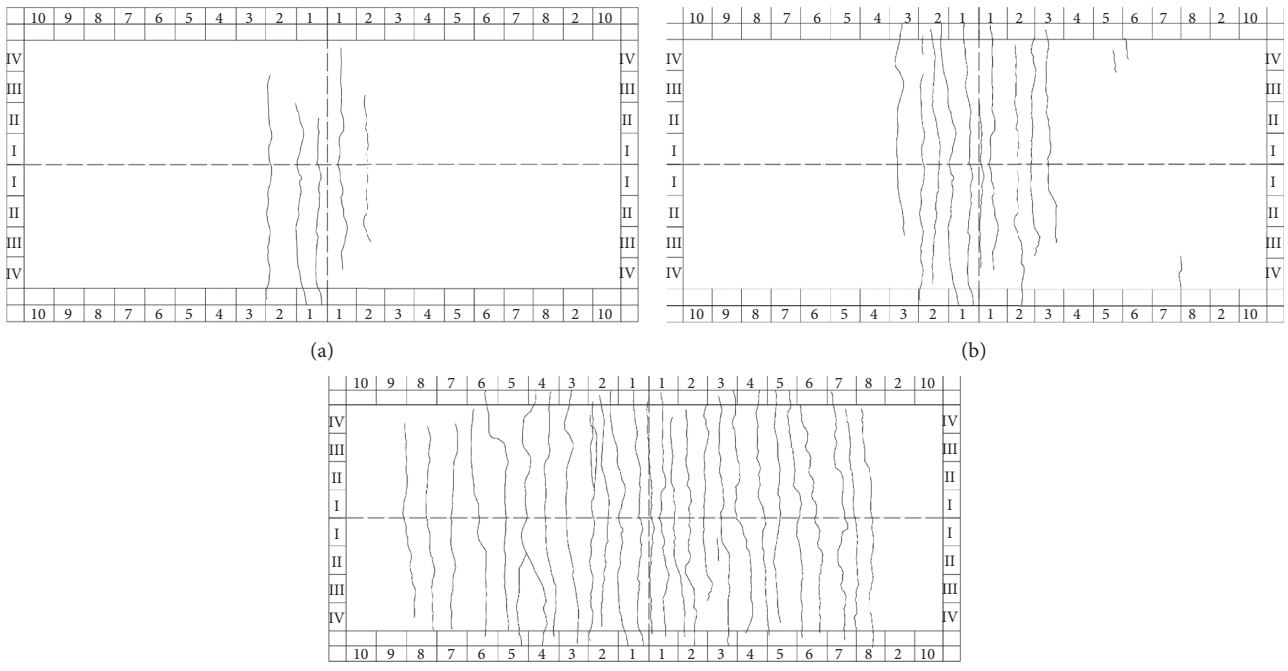

Figure 18: Distribution of cracks in the concrete slab of PLG-2. (a) 200 kN. (b) After 200,000 cycles. (c) After 1.5 million cycles.

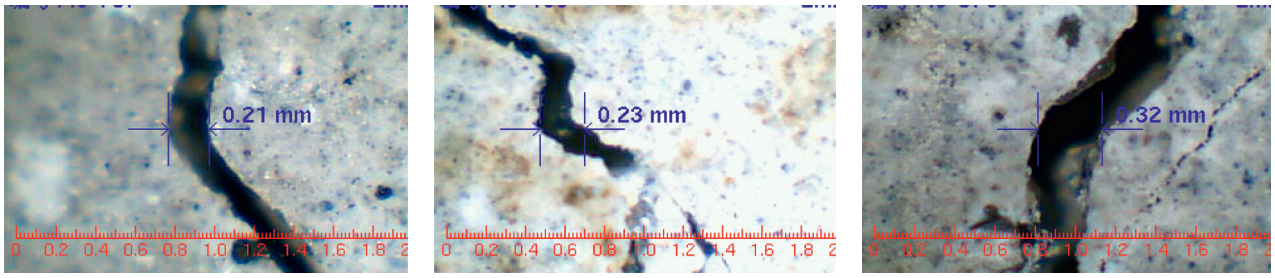

Figure 19: The largest crack in the concrete slab of PLG-2. (a) 200 kN. (b) After 200,000 cycles. (c) After 1.5 million cycles.

larger than that of the rest positions, which might be caused by the low reinforcement ratio of PLG-2, the insignificant shear lag effect, or the limited means of test. Figures 26 and 27 show the variation curve and comparison curve of reinforcement strain in concrete slab with load at the center line of PLG -1 and PLG -2. It can be seen that the strain of the reinforcement during the initial cracking of the concrete was greater than the strain of the reinforcement during repeated loading, which might be caused by the decrease in the stiffness of the concrete caused by repeated loading and the reduction of the shared moment of the concrete slab. Due to the influence of cracks, the strain of steel bars collected by strain gauge at the same section location was not the same. After the cracking of concrete, the load-strain relationship of reinforcement was close to linear in each static loading after repeated loading.

4.5. Strain of Steel Beam

4.5.1. PLG-1. Figure 28 shows the relationship between strain and load on the top flange of the steel beam at the center line section and at 0.5 times the beam height. It can be seen that the effect of fatigue load on the stiffness of the steel

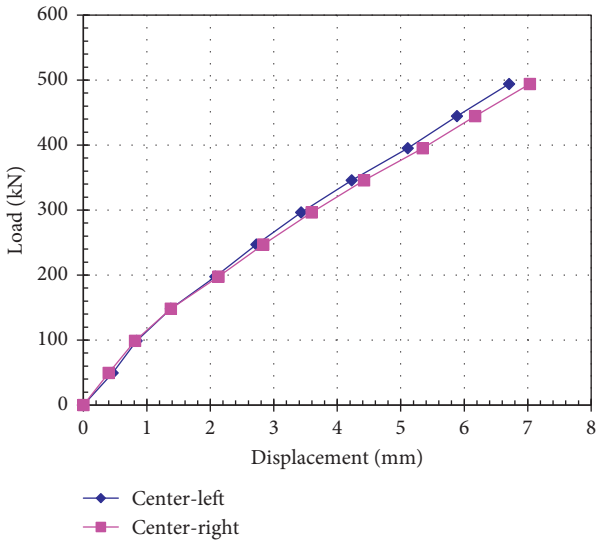

Figure 20: Load-displacement curve of PLG-1 midspan (before dynamic load).

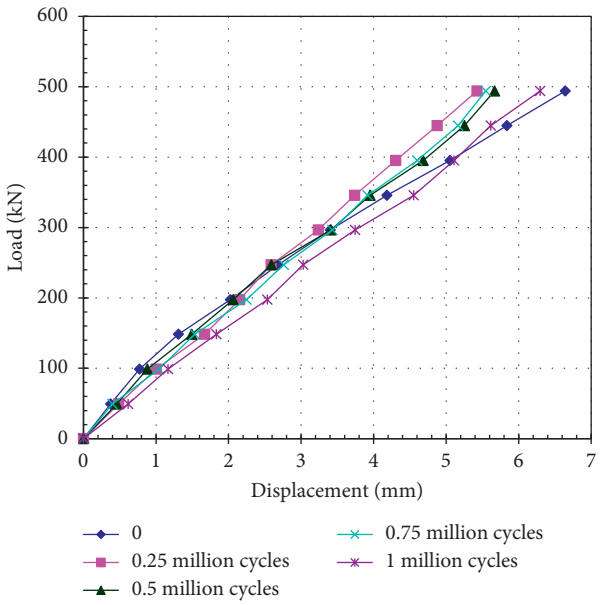

Figure 21: Comparison of midspan load-displacement curves (after dynamic loading of PLG-1).

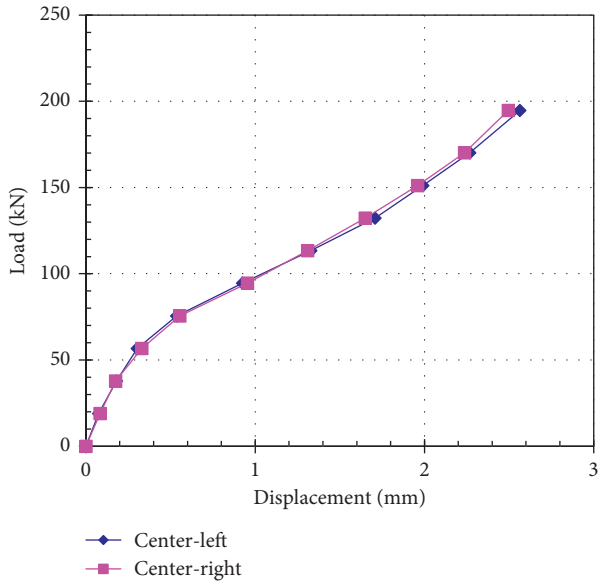

Figure 22: Load-displacement curve of PLG-2 midspan (before dynamic load).

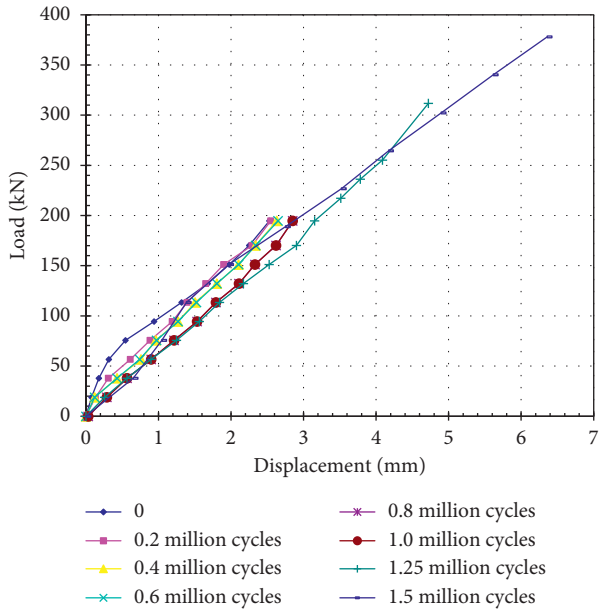

Figure 23: Comparison of midspan load-displacement curves (after dynamic loading of PLG-2).

beam was not obvious. After the first static load cracking of the concrete slab, the strain-load of the steel beam had a linear relationship and was in a lower stress state. With the increase of fatigue loading times, the strain of steel beam under the same load increases gradually.

Figure 29 shows the relationship between strain and section height on the top flange of the steel beam at the center line section and at 0.5 times the beam height. As can be seen from the figure, along the height of the section, the various strains were distributed in proportion to the distance from the neutral layer. As the load increases step by step, the strain was distributed in a straight line. The neutral layer was 150 mm away from the bottom edge of the section. After 1 million cycles, it can be seen that the strain at the height of 450 mm was basically the same, and the strain value at the 0.5 times beam height at the height of 0 mm was about twice the strain value of the central line section. The steel beam was in the elastic working range, and the section deformation conforms to the assumption of flat section.

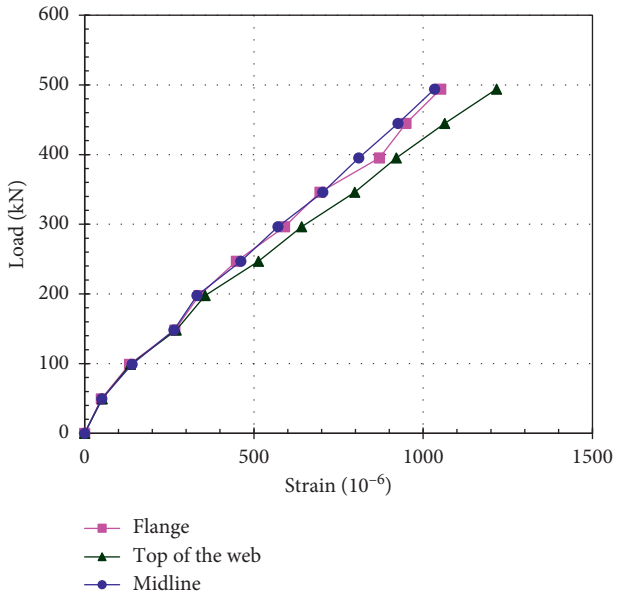

Figure 24: PLG-1 strain of midspan reinforcement after 1 million dynamic loads.

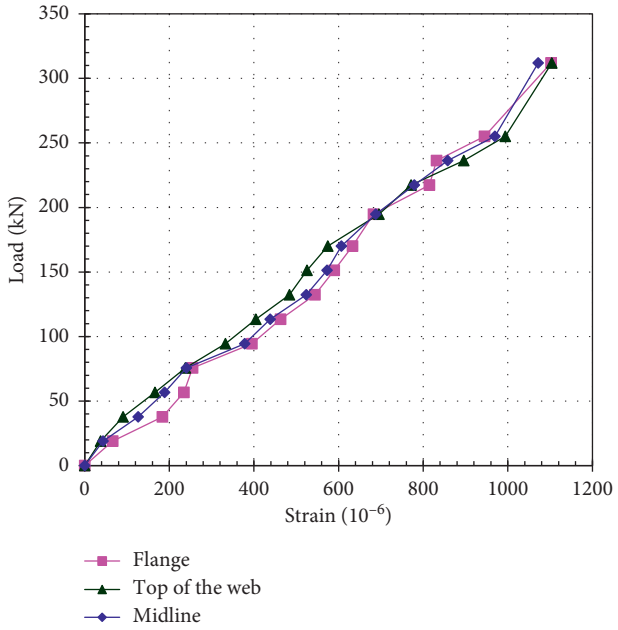

Figure 25: PLG-2 strain of midspan reinforcement after 1.25 million dynamic loads.

4.5.2. PLG-2. Figure 30 shows the variation curve of top flange strain with load at the center line section and 0.5 beams height section of PLG-2. It can be seen that the strain of the steel beam was not affected by the fatigue load. The load-strain relationship of steel beams after fatigue loading was linear. As the cycles of loadings increased, the strain of the steel beam under the same load gradually increased. Under the same static load, the strain after 1 million cycles of

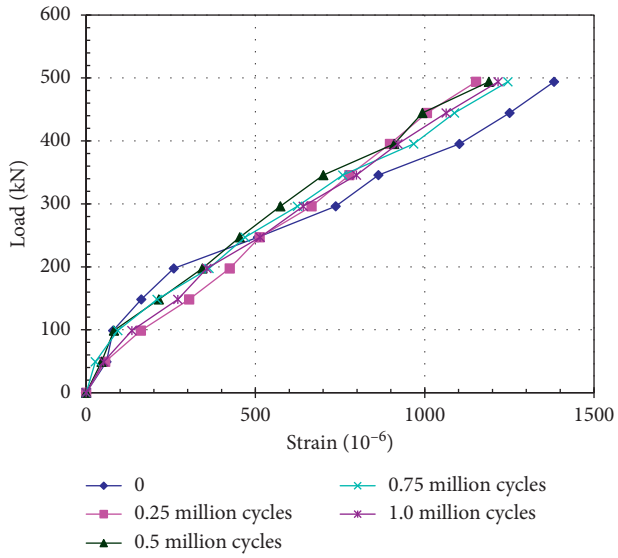

Figure 26: PLG-1 reinforcement strain comparison of midspan concrete slab.

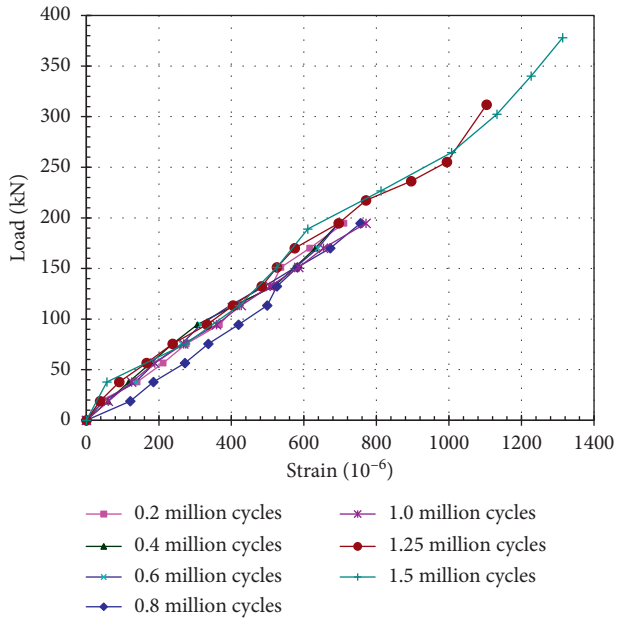

Figure 27: PLG-2 reinforcement strain comparison of midspan concrete slab.

fatigue loading increased by 2% compared with that after 200,000 cycles, but the strain after 1.25 million cycles of loading increased by 40% and that after 1.5 million cycles of loading increased by 50%, indicating that the rigidity of the steel beam before fatigue failure was significantly reduced.

Figure 31 shows the relationship between strain and section height on the top flange of the steel beam at the center line section and at 0.5 times the beam height. As can be seen from the figure, along the height of the section, the

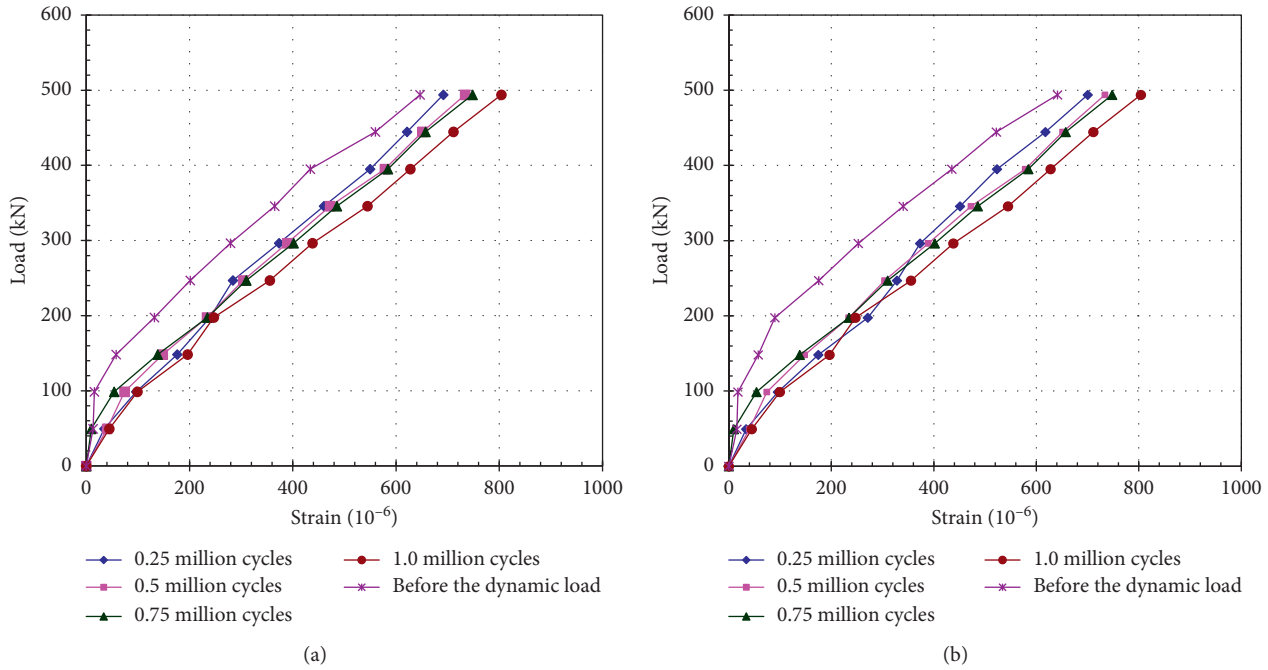

Figure 28: Curve of strain of PLG-1 steel beam with load. (a) Center line section. (b) 0.5 times the beam height section.

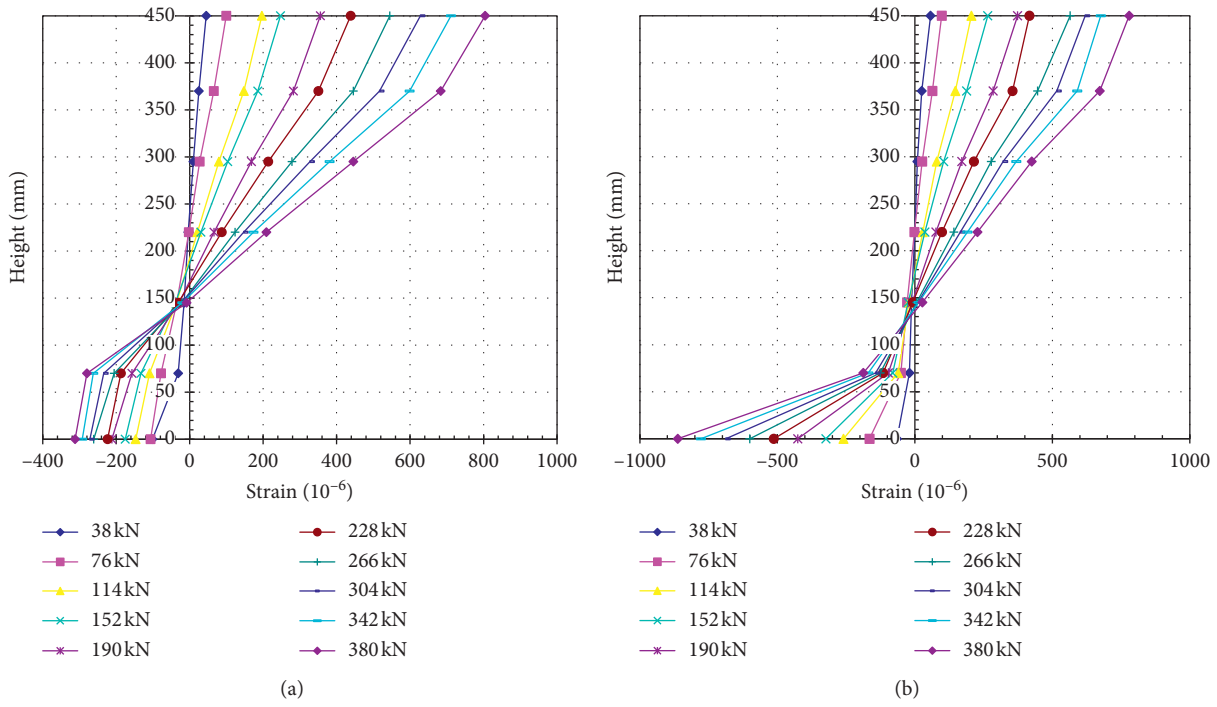

Figure 29: Curve of strain of PLG-1 steel beam with height. (a) Center line section (after 1 million cycles). (b) 0.5 times the beam height section (after 1 million cycles).

various strains were distributed in proportion to the distance from the neutral layer. As the load increases step by step, the strain was distributed in a straight line. The neutral layer was 150 mm away from the bottom edge. After 1 million cycles, it can be seen that the strain at the height of 450 mm was basically the same, and the strain value at the 0.5 times beam height at the height of 0 mm was about 1.5 times the strain value of the central line section. The steel beam was in the elastic working range, and the section deformation conforms to the assumption of flat section.

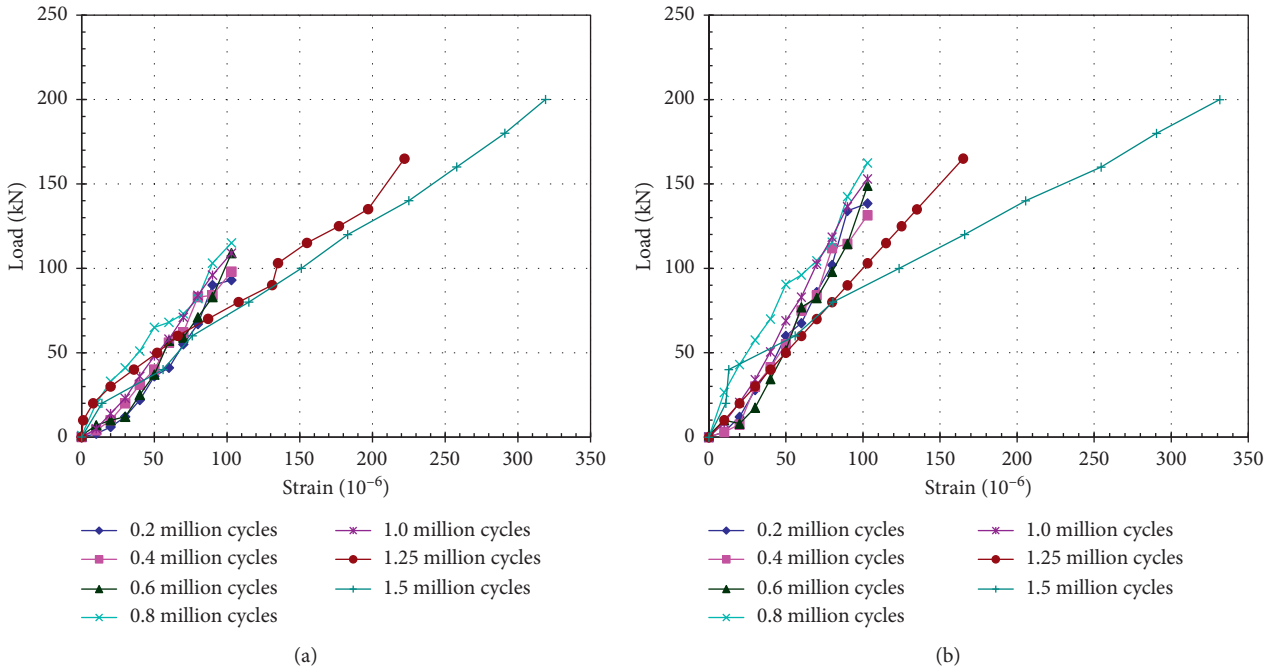

Figure 30: Curve of strain of PLG-2 steel beam with load. (a) Center line section. (b) 0.5 times the beam height section.

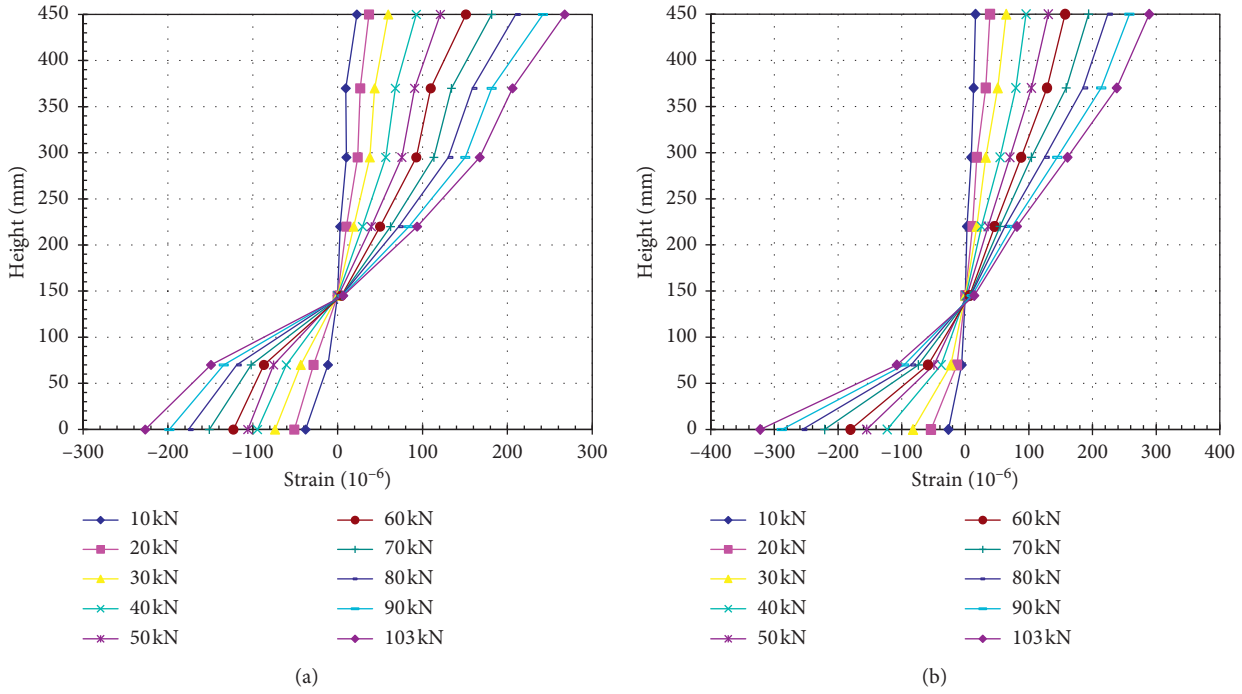

Figure 31: Curve of strain of PLG-2 steel beam with height. (a) Center line section (after 1 million cycles). (b) 0.5 times the beam height section (after 1 million cycles).

5. Conclusions

This work presents the results of the fatigue test and theoretical analysis of two composite beams with different reinforcement ratios used to obtain the variation law of the deflection, steel bar strain, steel beam strain, and crack growth of the composite beam under fatigue loading. Based on the experimental and theoretical results the following conclusions can be drawn:

(1) The failure modes of the composite beams with two reinforcement ratios designed in this paper were typical fractures of reinforcement, and there was no fatigue damage to the wailing nails and steel flange. The

cracking of the concrete in the negative moment region of the composite beam and the combined action between steel and concrete were not obvious, and the stress on the welding nails was small. However, there was stress concentration in the reinforcement at the crack, and the fatigue failure in the negative moment region of a composite beam was likely to be controlled by reinforcement, but welding nails.

(2) The reinforcement ratio of the concrete slab had little effect on the cracking load and crack distribution range of the test beam but had a greater effect on the crack width and crack spacing. The higher the concrete reinforcement ratio, the smaller crack distribution range, the denser crack spacing, and the smaller crack width.

(3) During the whole process of fatigue loading, the crack width growth trend of specimens with different reinforcement ratios was close to each other. When the reinforcement ratio of composite beams increased from 0.86% to 1.72%, the maximum crack width before fatigue failure decreases from 28% to 24% after one million times of fatigue tests. The fatigue resistance of the low reinforcement ratio specimen was much lower than the high reinforcement ratio specimen.

(4) The strains of the reinforcement and steel beams during the initial cracking were higher than those after repeated loading, and the stress concentration of reinforcement in the initial cracking was higher than that after repeated loading. As the number of loadings increases, the strain of the steel beam increased and the strain of the steel bar decreased; the internal force redistribution occurred in the section.

Data Availability

The data used to support the findings of this study are not available.

Conflicts of Interest

All authors declare that there are no conflicts of interest regarding the publication of this article.

Acknowledgments

This work was supported by the National Natural Science Foundation of China (no. 51878623), Innovative Research Team (in Science and Technology) in University of Henan Province (Grant no. 20IRTSTHN009), Program for Young Backbone Teachers in Colleges and Universities in Henan, (2018GGJS005), and Foundation for Postdoctoral Students in Henan Province (1901024).

References

[1] R. P. Johnson, *Composites Structures of Steel and Concrete: Beams, Slabs, Columns, and Frames for Buildings*, Wiley-Blackwell, Hoboken, NY, USA, 3rd edition, 2004.

[2] K. Rajan, "*The study on flexural behavior of steel-concrete composite continuous box girder*," M.S. thesis, Southeast University, Nanjing, China, 2019.

[3] F. Ding, J. Liu, and X. Liu, "Experimental investigation on hysteretic behavior of simply supported steel-concrete composite beam," *Journal of Constructional Steel Research*, vol. 144, pp. 153–165, 2018.

[4] J. Fan, J. Nie, H. Wang, and Q. Li, "Long-term behavior of composite beams under positive and negative bending I: experimental study," *Journal of Structural Engineering*, vol. 136, no. 7, pp. 849–857, 2010.

[5] P. Zhang, Y.-n. Zhao, C.-h. Liu, P. Wang, and T.-h. Zhang, "Combined effect of nano-SiO_2 particles and steel fibers on flexural properties of concrete composite containing fly ash," *Science and Engineering of Composite Materials*, vol. 21, no. 4, pp. 597–605, 2014.

[6] S. Han, Y. Cui, H. Huang, M. An, and Z. Yu, "Effect of curing conditions on the shrinkage of ultra high-performance fiber-reinforced concrete," *Advances in Civil Engineering*, vol. 2018, Article ID 5238278, pp. 1–8, 2018.

[7] P. R. Barnard and R. P. Johnson, "Plastic behavior of continuous composite beams," *Proceedings of the Institution of Civil Engineers*, vol. 32, no. 2, pp. 180–197, 1965.

[8] S. K. Mallick and S. K. Chattopadhyay, "Ultimate strength of continuous composite beams," *Building Science*, vol. 10, no. 3, pp. 189–198, 1975.

[9] S. Hamada and J Longworth, "Ultimate strength of continuous composite beams," *Journal of Structural Division*, vol. 102, no. 7, pp. 1463–1478, 1976.

[10] R. P. Johnson, R. D. Greenwood, and K. van Dalen, "Stud shear connectors in hogging moment regions of composite beams," *The Structural Engineer*, vol. 47, pp. 345–350, 1969.

[11] M. C. Hope-Gill and R. P. Johnson, "Tests on three three-span continuous composite beams," *Proceedings of the Institution of Civil Engineers*, vol. 61, no. 2, pp. 367–381, 1976.

[12] R. P. Johnson and I. M. May, "Partial-interaction design of composite beams," *Structural Engineer*, vol. 53, no. 8, pp. 305–311, 1975.

[13] R. P. Johnson and S Chen, "Local buckling and moment redistribution in class 2 composite beams," *Structural Engineering International*, vol. 1, no. 4, pp. 27–34, 1991.

[14] R. P. Johnson, *Composite structures of steel and concrete*, Blackwell Science, Boston, London, 2nd edition, 1994.

[15] J. A. Grant, C. Koeberl, W. U. Reimold, and P. H. Schultz, "Gradation of the Roter Kamm impact crater, Namibia," *Journal of Geophysical Research*, vol. 102, no. E7, pp. 16327–16338, 1997.

[16] B. G. Gautam, Y. Yiqiang, X. Liao, Z. Qiu, and S. Guo, "Experimental investigation of a slip in high-performance steel-concrete small box girder with different combinations of group studs," *Materials*, vol. 12, no. 17, p. 2781, 2019.

[17] R. G. Liao and J. W. Fisher, "Fatigue strength of shear connectors," *Fritz Laboratory Reports*, Lehigh University, Bethlehem, Pennsylvania, 1966.

[18] J. Y. R. Yen, Y. Lin, and M. T. Lai, "Composite beams subjected to static and fatigue loads," *Journal of Structural Engineering*, vol. 123, no. 6, pp. 765–771, 1997.

[19] N. Gattesco, E. Giuriani, and A. Gubana, "Low-cycle fatigue test on stud shear connectors," *Journal of Structural Engineering*, vol. 123, no. 2, pp. 145–150, 1997.

[20] S.-G. Youn and S.-P. Chang, "Behavior of composite bridge decks subjected to static and fatigue loading," *Journal of ACI*, vol. 95, no. 3, pp. 249–258, 1998.

[21] R. P. Johnson, "Resistance of stud shear connectors to fatigue," *Journal of Constructional Steel Research*, vol. 56, no. 2, pp. 101–116, 2000.

[22] B. Wang, Q. Huang, and X. Liu, "Deterioration in strength of studs based on two-parameter fatigue failure criterion," *Steel and Composite Structures*, vol. 23, no. 2, pp. 239–250, 2017.

[23] B. Wang, Q. Huang, X. Liu, and W. Li, "Experimental investigation of steel-concrete composite beams with different degrees of shear connection under monotonic and fatigue loads," *Advances in Structural Engineering*, vol. 21, no. 2, pp. 227–240, 2018.

[24] S. Liu, "Study on the mechanical performance of continuous composite box girder bridge in the negative moment zone," Ph.D. thesis, Tongji University, Shanghai, China, 2011.

Hindawi
Advances in Civil Engineering
Volume 2020, Article ID 8836643, 12 pages
https://doi.org/10.1155/2020/8836643

Research Article

Study on Variation of Surface Runoff and Soil Moisture Content in the Subgrade of Permeable Pavement Structure

Lijun Hou,[1] Yuan Wang,[1] Fengchun Shen,[1] Ming Lei,[1] Xiang Wang,[1] Xiaochong Zhao,[2] Shuling Gao ,[2] and Abdullah Alhaj[3]

[1]*Power China Roadbridge Group Co., Ltd., Beijing 100048, China*
[2]*School of Civil Engineering and Transportation, Hebei University of Technology, Tianjin 300401, China*
[3]*Department of Geosciences and Geological and Petroleum Engineering, Missouri University of Science and Technology, Rolla, MO 65409, USA*

Correspondence should be addressed to Shuling Gao; gsl200001@126.com

Received 17 May 2020; Revised 10 June 2020; Accepted 13 June 2020; Published 4 July 2020

Academic Editor: Yifeng Ling

The self-designed indoor simulated rainfall device was used to rain on five types of pavement structures with 4 types of rainfall intensity (2.5 mm/min, 3.4 mm/min, 4.6 mm/min, and 5.5 mm/min). The effect of rainfall intensity on the surface runoff, the relation between the subgrade soil moisture content changes, and the influence of initial soil water content on rain infiltration rate are studied. The test results show that the surface runoff coefficient of densely asphalted pavement is greater than 90% in drainage pavements and it has little influence on the reducing and hysteresis of the flood peak. The surface runoff coefficient of large-void asphalt pavement (permeable) is less than 40%. Although the large-void asphalt pavement (permeable) can reduce a small amount of surface runoff, it has no obvious effect on the reduction and hysteresis of the flood peak. In semipermeable pavement, with the increasing of the thickness of base (graded gravel), the surface runoff coefficient decreases at different rainfall intensities, parts of the surface runoff are reduced, and the arrival of flood peaks is delayed. In permeable roads, almost no surface runoff occurred. As time continued, the soil moisture content quickly reached a saturated state and presented a stable infiltration situation under the action of gravity and the gradient of soil water suction. As the initial moisture content increases, the initial infiltration rate decreases and the time to reach a stable infiltration rate becomes shorter. The drier the soil, the greater the initial infiltration rate and the higher the soil moisture content after infiltration stabilization. Permeable roads can greatly alleviate the pressure of urban drainage and reduce the risk of storms and floods.

1. Introduction

According to China's National Bureau of Statistics, China's urbanization rate had reached 57.35% in 2016 [1]. The densely asphalted road surface has increased significantly. During rain and snow, the accumulated water on the road surface causes serious inconvenience to pedestrian travel and vehicle driving. In the case of heavy rainfall, a large surface runoff will occur, increasing the drainage burden of the urban pipe network [2]. In addition, due to lack of rainwater penetration, groundwater is not effectively supplied, and many cities face severe water shortages and droughts [3, 4]. Since 1970, the United States, the United Kingdom, and Australia have successively developed a series of technologies to control urban runoff and introduced a series of rainwater management plans and guidelines [5–16].

Since October 2014, China has put forward the development strategy of "sponge city" urbanization on the basis of summarizing the concept of rainwater control in foreign cities. A series of policies and technical guidelines were issued.

At present, researchers are focusing on the effects of surface runoff control on permeable pavement structures (drainage pavements, semipermeable pavements, and permeable roads) [1–5].

Zhu [1] used storm water management model (SWMM) software to simulate the effects of different permeable pavement structures under different rainfall conditions on reducing surface runoff and controlling flood peaks. Guan [2] simulated the variation of surface runoff and soil moisture content in the subgrade of permeable roads. Xu [17] studied the relationship between rainfall and runoff in the area under four different underlying conditions by distributed water stability model. Cai [18] used SWMM to simulate the runoff and drainage condition under different rainfall conditions in Guangzhou. Zhao [19] studied the rainfall runoff model and runoff reduction of permeable asphalt pavement. The results show that the thickness of the pavement structural layer, the initial soil moisture content, and the saturated moisture content have a greater influence on the permeable function of the pavement.

However, it is not enough to study the comparative effects of three permeable pavement structures on urban rainwater surface runoff. The correlation between the base layer thickness and surface runoff and the change of soil moisture content in roadbed with time need to be studied further.

In order to study the influence of three types of permeable pavement structures on urban rainwater surface runoff, four types of artificial rainfall intensity (2.5 mm/min, 3.4 mm/min, 4.6 mm/min, and 5.5 mm/min) will be used to study five types of pavement structure section types used by self-designed indoor simulated rainfall device. Furthermore, the effect of base layer thickness on surface runoff, the relationship between soil moisture content and time, and the influence of initial soil moisture content on rainwater infiltration rate were analyzed.

The objective of this study is to provide more theoretical basis for the application of permeable pavement structure and theoretical support for the "sponge city."

2. Road Conditions

Urban roads are generally composed of traffic lanes, bicycle lanes, and sidewalks. These three types of roads have different requirements on traffic load and the distribution of drainage facilities.

Traffic lanes are mainly bearing urban traffic loads, while structural mechanics index and durability should also meet the requirements of traffic load except reducing the surface runoff. Therefore, the drainage road is adopted.

The load of bicycle lanes is smaller than that of traffic lanes, so semipermeable pavement is adopted. And the load of sidewalks is the least, while permeable road is adopted. The pavement lane distribution diagram is illustrated in Figure 1.

3. Rainfall Design

Four types of rainfall intensities were obtained from the average annual rainfall intensity in Huangdao District of Qingdao City in Shandong Province in China in recent years, which were 2.5 mm/min, 3.4 mm/min, 4.6 mm/min, and 5.5 mm/min, respectively, whose rainfall time was all lasting for 120 min.

The relationship between cumulative rainfall and rainfall duration is shown in Figure 2.

4. Pervious Pavement Structure

According to the technical specification of permeable asphalt pavement (CJJ/T190-2012) [20], the structures of drainage pavement, semipermeable pavement, and permeable pavement were studied, respectively.

In the drainage pavement structure, large-void asphalt mixture was only used for surface layer. Impervious asphalt material or asphalt sealing coating was used on the base layer, and rainwater was discharged from the surface of the sealing layer without penetrating below the base layer. This approach is generally applied to the roadway as shown in Figure 3.

In the semipermeable pavement structure, the surface layer adopted large-void asphalt mixture. The base layer adopted permeable graded gravel, and the cushion layer adopted medium sand. This kind of pavement structure is generally applied to the bicycle lanes, as shown in Figure 4.

In the permeable roads structure, the surface layer adopts large-void asphalt mixture. The base layer adopted permeable graded gravel, and the cushion was generally made of medium sand, while subgrade was made of sand with better permeability. This kind of pavement structure was generally applied to sidewalks as shown in Figure 5.

Polypropylene fiber can be used in cement-based materials to improve the toughness and anticracking performance of the matrix composite [21–23]. But, polypropylene fiber cannot bear high temperature, while basalt fiber not only can improve the material's bending resistance [24] but also can bear high temperature in asphalt concrete. So, basalt fiber is very suitable for use in large-void asphalt concrete.

As shown in Figures 3–5, the surface layer used a large-void basalt fiber asphalt mixture, whose void ratio was 19.3%. Its permeability coefficient was 3.35×10^{-2} cm/s and the transverse slope of the surface layer was 2%.

The base layer was made of graded crushed stone, whose void ratio was 38%. In order to reduce the surface runoff of the large-void asphalt pavement, the base layer thickness was not less than 15 cm.

The cushion layer used medium sand with a particle size of 1.3 mm, and its permeability coefficient was 2.4×10^{-3} cm/s.

The soil foundation used sandy soil and the soil permeability coefficient after compaction was 1×10^{-3} cm/s.

When the basalt fiber content was 0.3%, the indicators of each road performance reach the optimum. The test results are shown in Table 1.

5. Artificial Simulated Rainfall Experiment

5.1. Experimental Device. The artificial rainfall equipment was composed of test chamber, storage bucket, pump, water meter, and sprinkler.

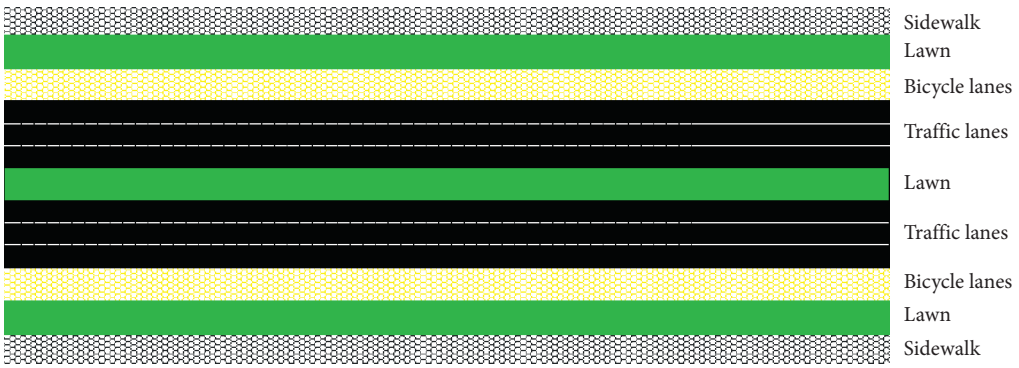

Figure 1: Pavement lane distribution.

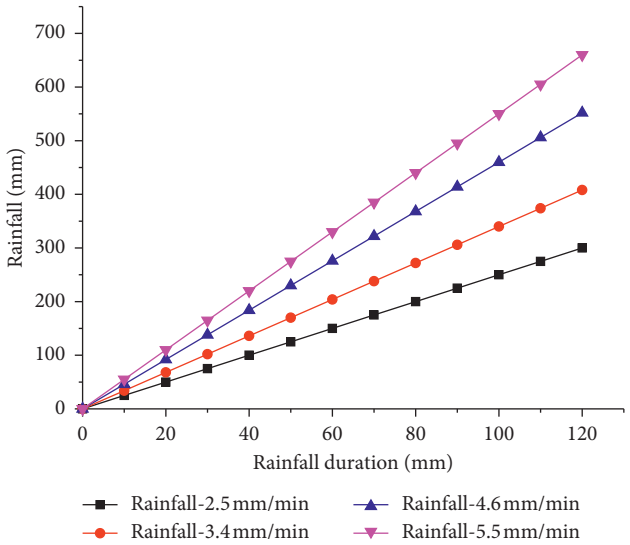

Figure 2: The relationship between cumulative rainfall and rainfall duration.

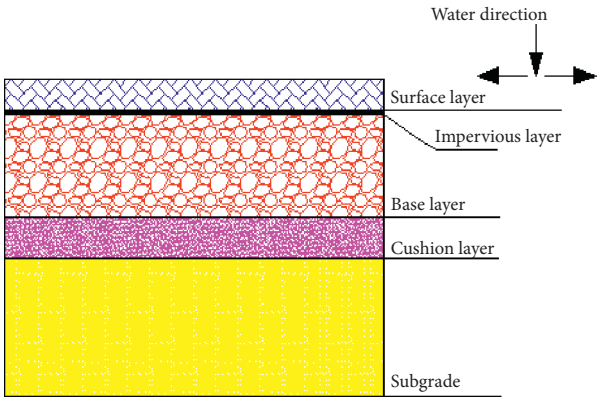

Figure 3: Drainage pavement structure.

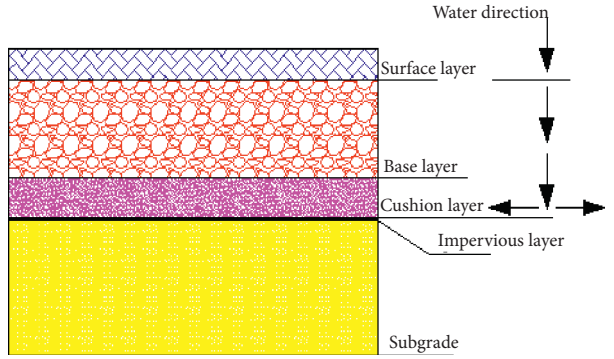

Figure 4: Semipermeable pavement structure.

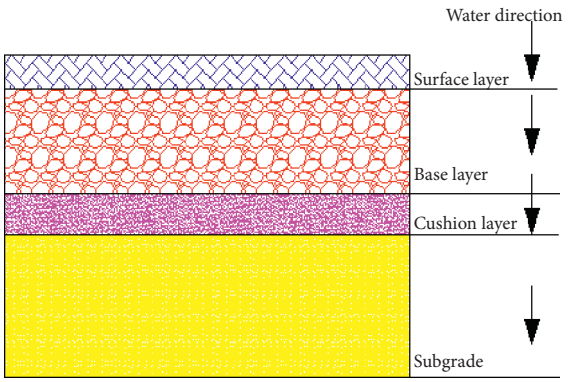

Figure 5: Permeable road structure.

As shown in Figures 6(a) and 6(b), the length, width, and height of the test chamber were 90 cm, 90 cm, and 100 cm, respectively. The one side of the test chamber shall be installed with transparent glass to observe the wetting front, and the box shall be paved with large-void asphalt pavement structure layer (surface layer, base layer, cushion layer, and subgrade). The other three sides of the box were provided with a certain number of drainage holes in order to collect surface runoff and the water discharged from the surface of the impervious sealing coating. There were drainage holes at the bottom of the box to collect the amount of rainwater seepage from the roadbed.

The water in the bucket was sent to the sprinkler by pump as shown in Figure 6(c). In order to simulate different rainfall intensities, the tee at the outlet of the pump was connected.

One pipe (Figure 6(c)-1) provided water and the other pipe (Figure 6(c)-2) controlled the different rainfall intensity by a valve in the water pipe.

Table 1: The indicators of large-void basalt fiber asphalt mixture (fiber content was 0.3%).

The indicators of performance test		Test results
High-temperature rutting experiment	Dynamic stability (time·mm^{-1})	4091
Freeze-thaw splitting test	Splitting tensile strength (MPa)	0.60
Low-temperature bending test (–10°C)	Bending strength (MPa)	10.75
	Maximum bending strain ($\mu\varepsilon$)	4957
	Bending stiffness modulus (MPa)	2172
Uniaxial compression experiment	Compressive strength (MPa)	4.50

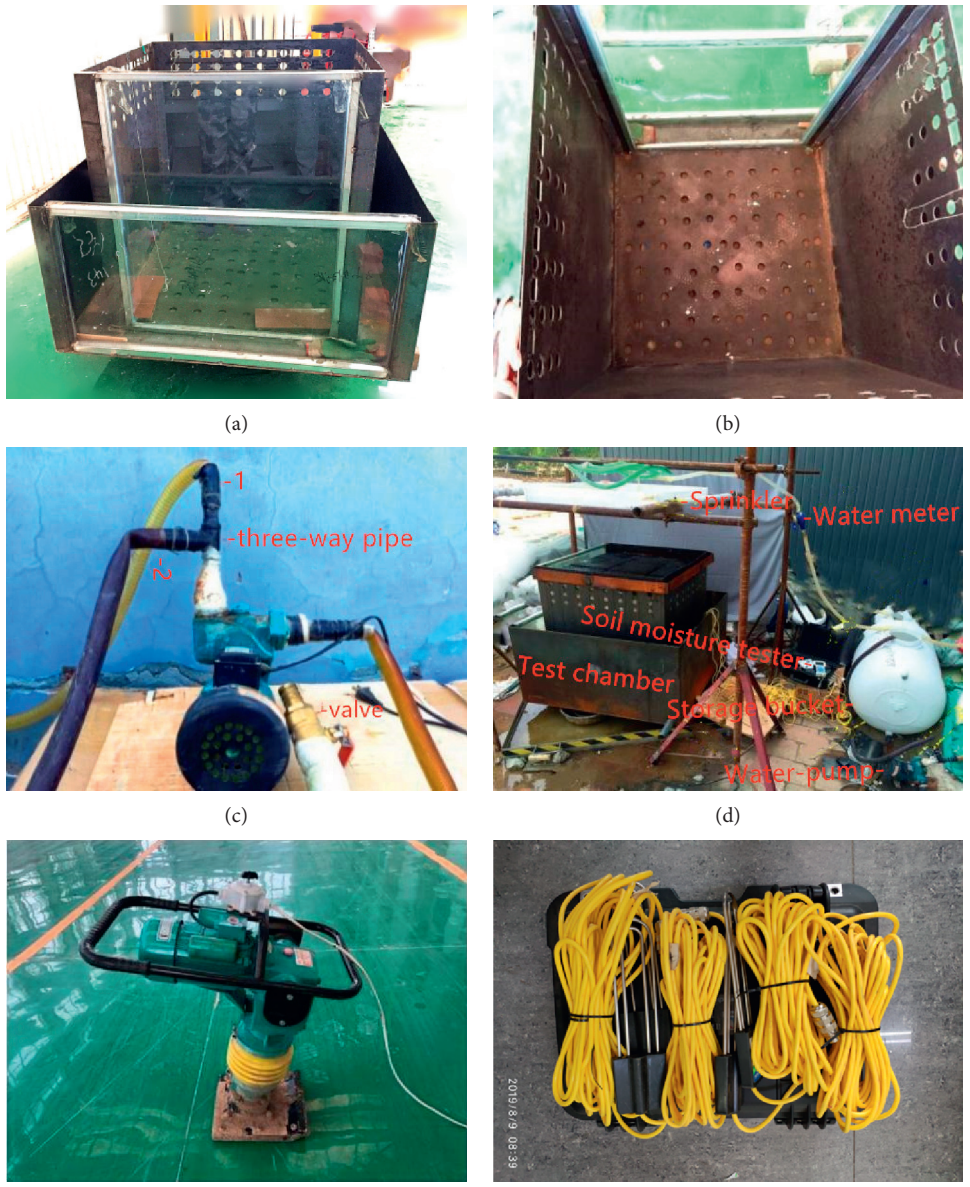

(a) (b) (c) (d) (e) (f)

Figure 6: Artificial rainfall experiment device, (a) test chamber, (b) the bottom of test chamber, (c) pump, (d) rainfall equipment, (e) impact tamping, and (f) moisture tester.

Water meters were used to record the amount of water passing through. The sprinklers were made of plastic, whose length, width, and height were 90 cm, 86.5 cm, and 15 cm, respectively.

In order to monitor the occurrence and ending time of surface runoff and surface runoff values under different rainfall intensities, a certain number of drainage holes were dug at a position that was parallel to the surface layer to

Table 2: Different pavement structure section types.

Number	Sectional type of pavement structure
1	Dense asphalt mixture surface layer 5 cm + base layer 30 cm + cushion layer 8 cm + subgrade 50 cm
2	Large-void asphalt mixture surface layer 5 cm + base layer 30 cm + cushion layer 8 cm + subgrade 50 cm
3	Large-void asphalt mixture surface layer 5 cm + base layer 25 cm + cushion layer 8 cm + subgrade 55 cm
4	Large-void asphalt mixture surface layer 5 cm + base layer 20 cm + cushion layer 8 cm + subgrade 60 cm
5	Large-void asphalt mixture surface layer 5 cm + base layer 15 cm + cushion layer 8 cm + subgrade 65 cm

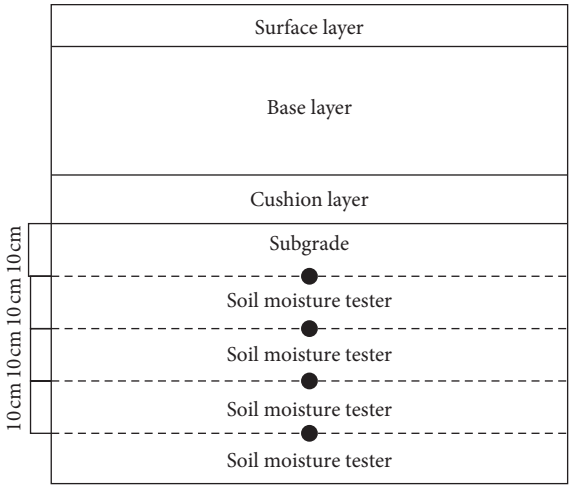

Figure 7: Schematic diagram of moisture analyzer layout.

collect rainwater from the surface runoff. The drainage hole diameter was 0.07 cm, who was dug at intervals of 3 cm. The water in each drainage hole can be collected into the same container through the surrounding sinks as shown in Figure 6(d).

In order to monitor the starting time, ending time, and seepage flow of different rainfall intensities, the water penetrated to the bottom of the pavement structure was collected in a collection container and determined by measuring the amount of water in the container. The artificial rainfall experiment equipment and devices are shown in Figure 6.

5.2. Experimental Process. The artificial simulated rainfall experimental device was used to test 5 types of structural section. The pavement structure is shown in Table 2.

In order to measure the change of soil water content during and after rainfall, 4 soil moisture analyzers were embedded in the soil to measure the soil water change at different depths. The layout diagram is shown in Figures 7 and 8.

6. Analysis of Experimental Results

6.1. Drainage Pavement (Travel Lane). Artificial rainfall experiments were performed on the 1 and 2 cross-section types by using 4 types of rainfall intensity (2.5 mm/min, 3.4 mm/min, 4.6 mm/min, and 5.5 mm/min).

The expression of surface runoff coefficient is shown in the following formula:

Figure 8: Moisture tester layout.

$$\text{surface runoff coefficient} = \frac{\text{surface runoff}}{\text{total rainfall}} \times 100\%. \quad (1)$$

The surface runoff and surface runoff coefficient are shown in Table 3.

The structural section of types 1 and 2 is shown in Figure 9; as the rainfall intensity was 4.6 mm/min, the runoff of rainwater lasted for 60 minutes.

As can be seen from Figure 10(a), when dense asphalt mixture was used as the surface layer, almost all the rainwater was discharged from the slope surface of the road surface and formed surface runoff.

As can be seen from Figure 10(b), when the large-void asphalt mixture was used as the surface layer, only a small

Table 3: Surface runoff coefficients at different rainfall intensities.

Structural section type	5.5 mm (min)		4.6 mm (min)		3.4 mm (min)		2.5 mm (min)	
	Surface runoff (mm)	Surface runoff coefficient (%)	Surface runoff (mm)	Surface runoff coefficient (%)	Surface runoff (mm)	Surface runoff coefficient (%)	Surface runoff (mm)	Surface runoff coefficient (%)
1	630	95.5	520	94.2	380	93.1	277	92.3
2	240	36	160	29	50	12	9	3

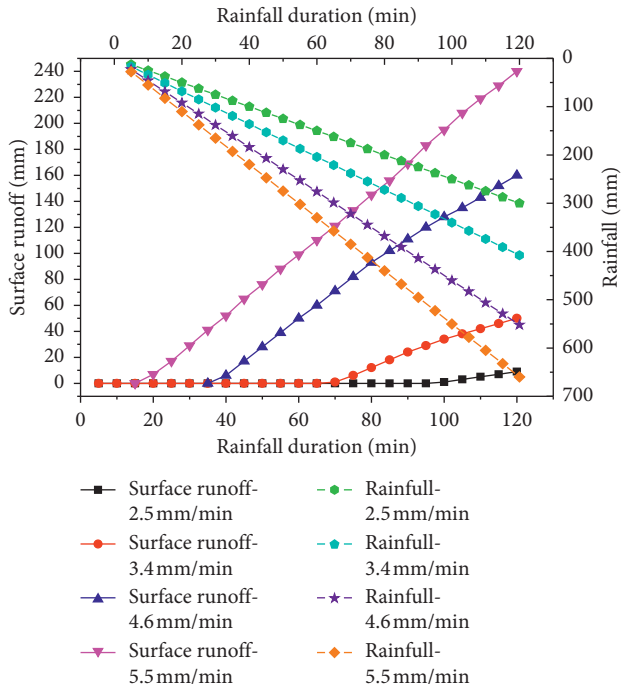

Figure 9: Large-void asphalt pavement.

(a) (b)

Figure 10: Rain intensity 4.6 mm/min (when the rainfall lasted 60 min). (a) Structural section type 1. (b) Structural section type 2.

part of the rain water was discharged from the slope surface of the road surface and formed surface runoff.

Under the conditions of different rainfall intensity, the relationship between the surface runoff and the rainfall duration is shown in Figures 9 and 11 about the structure section types 1 and 2.

As can be seen from Figure 11, the porosity of the dense asphalt mixture was 4% and the surface was almost impermeable. When the rainfall lasted for 5 minutes, the corresponding surface runoff was 5 mm, 9 mm, 16 mm, and 22 mm corresponding to the rainfall intensity with 2.5 mm/min, 3.4 mm/min, 4.6 mm/min, and 5.5 mm/min. When the rainfall lasted for 120 minutes, the corresponding surface runoff was 277 mm, 380 mm, 520 mm, and 630 mm and the corresponding surface runoff coefficients were 92.3%, 93.1%, 94.2%, and 95.5%. And the rainwater almost flowed into the water tank.

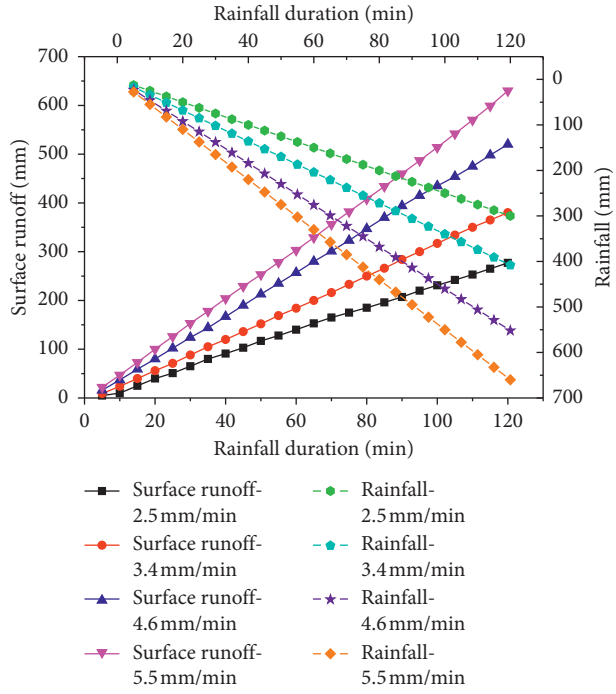

Figure 11: Dense asphalt pavement.

As can be seen from Figure 9, when the rainfall intensity was 2.5 mm/min and the rainfall lasted for 99 minutes, surface runoff began to occur. When the rainfall lasts for 120 minutes, the surface runoff was 9 mm, and the rest of the rainwater penetrated into the impermeable sealing coating and flowed into the tank through the drainage hole.

When the rainfall intensity was 3.4 mm/min and the rainfall lasted for 70 minutes, surface runoff began to be generated. When the rainfall lasted for 120 minutes, the surface runoff was 50 mm.

When the rainfall intensity was 4.6 mm/min and the rainfall lasted for 40 minutes, surface runoff began to be generated. When the rainfall lasted for 120 minutes, the surface runoff was 160 mm.

When the rainfall intensity was 5.5 mm/min and the rainfall lasted for 20 minutes, surface runoff began to be generated. When the rainfall lasted for 120 minutes, the surface runoff was 240 mm.

The corresponding surface runoff coefficients of the four rainfall intensities were 0.03, 0.12, 0.29, and 0.36. With the increasing of rainfall intensity, the surface runoff coefficient gradually increased, and the generation time of surface runoff was also earlier.

The reason for this phenomenon can be analyzed by the flow generation mechanism of large-void asphalt pavement as shown by part 6 in this paper. The experiment shows that the large-void asphalt pavement can greatly reduce the surface runoff compared with dense asphalt pavement.

6.2. Semipermeable Road (Bicycle Lane). Four types of thickness of 30 cm, 25 cm, 20 cm, and 15 cm (corresponding to pavement structure section types 2, 3, 4, and 5) were used to study the influence of the base layer thickness on surface runoff.

According to the experimental data in Table 4, when the rainfall intensity was 5.5 mm/min, the surface runoff coefficients were 5%, 13%, 20%, and 26% corresponding to the base layer thickness of 30 cm, 25 cm, 20 cm, and 15 cm. Therefore, as the increase of the base layer thickness, the surface runoff can be effectively reduced.

The permeability of the cushion was relatively small so that was used as the base layer. When the rainfall intensity was relatively high, the rainwater that penetrated from the surface layer of the large-void asphalt pavement cannot be discharged in time, while the base can temporarily store rainwater, so as to reduce the surface runoff.

The surface runoff was closely related to the thickness and voids of the base.

When the rainfall intensity was 2.5 mm/min, no surface runoff occurred on the 4 thickness pavement layers. So, the surface runoff coefficient was greatly affected by the thickness of water storage reservoir and rainfall intensity.

6.3. Permeable Road (Sidewalk). The variation of soil moisture content with rainfall intensity in the soil foundation and the effect of initial soil moisture content on rainwater infiltration were studied by four types of rainfall intensity of Section 2 pavement structure. The experimental results are shown in Table 5.

The surface runoff was 30 mm, when the rainfall intensity was 5.5 mm/min and the rainfall lasted for 120 min, while the surface runoff was 5 mm, when the rainfall intensity was 4.6 mm/min and the rainfall lasted for 120 min. The rainfall intensity was 3.4 mm/min and 2.5 mm/min,

Table 4: Surface runoff coefficients at different rainfall intensities.

Thickness of base layer (cm)	Rainfall intensity (5.5 mm/min)			Rainfall intensity (4.6 mm/min)			Rainfall intensity (3.4 mm/min)			Rainfall intensity (2.5 mm/min)		
	Total rainfall (mm)	Surface runoff (mm)	Surface runoff coefficient (%)	Total rainfall (mm)	Surface runoff (mm)	Surface runoff coefficient (%)	Total rainfall (mm)	Surface runoff (mm)	Surface runoff coefficient (%)	Total rainfall (mm)	Surface runoff (mm)	Surface runoff coefficient (%)
30	660	33	5	552	5	1	408	0	0	300	0	0
25	660	85	13	552	44	8	408	0	0	300	0	0
20	660	132	20	552	77	14	408	16	4	300	0	0
15	660	171	26	552	104	19	408	29	7	300	0	0

Table 5: Surface runoff coefficients at different rainfall intensities.

Structural section type	5.5 mm (min)		4.6 mm (min)		3.4 mm (min)		2.5 mm (min)	
	Surface runoff (mm)	Surface runoff coefficient (%)	Surface runoff (mm)	Surface runoff coefficient (%)	Surface runoff (mm)	Surface runoff coefficient (%)	Surface runoff (mm)	Surface runoff coefficient (%)
2	30	5	5	1	0	0	0	0

respectively; there is no surface runoff during 120 min rainfall.

As the rainfall continued, the large-void asphalt pavement structure tended to saturate and the rain began to penetrate from the subgrade. So, the amount of rainwater stored in the pavement was the difference between the rainfall and the permeability amount of the soil. The relationship between storage under various rainfall intensities and time is shown in Figure 12.

As can be seen from Figure 13, when the rainfall intensity was 5.5 mm/min, the infiltration started after 42 minutes. All the rainwater fallen was stored in the pavement structure during 42 minutes. As rainfall continued, the rainwater penetrated from the roadbed was less than the rainfall and the rainwater storage capacity of the pavement structure. The rainfall lasted more than 14 hours from start to the end of the infiltration, and the infiltration rainfall was 535 mm.

When the rainfall intensity was 4.6 mm/min, the infiltration started from 54 min. As the rainfall continued, the rainwater penetrated from the roadbed was less than the rainfall and the rainwater storage capacity of the pavement structure just like 5.5 mm/min. The rainfall lasted more than 14 hours from start to the end of the infiltration, and the infiltration rainfall was 438 mm.

When the rainfall intensity was 3.4 mm/min and 2.5 mm/min, the infiltration started from 67 minutes and 83 minutes, respectively. The rainfall lasted more than 14 hours from start to the end of the infiltration, and the infiltration rainfall was 294 mm and 190 mm, respectively.

With the decreasing of rainfall intensity, the infiltration start time was delayed, and the soil infiltration became slower. It can also be seen from Figure 13 that the final water storage capacity of the pavement structure was the same under different rainfall intensity, when the pavement structure section type was the same.

As can be seen from Figure 13, the relationship between infiltration start time and the intensity of rainfall is as follows:

$$y = 1.1x^2 - 21.7x + 130.2. \quad (2)$$

Adjusted R-square = 0.984, x is rainfall intensity, mm/minute; y is infiltration start time, minute.

Within a certain rainfall intensity, the infiltration rate increases with the increasing of rainfall intensity.

The soil moisture in the early stage was constant and the amount of rainwater accumulated in a short period will change with the rainfall intensity, so that the pressure on the roadbed will be different, resulting in different rainwater infiltration rates. With the increase of rainfall, the speed of rainwater infiltration in the subgrade also increased and the infiltration start time was earlier.

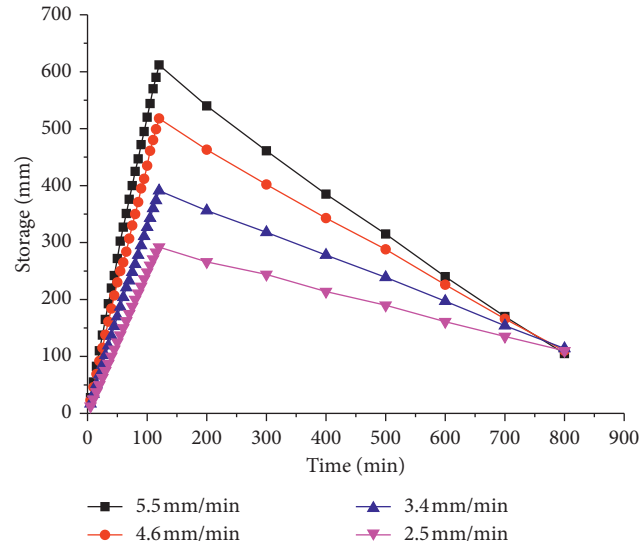

Figure 12: Relationship of storage under different rainfall intensities and time.

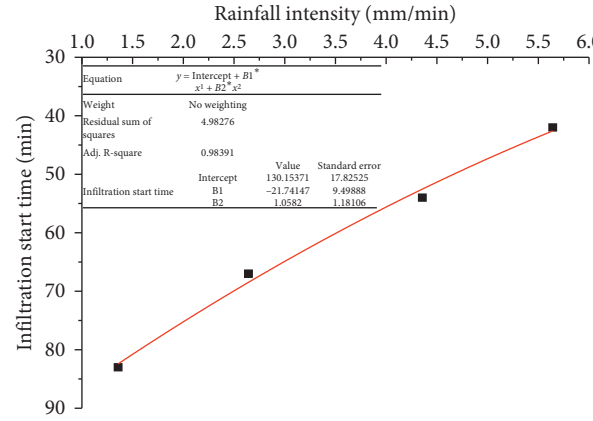

Figure 13: Relationship between rainfall intensity and infiltration start time.

6.4. The Analysis of Changes in Soil Moisture Content. Soil infiltration played an important role in the water cycle, which had great significance to the water resources, agricultural irrigations, and hydrological environment. Soil water infiltration was a dynamic process of water distributed in soil, so the change of soil water will affect the soil infiltration process [25–30].

6.4.1. During the Artificial Raining. According to Yanbin Guan's research on soil surface laminar flow [2], it was easy to meet the conditions for surface laminar flow formation,

when the soil texture had obvious stratification. Rainwater penetrated into the surface layer of the ground and flowed into the lower flow channel after flowing transversely, whose velocity was slower than surface runoff. And the seepage law of the large-void asphalt pavement structure was similar to the above. The relationship between the soil water content in each layer and time under a rainfall intensity of 5.5 mm/min is illustrated in Figure 14.

As can be seen from Figure 14, the soil water content of the depth of 10 cm, 20 cm, 30 cm, and 40 cm was 5.2%, 4.6%, 5%, and 5.6%, respectively, at the initial time. When the rainfall lasted 10 minutes, the soil water content was 20%, 7.5%, 5.2%, and 5.7%, respectively, which indicated that a small amount of rain began to penetrate into the soil to depth 10 cm. However, the soil water content did not reach a saturated state at 10 minutes.

As the rainfall continued, the rainwater penetrated further downward. After 40 minutes, the soil water content of the depth of 10 cm, 20 cm, 30 cm, and 40 cm was 32.6%, 32.2%, 29.5%, and 28.1%, respectively. From the experimental data in Figure 14, the soil water content of the entire roadbed tended to saturate, and the soil layer entered the stage of stable infiltration.

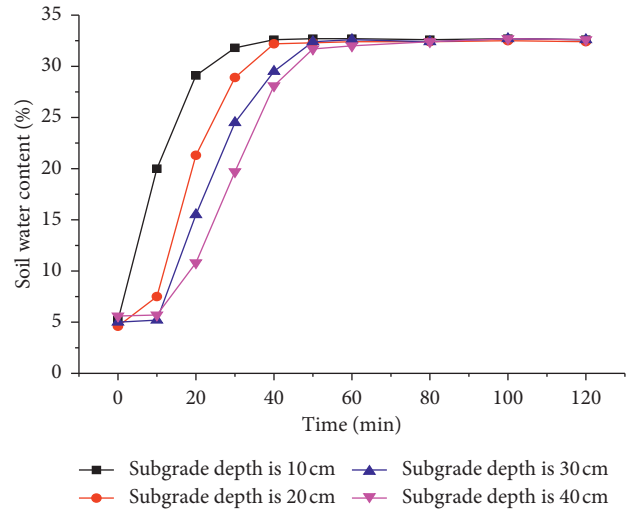

Figure 14: Relationship between soil water content and time.

6.4.2. As the Artificial Raining Ended. When the rainwater stopped and the ground water was exhausted due to evaporation or infiltration, the water in the subgrade soil still needed to penetrate downward for a long time. During the infiltration process, water was redistributed in the soil profile. The soil layer saturated cannot retain all the water, so part of the water continued to move to the deeper soil layer due to suction gradient and gravity of the soil water [31–34].

As can be seen from Figure 15, the soil water content began to decrease slowly with the time increasing at the 10 cm soil depth.

The soil water content decreased greatly within 1-2 days and the decrease ratio reached 39.9% after ending artificial rainfall.

Similarly, the soil water content at the 200 mm, 300 mm, and 40 cm soil depth decreased sequentially with time and the soil water content gradually tended to stabilize. In addition, the downward movement speed of the wet front was smaller found through the plexiglass side. The first reason is that the suction gradient between the two soil layers was correspondingly reduced, when the water of the moist soil layer was reduced and the water of the dry soil layer was increased. The second reason is that the dynamic process of soil moisture after infiltration became very complicated due to the existence of surface flow of large-void asphalt pavement.

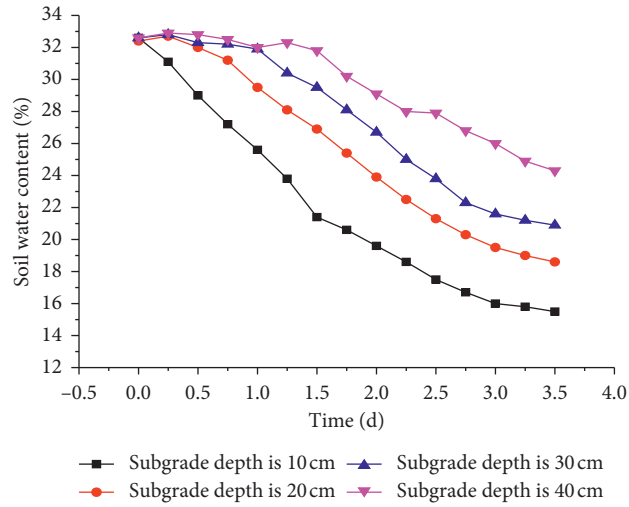

Figure 15: Relationship between soil water content and time at different soil depths.

6.4.3. Effect of Initial Water Content on Infiltration. The different initial water content of the soil will affect the infiltration of rain water and the runoff process [35–39]. So, four different initial soil moisture contents (5.3%, 9.1%, 12.8%, and 16.1%) were used to study the influence law with the same rainfall intensity of 5.5 mm/min. The test results are shown in Figure 16.

As can be seen from Figure 16, the initial infiltration rate was the largest and soil saturation needs the longest rainfall duration, when the initial water content of the soil was 5.3%. Mainly because the initial water content was low, the larger the magnitude of the matrix potential gradient, the larger the average suction force of the infiltration front. As the initial water content increased, the initial infiltration rate became smaller and the infiltration rate became shorter.

Combined with this experiment, when the initial soil moisture content was low, the soil moisture migration can be divided into two stages.

The first was the increasing stage of water content. After the wetting front moved to the layer, it was affected by gravity potential energy and matrix potential energy. The water content of the upper soil increased rapidly, but the water content did not reach saturation, and the soil moisture increased continuously.

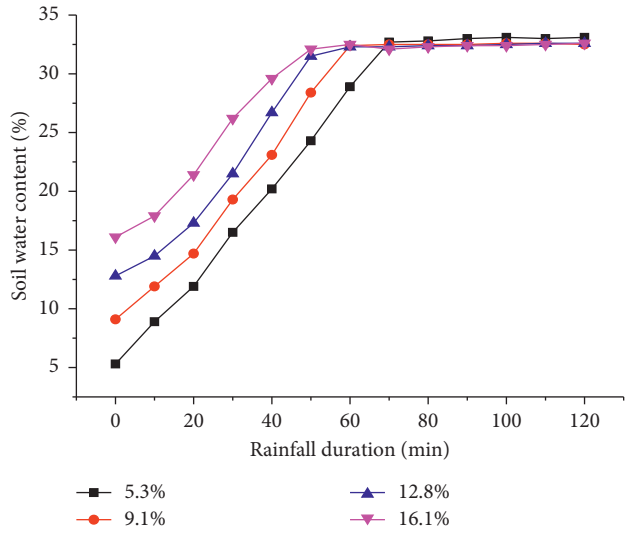

Figure 16: Effect of initial water content at 200 mm depth on infiltration.

The second stage was the stable stage of water content. When the soil moisture was close to saturation, the soil layer began stable infiltration, and the water flux of the soil layer became stable.

This is similar to Bodman's research on the initial water content of nonpermeable brick pavement soil [1].

7. Conclusions

The influence of several different pavement structures such as drainage pavements, semipermeable pavements, and permeable roads on surface runoff reduction was conducted. Secondly, the relationship between soil water content and rainfall duration was analyzed. Finally, the effect of initial water content on rainwater infiltration rates under different rainfall conditions was studied. The artificial rainfall device designed by authors was used to simulate rain on five types of pavement structures with 4 types of rainfall intensity. The conclusions are as follows:

(1) In the drainage pavement, the surface runoff coefficient of the dense asphalt pavement was more than 90%, while the large-void asphalt pavement was less than 40% under different rainfall intensities, which means that the large-void asphalt pavement can effectively reduce the surface runoff.

(2) In semipermeable roads and permeable roads, the surface runoff coefficient at each rainfall intensity decreased with increase of the base layer thickness, mainly because the permeability of the cushion and soil foundation was relatively weak and the base layer stored some water and delayed the generation of surface runoff, when the rainfall lasted for a long time or the rainfall intensity was heavy.

(3) With the increase of rainfall intensity, the surface runoff coefficients of the three pavement structures increased and the surface runoff occurred earlier. The sequence of the surface runoff generated in the three road structures was drainage road, semipermeable road, and permeable road.

(4) In the permeable road, the soil water content quickly reached a saturated state and a stable infiltration situation with the time increasing under the action of water gravity and the gradient of soil water suction. As the initial water content of the soil increased, the time of infiltration began to lag, and the amount of infiltration gradually decreased within 120 minutes of rainfall.

Groundwater level position, antifreezing layer, and traffic load condition will also affect the infiltration and drainage law of permeable pavement. In order to optimize the overall permeable performance of road surface, these factors need to be further studied in the future.

Data Availability

The data used to support the findings of this study are available from the corresponding author upon request.

Conflicts of Interest

The authors declare that they have no conflicts of interest.

Acknowledgments

This work was supported by the National Natural Science Foundation of China (51108151).

References

[1] H. R. Zhu, M. M. Yu, J. Q. Zhu, H. Z. Lu, and R. J. Cao, "Simulation study on effect of permeable pavement on reducing flood risk of urban runoff," *International Journal of Transportation Science and Technology*, vol. 132, pp. 121–130, 2018.

[2] Y. B. Guan, *Water Permeability Mechanism and Structure Design of Large Porous Asphalt Pavement*, Beijing Jiaotong University, Beijing, China, 2008.

[3] F. Gu, D. Watson, J. Moore, and N. Tran, "Evaluation of the benefits of open graded friction course: case study," *Construction and Building Materials*, vol. 189, pp. 131–143, 2018.

[4] Y. Xiong, "Analysis of the permeable asphalt pavement structure of urban roads," *Urban Roads Bridges and Flood Control*, vol. 33, no. 8, pp. 47–49, 2016.

[5] S. Saadeh, A. Ralla, Y. Al-Zubi, and R. Z. Wu, "Application of fully permeable pavements as a sustainable approach for mitigation of stormwater runoff," *International Journal of Transportation Science and Technology*, vol. 8, no. 4, pp. 338–350, 2019.

[6] L. Chu and T. F. Fwa, "Evaluation of surface infiltration performance of permeable pavements," *Journal of Environmental Management*, vol. 238, pp. 136–143, 2019.

[7] Q. Yang, S. Beecham, J. Liu, and D. Pezzaniti, "The influence of rainfall intensity and duration on sediment pathways and subsequent clogging in permeable pavements," *Journal of Environmental Management*, vol. 246, pp. 730–736, 2019.

[8] M. Legret and V. Colandini, "Effects of a porous pavement with reservoir structure on runoff water: water quality and fate

of heavy metals," *Water Science and Technology*, vol. 39, no. 2, pp. 111–117, 1999.

[9] C. J. Pratt, J. D. G. Mantle, and P. A. Schofield, "UK research into the performance of permeable pavement, reservoir structures in controlling stormwater discharge quantity and quality," *Water Science and Technology*, vol. 32, no. 1, pp. 63–69, 1995.

[10] W. Jiang, A. Sha, J. Xiao, Y. Li, and Y. Huang, "Experimental study on filtration effect and mechanism of pavement runoff in permeable asphalt pavement," *Construction and Building Materials*, vol. 100, pp. 102–110, 2015.

[11] M. Koohmishi and G. Shafabakhsh, "Drainage potential of reservoir course of porous pavement for various particle size distributions of aggregate," *Transportation Geotechnics*, vol. 16, pp. 63–75, 2018.

[12] R. Zhong, Z. Leng, and C.-s. Poon, "Research and application of pervious concrete as a sustainable pavement material: a state-of-the-art and state-of-the-practice review," *Construction and Building Materials*, vol. 183, pp. 544–553, 2018.

[13] A. K. Chandrappa and K. P. Biligiri, "Pervious concrete as a sustainable pavement material – research findings and future prospects: a state-of-the-art review," *Construction and Building Materials*, vol. 111, pp. 262–274, 2016.

[14] M. Kayhanian, H. Li, J. T. Harvey, and X. Liang, "Application of permeable pavements in highways for stormwater runoff management and pollution prevention: California research experiences," *International Journal of Transportation Science and Technology*, vol. 8, no. 4, pp. 358–372, 2016.

[15] L. Z. Hou, S. Y. Feng, and Z. W. Han, "Effect of pervious brick pavement cushion structure on urban rainwater infiltration process," *Journal of China Agricultural University*, vol. 11, no. 4, pp. 83–88, 2006.

[16] E. Z. Bean, W. F. Hunt, and D. A. Bidelspach, "Field survey of permeable pavement surface infiltration rates," *Journal of Irrigation and Drainage Engineering*, vol. 133, no. 3, pp. 249–255, 2007.

[17] Z. C. Xu and Y. C. Guo, "Simulated experimental study on rainfall runoff with different underlying surface conditions in the city," *South-to-North Water Transfer and Water Conservancy Science and Technology*, vol. 1, pp. 64–66, 2007.

[18] Q. Z. Cai, Z. H. Chen, X. Chen et al., "Simulation of urban rainwater control effect with low impact development measures," *Water Resources Protection*, vol. 33, no. 2, pp. 31–36, 2017.

[19] F. Zhao, S. H. Zhang, J. G. Chen et al., "Research on rainwater infiltration collection and runoff reduction technology in permeable pavement," *Water Supply and Drainage*, vol. 37, no. S1, pp. S1254–S1258, 2011.

[20] CJJ/T 190-2012, *Technical Specifications for Permeable Asphalt Pavement*, China Construction Industry Press, Beijing, China, 2012.

[21] Z. Peng and L. Qingfu, "Effect of polypropylene fibre on mechanical and shrinkage properties of cement-stabilised macadam," *International Journal of Pavement Engineering*, vol. 10, no. 6, pp. 435–445, 2009.

[22] P. Peng Zhang and Q. Qingfu Li, "Experimental study on shrinkage properties of cement-stabilized macadam reinforced with polypropylene fiber," *Journal of Reinforced Plastics and Composites*, vol. 29, no. 12, pp. 1851–1860, 2010.

[23] P. Zhang, Q. Li, and H. Wei, "Investigation of flexural properties of cement-stabilized macadam reinforced with polypropylene fiber," *Journal of Materials in Civil Engineering*, vol. 22, no. 12, pp. 1282–1287, 2010.

[24] Y. Zheng, P. Zhang, Y. Cai, Z. Jin, and E. Moshtagh, "Cracking resistance and mechanical properties of basalt fibers reinforced cement-stabilized macadam," *Composites Part B: Engineering*, vol. 165, pp. 312–334, 2019.

[25] J. L. Zhang, L. L. Zhou, R. M. Ma et al., "Influence of soil moisture content and soil and water conservation measures on time to runoff initiation under different rainfall intensities," *Catena*, vol. 182, pp. 104–172, 2019.

[26] J. Norambuena-Contreras, G. Arbat, P. J. García Nieto, and D. Castro-Fresno, "Nonlinear numerical simulation of rainwater infiltration through road embankments by FEM," *Applied Mathematics and Computation*, vol. 219, no. 4, pp. 1843–1852, 2012.

[27] M. Kamali, M. Delkash, and M. Tajrishy, "Evaluation of permeable pavement responses to urban surface runoff," *Journal of Environmental Management*, vol. 187, pp. 43–53, 2017.

[28] C. Zeng, Q. J. Wang, and J. Fan, "Effect of initial water content on soil vertical line source infiltration characteristics," *Transactions of the Chinese Society of Agricultural Engineering*, vol. 26, pp. 24–30, 2010.

[29] Y. Liu, Y. Xin, Y. Xie, and W. Wang, "Effects of slope and rainfall intensity on runoff and soil erosion from furrow diking under simulated rainfall," *Catena*, vol. 177, pp. 92–100, 2019.

[30] H. S. Chen, M. Shao, and Y. Xie, "Effects of initial soil moisture content on rainfall infiltration on slope and soil water redistribution," *Transactions of the Chinese Society of Agricultural Engineering*, vol. 22, no. 1, pp. 44–47, 2006.

[31] N. Xie, M. Akin, and X. Shi, "Permeable concrete pavements: a review of environmental benefits and durability," *Journal of Cleaner Production*, vol. 210, pp. 1605–1621, 2019.

[32] T. Lucke, F. Boogaard, and F. van de Ven, "Evaluation of a new experimental test procedure to more accurately determine the surface infiltration rate of permeable pavement systems," *Urban, Planning and Transport Research*, vol. 2, no. 1, pp. 22–35, 2014.

[33] L. Chu, B. Tang, and T. F. Fwa, "Evaluation of functional characteristics of laboratory mix design of porous pavement materials," *Construction and Building Materials*, vol. 191, pp. 281–289, 2018.

[34] L. Gholami, N. Karimi, and A. Kavian, "Soil and water conservation using biochar and various soil moisture in laboratory conditions," *Catena*, vol. 182, pp. 104–151, 2019.

[35] L. Zhao, R. Hou, F. Wu, and S. Keesstra, "Effect of soil surface roughness on infiltration water, ponding and runoff on tilled soils under rainfall simulation experiments," *Soil and Tillage Research*, vol. 179, pp. 47–53, 2018.

[36] H. Liu, T. W. Lei, and J. Zhao, "Effects of initial soil moisture content and rainfall intensity on infiltration performance of clay loess," *Science of Soil and Water Conservation*, vol. 7, pp. 1–6, 2009.

[37] C. Hernández-Crespo, M. Fernández-Gonzalvo, M. Martín, and I. Andrés-Doménech, "Influence of rainfall intensity and pollution build-up levels on water quality and quantity response of permeable pavements," *Science of the Total Environment*, vol. 684, pp. 303–313, 2019.

[38] M. X. Liu, Y. Nie, and J. Yu, "Infiltration process of clayey soil under different initial moisture content," *Acta Ecologica Sinica*, vol. 32, pp. 871–878, 2012.

[39] L. L. Song, J. F. Zhang, and R. Gao, "Effect of the initial moisture content of the upper soil layer on the water infiltration in the middle finger flow of layered soil," *Journal of China Agricultural University*, vol. 18, pp. 174–181, 2013.

Hindawi
Advances in Civil Engineering
Volume 2020, Article ID 8810440, 17 pages
https://doi.org/10.1155/2020/8810440

Research Article

Flexural Behavior of Fiber-Reinforced Self-Stressing Concrete T-Shaped Composite Beams

Boxin Wang, Ruichang Fang, and Qing Wang

College of Construction Engineering, Jilin University, Changchun 130021, China

Correspondence should be addressed to Boxin Wang; boxinwang@jlu.edu.cn

Received 16 March 2020; Revised 6 May 2020; Accepted 20 May 2020; Published 24 June 2020

Academic Editor: Yifeng Ling

Given the excellent crack resistance performance of steel fiber-reinforced self-stressing concrete (SFRSSC), the bending performance of some composite beams with SFRSSC laminated layers was studied. The experiment conducted in this study comprised a single-span composite beam test (including 3 test beams) and a two-span continuous composite beam test (including 2 test beams). All the test beams were T-shaped. The cracking load, yielding load, and ultimate load of all the test beams were recorded and comparatively analyzed. Experimental results showed that the cracking load of the test beam with an SFRSSC laminated layer is significantly increased. Mechanical analysis and numerical simulation of the test beams were conducted, and the obtained results agreed well with the experimental results. The composite beams under different working conditions were also numerically simulated. Through the simulation, reasonable ranges of precompressive stress and length of the SFRSSC laminated layer at intermediate support of continuous composite beam were obtained.

1. Introduction

As an important part of a bridge, a bridge deck pavement can protect road plates from direct wheel abrasion and the main girder from erosion by rain and other harmful substances. Furthermore, vehicle load is dispersed by deck pavement. Cement concrete and asphalt concrete are widely used for deck pavement, and these concrete types can meet the standard requirement [1]. When the deck pavement cracks, the main girders of the bridge will be exposed to the natural environment, affecting the normal service and durability of the bridge structure [2–5]. Thus, experts from China and other countries have conducted various studies on bridge deck pavement in recent years. Ultra-high-performance fiber-reinforced concrete (UHPFRC) [6–20], microexpansion polypropylene fiber concrete [21], ECC [22, 23], steel fiber polymer concrete [24–26], and other special materials have been introduced and studied for bridge deck pavement.

During the hardening process of steel fiber-reinforced self-stressing concrete (SFRSSC), the expansion of self-stressing concrete is limited by steel, steel fibers, and other constraint surfaces. A certain chemical precompressive stress generated in the concrete enhances the crack resistance of concrete. The concrete in the support area of the continuous concrete bridge easily cracks because of the negative moment. Given the excellent crack resistance performance of SFRSSC, the bending performance of some composite beams, which have SFRSSC laminated layers, was investigated in this study. The experiment included a single-span composite beam test and a two-span continuous composite beam test. All of the test beams were T-shaped. Furthermore, properties of the composite beams under different conditions were studied by numerical simulation. Different self-stress values and lengths of SFRSSC laminated layer were taken into account. The conclusion could provide a reference for the design of SFRSSC deck pavement.

2. Materials and Properties

2.1. Materials. Two kinds of cement are used in the experiment, Portland cement P.O. 32.5R for ordinary concrete (*C*) and steel fiber reinforced concrete (SFRC) and sulfur aluminate cement 4.0 for SFRSSC. The aggregate was composed of limestone with particle diameters ranging from

5 mm to 20 mm and high-quality river sand. The grading curves of the stone and sand are showed in Figures 1 and 2, respectively. The type of steel fiber used in the experiment was HE 0.75/35. The properties of the steel fiber are shown in Table 1. The yield strength of the reinforcement used in the test was 335 MPa, and the yield strength of the stirrup was 300 MPa. The tensile strength, ultimate elongation, and yield strength of reinforcement with different diameters were measured by a material mechanics test. Six specimens were tested for each kind of reinforcement, and the results are shown in Table 2. All concrete specimens in the experiment were prepared with tap water. Sika ViscoCrete 3301 water-reducing agent was used in the experimental specimens to increase the workability of concrete.

2.2. Properties of Concrete. Three kinds of concrete were used in experiment, including ordinary concrete, SFRC, and SFRSSC. The mixture ratios for these three kinds of concrete are shown in Table 3. Cubic compressive strength (f_{cu}), axial compressive strength (f_c), elastic modulus (E_c), and splitting tensile strength (f_{ts}) were measured for each kind of concrete. Six specimens were prepared to test every property of each kind of concrete. Table 4 shows the test results.

3. Experimental Investigation

3.1. Test Setup. The test includes two parts. The first part is the single-span composite T-shaped beam test. Three test beams were fabricated to simulate the force condition of the bridge structure with SFRSSC as deck pavement. The deck pavement of three test beams used ordinary concrete, SFRC, or SFRSSC. In the first part, the influence of the SFRSSC deck pavement on the crack resistance and flexural properties of the test beams is mainly investigated. The second part is a two-span continuous composite T-shaped beam test. This part includes two test beams, separately decked with ordinary concrete and SFRSSC. In this part, the bridge structure with SFRSSC deck pavement is simulated, and its working performance is investigated. The details of test beams are presented in Figures 3–7.

3.2. Specimen Preparation. The basic T-shaped beams were cast with ready-mix concrete after finishing the mesh reinforcement (Figure 7). The specimens were left at room temperature and covered with wet straw matting for 28 days. Subsequently, the concrete laminated layer was poured after a chiseled concrete surface was attained (Figures 8 and 9). The beams were aged for another 28 days (Figure 10). The details of the test beams are presented in Tables 5 and 6.

3.3. Test Program. For the single-span composite T-shaped beam test, beams were loaded with two concentrated loads (four-point bending scheme) which applied 1000 mm from the support (Figure 4). For the two-span continuous composite T-shaped beam test, beams were loaded with concentrated loads applied in the middle of every span. All the test loads were applied once. The experimental data

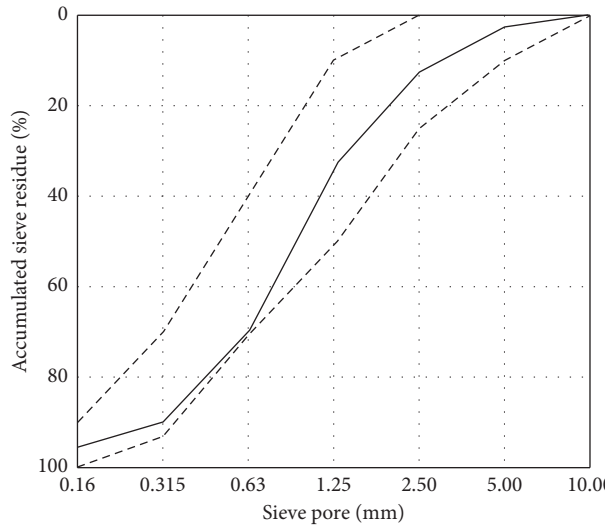

Figure 1: Grading curve of sand.

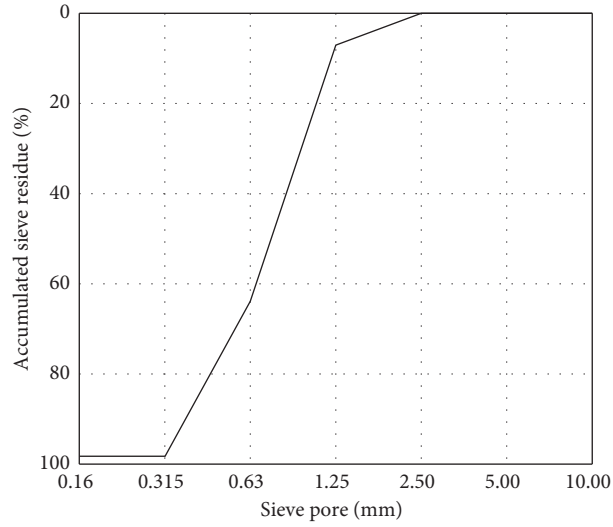

Figure 2: Grading curve of stone.

recorded during the test were as follows: cracking load, cracking deflection, ultimate bearing capacity, the strains of some special sections, deflection, crack width, and the relative slip between the laminated layer and the basic T-shaped beams. The instruments used in the experiment and their locations are shown in Figures 4, 7, 10, and 11.

4. Test Results

4.1. Single-Span Composite T-Shaped Beam Test Results

4.1.1. Crack Development. All experimental beams suffered flexural failure. The concrete in the compressive area was crushed as the test beams failed (Figure 12). The tests showed that beam CCB-1 cracked first, followed by SCB-1 and ZCB-1. As shown in Figure 13, the crack in CCB-1 developed faster than those in SCB-1 and ZCB-1 initially. However, when the test load reached 60 kN·m, the crack growth rate in SCB-1 suddenly accelerated, and the crack width

Table 1: Properties of steel fiber.

Length (mm)	Equivalent diameter (mm)	Tensile strength (MPa)	Ultimate elongation (%)	Elastic modulus (GPa)
35	0.7	600	12	200

Table 2: Properties of reinforcement.

Diameter (mm)	Elastic modulus (GPa)	Yield strength (MPa)	Tensile strength (MPa)	Ultimate elongation (%)
6.5	210	486.6	734.3	30
8	210	306.5	444.9	31.6
18	200	349.9	521.0	24.2
20	200	377.4	571.1	24.5

Table 3: Mixture ratios of different kinds of concrete (kg/m^3).

Concrete	Water	Cement	Sand	Stone	Sika3301	Steel fiber
C	193	350	645.7	1133	6.50	0
SFRC	172	541	765	974	5.41	25.6
SFRSSC	250	550	609	913	8.25	23.3

Table 4: Mechanical prosperities of concrete.

Concrete	f_{cu} (MPa)	f_c (MPa)	E_c (GPa)	f_{ts} (MPa)
C	48.7	45.2	33.5	3.5
SFRC	60.5	55.9	36.0	5.1
SFRSSC	59.9	52.0	33.4	5.2

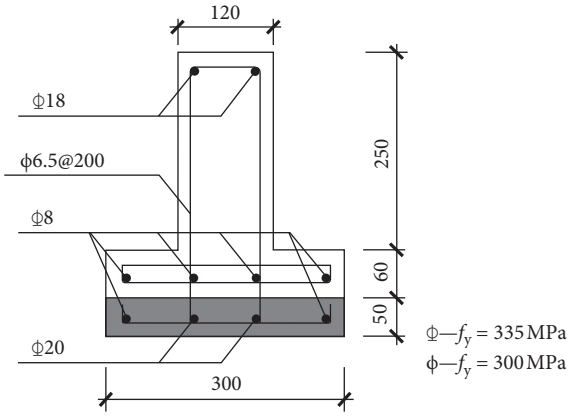

Figure 3: Reinforcement of single-span composite T-shaped beams.

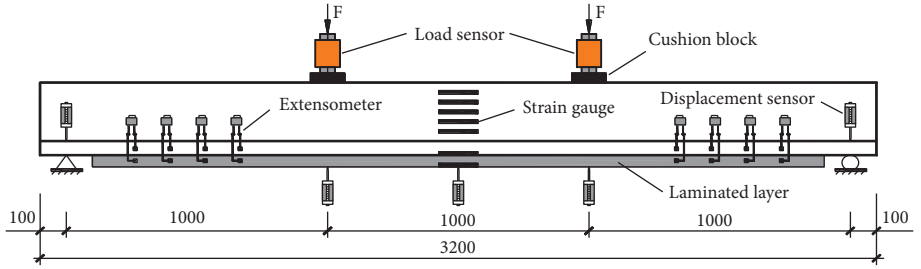

Figure 4: Details of single-span composite T-shaped beam test setup.

approached that in CCB-1. As the test beams started to yield, the crack width of CCB-1 reached 0.6 mm, whereas the crack widths of SCB-1 and ZCB-1 were only 0.4 mm and 0.2 mm, respectively. The development of the crack height in each of the three test beams is shown in Figure 14. As shown in Figure 14, the crack heights of the test beams developed at

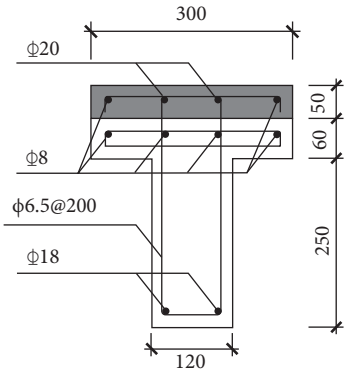

Figure 5: Reinforcement of the cross section at the middle support.

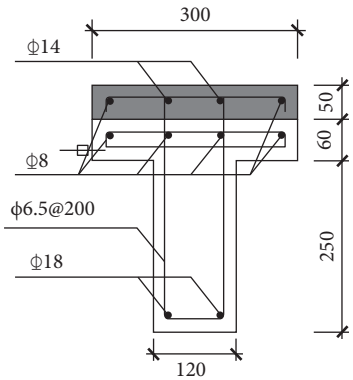

Figure 6: Reinforcement of the cross section at the midspan.

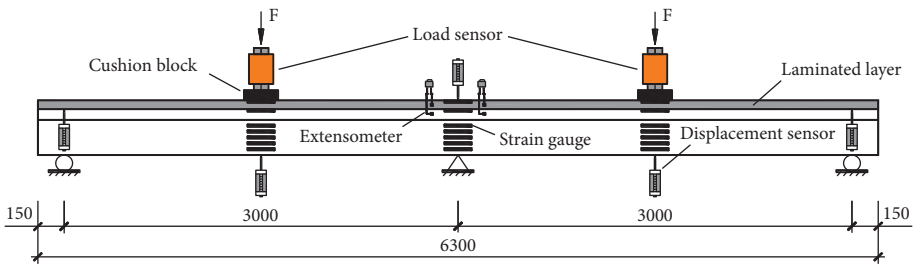

Figure 7: Details of the two-span continuous composite T-shaped beam test setup.

Figure 8: Bars.

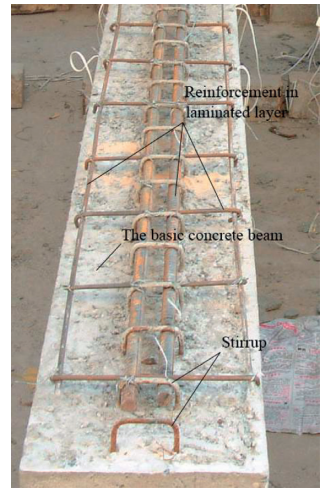

Figure 9: Chiseled basic T-shaped beams.

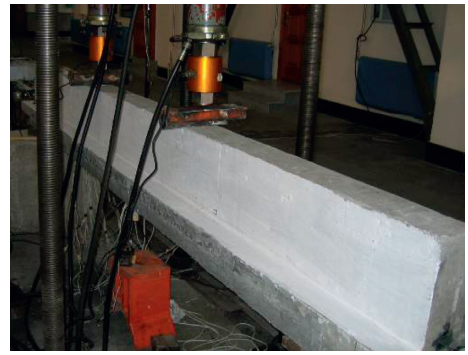

Figure 10: Single-span composite T-shaped beam.

Table 5: Details of single-span beams.

Beam	Concrete of laminated layer	Stirrup ratio (%)	Reinforcement ratio (%)
CCB-1	Ordinary concrete	0.24	4.86
SCB-1	SFRC	0.24	4.86
ZCB-1	SFRSSC	0.24	4.86

Table 6: Details of two-span continuous beams.

Beam	Concrete of laminated layer	Stirrup ratio (%)	Reinforcement ratio (%)
CCB-2	Ordinary concrete	0.24	0.97
ZCB-2	SFRSSC	0.24	0.97

the same speed, rapidly reaching 100 mm at the beginning. After a short plateau phase, the crack heights of CCB-1 and SCB-1 reached 200 mm within a short time. Compared with CCB-1 and SCB-1, ZCB-1 demonstrated a slow crack height development. Finally, before the test beams failed, the cracks in the test beams CCB-1, SCB-1, and ZCB-1 reached similar heights of 247 mm, 226 mm, and 238 mm, respectively.

When the test beams cracked, the transverse crack widths were minimal and insufficient to pull out the steel fiber. The steel fibers together with the steel bars partially bore the tension; thus, the crack development was impeded. For ZCB-1, aside from the steel fibers, the prepressing stress generated by the self-stressing concrete could also hinder crack development. At the beginning of the test, the prepressing stress offset the tensile stress caused by the test load. Thus, the cracking stage of the test beam was postponed; as a result, the cracking load of the composite beam was improved. This crack delay phenomenon is clearly shown in Figures 13 and 14.

4.1.2. Load-Displacement Curve Analysis. The load-displacement curves of the test beams are shown in Figure 15. According to Figure 15, every load-displacement curve of

Figure 11: Two-span continuous composite T-shaped beam actual test setup.

Figure 12: Cracked test beam SCB-1.

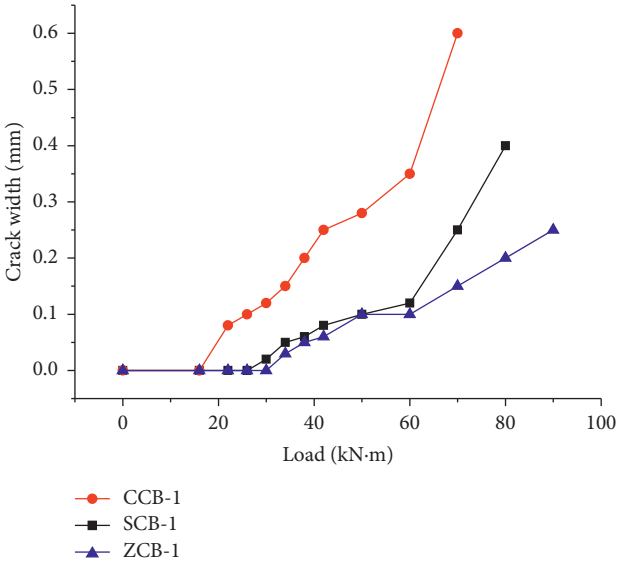

Figure 13: Development of crack width.

the three test beams consists of three phases: elastic, yielding, and destruction. The cracking load, yielding load, and ultimate load of every test beam were derived from Figure 15 and the test records and are shown in Table 7. As shown in Table 7, the SFRSSC laminated layer significantly improved the cracking loads of the composite beams. Compared with the cracking load of test beam CCB-1, the cracking load of SCB-1 increased by 16.83%, and the cracking load of ZCB-1 increased by 50.48%.

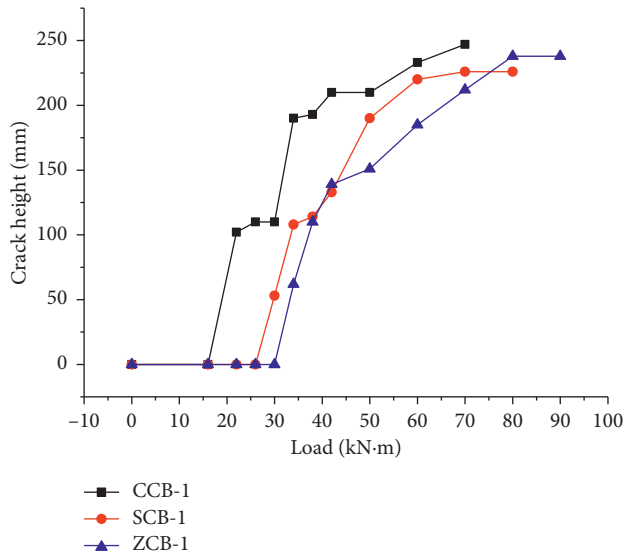

Figure 14: Development of crack height.

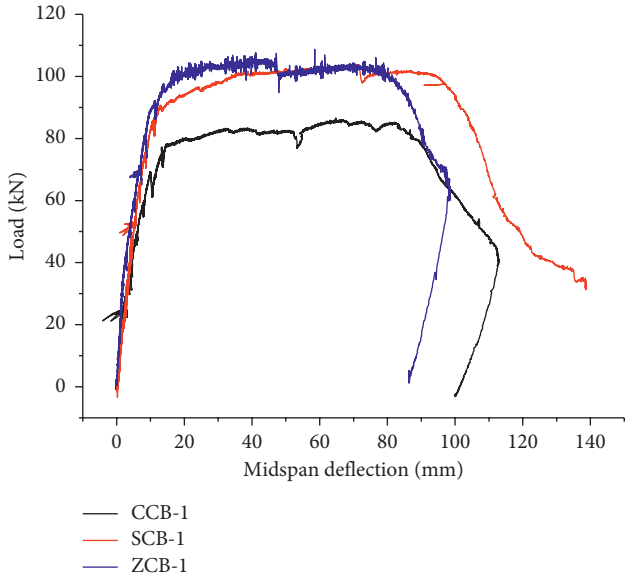

Figure 15: Load-displacement curves of the single-span composite T-shaped beams.

Table 7: Cracking load, yielding load, and ultimate load of test beams.

Test beams	Cracking load (kN)	Yielding load (kN)	Ultimate load (kN)
CCB-1	23.77	78.05	86.60
SCB-1	27.77	90.45	104.10
ZCB-1	35.77	93.63	105.71

4.2. Two-Span Continuous Composite T-Shaped Beam Test

4.2.1. Load-Displacement Curve Analysis. Two test beams were loaded to simulate the flexural properties of the continuous bridge structure with SFRSSC deck pavement and investigate its flexural properties. During the test, flexural failure occurred in all test beams (Figure 16). The load-displacement curves of the test beams are presented in Figure 17. The cracking load, yielding loads at the midspan and middle support, and ultimate deflection are presented in Table 8.

The results showed that the cracking load and yielding load of ZCB-2 were 120% and 14.05% higher than those of CCB-2, respectively. The SFRSSC laminated layer

Figure 16: Two-span continuous composite T-shaped beams at failure.

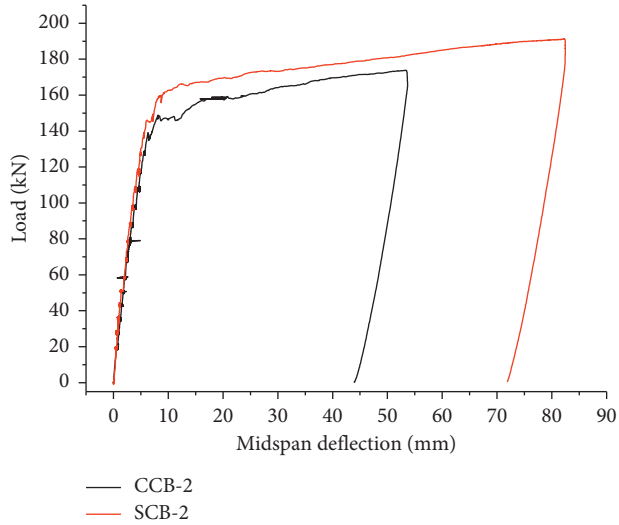

Figure 17: Load-displacement curves of the two-span beams.

Table 8: Test results of the two-span continuous composite T-shaped beams.

Test beam	Cracking load (kN·m)	Yielding load at the middle support (kN·m)	Yielding load at the midspan (kN·m)	Ultimate deflection (mm)
CCB-2	13.05	85.41	90.81	53.52
ZCB-2	28.84	97.41	92.21	81.96

significantly improved the crack resistance of the continuous T-shaped composite beams. Under the vertical load located in the adjacent span, a considerable negative moment occurred in the cross section at the intermediate support, mainly causing the cracking in the bridge. The SFRSSC used in the test exhibited good performance in terms of crack resistance because of the presence of its own self-chemical stress. Before the test even started, a certain precompressive stress generated by SFRSSC already existed in the laminated layer of ZCB-2. This precompressive stress postponed concrete cracking at the middle support when loading was initiated. Thus, the SFRSSC laminated layer enhanced the crack resistance of the test beams. After concrete cracking, the presence of steel fibers impeded the crack development in concrete, resulting in a slight improvement in the yielding load. However, the use of steel fibers is not a decisive factor on yielding load, whose increase is not significant.

For the cross section at the midspan, the SFRSSC laminated layer has minimal influence on the yielding load, as shown in Table 8. However, with regard to deformation, the ultimate deflection in beam ZCB-2 was 53.1% higher than that in beam CCB-2 when the test beams failed. During the experiment, the deflection in the test beams was recorded. As shown in Figure 17, in the initial stage, the deflection in ZCB-2 was significantly less than that in CCB-2. As the test load increased, the deflection gap between the two test beams was decreasing. At the beginning of experiment, the precompressive stress generated by SFRSSC delayed the cracking of concrete beams; thus, the stiffness of the test beams improved. Therefore, the deflection in ZCB-2 was less than that in CCB-2 under the same load. After the concrete around the intermediate support cracked, the precompressive stress inside the SFRSSC was released. Cracks gradually fully developed. The deflection gap between ZCB-2 and CCB-2 was decreasing with the dissipation of the precompressive stress. After the test beams entered the yield stage, the steel fibers in ZCB-2 enhanced its stiffness, resulting in its ultimate deflection to be significantly higher than that in CCB-2, as shown in Figure 17.

4.2.2. Crack Development. The crack development in each of the two test beams was observed during the test program. Figures 18–20 describe the crack width development and crack height development with respect to the test load. Figures 21 and 22 show the distributions of cracks in beams ZCB-2 and CCB-2, respectively. The development trends of the cracks around the middle support of the two-span continuous composite T-shaped beams are similar to those of the single-span composite T-shaped beams. The precompressive stress generated by SFRSSC delayed the crack in the concrete around the middle support. Thus, the width and the height developments of the crack in beam ZCB-2 lagged behind those in beam CCB-2. As the test load increased and the maximum precompressive stress dissipated, the crack widths and crack heights of the two test beams converged.

5. Theoretical Analysis

With the numerical simulation results and experimental results as reference, a theoretical analysis was conducted to calculate the cracking load of the single-span composite T-shaped beams.

The basic assumptions are as follows:

(1) The deformation of the composite beams is aligned with the plane section assumption.

(2) No relative slip exists between steel and concrete.

(3) The constitutive relations for steel and concrete are known.

(4) No relative slip exists between the laminated layer and basic concrete beam.

(5) The deformation of each of the composite beams meets the minimal deformation assumption.

According to the basic assumptions, cross-sectional strains of the single-span composite T-shaped beams are continuous when subjected to bending, as shown in Figure 23. Owing to the precompressive stress in the SFRSSC laminated layer, the stress broke down in the composition plane (Figure 23). Therefore, the sectional corner (φ) is

$$\varphi = \frac{\sigma_{zt} + \sigma_{z0}}{h - x}. \tag{1}$$

Two equilibrium relations are apparent in the cross section of the test beams including

$$\int_0^x b\sigma \mathrm{d}y + \sigma_s' A_s' \int_0^{h-x-h_f-h_p} b\sigma \mathrm{d}y + \int_{h-x-h_f-h_p}^{h-x-h_p} b_f \sigma \mathrm{d}y + \int_{h-x-h_p}^{h-x} b_f (\sigma - \sigma_0)\mathrm{d}y + \sigma_s A_s, \tag{2}$$

$$M = \int_0^x b\sigma y \mathrm{d}y + \sigma_s' A_s' (x - a_s') + \int_0^{h-x-h_f-h_p} b\sigma y \mathrm{d}y + \int_{h-x-h_f-h_p}^{h-x-h_p} b_f \sigma y \mathrm{d}y + \int_{h-x-h_p}^{h-x} b_f (\sigma - \sigma_0) y \mathrm{d}y + \sigma_s A_s (h - x - a_s). \tag{3}$$

The constitutive relation for concrete [27] is

$$\sigma_c = \begin{cases} \sigma_0 \left[2\left(\dfrac{\varepsilon_c}{\varepsilon_0}\right) - \left(\dfrac{\varepsilon_c}{\varepsilon_0}\right)^2 \right], & 0 \le \varepsilon_c \le \varepsilon_0, \\ \sigma_0 \left[1 - 0.15\left(\dfrac{\varepsilon - \varepsilon_0}{\varepsilon_u - \varepsilon_0}\right) \right], & \varepsilon_0 < \varepsilon_c \le \varepsilon_u. \end{cases} \tag{4}$$

The constitutive relation for steel is

$$\sigma_s = \begin{cases} E_s, & 0 \le \varepsilon_s \le \varepsilon_y, \\ f_y, & \varepsilon_y < \varepsilon_s. \end{cases} \tag{5}$$

According to our previous studies [28–30], the precompressive stress of SFRSSC can been calculated by

$$\sigma_{z0} = \sigma_{\mathrm{rz}} + \sigma_{\mathrm{rz},f} = \frac{\rho}{1 - \rho} E_s C e^{-\alpha\rho} + 0.368 \alpha_t \rho_f \frac{l_f}{d_f} f_{\mathrm{tk}}, \tag{6}$$

where ρ is the reinforcement ratio of the SFRSSC laminated layer, α and C are the parameters of SFRSSC, σ_{rz} is the precompressive stress caused by the limitation of steel, and $\sigma_{\mathrm{rz},f}$ is the precompressive stress caused by the limitation of steel fibers.

By substituting the parameters obtained from experiment into formula (6), the precompressive stress of SFRSSC used in this test is

$$\sigma_{z0} = 2.17\ \mathrm{MPa}. \tag{7}$$

With the solutions to (2)–(5), the theoretical crack moment of beam ZCB-1 can be derived as

$$M_{\mathrm{ZCB-1}} = 35.95\ \mathrm{kN \cdot m}. \tag{8}$$

The following theoretical crack moments of CCB-1 and SCB – 1 are derived by the same method:

$$\begin{aligned} M_{\mathrm{CCB-1}} &= 16.8\ \mathrm{kN \cdot m}, \\ M_{\mathrm{SCB-1}} &= 27.3\ \mathrm{kN \cdot m}. \end{aligned} \tag{9}$$

6. Numerical Simulation

6.1. Modeling. In this paper, a numerical simulation was performed with the software ANSYS. The numerical simulation analyses were performed for both the single-span composite T-shaped beams and the two-span continuous composite T-shaped beams. Furthermore, two additional variables were considered, namely, the precompressive stress and the length of the SFRSSC laminated layer.

The Solid65 element can be used in a 3D solid model with or without reinforcement. It was used in this study to simulate the concrete because of its capability to handle the nonlinearity of materials. The space bar element Link8 was used to simulate the reinforcement, which could withstand moments. In the nonlinear analysis, an integral model was used for the basic concrete beam, whereas a separate model was used for the concrete in the laminated layer. In all simulation beams, the bonding between concrete and steel was good, exhibiting the absence of a slip. For the model, the constitutive relation for concrete proposed by Hognestad and expressed in (4) was used, and five stress-strain

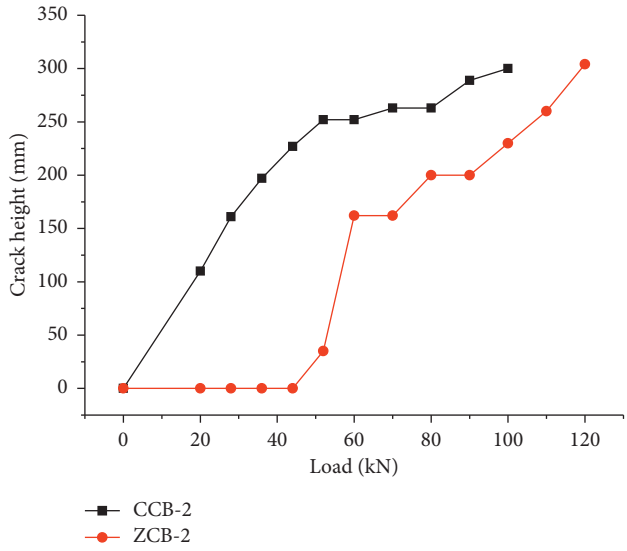

Figure 18: Development of crack height at the middle support.

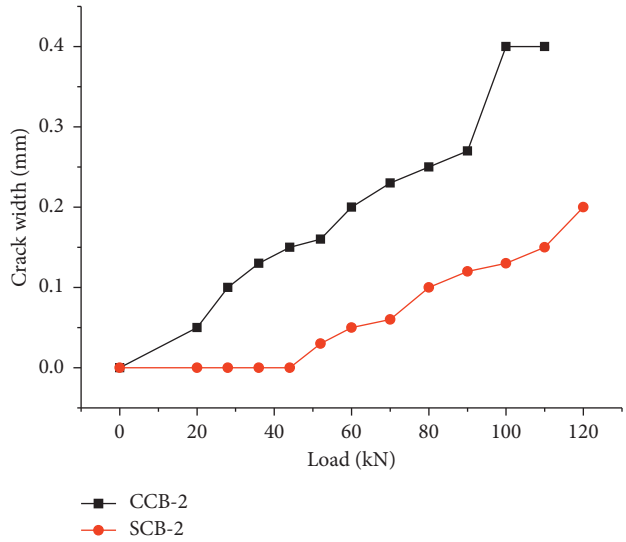

Figure 19: Development of crack width at the middle support.

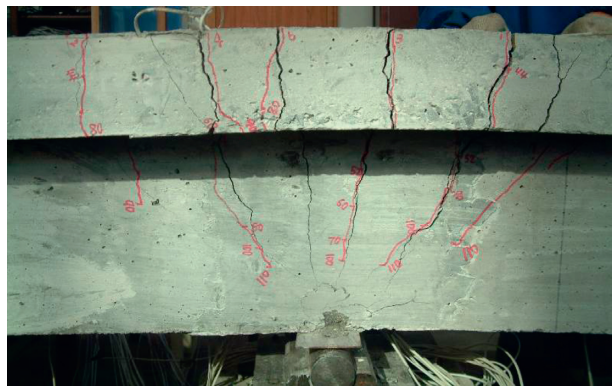

Figure 20: Cracks at the middle support.

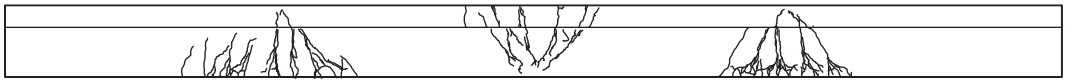

Figure 21: Cracks in test beam ZCB-2.

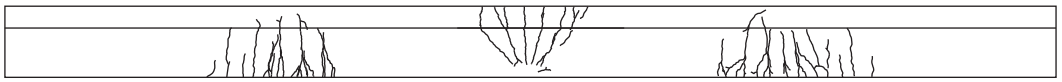

Figure 22: Cracks in test beam CCB-2.

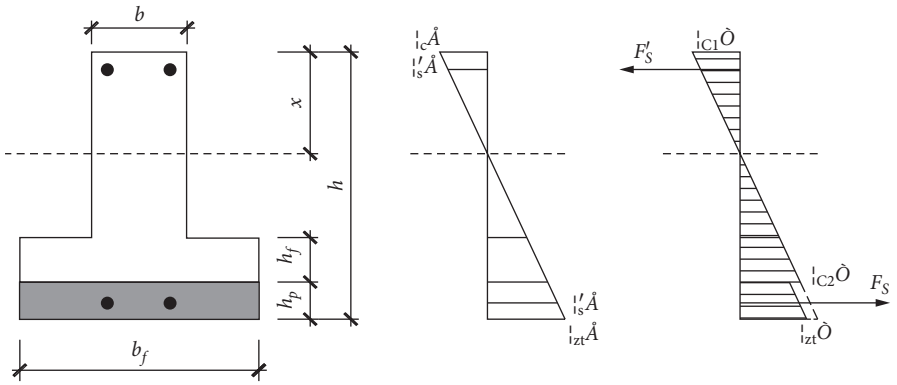

Figure 23: Stress and strain distributions of the single-span composite T-shaped beam.

relationship data were selected to define the curve simulated by the MISO model. Reinforcement is generally an elongated member. If the transverse shear force is disregarded, a complex stress situation will not exist. Accordingly, in this study, the constitutive relation for steel could be simulated with a bilinear isotropic hardening model (BISO). The models of the test beams are shown in Figure 24.

The thermal expansion coefficient of concrete was set to $\gamma_c = 1.0 \times 10^{-5}$ (°C), and the initial temperature was 25°C. The precompressive stress of SFRSSC was simulated by changing the temperature of concrete. The loads applied in the experiment were uniformly distributed surface loads. The force convergence criterion was used, and the convergence error was 5%.

6.2. Single-Span Composite T-Shaped Beam Simulation. The load-displacement curves of the test beams were presented in Figure 25. The simulated failure processes of the three test beams were similar to those in the experimental test described in Section 4.1. The curves presented three phases: elastic phase before cracking, elastic phase after cracking, and the yield phase. The simulated deflection values were less than the experimental values because the bond slip between steel and concrete was not considered in the simulation analysis. However, it had no influence on the characteristic load values. The stress history of the middle node on the bottom surface of the test beams is shown in Figure 26. The curves indicate that stress at this point increased with an increase in the test load. When the test load reached the cracking load, the stress decreased rapidly to zero, and the concrete at this point cracked. The test load at this moment was the cracking load, which corresponds with the load where the slope initially changed in the load-displacement curves. The simulation results for cracking loads are shown in Table 9. The theoretical cracking loads are in good agreement with the experimental results and simulation results.

6.3. Different Precompressive Stresses. In the experimental test, the effects of the different precompressive stresses of SFRSSC were not considered; thus, the flexural performance of the test beams for different precompressive stress was simulated and analyzed. Given that the precompressive stress of SFRSSC is simulated by changing the temperature of concrete in this part, the considered variable temperatures were 25°C, 27°C, 29°C, 31°C, 33°C, 35°C, 37°C, and 39°C. The time history plot is shown in Figure 27, and the stress nephogram is shown in Figure 28. The load-displacement curves obtained are presented in Figure 29. The cracking load of each beam can be determined from Figure 29, and the influence of the variation in precompressive stress on the cracking load is shown in Figure 30.

Figure 30 shows that the cracking load of the test beams could infinitely increase with increases in the precompressive stress of SFRSSC. When the precompressive stress values ranged within 1.5–2.5 MPa, the cracking load of the composite beams was the highest; thereafter, the cracking load exhibited a decreasing trend. This result is due to the cracking load of SFRSSC being limited by the steel and the top surface of the basic beam. With the generation of the precompressive stress in SFRSSC, a certain tensile stress appears in the concrete around the top surface of the basic

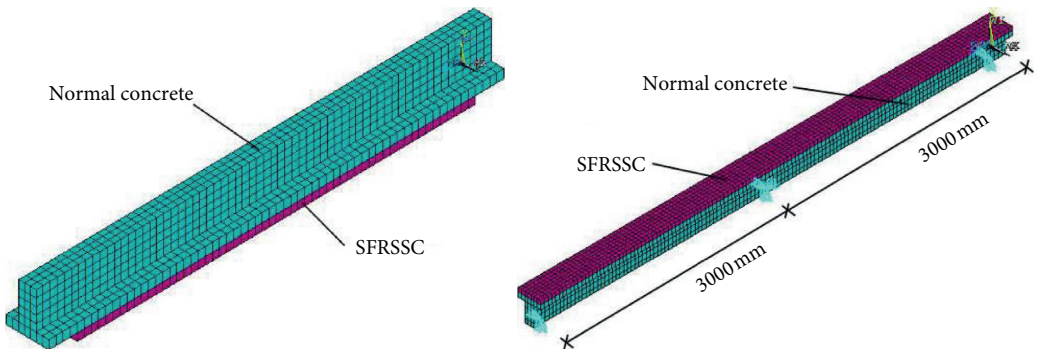

Figure 24: Models of test beams.

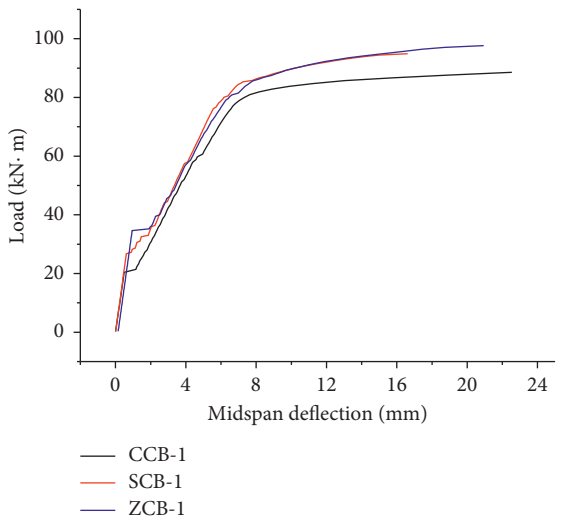

Figure 25: Load-displacement curves.

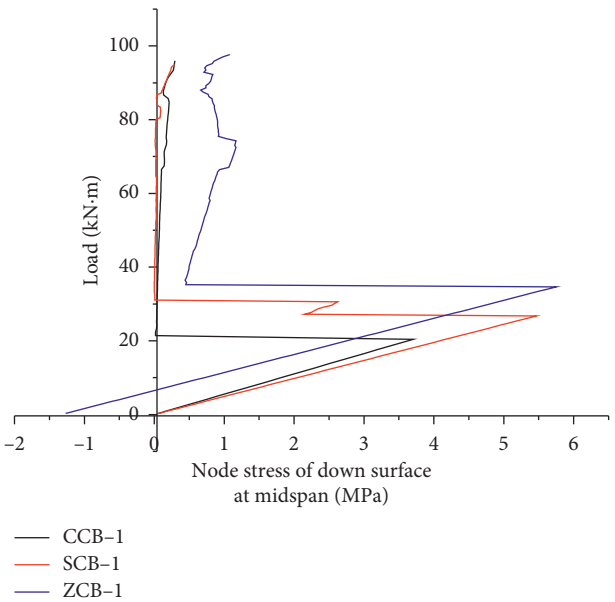

Figure 26: Stress history of the middle node on the bottom surface of the test beams.

Table 9: Cracking loads of the single-span composite T-shaped beams (kN·m).

Cracking load	CCB	SCB	ZCB
Experimental results	23.77	27.77	35.77
Theoretical results	16.85	27.32	35.95
Simulation results	20.43	26.76	34.65

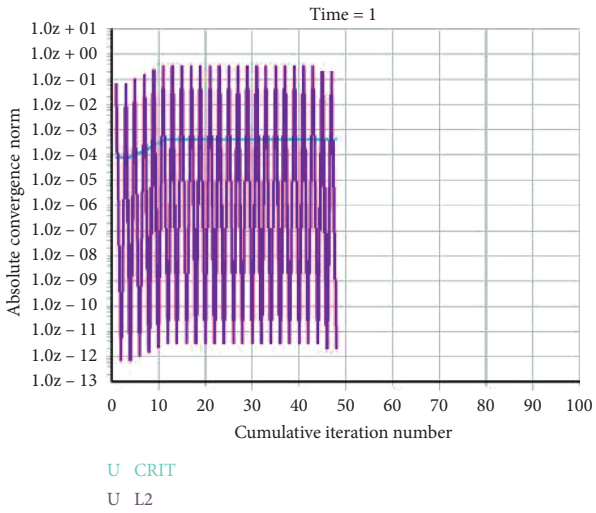

Figure 27: Time history plot.

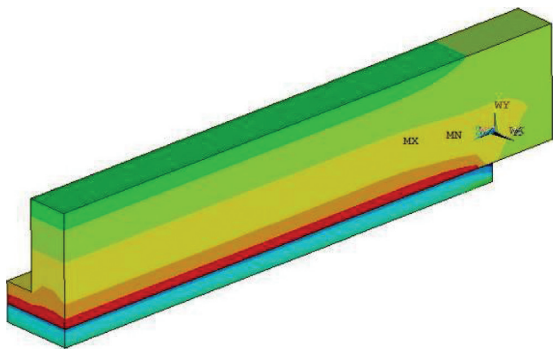

Figure 28: Stress nephogram.

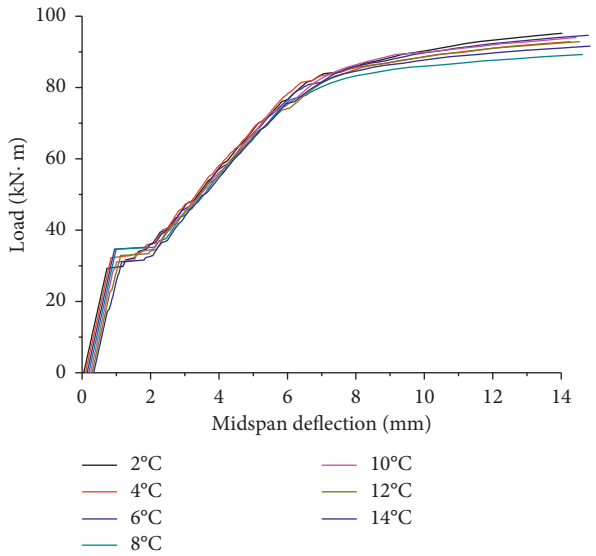

Figure 29: Load-displacement curves.

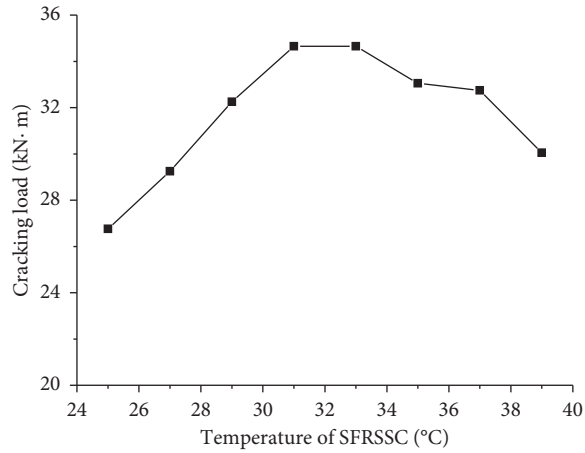

Figure 30: Relationship between cracking load and temperature.

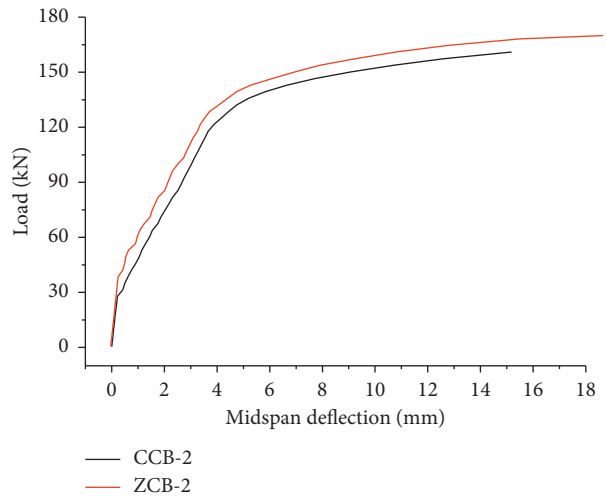

Figure 31: Load-displacement curves by simulation.

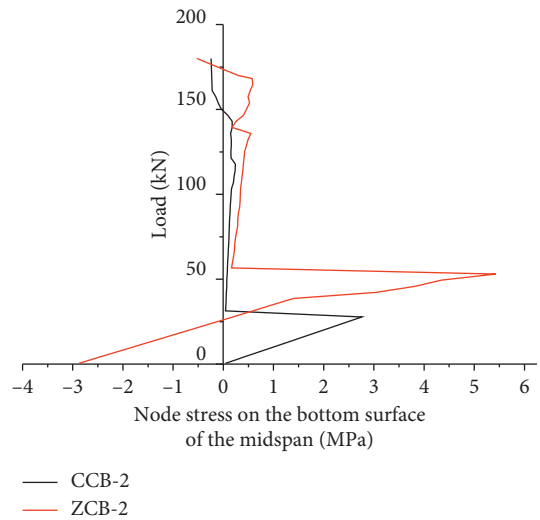

Figure 32: Stress history of the middle node on the top surface of the middle support.

Table 10: Cracking loads of the two-span continuous composite T-shaped beams.

Cracking load	Experimental results (kN·m)	Simulation results (kN·m)
CCB-2	13.05	15.64
ZCB-2	28.84	29.81

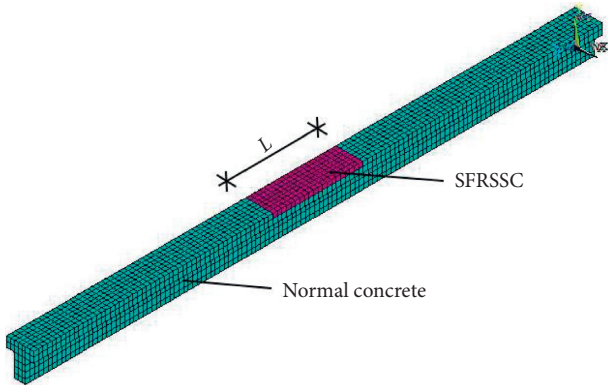

Figure 33: Model of condition II.

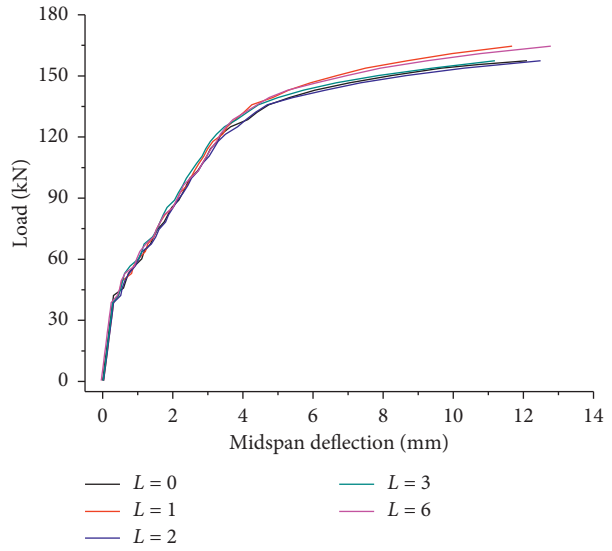

Figure 34: Load-displacement curves for different lengths of the SFRSSC laminated layer.

beam and increases as the precompressive stress increases. In the experiment, when the precompressive stress reached 2.5 MPa, the concrete around the top surface of the basic beam cracked earlier than the laminated layer, causing the reduction in the cracking load.

6.4. Two-Span Continuous Composite T-Shaped Beam Simulation. The properties of materials adopted in the simulation for the two-span continuous composite T-shaped beams are the same as those described in Table 8. The test beams' load-displacement curves obtained by simulation are displayed in Figure 31. Figure 32 shows the load-stress curves of the node on the top surface of the middle support. A certain precompressive stress evidently existed in the laminated layer of ZCB-2 before loading. The precompressive stress significantly enhanced the crack resistance of ZCB-2. The cracking loads are summarized in Table 10. Clearly, the theoretical results and the experimental results are in good agreement with the simulation results.

6.5. Influence of the Length of SFRSSC Laminated Layer on Flexural Behavior. For the two-span continuous composite T-shaped beams, the negative moment only existed at the middle support. Thus, in this study, a simulation analysis for condition II, that is, the SFRSSC was placed only in the middle support area, as shown Figure 33, was conducted. In the simulation, SFRSSC was placed around the middle support, with the support as the center. Normal concrete was

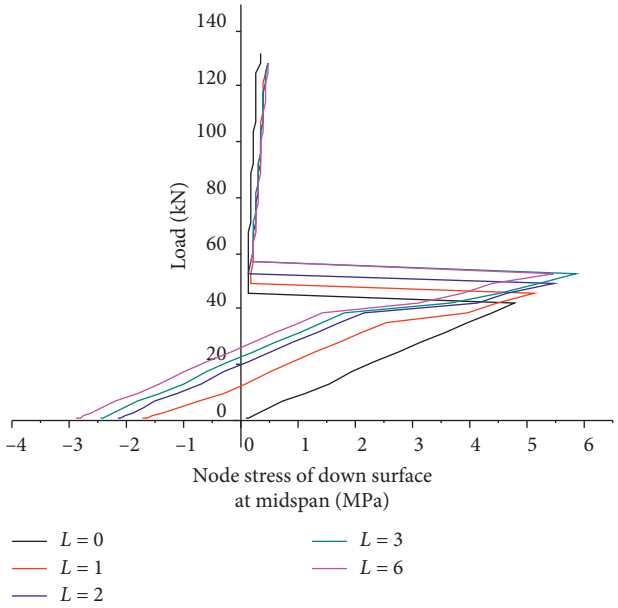

Figure 35: Stress history of the middle node on the top surface of the middle support.

Table 11: Cracking loads and precompressive stresses.

L (m)	0	1	2	3	6
M_{cr} (kN·m)	23.74	25.76	27.79	28.87	29.81
σ_{z0} (MPa)	0	−1.84	−2.22	−2.53	−2.92

poured into the remainder of the laminated layer. The lengths of SFRSSC were 1, 2, 3, and 6 m.

The test beams' load-displacement curves obtained by simulation are displayed in Figure 34. Figure 35 shows the load-stress curves of the node on the top surface of the middle support. The cracking loads (M_{cr}) and precompressive stresses (σ_{z0}) on the top surface of the beams were recorded and are summarized in Table 11. Figure 34 shows that the length of the SFRSSC laminated layer had minimal influences on the yield strengths and ultimate strengths of the test beams. Table 11 shows that the precompressive stress and cracking load decreased with a decrease in the length of the SFRSSC laminated layer. However, the cracking loads of the test beams were similar when the length of the SFRSSC laminated layer was 6, 3, or 2 m. Considering the material consumption and cracking resistance, the reasonable length of the SFRSSC laminated layer, as indicated by L in Figure 33, is 1/3 to 1/2 of the beam span.

7. Conclusions

(1) SFRSSC significantly improves the cracking load of two-span continuous composite T-shaped beams. Although the height of the laminated layer is only 14% of the height of the test beam, it allowed for the 2.2-fold increase in the cracking load in the negative moment area.

(2) A calculation method for the cracking load of the concrete composite beams with a SFRSSC laminated layer is established. The calculation or theoretical results are in good agreement with the experimental results.

(3) For the single-span composite T-shaped beams, the cracking load is desirable when the precompressive stress of SFRSSC ranges within 1.5–2.5 MPa.

(4) For the two-span continuous T-shaped composite beams, the reasonable length of the SFRSSC laminated layer is 1/3–1/2 of the beam span.

(5) The SFRSSC laminated layer has minimal influences on yielding load and ultimate load.

Data Availability

The data used to support the findings of this study are included within the article.

Conflicts of Interest

The author declares that there are no conflicts of interest regarding the publication of this paper.

Acknowledgments

This research work was financially supported by National Natural Science Foundation of China (Grants nos. 41430642, 41627801, and 51108207) and China Postdoctoral Science Foundation (Grant no. 2015M581403).

References

[1] L. Fan, *Bridge Engineering*, China Communications Press, Beijing, China, 2011.

[2] M. Jing, "Research on crack deterioration of long-span bridges deck pavement," Master's Thesis, Southeast University, Nanjing, China, 2005.

[3] J. Wang, "Method and research on deterioration of steel deck gussasphalt concrete pavement," Master's Thesis, Southeast University, Nanjing, China, 2005.

[4] L. Zhang, "Research on deterioration of jiang yin bridge deck pavement," Master's Thesis, Southeast University, Nanjing, China, 2004.

[5] J. Wang, "Causes analysis of early distresses and design method of asphalt concrete pavement for concrete bridge deck," Master's Thesis, Dalian University of Technology, Dalian, China, 2003.

[6] K. Habel, J.-P. Charron, E. Denarié, and E. Brühwiler, "Autogenous deformations and viscoelasticity of UHPFRC in structures part I: experimental results," *Magazine of Concrete Research*, vol. 58, no. 3, pp. 135–145, 2006.

[7] K. Habel, E. Denarié, and E. Brühwiler, "Time dependent behavior of elements combining ultra-high performance fiber reinforced concretes (UHPFRC) and reinforced concrete," *Materials and Structures*, vol. 39, no. 5, pp. 557–569, 2006.

[8] K. A. Harries and J. Moses, "Effect on superstructure stress of replacing a composite RC bridge deck with a GFRP deck," *Journal of Bridge Engineering*, vol. 12, no. 3, pp. 394–398, 2007.

[9] K. Coogler, K. A. Harries, B. Wan, D. C. Rizos, and M. F. Petrou, "Critical evaluation of strain measurements in glass fiber-reinforced polymer bridge decks," *Journal of Bridge Engineering*, vol. 10, no. 6, pp. 704–712, 2005.

[10] K. Habel, M. Viviani, E. Denarié, and E. Brühwiler, "Development of the mechanical properties of an ultra-high performance fiber reinforced concrete (UHPFRC)," *Cement and Concrete Research*, vol. 36, no. 7, pp. 1362–1370, 2006.

[11] B. Francesco, C. Antonio, and O. Luciano, "Numerical and analytical modeling of concrete beams with steel, FRP and hybrid FRP-steel reinforcements," *Composite Structures*, vol. 140, pp. 53–65, 2016.

[12] G. Kaur, S. P. Singh, and S. K Kaushik, "Mean and design fatigue lives of SFRC containing cement-based materials," *Magazine of Concrete Research*, vol. 68, no. 7, pp. 325–338, 2016.

[13] D.-Y. Yoo, N. Banthia, and Y.-S. Yoon, "Flexural behavior of ultra-high-performance fiber-reinforced concrete beams reinforced with GFRP and steel rebars," *Engineering Structures*, vol. 111, pp. 246–262, 2016.

[14] N. P. B. Tan, L. H. Keung, W. H. Choi et al., "Silica-based self-healing microcapsules for self-repair in concrete," *Journal of Applied Polymer Science*, vol. 133, no. 12, 2016.

[15] H. Gurdián, E. García-Alcocel, F. Baeza-Brotons, P. Garcés, and E. Zornoza, "Corrosion behavior of steel reinforcement in concrete with recycled aggregates, fly ash and spent cracking catalyst," *Materials*, vol. 7, no. 4, pp. 3176–3197, 2014.

[16] R. Siddique, K. Kapoor, E.-H. Kadri, and R. Bennacer, "Effect of polyester fibres on the compressive strength and abrasion resistance of HVFA concrete," *Construction and Building Materials*, vol. 29, pp. 270–278, 2012.

[17] K. Habel and P. Gauvreau, "Response of ultra-high performance fiber reinforced concrete (UHPFRC) to impact and static loading," *Cement and Concrete Composites*, vol. 30, no. 10, pp. 938–946, 2008.

[18] P. Zhang, Y. Zheng, K. Wang, and K. Zhang, "Combined influence of nano-CaCO3 and polyvinyl alcohol fibers on fresh and mechanical performance of concrete incorporating fly ash," *Structural Concrete*, vol. 21, no. 2, 2019.

[19] P. Zhang, Y. Ling, J. Wang, and Y. Shi, "Bending resistance of PVA fiber reinforced cementitious composites containing nano-SiO_2," *Nanotechnology Reviews*, vol. 8, no. 1, pp. 690–698, 2019.

[20] P. Zhang, L. Kang, J. Wang et al., "Mechanical properties and explosive spalling behavior of steel-fiber-reinforced concrete exposed to high temperature—a review," *Applied Sciences*, vol. 10, no. 7, p. 2324, 2020.

[21] J. Shan, *Study and application in high performance concrete for bridge deck overlays*, Ph.D. Thesis, Wuhan University of Technology, Wuhan, China, 2006.

[22] C. K. Y. Leung, Y. N. Cheung, and J. Zhang, "Fatigue enhancement of concrete beam with ECC layer," *Cement and Concrete Research*, vol. 37, no. 5, pp. 743–750, 2007.

[23] J. Zhang, C. K. Y. Leung, and Y. N. Cheung, "Flexural performance of layered ECC-concrete composite beam," *Composites Science and Technology*, vol. 66, no. 11, pp. 1501–1512, 2006.

[24] L. Luo, *Construction technology of SFRPC bridge deck pavement*, Ph.D. Thesis, South China University of Technology, Guangzhou, China, 2002.

[25] B. Wan, D. C. Rizos, M. F. Petrou, and K. A. Harries, "Computer simulations and parametric studies of GFRP bridge deck systems," *Composite Structures*, vol. 69, no. 1, pp. 103–115, 2005.

[26] W. C. Tang, R. V. Balendran, A. Nadeem, and H. Y. Leung, "Flexural strengthening of reinforced lightweight polystyrene aggregate concrete beams with near-surface mounted GFRP bars," *Building and Environment*, vol. 41, no. 10, pp. 1381–1393, 2006.

[27] Z. Guo, *Concrete Strength and Constitutive Relation-Principles and Applications*, China Industry Press, Beijing, China, 2004.

[28] R. V. Balendran, F. P. Zhou, A. Nadeem, and A. Y. T. Leung, "Influence of steel fibres on strength and ductility of normal and lightweight high strength concrete," *Building and Environment*, vol. 37, no. 12, pp. 1361–1367, 2002.

[29] L. Carin, W. Roberts, and W. S. Guirola, "Strength and performance of fiber-reinforced concrete composite slabs," *Journal of Structural Engineering*, vol. 130, no. 3, pp. 520–528, 2004.

[30] C. Huang, *Fiber Reinforced Concrete Structures*, Beijing Machinery Industry Press, Beijing, China, 2004.